INTERNATIONAL CONFERENCE GIS-IDEAS 2023

PROCEEDINGS

Geospatial Integrated Technologies for Natural Hazards and Environmental Problems

HUNRE, Ha Noi, Viet Nam

07-09 November 2023

PUBLISHING HOUSE FOR SCIENCE AND TECHNOLOGY

INTERNATIONAL CONFERENCE

GEOSPATIAL INTEGRATED TECHNOLOGIES FOR NATURAL HAZARDS AND ENVIRONMENTAL PROBLEMS

PUBLISHING HOUSE FOR SCIENCE AND TECHNOLOGY
HA NOI - 2023

Organized by

Hanoi University of Natural Resources and Environment (HUNRE)
Osaka Metropolitan University (OMU)
The Japan - Viet Nam Geoinformatics Consortium (JVGC)

Co-organizers

Hanoi University of Mining and Geology (Vietnam)
Japan Geotechnical Consultant Association
Japan Society of Geoinformatics

With the support and collaboration of

Department of National Remote Sensing (Vietnam)
Department of Survey, Mapping and Geographic Information (Vietnam)
Ho Chi Minh University of Natural Resources and Environment (Vietnam)
National Centre for Hydro-Meteorological Forecasting (Vietnam)
Vietnam Institute of Geosciences and Mineral Resources
Institute of Resources Geography, Ho Chi Minh (Vietnam)
Vietnam Disaster and Dyke Management Authority
Ho Chi Minh City Space Technology Application Center (Vietnam)
Institute of Marine Geology and Geophysics (Vietnam)
Nong Lam University, Ho Chi Minh (Vietnam)
NextTech Group of Technopreneurs (Vietnam)
Vietnam National University, Hanoi
Vietnam Academy for Water Resources
Vietnam National Forestry University
Association of Vietnam Geographers
Military Technology Academy (Vietnam)
Asian Institute of Technology (Thailand)
Naresuan University (Thailand)
Thuy Loi University (Vietnam)
University of Phayao (Thailand)
Everest Schools (Vietnam)

CONFERENCE FOUNDERS

Late Prof. Takashi FUJITA (Japan)

Dr. Nghiem Vu KHAI (Vietnam)

SYMPOSIUM CHAIRS

Prof. Dr. Huynh Thi Lan HUONG (Vietnam)

Prof. Venkatesh RAGHAVAN (Japan)

ORGANIZING SECRETARIES

Assoc. Prof. Dr. Le Thi TRINH (Vietnam)

Dr. Go Yonezawa (Japan)

CONFERENCE COORDINATORS

Ms. Tanyaluck CHANSOMBAT (Thailand)

Dr. Tatsuya NEMOTO (Japan)

Ms. Vu Thi Thuy NGAN (Vietnam)

Dr. Truong Xuan QUANG Vietnam)

STEERING COMMITTEE

Dr. Ho Dinh DUAN (Vietnam)

Dr. Duong Van HAI (Vietnam)

Prof. Dr. Tran Thanh HAI (Vietnam)

Assoc. Prof. Hoang Anh HUY (Vietnam)

Dr. Mai Van KHIEM (Vietnam)

Prof. Yasuyuki KONO (Japan)

Prof. Nguyen Kim LOI (Vietnam)

Prof. Truong Xuan LUAN (Vietnam)

Prof. Shinji MASUMOTO (Japan)

Prof. Alaa A MASOUD (Egypt)

Prof. Muneki MITAMURA (Japan)

Dr. Doan Thi Tuyet NGA (Vietnam)

Dr. Lam Dao NGUYEN (Vietnam)

Assoc. Prof. Huynh QUYEN (Vietnam)

Dr. Trinh Hai SON (Vietnam)

Assoc. Prof. Nguyen Canh THAI (Vietnam)

Prof. Nitin TRIPATHI (Thailand)

Dr. Chu Hai TUNG (Vietnam)

Prof. Yasushi YAMAGUCHI (Japan)

WORKSHOP COMMITTEE

DAO Hoang Tung (Vietnam)

Natraj VADDADI (India)

SCIENTIFIC COMMITTEE

Dr. Tran Thi AN (Vietnam)
Dr. Tran Van ANH (Vietnam)
Dr. Vansarochana CHAIWIWAT (Thailand)
Dr. Sittichai CHOOSUMRONG (Thailand)
Dr. Nguyen Dai DONG (Vietnam)
Dr. Nguyen Duc HA (Vietnam)
Prof. Dr. Pham Hoang HAI (Vietnam)
Assoc. Prof. Dr. Nguyen Hai HOA (Vietnam)
Dr. Pham Thi HOA (Vietnam)
Assoc. Prof. Dr. Nguyen Thanh HUNG (Vietnam)
Assoc. Prof. Dr. Trinh Le HUNG (Vietnam)
Dr. Atsushi KAJIYAMA (Japan)
Prof. Dr. Vo Chi MY (Vietnam)
Dr. Tatsuya NEMOTO (Japan)
Dr. Sarawut NINSAWAT (Thailand)
Dr. Susumu NONOGAKI (Japan)
Assoc. Prof. Dr. Pham Quy NHAN (Vietnam)
Dr. Nguyen Quoc PHI (Vietnam)
Dr. Vinayaraj POLIYAPRAM (Japan)
Assoc. Prof. Dr. Nguyen An THINH (Vietnam)
Assoc. Prof. Dr. Le Thi TRINH (Vietnam)
Assoc. Prof. Dr. Pham Thi Mai THAO (Vietnam)
Assoc. Prof. Dr. Nguyen Tien THANH (Vietnam)
Assoc. Prof. Dr. Phi Truong THANH (Vietnam)
Dr. Pham Thi Mai THY (Vietnam)
Dr. Pham Hong TINH (Vietnam)
Assoc. Prof. Dr. Nguyen Nhu TRUNG (Vietnam)
Dr. Le Quang TUAN (Vietnam)
Dr. Nghiem Van TUAN (Vietnam)
Assoc. Prof.Dr. Ho Thanh VAN (Vietnam)
Assoc. Prof.Dr. Pham Thi Mai THAO (Vietnam)

TABLE OF CONTENT

DETERMINATION OF THE OPTIMAL DENSITY CONTRAST IN THE SEAFLOOR DEPTH INVERSION FROM GRAVITY ANOMALIES USING THE GRAVITY-GEOLOGIC METHOD ON THE CENTRAL EAST SEA

Nguyen Dinh Hai[1], Nguyen Van Sang[2]*, Tran Tuan Dung[3,4]

[1]Vietnam's People Naval Hydrographic and Oceanographic Department, Hai Phong, Vietnam
[2]Hanoi University of Mining and Geology, Hanoi, Vietnam
[3]Institute of Marine Geology and Geophysics, VAST, Vietnam
[4]Graduate University of Science and Technology, Vietnam Academy of Science and Technology
*Corresponding author. Email: nguyenvansang@humg.edu.vn

ABSTRACT

In the seafloor depth inversion from gravity anomalies using the Gravity-Geologic Method, the density contrast between the seawater and the ocean bottom topographic mass needs to be determined. In this study, the iteration method was applied to determine the optimal density contrast. Firstly, a density contrast is given. Then, the seafloor depths are calculated and compared with the shipborne depths. In the next step, change the density contrast and repeat the calculation. Finally, the optimal density contrast is determined corresponding to the smallest deviation between the gravity anomaly-derived depths and the shipborne depths. The experiment calculations were carried out on the central East Sea with eight density contrast values, which varied from 1.10 g/cm^3 to 3.0 g/cm^3. The results show that the optimal density contrast in the study area is 1.40 g/cm^3.

1. INTRODUCTION

The world's oceans cover 71 % of the Earth's surface. Despite many attempts to measure, to date, only about 18 % of the ocean's area has been measured using echosounders (Wölfl, 2019). Measuring the entire ocean by direct depth measurement method is very difficult and expensive in terms of money and time.

Vietnam is a country with a coastline of up to 3260 km, a territorial sea area of over 64000 km^2 and an exclusive economic zone of nearly 1 million km^2. Seas and islands play an important role in the economic development of the country, security and defense work and international exchanges (Dang, 2008). Up to now, Vietnam has only established charts of 1:200,000 scale with about 53 % of the area of Vietnam's seas; completed seabed topographic surveys of about 24.5 % of Vietnam's sea area at the scales from 1:500,000 to 1:50,000 (Ministry of Natural Resources and Environment, 2019). Thus, there is still a large area of the East Sea that has not been measured and mapped. Measuring depth over the entire East Sea by direct measurement method is very difficult and expensive, especially not possible for the sea areas that are not directly accessible. In that context, indirect methods of depth determination need to be studied and applied. The Gravity Geologic Method (GGM) is one such indirect method.

In the GGM, it is very important to determine the optimal density contrast (DC) between the seafloor matter and seawater. Different seas have different density contrast. Globally, there

are some studies to determine the optimal density contrast: In the study (Yeon et al., 2018), the determined optimal contrast density over Korean waters is 5.0 g/cm^3. In the reference (Yu et al., 2011), the Downward Continuation Method (DWC) was used to determine density contrast in two study areas in southern Greenland. The results of this study show that the optimal density contrast in the first experimental area is 1.47 g/cm^3 and in the second area is 1.30 g/cm^3.

In this study, the iterative method will be studied and applied to determine the optimal density contrast for the area in the center of the East Sea.

2. STUDY AREA AND DATA

2.1 Study area

The study area is located in the center of the East Sea, between latitudes 8ºN and 14ºN and longitudes 110ºE and 115ºE (Figure 1), covering an area of about 363,000 km^2. This is an area located on the margin of the sea with diverse and complex architecture that has undergone a special geological development process, attracting the attention of many geophysicists and geologists in the world and abroad. The seafloor topography of the study area is diverse and complex. The Southeast of the study area is the sea of the Spratly Islands, with many submerged and floating islands. The Northeast of the study area is a deep depression of the East Sea, with the greatest depth is nearly 5,000 m. The Western side of the study area is the continental slope, with a depth of about 1,000 m to 2,000 m, a steep slope (Bui et al., 2005).

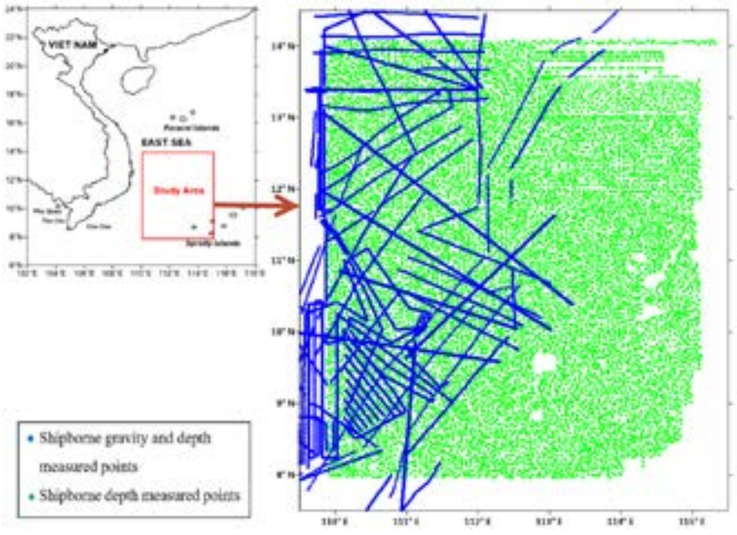

Figure 1. Study area and data.

2.2 Data used

2.2.1 Satellite-derived gravity anomaly data

In this study, the DTU17GRAV model is used. This is a model of the global marine gravity field, determined from satellite altimeter data and provided by the Technical University of Denmark (DTU) (Andersen et al., 2020). The gravity anomalies of this model are in the form of a square grid with a mesh size is 1 inch x 1 inch. The coordinates of this model are in the World Geodetic System WGS84. Over the study area, a total of 151,200 gravity anomalous values of this model were used. The maximum gravity value is 135.40 mGal; the smallest is -53.70 mGal; and the average of 9.98 mGal.

2.2.2 Shipborne gravity and depth data

In this study, the 19,226 points, measured simultaneous gravity and depth, were used (blue points in Figure 1). These data were measured in 1987, 1990 and 1992 in cooperation projects between Vietnam and Russia and Vietnam and France in the East Sea, specifically as follows: the geophysical surveying project was implemented in 1987; the survey project of the Gagarinsky ship carried out in 1990-1992; the survey project of the Atalante ship carried out in 1993. These data have high reliability, the parameters are very clear and the gravimetric accuracy is ± 1mGal (Bui et al., 2008). The coordinates of the measured points are in the World Geodetic System WGS-84. These data cover more than 0.5º study area.

2.2.3 Shipborne depth data

The shipborne depth data consists of 9,403 points (green points in Figure 1), measured by the Vietnamese Navy using a single-beam echosounder in 2009 and a multi-beam echosounder from 2010 to 2016. The measurement and process were carried out according to the standards of the International Hydrographic Organization (IHO). The coordinates of the measured points are in the WGS-84 (Khuong, 2018). The depths have been converted to the mean sea level of Vietnam based on the data of the tidal stations. It is important to note that the 9,403 points have the depth value only. Therefore, the gravity anomaly value for these points was further determined using the DTU17GRAV model.

The summary of the data used in this study is presented in (Table 1).

Table 1. Summary of the data used in this research.

No.	Data	Coverage (φ: latitude, λ: longitude	Number of points
1	DTU17GRAV model	$7.5^o \le \varphi \le 14.5^o$; $109.5^o \le \lambda \le 115.5^o$	151,200
2	Shipborne gravity and depth measured points	$7.5^o \le \varphi \le 14.5^o$; $109.5^o \le \lambda \le 115.5^o$	19,226
3	Shipborne depth measured points	$7.5^o \le \varphi \le 14.5^o$; $109.5^o \le \lambda \le 115.5^o$	9,403

2.2.4 Data preparation

A total of 28,629 shipborne points were used, including 19,226 points measured in the period of 1987, 1990-1993 and 9,403 points measured in the period of 2009-2016. After processing, these points have both depth and gravity anomaly values. For analysis, these 28,629 shipborne points were further randomly divided into two parts (Figure 2): Part 1 consisted of 14,404 points (black points in Figure 2) and was used to compute the seafloor depths. While Part 2 contained 14,225 points (red points on Figure 2) and was employed for estimating the accuracy of the depths.

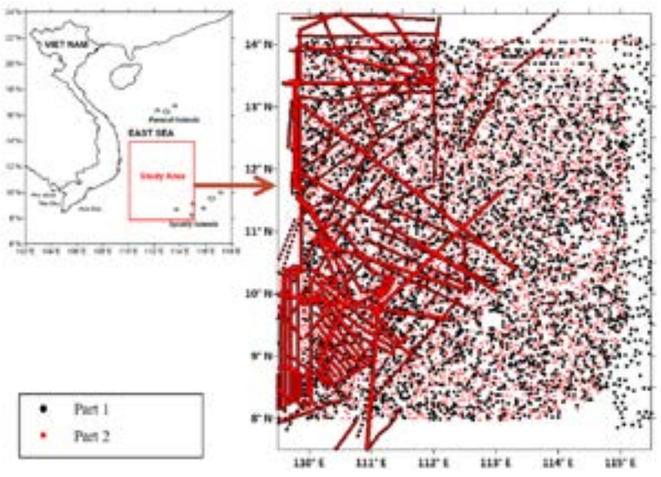

Figure 2. Shipborne data preparation.

3. THE METHOD OF DETERMINING THE OPTIMAL DENSITY CONTRAST IN THE SEAFLOOR DEPTH INVERSION FROM GRAVITY ANOMALIES

3.1 Principle of the seafloor depths inversion from gravity anomalies

To determine the depth of the gravity anomalies, according to studies (Yeon et al., 2018), (Yu et al., 2011), (Xueshuang et al., 2017), the gravity anomaly (Δg) is divided into 2 parts: the long-wavelength gravity anomaly (Δg^{long}) associated with deep and wide seafloor matter; and the short-wavelength gravity anomaly (Δg^{short}) related to the convexity of the seafloor topography.

For the points where the gravity anomalies and depths were known simultaneously, the short wavelength gravity anomaly is calculated using the equation:

$$\Delta g^{short} = 2\pi G\delta(D^{ship} - D_{max}) \quad (1)$$

where: G is the gravitational constant ($6{,}672 \times 10^{-8}$cm^3/gs^2); δ is the density contrast between the seawater and the ocean bottom topographic mass; D^{ship} is the shipborne seafloor depth; D_{max} is the maximum depth of the seafloor in the study area.

Then, the long-wavelength gravity anomaly is calculated by the equation:

$$\Delta g^{long} = \Delta g^{ship} - \Delta g^{short} \quad (2)$$

For the points where only gravity anomalies are known, depths should be determined (points of the DTU17GRAV model have been fitted with shipborne gravity anomaly, Δg^{fit}) and long-wavelength gravity anomalies are interpolated from the available points (Δg^{long}_{int}). Then, the short wavelength gravity anomalies of these points are calculated:

$$\Delta g^{short} = \Delta g^{fit} - \Delta g^{long}_{int} \quad (3)$$

The gravity anomaly-derived depth (D^{grav}) can be calculated using the equation:

$$D^{grav} = \frac{\Delta g^{short}}{2\pi G\delta} + D_{max} \quad (4)$$

3.2 Determination of the optimal density contrast between the seawater and the ocean bottom topographic mass by iterative method

To determine the optimal density contrast, the seafloor depth inversion from gravity anomalies is performed iteratively several times. At each time, a different density contrast is used: (1) First, a theoretically consistent density contrast value is given; (2) Next, the gravity anomaly-derived seafloor depths are calculated and compared with the shipborne seafloor depths to estimate the accuracy of these depths. Then, the density contrast value is changed and the calculation process is repeated. Finally, the optimal density contrast is determined corresponding to the smallest deviation between the gravity anomaly-derived depth and the shipborne depth. In other words, the accuracy of gravity depth is the best. The comparison between the gravity anomaly-derived depth with the shipborne depth is made as follows (Nguyen, 2023):

Depth deviations are calculated according to the equation:

$$\delta D_i = D_i^{grav} - D_i^{ship},\ i = 1, 2, \ldots, n; \quad (5)$$

where: n is the number of shipborne depth points; D_i^{ship} is the shipborne depth; D_i^{grav} is the gravity anomaly-derived depth.

The average depth deviation is calculated according to the equation:

$$\delta D_{ave} = \frac{1}{n}\sum_{i=1}^{n}\delta D_i \quad (6)$$

Standard deviation of the depth:

$$STD = \sqrt{\frac{1}{n-1}\sum_{i=1}^{n}(\delta D_i - \delta D_{ave})^2} \quad (7)$$

Root mean square of the deviation:

$$RMSD = \sqrt{\frac{1}{n}\sum_{i=1}^{n}\delta D_i^2} \quad (8)$$

The Pearson correlation coefficient between the gravity anomaly-derived depths and the shipborne depths (McKean et al., 2003):

$$R = \frac{\sum_{i=1}^{n}\left(D_i^{ship} - D_{ave}^{ship}\right).\left(D_i^{grav} - D_{ave}^{grav}\right)}{\sqrt{\sum_{i=1}^{n}(D_i^{ship} - D_{ave}^{ship})^2 . \sum_{i=1}^{n}(D_i^{grav} - D_{ave}^{grav})^2}} \quad (9)$$

Based on the root mean square of the deviation (RMSD), the standard deviation (STD), the Pearson correlation coefficient (R), the average depth deviation (δD_{ave}), the maximum deviation and the minimum deviation between the gravity anomaly-derived depths and shipborne depths and the optimal density contrast is selected in the study area.

4. RESEARCH RESULTS

According to the theory presented above, the experiments were performed with different density contrast options. Since the theoretical density contrast is 1.67 g/cm^3, the density contrast was investigated from 1.10 g/cm^3. The density contrast value in the next calculation time is determined based on the results of the previous calculation time, with the target being to minimize the *RMSD* value and maximize the *R* values. To find the optimal density contrast, the eight experimental options were calculated. The experimental results are summarized and presented in (Table 2).

Table 2. Summary results of the experimental options.

Expe. Options	Option 1	Option 2	Option 3	Option 4	Option 5	Option 6	Option 7	Option 8
DC (g/cm^3)	1.10	1.20	1.30	1.40	1.50	1.67	2.0	3.0
(m)	849.3	887.2	918.8	944.3	964.9	1,012.9	1,075.1	1,148.5
(m)	-913.7	-931.7	-948.5	-964.0	-972.9	-991.9	-1,023.7	-1,137.0
(m)	-1.5	-1.4	-1.3	-1.2	-1.1	-1.1	-1.0	-0.9
RMSD (m)	±87.9	±86.4	±85.7	±85.5	±85.9	±86.5	±87.7	±90.8
STD (m)	±87.9	±86.4	±85.7	±85.5	±85.9	±86.5	±87.7	±90.7
R	0.99679	0.99691	0.99697	0.99699	0.99697	0.99693	0.99685	0.99663

The chart of RMSD according to the experimental options is shown in (Figure 3).

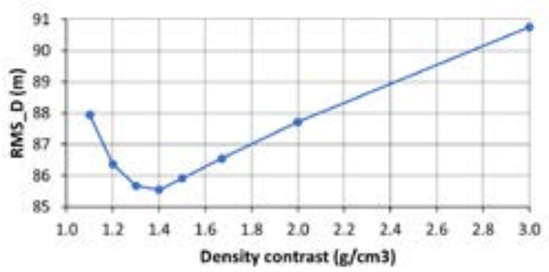

Figure 3. RMSD chart of the experimental options.

The chart of the Pearson correlation coefficient (R) according to the experimental options is presented in (Figure 4).

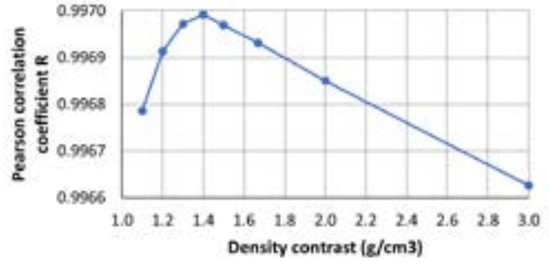

Figure 4. R chart of the experimental options.

The results of (Table 2), (Figure 3) and (Figure 4) show that as the contrast density (DC) increases from 1.10 g/cm^3 to 1.40 g/cm^3, the RMSD decreases from ±87.9 m to ±85.5 m, the Pearson correlation coefficient increases from 0.99679 to 0.99699. As the contrast density continued to increase from 1.40 g/cm^3 to 3.0 g/cm^3, the *RMSD* increased from ±85.5 m to ±90.8 m and the Pearson correlation coefficient decreased from 0.99699 to 0.99663. These results prove that the optimal density contrast in the study area is 1.40 g/cm^3.

5. CONCLUSION

The iterative method has been studied and applied to determine the optimal density contrast in the seafloor depth inversion from the gravity anomalies on the central East Sea. First, the density contrast is assigned a theoretically appropriate value. Then, the seafloor depths were calculated from the gravity anomalies corresponding to the given density contrast. Gravity anomaly-derived depths are compared with shipborne depths to evaluate their accuracy. Next, based on the accuracy evaluation results of the previous step to, change the density contrast value and repeat the calculation process. Finally, the optimal density contrast is selected based on the results of the accuracy evaluation of the experimental options.

From the experimental results of the eight options, the optimal density contrast on the central East Sea was selected as 1.40 g/cm^3. Corresponding to this optimal density contrast shows that the root mean square deviation is the smallest, RMSD = ±85.5 m and the Pearson correlation coefficient between gravity anomaly-derived depths and shipborne depths is the largest, R = 0.99699.

6. ACKNOWLEDGMENTS

The authors wish to thank the Vietnam National Project ĐTĐLCN.07/23, Project B2021-MDA-06 and the Scientific Contract 07/2021/Đ6-DATS (belong to the Project of General investigation of meteorology, oceanographic, geological and environmental factors in the Spratly area at scale 1:200.000) for funding this research.

7. REFERENCES

Andersen O. B., and Knudsen P., 2020. The DTU17 Global Marine Gravity Field: First Validation Results. In S. P. Mertikas, & R. Pail (Eds.), Fiducial Reference Measurements for Altimetry (pp. 83-87). *Springer. International Association of Geodesy Symposia.* Vol.150. https://doi.org/10.1007/1345_2019_65.

Bui Cong Que, Tran Tuan Dung, 2005. Building a map of basic features of natural and environmental conditions in Vietnam and adjacent waters. *State-level thesis summary report, code KT-09-02*. Marine Research Program KT-09, Hanoi. Vietnam.

Bui Cong Que, Tran Tuan Dung, Le Tram, 2008. Establishing a unified gravity anomaly map on the waters of Vietnam and adjacent. *Journal of marine science and technology*. No. 2, 29-41.

Dang Nam Chinh, 2008. Research to complete the technical criteria and the technological process of the marine surveying in Vietnam. *Ministry-level Science and Technology Project, code B-2007-02-35*. Ministry of Education and Training. Vietnam.

Khuong Van Long, 2018. Application of marine surveying technology and development orientation of the marine surveying industry after 2020. *Collection of reports of the National Conference on Science and Technology of Surveying and Cartography*. Vietnam Map and Resources Publishing House, ISBN: 978-604-952-272-7.

McKean J. W. and Sheather S. J., 2003. Statistic, Nonparametric. in R. A. Meyers Editor, *Encyclopedia of Phisical Science and Technology (Third Edition)* New York: Academic

Press, 891-914.

Ministry of Natural Resources and Environment, 2019. Summary of "Master project on basic investigation and management of marine natural resources and environment to 2010, vision to 2020". *Electronic newspaper of Natural Resources and Environment*.

Nguyen Van Sang, 2023. Research and propose a method to determine seafloor depth from gravity anomaly data in the East Sea area, code: B2021-MDA-06. *Ministry level project*, Ministry of Education and Training, Hanoi, Vietnam.

Wölfl, A.-C., Snaith, H., Amirebrahimi, S., 2019. Seafloor mapping-the challenge of a truly global ocean bathymetry. Frontiers in Marine Science, 283. https://doi.org/10.3389/fmars.2019.00283.

Xueshuang Xiang, Xiaoyun Wan, Running Zhang, Yang Li, Xiaohong Sui and Wenbin Wang, 2017. Bathymetry inversion with Gravity-Geologic Method: A study of long-wavelength gravity modeling based on adaptive mesh. *Marine Geodesy*. ISSN: 0149-0419 (Print) 1521-060X (Online). Doi: 10.1080/01490419.2017.1335257.

Yeon Yeu, Jurng-Jae Yee, Hong Sik Yun and Kwang Bae Kim, 2018. Evaluation of the Accuracy of Bathymetry on the Nearshore Coastlines of Western Korea from Satellite Altimetry, Multi-Beam and Airborne Bathymetric LiDAR. *Sensors, MDPI*. Doi:10.3390/s18092926.

Yu-Shen Hsiao, Jeong Woo Kim, Kwang Bae Kim, Bang Yong Lee and Cheinway Hwang, 2011. Bathymetry Estimation Using the Gravity-Geologic Method: An Investigation of Density Contrast Predicted by the Downward Continuation Method. *Terr. Atmos. Ocean. Sci.*, Vol. 22, No. 3, 347-358. Doi: 10.3319/TAO.2010.10.13.01.

IMPACT OF URBANIZATION ON SEAWATER QUALITY IN QUANG NINH PROVINCE

Nguyen Tran Dinh[1]*, Le Thanh Son[1], Nguyen Tran Dien [1], Vu Anh Tuan[2], Nguyen Hong Quang[2], Le Cao Khai[3]

[1]Institute of Environmental Technology (IET), Vietnam Academy of Science and Technology
[2]VietNam National Space Center (VNSC), Vietnam Academy of Science and Technology
[3]Department of Chemistry, Hanoi Pedagogical University, Vietnam
*Corresponding author. Email: dt195986@gmail.com

ABSTRACT

In this study, the authors use indicators to assess the level of water pollution, such as chemical and microbial pollution and measure the impact of urban factors, such as population growth, wastewater discharge and water consumption. In the survey results of seawater quality in two seasons, the rainy season and the dry season, there is a difference in some specific hydrological indicators, such as Coliform exceeding the allowable threshold in the dry season and iron and ammonium content tending to increase. In the rainy season, due to disturbance of the water layer, upwelling water and submerged water, the rest of the indicators are within the allowable limits according to Vietnamese standards on seawater quality QCVN 10 MT:2015/BTNMT. From the result analyses, the authors have made an overview of the impact of urbanization on seawater quality in Quang Ninh province. Thereby, the study points out the causes and effective solutions to minimize the impact of urbanization on seawater quality and protect the water resources of this area.

1. INTRODUCTION

The issues raised by the global scientific community's recent emphasis on the erosion of coasts have been widely publicized. There are two categories of human pressures on coastal areas: direct and indirect. First, one of the most dangerous degradation processes in Quang Ninh province is the loss of soil functions brought on by waterproofing the soil during the urbanization and infrastructure construction processes (Do Thi Thu Huong et al., 2021). This has a big impact on coastal regions worldwide, where tourism and urbanization are expanding more quickly (Ludlow, 2006; Wilby and Perry, 2006). This growth indicates a trend toward increase. Unwanted acts against natural systems, such as residential and commercial discharges that affect the structure of the coast, are referred to as indirect pressure (Brausch et al., 2012; Susan D Richardson and Thomas A Ternes, 2011). In recent years, Quang Ninh province has experienced rapid urbanization. According to statistics from (GOV, 2023), the province will have an urbanization rate of about 37.5 % in 2020, up from 30.8 % in 2010. Along with the development of industrial, tourism and service zones and many real estate and infrastructure projects being implemented, urban areas such as Ha Long, Uong Bi, Mong Cai and Cam Pha cities are growing strongly. Furthermore, urbanization growth poses many challenges for Quang Ninh province, including traffic overload, environmental pollution and the need to enhance infrastructure and public services to meet the growing needs of urban dwellers. In addition to traffic congestion, environmental pollution and the need to enhance infrastructure and public services, urbanization growth presents many other challenges for Quang Ninh province. One of them is the situation of cramped, scarce land in urban areas, especially in Ha

Long city, the tourism center of the province. The growth of urbanization also entails challenges for the protection and development of the natural heritage of Quang Ninh province, especially Ha Long Bay, Co To Island and Cua Dai mangrove forests. The management and protection of the architecture and ecological landscape around these heritage sites from pollution, illegal exploitation and overtourism are urgent issues in the province (Dinh et al., 2023). A study method of water quality-sampling-and instructions for sampling seawater were used according to Vietnam Standard TCVN 5998:1995 (ISO 5667-9:1992). This method has the advantage of having in-depth analysis and indicators of water quality in the sampling area. The analyzed water samples were selected by the authors based on the results of environmental monitoring in Quang Ninh in the period of 2018-2023.

2. RESEARCH AREA, SAMPLING METHOD, MONITORING

2.1 Research area

Quang Ninh Province is located in the northeast of Vietnam (Figure 1), bordering the East Sea to the east and Hai Duong province to the west. With an area of 6,100 km² of sea, Quang Ninh has great strengths and potential to develop marine economic sectors. It has the longest coastline of 250 km with 2,077 islands, accounting for two-thirds of the country's islands, of which over 1,000 have names. It also has a large aquaculture area of over 6,100 km², which is home to countless rare marine species. The Quang Ninh coast has many deep-water and airtight areas, which is a particularly important advantage favorable for the construction and development of a seaport system, especially a deep-water port that can receive ships of large tonnage and a seaport. Inland, especially in Ha Long city, Cam Pha city, Tien Yen district, Mong Cai city and Hai Ha district, to meet the needs of goods exchange with other provinces in the region. The province is also famous for many natural heritages, such as Ha Long Bay, one of the world's wonders; Co To Island; the 1,068-meter-high Yen Tu Peak; and Cua Dai mangrove forest (TTQN Electronic Library, 2018; Wikipedia, 2023).

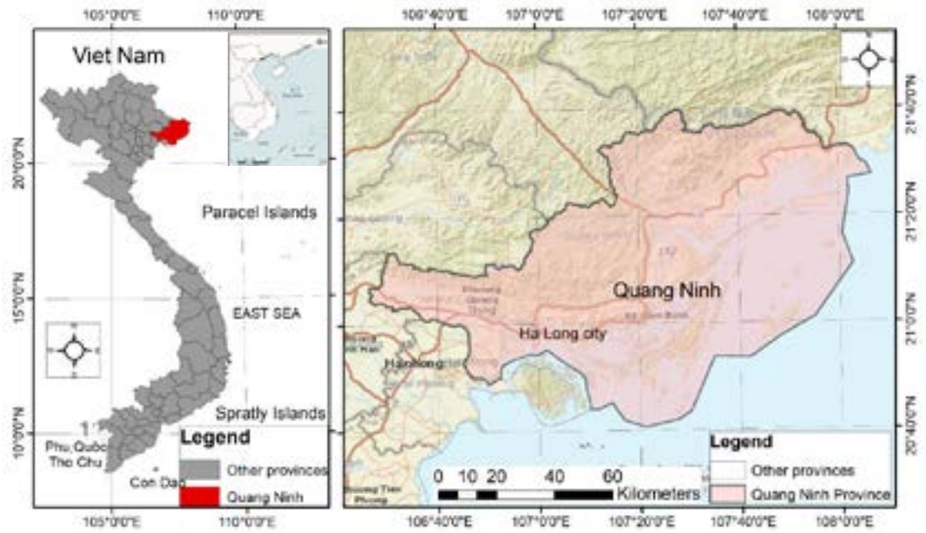

Figure 1. Location of Quang Ninh province in Vietnam.

2.2 Additional monitoring and analysis

The sampling process involved various steps to ensure accurate and comprehensive data collection. Initially, seawater samples were collected using a bucket and then transferred into a glass beaker for immediate measurements of key parameters such as pH and dissolved oxygen (DO). Subsequently, the samples were divided into different containers for preservation and analysis. Two 1-liter plastic bottles were used for cold storage, one containing HNO_3 and the other NaOH. Additionally, three 1-liter glass bottles were employed to preserve H_2SO_4, while two 1-liter glass bottles and one 0.5-liter glass bottle were designated for cold storage. Following the sample preparation, 0.5 liters of the seawater sample underwent filtration using filter paper. The filter paper, housing retained particles, was carefully preserved in a Falcon tube with 90 % ethanol. Simultaneously, the filtered water was retained for further analysis of CDOM (Chromophoric Dissolved Organic Matter) (Legal document, 1995).

To comprehensively assess the seawater quality in Quang Ninh Province, the research team established a strategic network of water quality monitoring points. These points were strategically located in various areas, including industrial zones, clusters, aquaculture zones, resorts, services and coastal estuaries, among others (refer to Figure 2). Seasonal variations were accounted for by collecting samples during both rainy and dry seasons, aiming to generate a comprehensive dataset for evaluating the overall seawater quality in Quang Ninh province. The execution of the sampling pattern adhered to specific locations, ensuring a thorough understanding of the impact of urbanization on seawater quality in the region.

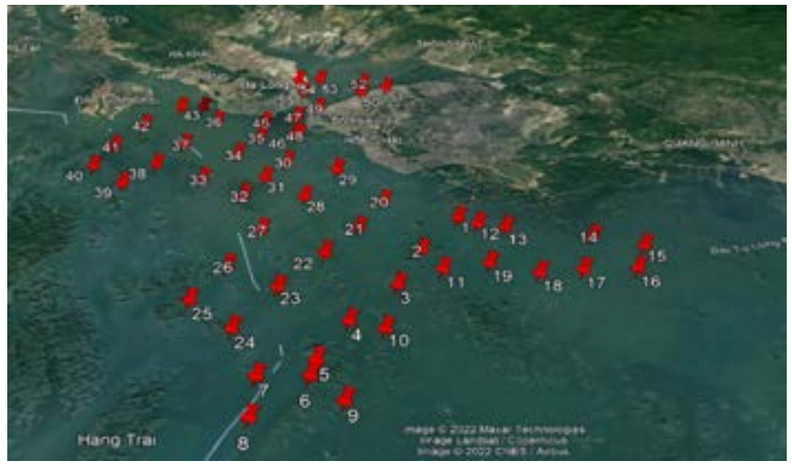

Figure 2. Sampling location in Quang Ninh province.

Collected seawater samples were analyzed in a laboratory with full Vimcert certificates (Vimcert 079, Vimcert 032, Vimcert 120); and Vilas (Vilas 386, Vilas 450, Vilas 366) conforming to the recognized international standard ISO/IEC 17025:2005 and a system of modern analytical equipment equipped by the JICA project of Japan and Korea's KOICA. The analysis parameters of coastal seawater samples comply with QCVN 10-MT:2015/BTNMT (Legal document, 2015) (National regulation on coastal water quality b, in which 25 indicators are evaluated: pH, DO, TSS, N-NH_4^+, P-PO_4^{3-}, F^-, CN^-, As, Pb, Cd, Cr_6^+, total Cr, Cu, Zn, Mn, Fe, Hg, Aldrin, BHC, Dieldrin, DDTs, Heptachlor & heptachlor epoxide, total phenol, total mineral grease, Coliform From the above data, combined with the data collected from the available seawater quality

monitoring system, it will be possible to assess the current state of seawater quality and the impact of urbanization on seawater quality in Quang Ninh province.

3. STATUS OF SEAWATER QUALITY IN SOME AREAS OF QUANG NINH PROVINCE

During the assessment of the current state of coastal water quality, we measured pH and DO in the field, the rest were analyzed in the laboratory. Rainy season symbols: MM; dry season: MK; QCVN 10-MT:2015/BTNMT: National technical regulation on seawater quality, applicable to: Region 1: aquaculture and aquatic conservation areas; Region 2: beach areas, water sports; Region 3: other places (Legal document, 2015).

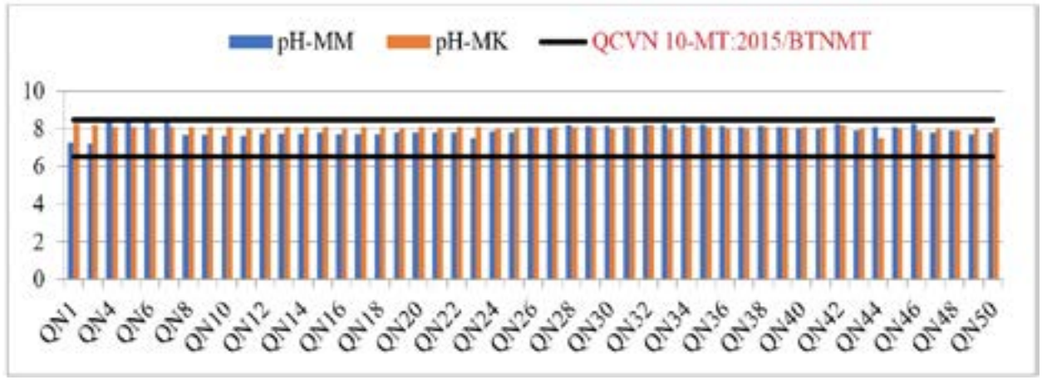

Figure 3. Seasonal pH value.

From the analysis results in Figure 3, it can be seen that the fluctuations of pH parameters are seasonal and by latitude. In the rainy season, the pH values fluctuate widely from 7.18 to 8.39 due to the change in water quality. In the rainy season, upstream water flows into the sea with a large flow, thereby reducing the pH value at each location and point, for the sampling location shows an average pH value of 7.93. In contrast to the dry season, the pH value fluctuates slightly from 7.5 to 8.3; the average pH value is 8.05. Thus, the pH of the rainy season is lower than that of the dry season and the pH values are satisfied with the limit of 6.5-8.5 according to all areas to be surveyed (Law Library, 2011).

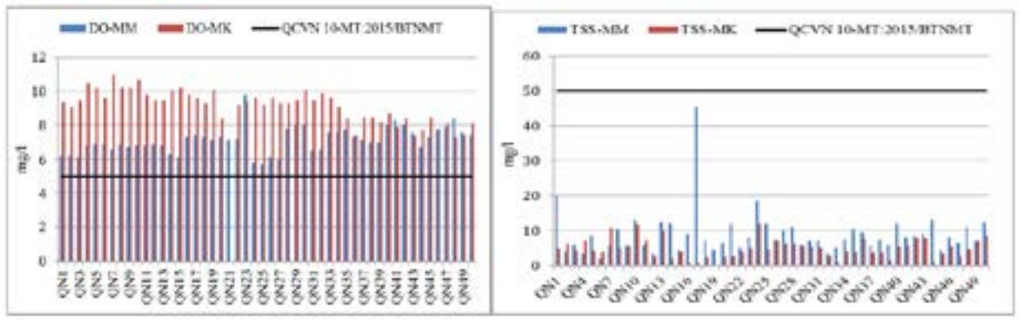

Figure 4. Seasonal DO, TSS values.

With the DO value in Figure 4, there is a seasonal change. Specifically, in the rainy season, the DO fluctuates in the range of 5.7-9.8, with an average of 7.12. In the dry season, the DO value fluctuates from 7.3 to 11.0, with an average of 9.15. The DO value depends on climatic and ecological conditions. The DO values in the rainy season and the dry season are all satisfied with the DO ≥ 5 limits according to Vietnam standards, which is the ideal condition for the aquatic ecosystem to develop (Law Library, 2004). With TSS, the values determined in the rainy season and the dry season are within the allowable limits of Vietnam standard for all regions; however, in the dry season, the average TSS value is 4.96 mg/L, which is lower than the average of the rainy season, which is 8.97 mg/L. The reason for the high rainy season is due to the water pouring in from the sources, so the suspended matter content in the water is higher than in the dry season. TSS fluctuations in both seasons fluctuated evenly; only the QN17 score for the rainy season reached 45.5 mg/L because, at the time of sampling, there were strong winds, big waves and whirlpools. The above value is still within the allowable limit of the Vietnam standard. Thus, the DO value depends on climatic and ecological conditions. The DO values in the rainy season and the dry season are all satisfied with the DO ≥ 5 limit according to Vietnam standards, which is the ideal condition for the aquatic ecosystem to develop (Mr. Carlos Manuel Robles, 2018).

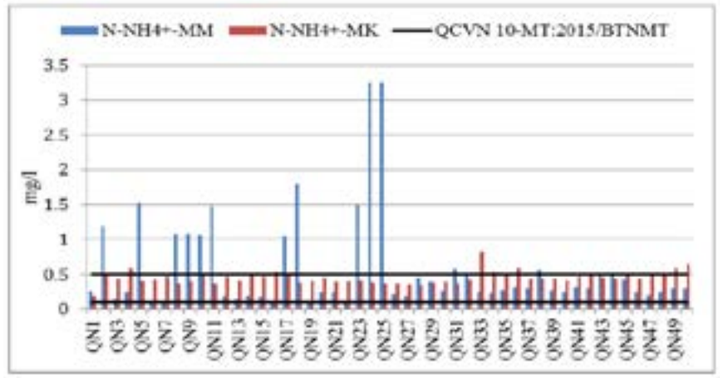

Figure 5. Seasonal NH_4^+ Value.

We find that the NH_4^+ values in Figure 5 are variable. The average rainy season (0.57 mg/L) is higher than the dry season average (0.45 mg/L) and the values determined in the dry season are stable and more uniform than in the rainy season. Specifically, in the dry season, there are 07 survey sites with a higher ammonium value than the limit of the Vietnam standard, the highest value being 1.65 times higher than the limit of the Vietnam standard applicable to beach areas, water sports and other places. All survey sites have ammonium content exceeding the standard compared to zone 1, so it is recommended to have close supervision when put into use for aquaculture or aquatic conservation purposes. In the rainy season, ammonium content fluctuates unevenly; specifically, there are 05 survey sites (QN6, QN7, QN19 and QN22) with ammonium content below 0.1 mg/L that meet the water quality standards for all three areas under the Vietnam standard. There are 30 sites with ammonium content below 0.5 mg/L meeting the water quality requirements for zones 2 and 3 and exceeding the threshold of zone 1, 15 points exceeding the threshold for all three regions and scores exceeding the threshold 6.52 times compared to the Vietnam standard applied to regions 2 and 3. The reason for the unusually high points in the rainy season may be due to the mixing of wastewater sources from the mainland associated with discharge activities from different waste sources at the time of the survey.

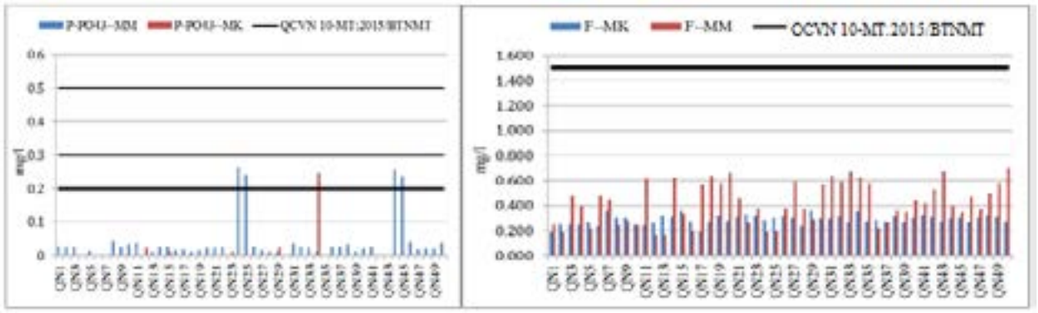

Figure 6. The PO_4^{3-}, F^- value according to season.

With the indicator PO_4^{3-} in Figure 6, 45 survey points all meet for all three regions; the remaining 5 points exceed the limit of zone 1 and are within the limit threshold for zones 2 and 3. The PO_4^{3-} at the measurement points have uniform values; only 5 points are slightly higher, but these values fluctuate by water, so these values do not affect much the purposes of use for all three regions. With F^-, all 50 survey sites are within the allowable threshold for all three regions; the average value in the dry season is 0.29 mg/L in the rainy season is 0.44 mg/L. In general, the rainy season is higher than the dry season, but the difference is not much.

With metal indicators such as As, Cd, Pb and Cr (VI), total Cr, Cu, Zn, Mn and Hg are all lower than the detection limit, or if detected, the value is very small. The above targets are within the allowable limits for all three areas of Vietnam standards and suitable for all uses on the seas. Organic indicators such as Aldrin, benzene hexachloride (BHC), dieldrin, DDTs, heptachlor, heptachlor epoxide and total phenol were all below the detection threshold of the test and all of the above criteria were within the allowable limits for all three regions under Vietnam standard, suitable for all uses on the seas.

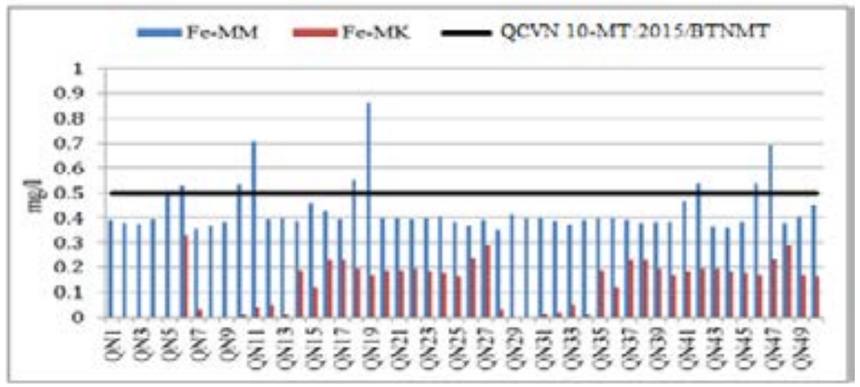

Figure 7. Fe value according to the season.

With Fe metal indicators, there are 41 survey sites with analytical results below the threshold for all three regions according to Vietnamese standards in both seasons Figure 7, so these locations can be used for both different purposes. In the dry season, the iron content in all 50 surveyed points is below the permissible threshold of Vietnamese standards. In the rainy season, 9 points exceed the limit from 1.06 to 1.726 times. However, these values are unevenly distributed and locally influenced by water from different sources flowing into the area daily, so there is no cause for concern.

Regarding the indicators of CN^- oil and total mineral, all 50 samples were below the allowable threshold. In the rainy season, most of the 50 survey sites were below the analytical limit. In the dry season, the CN^- content fluctuated in the range of 0.004-0.005 mg/L, while the total mineral oil and grease were mostly below the analytical detection threshold; some identified points were all at 0.3 mg/L. All bi-seasonal survey sites for these two indicators can be used for different purposes in all three regions according to Vietnam standards.

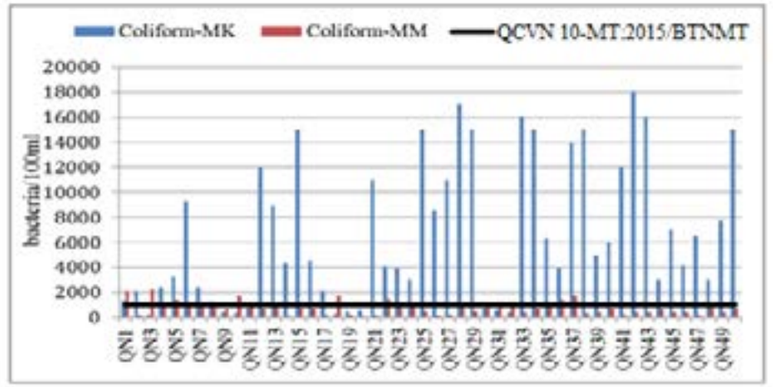

Figure 8. Seasonal Coliform values.

Figure 8 shows a clear difference between the two seasons. We see a clear difference between the two seasons. In the rainy season, the density of microorganisms is lower than in the dry season. The reason is that in the rainy season, there is a mix of other surface water sources at the time of sampling and marine tourism activities decrease sharply in contrast to dry buying, so it can be that this is the reason why the number of microorganisms increases sharply in the dry season. Specifically, in the rainy season, the determined values are evenly distributed according to the survey points. There are 17 points of permissible limit according to a limit of Vietnam standards and the excess value ranges from 1.1 to 2.2 times. This excess value is not worrisome because the rain always changes due to water from upstream to the sea; there is an exchange between flows, so the number of microorganisms is lower than in the dry season.

In the dry season, the coliform count exceeds the permissible limit of the Vietnam standard in a significant number of cases. Only 10 points fall within the allowed range, while the remaining 40 points exceed the limit by a factor of 1,3 to 18 times. The average value of the 50 points is 6726 (bacteria/100 m). To explain the fluctuations, it is known that aquaculture activities in the sea often result in excess food residues and high levels of ammonia, creating an ideal environment for microbial growth. Additionally, during the dry season, there is less rainfall and, consequently less water exchange. The increase in marine tourism activities during this period, combined with the hot weather, provides favorable conditions for vigorous microbial growth (Ogawa, 1974; Shen et al., 2020).

4. CAUSES AND SUGGESTED SOLUTIONS

4.1 The causes

In 2022, in Quang Ninh province, Ha Long has invested in building and operating an urban wastewater system with 5 wastewater treatment stations. However, these stations can only treat

about 45 % of domestic wastewater and the proportion of urban centers of grade 4 and above in the province with centralized wastewater treatment systems reaches over 21 % (Ministry of Natural Resources and Environment, 2016).

Regarding the issue of groundwater depletion, the urban areas in Quang Ninh province are currently in a phase of construction and development. Activities such as pond and lake reclamation and geological exploration not only alter the permeable environment but also reduce the amount of water infiltrating from the surface into the underground aquifers, thus diminishing the supplemental source for groundwater. This leads to a decline in extraction rates from wells, lowering the water table. Additionally, it creates favorable conditions for surface water contamination to easily infiltrate the aquifers, altering the existing environment of groundwater and resulting in groundwater pollution (Environmental Resources, 2022).

From 2011 to 2020, Quang Ninh Province achieved significant targets in environmental protection. The collection and treatment rate of municipal solid waste reached 96.2 %. The collection and treatment rates of hazardous waste and medical waste reached 100 %. The population‘s access to clean water reached 98 %, ranking second nationwide in the Environmental Governance Index (Environmental Resources, 2022). However, there are still many limitations in environmental protection within the province, particularly in terms of water pollution caused by domestic wastewater in urban areas. In 2020, the volume of domestic wastewater in the Ha Long area reached over 31,720 m^3/day and night. The city of Ha Long only has 5 wastewater treatment plants in operation with a capacity of 14,276 m^3/day and night. However, these plants can only treat about 45 % of the domestic wastewater discharged into the common receiving source. The remaining wastewater is still directly released into the general drainage system, flowing into the sea, posing a significant risk of pollution to Ha Long Bay‘s environment (Environmental Resources, 2022).

There are four main reasons behind the problems with environmental protection in Quang Ninh Province. First, the awareness and sense of responsibility of the authorities and the people are still limited and some levels of party committees and authorities focus on prioritizing economic development at the expense of the environment. Secondly, the drainage system of urban areas in the area is mostly old and degraded; many sewer lines in the urban area are encroached on and filled, causing flow congestion and local flooding in many localities during heavy and prolonged rain. Third, the rapid urbanization rate and the narrowing of natural ground and water surface areas such as ponds, lakes and canals have partly affected the drainage capacity of urban areas. Finally, investment funds for environmental protection work have not met the large investment capital needs for technical infrastructure for environmental treatment (Environmental Resources, 2022; Ministry of Natural Resources and Environment, 2016).

4.2 Solutions

To limit the impacts of urbanization on seawater quality in Quang Ninh province, it is necessary to have the following solutions:

- Effective urban waste management and treatment: Cities need to build urban wastewater treatment systems, protect rivers and canals and minimize pollution from urban waste sources.
- Control the growth of urbanization: strengthen supervision and control over the issuance of new construction permits, population management and orientation of sustainable urban development.
- Raise public awareness: Through communication, education and consulting campaigns, increase community awareness of environmental issues and environmental protection consciousness.
- Organization of volunteer activities: Organize volunteer activities such as green summer labor and volunteer programs to build wastewater treatment systems and protect and restore coastal areas to increase community awareness of environmental protection.
- Promoting the use of advanced technologies: using advanced technologies to manage and mitigate the effects of urbanization, such as wastewater treatment technologies, seawater quality analysis, environment management systems and remote monitoring.
- Promoting green economic development: encouraging green and sustainable economic activities, creating favorable conditions for attracting new investment projects and providing incentive policies to promote green economic development.
- Encourage the use of renewable energy sources: Promote the use of renewable energy sources such as solar energy, wind energy and hydroelectricity to reduce greenhouse gas emissions from traditional energy sources.
- Strengthening local and international cooperation: Strengthening local and international cooperation to exchange experiences and seek common solutions to problems related to the environment, including impacts of urbanization on seawater quality.

5. CONCLUSION

Therefore, the article has demonstrated that urbanization growth is negatively impacting the water quality along the coastal areas in Quang Ninh province, especially in rapidly developing urban regions like Ha Long and Cam Pha. These impacts include water pollution, the reduction of marine biodiversity and effects on human health. However, the article also proposes several solutions to mitigate the impact of urbanization on seawater quality, including the establishment of wastewater treatment systems, investment in clean water treatment technologies, monitoring, promotion of renewable energy sources and enhanced collaboration among relevant agencies and voluntary activities. The Ha Long Bay region holds special significance for Vietnam’s maritime economy, often experiencing the phenomenon of cold water tongues during northeast and southwest winds. The survey results of seawater quality in the rainy and dry seasons show differences in certain specific parameters influenced by hydrological factors. For example, coliform levels exceed the permissible limit during the dry season, while iron and ammonia levels tend to increase during the rainy season due to water layer mixing, upwelling and sinking. Other parameters remain within the allowable limits according to the Vietnam standard. In conclusion, further periodic surveys are necessary to provide a comprehensive and weather-condition-specific assessment to meet the usage purposes for each sampling location. This will enable appropriate water quality utilization or improvement aligned with research objectives. Therefore, implementing the aforementioned solutions will be an important step in environmental protection, conservation and the improvement of seawater quality in Quang Ninh province.

6. ACKNOWLEDGMENTS

This paper is supported by the Ministry of Science and Technology (MOST) through the protocol project with Australia entitled: “Building a support system for rapid assessment of landscape changes in service of planning and decision-making for coastal area management in Vietnam ”, Grant number: NDT/AU/21/15.

7. REFERENCES

Brausch J., Connors K., Brooks B., Rand G., 2012. Human Pharmaceuticals in the Aquatic Environment: A Review of Recent Toxicological Studies and Considerations for Toxicity Testing. *Reviews of environmental contamination and toxicology 218*, 1-99. https://doi.org/10.1007/978-1-4614-3137-4_1.

Dinh, N., Dien, N., Son, L., Khai, L., Trang, T., Tuan, V., Quang, N., Linh, N., 2023. Assessing sea water quality: Temperature, turbidity, chlorophyll-a, CDOM in Ha Long city, 44-46.

Do Thi Thu Huong, Nguyen Thi Thu Ha, Gia Do Khanh, Nguyen Van Thanh, Luc Hens, 2021. Sustainability assessment of coastal ecosystems: DPSIR analysis for beaches at the Northeast Coast of Vietnam | *SpringerLink* [WWW Document]. URL https://link.springer.com/article/10.1007/s10668-021-01648-x

Environmental Resources, 2022. Quang Ninh: Solving the problem of wastewater treatment in urban areas [WWW Document]. URL https://baotainguyenmoitruong.vn/quang-ninh-giai-bai-toan-xu-ly-nuoc-thai-tai-cac-do-thi-346494.html

GOV, 2023. Electronic information portal of the Department of Agriculture and Rural Development, Quang Ninh province planning for the period 2021-2030, vision to 2050 [WWW Document]. URL https://www.quangninh.gov.vn/So/sonongnghiepptnt/Trang/ChiTietTinTuc.aspx?nid=7415 (accessed 11.19.23).

Law Library, 2011. National standard TCVN 6492:2011 water quality - Determination of pH. [WWW Document]. URL https://thuvienphapluat.vn/TCVN/Tai-nguyen-Moi-truong/TCVN-6492-2011-chat-luong-nuoc-Xac-dinh-pH-904741.aspx

Law Library, 2004. Vietnam Standard TCVN 7325:2004 water quality - Determination of dissolved oxygen - Electrochemical probe method [WWW Document]. URL https://thuvienphapluat.vn/TCVN/Tai-nguyen-Moi-truong/TCVN-7325-2004-chat-luong-nuoc-xac-dinh-oxy-hoa-tan-phuong-phap-dau-do-dien-hoa-902783.aspx

Legal document, 2015. National standard QCVN 10-MT:2015/BTNMT on seawater quality [WWW Document]. URL https://hethongphapluat.com/quy-chuan-quoc-gia-qcvn-10-mt-2015-btnmt-ve-chat-luong-nuoc-bien.html (accessed 11.19.23).

Legal document, 1995. Vietnam Standard TCVN 5998:1995 (ISO 5667-9: 1992) on water quality - sampling - instructions for seawater sampling [WWW Document]. URL https://bachkhoaluat.vn/van-ban-luat/31708/tieu-chuan-viet-nam-tcvn-5998-1995-iso-5667-9--1992-ve-chat-luong-nuoc---lay-mau---huong-dan-lay-mau-nuoc

Ludlow, D., 2006. Urban sprawl in Europe - The ignored challenge. *European Environment Agency Report*. No 10.

Ministry of Natural Resources and Environment, 2016. Report on the current state of the national marine and island environment for the period 2016 - 2020 [WWW Document]. URL http://dwrm.gov.vn/index.php?language=vi&nv=download&op=Sa-ch-Ta-i-lieu-tham-kha-o/Bao-cao-hien-trang-moi-truong-bien-va-hai-dao-quoc-gia-giai-doan-2016-2020.

Mr. Carlos Manuel Robles, 2018. Sea Surface Temperature (SST) variability of the Eastern Coastal Zone of the Gulf of California [WWW Document]. URL https://www.mdpi.com/2072-4292/10/9/1434.

Ogawa, K., 1974. Some factors affecting the survival of coliform bacteria in seawater. *Journal of the Oceanographical Society of Japan 30*, 54-60. https://doi.org/10.1007/BF02112893

Shen, J., Zhou, X., Shan, Y., Yue, H., Huang, R., Hu, J., Xing, D., 2020. Sensitive detection of a bacterial pathogen using allosteric probe-initiated catalysis and CRISPR-Cas13a amplification reaction. *Nat Commun 11*, 267. https://doi.org/10.1038/s41467-019-14135-9

Susan D Richardson, Thomas A Ternes, 2011. Water analysis: emerging contaminants and current issues - PubMed [WWW Document]. URL https://pubmed.ncbi.nlm.nih.gov/21668018/.

TTQN Electronic Library, 2018. General introduction to Quang Ninh province [WWW Document]. URL https://thuviendientu.baoquangninh.vn/

Wikipedia, 2023. Quang Ninh province.

Wilby R. L., Perry G. L. W., 2006. Climate change, biodiversity and the urban environment: a critical review based on London, UK. Progress in Physical Geography: Earth and Environment 30, 73-98. https://doi.org/10.1191/0309133306pp470ra.review based on London, UK. *Progress in Physical Geography: Earth and Environment 30*, 73-98. https://doi.org/10.1191/0309133306pp470.

FORECAST OF SUBMARINE LANDSLIDES RELATED TO THE REACTIVE PROBABILITY OF THE FAULT SYSTEM IN THE SOUTHEAST VIETNAM CONTINENTAL SHELF AND ADJACENT AREAS

Tran Tuan Duong[1]*, Tran Tuan Dung[1,2], Nguyen Quang Minh[1], Tran Trong Lap[1]

[1]Institute of Marine Geology and Geophysics, Vietnam Academy of Science and Technology
[2]Graduate University of Science and Technology, Vietnam Academy of Science and Technology
*Corresponding author. E-mail: ttduong.humg@gmail.com

ABSTRACT

In this article, the fault's geometrical parameters in the Southeast Vietnam continental shelf and adjacent areas (such as the location, dip angle and strike angle as well as depth and length) are determined by gravity, seismic data and regional stress fields. For the faults, due to their high internal frictional coefficient, they accumulate more energy under the impact of the regional stress field. Sometimes, when they accumulate enough energy, they can react and disrupt the local geological structures, causing earthquakes and can penetrate the upper layers of the Earth's crust, forming favorable surfaces for submarine landslides.

The model of fault's reactive possibility is built based on analysis, overlayed integration of three informative layers determined, which are the slip tendency of the fault system and the relative vertical and horizontal displacement field of the Earth's crust. For fault's slip tendency and horizontal displacement, the classification of the fault's reactive possibility is based on their magnitude. For vertical displacement, where there is a large difference in amplitude, the fault's reactive possibility is higher and vice versa.

The reactive possibility of the fault system can be seen as a key factor in research on marine geological hazards such as earthquakes and submarine landslides in the Southeast Vietnam continental shelf and adjacent areas.

1. INTRODUCTION

Submarine landslides often occur on continental shelf margins and slopes, where the seafloor is usually steep slopes and loose sediments. Most of of them are caused by earthquakes in zones of active tectonic faults or by volcanism (Hühnerbach et al., 2004; Locat et al., 2000). This paper focuses on the assessment and forecast of submarine landslides by comprehensively analyzing four key factors, including slip tendency along faults, the magnitude of possible relative vertical and horizontal displacements in the crust and the reactive possibility of existent faults.

The theory of slip behavior of faults was first proposed by Wallace, (1951). Since then, there have been many further studies developed on inversed-stress methods based on the Wallace-Bott hypothesis (Angelier, 1990; Gephart et al., 1984; Morris et al., 1996). There are several relevant studies were launched under the Vietnam national projects. The main causes of submarine landslides were identified, such as earthquakes, active faults, geological structure, sedimentation and topography of the seabed. The results were published by Bui Cong Que et al., (2010); Tran Tuan Dung et al., (2015).

In spite of the numerous studies, accurate forecast of submarine landslides is still beyond our capabilities. Areas of possible submarine landslides are identifiable from seismic and multibeam profiling data, but it is difficult to forecast the occurrence of specific landslides. The numerical modeling of submarine landslides from the reactive possibility of faults is a necessary way to improve understanding of these phenomena. Such a model can be used to assess the damage and risks to human life caused by submarine landslides, as well as to mitigate the damage caused by them (Bui Cong Que et al., 2010; Tran Tuan Dung et al., 2015). The study area is located between 7-15° N and 106-114° E (Figure 1). In the area, including the continental shelf and slope, the topographic gradient of the seafloor varies most strongly. There are also many active faults in this area, which can be sources of earthquakes. Based on this basis, it can be said that the Southeast Vietnam continental shelf has a very high potential for submarine landslides.

2. DATA USED

2.1 Earthquake focal mechanisms

The earthquake's focal mechanisms (EFMs) provide reliable information on the stress field at depths greater than the drilling method (depth > 5km). This study has compiled a database of 135 earthquake focal mechanisms in the study area and adjacent areas, of which, there are 115 from the Global Centroid-Moment-Tensor Project up to 2022 (http://ds.iris.edu/spud/momenttensor) and 20 from Bui Cong Que et al., (2010). These intraplate EFMs were collected at depths > 5 km and magnitudes > 3Richter. The calculation was performed according to the steps described in the previous and updated until the present (Tran Tuan Dung et al., 2021). The present-day regional stress field in the region and adjacent area is determined by the earthquake's focal mechanism and it is shown in Figure 1.

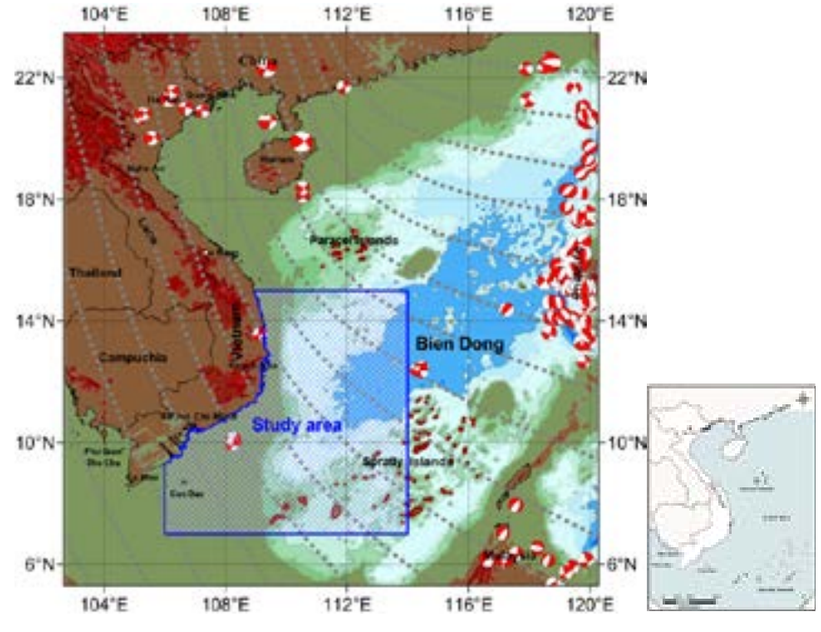

Figure 1. Study area, earthquake focal mechanisms and regional stress field.

2.2 Gravity data

The gravity data obtained from the continental shelf of South-Central Vietnam and adjacent areas are mainly collected from joint ship surveys of the Russian-Vietnamese expeditions onboard the R/V Professor Gagarinsky (1990-1992) and the R/V Professor Polshkov (2007-2008). In addition, satellite altimetry data was used. The authors have used the methods and results, which are proposed by Tran Tuan Dung et al., (2019) together with a new gravity dataset updated until the present (Tran Tuan Dung et al., 2023) to improve the accuracy of marine gravity anomalies (Figure 2a).

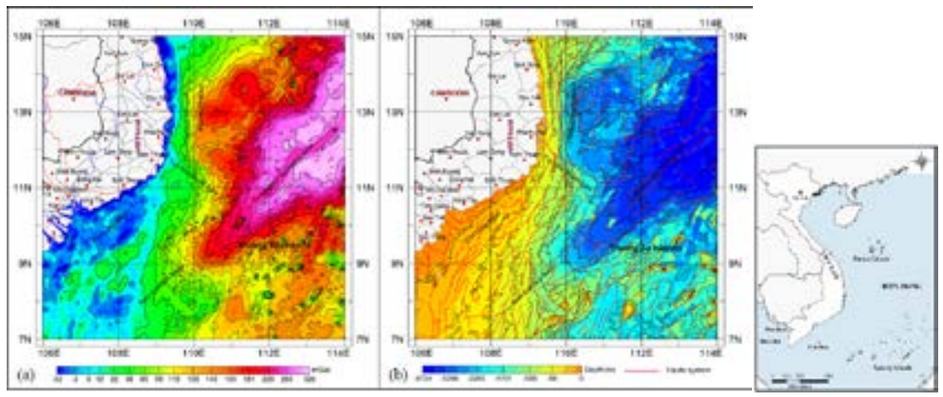

Figure 2. (a) Bouguer gravity field; (b) Bathymetry and faults system.

3. METHODS

3.1 Determination of fault systems

The method for determining faults in the Earth's crust was first described in Blakely et al., (1996) and then updated Tran Tuan Dung et al., (2021). According to this method, the maximum gravity horizontal gradient (MGHG) is used to identify the faults. Faults are mapped by linear zones of MGHG vectors of the same direction. The location and magnitude of the maximum gravity horizontal gradient $H[\Delta g]_{i,j}$ are defined by a second-order polynomial as follows (Blakely et al., 1996; Tran Tuan Dung et al., 2021):

$$X_{Max} = \frac{bd}{2a} \tag{1}$$

$$G_{Max} = aX_{Max}^2 + bX_{Max} + H[\Delta g]_{i,j} \tag{2}$$

where, d is the distance between grid intersections; a, b are developed coefficients of the polynomial, which are calculated from the grid of the gravity anomalies.

3.2 Determination of slip tendency on the fault surface

The slip tendency on the fault surface, which is affected by the present-day regional stress field, is defined as the ratio of the shear stress to the normal stress on the fault surface. In the present work, the methods for determining the contemporary regional stress field and fault slip tendency are partly inherited from our previous studies. According to Morris et al., 1996 and Tran Tuan Dung et al., 2021, the slip tendency (T_s) is determined as follows:

$$T_s = \frac{|\sigma_s|}{\mu|\sigma_n|} \tag{3}$$

where: σ_s is shear stress; σ_n is normal stress; μ is the static friction coefficient on the fault's surface, here μ is chosen as 0,65 (Schellar, 2000).

3.3 Determination of relative displacement in the Earth's crust based on fault parameters

The basic theory on the characteristics of displacements in the Earth's crust, which are influenced by the present-day stress field and fault behavior, is presented in the study of Okada Y (1992). The method for determining relative displacements in the Earth's crust in this work is partly inherited from previous studies (Tran Tuan Dung et al., 2021). The displacement field $u_i\ (x_1,x_2,x_3)$ caused by a dislocation $\Delta u_j\ (\xi_1,\xi_2,\xi_3)$ across a surface Σ in an isotropic space, it is represented by the formula:

$$u_i = \frac{1}{F}\iint_{\Sigma} \Delta u_j \left[\lambda\delta_{jk}\frac{\partial u_i^n}{\partial \xi_k} + \mu\left(\frac{\partial u_i^j}{\partial \xi_n} + \frac{\partial u_i^k}{\partial \xi_j}\right)\right] \nu_k \, d\Sigma \tag{4}$$

where, ν_k is the normal cosine to the surface element, i.e., $(0,-sin\delta,cos\delta)$. Based on the above formula, the internal displacement field (u^0) caused by each point source can be represented by joined forces of the strain nuclei ($\partial u^i/\partial \xi_k$) (Okada Y, 1992).

3.4 Probability of submarine landslides based on the integration of all information sources

Sources of information on factors contributing to underwater landslides are formed on the basis of reliable geological and geophysical data from modern and previous studies. The forecast of a potential submarine landslide is constructed according to the following formula:

$$H = \sum_{j=1}^{n} W_j X_{ij} \tag{5}$$

where, H is submarine landslide potentially index, W_j is the weight of the jth information layer, X_{ij} is the ith weight of the information layer j. The H index depends firstly on the weight of each component information layer and then on the weight of each level in each component information layer.

4. RESULTS AND DISCUSSION

4.1 Faults

In this study, the spatial parameters of the faults (depth, strike and dip) are determined based on the results, which are proposed by Tran Tuan Dung et al., (2021). The fault system is usually represented by the range of MGHG points and their directional vectors in the same direction. By analyzing and connecting the locations and magnitudes of the MGHG points in a suitable approach combined with the seismic data, the spatial distribution of the faults system is determined and shown in Figure 2b. As can be seen in Figure 2b, there are three directions of the fault system in the area: South-North, Northwest-Southeast and Northeast-Southwest. The system of meridional faults is mainly distributed in the west of the study area. Among them, the most prominent is the system of faults extending in the zone 109°30'-110°E. The NW-SE-

oriented fault system is mainly distributed in the Tuy Hoa shear zone. This zone reverses the direction of the fault system, extending along 109°30'-110°E. The NE-SW trending fault system is widespread in the outer zone of continental shelf uplift. This shows that the studied area is a place of intersection of different tectonic systems. Consequently, it can be assumed that these systems were formed and further influenced by many tectonic processes in different geological periods.

4.2 Relative horizontal and vertical displacement in the Earth's crust

Figure 3a shows the results of calculations of the relative horizontal displacements in the Earth's crust. As can be seen, the relative horizontal displacements connected with the meridional fault zone (109°30'-110°E) prevail in the study area. Although the displacement field occurs throughout the region, wherever the larger faults system exists, the displacement field has a greater magnitude. In Figure 3a, it can be seen the different strong and weak distributions in each specific area of the displacement field. In the study area, the relative horizontal displacement magnitude and the vector's direction indicate the strike-slip tendency of the faults system.

Figure 3b shows the distribution of relative vertical displacement. The general picture is a mosaic of local areas with upward or downward displacement tendencies. Against this background, the upward displacement tendency prevails in the western half of the study area and the downward displacement tendency prevails in the eastern half. The maximum upward displacement tendency is confined to the Tuy Hoa shear zone. The North and South of the Phu Khanh basin also show an upward displacement tendency and there is an area with a downward displacement tendency in its central part.

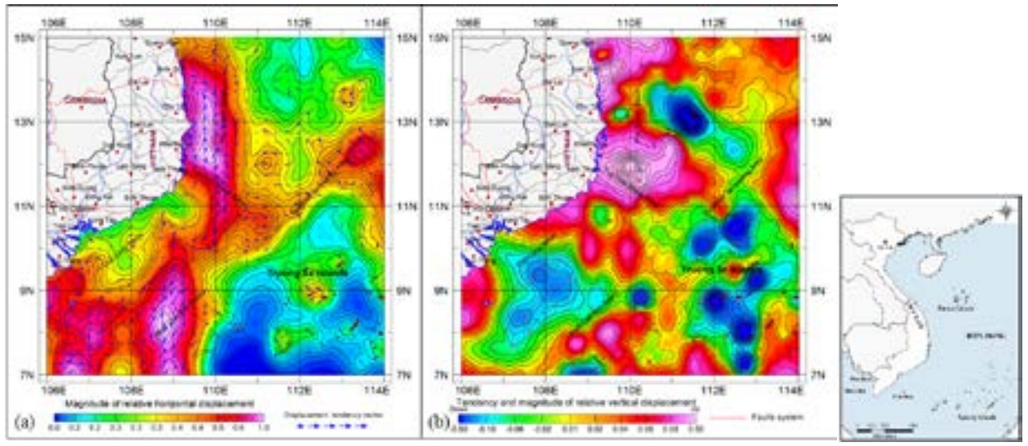

Figure 3. (a) Relative horizontal displacement; (b) Relative vertical displacement in the Earth's crust based on the parameters of the faults.

In all cases, these relative horizontal and vertical displacements are associated with the main faults in the study area - the meridional fault (109°30'-110°E) and the Tuy Hoa shear zone. It is possible to see that the fault system is strongly influenced by present-day stress fields, through which the fault's reactivity can be assessed.

4.3 The fault slip tendency

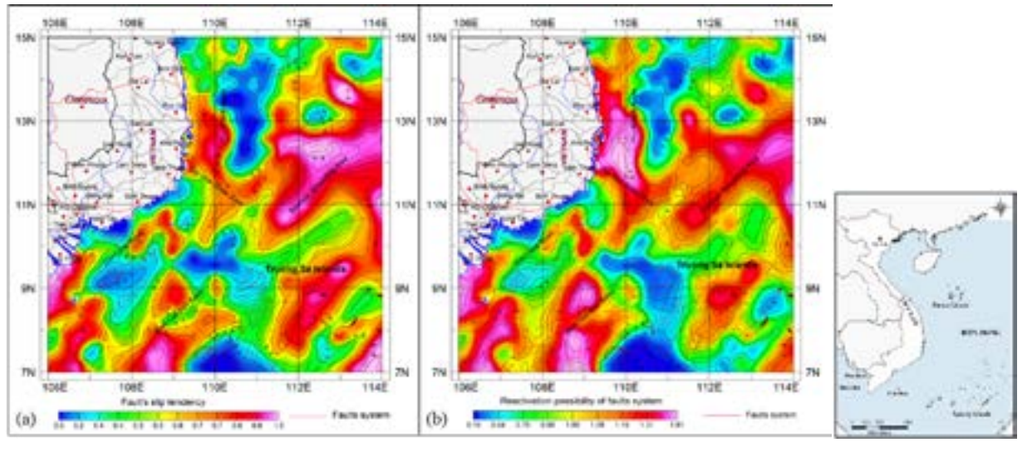

Figure 4. (a) Slip tendency of major tectonic faults; (b) Forecasted zonation of the faults reactivation probability.

The fault slip tendency was determined based on the present-day stress field (Tran Tuan Dung et al., 2021). In Figure 4a, it can be seen that the areas with large fault systems, such as the Tuy Hoa shear zone, seafloor spreading area, Truong Sa Islands, have high slip tendency. From there, it shows that the major fault system in the western Bien Dong is still impacted by distant tectonic forces and implies that their origin is closely related to the Indo-Asian collision (Tapponnier P et al., 1982).

4.4 Reactive probability of faults system

The model of faults system reactive possibility is built on the basis of analysis, overlayed integrates three informative layers determined, that are, the slip tendency of the faults system, the relative vertical and horizontal displacement field in the Earth's crust. Figure 4b shows clearly the forested zones and integrated coefficients on the reactive possibility of the faults system. Accordingly, the area with the bigger integrated coefficient, the higher the fault reactive possibility; the area with the smaller coefficient, the lower the fault reactive possibility. For the three layers of mentioned information above, each layer has different classified criteria on the reactive possibility of the faults system. With the slip tendency of the faults system and horizontal displacement, the classification is based on the magnitude of the slip vectors; with the vertical displacement, where there is a large difference in amplitude, the fault has a higher reactive possibility and vice versa. In Figure 4b, the faults system with high reactive possibility is concentrated in areas such as the Phu Khanh basin, Nam Con Son Uplift and the seafloor spreading area.

4.5 Zonation of the submarine landslides probability

The following information that used to forecast submarine landslides: (1) Relative horizontal displacements in the Earth's crust; (2) Relative vertical displacements in the Earth's crust; (3) Slip tendency on fault surface; (4) Reactive probability of existing fault system (Figure 5). For vertical displacement, where there is a large difference in amplitude, the fault's reactive possibility is higher and vice versa. The fault's slip tendency is assigned the greatest weight because it is directly estimated on each fault segment. Due to the common characteristics of the regional stress field is

strike-slip in the Northwest-Southeast direction, the horizontal displacement has a high role in the fault displacement, so it is assigned higher weight than that of the vertical displacement.

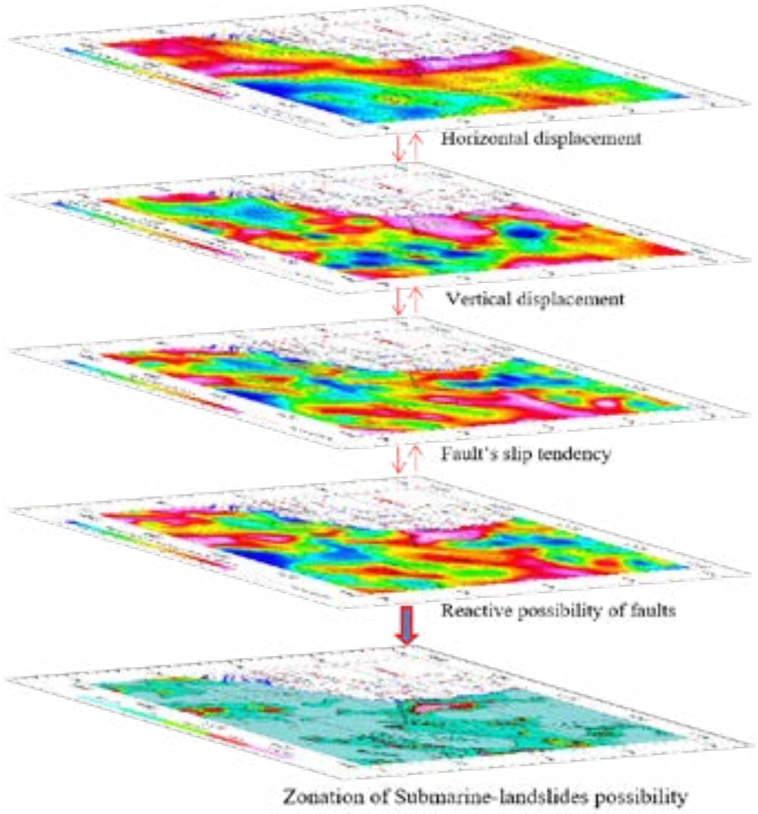

Figure 5. Contributed factors to submarine landslides.

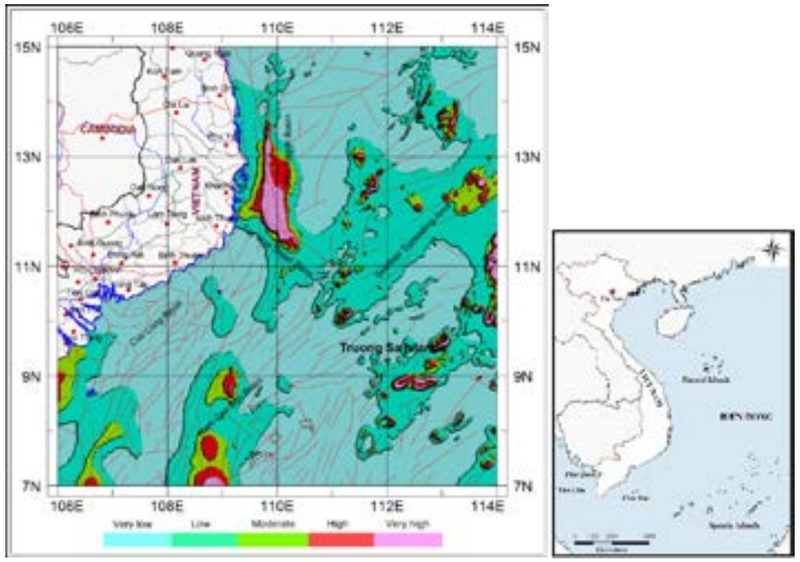

Figure 6. Forcasted zonation of the submarine landslides probability.

Figure 6 shows the zonation of the probability of submarine landslides. This probability is forecasted from very low to very high level based on the integrated weights of the above-mentioned information layers. The figure shows that a large area with a high probability of submarine landslides is located in the meridional fault zone (109°30'-110°E) and Tuy Hoa shear zone. As mentioned above, these faults have a high reactive probability and can be a source of earthquakes and cause submarine landslides. The area with a high landslide probability appears to be concentrated mainly in the central part of the study area. Areas with a low submarine landslide probability are located where fault's reactivation is low.

5. CONCLUSIONS

For deep faults, due to their high internal frictional coefficient, they accumulate more energy under the impact of the regional stress field. Sometimes, when they accumulate enough energy, they can reactivate and disrupt the local geological structures, causing earthquakes and are able to penetrate the upper layers of the Earth's crust, forming favorable surfaces for submarine landslides. Shallow faults with low internal frictional coefficients, which are always directly impacted by regional stress fields, are potential submarine landslide surfaces. This relationship can be seen as a key factor in research on marine geological hazards such as earthquakes and submarine landslides.

The model of submarine landslides possibility is built on the basis of analysis, overlayed integrates four informative layers determined, that are, the slip tendency of the faults system, the relative vertical and horizontal displacement field and reactive probability of existing fault system in the Earth's crust. The areas with high submarine landslide probability are located in the meridional fault zone (109°30'-110°E), the Tuy Hoa shear zone and Nam Con Son Uplift area. In the rest of the study area, the probability of submarine landslides is forecasted to be low. The exception may be the atolls, whose steep slopes could become sources of landslides. The results of the study enable decisions to be made on dealing with submarine landslides, reducing damage to people and property in coastal areas.

6. ACKNOWLEDGMENTS

The authors wish to thank the Institute of Marine Geology and Geophysics-VAST for supporting the necessary conditions to complete this research.

7. REFERENCES

Angelier, J., 1990. Inversion of field data in fault tectonics to obtain the regional stress, part 3. *Geophys. J. Int., 103*, 363-376.

Blakely, R, J. and Simpson, R.W., 1986. Approximating edges of source bodies from magnetic or gravity anomalies. *Geophysics, 51*, 1494-1498.

Bui Cong Que et al., 2010. Studying and assessing the hazard of earthquake and tsunami in the Vietnam coastal zone and Islands and proposing the solutions to prevent and mitigate their consequences. *National Project 2007G/45*.

Gephart, J. W., and D. W. Forsyth, 1984. An improved method for deter-mining the regional stress tensor using earthquake focal mechanism data: Application to the San Fernando earthquake sequence, *J. Geophys. Res., 89*, 9305-9320.

Hühnerbach. V, Masson. D.G, 2004. Landslides in the North Atlantic and its adjacent seas: An analysis of their morphology, setting and behavior. *Marine Geology, 213*, 343-362.

Locat, J. and Lee, H. J., 2000. Proceedings of the 8th International Symposium on Landslides. Cardiff, UK, 2000. *Canadian Geotechnical Journal*, *39*, 193-212.

Morris, A., D. A. Ferrill, and D. B. Henderson, 1996. Slip-tendency analysis and fault reactivation. *Geology, 24*, 275-278.

Okada Y., 1992. Internal deformation due to shear and tensile faults in half-space, *Bull. of the Seism. Soc. of America*, Vol. 82, No. 2, 1018-1040.

Schellart W.P., 2000. Shear test results for cohesion and friction coefficients for different granular materials: Scaling implications for their usage in analogue modeling. *Tectonophysics*. Vol. 324, 1-16.

Tapponnier P., Peltzer G., Le Dain A.Y., Armijo R., Cobbold P., 1982. Propagating extrusion tectonics in Asia: New insights from simple experiments with plasticine. *Geology, 10*, 611-616.

Tran Tuan Dung, 2015. Studying and warning the submarine landslide hazard in the Vietnam South central continental shelf. *National Project*, No. KC.09.11/11-15.

Tran Tuan Dung, 2023. Research to determine the gravity anomalous field on the continental shelf and Vietnam Sea from satellite altimeter data to identify deep and regional geological structures for mineral exploration. *National Project*, No. ĐTĐLCN.07/23.

Tran Tuan Dung, R. G. Kulinich, Tran Tuan Duong et al., 2021. A Study on the Possibility of the Reactivation of the Fault System in the Western Part of the Bien Dong as a Source of Geological Hazards. ISSN 1819-7140, *Russian Journal of Pacific Geology, 15,* 6, 555-569.

Tran Tuan Dung, R. G. Kulinich, Nguyen Van Sang, Tran Tuan Duong et al., 2019. Improving Accuracy of Altimeter-derived Marine Gravity Anomalies for Geological Structure Research in the Vietnam South-Central Continental Shelf and Adjacent Areas. ISSN 1819-7140. *Russian Journal of Pacific Geology, 13*, 4, 364-374.

Wallace, R. E., 1951. Geometry of shearing stress and relation to faulting, *J. Geol., 59*, 118-130.

APPLYING MACHINE LEARNING ALGORITHMS TO CLASSIFY FOREST COVER TYPE FROM SENTINEL 2 MSI DATA

Trinh Le Hung[1]*, Tran Xuan Bien[2], Pham The Trinh[3,4], Le Van Phu[1]

[1]Le Quy Don Technical University, Hanoi, Vietnam
[2]Hanoi University of Natural Resources and Environment, Vietnam
[3]Department of Science and Technology of Dak Lak province, Vietnam
[4]Tay Nguyen University, Buon Ma Thuot City, Dak Lak, Vietnam
*Corresponding author. Email: trinhlehung@lqdtu.edu.vn

ABSTRACT

Forest cover plays a very important role in regulating water sources, limiting floods and soil degradation as well as preserving ecosystems. In recent years, the forest cover has changed drastically due to the impact of socio-economic development, population growth and the effects of climate change. With outstanding advantages compared to traditional research methods, remote sensing data has been widely used in monitoring and evaluating changes in forest cover. This paper presents the results of forest cover classification in Dak Lak province from Sentinel 2 optical satellite image data using machine learning techniques. Sentinel 2 MSI images taken in November 2015 and December 2020 are used to classify forest cover objects and then evaluate forest cover changes in the period 2015-2020. The obtained results show that most of the forest cover objects in Dak Lak have a marked decrease in the period 2015-2020, especially evergreen forests, semi-evergreen forests and dipterocarp forests due to the conversion of natural forests to agricultural land, residential land, industrial crops such as rubber, coffee.

1. INTRODUCTION

Forest cover plays an important role, influencing surface energy exchange processes and acting as an interface between soil and atmosphere. In recent years, due to the impact of socio-economic development and population growth, there has been a rapid decline in forest cover, both in area and quality. Land cover, including forest cover data, is the basis of many studies on land resource management, ecological health and sustainable development. Monitoring and assessing forest cover changes is an urgent requirement, providing timely information for climate and environmental research models as well as serving state management.

There are many methods to evaluate forest cover changes, but the most popular and effective method is to use multi-temporal remote sensing data. With outstanding advantages such as a large coverage area and short update time, remote sensing technology has become a powerful way to obtain land cover data (Rogan and Chen, 2004).

Remote sensing image classification is of great importance for monitoring forest cover change. The need for higher classification accuracy has led to improvements in classification technology (Liu et al., 2022). Methods and algorithms to classify land use/land cover (LULC) from optical satellite images are developed on the basis of image spatial resolution characteristics. Traditional pixel-based classification methods, such as maximum likelihood, minimum distance and parallelepiped algorithms, are all based on the grey value of the pixel, in which only the

spectral information is used for classification. Pixel-based classification approaches have many limitations, especially for high-resolution remote sensing data (Sun et al., 2005). However, pixel-based classification methods may neglect the associations among objects and not utilize the spatial features of objects; thus, objects with the same spectral characteristics cannot be effectively classified (Lee et al., 2003). To overcome the above limitation, an object-oriented classification method is proposed and proves to be effective with high-resolution remote sensing data, especially in forest cover classification. In contrast to pixel-based classification methods, the object-based classification method first aggregates pixels into spectrally homogenous image objects using a segmentation algorithm and then classifies the individual objects (Liu and Xia, 2010).

Recently, machine learning techniques have been used effectively in classifying LULC from optical satellite images, helping to improve accuracy compared to traditional classification methods (Talukdar et al., 2020). In general, there are four types of machine learning algorithms: supervised, unsupervised, semi-supervised and reinforcement learning (Xie et al., 2022); however, the most used ones are supervised and unsupervised learning. The supervised learning techniques include support vector machine (SVM), random forest (RF), classification and regression tree (CART), artificial neural network (ANN)..., while the unsupervised learning techniques include fuzzy c-means algorithms, K-means algorithm, ISODATA...

Each machine-learning technique has different types of accuracy levels. In the study by Basheer et al., 2022 the authors experimented with different classification methods, including 3 types of machine learning techniques (SVM, RF, CART) and maximum likelihood method in classifying LULC through a case study for the city of Charlottetown in Canada. Results show that the SVM classifier presents the best performance compared to other classifiers, where overall accuracy reached 87 % with Landsat 8 and 92 % with Sentinel 2 (Basheer et al., 2022). The SVM algorithm is also used in LULC classification in the lower Tapi basin (India) from Landsat 8 data with the highest overall accuracy compared to ANFIS, M5tree, MARS and GEP techniques. Particularly for forest cover, the overall accuracy achieved in this study with the SVM algorithm reached 0.73. (Thakur and Manekar, 2020). Zhou et al., (2019) proposed an urban forest-type discrimination method from Sentinel 2A image based on linear spectral mixture analysis (LSMA) and SVM in the case study of Xuzhou, east China. Three different vegetation types, including broadleaved forest, coniferous forest and low vegetation and their abundances were extracted through LSMA and SVM algorithms (Zhou et al., 2019).

The study by Ouma et al., (2022) presents the results of urban LULC classification using decision tree-based classifiers comprising of gradient tree boosting (GTB), random forest (RF), in comparison with support vector machine (SVM) and multilayer perceptron neural networks (MLP-ANN). Based on the multi-temporal Landsat data for the period 1984 - 2020 in Botswana, the obtained results in this study show that the RF was the best classifier with an overall average accuracy of 92.8 % when compared to algorithms MLP-ANN (91.2 %), SVM (90.9 %) and GTB (87.8 %) (Ouma et al., 2022). The RF algorithm is also proven to have the highest accuracy compared to algorithms such as k-nearest neighbor (kNN), SVM and ANN when classifying LULC in the Mayo Rey area, northern Cameroon (Yuh et al., 2023). All four machine learning classifiers achieved a high accuracy of over 80 % when classifying LULC from Landsat images, in which the RF algorithm achieved over 90 %. The RF algorithm is also proven to have the highest accuracy when compared to SVM, artificial neural network (ANN), fuzzy adaptive resonance theory-supervised predictive mapping (Fuzzy ARTMAP), spectral angle mapper (SAM) and Mahalanobis distance (MD) algorithms for land cover classification in area of the river Ganga from Rajmahal to Farakka barrage (India) (Talukdar et al., 2020). Research by Kumar and Sinha shows that the RF algorithm achieves 94.6 % accuracy when classifying forest cover, compared to 70.8 % for traditional classification methods (Kumar and Sinha, 2020). The effectiveness of the RF algorithm in forest-type classification has also been demonstrated in studies (Carrion and Southworth, 2018; Cheng and Wang, 2019).

Alshari et al., (2022) proposed a model addressed by artificial neural networks (limited parameters) with random forest (hyperparameter) called ANN_RF for LULC classification from Landsat 8 and Sentinel 2 images. Combining ANN and RF techniques significantly improves LULC classification accuracy in the Sana area, Yemen, compared to using these techniques separately (Alshari et al., 2023).

This article presents the results of applying machine learning techniques in classifying forest cover in Dak Lak province from multi-temporal Sentinel 2 MSI image data. Sentinel 2A images taken in November 2015 and December 2020 in Dak Lak province were used to classify land cover and then evaluate forest cover changes in the study area. Three machine learning classification algorithms (Random Forest, Support Vector Machine (SVM), Classification and Regression Tree (CART)) and the maximum likelihood method are used to classify land cover/land use using Sentinel 2 images. Then, the algorithm with the highest accuracy will be selected to evaluate the change in forest cover in the study area. Area parameters will be additionally calculated in the research results.

2. MATERIALS AND METHODOLOGY

2.1 Study area

Dak Lak is a central mountainous province in the Central Highlands region in Central Vietnam, with a natural area of 13.152 km^2 and a population of 1.8 million people of 44 ethnic groups. It borders Gia Lai to the north, Phu Yen and Khanh Hoa to the east, Lam Dong and Dak Nong to the south and Mondulkiri of Cambodia to the west (https://daklak.gov.vn/).

Dak Lak has 608,886.2 hectares of forests, including 594,488.9 ha of natural forests and 14,397.3 ha of plantation forests. The forests are evenly distributed in Dak Lak's districts, especially the border corridor with Cambodia. Dak Lak's forests are abundant, diverse and generally structured in three layers, including wood trees playing a protective role and many kinds of specialty plants with economic and scientific value. Dak Lak's forests play an important role in soil erosion control, water flow regulation and natural disaster mitigation. However, in recent years, forest cover in Dak Lak has experienced profound fluctuations due to the influence of socio-economic development, population growth and the effects of climate change.

The geographical location of the study area is shown in Figure 1.

2.2 Materials

The Sentinel-2 mission consists of two satellites developed to support vegetation, land cover and environmental monitoring. The Sentinel-2A satellite was launched by ESA on June

23, 2015 and operates in a sun-synchronous orbit with a 10-day repeat cycle. A second identical satellite (Sentinel-2B) was launched on March 7, 2017. Together, they cover all of Earth's land surfaces, large islands and inland and coastal waters every five days. The Sentinel-2 MultiSpectral Instrument (MSI) acquires 13 spectral bands ranging from Visible and Near-Infrared (VNIR) to Shortwave Infrared (SWIR) wavelengths along a 290 km orbital swath. Characteristics of Sentinel 2 satellite bands are shown in Table 1 (Pahlevan et al., 2017).

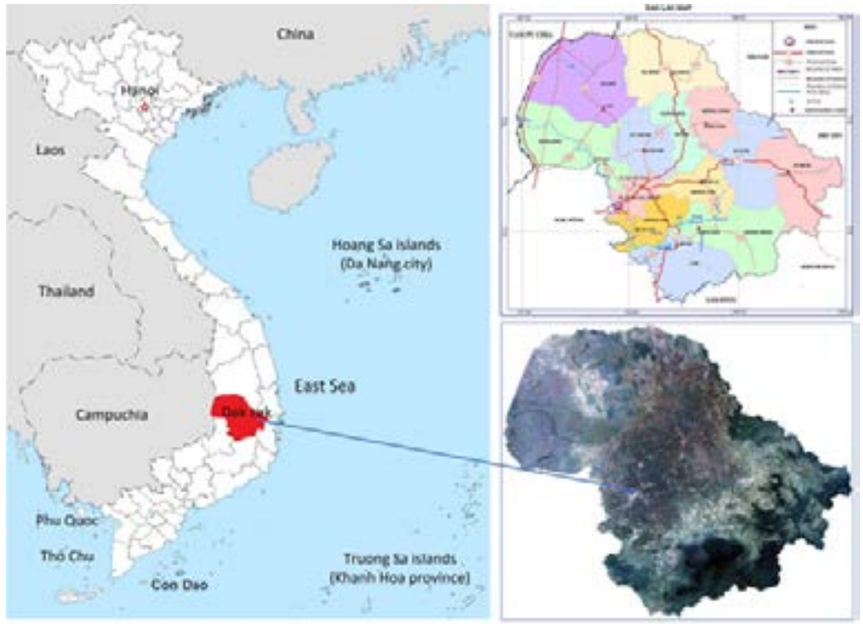

Figure 1: Geographical location of Dak Lak province.

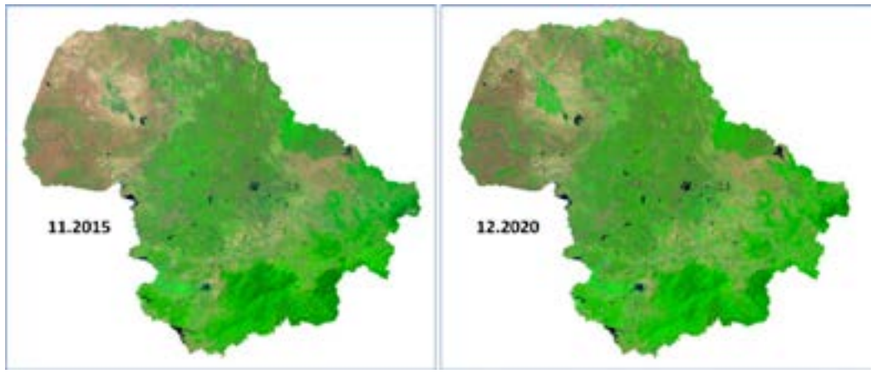

Figure 2. Sentinel 2A data in Dak Lak province in the period 2015-2020.

In this study, multispectral cloud-free Sentinel-2A images acquired between November 2015 and December 2020 were used for classifying and mapping land cover maps in the Dak Lak province (Figure 2). The Sentinel-2A data was the L2A level product, downloaded from the Copernicus Open Access Hub (https://scihub.copernicus.eu) website. The Level-2A product provides Bottom of Atmosphere (BOA) reflectance images derived from the associated Level-1C products. Characteristics of Sentinel 2A spectral bands are presented in Table 1.

Table 1. Sentinel-2 band characteristics.

Sentinel - 2 Bands	Central wavelength (µm)	Resolution (m)
Band 1 - Coastal aerosol	0.443	60
Band 2 - Blue	0.490	10
Band 3 - Green	0.560	10
Band 4 - Red	0.665	10
Band 5 - Vegetation Red Edge	0.705	20
Band 6 - Vegetation Red Edge	0.740	20
Band 7 - Vegetation Red Edge	0.783	20
Band 8 - NIR	0.842	10
Band 8A - Vegetation Red Edge	0.865	20
Band 9 - Water vapour	0.945	60
Band 10 - SWIR-Cirrus	1.375	60
Band 11 - SWIR	1.610	20
Band 12 - SWIR	2.190	20

2.3 Methodology

Sentinel 2 MSI satellite images, after being collected from the Copernicus database (https://scihub.copernicus.eu/dhus/#/home), are pre-processed to remove spectral and geometric errors and then cropped according to the boundaries of the study area. Sentinel 2 MSI spectral bands with 10 m spatial resolution (bands 2, 3, 4, 8) were used for land cover classification.

The flowchart methodology of this research is available in Figure 3.

In this study, 03 types of machine learning algorithms, including Random Forest (RF), Support Vector Machine (SVM), Classification and Regression Tree (CART), are tested to classify land cover from Sentinel 2 MSI image:

RF constructs an ensemble classifier and is one of the commonly used classifiers. RF generates many decision trees using a random selection of training datasets and factors. The two most essential input criteria for this classifier are the size of the training dataset and the number of trees generated (Han et al., 2020). Thus, RF randomly selects observations, builds a decision tree and takes the average result (Breiman, 2001). In classification using the RF algorithm, the number of decision trees (parameter NumberOfTrees) plays a very important role, greatly affecting the accuracy of the classification results.

SVM is one of the supervised learning techniques used to solve various problems related to regression and classification, first identified by Vladimir Vapnik and his colleagues in 1992. In the training phase, SVM classifiers generate an ideal hyperplane that splits several classes with the less misclassified pixels from input datasets. The kernel functions, cost parameters and gamma are key parameters for determining support vectors (Lopez et al., 2022). SVM has the advantage of being effective for large data samples such as remote sensing images and often achieves high accuracy compared to other supervised classification algorithms.

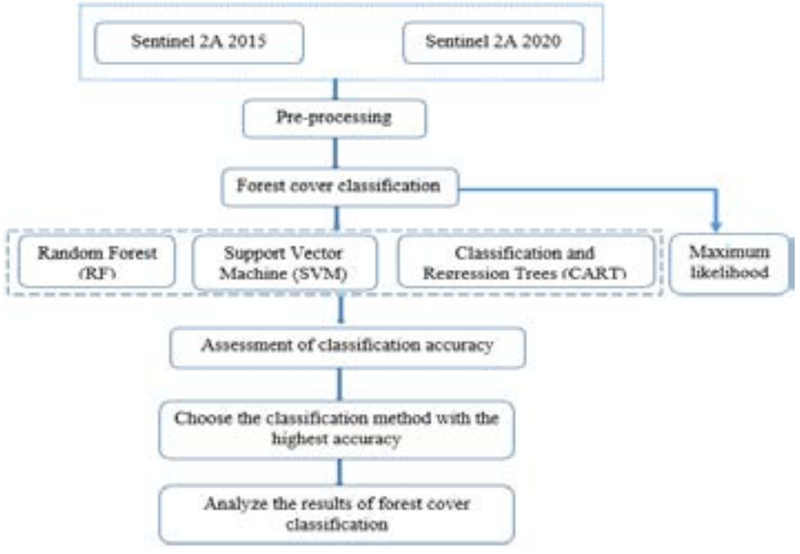

Figure 3. The flowchart of methodology for forest cover type classification using Sentinel 2 MSI.

CART is a supervised machine-learning technique commonly used in classifying objects from remote sensing images (Barragan et al., 2011; Yang and Li, 2013). Based on a predetermined threshold, CART runs by separating nodes until it reaches the terminal nodes. This method divides input data into further group sets and trees are generated using all but one of those group sets (Charbuty and Abdulazeez, 2021).

The maximum likelihood algorithm is very commonly used in classifying objects from remote sensing images and is considered the standard algorithm to compare with other classification algorithms. This supervised classification method is based on the Byes theorem.

Furthermore, the dataset is divided into training data and testing data, where training data is used to train machine learning models while testing data is used to evaluate the accuracy of the model. In this study, ten major land cover classes have been classified, including: (1) Evergreen forest, (2) Semi-evergreen forest, (3) Dipterocarpus forest, (4) Planted forest, (5) Rubber forest, (6) Coffee land, (7) Agricultural land, (8) Residential land, (9) Water body and (10) Bare land. The sample data set includes 250 samples, of which 175 samples are used to train machine learning models and 75 samples are used to evaluate the accuracy of classification results (training and testing datasets have a ratio of 7:3). Samples are polygon shaped, have different areas and are distributed over the entire region of interest. In addition, the traditional pixel-based classification method using the maximum likelihood algorithm was also tested to evaluate and compare with the classification results using machine learning algorithms. The classification accuracy is evaluated based on the Kappa index and overall accuracy, then the classification method with the highest accuracy is selected.

3. RESULTS AND DISCUSSION

Results of land cover classification in Dak Lak province (Central Highland region of Vietnam) from Sentinel 2 images, taken on November 2015 and December 2020 by using 3 machine learning classifiers (RF, SVM, CART) and maximum likelihood method are presented in Figures 4 and 5.

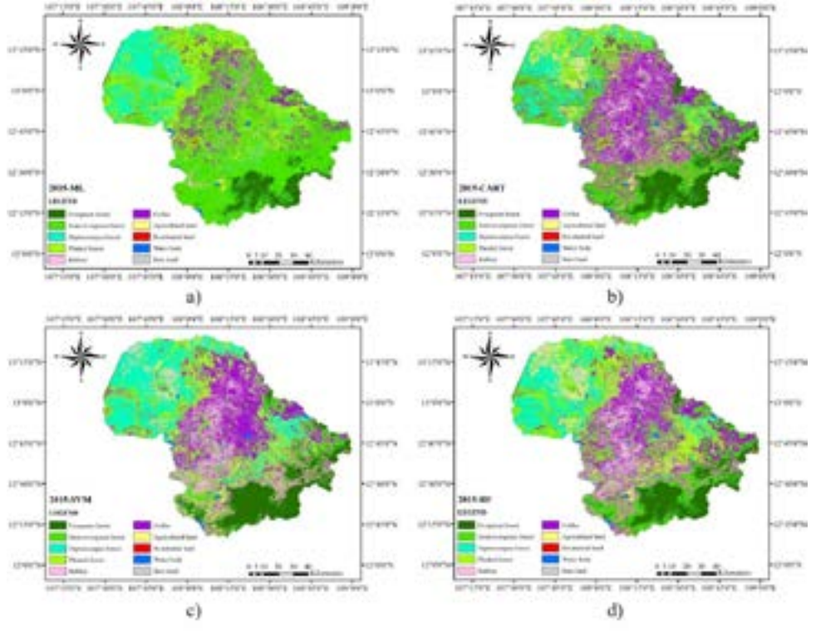

Figure 4. Results of land cover classification in Dak Lak province from Sentinel 2A images taken in November 2015 using different algorithms: a) maximum likelihood, b) CART, c) SVM, d) RF.

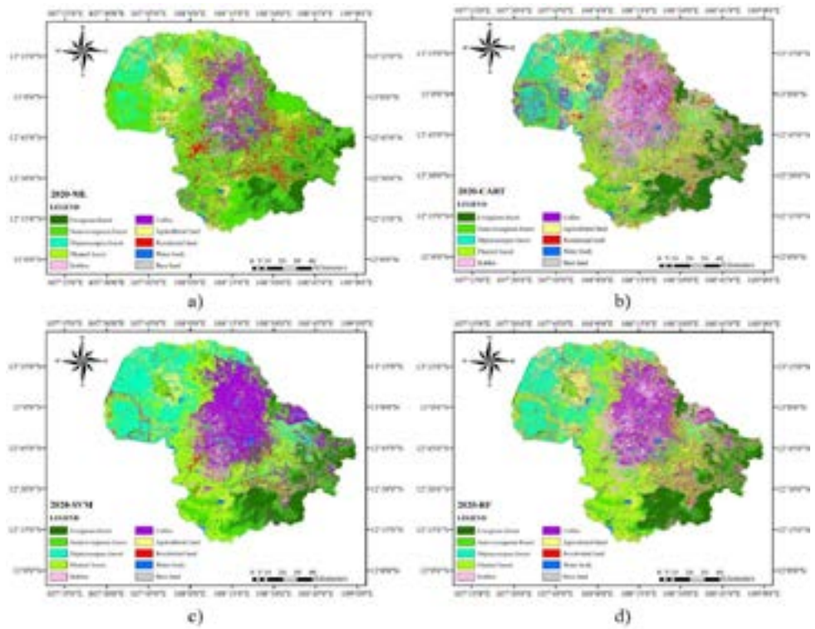

Figure 5. Results of land cover classification in Dak Lak province from Sentinel 2A images taken in December 2020 using different algorithms: a) maximum likelihood, b) CART, c) SVM, d) RF.

Table 2 presents the overall accuracy and Kappa coefficient when classifying land cover in Dak Lak province from Sentinel 2A images in 2015 using 4 different algorithms. It can be seen that the RF algorithm allows the highest accuracy of land cover classification, in which the overall accuracy and Kappa coefficient reach 90.56 % and 0.875, respectively. The CART algorithm has the second highest accuracy with overall accuracy values and the Kappa coefficient reached 87.52 % and 0.845, higher than the SVM algorithm (overall accuracy equal to 85.54 % and Kappa coefficient equal to 0.798).

Table 2. Overall accuracy and Kappa index based on classification results in 2015.

Accuracy	SVM	RF	CART	ML
Overall accuracy	85.54 %	**90.56 %**	87.52 %	75.56 %
Kappa index	0.798	**0.875**	0.845	0.695

While the maximum likelihood classifier has the lowest classification accuracy, the overall accuracy and Kappa coefficient reach 75.56 % and 0.695, respectively. Thus, with the 2015 Sentinel 2A image, machine learning techniques allow land cover classification in Dak Lak province with significantly higher accuracy than the traditional maximum likelihood method. The accuracy of classifying forest types using the RF algorithm, including (1) evergreen forest, (2) semi-evergreen forest, (3) dipterocarpus forest, (4) planted forest, (5) rubber forest, (6) coffee land from Sentinel 2A images in 2015 reached 86.71 %, 85.39 %, 81.56 %, 85 %, 86.84 % and 83.33 %, respectively.

Table 3 shows the overall accuracy and Kappa coefficient when classifying land cover in Dak Lak province from Sentinel 2A satellite images in 2020 using 4 different methods: RF, SVM, CART and maximum likelihood. Similar to the Sentinel 2A image taken in November 2015, the RF algorithm also achieved the highest accuracy of land cover classification compared to other algorithms using the Sentinel 2A image in December 2020, with overall accuracy and Kappa coefficient reaching 91.57 % and 0.883, respectively. The overall accuracy and Kappa coefficient when using SVM, CART and maximum likelihood algorithms reached 83.12 % and 0.784; 85.53 % and 0.805; 77.14 % and 0.723 (Table 3). The accuracy of classifying forest types using the RF algorithm, including (1) evergreen forest, (2) semi-evergreen forest, (3) dipterocarpus forest, (4) planted forest, (5) rubber forest, (6) coffee land from Sentinel 2A images in 2020 reached 85.31 %, 81.46 %, 80.45 %, 82.92 %, 83.76 % and 77.78 %, respectively.

Table 3. Overall accuracy and Kappa index based on classification results in 2020.

Accuracy	SVM	RF	CART	MD
Overall accuracy	83.12 %	**91.75 %**	85.53 %	77.14 %
Kappa index	0.784	**0.883**	0.805	0.723

Table 4. Changes in forest types in Dak Lak province during the period of 2015 - 2020.

Land cover objects	Area (km^2)	
	2015	**2020**
Evergreen forest	1127.30	1032.10
Semi-evergreen forest	1173.97	1006.12
Dipterocarpus forest	2194.94	2075.91
Planted forest	2980.04	2632.05
Rubber	2263.17	2355.61
Coffee	1693.72	1513.53

The results of forest cover change analysis in Dak Lak province in the period 2015 - 2020 are presented in Table 4. Analysis of the obtained results shows that most forest cover types in Dak Lak province have significantly decreased in the period 2015 - 2020, specifically:

+ Evergreen forest decreased by 95.2 km^2, from 1127.30 km^2 in 2015 to 1032.10 km^2 in 2020, equivalent to 8.44 % (about 1.69 %/year).

+ Semi-evergreen forest decreased by 167.85 km^2, from 1173.97 km^2 in 2015 to 1006.12 km^2 in 2020, equivalent to 14.30 % (about 2.86 %/year).

+ Dipterocarpus forest decreased by 119.03 km^2, from 2194.94 km^2 in 2015 to 2075.91 km^2 in 2020, equivalent to 5.42 % (about 1.08 %/year).

+ Planted forest decreased by 347.99 km^2, from 2980.04 km^2 in 2015 to 2632.05 km^2 in 2020, equivalent to 11.68 % (about 2.33 %/year).

Rubber forests increased by 92.44 km^2, from 2263.17 km^2 in 2015 to 2355.61 km^2 in 2020, equivalent to 4.08 % (about 0.82 %/year). Meanwhile, coffee land decreased by 180.19 km^2, from 1693.72 km^2 in 2015 to 1513.53 km^2 in 2020, equivalent to 10.64 % (about 2.13 %/year). The area of rubber and coffee land has opposite fluctuations due to the mutual conversion in the area of industrial crops in the study area.

4. CONCLUSION

Sentinel 2 MSI image data with 10 m spatial resolution (blue, green, red and NIR bands) can be used effectively for the forest cover types classification. In this study, 02 Sentinel 2A satellite images taken in November 2015 and December 2020 in Dak Lak province were used to classify 10 land cover objects, including 06 types of forest cover (evergreen forest, semi-evergreen forest, dipterocarpus forest, planted forest, rubber forest and coffee land). 03 common machine learning techniques, including RF, SVM and CART, were tested to classify the study area's land cover from Sentinel 2A images. In addition, the study also uses the maximum likelihood algorithm to classify land cover and compares it with the classification results by using machine learning techniques. Analysis of the obtained results shows that the RF algorithm achieved the highest accuracy of land cover classification, shown by the overall accuracy value and Kappa coefficient.

The results of classifying forest types in Dak Lak province using Sentinel 2A images show that natural forest types (evergreen forest, semi-evergreen forest, dipterocarp forest) have

significantly decreased in 2020 compared to 2015. The planted forests and coffee land areas also decreased, while the area of rubber forests increased by about 4.08 % in the period 2015-2020. The obtained results in the study provide objective and timely information that can help managers in monitoring and protecting forest resources.

5. ACKNOWLEDGEMENTS

This paper was supported by the Project: "Research and Application of artificial intelligence and geospatial technology to Build a System to Support and analyze forest resources under climate change conditions in Dak Lak Province". We would like to thank the Department of Science and Technology of Dak Lak province for funding this Project.

The authors are grateful to the European Space Agency for providing Sentinel 2 MSI images, to Google Earth for providing high-resolution remote sensing images and to Google Earth Engine for providing the image processing and storage environment.

6. REFERENCES

Alshari E., Abdulkareem M., Gawali B., 2022. Classification of land use/land cover using artificial intelligence (ANN-RF). *Frontiers in Artificial Intelligence*. Vol. 5, https://doi.org/10.3389/frai.2022.964279.

Barragan J., Ngugi M., Plant R., Six J., 2011. Object-based crop identification using multiple vegetation indices, textural features and crop phenology. *Remote Sensing of Environment, 115*, 1301 - 1316.

Basheer S., Wang X., Farooque A., Nawaz R., Liu K., Adekanmbi T., Liu S., 2022. Comparison of land use land cover classifiers using different satellite imagery and machine learning techniques. *Remote Sensing*, *14*(19), 4978, https://doi.org/10.3390/rs14194978.

Breiman L., 2001. Random Forests. *Machine Learning 45*, 5-32. https://doi.org/10.1023/A:1010933404324.

Carrion X., Southworth J., 2018. Understanding land cover change in a fragmented forest landscape in a biodiversity hotspot of coastal Ecuador. *Remote Sensing*. Vol. 10(12), 1980. Doi:10.3390/rs10121980.

Charbuty B., Abdulazeez A., 2021. Classification and regression tree algorithm for machine learning. *Journal of Applied Science and Technology Trends*. Vol. 2(1), 20-28.

Cheng K., Wang J., 2019. Forest type classification based on integrated spectral-spatial-temporal features and Random Forest algorithm - A case study in the Qinling mountains. *Forests*, *10*(7):559. https://doi.org/10.3390/f10070559.

Foga S., Scaramuzza P., Guo S., Zhu Z., Dilley R., Beckmann T., Schmidt G., Dwyer J., Hughes M., Laue B., 2017. Cloud detection algorithm comparison and validation for operational Landsat data products. *Remote Sensing of Environment 194*, 379-390. http://doi.org/10.1016/j.rse.2017.03.026.

Giang Thi Phuong Thao, Pham Thi Thu Huong, Pham Viet Hoa, Nguyen An Binh, 2023. Accuracy assessment of landcover classification based on various machine learning algorithms and remotely sensed data through Google EarthEngine: Application in Dak Lak province. *Science Journal of Natural Resources and Environment*. Vol. 46, 55-65.

Gomes V., Queiroz G., Ferreire K., 2020. An overview of platforms for big Earth observation data management and analysis. *Remote Sensing*, *12*, 1253. Doi:10.3390/rs12081253.

Han S., Kim H., Lee Y.S., 2020. Double random forest. *Machine Learning 109*, 1569-1586. https://doi.org/10.1007/s10994-020-05889-1.

Jeppesen J., Jacobsen R., Inceoglu F., Toftegaard T., 2019. A cloud detection algorithm for satellite imagery based on deep learning. *Remote Sensing of Environment*, *229*, 247-259.

Kumar A., Sinha N.,2020. Classification of forest cover type using Random Forest algorithm. *Advances in Data and Information Sciences, Part of the Lecture Notes in Networks and Systems book series* (LNNS), Vol. 94, 395-402.

Lee D.S., Shan J., Bethel J.S., 2003. Class-guided building extraction from ikonos imagery. *Photogrammetric Engineering and Remote Sensing*, *69*(2), 143-150. Doi:10.14358/pers.69.2.143.

Liu F., Dong L., Chang X., Guo X., 2022. Remote sensing image classification based on object-oriented convolutional neural network. *Frontiers in Earth Science*, *10*. https://doi.org/10.3389/feart.2022.988556.

Liu D., Xia F., 2010. Assessing object-based classification: Advantages and limitations. *Remote Sensing Letters*. Vol.1(4), 187 - 194. https://doi.org/10.1080/01431161003743173.

Lopez O., Lopez A., Crossa J., 2022. Support vector machine and support vector regression. Multivariate Statistical Machine Learning Methods for Genomic Prediction. *Springer, Cham*. https://doi.org/10.1007/978-3-030-89010-0_9.

Ouma Y., Keitsile A., Nkwae B., Odirile P., Moalafhi D., Qi J., 2023. Urban land-use classification using machine learning classifiers: comparative evaluation and post-classification multi-feature fusion approach. *European Journal of Remote Sensing*. Vol. 56(1), 2173659. https://doi.org/10.1080/22797254.2023.2173659.

Pahlevan N., Sarkar S., Franz B., Balasubramanian S., He J., 2017. Sentinel-2 MultiSpectral Instrument (MSI) data processing for aquatic science applications: Demonstrations and validations. *Remote Sensing of Environment*. Vol. 201, 47-56.

Rogan J., Chen D., 2004. Remote sensing technology for mapping and monitoring land cover and land use change. *Progress in planning*, *61*(4), 301-325. Doi:10.1016/s0305-9006(03)00066-7.

Sun X., Zhang J., Liu Z., 2005. A comparison of object-oriented and pixel-based classification approaches using QuickBird. *ISPRS Archives*, Volume XXXVI-2/W25, 3 pp.

Talukdar S., Singha P., Mahato S., Shahfahad, Pal S., Liou Y., Rahman A., 2020. Land use land cover classification by machine learning classifiers for satellite observation - a review. *Remote Sensing*, Vol. 12(7), 1135. https://doi.org/10.3390/rs12071135.

Tassi A., Vizzari M., 2020. Object-oriented LULC classification in Google Earth Engine combining SNIC, GLCM, and machine learning algorithms. *Remote Sensing, 12(*22), 3776. https://doi.org/10.3390/rs12223776.

Thakur R., Manekar V., 2020. Artificial intelligence-based image classification techniques for hydrologic applications. *Applied Artificial Intelligence*. Vol. 36(1), 2014185. https://doi.org/10.1080/08839514.2021.2014185.

Tran Anh Tuan, Nguyen Dinh Duong, 2019. Development of Landsat cloud free image data for classification of land cover, case study in Dak Lak province. *Vietnam National University Journal of Science: Earth and Environmental Sciences*. Vol. 35(4), 80-87.

Trinh Le Hung, Mai Dinh Sinh, Nguyen Nhu Hung, Le Van Phu, 2021. Automatic flood detection using Sentinel 1 images in Google Earth Engine. *Journal of Science and Technique*, *Section on Special Construction Engineering*. Vol. 8, 29-43.

Xie Y., Wang Y., Kandeepan S., Wang K., 2022. Machine learning application for short reach optical communication. *Photonics*. Vol. 9(1), 30. https://doi.org/10.3390/photonics9010030.

Yang B., Li S., 2013. Remote sense image classification based on CART algorithm. *Advanced Materials Research*. Volumes 864-867, 2782-2786.

Yuh Y., Tracz W., Matthews H., Turner S., 2023. Application of machine learning approaches for land cover monitoring in northern Cameroon. *Ecological Informatics*. Vol. 74, 101955, https://doi.org/10.1016/j.ecoinf.2022.101955.

Zhou X., Li L., Chen L., Liu Y., Cui Y., Zhang Y., Zhang T., 2019. Discriminating urban forest types from Sentinel-2A image data through linear spectral mixture analysis: A case study of Xuzhou, East China. *Forests 10(*6):478. Doi:10.3390/f10060478.

https://earthengine.google.com/. Accessed on 12 July 2023.

https://daklak.gov.vn/. Accessed on 12 July 2023.

https://scihub.copernicus.eu/dhus/#/home. Accessed on 12 July 2023.

EFFECTS OF THE STRONG EL NINO 2015-2016 ON THE SEA SURFACE SALINITY OVER SOUTHERN VIETNAM AS OBSERVED BY REMOTE SENSING DATA

Le Van Thien

Hanoi University of Natural Resources and Environment, Vietnam
Corresponding author. Email: lvthien@hunre.edu.vn

ABSTRACT

Observing and studying sea surface salinity variability is important owing to its role in atmosphere-ocean systems. Recently, the technological innovation in satellite remote sensing has provided a new chance for ocean study and observation. The effects of the strong El Nino 2015-2016 on sea surface salinity in the Southern Vietnam Sea are investigated using satellite observations. This strong El Nino event, fully established in spring 2015, reached its peak strength during November-December 2015 and has been rapidly developing into one of the three strongest El Nino episodes in recorded history. We show that a wide salinification is observed over most of the Southern Vietnam Sea during the mature phase of El Nino. Our results show that the spatial and temporal variability of sea surface salinity is different between the Southern Vietnam Sea during 2015-2016. In the northern regions, sea surface salinity increases during the mature phase of El Nino. The surface water tends to be saltier during El Nino time. The maximum sea surface salinity occurred in months with strong El Nino.

1. INTRODUCTION

With a coastline of more than 3,260 km in length, Vietnam has the potential for marine aquaculture. The government of Vietnam considers maricultural a priority in its overall strategy for marine economic development. The South Vietnam Sea is an open sea with many big islands (such as Phu Quy and Con Dao). This area has received the most considerable attention as it has the highest reserve of aquatic products in Vietnam.

Observing and studying Sea Surface Salinity (SSS) variability plays a crucial role in understanding ocean circulation and its impacts on global climate and natural water resources. The ocean salinity variability has significant effects on regional ocean circulation and indirect air-sea interactions and the resulting weather and climate events (Wang et al., 2021). Locally, variability in ocean salinity may also play a role in regulating deep circulation and heat and freshwater distribution (Qu et al., 2006). Vietnam's eastern sea is strongly influenced by major climate modes such as El Nino/Southern Oscillation (ENSO), which significantly changes evaporation, precipitation, wind, and ocean currents and further impacts the SSS. However, owing to limited historical observations, salinity remains one of the least understood fields of the ocean and climate system. Specifically, SSS variability and its relationship with ENSO in the Southern Vietnam Sea remain poorly understood. Recently, with advances in measuring technology, both in situ measurements and satellite remote sensing techniques, SSS variability has been studied extensively (Lagerloef et al., 2012; Mecklenburg et al., 2012; Fore et al., 2016). We select the strong 2015/2016 El Nino event as a case study to investigate the effects of El Nino on SSS over

the Southern Vietnam Sea.

2. STUDY AREA, DATA AND METHODS

2.1 Study area

Southern Vietnam Sea is an open sea including many large islands (Phu Quy, Con Dao). This area plays a significant role in the sea-related economy in Vietnam as it is the largest fishery production in the country. Based on natural conditions and topography, this sea area can be divided into two areas: the Southern Central Sea and the Mekong estuary.

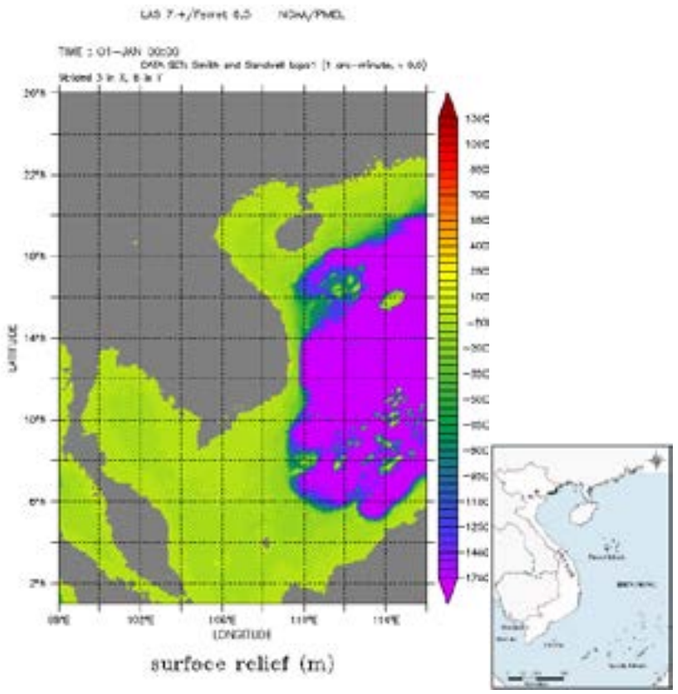

Figure 1. The study area is shown in the red box.

2.2 Data and Methods

To describe SSS variability in the Southern Vietnam Sea, this research uses remote sensing SSS products from the Mult-Mission Optimally Interpolated Sea Surface Salinity (OISSS) Level 4 V1.0 dataset (referred to as OISSS hereafter). This dataset maps the level-2 orbital swath data from the AQUARIUS/SAC-D mission, the Soil Moisture Active Passive (SMAP) mission, and the Soil Moisture and Ocean Salinity (SMOS) mission onto a 0.250 spatial and 4-day temporal grid using Optimal Interpolation (OI). The monthly SSS products are produced on a 0.25-degree spatial and a 4-day temporal grid using OI (Melnichenko et al., 2016).

Other observational data have been used to better understand the effects of El Nino on SSS. The precipitation from the GPCP (Rebert et al., 2003), the evaporation data from ECMWF Reanalysis Version 5 ERA5. The 500 hPa vertical velocity data is calculated from the ERA5 reanalysis system. In this study, anomalies of precipitation and 500 hPa vertical velocity are obtained by subtracting the climatology from its monthly values. The Nino 3.4 indexes obtained from the NOAA (National Oceanic and Atmospheric Administration) Physical Sciences Laboratory will also be used.

3. RESULTS

3.1 Monthly variability of Sea Surface Salinity during El Nino 2015-2016

To illustrate the monthly variability and annual cycle, monthly mean SSS fields are analyzed from the OI SSS over the period from 2015 to 2016. These three-month analyses are used to represent the time of season in Vietnam.

The distribution of SSS in December, January and February 2015 and 2016 in the study area is presented in Figure 2. In general, relatively low sea surface salinity (<31 psu) was found in most of the waters of the Gulf of Thailand in both two years. However, the distribution of SSS is contracyclically different between 2015 and 2016. In December, relatively high salinity was observed in the northern seas area in 2015, but relatively low salinity in 2016. The distribution of sea surface salinity this December is generally oriented South, with its value decreasing towards the South in 2015 and vice versa in 2016. The distribution of SSS is similar in January and February with high salinity observed in the Southern Sea and low in the northern sea in 2015. In contrast, the patterns display an opposite trend in 2016, in which SSS is higher in the northern sea than in the Southern Sea.

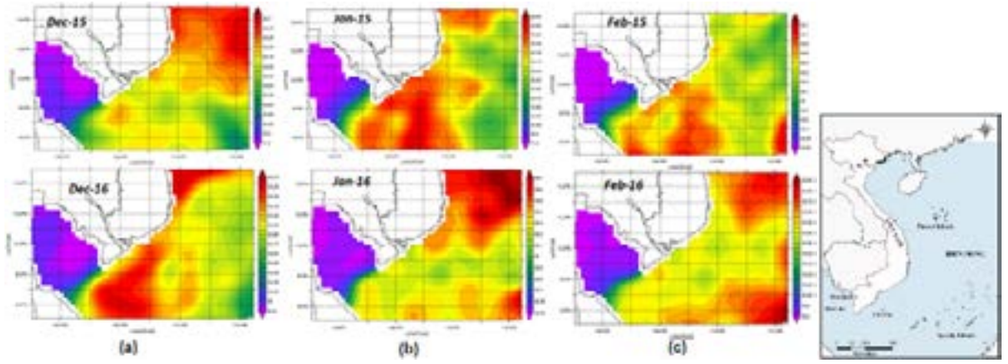

Figure 2. Spatial distribution of mean monthly SSS (psu) over the Southern Vietnam Sea in 2015-2016 in December (a), (b) January and (c) February.

Figure 3 shows the spatial distribution of mean SSS during the months of March, April and May of 2015 and 2016. SSS patterns in March are similar to those in April and May. The distribution of large-scale sea surface salinity is generally oriented South-North in 2015 and relatively uniform in 2016. In 2015, surface salinity decreased from about 34 PSU in the Southern part of the area to 33.5 PSU in the Northern part of the area. The lowest salinity, lower than 32.5 PSU, was observed in the entire Gulf of Thailand. The coastal salinity in 2016 is apparently higher than those in 2015. During these spring months, the SSS in the region becomes generally lower in most of the Northern part, saltier in the Southern part in 2015 and relatively uniform in 2016. The lowest salinity is observed in the Gulf of Thailand. Spring is a transition period from the winter monsoon to the combined monsoon with less rainfall and weak currents, such that no drastic changes in the distribution of sea surface salinity are observed.

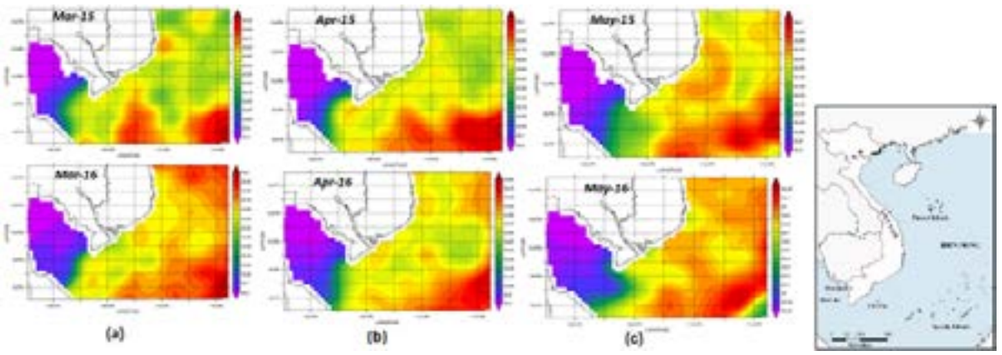

Figure 3. As Figure 2, but for (a) March, (b) April and (c) May.

SSS patterns in 2015 are similar to those in 2016 during the summer months in 2015 and 2016 (Figure 4). Salinity becomes lower in the Southwest and South, as well as slightly higher in the Northern and Eastern parts of the sea. The most noticeable changes exit in the South coastal area where a tongue of low SSS extends from the Gulf of Thailand Northeastward along the coast of Southern Vietnam, reaching as far as the center of the eastern sea of Vietnam. Relatively high salinities are observed along the coast of central Vietnam.

Compared to winter, the summer Southwest monsoon brings heavy rainfall, covering most of the East Sea and strong winds create a reverse vortex in the South. This may be a cause that may be responsible for these remarkable changes. The SSS minimum is found near the Mekong River delta and is related to a contribution from river outflows in this area.

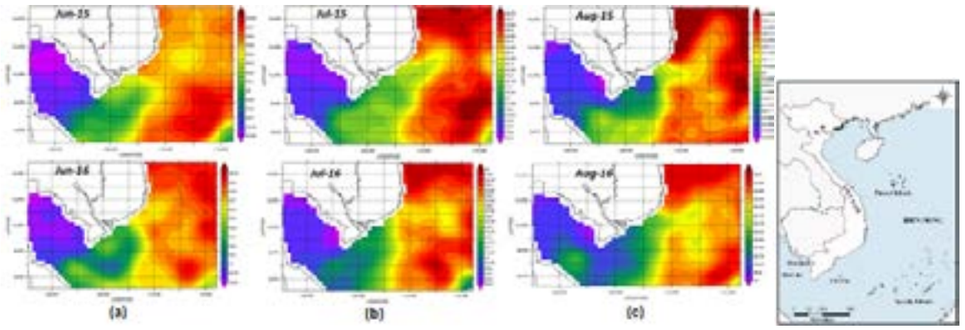

Figure 4. As Figure 2, but for (a) June, (b) July and (c) August.

The spatial distribution of SSS in 2015 and 2016 is generally similar during the autumn months (Figure 5). It should be noticeable that salinity decreases more extensively eastward in September and October than in November of two years in the Southern region. Compared with 2016, the high salinity in 2015 expanded more Southward and westward over the area. In addition, the minimum salinity of 32 PSU is found in the estuary area of the Mekong river Delta, where freshwater discharges from rivers. In general, the saltiest region is in the North of 11^{o}N and the freshest region is in the South and Gulf of Thailand. Freshwater flows from the Gulf of Thailand and the contribution of Mekong river runoff and rainfall may be favorable conditions for the minimum SSS in September and October.

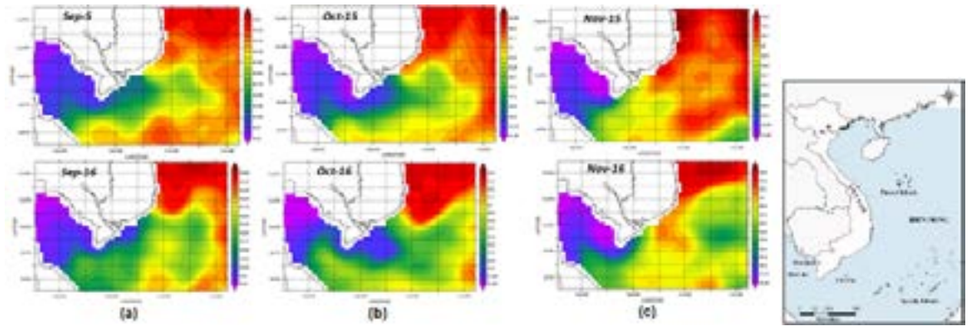

Figure 5. As Figure 2, but for (a) September, (b) October and (c) November.

3.2 El Nino 2015/2016 and SSS variability over Southern Vietnam Sea

The El Nino-Southern Oscillation (ENSO) has been previously studied extensively in the ocean-atmosphere system. Figure 6 shows the time series of the Nino 3.4 index from Jan 2015 to December 2016. From January 2015, the Sea Surface Temperature (SST) in the central equatorial Pacific began to increase and the standard deviation of sea surface temperature (SSTA) in the NINO 3.4 region reached 0.5 ^{o}C. This index continuously increased in the following months, showing that the El Nino phenomenon formed and peaked in December 2015 with a value of more than 2.5 ^{o}C. This value was lower than the maximum value during the 1997-1998 El Nino and El Nino 2015-2016 became the second strongest El Nino since available observed data. El Nino 2015-2016 ended in May 2016, lasting a total of 16 months. Thus, El Nino 2015-2016 is the longest El Nino since ENSO observation data. According to the National Oceanic and Atmospheric Administration's Oceanic Nino Index [ONI - a monthly index defined based on the three-month running mean SST anomalies averaged over the Nino3.4 region (5^{o}N-5^{o}S, 120-170^{o}W)], a super El Nino can be defined as one in which the ONI is greater than 2 ^{o}C (http://www.cpc.noaa.gov/products/analysis monitoring/ensostuff/ensoyears.shtml).

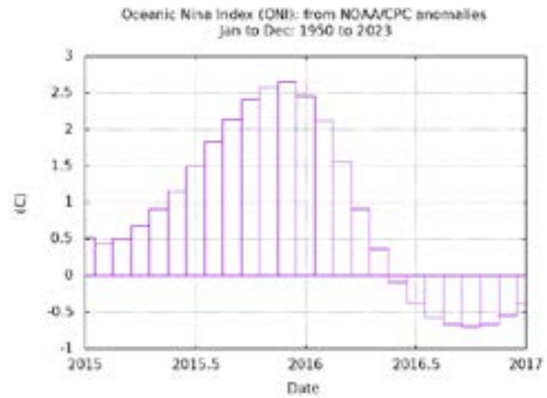

Figure 6. The anomaly Nino 3.4 index from Jan 2015 to December 2016.

Changes in SSS were observed in the Southern Vietnam Sea during the maturity of El Nino 2015/2016. To further clarify the relationship between El Nino and sea surface salinity in this area, further analyses of vertical velocity at 500 mb, evaporation and precipitation were performed using reanalyzed data from NCEP (Figure 7). The rainfall anomalies associated with El Nino are strongly month-dependent and vary most prominently from the El Nino developing month to the decaying

month. Figure 7 (bottom) shows the rainfall anomalies associated with the 2015/2016 El Nino in December of 2015 and 2016. The observations indicate harshly deficient rainfall in December 2015 but enhanced rainfall in December 2016 over the Southern Vietnam Sea. Many studies have recognized El Nino as the major source of precipitation (e.g., Wang and Li, 1990; Chang et al., 2000; Wu et al., 2003; Wang et al., 2009a; Yuan and Yang, 2012). El Nino caused the anomalous sinking of air (Fig. 7 top), leading to negative precipitation and evaporation anomalies in most of the Southern Vietnam Sea in December 2015. The situation was reversed in December 2016.

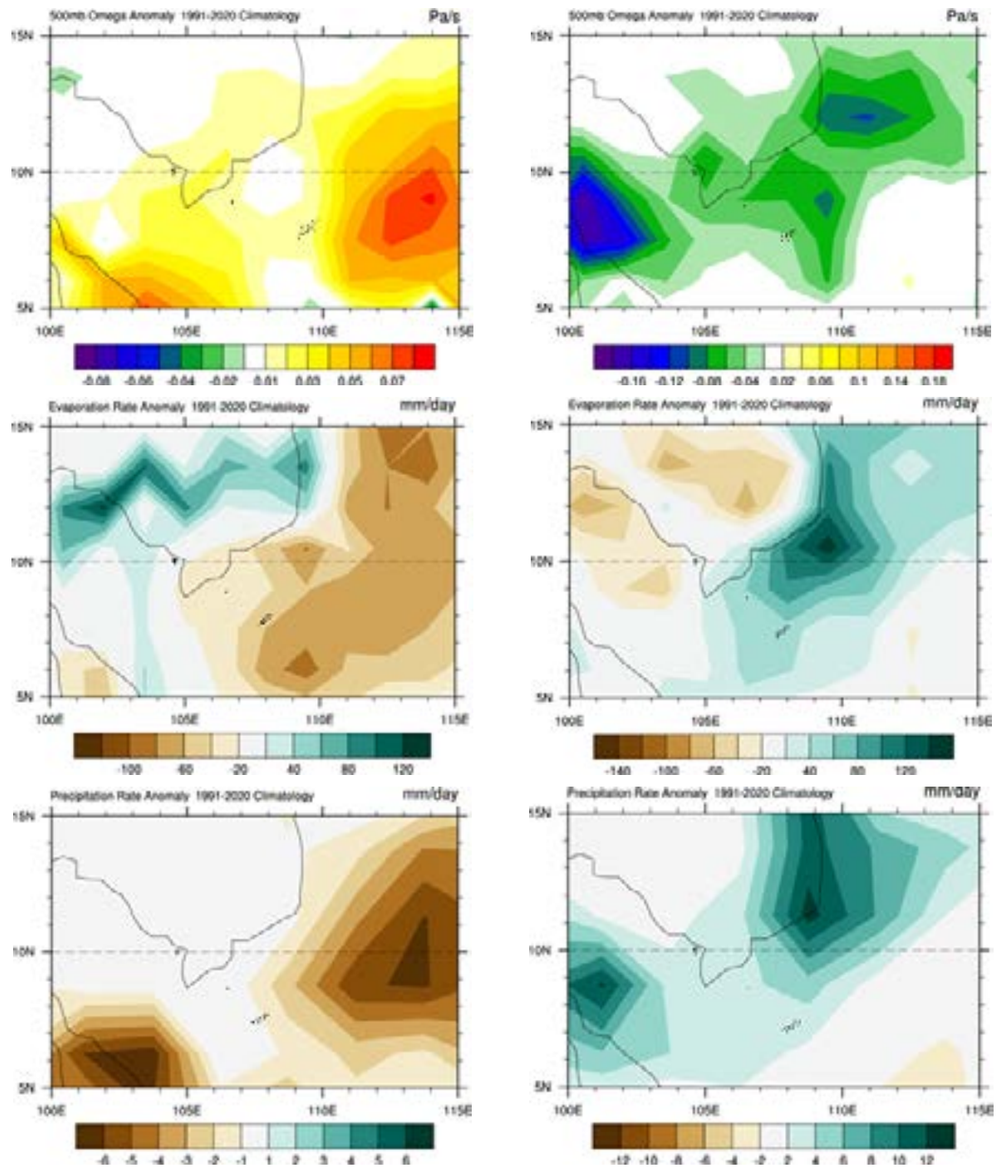

Figure 7. The anomaly vertical velocity at 500 hPa (Omega in Pa s^{-1}, positive values reflect subsiding motion), evaporation (mm/day) and precipitation (mm/day) in December 2015 (left) and 2016 (right).

Deficient or enhanced precipitation over the Southern Vietnam Sea occurs during the strong and decaying El Nino months. This is because El Nino can cause anomalous sinking of air, leading to a weakening of precipitation and a strengthening of evaporation in the Southern Vietnam Sea in December 2015. The situation was reversed in December 2016. We noted here that the spatial patterns of evaporation and precipitation in December 2015 are consistent with high values of SSS in the Northern area of 10 N but likely inconsistent in the Southern area of 10 N. This discrepancy could reflect other influences of ocean dynamics on the SSS distribution. In addition, low SSS found along the coast South of 10 N may be related to anomalous surface freshwater flux and Mekong river runoff during El Nino months. We will leave those subjects for future studies.

4. DISCUSSION AND CONCLUSION

The technological innovation in satellite remote sensing has provided a novel observation of the ocean. By using these new products, we have been able to investigate the spatial and temporal variability of SSS over the Southern Vietnam Sea during El Nino 2015-2026 months. The results show that the monthly distribution of SSS in the Southern Vietnam Sea gradually decreases Southwestward and becomes saltier in the eastern part of the region during the summer and fall time. There is a relatively uniform distribution of SSS found in most of the area during spring months. Spring is a transition period from the winter monsoon to the combined monsoon with less rainfall and weak currents, such that no drastic changes in the distribution of sea surface salinity are observed. The lowest salinity is observed in the Gulf of Thailand in whole years.

El Nino-Southern Oscillation (ENSO) was previously recognized to play an important role in the annual variations of the climate system in the East Sea. The SSS in the Southern Vietnam Sea appeared to be closely related to ENSO. During the mature months of El Nino, a wide salinification is observed over most of the region. Low SSS is visible only in a small region along the coast South of Vietnam and Mekong estuaries. In general, the SSS in the area is much saltier during the months of an active El Nino than in other months.

Our results show that evaporation, convection and precipitation responsible for SSS variability are different between 2015 and 2016 months. Deficient or enhanced precipitation over the Southern Vietnam Sea occurs during the strong and decaying El Nino months. This is because El Nino can cause anomalous sinking of air, leading to a weakening of precipitation and a strengthening of evaporation in the Southern Vietnam Sea in December 2015. The situation was reversed in December 2016. We noted here that the spatial patterns of evaporation and precipitation in December 2015 are consistent with high values of SSS in the Northern area of 10 N but likely inconsistent in the Southern area of 10 N. This discrepancy could reflect other influences of ocean dynamics on the SSS distribution.

5. REFERENCES

Chang, C.-P., Y. S. Zhang and T. Li, 2000. Interannual and interdecadal variations of the East Asian summer monsoon and tropical Pacific SSTs. Part I: Roles of the Subtropical Ridge. *J. Climate*, *13*, 4310-4325.

Fore A, Yueh S, Tang W, Stiles B and Hayashi A., 2016. Combined active/passive retrievals of ocean vector wind and sea surface salinity with SMAP IEEE Trans. *Geosci. Remote Sens*.

Wang X, Du Y, Zhang Y, Wang A and Wang T., 2021. Influence of two eddy pairs on high-salinity water intrusion in the East Sea during fall-winter 2015/2016. *Journal of Geophysical Research: Oceans, 126*, e2020JC0l6733.

Lagerloef G, Wentz F, Yueh S, Kao H Y, Johnson G C and Lyman J M., 2012. Aquarius satellite mission provides new, detailed view of sea surface salinity State of the Climate in 2011. *Bull. Am. Meteorol. Soc, 93*, S70-S711.

Mecklenburg S et al., 2012. ESA's soil moisture and ocean salinity mission: mission performance and operations IEEE Trans. *Geosci. Remote Sens, 50*. 1354-1366.

Melnichenko, O., Hacker, P., Maximenko, N., Lagerloef, G., & Potemra, J., 2016. Optimum interpolation analysis of Aquarius sea surface salinity. *Journal of Geophysical Research: Oceans*, *121*(1), 602-616.

Qu T, Du Y and Sasaki H., 2006. East Sea throughflow: A heat and freshwater conveyor. *Geophys. Res. Lett.33*. L23617.

Robert F. Adler, George J. Huffman, Alfred Chang, Ralph Ferraro, Ping-Ping Xie, John Janowiak, Bruno Rudolf, Udo Schneider, Scott Curtis, David Bolvin, Arnold Gruber, Joel Susskind, Philip Arkin and Eric Nelkin, 2003. The version-2 global precipitation climatology project (GPCP) monthly precipitation analysis (1979-present). *Journal of Hydrometeorology*, *4.* 1147-1167.

Wang and Li, 1990. Precipitation fluctuation over semiarid region in Northern China and the relationship with El Nino/Southern Oscillation. *J. Climate, 3*, 769-783.

Wu, R. G., Z.-Z. Hu and B. P. Kirtman, 2003. Evolution of ENSO related rainfall anomalies in East Asia. *J. Climate*, *16*, 3742-3758.

Wang, B., J. Liu, J. Yang, T. J. Zhou and Z. W. Wu, 2009a. Distinct principal modes of early and late summer rainfall anomalies in East Asia. *J. Climate, 22*, 3864-3875.

Yuan, Y., and S. Yang, 2012. Impacts of different types of El Nino on the East Asian climate: Focus on ENSO cycles. *J. Climate, 25*, 7702-7722.

RESEARCH THE APPLICATION OF TERRESTRIAL LASER SCANNING TECHNOLOGY FOR MINING MANAGEMENT (A CASE STUDY AT KHE CHAM MINE SITE, QUANG NINH PROVINCE)

Nguyen Ba Dzung[1]*, Dang Tuyet Minh[2], Vu Quoc Lap[3]

[1]Hanoi University of Natural Resources and Environment, Vietnam
[2]Thuyloi University, Ha Noi, Vietnam
[3]Geological and Mineral Survey company, Ha Noi, Vietnam
*Corresponding author. Email: nbdung@hunre.edu.vn

ABSTRACT

The technology of Terrestrial Laser Scanning allows a quick scan of the terrain surface and creates a database in the form of a point cloud to generate a digital model of hard-to-reach areas such as underground mines, transport rail, and mining pits where minerals have been exploited.

The paper presents the application of Terrestrial Laser Scanning technology and takes a case study at a mining pit of the Khe Cham coal mine for building digital spatial data of the mining tunnel system, transportation, ventilation, calculation of excavation volume and mining output over time in mining pit of Khe Cham coal mine, cycle 0 is 4070.19 m^3, cycle 1 is 13668.06 m^3 to ensure the coal mining management and to minimize the access and presence of people in dangerous underground mining areas.

1. INTRODUCTION

Most of the underground coal mines in Quang Ninh province have a complex geological structure. Because the mining depth of the underground mines is getting deeper and deeper, it requires more and more advances in mining science and technology to be converted to apply. This has become a challenge for coal mines belonging to the Vietnam National Coal and Mineral Industries Group. In fact, the number of accidents in underground mining has had an upward trend in recent times (Lap, 2018). Statistics show that, among the causes of accidents in underground coal mining, the most dangerous and serious cause is the collapse of the tunnel and the water bag, which often leads to a large amount of coal, soil, and rock falling into the pit area, the mining area buried people and mining vehicles, causing damage to people and machines. These two causes account for 45 % of the total number of pit accidents and occur frequently every year. For example, the accident on March 31, 2006, at the pit slope of Vu Mon area, belonging to Mong Duong coal joint stock company, and the terrible tunnel collapse on August 20, 2015, at Thanh Cong coal mine, belonging to the Hon Gai Coal Company has a serious impact to health and life of many workers due to occupational accidents. Some firms, such as Laica, Faro, and Geomax, have introduced and promoted terrestrial laser scanning systems in Vietnam. The An Thi Company used Faro's Focus3D X330 to test some caves in Quang Binh. Geomax laser scanning equipment has been applied by some authors, such as Vu Quoc Lap, Nguyen Viet Nghia, and other members in the field of mineral activities (Lap, 2018), and has initially had certain results. Eventually, researching

the application of new technologies in surveying, building a topographic database, determining the volume of excavations, and mining output in dangerous areas in underground mining is necessary for minimizing the dangers for workers directly in the mining area and serving the management of mineral exploitation in the underground mine.

2. OBJECTS AND RESEARCH METHODS

2.1 Research objects

Khe Cham coal mine belongs to Vietnam National Coal and Mineral Industries Group, located in the northeast of Cam Pha city. The North borders with Duong Huy and Bang Tay mine; The South borders with Khe Sim, Lo Tri, Deo Nai, and Coc Sau mine; the East borders with Quang Loi and Mong Duong mine; and The West borders with Khe Tam mine. The mine is currently exploiting down to -350 m with an output of about 3.5 million tons of coal per year by 2024 (Ha Long Coal company).

Figure 1. Experimental measurement area for terrestrial laser scanning Khe Cham coal mine, Cam Pha.

2.2 Research method

2.2.1 System of terrestrial laser scanner Geomax SPS Zoom 300

Geomax SPS Zoom300 was introduced and put on the market in 2014 with technical features that allow scanning according to the modes in Table 1.

With X-PAD software - a specialized data cloud processing tool for Geomax laser scanners, Geomax's scanner software includes 04 modules: BASIC, L-SCAN, TOPO, and X-CAD, which make it easy to process point clouds. X-PAD MPS software provides tools for collecting, processing, analyzing, sharing, and displaying point clouds (User manual, 2019).

Figure 2. Laser Scanner Geomax SPS Zoom 300.

Table 1. The scanning modes of Geomax SPS Zoom 300.

No	Scanning mode	Total points/ station	Scan time/ station	Resolution at 50 m	Resolution at 100 m
1	Fine	64.000.000	1h06'40"	1.96 cm	3.92 cm
2	Standard	16.000.000	0h16'40"	3.92 cm	7.85 cm
3	Fast	4.000.000	0h04'10"	7.85 cm	15.7 cm
4	Preview	1.000.000	0h01'02"	15.7 cm	31.41 cm

2.2.2 Testing the accuracy of the laser scanner Geomax SPS Zoom 300

a) Evaluation of the accuracy and odds of scanning position by laser scanning technology

To evaluate the accuracy of point location errors of Geomax SPS Zoom300 in actual conditions, a network of 6 monitoring points is arranged on the operating bench edge of a coal mine within a radius of 150 m. The distance and coordinates of the points determined by the Topcon GPT7501 electronic total station are used for comparison data. In which the angle measurement accuracy is 3"; distance measurement accuracy using mirrors is ± (2 mm + 2 ppm); mirrorless measurement accuracy is ±5 mm within a range of ≤ 250 m. Coordinates and distances between benchmark points are determined using by mirroless measurement method of the electronic total station GPT7501. When performing measuring operations, it is necessary to accurately capture the centers of the scoreboards and take the average from 3 measurements on both left and right circle positions. The signal used for positioning and scanning by laser is 20 × 20 cm in size. Its surface is covered with reflective paint in order to increase the surface reflection of the laser beam. The signs are arranged in straight lines perpendicular to the bench crest. Each bench arranges 5 benchmarks so that the maximum distance from the instrument to the target is equal to the farthest distance that the instrument can scan (Lap, 2018).

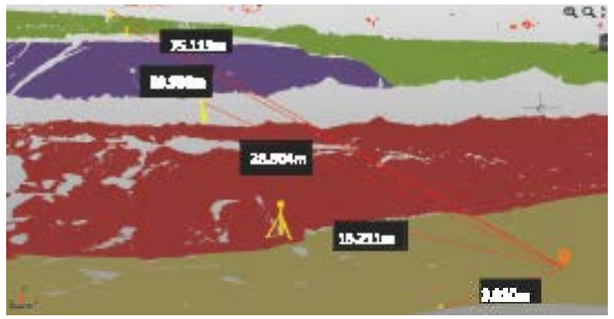

Figure 3. Diagram of checking location error of scan point by Geomax SPS Zoom 300.

The point position error determined by Geomax SPS Zoom 300 is calculated according to the following formula:

$$m_p^i = \pm\sqrt{\frac{[d^i d^i]}{n}} \quad (1)$$

di: Distance difference between measurement by electronic total station and measurement by Geomax SPS Zoom 300 at the ith measurement;

n: the number of comparative points;

The results of determining the measured distance difference between Geomax SPS Zoom 300 and Topcon GPT7501 at the mine site are shown in Figure 4.

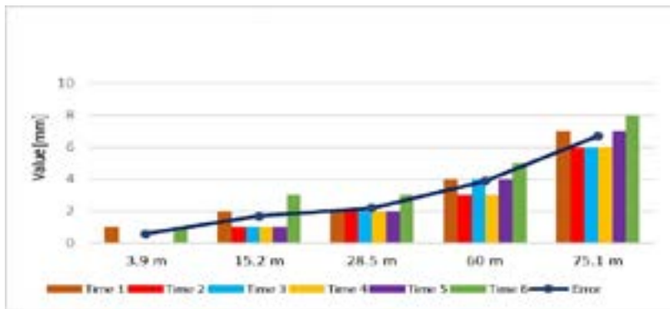

Figure 4. The chart shows the distance difference and the error of the midpoint position in determining the focal point using Geomax SPS Zoom 300 compared to Topcon GPT7501.

The test results show that the accuracy of the actual measurement result of the 3D laser scanner Zoom 300 at the pit slope of the open coal mine is consistent with the instrument's technical indicators and completely meets the requirements and technical standards in measuring and monitoring the pit slope deformation and terrain mapping (MONRE, 2013; MONRE, 2015).

b) Evaluation of the accuracy of the digital elevation model built by laser scanning technology

Evaluate the accuracy of the post-processed point cloud as well as the established digital elevation model, conduct field testing, and compare the coordinates and elevation of the digital elevation model with the coordinates, elevation of test measurement points, arrangement of measuring cross-section lines to check terrain elevation using Topcon GPT7501 electronic total station.

Table 2. Root mean squares to compare the elevation measured by Geomax SPS Zoom300 with Topcon GPT7501.

No	Actual field measurement at pit slope	Number of sections	Number of comparative points	Root mean squares (mh)
1	+ Cycle 0	6	182	± 0.0056 m
2	+ Cycle 1	6	141	± 0.0099 m

According to the test results, it is found that the accuracy of the digital elevation model built by terrestrial laser scanning meets the requirements of the research contents and consists of the instrument's specifications in order to measure and identify the movement and deformation of pit slopes (MONRE, 2013).

3. RESULTS AND RECOMMENDATION

3.1 Processing of terrestrial laser scanning data

3.1.1 Processing of point cloud data at each single scanning station

The scan data of each station is imported into the X-PAD MPS processing software through the "Import Point Cloud data" function of the processing software, and the parameters can be set to filter the scan data, such as the response strength, the distance from the scanning station to the scan point (Figure 5).

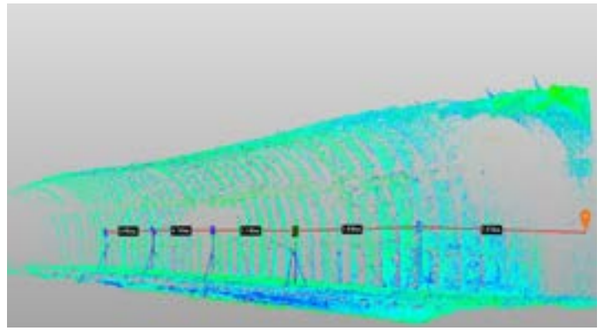

Figure 5. Single-station point cloud data after processing.

3.1.2 Pairing of scan stations, checking data coverage

To combine the scanning stations and convert the point cloud to the VN-2000 coordinate system, X-PAD MPS processing software is used as input parameters being the coordinates of the station points and the coordinates of the focus points. In the process of combining single scanning stations, it is essential to determine the common measurement criteria between the scanning stations. The accuracy of the point cloud model depends on the number of common points, the distance from the scanner to the scanning point, as well as the image quality of the target captured in the point cloud.

After merging the measuring stations to form a point cloud of the entire area, it is necessary to conduct preliminary processing of the data to check whether all the scanned data covers the scanning area or not, then compare coordinates and heights of overlapping points between 2 consecutive scanning stations to check whether the quality is satisfactory or not. Based on those

results, there will be a plan for compensating measurement (laser scanning or manual measurement with an electronic total station) if the error exceeds the permissible limit or lacks data (MONRE, 2013). The coordinates, elevation of the scanning station, and measurement criteria are entered through the "import text file" function of the X-PAD MPS processing software. In the process of pairing scanning stations, it is necessary to check the accuracy through the increments Δx, Δy, Δz of identical pairs.

3.1.3 Data standardization and additional measurements

- The point cloud data of the scanning stations is merged into a block. The data usually contains surface noise points from the discrete scanning stations before merging. The main purpose of this step is to correct and remove surface noises as well as help reduce storage capacity and speed up model data processing.

- After being filtered, the point cloud data needs to be classified by class with each attribute and must be designed so that the objects are well managed in both attributes and space, saving on storage capacity and helping manage and use in a simple and effective way.

+ The classification of data is conducted on the basis of combining intensity images, field surveys and digital images (if any). Before performing data classification, special attention should be paid to the structure of each type of mining gallery (mining pit, transport ways, ventilation channel)

+ After finishing this stage, the point data cloud must be separated into different layers based on its properties, such as ground rock, coal seam (mineral seam), and construction objects (columns, rails, electrical lines, ventilation pipes, etc.).

- Checking the point cloud data after being processed, filtered, and classified the object needs to identify areas that are missing or have no data, the areas with weak laser reflection strength, and the obscured areas; it is necessary to conduct additional measurement planning by laser scanning or by other direct measurement methods (by electronic total station, etc.).

- Topographic signals that are separated from the group of geologic signals will be the necessary data to build a digital elevation model (DEM). The 3D digital model is built using the "TOPO" module of the X-PAD MPS software or exported to a txt file (file format XYZ, RBG) to create a 3D digital model by other intermediate software, which serves to calculate the volume of soil and minerals exploited in a cycle.

- Based on the combination of coordinates, point cloud elevation, intensity, and digital images (if any), image interpretation and vector of objects are implemented. Conduct vectorization of objects to establish 3D models of the mining gallery system, and construction works to serve the mine management such as replacement, repair, fire prevention, and rescue (Nghia and Dung, 2016).

Object vectorization must ensure reasonableness between related object classes and unified data management and be deployed in the following order:

+ Boundaries of coal seams (minerals), geological constructions, geodetic control points, and geological faults.

+ Infrastructure: electrical system, ventilation, traffic, operational building, drainage system.

- After interpreting the images, it is necessary to print and conduct a comparative investigation of the objects in the field to eliminate errors.

- The digital model of the current state of the mining galleries must ensure to accurately represent the geometric relationship among the mining galleries, the underground mining constructions, the topography, and the constructions and architectures on the ground (if any) (Nghia, Long, Lap, 2017).

3.2 Terrestrial laser scanning for the construction of spatial data on the current state of the mining galleries system

In order to evaluate the applicability of terrestrial laser scanning technology, a test of terrestrial laser scanning technology is conducted to measure and collect data to create spatial data on the current state of the mining galleries system at Khe Cham coal mine, Quang Ninh: measurement time from May 15, 2017, to June 15, 2017;

In the mining galleries area, to ensure the detail of the 3D digital model, the Geomax ZOOM300 scanner is set to scan at the most detailed level of "Fine", in the panorama mode with a scanning radius (vertical/horizontal) of 270°/360°. The target for measuring 3D terrestrial laser scanning is the blackboard (25 × 25 cm) and reflective paint, which has conducted laser scanning measurement with the volume of the scanning station to serve the construction of spatial data with the current status of the mining galleries system is 9 stations;

With the ability to collect point cloud data with a resolution of up to 1.96 cm (measured at a distance of 50 m) combined with digital imaging, the SPS Zoom 300 terrestrial laser scanning technology is ideal for collecting spatial data for the establishment of 3D models of construction works, especially tunneling systems in underground mines. From the point cloud, the light-intensity image vectorizes the objects to reconstruct the 3D model of the mining galleries system (pillars, ventilation ducts, railways, and power grids) (Figure 6).

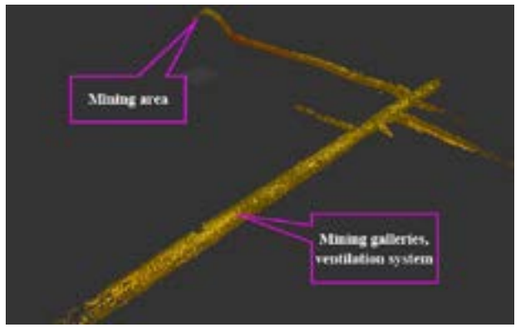

Figure 6. Line point cloud, mining area after connecting measuring stations.

3.3 Terrestrial laser scanning for mining mineral volume calculation

Experimenting with terrestrial laser scanning technology to measure and collect data for the calculation of the excavation volume and mineral output in the mining pit at Khe Cham coal mine, Quang Ninh, with 2 cycles:

+ Cycle 0 measured from May 25, 2017, to June 25, 2017;

+ Cycle 1 measured from July 18, 2017, to August 18, 2017;

In the market area, to ensure the detail of the 3D digital model, the Geomax ZOOM300 scanner is installed to scan at the most detailed level of "Fine", in panoramic mode with a scanning radius (vertical/horizontal) of 270°/360°. The target for 3D terrestrial laser scanning measurement is the blackboard (25 × 25) cm and reflective paint. Laser scanning has been carried out with the volume of the scanning station for the calculation of the excavation volume and mineral output 11 stations, of which period 0 is 5 stations, cycle 1 is 6 stations;

From terrestrial laser scanning data of period 0 and cycle 1 in the mining pit of Khe Cham coal mine, X-PAD MPS software is used to calculate the volume and volume of coal mined between 02 measurement cycles in Figure 7.

Figure 7. Khe Cham coal mine (mining pit) area point cloud measured at period 0 and period 1.

After processing point cloud data and filtering noise points, the function of X-PAD MPS software is used to generate a 3D surface model (TIN) of the mining galleries system of the mining area of 02 measurement cycles period, thereby calculating the volume and mass extracted at each cycle. Using the volumetric function from the 3D digital model (TIN) of the X-PAD MPS software (or its accompanying processing software), the volume of coal mined for two measurement cycles is shown in Table 3 (User manual, 2019).

Table 3. Coal mined volume between 2 cycles in underground mines.

No	Mining Cycle	Mining volume		Note
		Area (m^2)	Volume (m^3)	
1	Cycle 0	398.65	4070.19	
2	Cycle 1	1044.31	13668.06	
	Total	**1442.96**	**17738.25**	

4. CONCLUSION

3D Terrestrial laser scanning technology is being researched and manufactured with more and more complete measuring devices and data processing software (accuracy, scanning distance, speed, and scanning density). Laser scanning equipment was introduced by reputable manufacturers such as Leica, Faro, Trimble, Geomax, etc. to the Vietnam market with more and more affordable prices. Therefore, it is possible to research and apply 3D terrestrial laser scanning equipment in production practice for underground mining in Vietnam.

The result of 3D terrestrial laser scanning technology is point cloud data; after processing and building a digital model of the mining area has fully demonstrated the topography, topography as well as reflected the current state of the mining galleries and mining area, thereby allowing the calculation of the excavation volume and the volume of minerals to be exploited.

When comparing point cloud data, a digital elevation model with field measurements (measurement of longitudinal and transverse sections) is used to check accuracy. The comparison results show that the error of plane and height is less than or equal to ± 0.03 m. With this accuracy, terrestrial laser scanning technology can be applied to form a digital terrain model and calculate the volume of minerals exploited for underground mines while meeting the technical requirements when mining underground minerals.

5. REFERENCES

Vu Quoc Lap, 2018. Research and application of terrestrial laser scanning technology to improve the quality of geospatial data in order to improve State management capacity in mineral activities. *Summary report of the ministerial subject,* Code: 2015.07.10.

Nguyen Viet Nghia, Nguyen Quoc Long, Vu Quoc Lap, 2017. Application of terrestrial laser scanner GeoMax Zoom 300 for 3D mapping of Vietnam's open-pit mines. *Journal of Science and Technology Mining - Geology,* Vol. 58, Issue 4, 212-218, ISSN: 1859-1469.

Nguyen Viet Nghia, Vo Ngoc Dung, 2016. Study on the applicability of 3D terrestrial laser scanner in construction management - underground mining. *Journal of Science and Technology Mining - Geology*, Vol. 57, 65-73, ISSN: 1859-1469.

Ministry of Natural Resources and Environment (MONRE), 2013. Circular No. 02/2013/TT-BTNMT of March 1, 2013. Regulating the making of land status quo maps, current cross-sectional drawings of areas permitted for mineral mining; statistics and inventory of mineral reserves.

Ministry of Natural Resources and Environment (MONRE), 2015. Circular No. 68/2015/TT-BTNMT of December 12, 2015, Technical regulating of direct topographic measurement for the establishment of topographic maps and geographic base databases at scales 1:500, 1:1000, 1:2000, 1:5000.

Ha Long Coal company, 2016. Decision No 098 of May 9, 2016, focusing on leading and promoting the implementation of the Khe Cham coal mine underground mining project.

User manual for X-PAD MPS software from GeoMax, 2019.

APPLICATION FOR GIS TECHNOLOGY TO COMPARISON OF ORDINARY LEAST SQUARES AND GEOGRAPHICALLY WEIGHTED REGRESSION MODEL IN THE ASSESSMENT OF THE MARKET RESIDENCE LAND IN THUY VAN WARD, HUE CITY, VIETNAM

Le Huu Ngoc Thanh*, Nguyen Huu Ngu, Pham Thi Thao Hien, Duong Quoc Non

University of Agriculture and Forestry, Hue University, Vietnam
*Corresponding author. Email: lhnthanh@hueuni.edu.vn

ABSTRACT

The objective of this paper is to compare the application of GIS technology to compare ordinary least squares (OLS) and Geographically Weighted Regression (GWR) regression models in determining market land prices at Thuy Van ward. Research results show that both models identify the same variables affecting land prices in the market, including the following factors: Area of the land, width of road attached to the land plot, distance to hospital, being able to generate cash flow, planning information with different equation coefficients. However, the level of R^2 interpretation of both models is quite similar to the GWR model, which is 76 % lower than 78 % of the OLS model. Besides, the difference between the market land price and the estimated land price from the two models is quite similar when about 75 % of the difference goes under about 3 million VND per m^2. Thus, both models are easy to apply and have high accuracy in valuing residential land in series; also, these models contribute to improve the efficiency of land valuation.

1. INTRODUCTION

The field of Geographic Information Systems (GIS) technology has seen significant as a big and rapid progress in recent years (Li & Li, 2012). GIS technology has been widely applied to the following contents: determining land suitability (Chandio et al., 2011), real estate (Qian, 2013), land information (Longley & Cheshire, 2017), and land price (Xu & Li, 2014). Nowadays, Geographic Information Systems (GIS) and web service technologies facilitate the dissemination, exploration, and examination of land price data. The principal benefit of the GIS-based web approach resides in its incorporation of spatial-temporal analysis models and web GIS technology. Thereby, it enables a greater number of investors and administrators with restricted domain expertise in order to acquire a more comprehensive comprehension of the evolving pattern and spatial arrangement of land prices (Yang et al., 2015). The problem of determining land price is an important, a complicated and complex issue, therefore it is necessary to combine many different research methods to find the most optimal models of land price determination. In GIS technology, there are many different models to determine land prices. In this study, the author uses two models: Ordinary Least Squares (OLS) and Geographically Weighted Regression (GWR). Ordinary least-squares (OLS) regression is a statistical technique used to model a single response variable that has been measured on at least an interval scale. The technique can be applied to both single and multiple explanatory variables, including categorical variables that have been appropriately coded (Dismuke & Lindrooth, 2006). GWR is one of the collections of spatial regression methodologies that are employed in the field of geography and other related disciplines. GWR assesses a localized model of the particular variable or procedure that one aims to comprehend or anticipate through the process of fitting a regression equation to each and every characteristic within the dataset given. Subsequently, GWR formulates these distinct equations by assimilating the dependent and explanatory variables of the characteristics that are situated within the vicinity of every designated characteristic (Wheeler & Páez, 2009). There have been numerous scholarly endeavors employing these two models for investigation. In Thailand, the team of researchers has constructed a model encompassing the evaluation and market prices of land within the metropolitan region of Bangkok (Malaitham et al., 2020). An analysis of the determinants of commercial land prices in the city of Hangzhou, China, using Geographically Weighted Regression (GWR) and Ordinary Least Squares (OLS) techniques (Garang et al., 2021) and analyzing the changes in real estate prices in Taitung City, Taiwan (Wang et al., 2019). In Vietnam; particular in Hanoi, researchers have built a market house price model (Phe et al., 2016). Research results in the world as well as in Vietnam, show that the use of OLS and GWR methods in determining land prices is appropriate. However, my explicit knowledge, there has been not any single research to compare the land price model in Thuy Van ward, Hue city, Vietnam. Therefore, this is the first study as well as valuable potential one with the aim of assessing the market residence land in Thuy Van ward, Hue city, Vietnam by using OLS and GWR models to build on QGIS software. The research results have contributed to straightforward mass land valuation for this area and found the advantages of two models in determining land prices.

2. STUDY AREA AND MATERIALS

2.1 Study area

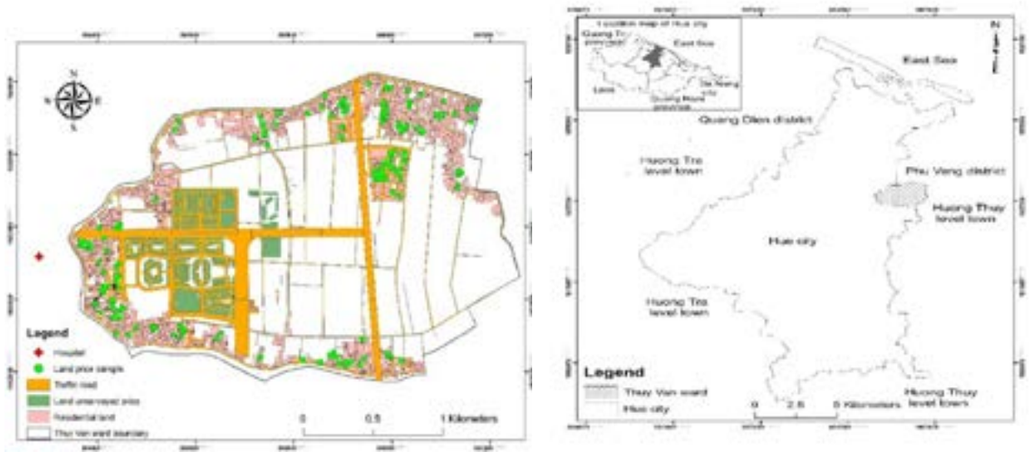

Figure 1. Cadastral map of Thuy Van ward and land price sampling point.

Thuy Van ward has a natural area of 4.92 km^2 and a population of 7,932 inhabitants. According to the 2022 socio-economic report of Hue City, in-addition, Thuy Van ward has a plain terrain located in the planning area of An Van Duong new urban area. At the same time, there is an arterial traffic route of the 49th National Highway through the connections with nationwide others, convenience for exchanges with many regions in among towns and provinces, and is a destination attracting domestic and foreign investment, and it is really creating favorable conditions for

infrastructure development and boosting up the local economy. Thuy Van ward is located as a suburban area towards the south of Hue City with much potential for urban development and a high urbanization rate when it borders Huong Thuy town to the east and Vy Da ward to the west. It is bordered by a line of distinction between An Dong ward and Xuan Phu ward to the South and the North by Phu Thuong ward and Phu Vang district.

2.2 Materials

The study uses the following data collected, such as cadastral maps from the Information Technology Center, Department of Natural Resources and Environment of Thua Thien-Hue province. In addition, we collected 200 transferred land plots, and the factors affecting the land price were determined to be suitable for the area. It aims to collect information about transferred land plots, including land prices and other information in Thuy Van ward, Hue City to run 2 models in QGIS.

3. METHODOLOGY

The research process consists of 5 stages as follows:

Figure 2. Data processing process.

Stage 1: Collecting land price data, factors which are affecting land price, cadastral map

The study was conducted to collect 200 transferred land plots, and the factors affecting the land price were determined suitable for the area, including the area of the land, width of road attached to the land plot, distance to the hospital, Ability to generate cash flow; Planning information and information about residential land price as shown in Table 1 and the cadastral map in 2022.

Stage 2: Building a current map

The study was conducted using the FME tool to convert all data to the current status map with the VN2000 coordinate system with a 3-degree projection zone of Thua Thien-Hue province.

Stage 3: Giving land price data and land parcel information, factors which are affecting land price

Use the important tool to bring all information from Excel linked to the land plot information so that the land plot has all the data to ensure the process of running the model.

Stage 4: Running OLS, GWR models

This study applies the OLS model and GWR model with tools on QGIS and edited/renewed the results from the two models mentioned above.

Stage 5: Comparing the results of two models

The results of the two models are compared from parameters such as R2, AICC, multi-collinearity, significance level of variables, residuals, and normal distribution.

Table 1. Variable format for land price model.

No.	Variable symbol	Description	Unit	Type
1	LP	Land price (Dependent variable)	million vnd/m^2	Quantitative
2	AL	Area of the land	m^2	Quantitative
3	WD	Width of road attached to the land plot	m	Quantitative
4	DH	Distance to hospital	m	Quantitative
5	CF	Ability to generate cash flow	1= yes; 0 = no	Dummy variable
6	PI	Planning information	1= yes; 0 = no	Dummy variable

4. RESULT AND DISCUSSION

In the process of evaluating and building a land valuation model, several models can be selected, but this study focuses on comparing the two models, OLS and GWR, as a case to illustrate for this paper.

4.1 OLS model

Using the OLS tool in Spatial Statistics in QGIS to run the model results, the results are shown in Table 2 below.

Table 2. Summary of OLS results - model variables.

Variable	Symbol	Coefficient [a]	Std. Error	t- Statistic	Probability [b]	VIF (c)
Intercept		19.148	1.439	13.308	0.0000	
Area of the land	AL	-0.023	0.003	-7.818	0.0000	1.063
Width of road attached to the land plot	WD	0.416	0.028	14.982	0.0000	1.556
Distance to hospital	DH	-0.002	0	-6.999	0.0000	1.408
Ability to generate cash flow	CF	2.091	0.639	3.271	0.0010	1.386
Planning information	PI	4.826	0.954	5.057	0.0000	1.257

Adjusted R-Squared [d]: 0.78000l; Prob(>F), (5.165) degrees of freedom: 0.000000*

Akaike's Information Criterion (AICc) [d] = 880

The data results from Table 2 show that the OLS land pricing model is significant with sig = 0.00 < 0.05, and the model explains 78 % of the land price variation with the following influencing factors: Area of the land; Width of road attached to the land plot; Distance to hospital; Ability to generate cash flow; Planning information. The AICc value is achieved at 880, and the VIF results are all < 2, so there is no multi-collinearity phenomenon. The variables are entirely independent of the impact on land prices. Thus, the OLS model builds the land price determination equation as follows:

$$LP = 19.148 - 0.23 \times AL + 0.416 \times WD - 0.002 \times DH + 2.091 \times CF + 4.826 \times PI$$

Table 3. The importance of the factors affecting the land price of the OLS model.

No.	Variable symbol	Description	The absolute value of the coefficient	Percentage (%)	Rank
1	AL	Area of the land	0.023	0.31	4
2	WD	Width of road attached to the land plot	0.416	5.65	3
3	DH	Distance to hospital	0.002	0.03	5
4	CF	Ability to generate cash flow	2.091	28.42	2
5	PI	Planning information	4.826	65.59	1
		Total	**7.358**	**100.00**	

At the same time, the results of Table 3 also show that the influence of the factors on the price is evaluated in order, with the most important factor being planning information at 65.59 % and the least influential factor being distance to hospital with 0.03 %. This is consistent with the fact that when the price of land in this area increases, it is concentrated in areas with planning information related to road widening and construction of housing projects such as Ecogarden, Royal Park, and Parks. FPT technology, eco-tourism area, etc. The rest of the remaining areas do not have projects, and land prices are often less volatile and low because the degree of urbanization here is relatively low, reflecting the current situation of rural landscape in residential areas.

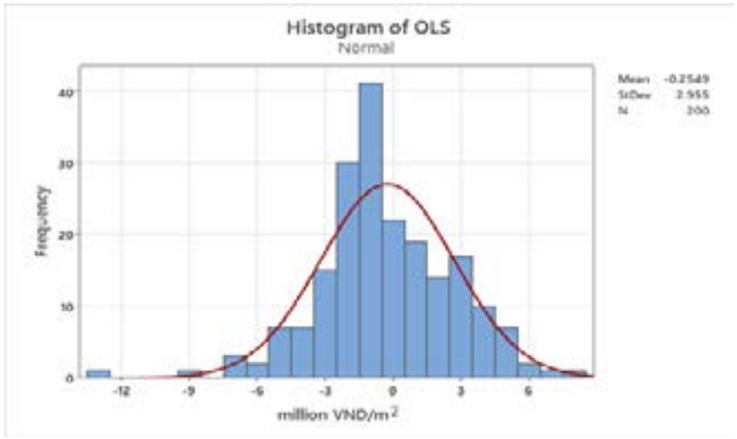

Figure 3. Average distribution histogram OLS model.

In addition to the results of the model's variable parameters, the research results also show that the model's residuals are normally distributed with a relatively low standard deviation of 2.955, and the mean is -0.2549.

4.2 GWR model

Using the GWR tool in Spatial Statistics in QGIS to run the model results, the results are shown in Tables 4 and 5.

Table 4. Results of OLS and GWR models.

	OLS	GWR
Adjusted R^2	0.78	0.76
AICc	880	898

The results from Table 4 show that the GWR model has an Adjusted R2 = 0.76 value with a significant explanation for land price change of 76 %, which is 78 % lower than that of the OLS model in addition. AICc value of 898, which is greater than 880 of the OLS model, also shows that the OLS model has higher performance and better fits to the data set. In addition, the values of conditional Number (CN) range from 10-29, so there is no multi-collinearity. The GWR model builds the land price determination equation as follows:

$$LP = 15.176 - 0.020 \times AL + 0.519 \times WD - 0.004 \times DH + 2.45 \times CF + 4.433 \times PI$$

Table 5. Summary of OLS, GWR results.

Variable	Symbol	Coefficient of OLS	Coefficient of GWR
Intercept		19.148	15.176
Area of the land	AL	-0.023	-0.020
Width of road attached to the land plot	WD	0.416	0.519
Distance to hospital	DH	-0.002	-0.004
Ability to generate cash flow	CF	2.091	2.45
Planning information	PI	4.826	4.433

Table 6. The importance of the factors affecting the land price of the GWR model.

No.	Variable symbol	Description	The absolute value of the coefficient	Percentage (%)	Rank
1	AL	Area of the land	-0.020	0.27	4
2	WD	Width of road attached to the land plot	0.519	6.99	3
3	DH	Distance to hospital	-0.004	0.05	5
4	CF	Ability to generate cash flow	2.45	32.99	2
5	PI	Planning information	4.433	59.70	1
		Total	**7.426**	**100.00**	

The data results in Tables 5 and 6 show that both models have the same variables with positive correlation with the width of the road attached to the land plot, ability to generate cash flow; planning information and negatively correlated with distance to the hospital and area of the land. At the same time, the results also show that both models have the same order of factors affecting land price, only the percentage is different. The GWR model with the most critical factor is planning information at 59.70 %, and the least influential factor is to keep a distance from the hospital at 0.27 %.

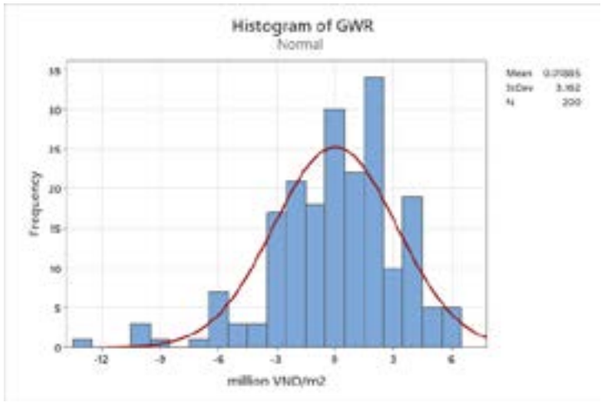

Figure 4. Normal distribution histogram GWR model.

In addition to the results of the model's variable parameters, the research results also show that the model's residual normal distribution has a higher standard deviation (SD) than the OLS model when the value is 3.162 and the mean value is 0.01885.

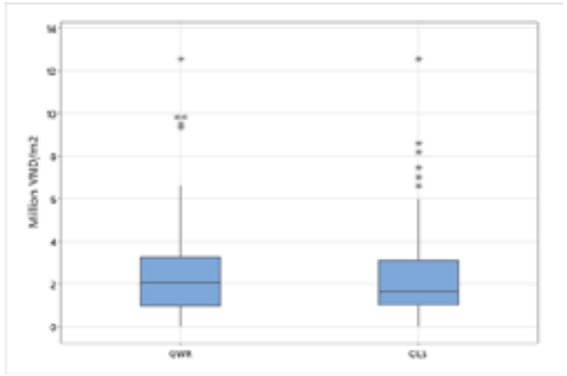

Figure 5. Residual absolute value boxplot of 2 models.

The results show that after taking the absolute value of the residuals of the two models, the errors of the two models are similar when both models have 75 % error at less than 3 million VND/m^2. However, the OLS model shows that at less than 50 %, the GWR model shows a result of 2 million VND/m^2, while the OLS model is only about 1,6 million VND/m^2 lower. Thus, the OLS model with a normal distribution of residuals shows that the level of prediction error is relatively lower than that of the GWR model.

The research results show that the land price determination model built by the OLS model has a higher level of significance and relevance. However, the GWR model has the advantage that there are map layers of each variable representing the distribution in space, supporting the observation of the impact of variables on land prices.

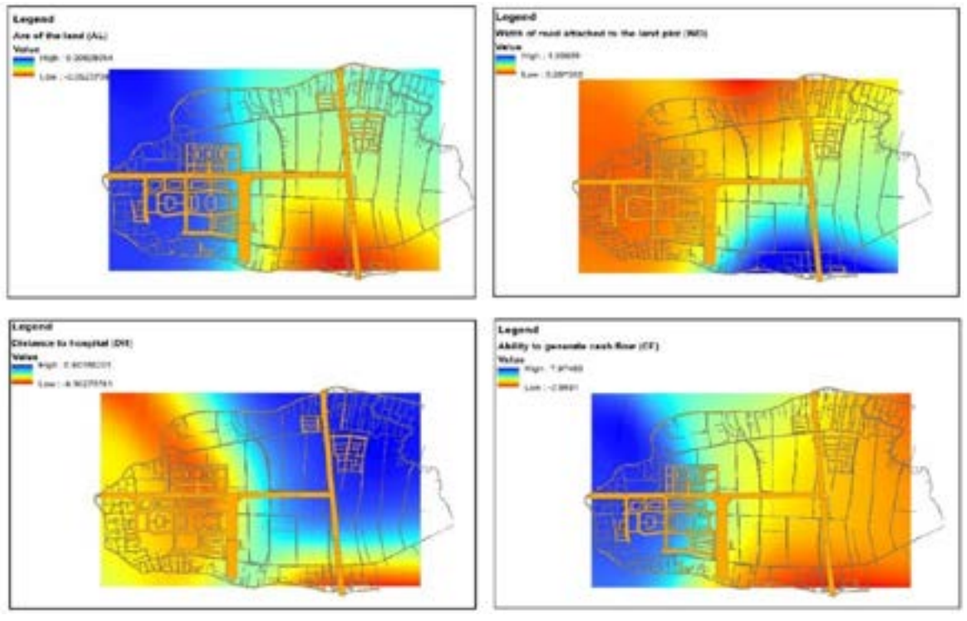

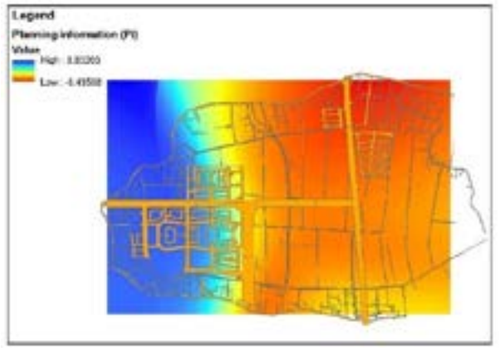

Figure 6. The distribution of the influence of factors on land prices in Thuy Van ward.

In Figure 6, the blue portion indicates a significant level of influence for that particular factor and vice versa for the red color. The results obtained from conducting spatial analysis on each factor concerning residential land prices, using the GWR model, reveal that the western area of Thuy Van ward, bordering the center of Hue city and housing projects, exhibits notable characteristics. When the concentration of blue is observed in the western region, it signifies the area favorable suitability for business activities. Furthermore, factors such as cash flow and planning information contribute to the influence on land prices. On the contrary, the eastern area of Thuy Van ward is affected by the distance factor to the hospital because this area is quite far from the hospital and the greater the distance to the hospital, the lower the land price will tend to be. The support of spatial analysis in the GWR model is clearly an advantage in assessing the factors affecting land prices in terms of surface space, which the OLS model does not provide.

5. CONCLUSION

Research results have built two land valuation models, OLS and GWR, which are being supported by GIS technology. The study analyzed the similarity of both models that have been significant with the factors affecting land price, including area of the land; width of road attached to the land plot; distance to the hospital; ability to generate cash flow; and planning information. In the same vein, the level of explanatory significance of both OLS models and GWR are both high, 78 % and 76 %, respectively. However, the results also show that the GWR model brings about image results in terms of spatial analysis of factors, supporting in terms of factor evaluation according to the spatial surface area.

6. REFERENCES

Chandio I, A, Matori A,-N., Lawal D, U., & Sabri S., (2011). GIS-based land suitability analysis using AHP for public parks planning in Larkana city. *Modern applied science, 5*(4): 177.

Dismuke C., & Lindrooth R., (2006). Ordinary least squares. *Methods and Designs for Outcomes Research, 93*(1): 93-104.

Garang Z., Wu C., Li G., Zhuo Y., & Xu Z., (2021). Spatio-temporal non-stationarity and its influencing factors of commercial land price: a case study of Hangzhou, China. *Land 10*(3): 317.

Li X., & Li S., (2012). Research and development of virtual 3D geographic information systems

based on skyline. *AISS 4*(2), 118-125.

Longley P, A., & Cheshire J, A., (2017). Geographical information systems. The Routledge Handbook of Mapping and Cartography. *Routledge*, 251-258.

Malaitham S., Fukuda A., Vichiensan V., & Wasuntarasook V., (2020). Hedonic pricing model of assessed and market land values: A case study in Bangkok metropolitan area, Thailand. *Case Studies on Transport Policy, 8*(1): 153-162. https://doi.org/10.1016/j.cstp.2018.09.008.

Phe H, H., Comber A., Harris P., Nguyen Q., Chi K., & Tran H., (2016). Local variation in hedonic house pricing in Hanoi, Vietnam: A spatial analysis of status qualit. *Issue: International Conference on GIS cience Short Paper Proceedings, 1* (1),

Qian R., (2013). The application of GIS in the real estate management system. Proceedings of the 2012 international conference of modern computer science and applications. *Springer*, 553-558.

Wang W,C., Chang Y,J., & Wang H,C., (2019). An application of the spatial autocorrelation method on the change of real estate prices in Taitung city. *International Journal of Geo-Information, 8*(6), 249.

Wheeler D, C., & Páez A., (2009). Geographically weighted regression, In: Handbook of applied spatial analysis: Software tools, methods and applications. *Springer*, 461-486.

Xu Z., & Li Q., (2014). Integrating the empirical models of benchmark land price and GIS technology for sustainability analysis of urban residential development. *Habitat International, 44*,79-92.

Yang Y., Sun Y., Li S., Zhang S., Wang K., Hou H., & Xu S., (2015). A GIS-based web approach for serving land price information. *International Journal of Geo-Information, 4*(4): 2078-2093.

QUANTITATIVE CORRELATION OF FRACTURE ORIENTATION DISTRIBUTION AND THEIR RELATIONSHIP WITH TECTONIC CHARACTERISTICS IN NAM DU ARCHIPELAGO AREA, KIEN HAI DISTRICT, KIEN GIANG PROVINCE, VIETNAM

Phi Truong Thanh[1]*, Vu Ngoc Binh[2], Van Duc Tung[3], Nguyen Quang Minh[4], Do Manh Tuan[1], Vu Thi Hong Cam[1]

[1]Hanoi University of Natural Resources and Environment, Vietnam
[2]Hydraulic Construction Institute, Vietnam Academy for Water Resources
[3]Institute of Geological Science, Vietnam Academy of Science and Technology
[4]Hanoi University of Mining and Geology, Vietnam
*Corresponding author. Email: ptthanhdc@hunre.edu.vn

ABSTRACT

This paper presents the analytical results of the quantitative correlation of fracture orientation distribution of 3016 measurements at 102 survey sites at three islands of Hon Lon, Hon Ngang and Hon Mau belonging to Nam Du Archipelago Area in Kien Hai district, Kien Giang province of Vietnam. The obtained analytical results have shown that the smallest correlation value among survey sites on the Hon Lon island is 0.71 % and their highest correlation value is 0.98 %; between the Hon Lon island and Hon Ngang island is 0.60 %; between Hon Ngang island and Hon Mau island is 0.67 %. The analytical results of the quantitative correlation of fracture orientation distribution between survey sites on the Hon Lon island and among these islands clearly reflect the tectonic stress field caused rock deformation according to the compression directions: NE-SW, NW-SE, sub-longitude and sub-latitude, suitable to regional tectonic conditions.

1. INTRODUCTION

A fracture domain is characterized by the volume of rock mass with similar properties: orientation, trace length and spacing. Piteau and Russell, (1971) used the fracture orientation in rock mass measured along a scan line to propose a cumulative sum technique to indicate the location of structural domains. Miller, (1983) plotted the discontinuity orientations on a stereonet as poles by using the lower-hemisphere Schmidt projection, then compared the stereonets with data from different areas of the rock mass using a contingency table derived by the chi-square method. Kulatilake PHSW et al., (1990) and Truong Thanh et al., (2021) analyzed the structural homogeneity of rock masses. Mahtab and Yegulalp, (1984) subsequently divided the upper-hemisphere Schmidt diagram into 100 quadrilateral squares of equal area to identify the structural domains. Dershowitz et al., (1998) used fracture orientation and their frequency along a borehole to determine structural domains. Martin et al., (2004) used the method of quantitative correlation of fracture distribution to divide into structure domains at the EKATI Diamond Mine in northern Canada. Phi et al., (2012) used the method for identifying structural domain boundaries along the tunnel. Li et al., (2015) used the correlation coefficient to quantify the degree of similarity between two populations by considering nine fracture parameters. However, they are not considered simultaneously. Truong Thanh et al., (2015) delineated the fracture domain's boundary along the borehole by using lower

fracture correlation coefficients. Recently, Truong Thanh and Hong Thinh, (2018) used the method of the fracture correlation coefficients among survey sites to determine the relationship between the fracture domain and deformation phases on the Co To - Thanh Lan island in Quang Ninh province of Vietnam.

2. METHOD

This study uses the correlation method to calculate the correlation coefficient of fracture frequency distribution between two stereonet windows of two different survey sites. The calculation is carried out based on the number of fracture poles in each cell on the stereonet window, which is plotted on the lower hemisphere projection (Figure 1).

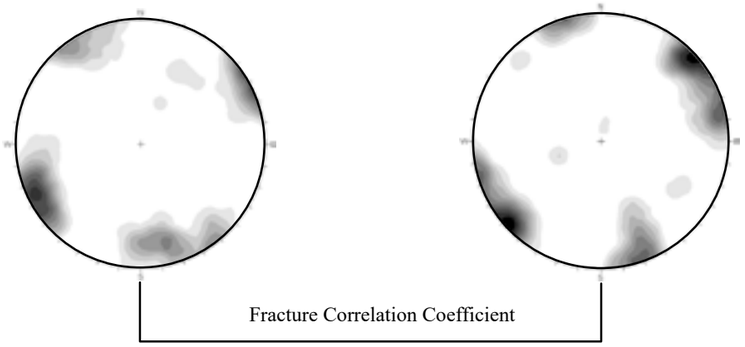

Figure 1. Stereonet contour poles of two survey sites (two stereonet windows).

The calculation of the fracture correlation coefficient between two stereonet windows is carried out by using Equation 1.

$$R(x,y) = \frac{\sum_{i=1}^{n}(x_i - \overline{X})(y_i - \overline{Y})}{\sqrt{\sum_{i=1}^{n}(x_i - \overline{X})^2}\sqrt{\sum_{i=1}^{n}(y_i - \overline{Y})^2}} \quad (1)$$

Where: (x_1, y1), (x_2, y2), ..., (x_n, yn) are n pairs of observations of a random sample of two random variables X and Y; $\overline{X}$ and $\overline{Y}$ are the average values of a fractured number of two stereonet windows, while x_i is the fracture number which appears in each cell of the first stereonet window and y_i is the fracture number which appears in each cell of the second stereonet window.

The values of x_i and y_i can occur within 324 cells in each stereonet window if each cell is divided into 10×10° according to the values of dip direction and dip angle. The correlation coefficient expresses the strength of the association between the two variables from two stereonet windows. These values always lie within (-1, 1) and they are independent of the magnitude of the variables. If the correlation coefficient is -1, it means perfect negative correlation; if the correlation coefficient is 0, it means no correlation; and if the correlation coefficient is 1, it means perfect positive correlation.

3. DATA

3.1 Fracture orientation collection on Hon Lon island

Fracture orientation collection on Hon Lon island at 63 survey sites is presented in Figure 2.

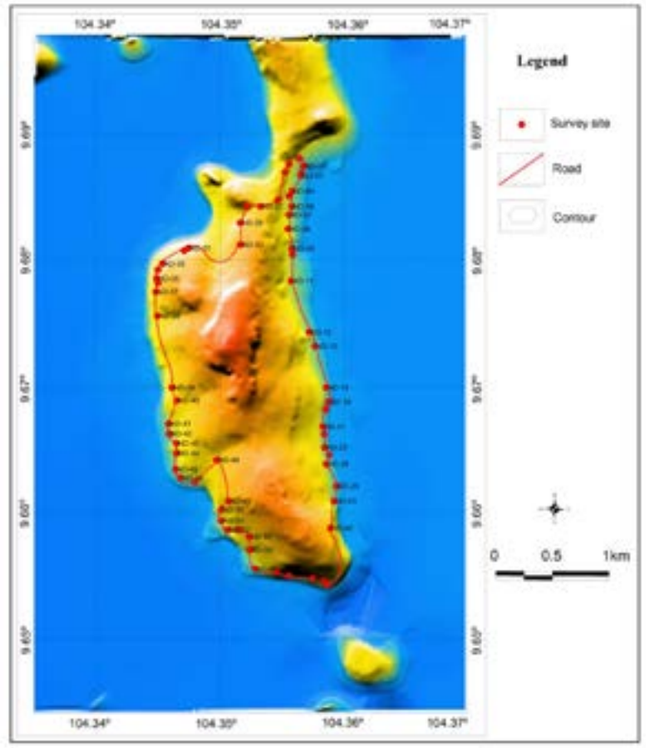

Figure 2. Location map of survey sites for collecting fracture orientation on Hon Lon island.

3.2 Fracture orientation collection on Hon Ngang island

Fracture orientation collection on Hon Ngang island at 20 survey sites is presented in Table 1 and Figure 3.

Table 1. Locations and fracture number at survey sites on Hon Ngang island.

No	Survey site	Longitude	Latitude	Fracture number	No	Survey site	Longitude	Latitude	Fracture number
1	HN-01	104.400159°	9.670687°	92	7	HN-14	104.400526°	9.665553°	65
2	HN-03	104.402259°	9.674153°	92	8	HN-15	104.400309°	9.665320°	10
3	HN-04	104.401826°	9.674387°	102	9	HN-16	104.396992°	9.663853°	36
4	HN-07	104.399126°	9.672653°	107	10	HN-18	104.396192°	9.663903°	76
5	HN-11	104.399703°	9.675327°	89	11	HN-20	104.395226°	9.663970°	102
6	HN-12	104.402076°	9.672700°	64					

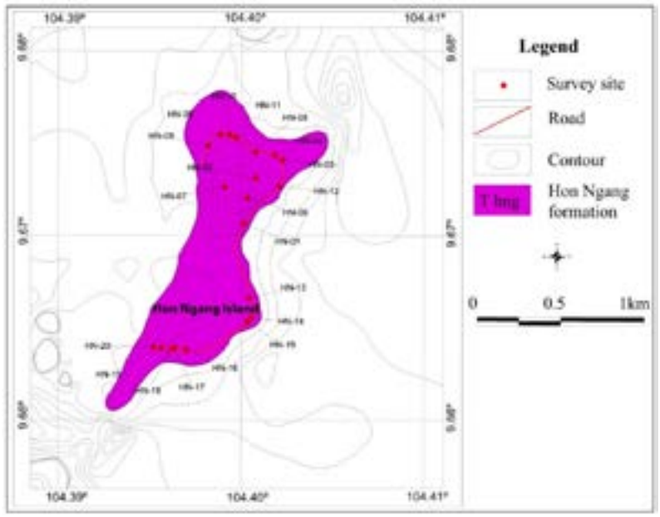

Figure 3. Location map of survey sites for collecting fracture orientation on Hon Ngang island.

3.3 Fracture orientation collection on Hon Mau island

Fracture orientation collection on Hon Mau island at 7 survey sites is presented in Table 2 and Figure 4.

Table 2. Locations and fracture number at survey sites on Hon Mau island

No	Survey site	Longitude	Latitude	Fracture number	No	Survey site	Longitude	Latitude	Fracture number
1	HM-01	104.4005332°	9.63723952°	103	2	HM-03	104.4030002°	9.63927347°	11

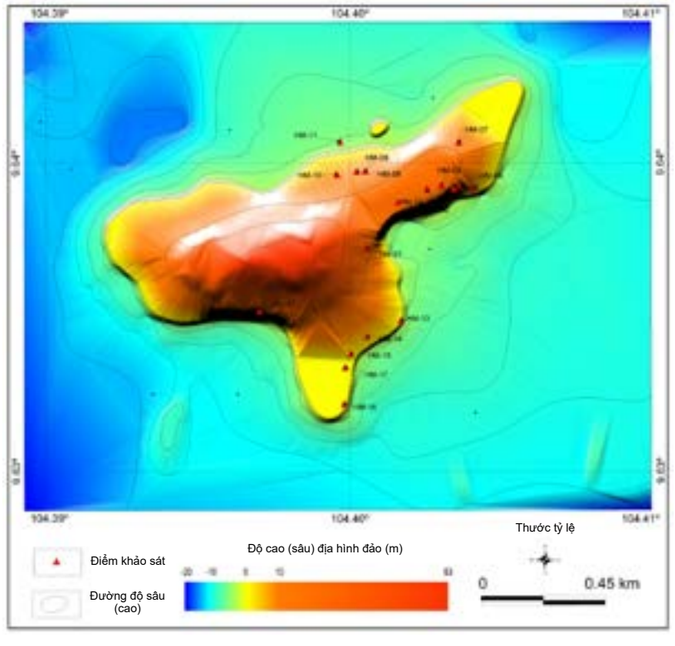

Figure 4. Location map of survey sites for collecting fracture orientation on Hon Mau island.

4. RESULTS

4.1 Quantitative correlation calculation of fracture orientation distribution

Quantitative correlation calculation of the fracture orientation distribution on the islands of Hon Lon, Hon Ngang and Hon Mau, belonging to the Nam Du archipelago, is conducted at survey sites on each island and among pairs of islands.

4.1.1 Quantitative correlation calculation of fracture orientation distribution at survey sites on Hon Lon island

Quantitative correlation calculation of the fracture orientation distribution on Hon Lon island is carried out by grouping adjacent survey sites into groups (Figure 5) and calculating the quantitative correlation between them.

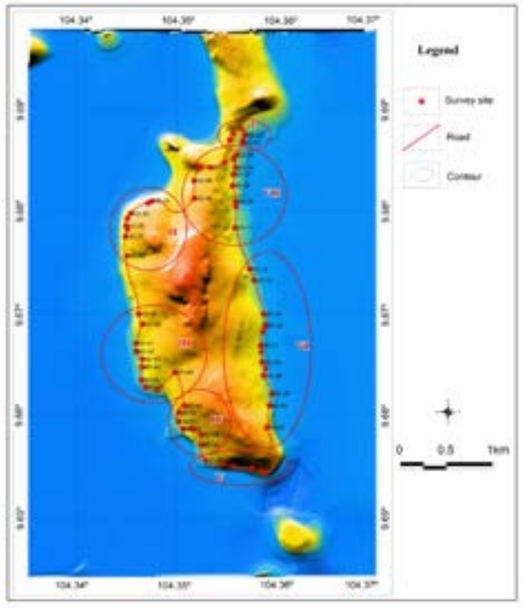

Figure 5. Map of groups of survey sites on Hon Lon island.

Accordingly, adjacent survey sites are grouped into groups and the quantitative correlation calculation of fracture orientation distribution among them. On Hon Lon island, 63 survey sites are grouped into 7 groups in order from I to VII (Figure 5). The results of the quantitative correlation calculation of fracture orientation distribution among groups of survey sites on Hon Lon island and between Hon Lon, Hon Ngang and Hon Mau islands are recorded in Table 3.

Table 3. Results of quantitative correlation calculation of fracture orientation distribution between groups of survey sites on Hon Lon island and between Hon Lon, Hon Ngang and Hon Mau islands.

No	Quantitative correlation of fracture orientation distribution between groups and islands	Correlation values	No	Quantitative correlation of fracture orientation distribution between groups and islands	Correlation values
1	Group of I and II	0.902	6	Group of VI and VII	0.883

No	Quantitative correlation of fracture orientation distribution between groups and islands	Correlation values	No	Quantitative correlation of fracture orientation distribution between groups and islands	Correlation values
2	Group of and III	0.819	7	Group of I and VII	0.985
3	Group of III and IV	0.713	8	Hon Lon and Hon Ngang islands	0.885
4	Group of IV and V	0.726	9	Hon Lon and Hon Mau islands	0.602
5	Group of V and VI	0.826	10	Hon Ngang and Hon Mau islands	0.679

Table 3 shows that the correlation value of fracture orientation distribution among groups on Hon Lon island varies from 0.7 to 0.98 %; between Hon Lon island and Hon Ngang island is greater than 0.8 % and between the remaining islands is greater than 0.6 %. These results clearly reflect the characteristics of tectonic activity in the area and their dependence on the number of fracture orientations number obtained at each survey site on the islands.

4.2 The relationship between fracture orientations and tectonic characteristics in Nam Du archipelago area, Kien Hai district, Kien Giang province

The Nam Du archipelago area, Kien Hai district, Kien Giang province, Vietnam, has a complex geological development history with many phases of tectonic activity that occurred during the Cenozoic period. The analytical results of the fault plane and striations at survey sites on Hon Lon and Hon Ngang islands have identified four phases of tectonic activity in sub-longitude direction compression, sub-longitude direction extension, sub-latitude direction compression, NE-SW and NW-SE direction compression on Hon Lon island; NE-SW direction compression and NE-SW direction extension on Hon Ngang island in magmatic rocks of the Hon Ngang formation. The impact of the stress field in these directions has created fault zones that move right, left, normal and reverse and fracture systems that develop in the sub-longitude direction, sub-latitude direction, NE-SW and NW-SE directions. This result is also consistent with previous studies by Phi Truong Thanh, (2018, 2019) in the northeast region of Vietnam.

The tectonic movement phases have formed fracture systems with high correlation values between Hon Lon and Hon Ngang islands to be 0.885, Hon Lon and Hon Mau islands to be 0.602, Hon Ngang and Hon Mau islands to be 0.679. The distribution of fracture systems on these islands is clearly shown in the Rose diagram in Figure 6.

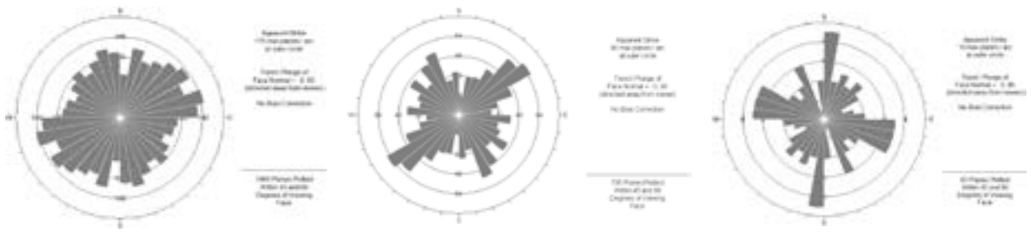

Hon Lon island ***Hon Ngang island*** ***Hon Mau island***

Figure 6. Rose diagram of fracture systems on Hon Lon, Hon Ngang and Hon Mau islands.

5. CONCLUSIONS

The results of calculating the distribution of fracture orientation at three islands, Hon Lon, Hon Ngang and Hon Mau, belonging to the Nam Du archipelago, have been determined. The correlation value varies from 0.6 to 0.9 %, corresponding to a range from 0.6 to 0.7 being 20 %, from 0.7 to 0.8 being 20 %, from 0.8 to 0.9 being 40 %, the remaining from 0.9 to 1 to be 20 %. This result shows that the fracture systems are formed by tectonic destruction phases of sub-longitude compression direction, sub-longitude extension direction, sub-latitude compression direction, NE-SW and NW-SE compression direction on Hon Lon island; NE-SW direction compression and NE-SW direction extension on Hon Ngang island in magmatic rocks of the Hon Ngang formation.

6. ACKNOWLEDGMENTS

This paper is supported by the project: “Research and propose a technology for efficient and sustainable water supply in some large islands, belonging to Nam Du archipelago, Kien Giang province, Vietnam”, project code: ĐTĐL.CN- 38/19, Ministry of Science and Technology of Vietnam.

7. REFERENCES

Dershowitz W., LaPoint P., Cladouhos T., (1998). Derivation of fracture spatial pattern parameters from borehole data. Int. J. Rock Mech. Min. *Sci. Geomech.* Abstr. 35 (4/5), No. 134.

Hoek E., Bray JW., (2004). *Rock slope Engineering*. Taylor & Francis Group, London and New York, 431 p.

Kulatilake PHSW., Wathugala DN., Poulton M., Stephansson O., (1990). Analysis of structural homogeneity of rock masses. *Engineering Geology, 29*, 195-211.

Li Y, Wang Q., Chen J., Song S., Ruan Y., Zhang Q., (2015). A multivariate technique for evaluating the statistical homogeneity of jointed rock masses. *Rock Mechanics and Rock Engineering*, Vol. 48, No. 5, 1821-1831.

Mahtab MA., Yegulalp TM., (1984). A similarity test for grouping orientation data in rock mechanics. *Proceedings of the 25th US symposium on rock mechanics*, NewYork, 495-502.

Martin MW., Tannant DD., (2004). A technique for identifying structural domain boundaries at the EKATI Diamond Mine. *Engineering Geology*, *74*, 247-264.

Miller SM., (1983). A statistical method to evaluate homogeneity of structural populations. *Mathematical Geology*, *15*, 317-328.

Phi NQ., Gi HS., Thanh PT., Phuong N., (2012). Structural domain identification by fracture orientation and fracture density in rock mass. *International Journal of Geoinformatics, 8*, 35-40.

Phi Truong Thanh, (2019). Tectonic activity phases of the Cenozoic period in Xuat Hoa area, Bac Kan province, northeastern region, Vietnam. *Indonesian Journal on Geoscience*. Vol. 6, No.3 311-325.

Piteau DR., Russell L., (1971). Cumulative sums technique: a new approach to analyzing joints in rock. *Proceedings of the 13th US symposium on rock mechanics, Urbana*, 1-29.

Thanh PT., Thinh PH., (2018). Some experimental results of analyzing quantitative correlation of fracture frequency distribution: Case study in quang ninh province, Vietnam. *Geodynamics & Tectonophysics*. Vol.9, Issue 2, 557-567. https://doi.org/10.5800/GT-2018-9-2-0361.

Thanh PT., Thinh PH., Ha NV., (2018). Rock slope failure blocks and their relation to tectonic activity: A case study in 3B highway, Xuathoa area, Backan province, Vietnam. *Bulletin of the Iraq Natural History Museum*, Vol 15 No 2, 207-223. Doi: https://doi.org/10.26842/binhm.7.2018.15.2.0207.

Thanh PT., Gi HS., Phi NQ., (2015). Delineate structural boundary from fracture correlation coefficients. *Vietrock 2015 an ISRM specialized conference,* Hanoi, 243-251.

Truong Thanh Phi, Hong Thinh Phi, (2018). Some experimental results of analyzing the quantitative correlation of fracture frequency distribution: A Case study in Quang Ninh province, Vietnam. *Geodynamics & Tectonophysics 9*(2):557-567. Doi:10.5800/GT-2018-9-2-0361

Thanh Truong Phi, Pinnaduwa H.S.W. Kulatilake, Mawuko Luke Yaw Ankah, Desmond Talamwin Sunkpal, Xiaokang Zhao, Ha Viet Nguyen, Tung Duc Van, (2021). Rock mass statistical homogeneity investigation along a highway corridor in Vietnam. *Engineering Geology,* 289.

APPLICATION OF RANDOM FOREST ALGORITHM AND GOOGLE COLAB FOR LAND COVER CLASSIFICATION

Hoa Thanh Thi Pham[1,2]*, Ngoc Quang Vu[3], Nghi Thanh Le [1,2], Nam Phuong Thi Doan[1,2]

[1]Faculty of Geomatics and Land Administration,
Hanoi University of Mining and Geology, Vietnam
[2]Geomatics in Earth Sciences Research Group,
Hanoi University of Mining and Geology, Vietnam
[3]Engineering Faculty, University of Transport Technology, Vietnam
*Corresponding author. Email: phamthithanhhoa@humg.edu.vn

ABSTRACT

Land cover is important information for the management and monitoring environment including disaster assessment in terms of flood, erosion, forest fire, landslide, and so on. Nowadays, many machine learning methods have been used to map land cover. Scientists assessed Random Forest (RF) to have more advantages than other image classification methods in its accuracy, its flexibility, and it is an easy-to-use algorithm. Especially, the appearance of Google Colab has brought the potential for RF in land cover classification. Google Colab allows researchers to run Python code through the browser, which not only requires no installation to use or upgrade computer hardware but also provides access free of charge to computing resources. Therefore the research is to provide the approach RF with Google Colab environment for classifying land cover in Quang Binh province, Vietnam using sentinel - 2 image in August 2021. The results have indicated the ability of this research direction with an overall accuracy above 80 %.

1. INTRODUCTION

Land cover is the observed (bio)physical cover on the earth's surface (FAO, 1998). It is important information for the management and monitoring environment including disaster assessment in terms of flood, erosion, forest fire, landslide, and so on. Many methods have been used for land cover classification. Remote sensing is still an effective tool for studying land cover at large scales (Friedl et al., 2010). Many commonly used open-access satellite imagery for mapping land cover are Landsat (Yang and Lo, 2002; Yuan et al., 2005), Sentinel 2 (Majidi Nezhad et al., 2019),…

Today, technological advances in storage and processing have enabled the creation of innovative algorithms for remote sensing applications based on machine learning. One of the most widely used algorithms is Random Forest (RF) (Breiman, 2001). It is the result of the development of the decision trees algorithm. In the world, scientists have used the Random Forest (Alonso Martínez et al., 2021; Gislason et al., 2006; Horning, 2010; Jin et al., 2018; Tokar et al., 2018). (Tokar et al., 2018) used this algorithm for land cover classification of Landsat 8 and gave an overall accuracy of 84,6 % and Kappa 0,808 for classes including cloud, water, urban and grassland (accuracy more than 90 %), forests (accuracy nearly 75 %). (Kulkarni and Lowe, 2016) assessed Random Forest to have more advantages than other image classification methods (Maximum likelihood, Minimum distance, Decision trees, Neural networks and Support Vector

Machine) in accuracy, although they had the same training and testing sample.

In Vietnam, RF has started to be used recently (Le et al., 2022; Nguyen et al., 2018; Tran et al., 2021). (Tran et al., 2021) established a land cover map for the study area of Ca Mau, Vietnam with the application of RF and Sentinel 1 Radar, (Nguyen et al., 2018) approached RF in the R software environment for classifying with Landsat 8. Therefore, it can be seen that RF has brought the potential in land cover classification.

Especially, the appearance of Google Colab (GC) which runs entirely on the cloud platform, allows researchers to execute code for image processing through the browser and is especially well suited to machine learning (according to Google Research). However, only a few studies have used GC (Lilay and Taye, 2023) for mapping land cover. Therefore, the research aims to provide the approach RF with Google Colab environment for classifying land cover in Quang Binh province, Vietnam using Sentinel-2 images.

2. STUDY AREA AND MATERIAL

2.1 Study area

Figure 1. The study area.

Quang Binh province is in the North Central area of Vietnam with coordinates 16°55' to 18°05' North and 105°37' to 107°00' East. It borders Ha Tinh province on the North, Quang Tri province on the South, Laos on the West, and the East Sea on the East. The provincial terrain is narrow and sloping from the West to the East. The area is divided into specific zones: 85 % high mountainous area and hill in the West, while the remaining is plain and coastal sandy area in the East of the province. The seaside sand dunes belt is a natural dam that protects the land from ocean tides (according to Quang Binh Portal).

2.2 Data resources

The study used Sentinel-2 (S2) with cloud cover of less than 30 % in August 2021. S2 Multispectral Instrument (MSI) is a European wide-swath, high-resolution, multi-spectral imaging mission. The full mission with twin satellites flying in the same orbit but phased at 180°, is designed to give a high revisit frequency of 5 days at the Equator. The orbital swath width is 290 km. S2 carries an optical instrument payload that samples 13 spectral bands: Four bands at 10 m, six bands at 20 m and three bands at 60 m spatial resolution (ESA). The characteristics of the S2 are presented in Table 1.

Tab 1. The characteristics of Sentinel-2.

Band Number	Pixel Size	Description
B1	60 meters	Aerosols
B2	10 meters	Blue
B3	10 meters	Green
B4	10 meters	Red
B5	20 meters	Red Edge 1
B6	20 meters	Red Edge 2
B7	20 meters	Red Edge 3
B8	10 meters	Near infrared (NIR)
B8A	20 meters	Red Edge
B9	60 meters	Water vapor
B10	60 meters	Shortwave infrared/Cirrus
B11	20 meters	Shortwave infrared 1(SWIR 1)
B12	20 meters	Shortwave infrared 2 (SWIR 2)

Source: https://sentinels.copernicus.eu

3. METHODOLOGY

3.1 Google Colab

The study used Google Colab (GC) in land cover classification. Google Colab (short for Colaboratory) is a powerful cloud platform and is based on the Jupyter Notebook open-source environment. It is designed to help scientists work more efficiently, especially in machine learning fields.

Google Colab allows researchers to run Python code through the browser, which not only requires no installation to use or upgrade computer hardware but also provides access free of charge to computing resources. They are also the advantage of GC.

Figure 2. Google Colab Interface.

Google Colab ingrates Python with a full of popular and pre-installed data science libraries for data analysis and visualization. Python is an interpreted, object-oriented, high-level programming

language. It is assessed as simple, easy to learn and mostly applies on many different platforms.

Generally, Google Colab is appropriate for people who need to work with multiple devices, for instance, computers or laptops, tablets, and even work in many places such as home, office,… because it has the ability to sync seamlessly between devices.

3.2 Random Forest

Random forest is one of the most popular supervised machine-learning algorithms which can be used to solve both classification and regression issues. Random forest is a combination of tree predictors such that each tree depends on the values of a random vector sampled independently and with the same distribution for all trees in the forest (Breiman, 2001). Theoretically, a forest obtains numerous trees, and the more trees more it will be stronger. Thus, one of the major advantages of RF is that it comprises a great number of trees leading to high accuracy and preventing the problem of overfitting. Feature bagging also makes the Random Forest classifier an effective tool for estimating missing values as it maintains accuracy when a portion of the data is missing (IBM).

With random forest classification, decision trees are created by using different random subsets of the given data and features. Each tree will provide its prediction to classify the data. RF is based on the majority votes of predictions and takes the most popular result to the final output.

The below diagram illustrates how the Random Forest algorithm works.

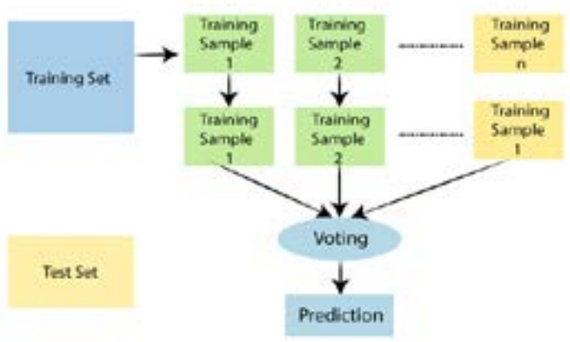

Figure 3. Random Forest.

Source: https://www.javatpoint.com/machine-learning-random-forest-algorithm

There are 4 steps:

Step 1: Select random samples from a given data

Step 2: Construct a decision tree for every sample and get the prediction result from every decision tree.

Step 3: Perform the votes for every predicted target

Step 4: Choose the most voted prediction result as the final prediction result.

Random forest algorithms have three main hyperparameters which need to be set before training. They are node size, the number of trees, and the number of features sampled.

3.3 Image Processing and Classification

Firstly, we installed and imported some libraries and maps in Google Colab such as Numpy, Geemap,… Because Google Earth Engine platform has provided a large of remote sensing imagery, so we used it to import Sentinel-2 for this study.

```
# Time
START_DATE = ee.Date('2021-08-01');
END_DATE = ee.Date('2021-08-31');
MAX_CLOUD_PROBABILITY = 30;

# Study Area
provinceName = 'Quang Binh'
bound_vn = ee.FeatureCollection("projects/ee-thanhhoa/assets/gadm41_VNM_1")
province = bound_vn.filter(ee.Filter.eq('VARNAME_1',provinceName))
Map.addLayer(province, {'color': 'grey', 'fillColor': 00000000}, 'Study Area')
Map.centerObject(province,8)

# Load Sentinel 2 data
s2Sr = ee.ImageCollection('COPERNICUS/S2_SR')
s2Clouds = ee.ImageCollection('COPERNICUS/S2_CLOUD_PROBABILITY')

#Visualize
bands = ['B4', 'B3', 'B2'];
visParams = {'bands': bands,'min': 0,'max': 2000, 'gamma':1.3};
```

Figure 4. Set time and cloud coverage, select the study area and Sentinel-2.

Then, a set of Sentinel-2 images was filtered in August 2021 with less than 30 % cloud coverage (Figure 4). A cloud mask was applied using the “probability” band. The composite images were created by determining the median values of each pixel (in all bands) in the images. The final image was clipped within the study area boundary.

Besides, adding spectral indices can increase the information and improve the results of the classification (Praticò et al., 2021). Therefore, two indices NDVI (Normalized Difference Vegetation Index) and NDWI (Normalized Difference Water Index) were used in the study and added as bands in images. NDVI is a simple index but it can help recognize the difference between the forest and cropland (Tran et al., 2022). The NDVI is calculated as formula (1) (Tucker, 1979). While NDWI is used to highlight water bodies against the soil and vegetation: positive values for water features and negative ones (or zero) for soil and vegetation (McFeeters, 1996).

$$NDVI = \frac{NIR - RED}{NIR + RED} \quad (1)$$

$$NDWI = \frac{GREEN - NIR}{GREEN + NIR} \quad (2)$$

Where RED, GREEN and NIR stand for the spectral reflectance measurements acquired in the red, green and near-infrared bands.

We used Random Forest for land cover classification in Quang Binh. Sample data for 5 classes: Forest, Cropland, Fallow, Waterbody, and Build-Up were created based on the geodatabase of the study area, visually integrating information from Bing Map, Google Satellite, Sentinel-2 in QGIS software. They were divided randomly with 80 % for training and 20 % for validation. For each class, we assign a number to the property named ‘landcover’.

Figure 5 presents code for RF method with a tree number of 300 and bands used for the classification (band 2, band 3, band 4, band 8, NDVI and NDWI at 10m spatial resolution).

```
# Select bands for training
bands =['B2', 'B3','B4','B8', 'NDVI', 'NDWI'];
### RF Classifier Model Building
# ee.Classifier.smileRandomForest(numberOfTrees, variablesPerSplit, minLeafPopulation, bagFraction, maxNodes, seed)
RFclassifier = ee.Classifier.smileRandomForest(300).train(**{
    'features': trainingsample,
    'classProperty': 'Class',
    'inputProperties': bands,
})
# Classify the image
Classified = S2_StudyArea.select(bands).classify(RFclassifier)
```

Figure 5. Random Forest code in Google Colab.

4. RESULTS AND DISCUSSION

Google Colab allows displaying results in its interface via Geemap.

a ***b***

Figure 6. a) Sentinel-2 (True RGB color), b) Dislay results in Google Colab.

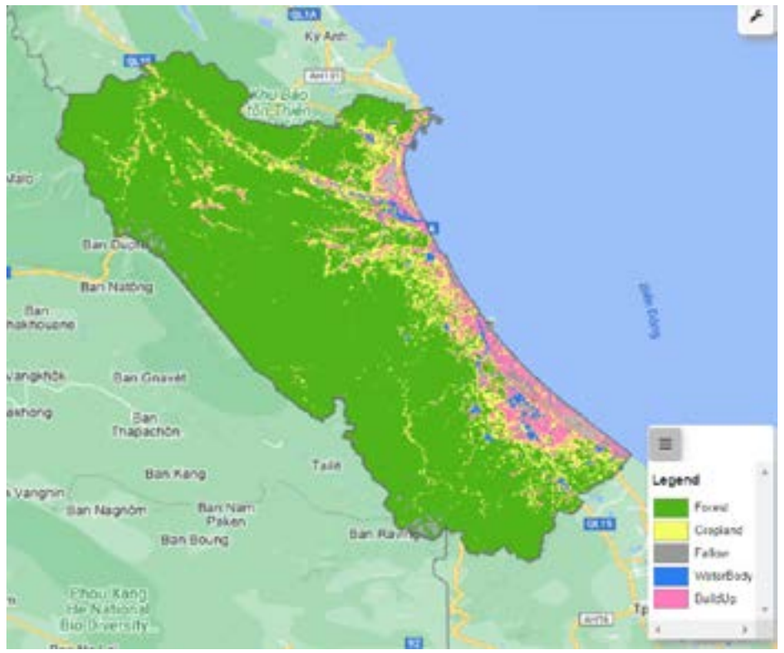

Figure 7. Land cover of Quang Binh province in Google Colab.

Figure 7 shows the land cover of the study area in August 2021 with 5 classes: Forest, Cropland (also known as Agricultural land), Fallow (including Sand, Barren Land), Waterbody, and Build-Up (also including Resident/homestead land). Generally, most of the forest area was concentrated in the west of Quang Binh province, and part of the forest was in the coastal area in the east. With the large forest area in the west, there is a famous forest Ke Bang within Phong Nha-Ke Bang National Park which was recognized as a World Natural Heritage Site by UNESCO in 2003. In addition, other land cover was scattered throughout the entire area and the eastern area. Fallow, especially sand, was distributed in the coastal area. The water bodies contain rivers such as Gianh, Nhat Le,... and numerous ponds.

Finally, the result of the classification is evaluated.

- Overall Accuracy (OA): OA is calculated by dividing the sum of the number of correct classifications (the diagonal of the matrix) by the total number of samples taken (Story et al., 1986).

- Producer's Accuracy (PA): is calculated by dividing the number of correctly classified reference points by the total number of reference points for that class.

It corresponds to the map accuracy from the point of view of the map maker. It represents how often real features on the ground are correctly shown on the classified map or the probability that a certain land cover of an area on the ground is properly classified (Alonso Martínez et al., 2021).

- User's Accuracy (UA): is computed by dividing the total number of classified pixels that agree with the reference data by the total number of classified pixels for that class. This value represents the reliability of the map or the probability that a pixel classified into a given category actually represents that category on the ground (Alonso Martínez et al., 2021).

- Kappa Coefficient: It is generated to evaluate the accuracy of classification. It compares the accuracy obtained in the classification to the accuracy that would be obtained randomly. A negative number indicates the classification is significantly worse than random. A value close to 1 indicates that the classification is significantly better than random.

Table 1 shows the results of the accuracy assessment including the Consumer's accuracy and the Producer's accuracy of each class in the land cover. Besides, the overall error (OA) = 86.7 %, Kappa = 0.8.

Table 2. Accuracy of Land cover classification result.

Class	UA (%)	PA (%)
Forest	75	88.2
Cropland	85.3	78.3
Fallow	81.8	99
Waterbody	75	99
Build-Up	94.2	89.1

The UA and PA of cropland were lower than others. The main reason is that, in the image of the study area, pixels distinguished between Cropland, Forest, and a part of Water were quite similar. Therefore, this study used NDVI to add in Random Forest algorithm, helping to improve the accuracy of results (above 75 %). Water bodies were recognized with high accuracy due to

adding NDWI. The OA above 80 % and Kappa coefficient above 0.8 show that the result of classification is generally good with Sentinel-2 and Random Forest.

Unlike other similar studies based on commercial software, Google Colab has brought the point of novelty of our research in this field. It is an effective tool because it allows users to run Python in the browser without the need for complex configuration, and the results were obtained in a short time.

5. CONCLUSION

In this study, based on the Sentinel-2 and Random Forest Algorithm, 5 classes of land cover were classified in Quang Binh province in 2021: Forest, Cropland, Fallow, Waterbody, and Build-Up. The accuracy of classification is generally high. Furthermore, the study also indirectly highlights how the possibility of exploiting the potential of Google Colab in this field. The problem is the time limit of free Google Colab sessions, the internet connection and the limited availability of data. Therefore, the improvement in this direction will bring outstanding results. Future research will apply different remote sensing imagery, more spectral indices, and other data such as DEM in land cover classification.

6. ACKNOWLEDGEMENTS

The study is supported and funded by Project No T23-41 of Hanoi University of Mining and Geology, Vietnam.

7. REFERENCES

Alonso Martínez, L., Picos, J., and Armesto, J., 2021. Forest Land Cover Mapping at a Regional Scale Using Multi-Temporal Sentinel-2 Imagery and RF Models. *Remote Sensing*, *13*, 2237. Doi:10.3390/rs13122237.

Breiman, L., 2001. Random Forests. *Machine Learning*, *45*(1), 5-32. Doi:10.1023/A:1010933404324.

FAO, 1998. Land cover and Land use. *The FAO AFRICOVER Programme*.

Friedl, M., Sulla-Menashe, D., Tan, B., Schneider, A., Ramankutty, N., Sibley, A., and Huang, X., 2010. MODIS Collection 5 Global land cover: Algorithm refinements and Characterization of new datasets. *Remote Sensing of Environment, 114*, 168-182. Doi:10.1016/j.rse.2009.08.016

Gislason, P. O., Benediktsson, J. A., and Sveinsson, J. R., 2006. Random Forests for land cover classification. *Pattern Recognition Letters, 27*(4), 294-300. Doi: https://doi.org/10.1016/j.patrec.2005.08.011

Horning, N., 2010. Random Forests : An algorithm for image classification and generation of continuous fields data sets. *International Conference on Geoinformatics for Spatial Infrastructure Development in Earth and Allied Sciences 2010*.

IBM, (2023). What is random forest? Retrieved from https://www.ibm.com/topics/random-forest#:~:text=Random%20forest%20is%20a%20commonly,both%20classification%20and%20regression%20problems. [Accessed on 12 June 2023].

Jin, Y., Liu, X., Chen, Y., and Liang, X., 2018. Land-cover mapping using Random Forest classification and incorporating NDVI time-series and texture: a case study of central Shandong. *International Journal of Remote Sensing, 39*(23), 8703-8723. Doi:10.1080/01431161.2018.1490976.

Kulkarni, A. D., and Lowe, B., 2016. Random Forest Algorithm for Land Cover Classification. *International Journal on Recent and Innovation Trends in Computing and Communication, 4*(3), 58-63.

Le, H., Pham, L., Hoang, T., and Dinh, T., 2022. Land-cover classification using Random Forest and incorporating NDVI time-series and topography: a case study of Thanh Hoa province, Vietnam. *VNUHCM Journal of Earth Science and Environment, 5*(S3), 40-53. Doi: https://doi.org/https://doi.org/10.32508/stdjsee.v5iSI2.681.

Lilay, M. Y., and Taye, G. D., 2023. Semantic segmentation model for land cover classification from satellite images in Gambella National Park, Ethiopia. *SN Applied Sciences, 5*(3), 76. Doi:10.1007/s42452-023-05280-4.

Majidi Nezhad, M., Heydari, A., Fusilli, L., and Laneve, G. (2019). Land Cover Classification by using Sentinel-2 Images: A case study in the city of Rome. *Proceedings of the 4th World Congress on Civil, Structural and Environmental Engineering (CSEE'19)*.

McFeeters, S. K., 1996. The use of the Normalized Difference Water Index (NDWI) in the delineation of open water features. *International Journal of Remote Sensing, 17*(7), 1425-1432. Doi:10.1080/01431169608948714.

Nguyen, H. T. T., Doan, T. M., and Radeloff, V., 2018. Applying random forest classification to map land use/land cover using Landsat 8 OLI. *Int. Arch. Photogramm. Remote Sens. Spatial Inf. Sci.*, XLII-3/W4, 363-367. Doi:10.5194/isprs-archives-XLII-3-W4-363-2018.

Praticò, S., Solano, F., Di Fazio, S., and Modica, G., 2021. Machine Learning Classification of Mediterranean Forest Habitats in Google Earth Engine Based on Seasonal Sentinel-2 Time-Series and Input Image Composition Optimisation. *Remote Sensing, 13*, 586. Doi:10.3390/rs13040586.

Story, M., Congalton, R. G. J. P. E., and Sensing, R., 1986. *Accuracy assessment: A user's perspective, 52*, 397-399.

Tokar, O., Olena, V., Lubov, K., Havryliuk, S., and Korol, M., 2018. Using the Random Forest Classification for Land Cover Interpretation of Landsat Images in the Prykarpattya Region of Ukraine. *2018 IEEE 13th International Scientific and Technical Conference on Computer Sciences and Information Technologies (CSIT)*, 241-244. Doi:10.1109/STC-CSIT.2018.8526646.

Tran, V. A., Le, M. H., Tran, H. H., Le, T. N., Tran, T. A., Nguyen, C. C., and Ha, T. K., 2022. Land cover mapping in Camau province by machine learning algorithms using Sentinel-2 imagery. *The 43th Asian Conference on Remote Sensing (ACRS 2022)*.

Tran, V. A., Le, T. L., Tran, H. H., and Le, T. N., 2021. Monitoring Vegetation Cover Changes by Sentinel-1 Radar Images Using Random Forest Classification Method. *Journal of the Polish Mineral Engineering Society, 1*, 441-452.

Tucker, C. J., 1979. Red and photographic infrared linear combinations for monitoring vegetation. *Remote Sensing of Environment, 8*(2), 127-150. Doi: https://doi.org/10.1016/0034-4257(79)90013-0.

Yang, X., and Lo, C. P., 2002. Using a time series of satellite imagery to detect land use and land cover changes in the Atlanta, Georgia metropolitan area. *International Journal of Remote Sensing, 23*(9), 1775-1798. Doi:10.1080/01431160110075802.

Yuan, F., Sawaya, K. E., Loeffelholz, B. C., and Bauer, M. E., 2005. Land cover classification and change analysis of the Twin Cities (Minnesota) Metropolitan Area by multitemporal Landsat remote sensing. *Remote Sensing of Environment, 98*(2), 317-328. Doi: https://doi.org/10.1016/j.rse.2005.08.006.

ESTIMATION OF LAND SURFACE TEMPERATURE AND VEGETATION DRYNESS INDEX (TVDI) IN BAC BINH - BINH THUAN USING REMOTE SENSING IMAGES

Linh Nguyen Thi Thuy*, Minh Hoang Thi Nguyet, Linh Phung Thi

Ha Noi University of Natural Resources and Environment, Vietnam

*Corresponding author. Email: nttlinh.tnn@hunre.edu.vn

ABSTRACT

Nowadays, drought is regarded as one of the most destructive natural disasters which causes negative impacts on societies around the globe. Especially in Binh Thuan province - Vietnam, the drought tends to increase in both scale and intensity, but it is harder to forecast. In recent years, with the development of remote sensing technology, its products have been used effectively in studying, monitoring and reacting to drought. Thus, in this study, we aim to determine the progress of drought through the years in Bac Binh district - Binh Thuan province by using remote sensing images. In detail, we use images from Landsat 7 ETM+ (2002, 2005, 2010) and Landsat 8 OLI (2014 and 2017) to estimate dryness indices: temperature vegetation dryness index (TVDI) and improved temperature vegetation dryness index. These two dryness indices are based on normalized difference vegetation index (NDVI) and land surface temperature (LST) for TVDI and gradient of temperature (Ts-Ta) for iTVDI. The obtained results show that almost Bac Binh's area is estimated to have medium and higher drought risk and its severe drought areas increased rapidly in 2014 and 2017. High drought-risk areas are found mostly in agricultural or non-vegetated areas in the center of Bac Binh.

1. INTRODUCTION

Drought is regarded as a natural phenomenon that has serious effects on the economies and societies of most countries worldwide. Also, drought stands third in the list of the most destructive natural disasters, such as floods and storms. Especially, drought events tend to increase in both scale and intensity in recent years and it is more difficult to predict the impact of climate change. In Vietnam, most of the areas are suffering from drought at different degrees at different times. Nevertheless, the situations in the middle areas of Vietnam and Tay Nguyen regions are the worst, where severe droughts occur more frequently and cause damage to the local economy, society and agriculture production.

Assessing drought probability for agricultural areas in Africa with coarse resolution remote sensing imagery study used the per-pixel Vegetation Health Index (VHI) from the Advanced Very High-Resolution Radiometer (AVHRR) averaged over the crop season as the main drought indicator. After that, the per-pixel average VHI was aggregated for agricultural areas at the sub-national level to obtain a drought intensity indicator (Rojas, Vrieling & Rembold, 2011) often with devastating consequences for the food security of agricultural households. This study proposes a novel method for calculating the empirical probability of having a significant proportion of the total agricultural area affected by drought at sub-national level. First, we used the per-pixel Vegetation Health Index (VHI. Nevertheless, the main data in this study (NOAA AVHRR) are 16 km resolution (for VHI data) and 8 km (for the Normalized Difference Vegetation Index) resolution, so the estimation of results will be affected if a study area is a small one.

In another study of monitoring meteorological drought in semi-arid regions using multi-sensor microwave remote sensing data using the Microwave Integrated Drought Index (MIDI) by integrating three variables, including Tropical Rainfall Measuring Mission (TRMM) derived precipitation, Advanced Microwave Scanning Radiometer for EOS (AMSR-E) derived soil moisture and AMSR-E derived land surface temperature. The results showed that MIDI with proper weights of three components outperformed individual remote sensing drought indices and other combined microwave drought indices in monitoring drought (Zhang & Jia, 2013). In this study, the Land Surface Temperature and soil moisture are not entirely independent according to the LPRM algorithm (Liu et al., 2010; Owe et al., 2008). Further studies using independent datasets of MIDI components derived from different algorithms or sensors are needed and will be included in subsequent studies.

Droughts often occur on a large scale. Therefore, observing and studying by using in situ stations is not an effective method, as the installation of the stations can be very costly. Meanwhile, remote sensing technology provides information about the earth's surface in different bands and has a fair spatial and temporal resolution that is then useful for drought study. In the past few years, many studies have been conducted about the application of remote sensing using a thermal infrared band that estimates land surface temperature and soil moisture to evaluate droughts. In Vietnam, some researchers working in this area used thermal images from MODIS, NOAA/AVHRR. However, because of the coarse spatial resolution of MODIS and NOAA/AVHRR, it is not suitable for some specific studies.

In this study, we used the thermal infrared LANDSAT images to evaluate drought risk in Bac Binh - Binh Thuan which the resolution is 30×30 m. These data will provide information in more detail about changes in the land surface compared to MODIS and NOAA/AVHRR images.

2. STUDY AREA AND DATASETS

2.1 Study area

Bac Binh is one of two districts in Binh Thuan province which has the highest land degradation and desertification risk in Vietnam. Because of its natural climate and topography, Bac Binh district annually suffers from severe droughts.

According to statistical data at Bau Trang station from 1960 to 2010, the annual average rainfall in Bac Binh is between 700 to 1000 mm, only occurs in the rainy season (from May to October), while in the dry season (from November to April), the amount of rainfall is low. With Tuy Phong district in Binh Thuan, Bac Binh was also predicted as the highest drought risk area in Binh Thuan (Grade 4 - Meteorology index). In recent years, the causes of climate change and the effects of negative activities from people have made drought situations in the South-Central coast as well as Binh Thuan province become even more serious. Drought events usually occur in the dry season but also in the rainy season. That problem has affected production activities as well as the lives of people who live there. Therefore, applying remote sensing data to monitor and cope with a drought becomes signification.

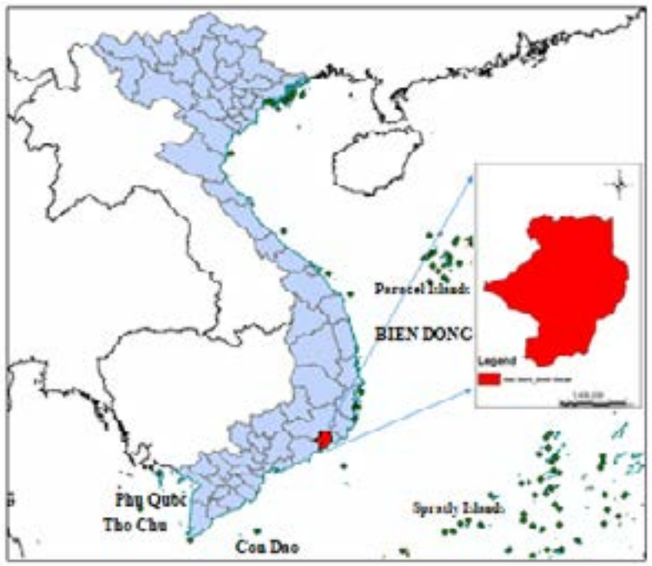

Figure 1. Study area boundary of Bac Binh district in Binh Thuan, Vietnam.

2.2 Datasets

Remote sensing data used in this study include Landsat 7 ETM+ (5th January 2002, 13th January, 12th February 2010) and Landsat 8 OLI (15th February 2014, 23rd February 2017). Figure 1 shows the study area boundary which is performed in this study. Images were taken in the dry season, which was a high drought in the central area and highlands of Vietnam. MODIS images will be used to compare temperature distribution between Landsat's temper images and MODIS images. The respective MODIS images include 5th January 2002, 13th January 2005, 12th February 2010, 15th February 2014 and 23rd February 2017 to validate the temperature images. Because of the different time periods, the two types of images have different limitations.

The resolution of the data is 30×30 m for all of the bands. Actually, the thermal infrared bands with Landsat 7 ETM+ at the 60-meter resolution and Landsat 8 OLI at the 100-meter resolution. However, they were resampled to 30 meters in delivered data product after 25th February 2010. Especially, Landsat images are provided totally free for a period of 16 days, so these images become precious and important data for studying the natural environment and monitoring the environment.

Ambient air temperature from 6 meteorological stations for the period years 2002-2014 was used for this retrieving T_s-T_a maps. Temperature data were interpolated using the smart interpolation method (Willmott and Matsuura, 1995). For using this method, sixteen Radar Topography Mission (SRTM) DEM images (30 m) of the study area were obtained from Global Land Cover Facilities (GLCF). Considering the general value of the lapse rate (0.6 °C/100 m) is inaccurate and may differ in different places and different months, in this research, environmental lapse rates were calculated using linear regression between air temperature and elevation in each month for available meteorological stations (Rahimzadeh-Bajgiran, Omasa and Shimizu, 2012).

3. METHODOLOGY

3.1 The Temperature Vegetation Dryness Index

Many studies around the world have shown that land surface temperature and vegetation index are important factors that can provide information about surface moisture. Temperature can quickly increase when the surface is drought or vegetation does not have enough water. In this study, we use a temperature vegetation dryness index (TVDI) to estimate the surface drought grades based on the study of Saldholt I in 2002 (the relationship between surface temperature and vegetation cover). The temperature vegetation dryness index is estimated by the equation below:

$$TVDI = \frac{T_s - T_{s\min}}{T_{s\max} - T_{s\min}} \quad (1)$$

where: T_s is the surface temperature of a pixel; T_{smin}, T_{smax} are the minimum and maximum surface temperature and both of them are the linear functions of the vegetation index

$$T_{s\max} = a_{\max} \times NDVI + b_{\max}$$
$$T_{s\min} = a_{\min} \times NDVI + b_{\min} \quad (2)$$

where a_{max}, b_{max} = linear regression parameters for dry edge; a_{min}, b_{min} = linear regression parameters for wet edge.

Theoretically, the scatter plot formed by vegetation index and land surface temperature should be like a triangle (Figure 2). The upper edge of the triangle is defined as a dry edge, while the lower one is a wet edge. Pixels close to the dry edge are comparatively drier, while those close to the wet edge are wetter. The position of the pixel in the scatter plot defines its moisture condition. Thus, the core issue of the triangle method is to calculate the ideal dry edge and wet edge. In previous research, people only calculate the dry edge while considering the wet edge as a horizontal line, but in real situations, the wet edge may not be horizontal but a little oblique. In this paper, a linear function is applied to both the upper and lower envelope of the triangle to calculate the dry edge and cold edge, respectively (Han, Li, Wang, Liu and Jiao, 2004). The higher the TVDI, the higher the drought risk the area can be. In the dry edge, the TVDI equals 1, while in the wet edge, the TVDI equals 0 (Figure 2).

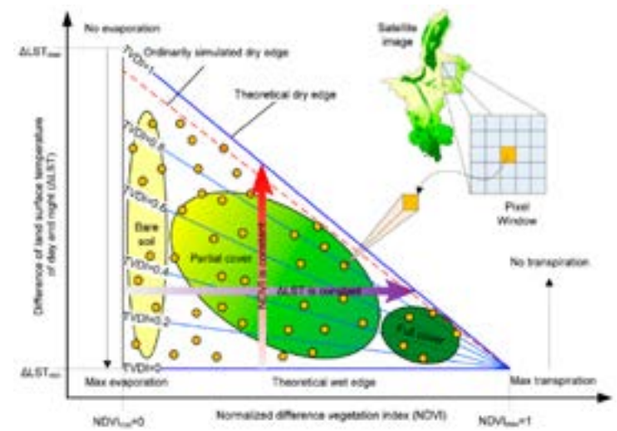

Figure 2. The triangle temperature T_s/NDVI (or Ts-Ta/NDVI).

To determine the surface temperature, the original values from the Landsat image transfer to the real value of electromagnetic radiation (Wm^{-2} μm-2).

For Landsat 7, ETM+ spectral radiance is calculated by using the equation below:

$$L_\lambda = \frac{L_{\max} - L_{\min}}{DN_{\max} - DN_{\min}}\left(DN - DN_{\min}\right) + L_{\min} \quad (3)$$

where, L_λ is spectral radiance; L_{max}, L_{min} are spectral radiance correspondence with DN_{max} and DN_{min} in the thermal infrared band and are provided in the metadata file of Landsat images. For Landsat 8 OLI, spectral radiance is determined by using the equation:

$$L_\lambda = M_L.Q_{cal} + A_L \quad (4)$$

where, M_L, A_L are conversion coefficients that are provided in the metadata file of Landsat 8; Q_{cal} is band values.

The brightness temperature is calculated from the spectral radiance as the equation:

$$T_B = \frac{K_2}{\ln\left(1 + \frac{K_1}{L_\lambda}\right)} \quad (5)$$

where, K_1 and K_2 coefficients are provided in the metadata file of Landsat.

Brightness temperature is validated based on surface emissivity to determine the land surface temperature as the equation:

$$LST = \frac{T_B}{1 + \left(\frac{\lambda.T_B}{\rho}\right) * \ln\varepsilon} \quad (6)$$

where, λ is the average wavelength value in the thermal infrared band;

$\rho = \frac{h.c}{\sigma}$ with σ is Stefan - Boltzmann constant ($\sigma = 1.38 * 10^{-23}\ J/K$)

h: Plank constant ($h = 6.626 * 0^{-34}\ J.\text{sec}$)

c: bright velocity ($c = 2{,}998 * 0^{8}\ m/s$)

ε: surface emissivity

The surface emissivity can be determined from remote sensing data based on the kinds of vegetation covers or the normalized difference vegetation index (NDVI). However, the method bases on the NDVI index has advantages caused this method can be determined by each pixel. To estimate the surface emissivity, this study uses a method of Valor E., Caselles V that, based on the NDVI, applies to heterogeneous areas with many kinds of vegetation. In this method, the surface emissivity of each pixel is calculated by the sum of its component emissivity.

$$\varepsilon = \varepsilon_v P_v + \varepsilon_s\left(1 - P_v\right) \quad (7)$$

where, ε_v, ε_s are emissivity that represents the hot and cold pixels. A hot pixel is regarded as the location of a dry and non-vegetated (or sparsely vegetated) area and a cold pixel is a well-watered, healthy and fully vegetated area. P_v is a value that equals 0 for the vacant land area and equals 1 for the full vegetation area. P_v is determined by the equation:

$$\varepsilon = \varepsilon_v P_v + \varepsilon_s\left(1 - P_v\right) \quad (8)$$

where, NDVI is the observed normalized difference vegetation index and it can be defined as:

$$P_v = \left[\frac{NDVI - NDVI_{\min}}{NDVI_{\max} - NDVI_{\min}}\right]^2 \quad (9)$$

where, ρ_{nir} is the near-infrared band reflectance and ρ_{red} is the red band reflectance. In this study, NDVI was calculated using LANDSAT-7 ETM+ Band 3 (the red band) reflectance, Band 4 (the near-infrared band) reflectance and LANDSAT-8 OLI Band 4 (the red band) reflectance and Band 5 (the near-infrared band) reflectance.

3.2 The improved Temperature Vegetation Dryness Index

A modified approach towards the Temperature Vegetation Dryness Index (TVDI) concept, incorporating air temperature and a Digital Elevation Model (DEM) to develop the improved TVDI (iTVDI), is also estimated and the results are compared with the original TVDI.

As it is assumed that the main source of variation in the TVDI is soil moisture, air temperature is not considered in the model, which may increase the uncertainty of the TVDI for larger areas and higher NDVI values (Sandholt et al., 2002). An inherent assumption when applying the TVDI is that Ta is constant for the subset or window over which the index is estimated. A typical error in studies based on the TVDI is that this assumption is violated in selecting too large an area. On the other hand, when using the TVDI to estimate soil moisture status, heterogeneity of the earth's surfaces increases the uncertainty of the TVDI to estimate soil moisture. Therefore, the TVDI should ideally only be applied in regions with little topography. To correct the effect of topography, Ran et al., (2005) used an approach to correct Ts with a DEM before constructing the AVHRR Ts/NDVI space. Hassan et al., (2007) proposed a correction method to use a DEM to infer local pressure from altitude and then transform surface temperature to potential temperature.

Air temperature decreases as altitude increases, a phenomenon known as the environmental lapse rate. Therefore, a Digital Elevation Model (DEM) of the study area has also been used to calculate the lapse rate to improve the performance of the index to estimate evapotranspiration at different altitudes in each specific month. The new index, hereafter called the improved TVDI (iTVDI) is calculated using the below equation and is schematically presented in Figure 2.

$$NDVI = \frac{\rho_{NIR} - \rho_{RED}}{\rho_{NIR} + \rho_{RED}} \quad (10)$$

where, ΔT_{obs} is observed Ts-Ta and Ta are observed air temperature calibrated using DEM. $\Delta T_{\min}$ and $\Delta T_{\max}$ are the minimum and maximum ΔT, respectively, for the same vegetation index value (here the NDVI). AB and BC are the distances represented in Figure 2, between the dry edge and wet edge in the ΔT vs. NDVI scatter plot as described by Sandholt et al. (2002). The iTVDI is lower for wet and higher for dry conditions and similar to the TVDI, varies between 0 and 1.

4. RESULTS AND DISCUSSIONS

4.1 Determining the corresponding parameters

4.1.1 The Normalized Difference Vegetation Index (NDVI)

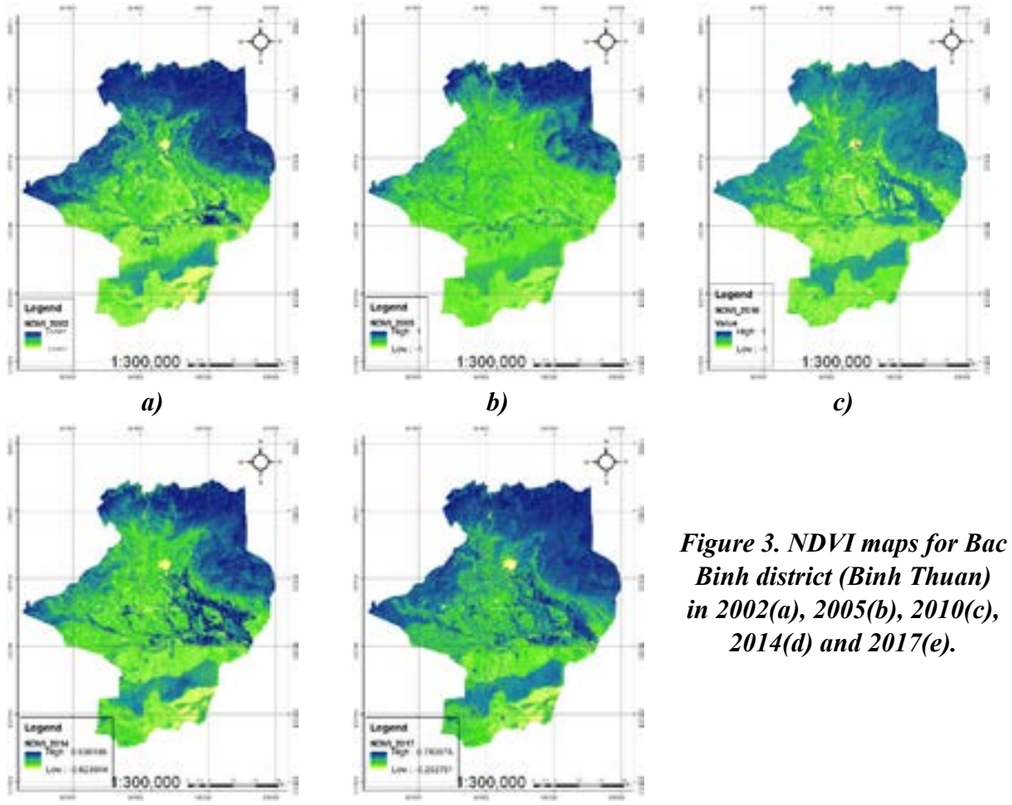

a) *b)* *c)*

d) *e)*

Figure 3. NDVI maps for Bac Binh district (Binh Thuan) in 2002(a), 2005(b), 2010(c), 2014(d) and 2017(e).

To estimate the emissivity based on NDVI, we need to know the emissivity of the hot and cold pixels. Many former types of research took these emissivities by getting the result of experimental measurement in representative samples. However, in this study, the condition does not allow us to conduct the measurements. Instead, we get the values from another report that has been done with the measurements in the same area**.** The values of NDVI for a hot and cold pixel are 0.127 and 0.515. Using the Van De Griend method, the emissivity for a hot and cold pixel can be estimated by the following equation:

$$\varepsilon = 1.0094 + 0.047\ln(NDVI) \quad (7)$$

4.1.2 The Land Surface Temperature (LST)

The results of land surface temperature in the area of Bac Binh district (Binh Thuan) are presented in Figure 4. Through these results, it is clear to be seen that there are some areas with high temperatures, which are found mainly in the non-vegetated regions. The differences in temperature between vegetable areas and non-vegetable areas are significant, with 24.45, 28.78, 28.56, 25.56, 18.00 degree in the year 2002, 2005, 2010, 2014 and 2017, respectively.

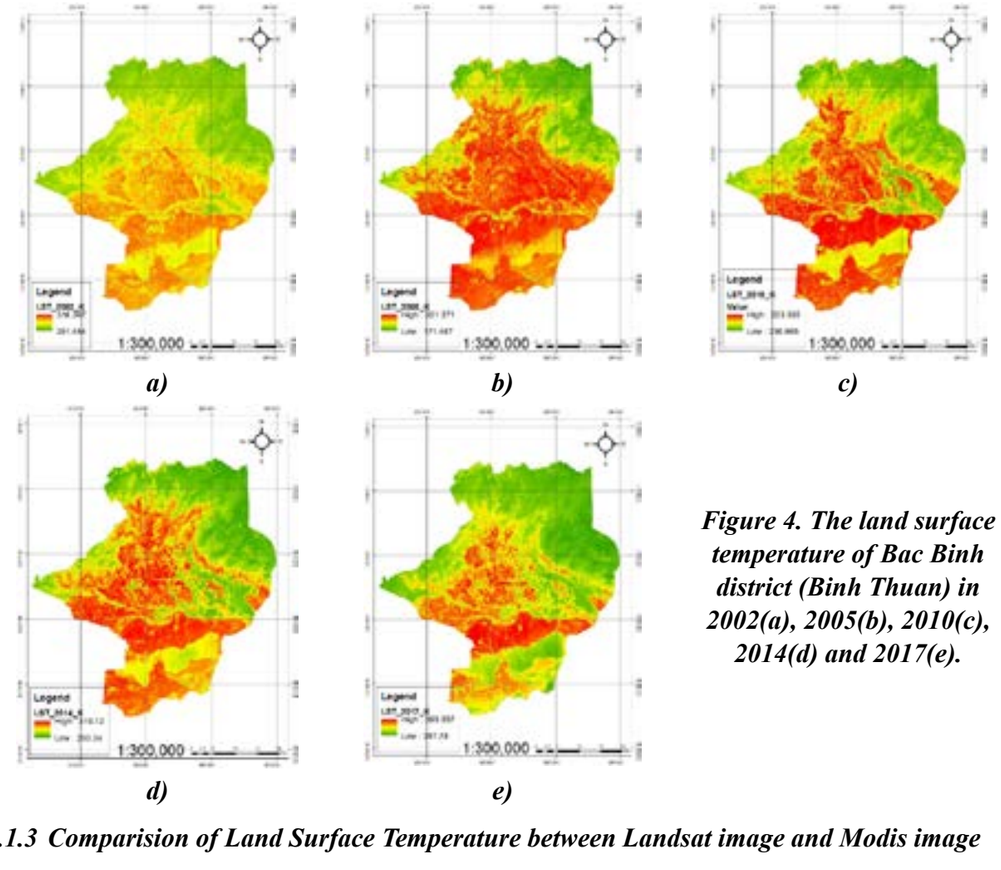

a) *b)* *c)*

d) *e)*

Figure 4. The land surface temperature of Bac Binh district (Binh Thuan) in 2002(a), 2005(b), 2010(c), 2014(d) and 2017(e).

4.1.3 Comparision of Land Surface Temperature between Landsat image and Modis image

The Land Surface Ttemperature (LST) calculated from the Landsat image is compared to the product of MODIS. Due to the different resolutions of the two images (Landsat and Modis), Landsat's LST is downscaled. The value of pixels is scattered on a two-dimensional space. Figure 5 shows the relationship between the values of the two temperature images from 2002 to 2014. The correlation coefficients (R^2) are relatively low (< 0.15). This is because of the downscaling and there is a difference between the calculated time of the two images, Landsat and Modis. However, one thing to note is that, in general, the temperature calculated from the Landsat image is 5 ^oC lower value compared to the Modis image.

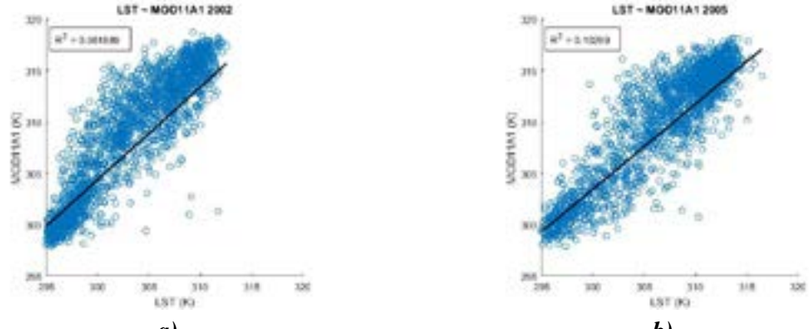

a) *b)*

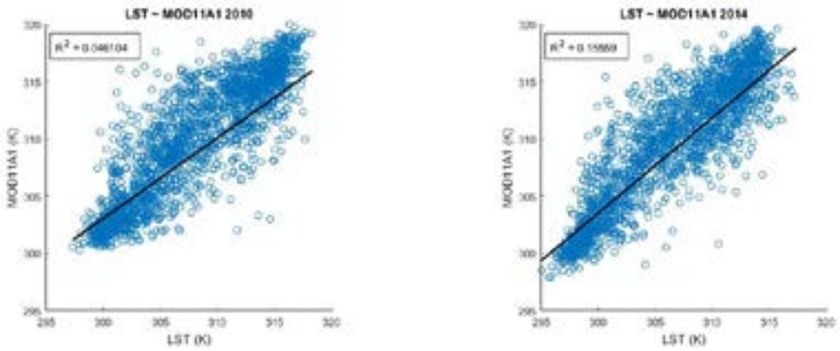

c) *d)*

Figure 5. Comparison of LST between Landsat image and Modis image in 2002(a), 2005(b), 2010(c) and 2014(d).

4.1.4 The observed Ts-Ta temperature

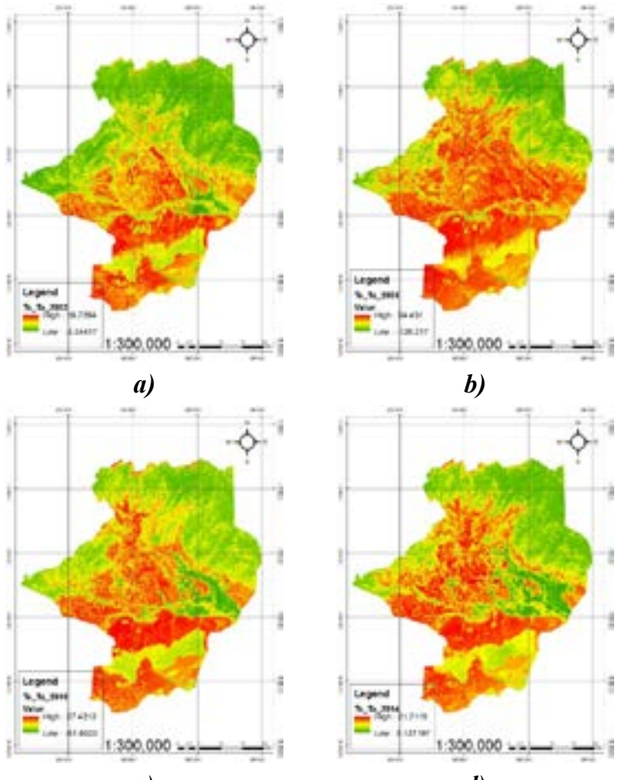

a) *b)*

c) *d)*

Figure 6. The Ta of Bac Binh district (Binh Thuan) in 2002(a), 2005(b), 2010(c) and 2014(d).

Using the DEM image with 30×30 meters resolution (Digital Elevation Model) to calibrate the observed air temperature Ta, after that, the land surface temperature is used to calculate the Ts-Ta. To correct the effect of topography, we used Ts-Ta to consider local pressure from altitude and transform surface temperature to potential temperature.

4.1.5 The maximum and minimum temperature in the relationship of NDVI/LST or Ts-Ta

To determine the dry edge of the relationship between LST and NDVI as well as Ts-Ta (ΔT) and NDVI, in this study, we divided the NDVI into 15 segments and determined the maximum temperature at these segments.

Figure 7 shows the results of the scatter diagrams between the land surface temperature and the Normalized Difference Vegetation Index by years from 2002 to 2017 to determine the equations of dry edge and wet edge. The details of these equations are in Table 1. Similarly, with the LST/NDVI, the triangular shapes of ΔT/NDVI relationship are shown in Figure 8 and the equations of ΔT_{max} and ΔT_{min} presented in Table 2.

These results show that surface temperature decreases with increasing vegetation cover when the trapezoid shape can change to a triangular shape, according to lots of remote data. For a heterogeneous surface, the temperature is an indicator of surface energy fluxes partitioning rather than an indicator of soil moisture. Thus the warm edge is more likely to represent limiting values for surface evaporation rather than a purely dry soil surface. Within each type of land surface, the warm edge of the triangle is the lower bound of evapotranspiration and the upper bound of vegetation foliage temperature. The cold edge of the triangle is the upper bound evapotranspiration when actual evapotranspiration is equal to potential evapotranspiration in some range near the cold edge.

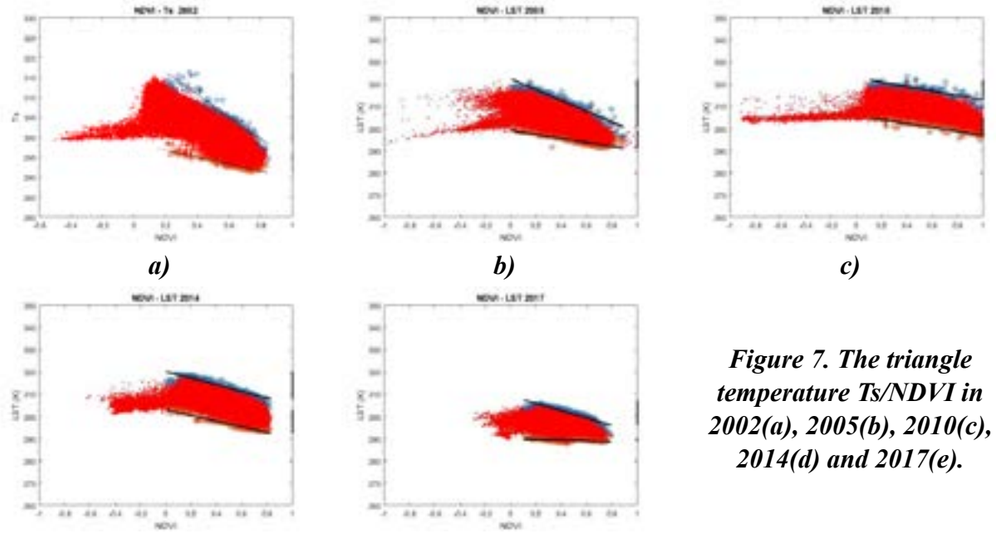

a) *b)* *c)*

d) *e)*

Figure 7. The triangle temperature Ts/NDVI in 2002(a), 2005(b), 2010(c), 2014(d) and 2017(e).

Table 1. The dry edge and wet edge (LST/NDVI) for the years 2002, 2005, 2010, 2014 and 2017.

Year	LST_{max} (K°)	LST_{min} (K°)
2002	-27.8631 NDVI + 321.8861	-8.9040 NDVI + 298.6472
2005	-24.1558 NDVI + 322.3543	-8.9730 NDVI +299.0820
2010	-9.9723 NDVI +322.9200	-8.9609 NDVI +305.8564
2014	-14.8577 NDVI +320.1936	-12.7504 NDVI +303.0350
2017	-16.5339 NDVI +309.2286	-1.4143 NDVI +289.9726

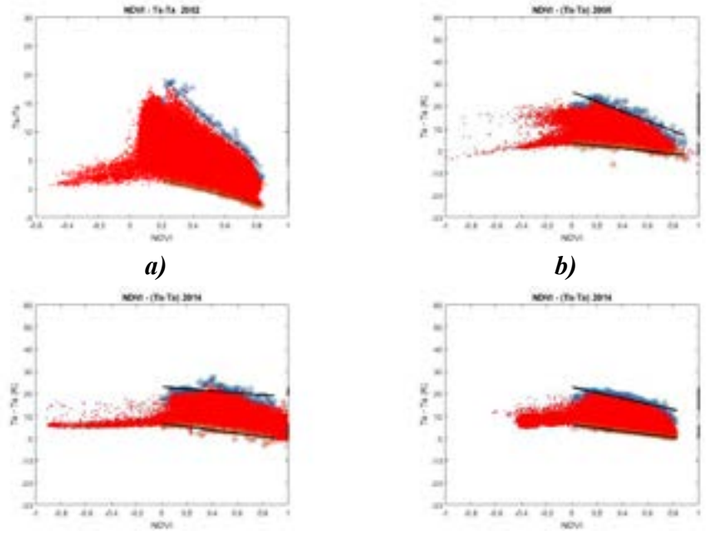

a) *b)* *c)* *d)*

Figure 8. The triangle temperature Ts-Ta/NDVI in 2002(a), 2005(b), 2010(c) and 2014(d).

Table 2. The dry edge and wet edge (Ts-Ta/NDVI) for the years 2002, 2005, 2010 and 2014

Year	ΔT_{max} (K°)	ΔT_{min} (K°)
2002	-24.4810 NDVI + 24.3367	-6.8970 NDVI + 2.9584
2005	-21.9738 NDVI + 26.4341	-5.8838 NDVI +3.3268
2010	-4.4785 NDVI + 23.0267	-7.4154 NDVI + 6.5539
2014	-12.6023 NDVI + 22.9592	-6.9774 NDVI + 5.8902

4.2 Estimating the TVDI and iTVDI

The TVDI or iTVDI values range from 0 to 1. We classified the levels for temperature vegetation dryness index, which is shown in Table 3. In particular, the TVDI or iTVDI values, which are smaller than 0.2, represent the no drought risk area (well-watered, healthy and fully vegetated agricultural land). If the value lies between 0.2 and 0.4, the area will have a low risk of drought (forest area). For the next 2 segments (0.4 - 0.6 and 0.6 - 0.8), the areas are regarded as medium drought risk and drought risk areas. If the TVDI is larger than 0.8, this area will have severe drought risk.

Table 3. Classification of the drought risk for the TVDI map

No.	TVDI/iTVDI values	Drought grade
1	0 - 0.2	Not drought
2	0.2 - 0.4	Light drought
3	0.4 - 0.6	Medium drought
4	0.6 - 0.8	Drought
5	0.8 - 1	Severe drought

Source: (Trinh Le Hung, 2015)

4.2.1 The Temperature Vegetation Dryness Index (TVDI)

The classified TVDI maps for Bac Binh district (Binh Thuan) based on LST and TVDI are shown in Figure 9. As a result, it is clear to be seen that a large area of Bac Binh district is regarded as having medium and higher drought risk and concentrated in the centre part of the area. Areas with low drought risk are located mainly in the north of Bac Binh. In fact, this is a hilly area covered with forest.

Table 4 shows the proportions of each classified drought risk area by TVDI and iTVDI. It can be seen that the Drought and Severe Drought areas account for about 40 to 50 %. Although this proportion tended to remain constant (from 46.22 % in 2002 to roughly 47 % in 2017), the change is significant, moving from Drought to Severe Drought. In other words, the intensity of drought in Bac Binh rose through time. This can be clearly seen in the results of TDVI in 2014 and 2017 when the proportions of severe drought risk areas soared up to 17.18 % in 2014 and 14.77 % in 2017 compared to less than 0.3 % in the former years.

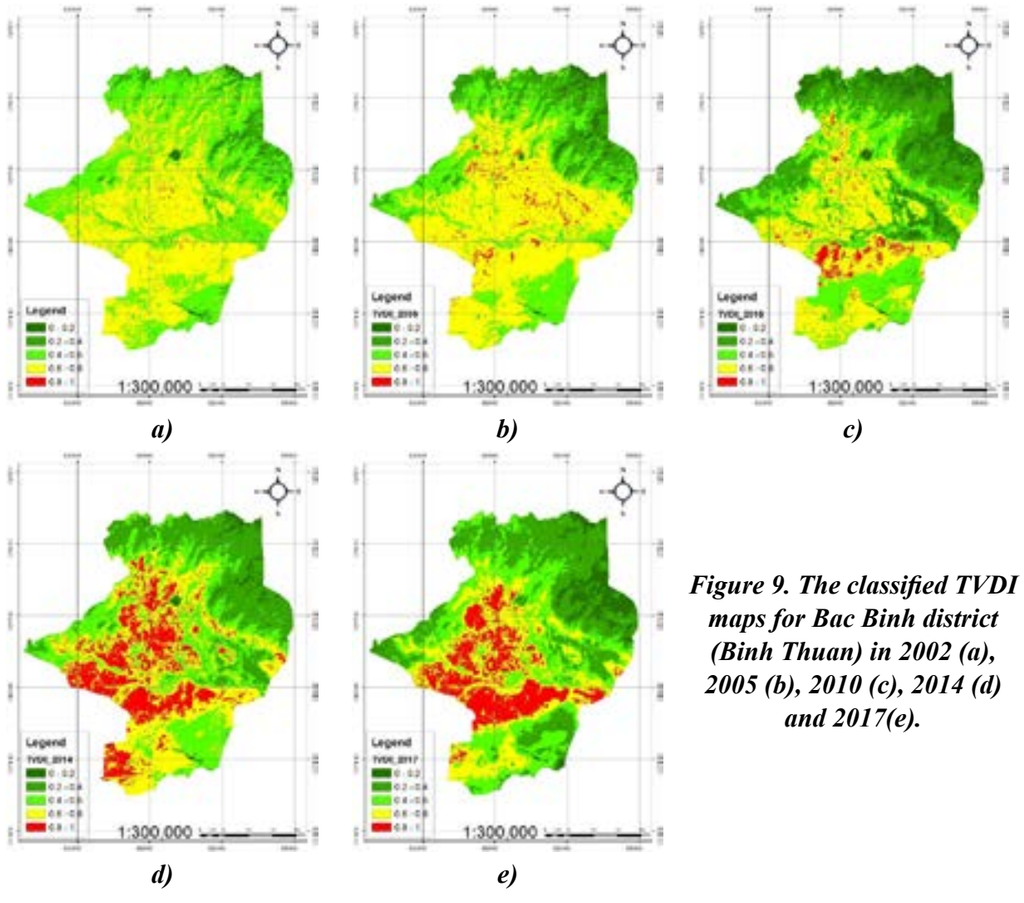

a) *b)* *c)* *d)* *e)*

Figure 9. The classified TVDI maps for Bac Binh district (Binh Thuan) in 2002 (a), 2005 (b), 2010 (c), 2014 (d) and 2017(e).

4.2.2 The improved Temperature Vegetation Dryness Index (iTVDI)

The outcomes of iTVDI from 2002 to 2014 are presented in Figure 10. Overall, in terms of dryness trend, the iTVDI has the same results as the TVDI. The area is classified as Drought

and Severe Drought, mainly found in the center of the area and the level of drought has increased sharply since 2014. However, compared to TVDI results, the value of iTVDI is lower. Percentage of Drought and Severe Drought range from 20 - 40 %. This number in 2002 is only 5 %.

A comparison between the histogram of the 2 dryness indices images from 2002 to 2014 is shown in Figure 10. These figures show that the shapes of histograms are similar. However, the iTVDI value is shifted to the lower value domain compared to TVDI. This, again, confirms that the iTVDI, with the use of air temperature collaborated with DEM, has reduced the value of the dryness index over the years.

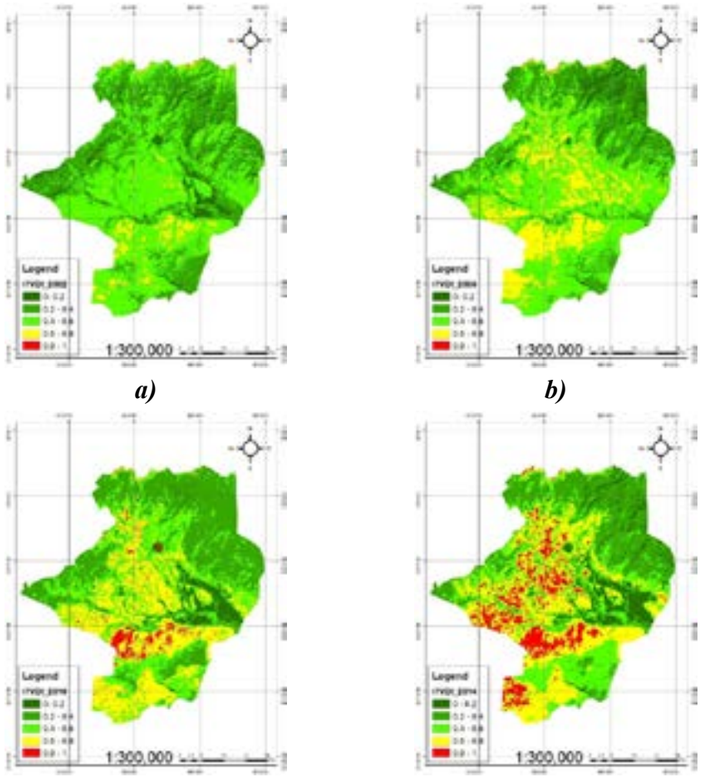

a) *b)*

c) *d)*

Figure 10. The classified iTVDI maps for Bac Binh district (Binh Thuan) in 2002 (a), 2005 (b), 2010 (c) and 2014 (d).

Table 4. Proportions of each classified drought risk area (Bac Binh).

Year	Areas (%)									
	No drought		Low drought		Medium drought		Drought		Severe drought	
	TVDI	iTVDI	TVDI	iTVDI	TVDI	iTVDI	TVDI	iTVDI	TVDI	iTVDI
2002	0.99	6.81	9.60	37.18	43.20	50.47	45.66	5.49	0.56	0.06
2005	2.45	6.08	16.38	26.46	28.97	46.91	49.98	20.42	2.22	0.12
2010	10.24	3.94	27.29	36.50	28.10	29.70	31.26	26.87	3.11	2.98
2014	2.28	6.82	22.66	28.38	26.99	25.78	30.89	29.23	17.18	9.80
2017	5.91		28.78		27.28		23.27		14.77	

5. CONCLUSIONS

In conclusion, this study conducted a drought assessment in Bac Binh, Binh Thuan, Vietnam, using TVDI and iTVDI. The results of surface temperature calculations are compared with the results from the MODIS image to check the accuracy of the calculation. The results of the drought assessment from 2002 to 2014 by the TVDI and iTVDI indices indicate that the area of significant area is at high risk of severe drought and drought. The study also compared the two drought indices and found that TVDI tended to have a higher drought rating than the iTVDI.

There are some limitations to the study. The comparison of land surface temperature between Landsat and Modis images for the correlation coefficient is not high due to the downscaling Landsat image. Another issue is that the drought index changed significantly from 2010 (Landsat 7) to 2014 (Landsat 8) in both indices. There is, therefore, a need to study whether this change is due to the difference between the two satellites' images or, indeed because the drought rate in the study area has increased.

6. REFERENCES

Arnon Karnieli, Nurit Agam, Rachel T. Pinker, Martha Anderson, Marc L. Imhoff, Garik G. Gutman, Natalya Panov, Alexander Goldberg, 2009. Use of NDVI and land surface temperature for drought assessment: merits and limitations. *Journal of Climate*, Vol. 23, No. 3, 618-633.

Han, L., Li, X., Wang, J., Liu, S., & Jiao, Z., (2004). A simple interpretation of NDVI-Ts space combining LAI and evapotranspiration. *Geoscience and Remote*, 3611-3614. https://doi.org/10.1109/IGARSS.2004.1369899.

Hassan, Q.K., Bourque, C.P.A., Meng, F.R., Cox, R.M., 2007. A wetness index using terrain corrected surface temperature and NDVI derived from standard MODIS products: an evaluation of its use in a humid forest dominated region of eastern Canada. *Sensors 7*(10), 2028-2048.

Liu, Y. Y., Evans, J. P., McCabe, M. F., De Jeu, R. A. M., van Dijk, A. I. J. M., & Su, H., (2010). Influence of cracking clays on satellite estimated and model simulated soil moisture. *Hydrology and Earth System Sciences, 14*, 979-990.

Lu Yuan, Tao Heping, Wu Hua, 2007. Dynamic drought monitoring in Guangxi using revised temperature vegetation dryness index. *Wuhan University Journal of Natural sciences, 12*, 663-668.

Moron M S, Clarke T R, Inoue Y, et al., 1994. Estimating crop water deficit using the relation between surface air temperature and spectral vegetation index [J]. *Remote Sensing of Environment, 49*, 246-263

Owe, M., De Jeu, R. A. M., & Holmes, T. R. H., (2008). Multi-sensor historical climatology of satellite-derived global land surface moisture. *Journal of Geophysical Research, 113*, F01002.

Ran, Q., Zhang, Z., Zhou, Q., Wang, Q., 2005. Soil moisture derivation in China using AVHRR data and analysis of its affecting factors. In: Geoscience and Remote Sensing Symposium, IGARSS 05 Proceedings. *IEEE International,* 4497-4500.

Rahimzadeh-Bajgiran, P., Omasa, K., & Shimizu, Y., (2012). Comparative evaluation of the Vegetation Dryness Index (VDI), the Temperature Vegetation Dryness Index (TVDI) and the improved TVDI (iTVDI) for water stress detection in semi-arid regions of Iran. *ISPRS Journal of Photogrammetry and Remote Sensing, 68*(1), 1-12. https://doi.org/10.1016/j.isprsjprs.2011.10.009.

Rojas, O., Vrieling, A., & Rembold, F., (2011). Assessing drought probability for agricultural areas in Africa with coarse resolution remote sensing imagery. *Remote Sensing of Environment, 115*(2), 343-352. https://doi.org/10.1016/j.rse.2010.09.006.

Trinh Le Hung, 2014. The distribution of land surface temperature using LANDSAT data. *Earth Science Journal*, *36*(1). Doi:10.15625/0866-7187/36/1/4145.

Trinh Le Hung, D. K. H., (2015). Drought risk evaluation using remote sensing: a case study in Bac Binh district, Binh Thuan province. *Journal of Science, 88*(12), 128-139.

Van de Griend A.A., Owen M., 1993. On the relationship between thermal emissivity and the normalized difference vegetation index for natural surface. *International journal of remote sensing, 14*, 1119-1131.

Willmott, C.J., Matsuura, K., 1995. Smart interpolation of annually averaged air temperature in the United-States. *Journal of Applied Meteorology 34*(12), 2577-2586.

Sandholt I., Rasmussen K., Anderson J., 2002. A simple interpretation of the surface temperature/ vegetation index space for assessment of the surface moisture status. *Remote Sensing of Environment*, vol.79, issues 2-3, 213-224. https://doi.org/10.1016/S0034-4257(01)00274-7.

Sandholt Inge, Rasmussen Kjeld, Andersen Jens, 2002. A simple interpretation of the surface temperature/vegetation index space for assessment of surface moisture status. *Remote Sensing of Environment, 79*, 213-224.

Zhang, A., & Jia, G., (2013). Monitoring meteorological drought in semi-arid regions using multi-sensor microwave remote sensing data. *Remote Sensing of Environment, 134*, 12-23. https://doi.org/10.1016/j.rse.2013.02.023.

COLORIZATION OF BLACK-AND-WHITE AERIAL PHOTOGRAPHS USING DEEP LEARNING FOR OBJECT-BASED IMAGE ANALYSIS LAND USE CLASSIFICATION

Arunothai Waesonthea[1], Sarawut Ninsawat[2]*, Nitin Kumar Tripathi[2], Sanit Arunplod[2], Thantham Khamyai[2]

[1]Department of Lands, Survey and Mapping Building, Chaeng Wattana Road, Pak Kret district, Nonthaburi, Thailand

[2]Remote Sensing and GIS, School of Engineering and Technology, Asian Institute of Technology, Klong Luang, Pathum Thani, Thailand

*Corresponding author. Email: sarawutn@ait.ac.th

ABSTRACT

The archive of multispectral images that comprise various spectral wave ranges provides a high potential for land use and land cover classification. This strength has been commonly used to trace land use in the past. In Thailand, it also has been used as legal evidence that can help in considering the possession right of the land or determine the encroachment on land. However, the critical period for judgment has only black-and-white images available. In this study, deep learning techniques to simulate the color channels of a grayscale image are adopted. Then, object-based image analysis is used to classify land use, both colorized images from deep learning and the original black-and-white image, to evaluate the capabilities of colorized images for land use classification. This study uses aerial photographs from the WWS project in 1954, Maha Sarakham province. The project has been used to prove the possession right by considering traces of land use for consideration of the issuance of title deeds, but it has only a black-and-white image available. In addition, this study also compares techniques of land use classification between pixel-based and OBIA techniques with colorized images to determine the most suitable method of land use classification. As a result, land use classifications on colorized images showed significant improvements in overall accuracy over grayscale images at +5.02 %. The study reveals that colorized images outperform grayscale images in land use classification using the OBIA technique. It can reduce confusion between cropland and nature shrubs, and this can be implemented in proving the right for encroachment on land or consideration about issuing title deeds in Thailand.

1. INTRODUCTION

Land title deeds are vital documents that can be used to confirm land ownership and transfer history. In Thailand, the Department of Lands operates and verifies the right of ownership of land and other land-related processes (Williamson, 1983). One of the Department of Land's tasks is to investigate and verify the right of ownership when the land has a disputed area or claims ownership from people. Thus, the inspection to certify land ownership needs to use the interpretation of the aerial photography technique with historical aerial photographs to help consider the trace land use scientific proof. However, the present technology utilized in operations frequently confronts issues with operational reliability and complications that cause delays (Entwisle et al., 1998). Also, most historical aerial photographs in Thailand that are used to interpret trace land use in the past are

black-and-white. The absence of spectrum information in this historical aerial photography is a limitation in classifying land use, which seriously needs spectral data for the divide of segmenting land use type (Poterek et al., 2020). Currently, there are attempts to improve the image interpretation capability from grayscale images, such as legacy aerial photographs. Image colorization now popularly uses deep learning due to the image-to-image interpretation strategy and proves that numerous computer vision and image processing methods work (Žeger et al., 2021). Moreover, it efficiently enhances land cover classification performance (Farella et al., 2022; Poterek et al., 2020). In the past, land use classification was usually divided by land use using a pixel-based technique (Enderle and Weih, 2005). The pixel-based technique analyzes the spectral properties of a pixel entity but ignores spatial or contextual information. With higher-resolution imagery, this could improve land use classification accuracy (Weih and Riggan., 2010). The possibility of creating a fully automated classification procedure that would exceed the effectiveness of pixel-based methods in the recent (Blaschke et al., 2000; Csathó et al., 1999). The object-Based Image (OBIA) technique uses image segmentation and feature extraction to manage class complexity and categorize land use (Hossain and Chen, 2019). Although high-resolution satellites represent fewer pixel sizes, they bring about pixel-based classification less effective (Veljanovski, 2011). Object-based analysis employing a multi-resolution algorithm and the random forest classifier can reliably categorize crops from black-and-white aerial photos (Vogels et al., 2017). To measure the performance of land use classification, the original black-and-white and colorized images as RGB color from deep learning are prepared in order to implement OBIA analysis for land use classifications. Land use maps are compared to evaluate accuracy.

2. MATERIALS AND METHODS

2.1 Study area

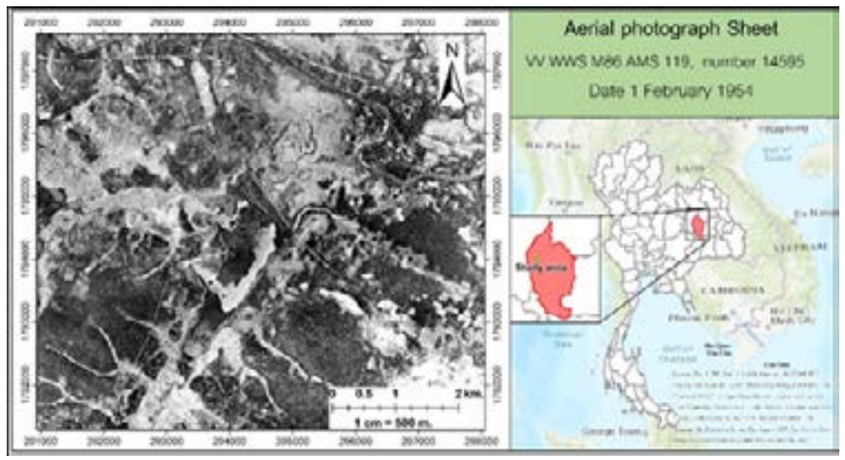

Figure 1. Shows the study area.

This study area is located in that is the northeast region of Thailand, which is mostly a mountain plateau that is not steep. The characteristic topography in the study area is plains, which cover agriculture, a few forests, bodies of water, and urban areas, as shown in Figure 1.

2.2 Overall methodology

Aerial photographs, the WWS project in 1954 has a 1-meter ground resolution with a map scale of 1:50,000 and covers an area of 36. They are black-and-white aerial photographs recorded by panchromatic film and are scanned from the films at a resolution of 20 microns using a high-precision photogrammetric scanner.

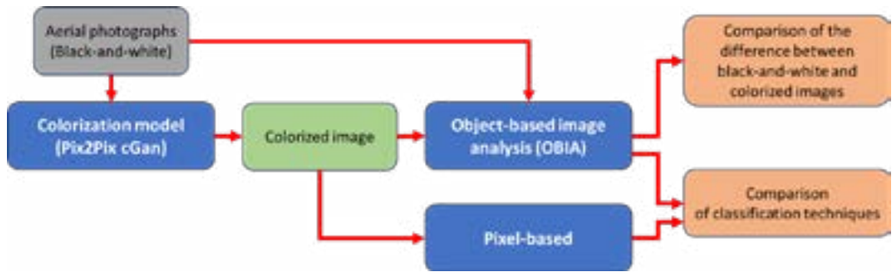

Figure 2. Outline chart of the methodology.

The overall methodology is explained in Figure 2. Outline chart of the methodology in two main processes. Firstly, the colorization model is the first process to improve the quality of images from black-and-white as RGB color. It is called a colorized image. Aerial photographs in the WWS project are improved color as RGB images based on the deep learning technique. Pix2Pix is used to train on the RGB-grayscale paired image conducted in a conditional Generative Adversarial Network (GAN). Isola et al., (2017) explained that the GAN model generates 2-channel output from a grayscale picture as x. The discriminator binds grayscale picture x to 2 channels y. The authenticity of the 3-channel image is also determined. Conditional GANs, are as follows in Eq 1.

$$\mathcal{L}_{cGAN}(G,D) = \mathbb{E}_{x,y}[\log D](x,y)] + \mathbb{E}_{x,z}[\log(1 - D\,(x, G(x,z))] \quad (1)$$

where, x is a grayscale image, y is the 2-channel image, and z is a random noise vector, G tries to minimize this function, but an adversarial D tries to maximize it.

Next process, land use classification on images is computed in two techniques, including object-based image analysis and pixel-based. Finally, the accuracy assessment considers land use classification results with an evaluation metrics equation. There is a comparison accuracy between black-and-white and colorized images on object-based image analysis. Moreover, still considered the different classification techniques between object-based analysis and pixel-based for inspecting and comparing the accuracy of the two methods. This study represents the calculation of many evaluation metrics. As given by the following equations:

$$precision = \frac{TP}{TP + FN} \quad (2)$$

$$recall = \frac{TP}{TP + FP} \quad (3)$$

$$F1 = 2 \times \frac{precision \times recall}{precision + recall} \quad (4)$$

$$IoU_c = \frac{TP_c}{TP_c + FP_c + FN_c} \quad (5)$$

$$Overall\ accuracy = \frac{\sum((TP+TN))}{Total\ classes} \quad (6)$$

$$Kappa = \frac{Total\ accuracy - Random\ accuracy}{1 - Random\ accuracy} \quad (7)$$

The TP, FP, and FN represent true positives, false positives, and false negatives, respectively, to explain the prediction proportionately as well as the correct pixels.

2.3 Land use classification

The determination types of land use classification in this study were referred by the Department of Lands to assign classes, including built-up, paddy field, field crop, forest, shrub, wetland, sand/beach, water, and transportation. This reference data for evaluation was digitized from the human visual interpretation technique using a mirror stereoscope equipment of aerial photographs acquired in the 1954 WWS project.

2.3.1 Comparison of the colorized and black-and-white images

The study aims to assess the effectiveness of different image types for accurate land use classification using Object-based image analysis. The colorized image from training deep learning is classified to compare the accuracy of land use with black-and-white images. There are two main processes. Firstly, the segmentation process extracts objects on the image by following a parameter set that consists of scale, shape, and compactness. As shown in Table 1, from Drăgut et al., 2010 used the multi-resolution segmentation algorithm to extract sub-objects for land use area grouping.

Table 1. Details of the parameter set are set in the experiment.

Parameter	Values			
Scale	50	100	200	300
shape	0.3	0.5	0.8	
Compactness	0.3	0.5	0.8	

To develop model, images are used to extract objects to classify land use types, and they are indicated by the area fit index (AFI) to consider the quality of the segmentation (Luciceer, 2004). The efficiency of segmented objects, compared to a reference polygon, can be expressed as:

$$AFI = \frac{A_{Rj} - A_{Si}}{A_{Rj}} \quad (1)$$

where A_{Rj} is the reference total area R_j, A_{Si} is the total area of the corresponding terrain segment S_i and A is an area in pixels.

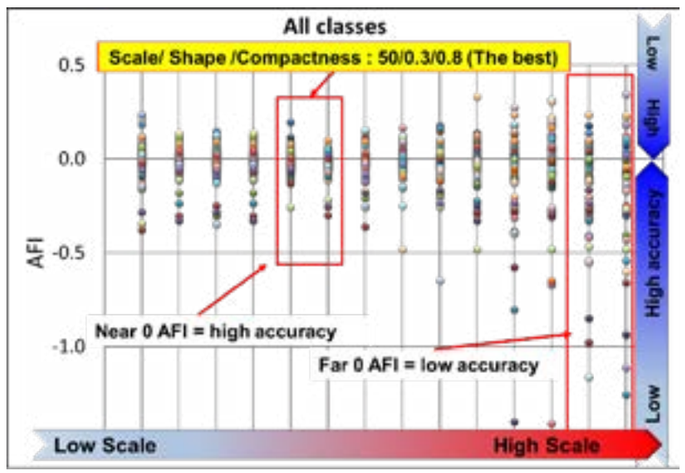

Figure 3. Shows the AFI graph result that represents 70 samples on a scale of 100.

As shown in Figure 3, that graph represents the AFI graph results on a scale of 100; all classes (70 samples) and 14 parameter sets are used to consider the best parameter sets. Lucieer and Stein. (2002) explained that the AFI value that is far from 0, the accuracy is low. On the other hand, the AFI value is close to 0, this is high accuracy. Thus, the suitable scale for an image in the WWS project is 100, then the shape and compactness parameters are 0.3 and 0.8, respectively, aligning with a previous study (Mesner N., and Oštir, K., 2014).

Then, the suitable parameter set is used to extract objects from the image by the eCognition software Developer 64 version 9.0. As a result, the nearest neighbor model classifies land use types from segmented objects. The methodology included refining classification results using the Edit Standard Nearest Neighbor Feature Space and considering GLCM texture measurements for each band to improve classification accuracy. The processes are performed with both black-and-white and colorized images to compare the accuracy. To inspect the accuracy, there is a comparison between land use classification results from original and colorized images.

2.3.2 Comparison of object-based image analysis (OBIA) and Pixel-based techniques

This content compared the efficiency of land use classification between OBIA and pixel-based with colorized images, which is conducted. Typically, the process of the pixel-based technique involves the automatic assignment of land cover classes or themes to individual pixels within an image based on their characteristics. Moreover, multispectral data is employed, wherein the spectral pattern inherent in the data for each pixel serves as the quantitative foundation for classification (Gao, Y., & Mas, J. F., 2008). However, the OBIA technique divides similar features on an image into smaller objects by gathering pixels from the size, shape, and compactness of objects in the imagery (Guo et al., 2022; Li et al., 2022). To compare the performance of land use classification on aerial photographs in this research, these techniques are also compared by an accuracy assessment with simulated images.

3. RESULTS

3.1 Land use classification between the colorized and black-and-white images

The efficiency of the land use classification was evaluated by an accuracy assessment with the reference dataset. The results were analyzed using the confusion matrix. The confusion matrix allowed us to determine various metrics indicating how accurate and precise: overall accuracy (OA), the Kappa coefficient, precision, recall, F1-score, and Intersection Over Union (IOU). These metrics are calculated and result in the black-and-white and colorized image classifications. Land use classification results can be observed in Figure 4.

There are illustrations of the evaluation metrics, including precision, recall, F1-score and IOU, as shown in Figure 5. It reveals that the classification results of colorized images exhibit higher accuracy compared to black-and-white images across all land use types. The bar charts visualize the accuracy percentages from different black-and-white and colorized images for each class: built-up, paddy field, field crop, forest, shrub, wetland, sand/beach, water, and transportation. In addition, the overall accuracy and kappa coefficient are represented in the overview of land use classification accuracy of black-and-white and colorized images. For 1954 in the WWS project, overall accuracy improved from 79.51 % (black-and-white) to 84.53 % (colorized), indicating an

improvement due to the colorization process. The Kappa coefficient classification ranges from 65.80 to 74.83 %, indicating moderate to substantial agreement in land use classification, especially in colorized images, with a high 75 % agreement, as shown in Table 2. Thus, it has high accuracy in both black-and-white and colorized images, which shows this technique is suitable for aerial photographs in the WWS project of resolution 1 meter, especially the colorized image.

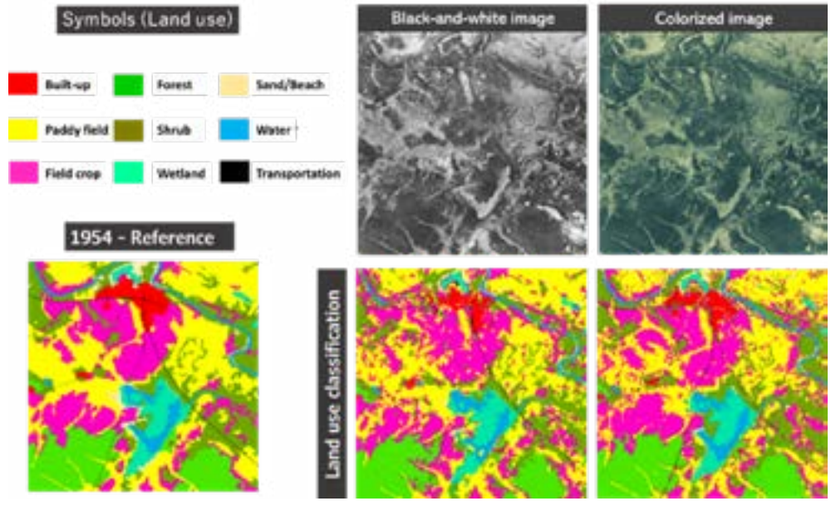

Figure 4. Land use classification results in black-and-white and colorized images.

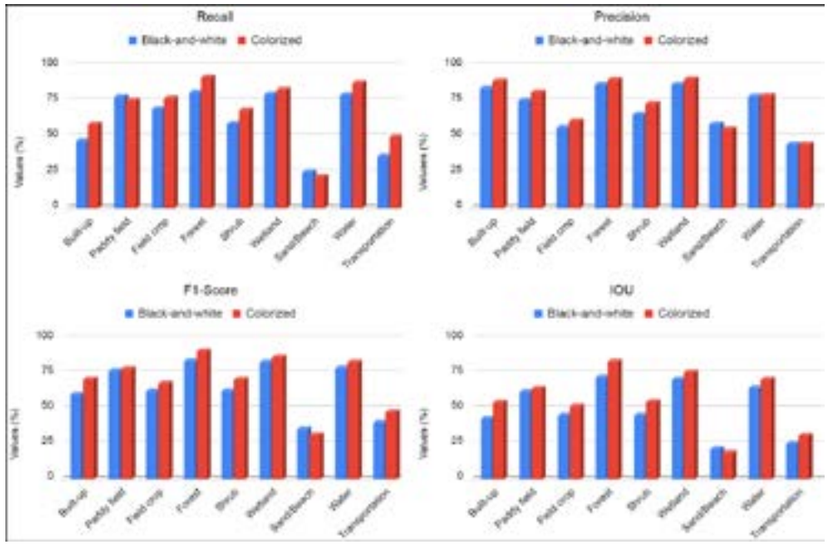

Figure 5. The bar charts represent an accuracy assessment that compares land use classifications between black-and-white and colorized images.

Table 2. Accuracy comparison among black-and-white and colorized images.

Image	Overall accuracy	kappa coefficient
Black-and-white	79.51 %	65.80 %
Colorized	84.53 %	74.83 %

3.2 Comparison of pixel based and OBIA on colorized image

Land use classification accuracy between pixel-based and OBIA techniques in this study. The accuracy in each land use of the pixel-based method is lower than another. Figure 6 shows the comparison of the land use classification accuracy between pixel-based and OBIA techniques. It found that all classes of land use with pixel-based techniques have lower accuracy than the land use classification using OBIA.

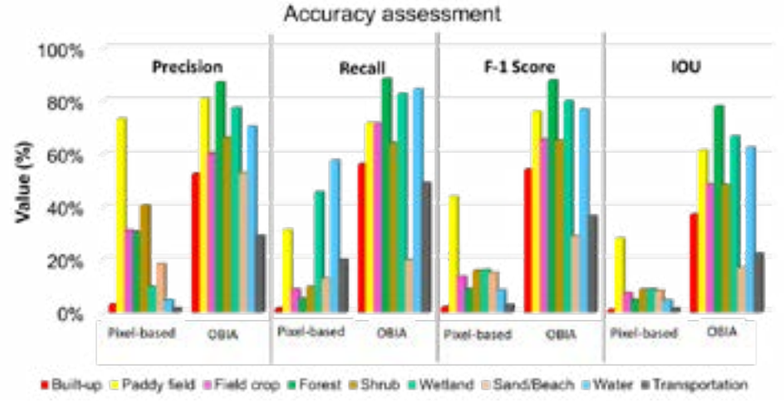

Figure 6. The bar charts represent an accuracy assessment that compares land use classifications between black-and-white and colorized images.

Table 3. Accuracy comparison among black-and-white and colorized images.

Image	Overall accuracy	Kappa coefficient
Pixel-based	18.99 %	69.05 %
Object-based image analysis	84.53 %	74.83%

As well as the overall accuracy and kappa coefficient of 18.99 % and 69.05 %, respectively, for the pixel-based, which is lower compared to the OBIA technique of 84.53 % and 74.83 %, respectively, as shown in Table 3. This table can summarize that OBIA outperforms the pixel-based technique because there is high overall accuracy and a high Kappa coefficient. However, we still found that pixel-based models have a high kappa coefficient. They are 69.05 %, which shows the accuracy of classification in the dataset is better than random within an acceptable range of moderate. On the other hand, the low overall accuracy means that land use classification is highly mixed with other classes.

4. DISCUSSION

For the object-based image analysis technique, the difference between black-and-white and the colorized image impacts classifying land use. We found the accuracy of land use classification using colorized images to be higher th444an black-and-white images by about 5.02 %. Land use classification on the colorized images can classify more precise classes, especially mixing land of agriculture and shrubs. In contrast, some areas reflected that bright color and were often confused to distinguish classes, such as beaches and sand, which are usually found to mix with the paddy field after harvesting. Thus, it leads to low land use classification accuracy while still classifying land use higher than the black-and-white image.

In the techniques for land use classification, the OBIA technique is there to distinguish land use, although the pixel-based method has been popularly used with the multispectral image. However, most results found that the pixel-based technique has the effect of "salt and pepper" when applied to high-resolution images. Thus, it leads to a lack of precision in the classification (Gao and Mas, 2008; Van de Voorde et al., 2004). On the other hand, the OBIA technique considers spatial and contextual information, such as the shape, size, and texture of objects and their relationships. From causes why the pixel-based has low performance when compared with the OBIA techniques in this study. The spectral information of the colorized image in this study as RGB colors provided is spectrally insufficient to distinguish land use the pixel-based method performance. Because pixel-based mainly relies on spectral features for the classification but has only three bands in this study. The accuracy of the RGB image processing, when considering all evaluated vegetation, exhibited confusion as the spectral information diminished (Öztürk and Çölkesen, 2021).

5. CONCLUSION

Many limitation for historical aerial photographs that are used to investigate the trace land use in the past is the quality of spectral only black-and-white color and resolution from the scanned film. From this study, object-based image analysis has higher performance than pixel-based techniques for the classification of images that have high resolution. Moreover, land use classification was better by 5.02 % when colorized images from testing the colorization model were used, compared to black-and-white ones, but the accuracy in classifying highly reflective areas like sand bars or harvested paddy fields has still confused classification. Thus, the multispectral image as RGB channels is still not enough to distinguish land use for these techniques. Despite the shortcomings, the study underlines the importance of color in helping land use classification in a remote sensing context. It shows the approach to improving historical aerial photographs with remote sensing techniques and deep learning. The model proved useful in identifying primary land use categories. Finally, a human visual assessment was still needed to investigate sub-classes, or land uses requiring more detailed types.

6. REFERENCES

Barcia P. A. U. L. O., Bugalho M. N., Campagnolo M. L., and Cerdeira J. O., 2007. Using n-alkanes to estimate diet composition of herbivores: A novel mathematical approach. *Animal*, *1*(1), 141-149.

Cao L., Jiao L., Li Z., Liu T., Zhong Y. (2017). Grayscale image colorization using an adaptive weighted average method. *Journal of Imaging Science and Technology, 61*(6), 60502–1. https://doi.org/10.2352/J.ImagingSci.Technol.2017.61.6.060502

Csathó B., Schenk T., Lee D.C., and Filin S., 1999. Inclusion of multispectral data into object recognition. *International Archives of Photogrammetry and Remote Sensing*, *32*(7-4), 53-61.

Drăgut L., Tiede D., and Levick S.R., 2010. ESP: A tool to estimate scale parameter for multi-resolution image segmentation of remotely sensed data. *International Journal of Geographical Information Science*, *24*(6), 859-871.

Enderle D.I., Weih Jr R.C., 2005. Integrating supervised and unsupervised classification methods to develop a more accurate land cover classification. *Journal of the Arkansas Academy of Science*, *59*(1), 65-73.

Entwisle B., Walsh S.J., Rindfuss R.R., and Chamratrithirong A., 1998. Land-use/land-cover and population dynamics, Nang Rong, Thailand. *People and pixels: Linking remote sensing and social science*, 121-144.

Farella E.M., Malek S., and Remondino F., 2022. Colorizing the Past: Deep Learning for the Automatic Colorization of Historical Aerial Images. *Journal of Imaging*, *8*(10), p. 269.

Gao Y., and Mas J.F., 2008. A comparison of the performance of pixel-based and object-based classifications over images with various spatial resolutions. *Online journal of earth sciences*, *2*(1), 27-35.

Hossain M.D., and Chen D., 2019. Segmentation for Object-Based Image Analysis (OBIA): A review of algorithms and challenges from remote sensing perspective. *ISPRS Journal of Photogrammetry and Remote Sensing*, *150*, 115-134.

Isola P., Zhu J. Y., Zhou T., & Efros A. A., (2017). Image-to-image translation with conditional adversarial networks. *Proceedings of the IEEE conference on computer vision and pattern recognition*, 1125-1134.

Lucieer A., & Stein A., (2002). Existential uncertainty of spatial objects segmented from satellite sensor imagery. *IEEE Transactions on Geoscience and Remote Sensing, 40(11)*, 2518-2521.

Lucieer A., (2004). Uncertainties in Segmentation and their Visualization. *Doctoral dissertation*, Utrecht University and International Institute for Geo-Information Science and Earth Observation (ITC).

Marpu P.R., Niemeyer I., Nussbaum S., and Gloaguen R., 2008. A procedure for automatic object-based classification. *Object-based Image analysis: spatial concepts for knowledge-driven remote sensing applications*, 169-184.

Mesner N., and Oštir K., 2014. Investigating the impact of spatial and spectral resolution of satellite images on segmentation quality. *Journal of Applied Remote Sensing*, *8*(1), 083696-083696.

Öztürk M.Y., and Çölkesen İ., 2021. The impacts of vegetation indices from UAV-based RGB imagery on land cover classification using ensemble learning. *Mersin Photogrammetry Journal*, *3*(2), 41-47.

Poterek Q., Herrault P.A., Skupinski G., and Sheeren D., 2020. Deep learning for automatic colorization of legacy grayscale aerial photographs. *IEEE Journal of Selected topics in Applied Earth Observations and Remote Sensing*, *13*, 2899-2915.

Thomas Blaschke, Stefan Lang, Eric Lorup, Josef Strobl and Peter Zeil, 2000. Object-oriented image processing in an integrated GIS/remote sensing environment and perspectives for environmental applications. Environmental Information for Planning, Politics and the public vol. 2, (Cremers, A. and Greve, K., editors). *Metropolis*, Marburg, 555-570.

Van de Voorde T., W. De Genst., F. Canters., N. Stephenne., E. Wolff and M. Binard, 2004. Extraction of land use/land coverrelated information from very high-resolution data in urban and suburban areas, Remote Sensing in Transition. Proceedings of the 23rd Symposium of the European Association of Remote Sensing Laboratories. *Mill Press*, Rotterdam, 237-244.

Veljanovski T., Kanjir U., and Ostir K., 2011. Object-based image analysis of remote sensing data. *Geodetski vestnik*, *55*(4), 678-688.

Vogels M.F., De Jong, S.M., Sterk G., and Addink E.A., 2017. Agricultural cropland mapping using black-and-white aerial photography, object-based image analysis and random forests. *International journal of applied earth observation and geoinformation*, *54*, 114-123.

Weih R.C., and Riggan N.D., 2010. Object-based classification vs. pixel-based classification: Comparative importance of multi-resolution imagery. *Int. Arch. Photogramm. Remote Sens. Spat. Inf. Sci. 38,* C7

Williamson I.P., 1983. Cadastral survey techniques in developing countries with particular reference to Thailand. *Australian surveyor*, *31*(7), 496-512.

Ye Z., Yang K., Lin Y., Guo S., Sun Y., Chen X., Lai R., and Zhang H., 2023. A comparison between Pixel-based deep learning and Object-based image analysis (OBIA) for individual detection of cabbage plants based on UAV Visible-light images. *Computers and Electronics in Agriculture, 209*, 107822.

Žeger I., Grgic S., Vuković J., and Šišul G., 2021. Grayscale image colorization methods: Overview and evaluation. *IEEE Access*, *9*, 113326-113346.

SPATIAL-TEMPORAL ANALYSIS OF NO_2 CONCENTRATION IN BINH DUONG PROVINCE, VIETNAM

Nguyen Thi Bich Ngoc[1], Pham Thi Mai Thy[2], Nguyen Le Tan Dat[1], Tran Thi An[1]*

[1]Faculty of Management Science, Thu Dau Mot University, Ho Chi Minh city, Vietnam
[2]Ho Chi Minh city Space Technology Application Center, Vietnam
*Corresponding author. Email: antt@tdmu.edu.vn

ABSTRACT

This study aims at using Sentinel-5P satellite data for analyzing NO_2 concentrations in Binh Duong province, Vietnam. Google Earth Engine, which is a cloud-based geospatial analysis platform, has been used to collect satellite data and extract information on NO_2 concentrations in Binh Duong in the period from 2018 to 2023. Based on the analysis over time, NO_2 dispersion is dependent on seasonal variation and spatial distribution. The average NO_2 density is ranging from 17.2 to 41.86 µmol/m^2 in the period from 2018 to 2023. The average NO_2 concentration in the areas with a high density of industrial factories is higher than in other regions in Binh Duong province. Based on the spatial analysis of NO_2 concentration in Binh Duong, the NO_2 index is highest in Di An city and lowest in Phu Giao district. Results from this study are valuable for air pollution monitoring in Binh Duong as well as other industrial provinces in Vietnam.

1. INTRODUCTION

Air pollution is a significant concern for sustainable development and public health in many countries. Due to the industrialization and urbanization progress, the increasing emissions from industrial and transportation sources contribute to the degradation of air quality. The rapid population growth, along with the rising number of vehicles and inadequate infrastructure, exacerbates the severity of the current pollution problem. NO_2, a gas known for its high solar radiation absorption capacity, primarily originates from transportation and industrial activities (Solomon et al., 1999). Despite the ongoing economic development in Vietnam, the issue of air pollution, including NO_2 pollution, has not been adequately addressed. In this context, research on the assessment of the current NO_2 pollution is crucial and valuable for the mitigation of air pollution issues, ensuring long-term sustainability and aligning with the country's realities.

Binh Duong is a province located in the Southeast region of Vietnam, and it serves as an important hub connecting various provinces and cities in the Southern key economic zone. Currently, the province has the highest per capita income in the country (General Statistics Office, 2020). With the rapid growth of businesses and industrial zones in Binh Duong province in recent years, controlling air quality and ensuring sustainable industrial development have become urgent priorities.

Satellite-based remote sensing has become an ideal alternative solution for long-term monitoring of air quality in different spatial and temporal scales (Aldabash et al., 2020). Satellite imagery has been studied in Vietnam since the 1980s and has been applied using remote sensing technology for many years. Monitoring air pollution through satellite remote sensing is a valuable method for researchers to easily analysis of temporal and spatial changes. Air quality resources are

directly linked to human survival, but the advanced application of remote sensing technology for air quality monitoring is currently limited in Vietnam (Tran Thi Van et al., 2012). The Copernicus Sentinel-5P is one of the powerful remote sensing data that is currently widely used in air quality monitoring (Aldabash et al., 2020; Verhoelst et al., 2021; Faisal and Muhamad, 2023). The Sentinel-5P satellite is specifically for monitoring air quality, which is Nitrogen Dioxide (NO_2), climate, and the ozone layer, with global coverage and daily temporal resolution (Faisal and Muhamad, 2023).

Numerous tools have been developed to facilitate the analysis of satellite imagery. Google Earth Engine (GEE) is a highly advanced tool for assessing current air pollution. By utilizing various analysis algorithms and data processing capabilities within this platform, researchers can generate maps that depict the levels of air pollution and identify areas with high pollution levels. GEE has the capacity to handle large-scale geospatial datasets with global coverage, and the processing techniques can be implemented through its code editor.

Despite conducting numerous studies on air pollution, the evaluation of long-term variations in tropospheric NO_2 remains limited in the province. Therefore, applying the Google Earth Engine platform to monitor air quality in Vietnam as well as Binh Duong province is a highly practical issue. The research aims to analyze the temporal and spatial variations of tropospheric NO_2 data in Binh Duong province using GEE for the period from 2018 to 2023. The results from this study are an important background for local government to propose effective, responsible strategies for air pollution in the province.

2. METHODOLOGY

The research process is summarized in Figure 1 determining the tropospheric NO_2 concentrations in the Binh Duong area during the study period from 2018 to 2023. The authors conducted the data collection and literature review. Next, the collected data was processed and analyzed, categorized into two types: spatial analysis and temporal analysis of NO_2 data.

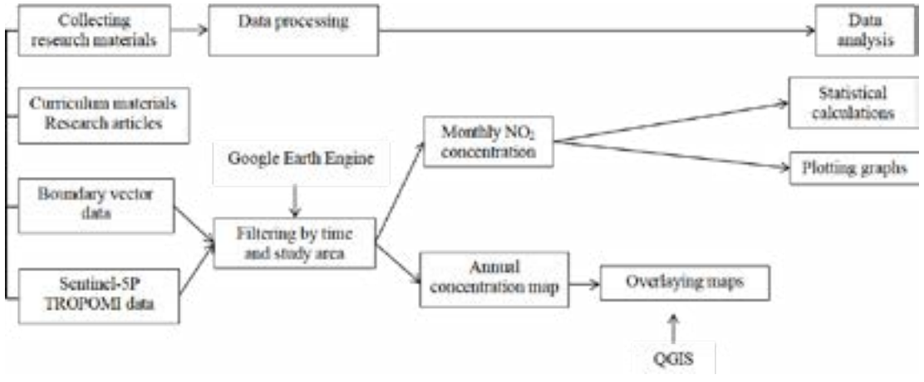

Figure 1. The research workflow on NO_2 concentration in Binh Duong province.

2.1 Data collection methods

The tropospheric NO_2 data was extracted from the TROPOMI sensor onboard the Sentinel-5P satellite (Sentinel-5 Precursor/Sentinel-5P). The Copernicus Sentinel-5P consists of a satellite carrying the TROPOspheric Monitoring Instrument (TROPOMI) instrument. The TROPOMI mission is to perform atmospheric measurements with high spatio-temporal resolution, to be used for air quality, ozone and and UV radiation, and climate monitoring and forecasting (ESA, 2017). The Sentinel-5P satellite was successfully launched in October 2017 from the Plesetsk Cosmodrome in Russia (Verhoelst et al., 2021), and it is a result of collaboration between ESA, the European Commission, and the Netherlands Space Office. TROPOMI is an advanced Differential Optical Absorption Spectroscopy (DOAS) instrument with a wide swath of 2600 km (approximately 104°) and a spatial sampling of 7 × 7 km² (Veefkind et al., 2012). The satellite operates in a sun-synchronous orbit at an altitude of 824 km and has an orbital cycle of 17 minutes with an inclination of 98.742°. Data from Sentinel-5P includes total Columns of Ozone (O3), Nitrogen Dioxide (NO_2), Carbon Monoxide (CO), Cloud and Aerosol information, such as Formaldehyde, Sulphur Dioxide, and total Columns of Methane (ESA, 2017). Its temporal resolution is 1 day, allowing for the monitoring of air quality variations over time. TROPOMI is capable of observing the atmosphere under various lighting conditions, including both day and night. This enables continuous and comprehensive data collection on air quality.

In this study, all remote sensing data collection steps are performed online on the official website of GEE using code. Additionally, the research also collects supplementary data from websites of various organizations, research groups, and dissertations, both domestic and international, as well as data related to the NO_2 index and the GEE platform.

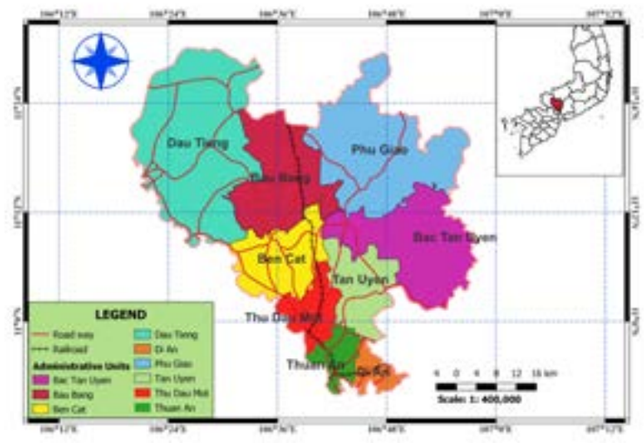

Figure 2. Administrative map of Binh Duong province.

The administrative data of Binh Duong province is downloaded from the website https://gadm.org/download_country.html to archive the GIS data in shapefile format. QGIS 3.28.3 software is used to clip the boundaries of the region. The location of Binh Duong is selected on the map, and the boundaries are clipped accordingly. Subsequently, the saved boundaries are used and added to the main page of the GEE code editor for data processing methods.

2.2 Data processing methods

The extraction of NO_2 concentration data is directly carried out through the GEE platform using the Earth Engine Code Editor (https://developers.google.com/earth-engine/guides). The research area boundaries are saved on the main GEE page as a *FeatureCollection*. The study period is selected using the *ee.Date()* tool, where the start and end times are inputted on a

monthly basis throughout the research period. The satellite image level is utilized through the *ee.ImageCollection()* function and *ee.select()* to combine with the desired spectral bands. Since the NO_2 concentration is in small units, the unit is converted from mol/m^2 to µmol/m^2 for easier analysis using the *image.multiply()* function. The *Image.reduceRegion()* function is performed on the ImageCollection using specific functions to calculate the average NO_2 concentration values. The *ee.batch.Export.image.toDrive* tool is used to store all the maps in Google Drive for further analysis on other platforms. The NO_2 values are stored as data, and the pollution maps are extracted in Raster format.

After the maps are stored, the satellite image data will be used to create a map depicting the NO_2 concentration changes in Binh Duong. This process is performed using QGIS 3.28.3 software. The overlapping of annual concentration maps into a map for the research period of 2018-2023 is carried out using the Raster Calculator tool.

2.3 Data analysis methods

The process involves constructing charts and performing statistical calculations using Microsoft Excel Office 365 software. A comparison is made between NO_2 data results using Sentinel-5P satellite imagery in terms of spatial and temporal dimensions. Specifically, the differences are compared across months and years within the research period of 2018-2023, as well as the distribution of NO_2 concentration among different provinces and cities. From these comparisons, the results are combined to provide analysis and conclusions regarding the variations in NO_2 concentration over the years. Finally, an objective analysis of the NO_2 data situation during the research period is presented.

3. RESULTS AND DISCUSSION

3.1 Analysis of NO_2 concentration trends in Binh Duong over the period 2018-2023

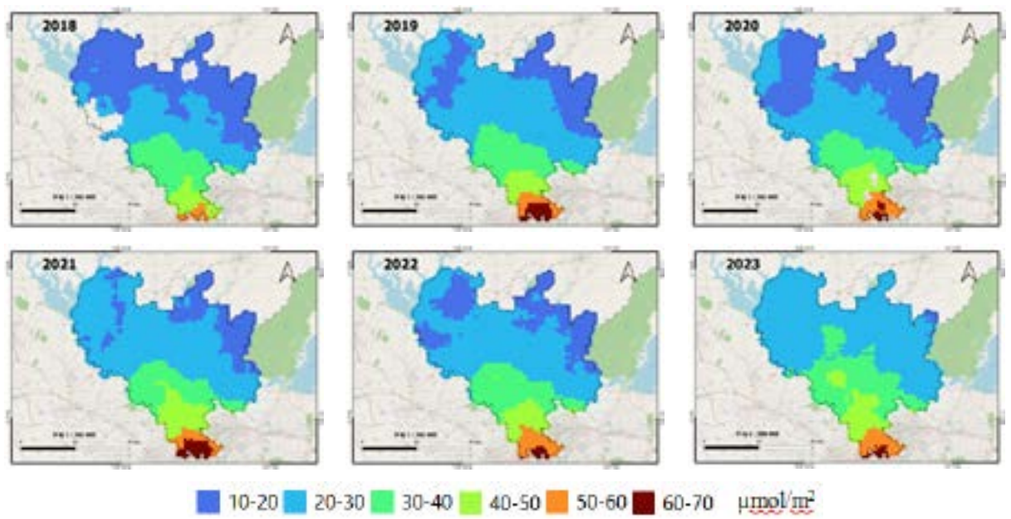

Figure 3. Map of NO_2 concentration evolution in the period 2018-2023 in Binh Duong.

Fig. 3 presents a map depicting the variations in tropospheric NO_2 concentrations for each year within the 2018-2023 period in Binh Duong province. In general, the map shows significant changes in the distribution of NO_2 data over the years. In 2018, the lowest values were observed, with the majority of the area having concentrations ranging mostly from 10 to 40 µmol/m^2 and no areas with high concentrations above 60 µmol/m^2. In 2023, the highest average concentrations were found, ranging from 20 to 50 µmol/m^2. Moreover, in 2019 and 2021, there were notable areas with high concentrations ranging from 60 to 70 µmol/m^2 during the research period. Through the analysis, it is evident that the tropospheric NO_2 data shows an increasing trend over the years.

Table 1 presents the results of the average monthly NO_2 charts for the study period in Binh Duong province. Due to the results extracted from the Sentinel-5P satellite, launched at the end of 2017 via the GEE platform, the data for the first five months of 2018 has not been updated in the study area. The highest average NO_2 density ranges from 20.93 to 41.86 µmol/m^2 in 2023, while the lowest ranges from 17.97 to 27.07 µmol/m^2 in 2018.

The average concentration in 2020 (25.02 µmol/m^2) tends to decrease compared to 2019 (26.06 µmol/m^2) due to the emergence of the COVID-19 pandemic in Vietnam, leading to the implementation of social distancing measures. As a result, there was a reduction in travel and goods production, leading to a decrease in NO_2 emissions into the atmosphere. Consequently, the tropospheric NO_2 concentration also improved during this period as the primary sources of NO_2 emissions are from transportation and industrial activities.

Table 1. Average tropospheric NO_2 concentration (µmol/m^2) during the 2018-2023 period in Binh Duong.

Month	2018	2019	2020	2021	2022	2023
1		32.98	28.05	35.55	33.85	28.73
2		29.81	27.55	35.38	24.09	27.68
3		41.64	27.37	34.17	33.29	40.15
4		30.61	27.00	33.65	26.61	41.86
5		26.91	27.07	29.43	25.47	32.45
6	27.07	22.02	25.59	24.27	26.36	23.23
7	19.25	19.74	25.56	20.86	23.29	25.97
8	17.97	17.95	17.92	19.02	23.64	20.93
9	22.95	17.20	20.79	18.11	23.52	
10	26.92	23.02	23.38	20.24	23.20	
11	25.10	22.80	22.77	24.38	27.67	
12	25.40	28.06	27.17	29.45	28.71	
Average	**23.52**	**26.06**	**25.02**	**27.04**	**26.64**	**30.12**

The concentration of NO_2 in the tropospheric layer is influenced by seasonal variations in climate, as depicted in Fig. 4. During the rainy season, the emission levels are lower compared to the dry season due to better dispersion capabilities of pollutants in rainy weather conditions. In the dry season, factors such as weak winds, low temperatures, less rainfall, and high humidity reduce the dispersion of pollutants in the air. This leads to an increase in NO_2 concentration as the air cannot escape to higher regions or move to other areas. Thus, the average concentration from April to November, which corresponds to the dry season in Vietnam, shows an increasing trend in NO_2 concentration in the Binh Duong region compared to the rainy season from May to October.

From the chart in Figure 3, it can be observed that the months with the highest average concentration during the dry season are March and April, with tropospheric NO_2 data of 35.33 µmol/m² and 31.95 µmol/m², respectively. In the rainy season, the lowest concentration is observed in August, with 19.57 µmol/m² (Table 1).

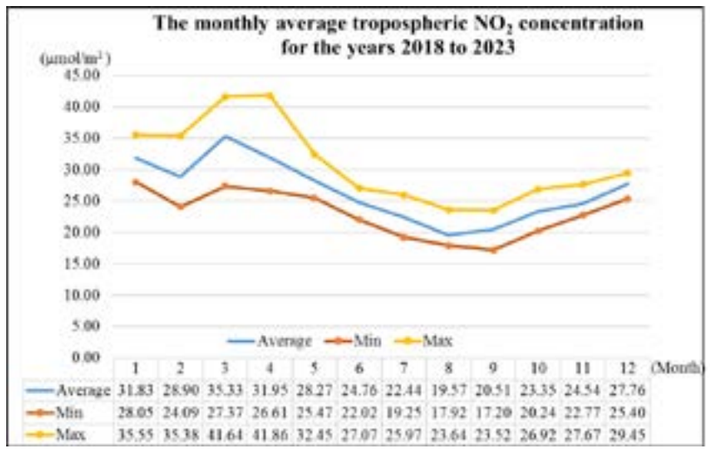

Figure 4. Average monthly tropospheric NO_2 concentration 2018-2023.

3.2 Analysis of spatial variations in NO_2 Concentration in Binh Duong province

Fig. 5 presents the results of the tropospheric NO_2 concentration in Binh Duong province, including 4 districts, 1 town, and 4 cities, during the period from 2018 to 2023. The map provides a visual representation of the data, with areas of high concentration located in economically developed districts. Based on the map, Di An and Thuan An are the areas with the highest concentration of tropospheric NO_2, with an average index ranging from 50 to 70 µmol/m². The areas of Thu Dau Mot, Tan Uyen and Ben Cat exhibit a lower distribution, ranging from 30 to 60 mol/m². The lowest concentrations are observed in the areas of Dau Tieng, Bau Bang, Phu Giao, and Bac Tan Uyen, with concentrations ranging from 10 to 30 mol/m². From these findings, it can be concluded that there is a significant disparity in NO_2 concentration levels among the provinces and cities within the Binh Duong region.

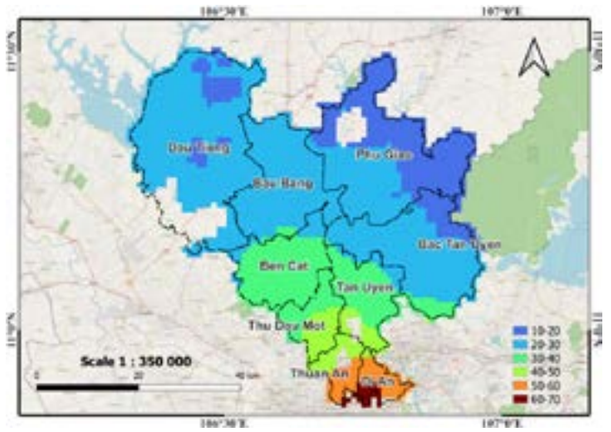

Figure 5. Spatial tropospheric NO_2 concentration in Binh Duong region.

Fig. 6 provides a visual representation of the NO_2 levels in different areas, showing the fluctuation over a specific period. Based on the chart, Di An has the highest levels compared to other districts, with an average concentration ranging from 51.19 to 64.75 µmol/m². The lowest concentration is observed in Phu Giao, ranging from 17.71 to 24.65 µmol/m² during the study period. The average concentration also varies significantly between high and low areas, with a difference of 2.8 times. These results align with reality, as Di An serves as an economic center with transportation and industrial development in Binh Duong, while Phu Giao is primarily focused on agriculture. The remaining areas exhibit similar concentrations, ranging from 19.72 to 56.47 µmol/m². Additionally, based on the chart, it can be concluded that the NO_2 levels tend to decrease uniformly during the pandemic period in 2020 across all districts and cities.

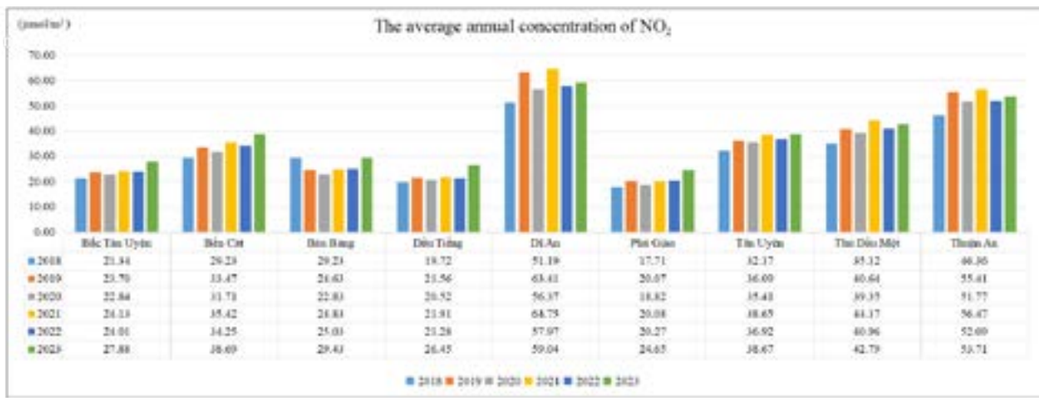

Figure 6. Chart of average NO_2 concentration in different areas of Binh Duong province.

4. CONCLUSION

In this research, the tropospheric NO_2 data was retrieved from the Sentinel-5P TROPOMI satellite through the Google Earth Engine platform for the period of 2018 to 2023 in Binh Duong province. The study has analyzed the distribution of tropospheric NO_2 in Binh Duong province both spatially and temporally. The results show that the average tropospheric NO_2 concentration in the study area fluctuates insignificantly. Due to the emergence of the Covid-19 pandemic, the obtained concentration data tends to decrease during the outbreak period, attributed to reduced transportation and industrial activities. Furthermore, the temporal analysis reveals that the NO_2 concentration is influenced by seasonal variations, contributing to the dispersion of pollutants. In 2023, the highest average concentration reached 30.12 µmol/m², while the lowest average concentration was recorded in 2018 at 23.52 µmol/m². Based on the average results, it can be concluded that the highest NO_2 index is found in the Di An area, while the lowest is in the Phu Giao area, with a significant variation in average concentration between high and low areas, due to the high density of industrial activities in Di An. The results demonstrate the potential application of Google Earth Engine in air quality monitoring. In addition, results from this study could provide important background for local government on building strategies for mitigation of air pollution in the province.

5. REFERENCES

Aldabash M., Balcik F. B., & Glantz P., 2020. Validation of MODIS C6.1 and MERRA-2 AOD using AERONET observations: A comparative study over Turkey. *Atmosphere, 11*(9). https://doi.org/10.3390/ATMOS11090905

Faisal M., and Muhamad J. L., 2023. Spatio-temporal analysis of nitrogen dioxide (NO2) from Sentinel-5P imageries using Google Earth Engine changes during the COVID-19 social restriction policy in Jakarta. *Natural Hazards Research*. Volume 3, Issue 2, 2023, 344-352, https://doi.org/10.1016/j.nhres.2023.02.006.

General Statistics Office, 2020. Statistical Yearbook 2020. *General Statistics Office*, Statistical Publishing House.

Solomon S., Portmann R. W., Sanders R. W., Daniel J. S., Madsen W., Bartram B., & Dutton E. G., 1999. On the role of nitrogen dioxide in the absorption of solar radiation. *Journal of Geophysical Research: Atmospheres, 104* (D10), 12047-12058.

The European Space Agency (ESA), 2017. *The Sentinel missions*. Available on: https://www.esa.int/Applications (Accessed on August 10th, 2023).

Tran Thi Van, Trinh Thi Binh, Ha Duong Xuan Bao, 2012. Study on the detection capability of dust pollution in Urban Areas using Remote Sensing Technology to Support Air Environmental Monitoring. *Journal of Science and Technology Development*. Volume 15, Issue M2-2012.

Veefkind J. P., Aben I., McMullan K., Förster H., De Vries J., Otter G., & Levelt P. F., 2012. TROPOMI on the ESA Sentinel-5 Precursor: A GMES mission for global observations of the atmospheric composition for climate, air quality and ozone layer applications. *Remote sensing of environment, 120*, 70-83.

Verhoelst T., Pinardi G., Eskes H. J., Fjaeraa A. M., Folkert Boersma K., Levelt P. F., Navarro-Comas M., Piters A. J. M., Sinyakov V. P., Strong K., Verhoelst T., Compernolle S., Pinardi G., Lambert J. C., Eichmann K. U., Granville J., Niemeijer S., Cede A., Tiefengraber M., Zehner C., 2021. Atmospheric Measurement Techniques. *European Geosciences Union, 14*(1), 481-510. https://doi.org/10.5194/amt-14-481-2021ï.

DEVELOPMENT OF WEB GIS FOR INVENTORY OF VIETNAM MARINE PROTECTED AREAS

Van Ngoc Truc Phuong

Department of Geodesy, Cartography and GIS.
HCMC University of Natural Resources and Environment, Vietnam
Corresponding author. Email: vntphuong@hcmunre.edu.vn

ABSTRACT

Marine protected areas (MPAs) have become a strategy for marine biodiversity conservation. Inventories are useful assessments that inform balanced resource management and conservation efforts in marine ecosystems. The advancement of GIS technologies has enabled geospatial data inventories. Particularly, dashboards have been used to create web maps that support interactive visualizations dynamically and spatially display statistics. Several web GIS dashboards were launched for marine biodiversity inventories. In Vietnam, the system of MPAs has been established since 2003 and inventories of MPAs' biodiversity are compulsory. Efforts have been made to support the need at the very initial stage. This paper aims to develop a dashboard for an inventory of Vietnam MPAs system. Based on biodiversity conservation policies and regulations, indicators are selected. Geospatial data are pulled from Protected Planet and Open Development Vietnam. Statistical data are collected from legal documents, journal articles, conference proceedings, MPAs' websites and books from 2010 to 2023. ArcGIS platform was used to build experiment data, create the web map and develop the Dashboard. The results are indicators for MPAs' biodiversity and a web GIS dashboard. The Dashboard is composed of a multi-scale map, an indicator, a list and charts. Statistical indicators are presented on the Dashboard to interactively link the map to infographics and vice versa. Despite the lack of biodiversity data, the Dashboard helps users to understand MPAs' biodiversity quickly and easily, facilitating decision-making. The study results are applicable to the inventory of other types of Vietnam protection areas.

1. INTRODUCTION

Marine Protected Areas (MPAs) have become a strategy for marine biodiversity conservation. Biodiversity inventories are useful assessments that inform balanced resource management, conservation and restoration efforts in marine ecosystems. They help to explain the existence of marine life, make predictions and set long-term conservation and restoration targets. Vietnam PAs have been established since 1977 (Decision 41/TTg, 1977). Vietnam's PAs system targets to increase the area of terrestrial PAs up to 9 % of the national territorial area to increase that of MPAs up to 5 % of the marine area (Decision 218/QĐ-TTg, 2014). However, the starting point for establishing MPAs was not until 2003, marked by the approvals of the strategy for management of Vietnam PAs until 2010 (Decision 192/2003/QĐ-TTg, 2003) and of the Fishery Law (Constitution, 2003). Out of approximately 230 PAs, the MPAs system includes 11 existing and 18 planned MPAs and many other proposed marine effective area-based conservation measures (MARD, 2023). Despite their small numbers, MPAs are responsible for maintaining current levels of mangrove forests, seagrass beds and coral reefs; improving the quality and populations of endangered, rare and

precious species; and compiling an inventory for storing and conserving native endangered, rare and precious genetic resources (MONRE, 2019). Hence, the inventory, monitoring and reporting of the status of biodiversity is a need.

A national program for inventory, monitoring, reporting and building the National Biodiversity Database by 2030, with a vision to 2050, was promulgated in 2021 (Decision 2067/QĐ-TTg, 2021). Initiatives for the inventory of biodiversity in Vietnam have not been focused on MPAs. Particularly, the national biodiversity database systems (NBDS) for decision-makers, governmental officers, researchers and the public (VED, 2015) and a geodatabase of biodiversity in BacKan province were developed and published as a web map (Bac Kan DONRE, 2022). The NBDS provides better support to users for searching (1) biodiversity information by declaring organization, date of declaration, PA and species taxon; and (2) PAs by locations (region and province), types of PAs, status of designation and management authority's level. Searching results are a list of PAs and a list of species' taxa of individual PAs without linking to the map. Meanwhile, the provincial geodatabases support only searching each species and displaying its distribution on maps.

Recent GIS advancement, particularly the Dashboard, allows creation-web maps that support interactive visualizations and dynamically and spatially display statistics of biodiversity on the whole and MPA's biodiversity in particular. On a global scale, the Terrestrial Dashboard of World Database of Protected Areas (WDPA) is published as a dashboard for the terrestrial PAs in many countries (except for Canada, Vietnam and some other Asia countries), which count the number and areas of PAs by IUCN category (WDPA, n.d.). On a regional scale, the Regional Centre for Mapping of Resource for Development launched dashboards for the Eastern and Southern African countries, which chart and count various types of PAs (RCMRD, 2020, 2022a), forest cover trend, forest cover percentage and forest ownership percentage…by country (RCMRD, 2022b). Besides, the Dashboard of the Gulf of Mexico Benthic Habitat Inventory dynamically displays statistics for habitat units, focusing on biogeographical and geomorphological features (Rose & Cebrian, 2022). On a national scale, NOAA's MPA Inventory Dashboard (NOAA, 2018) and Australian PAs Dashboard (Collaborative Australian PAs Database, 2020) visualized the area and numbers of various US MPAs and Australian PAs categories. Besides those indicators, the Canadian MPAs dashboard dynamically visualize the stage of MPA establishment by region and a list of activity snapshot for each MPAs (Canadian Parks and Wilderness Society, 2021) and the MPAs dashboard of Tanzania chart the year of MPAs establishment (Nairobi Convention, 2021). These inventory dashboards help to measure habitat diversity including the existence of distinct habitats, their locations, magnitudes and intensities. Genetic diversity and species diversity of natural ecosystems are not mentioned.

This study aims to build a web GIS dashboard of Vietnam MPAs for biodiversity inventory purposes. It is an experiment for the development of a web GIS-based dashboard for biodiversity inventory of all types of Vietnam PAs systems.

2. METHODS

2.1 Indicator identification for an inventory of Vietnam marine protected areas' biodiversity

There are no indicators designated to Vietnam MPAs' biodiversity. In this study, the indicators of Vietnam MPAs' biodiversity are identified based on legal documents related to information and data on Vietnam biodiversity (Table 1). At first, the indicators are selected from the Guidance on Development of Biodiversity Report. The guidance was promulgated in 2006 by the Vietnam Environment Administration, which includes a proposed set of biodiversity indicators for terrestrial, inland wetlands and coastal and marine ecosystems. These indicators are applicable to the investigation, monitoring and inventory of biodiversity for building national, provincial and PA biodiversity. The category of MPAs' species is also developed from the guidance. Then, a list of endangered, precious and rare species of MPAs are categorized according to Vietnam Red Data Book 2007, IUCN Red List of Threatened Species 2009, Decision 74/2008/QĐ-BNN, Decree 32/2006/NĐ-CP and Decree 160/2013/NĐ-CP.

Table 1. Legal documents related to information and data on Vietnam biodiversity.

Document no/Author	Name of (attached) document	Date of approval
Official note 2149/ TCMT-BTĐDSH	Guidance on the development of biodiversity report	September 14, 2016
Decree 160/2013/NĐ-CP	Criteria to determine species and the regime of managing species under lists of endangered, precious and rare species prioritized for protection	November 12, 2013
Decree 32/2006/NĐ-CP	Management of endangered, precious and rare forest plants and animals	March 30, 2006
IUCN, 2009	IUCN Red List of Threatened Species 2009	2009
Ministry of Science and Technology & Vietnamese Academy of Science and Technology	Vietnam Red Data Book	2007
Decision 74/2008/QĐ-BNN	The list of species of wild animals and plants stipulated in annexes of the Convention on International Trade of Endangered Wild Fauna and Flora (CITES 2008)	June 20, 2008

2.2 Building experiment data

Geospatial data are pulled from the World Database on Protected Areas, Protected Planet and Open Development Mekong. Statistical biodiversity data are collected from legal documents, journal articles, conference proceedings, MPA websites and books (Table 2). They are publications for results of projects and programs for biodiversity investigations, inventory and monitoring from 2010 to 2023.

Table 2. Data collection.

No	Sources of geospatial dataset/ statistical data
1	UNEP-WCMC and IUCN, 2023. Protected Planet: The World Database on Protected Areas (WDPA) and World Database on Other Effective Area-based Conservation Measures (WD-OECM) [Online], September 2023. *Cambridge*, UK: UNEP-WCMC and IUCN. Available at: www.protectedplanet.net
2	Open Development Vietnam, 2021. National PAs of Vietnam. Available at: https://data.opendevelopmentmekong.net/dataset/national-protected-areas-in-vietnam
3	Decision 218/QD-TTg dated February 7, 2014, on Approving the Strategy for Management of systems of special-use forests, MPAs and inland wetland PAs of Viet Nam by 2020, with a vision toward 2030
4	Vo S. T., Nguyen H. Y., 2010. Hermatypic corals in the waters bordering Con Co island (Quang Tri province). *Collection of Marine Research Works*, XVII: 147-154.

No	Sources of geospatial dataset/ statistical data
5	Luu T. A., Nguyen D. K., Ha Q. Q., Nguyen H. N., 2013. Biodiversity of Hon Me Aprchipelago, Thanh Hoa Province. *The 5th National Conference Proceedings on Ecology and Biological Resource*, 371-378, Ha Noi.
6	Luu T. A., Nguyen D. K., Ha Q. Q., 2011. Biodiversity conservation of Hon Cau - Ca Na MPA. *The 4th National Conference Proceedings on Ecology and Biological Resource*, 457-462, Ha Noi.
7	Tran D. T., Tran D. L, Nguyen V. Q., Nguyen T. M. H., Dinh V. H., 2014. Bach Long Vy national MPA: potential and solution for promoting values. *Journal of Marine science and technology*, *14*(3A): 281-291.
8	Cat Ba National Park homepage. https://catbanationalpark.vn/, last accessed 2023/6/10.
9	Nui Chua National Park homepage. http://www.vqgnuichua.vn/, last accessed 2023/7/01.
10	Management Board of Cham island MPAs homepage. https://culaochammpa.com.vn/, last accessed 2023/7/10.
11	Con Dao National Park homepage. https://www.condaopark.com.vn/. Accessed on 21/8/2023.
12	Management board of Nha Trang bay homepage. https://vinhnhatrang.net/. Accessed on 10/9/2023.
13	Nguyen V. Q., Nguyen D. T., Nguyen V. C (editors)., 2023. Biodiversity values, conservation potentials and Integrated Management Approach towards Co To - Tran Island MPA, Quang Ninh province. *Science and Technology*.
14	Hoang X. B, Nguyen V. L., Hua. T. T., Phan K. H., Thai M. Q., 2018. Biodiversity and characteristics of coral reef communities in Ly Son MPA, Quang Ngai province. *Journal of Marine Science and Technology, 18*(2): 150-160.

2.3 Development of web GIS dashboard for Vietnam marine protected areas

The web GIS dashboard is developed via the ESRI platform. Geospatial data are processed and composed as multi-scale maps in ArcPro. Then, the map is shared as a web map to ArcGIS online, from which the web GIS dashboard is developed by ArcGIS dashboards.

3. RESULTS AND DISCUSSIONS

3.1 Biodiversity indicators for the web GIS

This study builds indicators for web GIS MPAs' biodiversity, including basic information, area of MPAs, area of biodiversity distribution, quality of critical ecosystems and quantity of important species (Table 3). For the statistics related to species, the number of species is listed by fungi, floral and faunal classes. Accordingly, floral species are counted by taxon, ranging from division class to order. Meanwhile, faunal species are grouped into 6 groups (Insecta, Amphibian, Reptile, Aves, Mammalia and Marine plants and Animals). Marine plants and animals are sub-divided into phytoplankton, zooplankton, seaweed, algae, seagrass, coral, crustacea, Mollusca, Echinodermata, fish, marine reptiles and marine animals. Levels of priority for protection of endangered, precious and rare species/individuals are classified into 6 categories (Table 4).

Table 3. Indicators for the current status of MPAs' biodiversity.

No	Indicators	Sub-indicators
1	Basic information	Name and types of MPAs, management level, decision number of establishment, area by functional zone, buffer areas, main species protected and co-management
2	Area of MPAs	Area and MPAs area percent of marine surface
3	Area of biodiversity distribution	Area of mangrove forest (including new plant forest) and area and cover percentage of coral reef and seagrass bed
4	Quality of critical ecosystems	Forest ecosystems: number of forest plant species, tree density, forest biomass and volume; wetland ecosystem: aquatic species composition, tree density and forest biomass; mangrove forest ecosystem: number of mangrove plant species, tree density and biomass; area of newly died mangrove forest; area of newly died coral reef; area of newly died seagrass bed; and area of mangrove newly converted to other land uses
5	Quantity of important species	Number of floral and faunal species; the number of marine endangered, precious and rare species and individuals; number of extinct marine precious and rare species

Table 4. Protection priority of MPAs' endangered, precious and rare species/individuals.

No	Categories	Levels of priority for protection
1	Vietnam Red Data Book 2007	Critically endangered, endangered, vulnerable, lower risk
2	IUCN Red List of Threatened Species 2009	Critically endangered, endangered, vulnerable, near threatened, least concerned, data deficient, not evaluated
3	CITES 2008	N/A
4	Decree 32	Group IA, IIA, IB, IIB
5	Decree 160	N/A
6	Endemic	Local, regional, Vietnamese, Indochinese, Southeast Asian

3.2 Web GIS dashboard

The final result is a web GIS for the inventory of Vietnam MPAs, which is accessible via https://vanntphuong.maps.arcgis.com/apps/dashboards/e23b7913b1d045619064aa0afb5a226d. In terms of dashboard architecture, the user interface consists of an information panel and a map panel. The data component includes a thematic layer and base layer for multi-scale mapping. (Figure 1). The Dashboard is designed to display multiple visualizations that work together, enabling users to convey information by presenting location-based analytics using intuitive and interactive data visualizations on a single screen (Figure 2). It is composed of a multi-scale map, a list, a pie chart, 4 serial charts (2 grouped and 2 stacked charts) and an indicator. The map introduces (1) the location of MPAs as points and polygons and (2) levels of administrative boundaries at smaller and larger scales, respectively (Figure 3). It is configured to interact with the list, charts and indicators for inventory and vice versa. The list shows the basic information of MPAs, such as name, type, year and decision of establishment, main species protected and co-management, in a map view (Figure 2). The pie and two stacked charts are added to the stack at the upper right of the Dashboard. Each slice of the pie chart displays the sum of the area by functional zone of all MPAs in a map view. A stacked chart compares areas of functional zones among MPAs and the other compares numbers of marine endangered, precious and rare species. The two other stacked charts are also added to the stack at the bottom of the Dashboard. One compares the numbers of terrestrial fauna species and the other compares the numbers of marine plants and species in a map view. The indicator (in the upper left) shows the sum of marine areas of all MPAs in a map view.

The Dashboard visualizes the status of MPAs' biodiversity, facilitating users the ability to slice the data to get the answers they need quickly and easily. Some indicators listed in Table 3 are excluded from the Dashboard due to the lack of data. It could be improved when more data available and when end users consulted.

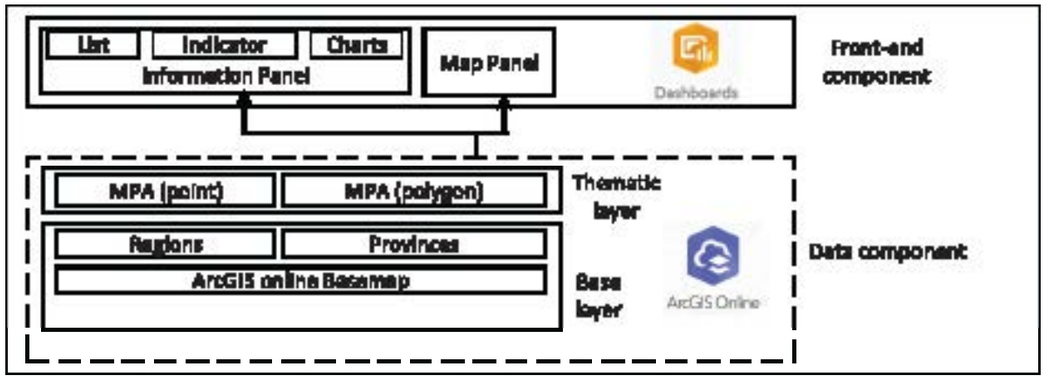

Figure 1. Dashboard architecture.

Figure 2. Interface of web GIS dashboard.

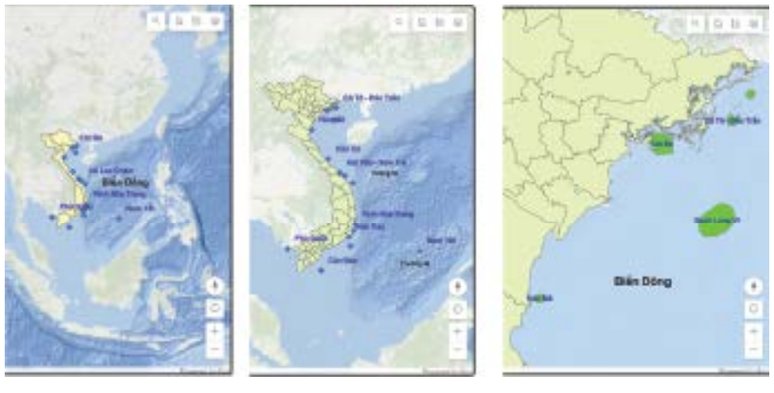

Figure 3. Illustration of different map zooms.

4. CONCLUSION

Vietnam MPAs' systems have become a strategy for marine biodiversity conservation. Inventory the status of MPAs' biodiversity is a need. Efforts have been made to support the need. However, they are at a very initial stage. This paper aims to develop a web GIS dashboard for the inventory of the Vietnam MPAs system. Based on national biodiversity conservation policies and regulations, MPA's biodiversity indicators are selected. Then, the ArcGIS platform is applied to develop web GIS dashboard. The results are indicators MPAs' biodiversity and a web GIS dashboard. The Dashboard is composed of a map, indicator, list and charts, enabling users to convey information by presenting location-based analytics using intuitive and interactive data visualizations on a single screen. Although there is a lack of biodiversity data, the Dashboard helps users to understand MPAs' biodiversity quickly and easily, facilitating decision-making. The study results are applicable to the inventory of other types of Vietnam protection areas.

5. REFERENCES

Bac Kan Department of Natural Resources and Environment, 2022. Database of biodiversity in Bac-Kan province. Retrieved September 21, 2023, from http://moitruong.backan.gov.vn:88/ddsh/-index.php?com=map

Canadian Parks and Wilderness Society, 2021. Asseing Canada's marine protected areas. Retrieved July 29, 2023, from www.arcgis.com/apps/dashboards/21f5eec7e2d04ef0908ec8f0e8b8be63

Collaborative Australian Protected Areas Database, 2020. Australian protected areas dashboard. Retrieved September 27, 2023, from www.dcceew.gov.au/environment/land/nrs/science/capad/-dashboard

Ministry of Agriculre and Rural Development, 2023. Draft program for widenning and establishing marine protected areas by 2030, Ha Noi.

Ministry of Natural Resources and Environment, 2019. The sixth national report to the United Nations Convention on Biological Diversity, Ha Noi.

Nairobi Convention, 2021. United Republic of Tanzania: Marine protected areas dashboard. https://experience.arcgis.com/experience/ab42dbbed9ce41948c97d17b20cd7be1

National Assembly of the Socialist Republic of Vietnam, 2003. Fishery Law, Ha Noi.

NOAA, 2018. The State of Marine Protected Areas. https://noaa.maps.arcgis.com/apps/MapJournal/index.html?appid=9dc129dade0044869695d65c4eadb474#.

Prime Minister of the Socialist Republic of Vietnam (2003). Decision 192/2003/QĐ-TTg on Approving the strategy for management of Vietnam protected areas system by 2010. Dated September 17, 2003, Ha Noi.

Prime Minister of the Socialist Republic of Vietnam (2014). Decision 218/QĐ-TTg on Approving the Strategy for management of systems of Vietnam special-use forests, marine protected areas and inland wetland protected areas by 2020, with a vision toward 2030. Dated February 07, 2014, Ha Noi.

Prime Minister of the Socialist Republic of Vietnam (2021). Decision 2067/QĐ-TTg on Approving Program for Inventory, monitoring, building report and developing national biodiversity database by 2030, with a vision toward 2050. Dated December 08, 2021, Ha Noi.

Prime Minister of the Socialist Republic of Vietnam, 1977. Decision 41/TTg on Regulations for forbidden forest. Dated January 24, 1977, Ha Noi.

Regional Centre for Mapping of Resource for Development, 2020. Eastern & Southern Africa protected areas dashboard. https://esahub.rcmrd.org/en/

Regional Centre for Mapping of Resource for Development, 2022a. Protected areas for OFESA covered countries. https://ofesa-geoportal.rcmrd.org/apps/rcmrd::regional-forest-reserves-dashboard-ofesa/explore

Regional Centre for Mapping of Resource for Development, 2022b. Regional forest reserves dashboard OFESA. https://ofesa-geoportal.rcmrd.org/apps/rcmrd::regional-forest-reserves-dashboard-ofesa-/explore

Rose, K. and Cebrian, J., 2022. Inventorying Benthic Habitats for Well-Managed Marine Ecosystems with Dashboard. *ESRI Ocean, Weather and Climate Forum 2021*. https://mediaspace.esri.com-/media/t/1_fq7h3ts3

Vietnam Environment Administration, 2015. National biodiversity database systems. Retrieved August 1, 2023. https://nbds.ceid.gov.vn/

WDPA. (n.d.). The terrestrial dashboard of world database of protected areas. Retrieved September 21, 2023. https://www.arcgis.com/apps/dashboards/3d12bb4fabb24299a1bdf1ebeb5f2f3f

MONITORING SURFACE WATER BODIES CHANGES FROM SENTINEL-2A IMAGERY WITH MODIFIED NORMALIZED DIFFERENCE WATER INDEX: APPLICATION IN DALAT, LAM DONG, VIET NAM

Trung Van Nguyen [1,2]*, Ha Thu Thi Le[1,2]

[1]Faculty of Geomatics and Land Administration,
Hanoi University of Mining and Geology, Vietnam
[2]Geomatics in Earth Sciences Research Group,
Hanoi University of Mining and Geology, Vietnam
*Corresponding author. Email: nguyenvantrung@humg.edu.vn

ABSTRACT

Accurately monitoring open water bodies is a fundamental and crucial task in remote sensing. Numerous techniques for mapping water bodies have been devised to extract them from multi-spectral images. One of the most widely used techniques is the method relying on the spectral water index, particularly the Modified Normalized Difference Water Index (MDNWI), which is derived from the green and Shortwave-Infrared (SWIR) bands. The purpose of the study is to identify surface water body changes using Sentinel-2 MSI (Multi-Spectral Instrument) data, one of the latest types of remote sensing satellite data. The results of the research show that by using Sentinel-2 MSI imagery, MNDWI (Modified Normalized Water Index) is the appropriate parameter to detect surface water areas in the studied area, with an overall accuracy > 0.92 and Kappa coefficient > 0.84. Additional research is required, specifically targeting diverse geographical conditions and exploring other regions within Vietnam.

1. INTRODUCTION

Monitoring surface water body changes has a great significance in understanding hydrology processes and managing water resources (Roberts et al., 1993; Vorosmarty et al., 1997; Papa et al., 2008). Recently, remote sensing has become a suitable approach for monitoring surface water body changes because the acquired data can provide real-time, dynamic and cost-effective information, which is substantially different from conventional *in situ* measurements (Chen et al., 2004; Du et al., 2011; and Feng et al., 2012). There were various methods developed in order to extract water bodies from different remote sensing images, include single band density slicing (Work and Gilmer, 1976), unsupervised and supervised classification (Sivanpillai et al., 2010; and Huang et al., 2014ab) and spectral water indexes (Hui et al., 2008; Li et al., 2013; Du et al., 2014; Xie et al., 2014; Jiang et al., 2014; Mizuochi et al., 2014; Yao et al., 2015; and Li et al., 2016). To select the water body mapping methods, the spectral water index-based method is chosen because it is efficient and has low computational cost (Ryu et al., 2002). In the past several decades, the Normalized Difference Water Index (NDWI) was proposed by McFeeters, 1996, using the green and Near Infrared (NIR) bands of remote sensing images relied on strong absorbability and low radiation of the water bodies in the range from visible to infrared wavelengths. In most cases, the water information is effectively enhanced by using NDWI. However, it is sensitive to built-up

land. To overcome the foible of NDWI, Xu, (2006) developed the Modified Normalized Difference Water Index (MNDWI) (Xu et al., 2006) that uses the Shortwave Infrared (SWIR) band instead of the NIR band used in NDWI. Many previous research works have demonstrated that MNDWI is more suitable to extract water bodies with greater accuracy than NDWI (Xu et al., 2006; Li et al., 2013; Du et al., 2014; Singh et al., 2015).

More recently, MNDWI has been widely applied to produce water body maps at different scales. In practice, the spatial resolutions of both the SWIR and green bands directly affect the accuracy of mapped water bodies. For instance, MODerate-resolution Imaging Spectroradiometer (MODIS) images at 250-m spatial resolution have been popularly used to generate water bodies at both global and regional scales (Caroll et al., 2009; Huang et al., 2012). For regional studies, images at 30-m spatial resolution provided by the Thematic Mapper (TM), the Enhanced Thematic Mapper Plus (ETM+) and the latest Operational Land Imager (OLI) from Landsat series satellites are relevant datasets (Hui et al., 2008; Du et al., 2014; and Rokni et al., 2014). Although the Landsat TM, ETM+ and OLI images can extract water bodies with more accurate boundaries, the spatial resolution of Landsat series images is still not good enough to detect smaller-sized open water bodies, such as narrow gutters and small pools in urban areas. By rapid development of remote sensing data consisting of SPOT6/7, IKONOS and Quick-bird having spatial resolution under 1-m, these small-sized water bodies can be monitored. However, these very high spatial resolution images have no SWIR band, making it impossible to use the MNDWI method.

For convenience, the European Space Agency (ESA) launched a new Sentinel-2 satellite on 23 June 2015. The Sentinel-2 images can provide for regional water body's maps due to their reasonable properties (*i.e.*, the 10-m spatial resolution for four bands and the 10-day revisit frequency) and the free access. The Sentinel-2 carries the Multi-spectral Imager (MSI). This sensor has a total of 13 spectral bands, in which four bands (blue, green, red and NIR) have a spatial resolution of 10 m and six bands (including the SWIR band) have a spatial resolution of 20 m. Since the green and SWIR bands are included, the MNDWI method gathers water bodies from the Sentinel-2 images. The objectives of this study are to (1) produce MNDWI from the Sentinel-2 image by the green and the SWIR bands; (2) use the produced MNDWI to extract water bodies; and (3) evaluate the map-level accuracy of the resultant water body map.

2. STUDY AREA & DATA SET

2.1 Study Area

Da Lat city is situated on the Lam Vien plateau, serving as the administrative center of Lam Dong province. It is approximately 300 kilometers to the northeast of Ho Chi Minh city, 110 kilometers west of Phan Rang and 130 kilometers to the northeast of Nha Trang. Da Lat holds a central role in Lam Dong province, serving as its political, administrative, economic, cultural and service hub. It also plays a crucial role as a significant economic trading center and a focal point for various forms of tourism, particularly sightseeing tours, resorts, conferences, seminars and ecological activities within the country and the surrounding region. Furthermore, it stands as one of the nation's primary institutions for diverse education and advanced scientific research.

Despite the limited availability of surface water resources in Da Lat, they are sufficient to cater to the socio-economic needs of a city primarily oriented toward tourism, services, education and scientific research. The primary preference for sourcing water remains surface water, with underground water reserved for use in suburban residential areas only when centralized water supply systems are absent. Although the water quality in several significant reservoirs such as Dan Kia, Suoi Vang, Tuyen Lam, Chien Thang and Da Thien remains favorable at present, it is essential to maintain a long-term focus on protective measures to reduce the risk of pollution and sedimentation. (Figure 1).

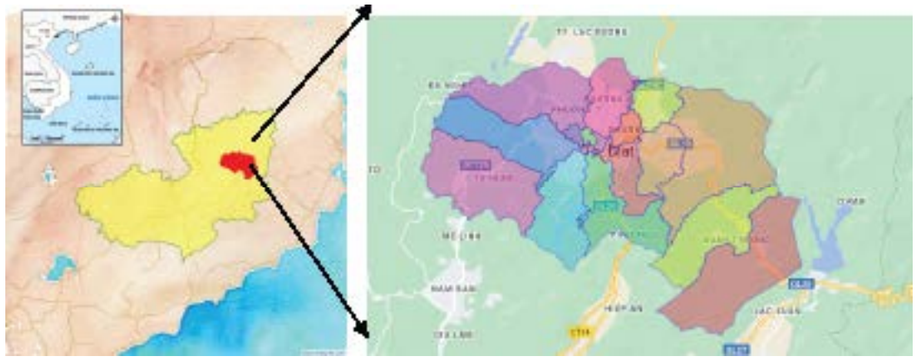

Figure 1. The study area.

https://bandovietnam.com.vn/ban-do-thanh-pho-da-lat

2.2 Data set

In this research, time series of Sentinel-2A (Level_2A) images with a cloud cover of less than 1 % have been used. The reason for the very low cloud coverage is that in the continuation of the classification process, we need to obtain the area of the water class in each image. For this reason, the presence of clouds can create many problems in our calculations.

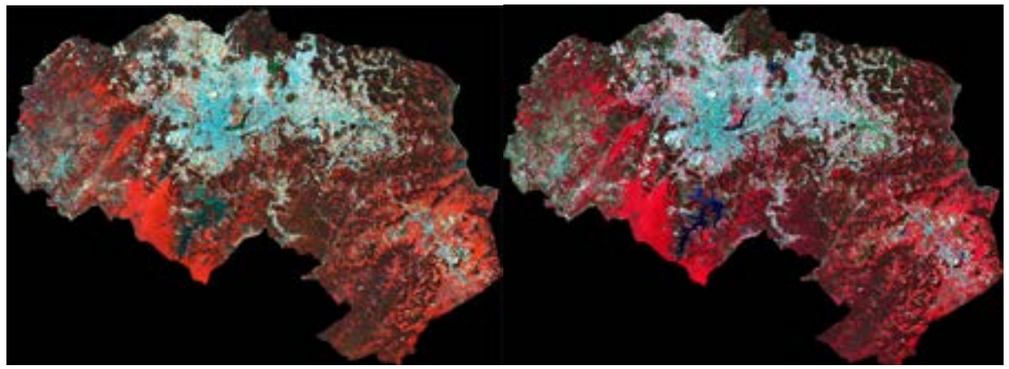

(a) ***(b)***

Figure 2. Satellite images cut by the boundaries of Dalat city on the dry (a) and the flood season (b).

Table 1. Acquisition date of the Sentinel-2A satellite images used during 2022 in Dalat city.

Number	Sensing Date	Mission
1	12 March 2022	Sentinel-2A

Number	Sensing Date	Mission
2	18 November 2022	Sentinel-2A

Sentinel-2 is an Earth observation mission developed by ESA as part of the Copernicus Program to carry out ground-based observations in support of services such as forest monitoring, land area change detection and disaster management. It consists of two identical satellites built by Airbus DS, Sentinel-2A and Sentinel-2B.

The Sentinel-2 mission has the following capabilities:

• Multi-spectral data with 13 bands in the visible, near-infrared, infrared and shortwave portions of the spectrum;

• Systematic global coverage of land surfaces from 56°S to 84°N, coastal areas and all of the Mediterranean Sea;

• Repeat every 5 days under the same view. Sentinel-2 repeat shooting cycle will be shorter than 5 days at high latitudes or shooting with different viewing angles;

• Spatial resolution of 10 m, 20 m and 60 m;

• The scanning range is 290 km wide;

• Free and open data policy.

3. METHODOLOGY

Figure 3 shows the flowchart of the implemented method for the detection and analysis of the change in bodies of water in two seasons. Our research consists of three main steps: (1) Selection of bands and indicators of water body extraction, (2) Surveying thresholds of water index to classify the images into two water and non-water classes and (3) Analysis and interpretation of changes.

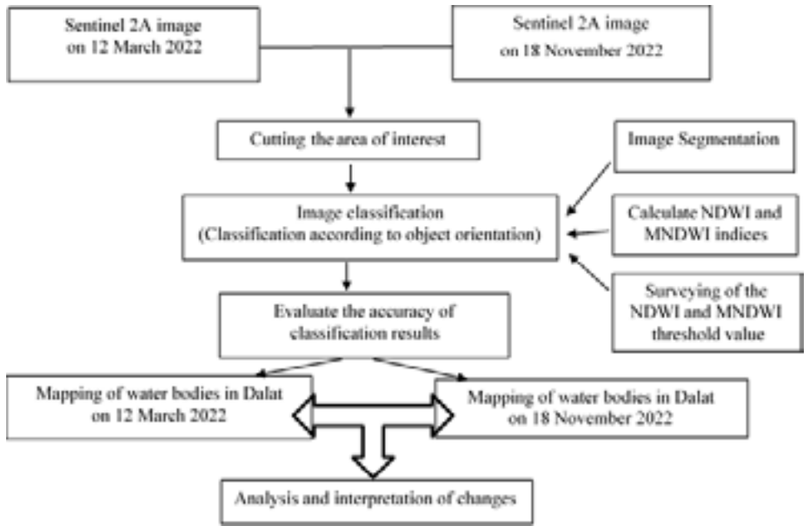

Figure 3. Flowchart of the implemented method for detection and analysis of the change in bodies of water in two seasons.

4. RESULTS

4.1 Results of surface water extraction using the MNDWI index method

A positive value in the NDWI index signifies the presence of surface water, making it a valuable tool for identifying and assessing alterations in surface water coverage. The NDWI index, as introduced by McFeeters, strives to (a) enhance the reflectivity of surface waters in the green band and (b) diminish the reflectivity of surface waters in the near-infrared (NIR) band, as expressed by the following formula:

$$NDWI = \frac{\rho_{Green} - \rho_{NIR}}{\rho_{Green} + \rho_{NIR}} \quad (1)$$

For Sentinel 2A images, the NDWI index is determined as follows:

$$NDWI = \frac{\rho_{Band\ 3} - \rho_{Band\ 8}}{\rho_{Band\ 3} + \rho_{Band\ 8}} \quad (2)$$

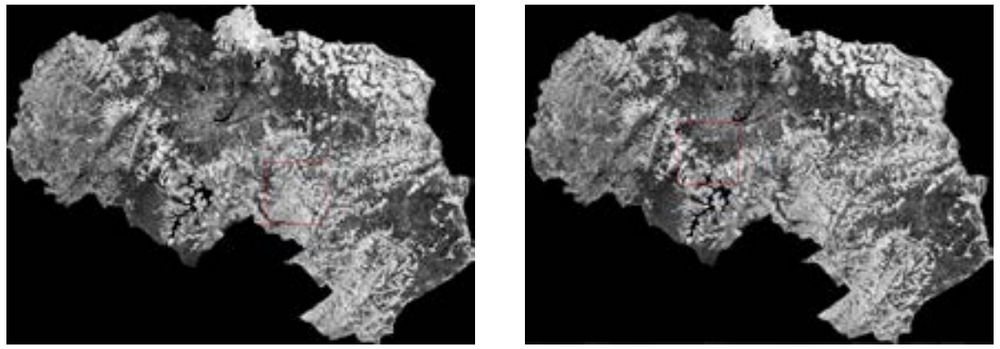

(a) ***(b)***

Figure 4. The NDWI index image outcomes within Da Lat City on the dry (a) and the flood season (b).

4.2 Results of surface water extraction using the MNDWI index method

One significant drawback of the NDWI index is its tendency to be mistaken for built-up areas. Xu et al., (2006) identified that it's possible to differentiate between surface water areas and built-up regions by examining the short wavelength infrared (SWIR) band. Consequently, the MNDWI index is introduced and calculated as follows:

$$MNDWI = \frac{\rho_{Green} - \rho_{SWIR}}{\rho_{Green} + \rho_{SWIR}} \quad (3)$$

For Sentinel 2A images, the MNDWI index is determined as follows:

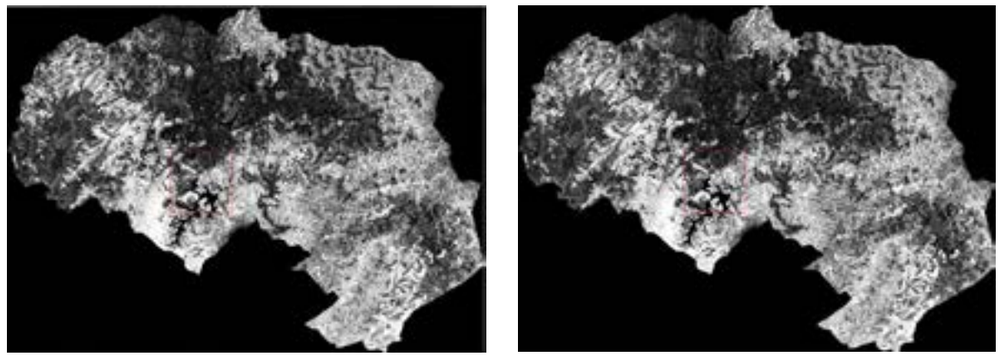

(a) *(b)*

Figure 5. The MNDWI index image outcomes within the Da Lat city on the dry (a) and the flood season (b).

Following the generation of the NDWI and MNDWI index images, surface water bodies are identified through a thresholding process. Typically, NDWI and MNDWI index values fall within the range of [-1, 1], with 0 serving as the commonly used threshold to differentiate between water and non-water.

In this research, both NDWI and MNDWI indices were computed. The study employed these indices to extract surface water features, selecting the suitable water separation index for each type of surface water resource.

4.3 Evaluate the accuracy of classification results

The accuracy of the extracted current surface water distribution from two sets of Sentinel 2A satellite images was assessed using a combination of direct surveys conducted on the 1-meter spatial resolution satellite images.

Random control samples were taken across the entire study area, totaling 80 regions encompassing two surface types (water and others). These regions were subsequently overlaid with high-resolution satellite image data from 2022 to calculate statistics measuring the actual level of correspondence between objects. The Kappa coefficient, calculated according to Congalton's formula, revealed that the classification accuracy of the 2022 surface water distribution based on the MNDWI index image was 94.07 %, which matches the current classification accuracy of 94.07 %. In contrast, the accuracy for the surface water distribution status in 2022 derived from the NDWI index image was 88.64 %.

Consequently, this study opted for MNDWI index images to extract surface water information, confirming their suitability for characterizing the distribution of surface water resources within the project's study area.

4.4 The findings from evaluating the present state of surface water distribution within the city of Da Lat, encompassing two distinct research periods

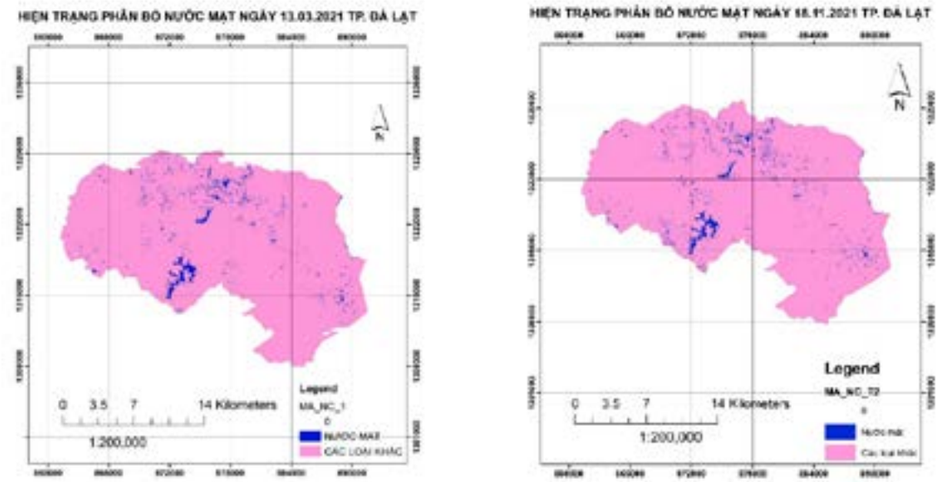

(a) *(b)*

Figure 6. Results of surface water extraction from Sentinel 2A satellite images in Da Lat City on the dry (a) and the flood season (b).

Table 2. Statistics on surface water area for two periods, March and November 2022, in Dalat city.

Land cover	12 March 2022 (ha)	18 November 2022 (ha)	Change (ha)
1-Water	691,430	759,939	+ 68.51
2-Non-water	38,768.330	759,939	- 68.51
Total (ha)	39,459.760	39,459.760	0

Examining the outcomes regarding the spatial distribution of surface water resources in Da Lat city within Lam Dong province, in conjunction with the statistical data, it becomes evident that Da Lat encompasses surface water resources that make up nearly 2 % of the city's total area. These resources are primarily in the form of rivers, streams and lakes, with a predominant concentration in the form of large lakes such as Xuan Huong, Than Tho and Tuyen Lam.

Simultaneously, over the past two decades, the sectors of agriculture, tourism and population have all experienced significant growth. Consequently, Da Lat city finds itself in need of pragmatic water management solutions. This is especially critical to safeguard the purity of the surface water environment, as it plays a pivotal role in preserving the aesthetics necessary for tourism development and is closely linked to the well-being of the local population.

5. DISCUSSION

Da Lat's flow pattern is contingent upon the climate and can be categorized into two distinct seasons: the flood season and the dry season. In May, Da Lat transitions into its rainy season, during which streams that had previously dried up due to the dry period do not initially produce surface runoff; instead, the initial rains are absorbed into the soil. Thanks to its excellent permeability, the streams become inundated, typically occurring 1.5 to 2 months after the onset of the rainy season.

The period spanning from May to July signifies the transitional phase from dry to flood conditions in Da Lat's streams. During this transitional phase, the basin accumulates more moisture,

eventually culminating in the flood season in July. This coincides with the heavy and prolonged rainfall that characterizes the rainy season.

The rainy season concludes in November and the transition from the flood season to the dry season is gradual. During this receding phase, stream waters gradually decrease, but significant floods can still occur due to late rains falling on already water-saturated basins. As the transition progresses from flood to dry conditions, groundwater plays a crucial role in moderating stream water levels, reducing the disparity in flow patterns. Effectively, the flood season extends until the end of November.

Throughout the flood season, approximately 70 % of the annual water volume is contained within the streams. The peak flood months typically occur in September and October, contributing to around 20 % of the total annual water volume. Early-season floods are often triggered by thunderstorms, while major floods during the peak flood season result from storms and tropical convergence zones. Late-season floods are usually induced by storms or by heavy rainfall, occasionally.

Once the rainy season concludes, the streams quickly begin to lose water. By the time April arrives, they reach their lowest point, constituting just about 2 % of the total annual water volume. Streams with smaller drainage areas (less than 5 square kilometers) found in the southwest and southeast corners of the city originate from elevated areas that lack forest vegetation cover and possess only a weathered surface layer. Consequently, they frequently run dry and cease to flow.

The contrast in precipitation between the dry and rainy seasons is quite noticeable. Nonetheless, as per the findings detailed in Table 2, the expansion of surface water within Da Lat city has been limited to nearly 70 hectares. This restriction is primarily attributed to the city's steep topography, which impedes the retention of substantial surface water during the rainy season. Therefore, to enable the growth and advancement of high-quality agriculture, alternative water sources or modern water-saving technologies are imperative.

6. CONCLUSION

The investigation involved the extraction of surface water resource data by establishing thresholds for the NDWI and MNDWI indices. The indices derived from Sentinel 2A imagery have demonstrated their efficacy in surface water area analysis. Findings from the study indicate that the utilization of NDWI and MNDWI water extraction indices facilitates a more straightforward separation of surface water entities. This is particularly advantageous when distinguishing water bodies within residential and industrial areas and during construction processes, resulting in increased accuracy in satellite image classification outcomes. Consequently, it can be inferred that optical remote sensing images offer a superior solution for surface water research.

Nonetheless, there exist certain limitations and challenges in terms of data and methodologies that warrant further investigation. To enhance precision and dependability, novel threshold determination techniques may be employed. The crucial aspect of implementing these new thresholding methods, which involve statistical analysis functions, lies in the requirement for significantly larger and more detailed field data. This data should also be collected over an extended timeframe for comparison with specific scenes, enabling the selection of precise thresholds for each distinct research area.

Furthermore, it is imperative to persist in the development of this research avenue and its application within the emerging realm of artificial intelligence and machine learning algorithms. While optical remote sensing image data has proven effective in surface water research, it's essential to acknowledge its primary limitation-vulnerability to cloud cover and adverse weather conditions. This can lead to information gaps or inaccuracies, particularly in Vietnam's mountainous regions. In this regard, radar remote sensing image data emerges as a viable approach for mitigating the influence of clouds and rainfall in surface water research. By amalgamating this data with optical images and incorporating innovative technologies such as drones, a comprehensive solution can be devised for studying and mapping the current status and fluctuations in surface water resources.

7. REFERENCES

Carroll, M. L., Townshend, J. R., DiMiceli, C. M., Noojipady, P., and Sohlberg, R. A., 2009. A new global raster water mask at 250 m resolution. *Int. J. Digit. Earth, 2*, 291-308.

Chen, Q. L., Zhang, Y. Z., Ekroos, A., Hallikainen, M., 2004. The role of remote sensing technology in the EU water framework directive (WFD). *Environ. Sci. Policy, 7*, 267-276.

Du, Y., Xue, H. P., Wu, S. J., Ling, F., Xiao, F., and Wei, X. H., 2011. Lake area changes in the middle Yangtze region of China over the 20th century. *J. Environ. Manag, 92*, 1248-1255.

Du, Z. Q., Li, W. B., Zhou, D. B., Tian, L. Q., Ling, F., Wang, H. L., Gui, Y. M., and Sun, B. Y., 2014. Analysis of Landsat-8 OLI imagery for land surface water mapping. *Remote Sens. Lett., 5*, 672-681.

Feng, L., Hu, C. M., Chen, X. L. Cai, X. B., Tian, L. Q., and Gan, W. X., 2012. Assessment of inundation changes of Poyang Lake using MODIS observations between 2000 and 2010. *Remote Sens. Environ., 121*, 80-92.

Huang, C., Chen, Y., and Wu, J. P., 2014b. Mapping spatio-temporal flood inundation dynamics at large river basin scale using time-series flow data and MODIS imagery. *Int. J. Appl. Earth Obs. Geoinf., 26*, 350-362.

Huang, C., Chen, Y.,and Wu, J. P., 2014a. DEM-based modification of pixel-swapping algorithm for enhancing floodplain inundation mapping. *Int. J. Remote Sens., 35*, 365-381.

Huang, S. F., Li, J. G., and Xu, M., 2012. Water surface variations monitoring and flood hazard analysis in Dongting Lake area using long-term Terra/MODIS data time series. *Nat. Hazards, 62*, 93-100.

Hui, F. M., Xu, B., Huang, H. B., Yu, Q., and Gong, P., 2008. Modelling spatial-temporal change of Poyang Lake using multitemporal Landsat imagery. *Int. J. Remote Sens, 29*, 5767-5784.

Jiang, H., Feng, M., Zhu, Y. Q., Lu, N., Huang, J. X., and Xiao, T., 2014. An automated method for extracting rivers and lakes from landsat imagery. *Remote Sens, 6*, 5067-5089.

Li, W. B., Du, Z. Q., Ling, F., Zhou, D. B., Wang, H. L., Gui, Y. M., Sun, B. Y., and Zhang, X. M., 2013. A comparison of land surface water mapping using the normalized difference water index from TM, ETM plus and ALI. *Remote Sens., 5*, 5530-5549.

Li, W., Qin, Y., Sun, Y., Huang, H., Ling, F., Tian, L., and Ding, Y., 2016. Estimating the relationship between dam water level and surface water area for the Danjiangkou Reservoir using Landsat

remote sensing images. *Remote Sens. Lett., 7*, 121-130.

McFeeters, S. K., 1996. The use of the normalized difference water index (NDWI) in the delineation of open water features. *Int. J. Remote Sens., 17*, 1425-1432.

Mizuochi, H., Hiyama, T., Ohta, T.,and Nasahara, K. N., 2014. Evaluation of the surface water distribution in north-central namibia based on MODIS and AMSR series. *Remote Sens., 6*, 7660-7682.

Papa, F., Prigent, C., and Rossow, W. B., 2008. Monitoring flood and discharge variations in the large siberian rivers from a multi-satellite technique. *Surv. Geophys., 29*, 297-317.

Roberts, N., Taieb, M., Barker, P., Damnati, B., Icole, M., and Williamson, D., 1993. Timing of the younger dryas event in east-Africa from lake-level changes. *Nature 366*, 146-148.

Rokni, K., Ahmad, A., Selamat, A., and Hazini, S., 2014. Water feature extraction and change detection using multitemporal landsat imagery. *Remote Sens., 6*, 4173-4189.

Ryu, J. H., Won, J. S., and Min, K. D., 2002. Waterline extraction from Landsat TM data in a tidal flat-A case study in Gomso Bay, Korea. *Remote Sens. Environ., 83*, 442-456.

Sheng, Y. W., Shah, C. A., and Smith, L. C., 2008. Automated image registration for hydrologic change detection in the lake-rich Arctic. *IEEE Geosci. Remote Sens. Lett., 5*, 414-418.

Singh, K.V., Setia, R., Sahoo, S., Prasad, A.,and Pateriya, B., 2015. Evaluation of NDWI and MNDWI for assessment of waterlogging by integrating digital elevation model and groundwater level. *Geocarto Int. 30*, 650-661.

Sivanpillai, R.,and Miller, S. N., 2010. Improvements in mapping water bodies using ASTER data. *Ecol. Inform. 5*, 73-78.

Vorosmarty, C. J., Sharma, K. P., Fekete, B. M., Copeland, A. H., Holden, J., Marble, J., and Lough, J. A., 1997. The storage and aging of continental runoff in large reservoir systems of the world. *AMBIO 26*, 210-219.

Work, E. A.,and Gilmer, D. S., 1976. Utilization of satellite data for inventorying prairie ponds and lakes. *Photogramm. Eng. Remote Sens. 42*, 685-694.

Xie, H., Luo, X., Xu, X., Tong, X. H., Jin, Y. M.; Pan, H. Y.,and Zhou, B. Z., 2014. New hyperspectral difference water index for the extraction of urban water bodies by the use of airborne hyperspectral images. *J. Appl. Remote Sens. 8*, 085098.

Xu, H. Q., 2006. Modification of normalised difference water index (NDWI) to enhance open water features in remotely sensed imagery. *Int. J. Remote Sens. 27*, 3025-3033.

Yao, F. F., Wang, C., Dong, D., Luo, J. C., Shen, Z. F., and Yang, K. H., 2015. High-resolution mapping of urban surface water using ZY-3 multi-spectral imagery. *Remote Sens. 7*, 12336-12355.

METHOD FOR FORECASTING LANDSLIDE RISKS AND IDENTIFYING LANDSLIDE FORMS FOR RESETTLEMENT AREAS OF SONLA HYDROPOWER PLANT

Phung Vinh An[1], Nguyen Van Thang[2]*

[1]Hydraulic Construction Institute (HYCI), Hanoi, Vietnam
[2]Faculty of Civil Engineering, Thuyloi University, Hanoi, Vietnam
*Corresponding author. Email: thangnv@tlu.edu.vn

ABSTRACT

The abnormal increase in landslide occurrences poses significant threats to the resettlement areas of the Son La hydropower plant, resulting in substantial harm to people and infrastructure. This paper presents a methodological approach for predicting and identifying landslide risks in these areas, which is crucial for implementing timely prevention measures. The study integrates four essential factors: layout methodology, infrastructure type, natural factors and an understanding of the living environment in the Son La hydropower resettlement areas. Utilizing topographic, geological and hydrogeological databases alongside historical landslide events, precipitation thresholds and a comprehensive landslide prediction matrix is established. This matrix categorizes factors, such as rainfall, weathering crust, slope, etc., into high, medium and low-risk levels. The four-step process involves building a set of identification criteria, standardizing identification criteria, utilizing the Analytical Hierarchy Process (AHP) for factor analysis and forecasting landslide risks and landslide types. Testing application of the method in the Son La hydropower resettlement areas demonstrates its suitability for defined residential zones with limited natural conditions despite limitations in scalability for larger regions. Comparisons with similar methods underscore its effectiveness for specific, narrow areas like the Son La hydropower resettlement site.

1. INTRODUCTION

The landslides seriousness in Son La Hydroelectric is studied and highlighted in some research (Pham et al., 2015; Nguyen, 2020). A landslide is one of the natural disasters that have a severe impact on the Son La Hydroelectric Resettlement Areas (HRAs) (Phung, 2022a). Various methods have been studied and applied in Vietnam to prevent and mitigate the consequences of landslides, including landslide susceptibility mapping, landslides monitoring and landslide prediction methods based on numerical models (Gian et al., 2017; Bui et al., 2016; Le et al., 2021; Tran et al., 2021). However, applying the mentioned study methods under the specific conditions of the Son La HRAs poses certain difficulties in terms of both technological aspects and the construction and operation costs. Therefore, it is practically meaningful to develop and implement a landslide risk identification method that is suitable for the conditions of the Son La HRAs (Phung et al., 2023b; Phung, 2022b). This study introduces a method for identifying and predicting landslide risks based on the data layers investigated at 190 landslide points in the study area. Although methodologically there are similarities with methods for mapping landslide susceptibility, it differs by not utilizing input maps such as rainfall maps or weathered layers characteristic maps and does not produce output maps. The core of this method relies on data collected on the probability of

landslide occurrences related to factors such as annual rainfall, weathering mantle, slope thickness, gradient and absolute elevation. These data factors are evaluated hierarchically to serve as a basis for calculating the Landslide Susceptibility Index (LSI) for research targets in the Son La HRAs.

2. THE SCIENTIFIC BASIS OF METHODS FOR FORECASTING AND IDENTIFYING LANDSLIDE HAZARD

The method is derived from four specific factors: the layout method, infrastructure structure, natural conditions and understanding of the living area in the Son La HRAs, as detailed in the references (Phung et al., 2023b; Phung, 2022b; Cruden and Varnes, 1996):

2.1 Landslide risk identification factors

This method aims to predict the landslide risks in the study area by considering factors such as topography, geology landslide signs, as well as rainfall amounts. Additionally, it anticipates the types of landslides that may occur by identifying the thickness and mechanical characteristics of the rock and soil layers within the research area. The factors to be considered are specifically explained as follows:

2.1.1 Terrain conditions

In the Son La HRAs, terrain plays a crucial role in landslide susceptibility. Field surveys or available topographic maps, such as 1:10,000 scale maps, DEM (Digital Elevation Maps), Google Earth and Google Maps, can help identify typical slopes and the extent of areas prone to landslides. Furthermore, the absolute elevation of residential areas can be determined using topographic documents and GIS tools.

Analysis of landslide data collected in the study area since the construction and operation of the Son La HRAs until 2022 reveals that landslide occurrences are not evenly distributed across different elevation ranges but tend to concentrate in specific elevation ranges (Phung et al., 2023a). Thus, by determining the absolute elevation of residential areas, it becomes possible to partially predict landslide risk. In essence, knowledge of the absolute elevation of a location within the Son La HRAs can help identify the likelihood of landslides when adverse conditions such as rainfall are present.

The angle of excavation slopes or fill slopes is also a critical factor in landslide risk assessment. Theoretically, steeper slopes are associated with a higher risk of landslides. Gentler slopes tend to be more stable, even under unfavorable geological and hydrogeological conditions. Statistical findings from landslides in the study area indicate that slopes with angles ranging from 8° to 25° have witnessed the highest number of landslides (Phung et al., 2023a).

2.1.2 Geological and Hydrogeological databases

In the Son La HRAs, where various infrastructure projects, such as civil works and roads, have been predominantly developed, we possess a substantial collection of geological survey documents. These survey records are notably comprehensive and detailed, with most drill holes reaching down to the bedrock layer. Furthermore, during the construction of projects in the area, the excavation for construction foundations provides a clear depiction of the geological structure within the resettlement areas. These documents have been gathered for research purposes

(Phung et al., 2023a). Analysis of landslide occurrences in specific resettlement areas reveals that landslides primarily manifest in particular types of soil and rock.

Records related to hydrogeological phenomena associated with landslides within the resettlement area are systematically maintained and updated. For instance, the recurring or seasonal presence of groundwater on slopes and inclines is documented.

2.1.3 Warning signs appearance

Within the Son La HRAs, unusual signs, the emergence of unusual signs, such as sudden bulges on roads, foundation settlements,… must be consistently investigated and documented. In areas with a high risk of significant and hazardous landslides, monitoring the development of these signs is mandatory. Various methods need to be employed, such as visual observation or modern monitoring systems. These signs play a critical role in the evaluation and prediction of landslide possibilities.

2.1.4 Influence of rainfall and domestic water usage on slope failures

In the Son La HRAs, rainfall is a significant factor that triggers landslides. Human activities have largely depleted the vegetation in this region. Additionally, the weathered layers have a relatively high permeability coefficient, allowing rainwater to infiltrate into the slopes and trigger landslides. Research findings indicate that areas with high average annual rainfall tend to experience more landslides compared to areas with lower rainfall averages (Phung, 2022a; Phung, 2022b). Specifically, regions with an average annual rainfall of approximately 1,600 to 1,700 mm per year exhibit the highest landslide susceptibility. Conversely, areas with annual rainfall below this threshold experience fewer landslides.

Residents in Sonla HRAs often have the habit of pouring wastewater from daily activities directly onto the ground instead of collecting it through ditches or pipes. Consequently, a portion of this wastewater seeps directly into the ground, while the rest flows over the slopes and gradually makes slopes saturated. This process results in increasing sliding weight and reducing the shear resistance of the soil. Research results indicate that each person in this area consumes an average of around 50 liters of water per day, meaning a household of four uses approximately 200 liters daily (Phung et al., 2023a). This wastewater saturates the ground beneath the stilt houses and the slopes behind them. With additional rainfall, the slopes reach a saturated state in just over 24 hours. Statistical data from 2015 to 2022 reveals that up to 90 % of landslides in resettlement areas occur within a 24 to 36-hour period after heavy rain (Phung et al., 2023a).

2.2 Developing a process for predicting landslide risks and forms

The process of predicting landslide risks in the Son La HRAs is initially built on a comprehensive understanding of these regions, as referenced in (Phung et al., 2023a, 2023b; Phung, 2022a). This understanding encompasses specific factors such as layout methods, infrastructure structures, natural conditions and the unique characteristics of the residential areas within the resettlement zones, as depicted in Figure 1.

2.2.1 Step 1: Building a set of identification criteria

The landslide identification criteria set is built based on the references in the studies (Phung et al., 2023b; Phung, 2022b; Cruden and Varnes, 1996). Firstly, field surveys are implemented

to initially identify areas within the resettlement zone that are at a high risk of landslides. Then, the relevant factors are considered, including additional investigations. Based on such basics, the hazard factors related to high-risk areas are identified, such as absolute elevation and angle slope. These identifications will serve as crucial information for making decisions regarding landslide risk forecasting and landslide type identification. Secondly, geological and hydrogeological data are collected from topographical and geological survey documents during the design step of Son La HRAs. If necessary, additional geological surveys can also be conducted to further clarify information of concern. From there, identify factors such as colluvium thickness, weathered layer characteristics, strata, etc. Finally, the average annual rainfall over many years is considered to determine the relative trend of landslide occurrence and rainfall. Additionally, real-time rainfall can be used to forecast short-term landslides more accurately. Eventually, a set of criteria to identify landslide risks is introduced based on factors such as slope angle, the absolute elevation of the terrain, a weathered cover layer, colluvium layer thickness and average annual rainfall (Phung et al., 2023a).

2.2.2 Step 2: Standardizing identification criteria

Figure 1. Flow chart of landslide risk identification process in Son La HRAs.

In this step, evaluation criteria are standardized according to a common scale to allow for meaningful comparisons. Specifically, each indicator is categorized into three landslide susceptibility levels: high, medium and low. This categorization is based on collected data on landslide locations and statistical analysis for each criterion (Phung et al., 2023a, 2023b; Phung, 2022a), which determines the sensitivity level of each criterion. The standardized scales are assigned to each landslide susceptibility level based on Table 1. Since the Son La HRAs are located in three northern mountainous provinces, the impact factors for landslide risk have similarities. These factors are standardized in their identification in Tables 2, 3 and 4. In addition, factors unique to each province of Son La, Dien Bien and Lai Chau, such as absolute elevation and colluvium thickness, are also standardized and documented in Tables 5, 6, 7, 8, 9 and 10.

Table 1. Classification (identification) scale of landslide susceptibility.

No.	Susceptibility level	Score
1	High (H)	9
2	Medium (M)	6
3	Low (L)	3

Table 2. Slope angle classification.

Characteristics	Hazard classification		
	High	Medium	Low
Average slope angle (°)	8-25	3-8; 25-35	<3; >35
Normalized score	9	6	3

Table 3. Average annual cumulative rainfall classification.

Characteristic	Rainfall threshold (mm)		
	High	Medium	Low
Average annual cumulative rainfall (mm)	>1,600	1,500-1,600	1,300-1,500
Normalized score	9	6	3

Table 4. Weathered layer characteristic factor identification.

Characteristics	Hazard classification		
	High	Medium	Low
Weathering level	Completely weathered	Strongly weathered	Moderate weathered
Normalized score	9	6	3

Table 5. Absolute terrain elevation factor identification for Son La province.

Characteristics	Hazard classification		
	High	Medium	Low
Absolute Elevation	250-500	(100-250) and (500-1,000)	>1,000 and <100
Normalized score	9	6	3

Table 6. Colluvium thickness factor identification for Son La province.

Characteristics	Hazard classification		
	High	Medium	Low
Thickness (m)	2-10	< 2	>10
Normalized score	9	6	3

Table 7. Absolute terrain elevation factor identification for Dien Bien province.

Characteristics	Hazard classification		
	High	Medium	Low
Absolute Elevation		100 - 250	> 250 and < 100
Normalized score	9	6	3

Table 8. Colluvium thickness factor identification for Dien Bien province.

Characteristics	Hazard classification		
	High	Medium	Low
Thickness (m)	2-10	< 2	>10
Normalized score	9	6	3

Table 9. Absolute terrain elevation factor identification for Lai Chau province.

Characteristics	Hazard classification		
	High	Medium	Low
Absolute Elevation	250-500	100-250 and 500-1,000	>1,000 and <100
Normalized score	9	6	3

Table 10. Colluvium thickness factor identification for Lai Chau province.

Characteristics	Hazard classification		
	High	Medium	Low
Thickness (m)	2-10	< 2	>10
Normalized score	9	6	3

2.2.3 Step 3: Calculating weights

The factors' weights were calculated using the Analytical Hierarchy Process (AHP) according to the Saaty-Saaty analytical hierarchy method. The weight calculation is done by dividing each value in each column of the matrix by the total number of values in that column, which will give a new matrix with values between 0 and 1. The average on each row of the matrix corresponds to the weight of the indicator in that row. The pairwise comparison matrix for each criterion is built based on the opinion of experts according to T.Saaty's rating scale. The pairwise comparisons between criteria and the importance of these criterion pairs are assessed to assign priority levels (aij values) according to the pairwise comparisons, typically using positive integer values from 1 to 9 or their inverses. This generates a square matrix (n × n), in which the "Total" row is calculated by each column (as illustrated in Table 12). The evaluation criteria weighting matrix is created by dividing the value of each cell in the evaluation criteria matrix by the total in each column. The consistency rate (CR) was calculated using criterion weights and a pairwise comparison matrix. The values of this index need to be guaranteed to be less than 10 % to ensure consistency in the evaluation process.

Table 11. Importance evaluation scale for criteria pairs based on the T. Saaty method.

Level	Definition	Explanation
1	Equal Importance	Two factors, A and B, contribute equally
3	Slightly Dominant Importance	Factor A is slightly prioritized over factor B in the contribution
5	More Importance	Factor A contributes more than B
7	High Importance	Factor A contributes significantly more than B, clearly evident in a specific case.
9	Extremely important, completely dominant	Factor A demonstrates completely dominates Factor B
2, 4, 6, 8	Intermediate level between the above levels	Consideration is needed between the two levels

Table 12. Matrix for comparing evaluation criteria.

Factor	(A)	(B)	(C)	(D)	(E)
Slope angle (A)	1	9	3	4	3
Absolute Elevation (B)	0.111	1	1/3	1/3	1/5
Weathered layer (C)	0.333	3	1	1	3
Colluvium Thickness (D)	0.250	3	1.000	1	3
Rainfall (E)	0.333	5	0.333	0.333	1
Total	2.028	21	5.667	6.667	10.2

2.2.4 Step 4: Forecast landslide risk and identify landslide types

The Landslide Susceptibility Index is an index used to assess the susceptibility of landslides. The LSI value for each HRA is calculated using the constructed identification criteria from Step 2 and their corresponding weights as follows:

$$LSI = 0.4691 \times A + 0.0462 \times B + 0.1856 \times C + 0.1773 \times D + 0.1219 \times E \quad (1)$$

where, A, B, C, D and E correspond to the scoring values of the factors: slope, absolute terrain elevation, weathering crust, residual slope cover and rainfall, which were determined in the previous steps.

- *Predicting landslide risk based on LSI score:* According to the standardized scoring in Table 1, the range of LSI values for assessing landslide susceptibility at resettlement sites falls within the range of 3.0 to 9.0. Therefore, categorize the sensitivity levels based on the LSI value ranges as follows: LSI < 5.0 - "Low" risk; LSI = 5.0 ÷ 7.0 - "Medium" risk; LSI > 7.0 - "High" risk. In this step, also consider other relevant information, such as any signs that may affect landslides at the surveyed locations, based on the information recorded during the field survey in Step 1.

- *Identifying the form and scale of landslides:* Based on the data collected and analyzed during the research on landslides in resettlement areas (Phung, 2022a), the following patterns are observed:

Rotational landslides typically occur in areas with a thick and completely weathered layer, resulting in large-scale sliding blocks. Translational landslides often occur in locations with a thin cover on hard ground (base rock) that is weak to moderately weathered, with a colluvium layer thickness of less than 3.0 m. The sliding block scale in these cases ranges from small to very small. Compound landslides represent an intermediate state between translational landslides and rotational landslides, with a moderate-scale sliding block. Compound landslides occur when the colluvium layer is larger than 3.0 m thick.

It should be noted that for the specific study sites, all identified criteria can be considered constant criteria, with the exception of precipitation. Therefore, it is possible to predict landslide occurrence and landslide form according to rainfall data based on the proposed criteria datasets.

3. RESULTS OF THE METHOD APPLICATION FOR STUDY SITES

To assess the feasibility of the developed method and validate the constructed data, the research team utilized historical landslide records in the Son La HRAs. The statistical analysis revealed a strong correlation between the average annual rainfall and the number and type of landslides in this region based on the proposed dataset. Therefore, the dataset used for preliminary testing in this study is as outlined below:

3.1 Input data used for analysis and forecasting

The input data used for analysis are referenced from documents (Phung, 2022a, Phung, 2022b). The absolute elevation of the study sites is taken from 30-meter resolution DEMs of Dien Bien, Son La and Lai Chau provinces. The slope gradient is created based on DEMs. The weathered layer and geology information are referenced from available documents. The groundwater data and recorded landslides for the study areas are investigated. Furthermore, the rainfall data used is the average annual rainfall records from representative rain stations (including Muong Lay district, Tuan Giao district, Muong La district, Thuan Chau district, Quynh Nhai district, Mai Son district, Song Ma district, Moc Chau district, Son La city, Muong Te - Nam Nhun district, Sin Ho district,…).

3.2 Prediction results for risk, form and scale of landslides

Based on the four-step process developed previously and the collected database to determine factors such as slope, rainfall, weathering cover, absolute terrain elevation and colluvium layer thickness for numerous locations across the three provinces of Dien Bien, Son La and Lai Chau. Then, the Landslide Susceptibility Index (LSI) is calculated using Formula 1 for these target sites in the Son La HRAs. Based on the LSI values and the surveyed danger signs at Step 1, the risk, form and scale of landslides at these locations are predicted and presented in Tables 13, 14 and 15. Tabs 13, 14 and 15 reveal that the predicted results are generally relatively consistent with historical landslide records in most study sites except Muong Bu commune. However, there are notable discrepancies in the type and scale of landslides specifically within Muong Bu commune. According to the collected historical documents, the majority of landslides in Muong Bu commune were translational landslides while predicted results are compound landslides. It's worth noting that these differences may be attributed to the representativeness of the collected data. Further investigation and refinement of these data are expected to improve the accuracy of landslide predictions.

Table 13. Landslide prediction results at resettlement areas in Lai Chau province.

No.	Places	Prediction results		
		Risk	Landslide type	Scale
A	Sin Ho district			
I	Nam Han commune	High	Compound and Rotational Landslide	Medium-Large
1	Nam Han 1	High	Compound Landslide	Small-Medium
2	Nam Han 2	High	Compound Landslide	Small-Medium
3	Nam Han 3	High	Compound Landslide	Small-Medium
II	Can Co commune	High	Compound Landslide	Medium-Large
1	Can Co 1	High	Rotational Landslide	Large
2	Can Co 2	Medium	Compound Landslide	Small-Medium
3	Can Co 3	Medium	Compound Landslide	Small-Medium
III	Nam Ma commune	High	Compound Landslide	Small-Medium
1	Nam Ma 1	High	Compound Landslide	Small-Medium
2	Nam Ma 2	High	Compound Landslide	Small-Medium
3	Nam Ma 3	High	Compound Landslide	Small-Medium
IV	Nam Cha commune	High	Rotational Landslide	Large
1	Nam Cha 1	High	Rotational Landslide	Large
2	Nam Cha 2	High	Rotational Landslide	Large
3	Nam Cha 3	High	Rotational Landslide	Large

Table 14. Landslide prediction results at resettlement areas in Dien Bien province.

No.	Places	Prediction results		
		Risk	Landslide type	Scale
I	Tua Thang commune	High	Compound and Rotational Landslide	Medium-Large
1	Tua Thang 1	High	Rotational Landslide	Large
2	Tua Thang 2	High	Rotational Landslide	Large
3	Tua Thang 3	High	Rotational Landslide	Large
II	Lay Nua commune	High	Rotational Landslide	Medium-Large
1	Lay Nua 1	High	Compound Landslide	Small-Medium
2	Lay Nua 2	High	Rotational Landslide	Large
3	Lay Nua 3	Medium	Translational Landslide	Small

Table 15. Landslide prediction results at resettlement areas in Son La province.

No.	Places	Prediction results		
		Risk	Landslide type	Scale
I	Nam Gion commune	Medium	Compound and Rotational Landslide	Medium-Large
1	Nam Gion 1	Medium	Translational Landslide	Small
2	Nam Gion 2	Medium	Compound Landslide	Small-Medium
3	Nam Gion 3	Medium	Compound Landslide	Small-Medium
II	Muong Bu commune	Medium	Compound and Rotational Landslide	Medium-Large
1	Muong Bu 1	Medium	Compound Landslide	Small-Medium
2	Muong Bu 2	Medium	Compound Landslide	Small-Medium
3	Muong Bu 3	Medium	Compound Landslide	Small-Medium

No.	Places	Prediction results		
		Risk	Landslide type	Scale
III	Muong Chum commune	Medium	Compound and Rotational Landslide	Medium-Large
1	Muong Chum 1	Medium	Compound Landslide	Small-Medium
2	Muong Chum 2	Medium	Compound Landslide	Small-Medium
3	Muong Chum 3	Medium	Compound Landslide	Small-Medium

4. CONCLUSIONS AND RECOMMENDATIONS

Landslides have consistently posed a significant threat to both lives and property in the Son La HRAs ever since the relocation of people from the lake bed to these resettlement zones. The most effective strategy for mitigating this threat is to predict landslide risks and implement appropriate preventive measures. Therefore, this study has leveraged field investigations and the analysis of historical landslide events to elucidate the nature of destruction and the characteristics of landslides, considering factors such as rainfall, terrain, geology, slope gradient and weathered cover layer. This effort has proposed a potential method for identifying landslide risks and landslide forms for the Son La HRAs.

The method offers the distinct advantage of having all identification criteria already established, with the exception of the rainfall criterion. Therefore, whenever rainfall forecasts are available, they can be harnessed to predict the landslide risk. Additionally, the method enables the prediction of landslide types and scales.

The results obtained through applying this method to Son La hydropower resettlement areas have been verified based on historical landslide data collected. The results show consistency between forecast and actual landslides in both form and scale. This integrated approach holds promise for improving the overall effectiveness of landslide prevention and management strategies for Son La HRAs.

5. ACKNOWLEDGMENTS

This study is a component of the research outcomes from the State project titled “Research on methods for identifying the risk of slope landslides and proposing environmentally friendly, cost-effective solutions using on-site materials and labor, suitable for densely populated areas within the resettlement points of the Son La hydroelectric power project”, Project code ĐTĐL. CN-80/21. The project is managed by the Ministry of Science and Technology and executed by the Vietnam Institute of Water Resources Science.

6. REFERENCES

Bui T. D., Tran A. T., Hoang N. D., Nguyen Q. T., Nguyen B. D., Ngo V. L. & Pradhan B., 2016. Spatial prediction of rainfall-induced landslides for the Lao Cai area (Vietnam) using a hybrid intelligent approach of least squares support vector machines inference model and artificial bee colony optimization. *Landslides, 14*, 447-458.

Cruden D. M., & Varnes D. J., 1996. Landslide types and processes. *Special report, 247*, 36-75.

Gian Q. A., Tran D. T., Nguyen D. C., Nhu V. H., & Bui D. T., 2017. Design and implementation of site-specific rainfall-induced landslide early warning and monitoring system: a case study at Nam Dan landslide (Vietnam). *Geomatics, natural hazards and risk, 18:2*, 1978-1996.

Le T. T. T., Tran T. V., Hoang V. H., Bui V. T., Bui T. K. T., & Nguyen H. P., 2021. Developing a landslide susceptibility map using the analytic hierarchical process in Ta Van and Hau Thao communes, Sapa, Vietnam. *Journal of Disaster Research, 16:4*, 529-538.

Nguyen V. D., 2020. Research on warning of the risk of landslides in Son La hydropower reservoir area using analysis of high-resolution remote images and geographic information system. *VNU University of Science*.

Pham V. H., Pham Q. S. & Nguyen V. D., 2015. The study evaluated arming of risk of landslide in Hoa Binh and Son La reservoir hydropower area on the basis of analyzing high-resolution remote sensing and geographic information systems. *Vietnam Journal of Earth Sciences, 37:3*, 193-203.

Phung V. A., 2022a. Report assessing the current status of landslides in Son La hydropower resettlement areas. *State project: Research on methods to identify slope landslide risks and propose environmentally friendly, low-cost solutions, using on-site materials and labor, suitable for residential areas concentrated in the resettlement sites of Son La hydropower plant*.

Phung V. A., 2022b. The report proposes to develop landslide criteria. *State project: Research on methods to identify slope landslide risks and propose environmentally friendly, low-cost solutions, using on-site materials and labor, suitable for residential areas concentrated in the resettlement sites of Son La hydropower plant*.

Phung V. A., Nguyen D. H., To Q. T., & Tran Q. L., 2023a. Results of forecasting and identifying landslide risks for Son La hydropower resettlement areas. *Journal of Irrigation Science and Technology.* Special issue (Celebrating the 15th Anniversary of the Institute of Water Engineering) in 2023, 41-48.

Phung V. A., Nguyen D. M., & Nguyen V. L., 2023b. Analysis of landslide types in the resettlement areas of the Son La hydropower plant and proposed remediation strategies. *Journal of Irrigation Science and Technology, 76*, 77-86.

Tran T. V., Alvioli M., & Hoang V. H., 2021. Description of a complex, rainfall-induced landslide within a multi-stage three-dimensional model. *Nat Hazards, 110*, 1953-1968.

APPLICATION OF AHP MODEL TO ESTABLISH A LANDSLIDE PROBABILITY ZONING MAP IN A LUOI DISTRICT, THUA THIEN-HUE PROVINCE, VIETNAM

Nguyen Thi Thuy Hanh*, Quach Thi Chuc

Hanoi University of Natural Resources and Environment, Vietnam
*Corresponding author. Email: ntthanh.tdbd@hunre.edu.vn

ABSTRACT

A Luoi is a mountainous district of Thua Thien-Hue province, Vietnam, with rugged terrain, steep slopes and many valleys. Every year, A Luoi district bears many risks of natural disasters such as storms, floods, droughts and especially landslides. This study applied the AHP (Analytical Hierarchy Process) model with the GIS tool on the input database of Sentinel-2B Image, DEM and geographic background data to evaluate the influence of 5 factors: slope, elevation, aspect, land cover and vegetation to generate a landslide hazard zoning map, scale 1:50,000. The results show that the sites with a high risk of landslides are concentrated mainly in the communes of Hong Kim, Hong Ha, Son Thuy, Hong Thuong, Phu Vinh and Huong Nguyen. Thereby helping people avoid and minimize vulnerabilities caused by landslides.

1. INTRODUCTION

Landslides are one of the most popular geological hazards (Chalkias et al., 2014). Landslides often cause loss of life and property as well as serious damage to natural resources worldwide. Landslides occur due to natural factors or man-made activities. Natural activities include changes in climate, such as heavy rainfall, prolonged rainfall, complex terrain, etc. Human activities consist of changing land use purposes, cutting down forests for farming, changing slopes and building infrastructure (Zaruba and Mencl, 2014). Landslide risk mapping is necessary to devise feasible prevention measures and evacuation plans to avoid loss of life and property. Furthermore, landslide hazard maps greatly help planners in selecting suitable areas for economic development in any region (Cirianni et al., 2012; Cirianni et al., 2008).

Scientists have been focused on landslide risk topics since the 1970s with many different levels and approaches (Reichenbach et al., 2018). Varnes and Guzzetti et al. have divided landslides into 5 levels (Varnes, 1984; Guzzetti et al., 2005). Landslide risk assessment methods are divided into 2 groups, qualitative and quantitative, or can be divided into 3 types: heuristic method, statistical method and deterministic method. For the heuristic method, investigators rank and evaluate the weights of landslide-causing factors based on the assumption or importance of factors leading to landslides (Cirianni et al., 2012; Guzzetti et al., 2005; Hansen, 1984). This is a qualitative method, which is likely to lead to errors due to its reliance on the opinions of experts in determining the weight of factors causing landslides (Cirianni, 2008; Hansen et al., 1995; Dahal et al., 2008). The deterministic method belongs to the quantitative method, based on the calculation and analysis of stable or unstable conditions of the slope. This is a stable and highly accurate method (Cirianni, 2012; Dahal et al., 2008; Pourghasemi et al., 2018). The statistical method is a quantitative method based on the spatial distribution of factors causing landslides in the past to analyze and make predictions about the risk of landslides in the future (Alvioli and Baum, 2016). Among landslide risk assessment methods, deterministic methods and statistical methods are considered highly effective and are widely used in current research (Cirianni, 2012). In particular, the deterministic method can only be applied to small areas because it is necessary to collect detailed information about the topographic, geological and hydrological characteristics of the slope (Dahal, 2008; Huang and Zhao, 2018). For large areas, statistical methods are the most common choice (Alvioli and Baum, 2016). Some qualitative methods become semi-quantitative by combining rankings and weights (Youssef, 2016; Ayalew, 2005), as is the case with the analytic hierarchy process (AHP), a multi-criteria decision-making method has been widely applied to solve deterministic problems (Jazouli et al., 2019).

This method is based on a hierarchical analysis system of related factors and comparisons between different pairs of factors to be able to assign an appropriate ratio for each factor. Thereby, it is possible to estimate the weight of each considered factor through the linear correlation of each factor with other factors. The correlation among various factors has made this method a valuable tool in the establishment of landslide hazard maps obtained by correlating and comparing a large number of factors (Saaty, 1990).

Therefore, the management of a large number of correlated factors and estimates to determine the extent of landslides is carried out, in most cases, through the use of geographic information systems (GIS) (Ayalew et al., 2005). GIS uses data integration techniques, which are a highly suitable tool for landslide hazard mapping. In reality, due to the increasing availability of high-resolution spatial data sets, GIS, remote sensing and high-speed computing, landslide risk assessment and hazard mapping procedures can become partial automation and, thus, fieldwork minimized (Saaty, 1990). The reliability of these maps depends largely on the methodology and available data used to estimate disaster risk. Furthermore, GIS is an excellent and useful tool for mapping the susceptibility of an area at risk of landslides (Saaty, 1990). In Vietnam, landslides mainly occur during the rainy season in the Northern mountainous provinces and the Central-Central Highlands region (Doan et al., 2020). Among them, A Luoi, Thua Thien-Hue province, in the Central region, is one of the districts that often suffer from many consequences caused by landslides, causing deaths and damage to plenty of property.

This study aims to establish a landslide risk map for A Luoi district through the AHP model in a GIS environment, based on 5 characteristic factors: slope, elevation, direction, land cover and vegetation density. Finally, it is possible to zone sites at high risk of landslides and support people and local authorities to minimize vulnerabilities.

2. STUDY AREA AND DATA

2.1 Study area

A Luoi is a mountainous district on the western border of Thua Thien-Hue province, with an area of about 1224.63 km^2. A Luoi's terrain is strongly divided, including two parts, East Truong Son and West Truong Son, with an average altitude of 600-800 m above sea level and an average slope of 20-25^o. The eastern part of Truong Son has rugged terrain and steep slopes, with high peaks such as Dong Ngai (1,774 m), Co Pung Peak (1,615 m), Re Lao (1,487 m),

Tam Voi (1,224 m) (Local Committee of A Luoi district, 2023).

In addition, the weathered crust in A Luoi is highly diverse in depth, structure, geomorphology, characteristics and origin of chemical-mineralogical and geochemical components. The rainy season in the study area lasts about 4 months, from September to December, containing about 70-80 % of the total rainfall every year. The rainfall in each month of the year ranges from 2,900-5,800 mm (Local Committee of A Luoi district, 2023). The hot and humid conditions of tropical climates strongly affect landslide-related materials, causing rapid weathering processes to take place, weakening and strongly damaging regolith coatings.

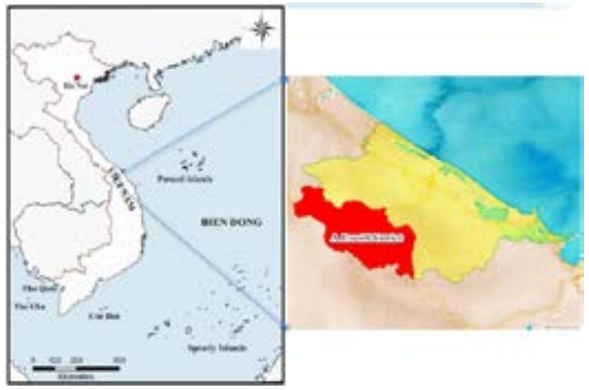

Figure 1. Location of study.

A Luoi also possesses large resources and vegetation, in which the forest coverage rate in 2010 reached 75 %, average reserve of 6-7 million m^3 (Local Committee of A Luoi district, 2023). However, in recent years, natural vegetation has also been rapidly changed by local deforestation activities or leaving land bare, so the risk of landslides is very high. Therefore, in this study, the authors chose 5 typical factors, including slope, elevation, aspect, land cover and vegetation density, as input data to build the landslides model in A Luoi district.

2.2 Data

A data set used in the project includes a Sentinel 2B satellite image (ESA, 2023) and a Digital elevation model (DEM) with a resolution of 12.5 m (Alaska Satellite Facility, 2023). The image was aquired on January 15th, 2023 at 10 m of spatial resolution. The ID of the image is S2B_MSIL1C_20230115T032059. Bands 2,3,4,8 of the image are employed to classify land cover and calculate the Normalized Difference Vegetation Index (NDVI). The slope and aspect maps generated by the DEM. Consequently, 5 factors consisting of slope, elevation, aspect, land cover and NDVI density are ready to put in the landslide model.

3. METHODS

AHP was developed in the 1970s by Thomas L. Saaty and has since been extensively studied and is currently used in decision-making for complex scenarios (Bhushan & Rai, 2004). The application of AHP begins with a problem being decomposed into a hierarchy of criteria so as to be more easily analyzed and compared in an independent manner. After this logical hierarchy is constructed, the decision-makers can systematically assess the alternatives by making pairwise comparisons for each of the chosen criteria (Saaty, 2008). AHP transforms the comparisons, which are most often empirical, into numerical values that are further processed and compared. The weight of each factor allows the assessment of each one of the elements inside the defined hierarchy. This capability of converting empirical data into mathematical models is the main distinctive contribution of the AHP technique when contrasted with other comparing techniques. AHP is applied to generate a landslide probability zoning map for A Luoi district, as shown in Figure 2.

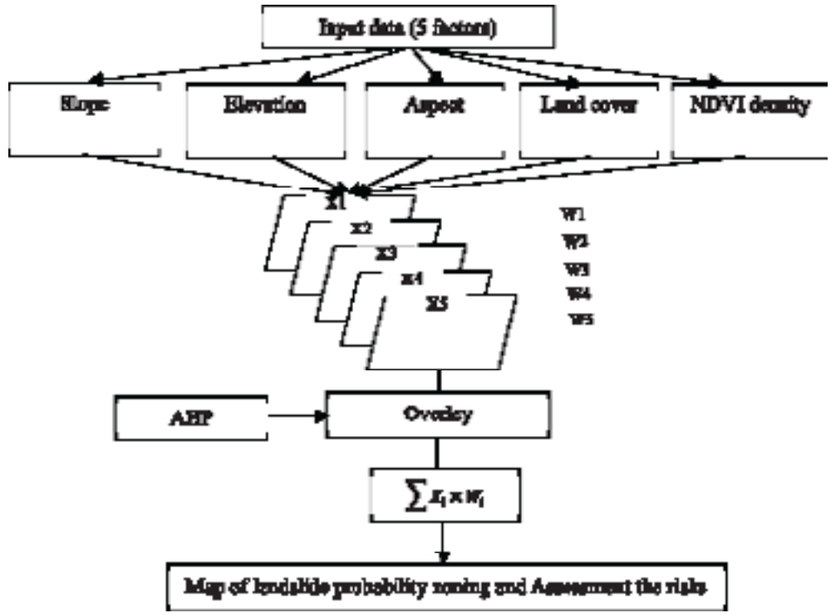

Figure 2. Flowchart of estimate landslide model.

3.1 Identifying typical factors to put into the landslide model

Landslides occur due to the resistance of the soil or rock forming the slope against gravity and landslides occur when gravity is imbalanced. This balance can be changed by both natural and man-made factors. The factors that influence slope stability are diverse and interact in complex and dangerous ways (Varnes, 1984). Besides man-made factors, natural factors affect landslides, such as seismicity, soil strength, chemistry and mineralogy, geology, geomorphology and hydrology.

Identifying the influence of each factor driving landslides or decentralizing the influence of each factor is based on the properties of the drivers. Based on analyzing the mechanism of landslide formation and identifying the main causes of landslides, based on analysis of specific characteristics of the study area and on the basis of previous publications, it is possible to determine qualitatively the main factors affecting the landslide process of the study area as follows: slope, elevation, aspect, geology, weathering crust and soil, geomorphology, fault density, river and stream density, land cover, vegetation density, rainfall and depth of cleavage. From there, we selected 5 typical factors leading to landslides in A Luoi district, Thua Thien Hue province, including slope, elevation, aspect, land cover and vegetation density to analyze.

Table 1. Scores of priority to the factors (the higher score, the higher level of priority).

Fators	Slope	Elevation	Aspect	Land cover	NDVI density
Level	1	2	2	3	3

Table 2. Correlated matrix.

Factors	Slope	Elevation	Aspect	Land cover	NDVI density
Slope	1	2	2	3	3
Elevation	0.5	1	1	1.5	1.5
Aspect	0.5	1	1	1.5	1.5
Land cover	0.33	0.67	0.67	1	1
NDVI density	0.33	0.67	0.67	1	1
Sum	2.67	5.33	5.33	8	8

Table 3. Weight matrix of the factors.

Factors	Slope	Elevation	Aspect	Land cover	NDVI density	Weight
Slope	0.38	0.38	0.38	0.38	0.38	0.38
Elevation	0.19	0.19	0.19	0.19	0.19	0.19
Aspect	0.19	0.19	0.19	0.19	0.19	0.19
Land cover	0.13	0.13	0.13	0.13	0.13	0.13
NDVI density	0.13	0.13	0.13	0.13	0.13	0.13

3.2 Generating thematic maps according to each element

The scale for assessing the risk of disasters and landslides, in particular, usually has at least 2 levels and at most 7 levels. The number of levels depends on the objectives, data adequatation and scale of projects. The risk assessment scale is often expressed in increasing levels as follows: low, medium and high for a 3-level scale; very low, low, medium, high and very high for a 5-level scale. This project used the latter when producing the maps.

3.2.1 Establishing landslide risk maps due to the influence of slope, elevation and aspect

DEM is important data for landslide research and supports the generation of the slope, elevation range and aspect maps using various tools in GIS. There are many types of slopes, such as slopes in certain directions, North, South, East, West and average slope. Here, we utilized the average slope and the unit of measurement is degrees. Then, the slope map is thresholded based on the physical features of the site. In each slope interval, weights affecting landslides are calculated according to the model's formulas based on referencing the existing landslide map. Statistically, the higher the weight, the higher the likelihood of landslides to that factor.

The influence of elevation on landslides is often indirect relationships. Weathering factors play a crucial role in landslides and are closely related to the altitude of the terrain; for example, at high altitudes, more erosion occurs, resulting in less weathering depth. The statistics showed that altitude values in A Luoi district, Thua Thien Hue province, vary from 22 m to 1,800 m. Terrain with elevation < 300 m accounts for 18.13 %, areas with elevation from 300-900 m account for 70.09 % and areas with elevation from 900 m to 1,200 m account for 8.88 %. Areas with altitudes above 1,200 m account for only 2.9 %. The elevation map, after being established and statistically divided into 5 classes corresponding to the level of its impact on different landslide risks.

Table 4. The levels of landslide risks according to elevation.

Levels	Elevation (m)	Scale of landslide risks	Areas (ha)	Percentage (%)
1	22 - 300	Very low	22,237.26	18.13
2	300 - 600	Low	44,046.02	35.92
3	600 - 900	Medium	41,894.45	34.17
4	900 - 1,200	High	10,883.92	8.88
5	1,200 - 1,800	Very high	3,559.96	2.90

The slop direction has an indirect impact on the landslide process through the relationship between terrain and climate. Slopes facing the wind have moisture and vegetation cover that differs from slopes without wind, which also leads to different levels of slope stability. The study area has aspects from the Northeast to the Southeast, accounting for 45.6 %, the South, accounting for 20.78 % and the direction from the West to the Northwest, accounting for 33.61 %. The aspect map is divided into 5 ranges corresponding to the level of its impact on different landslide risks.

Table 5. The levels of landslide risks according to aspect.

Levels	Aspect	Scale of landslide risks	Areas (ha)	Percentage (%)
1	North East	Very low	27,630.86	22.56
2	South East	Low	28,218.51	23.04
3	South	Medium	25,447.67	20.78
4	West	High	20,724.33	16.92
5	North	Very high	20,436.81	16.69

Slope statistics in A Luoi district, Thua Thien-Hue province, show that slope values vary from 0-75°. Areas with a slope < 18° account for 43.78 %, areas with a slope from 18° to 25° account for 23.54 % and areas above 25° account for 32.68 %. The slope retrieved map is divided into 5 threshes corresponding to the level of its impact on different landslide risks.

Table 6. The levels of landslide risks according to slope.

Levels	Slope (°)	Scale of landslide risks	Areas (ha)	Percentage (%)
1	< 3°	Very low	6,088.33	4.97
2	3 - 8°	Low	12,077.87	9.85
3	8 - 18°	Medium	35,502.18	28.96
4	18 - 25°	High	28,858.75	23.54
5	>25°	Very high	40,061.8	32.68

3.2.2 Establishing landslide risk maps due to vegetation density

Studying landslides for the vegetation cover plays a very important role. It is closely related to the stability of slopes. For areas covered with dense vegetation, large coverage and developed root systems, the probability of landslides is low and vice versa. Thus, establishing a vegetation map is critical to landslide research. In this study, vegetation was evaluated through NDVI density maps; NDVI is calculated based on the red band and near-infrared band of the Sentinel 2B satellite image, as shown below.

$$NDVI = \frac{NIR - RED}{NIR + RED} \quad (1)$$

Different NDVI values reflect different plant quality in each pixel. The NDVI index in the area interested varies from - 0.22 to 0.62 and are thresholded into 5 levels corresponding to the

landslide risk levels, in which areas with little or no vegetation have a high likelihood of landslides and vice versa.

Table 7. The levels of landslide risks according to NDVI density.

Levels	NDVI	Scale of landslide risks	Areas (ha)	Percentage (%)
1	0.42 - 0.62	Very low	31,106.43	25.30
2	0.34 - 0.42	Low	46,258.13	37.63
3	0.24 - 0.34	Medium	30,006.18	24.41
4	0.09 -0.24	High	13,146.83	10.69
5	(-0.22) - 0.09	Very high	2,421.64	1.97

3.2.3 Establishing landslide risk maps due to land cover

Sentinel images are used for land cover classification. There are two main classification methods: supervised classification and unsupervised classification. In the study, the authors used a supervised classification method and performed classification with types, including Forests, Bare soils, Water bodies, Impervious surfaces and Agricultures.

In the study area, forest and agricultural areas dominate 54.66 %. Bare soil and impervious surfaces, especially traffic systems, mainly cause landslides, accounting for up to 33.42 %. Recently, natural vegetation has been drastically altered by human activities such as agriculture and timber production; local people clear forests and leave bare soil, so the risk of landslides is very high. Levels of landslide risks corresponding to land cover classes are presented in Table 8.

Table 8. The levels of landslide risks according to land cover.

Levels	Land cover classes	Scale of landslide risks	Areas (ha)	Percentage (%)
1	Water bodies	Very low	14,656.85	11.91
2	Forests	Low	31,789.87	25.84
3	Agricultures	Medium	35,462.9	28.82
4	Impervious surfaces	High	28,511.12	23.17
5	Bare soils	Very high	12,609.15	10.25

3.3 Establish a landslide probability zoning map

There are many factors that affect the landslide process; however, their roles are not similar. Therefore, determining the weight of each driver is very necessary. This study determines the weights by comparing the correlation among influencing factors. Intermediate maps, which are weight value maps showing the relationship between the landslide process and each factor, are integrated into GIS to produce a landslide risk zoning map for the study area. The probability of landslide is calculated in the GIS system for an area based on the following Van Westen formula:

$$LSI = \sum_{j=1}^{n} X_{ij} W_j \quad (2)$$

where: LSI: Landslide risk index;

Wj: Weight of the factor j;

Xij: is the score of class i in the factor j;

n: Number of agents causing landslides in the study area.

After considering and evaluating the level of landslide risk, we classify the level of landslide risk from low level to extremely dangerous level (determine the level of no landslide risk, low risk, high risk, corresponds to value ranges), then group the values in the same range together. Then, all sites on the map in a range face the same landslide risk level.

The above formula adapted for A Luoi district to result in the below equation:

$$LSI = 0.38\times A + 0.19\times B + 0.19\times C + 0.13\times D + 0.13\times E \quad (3)$$

where: A is a slope, B is elevation, C is aspect, D is land cover and E is NDVI density.

The result is a map of landslide probability with different values on each pixel. Then, the map is reclassified as 5 corresponding risk levels consisting of very low, low, medium, high and very high. The thresholds are selected based on statistical value, resulting in a cumulative probability curve with the following parameters: $LSI_{min} = 1.15$; $LSI_{max} = 4.84$

The intervals are calculated according to the below formula:

$$\Delta_{TL\text{Đ}} = \frac{\text{LSImax - LSImin}}{n} = \frac{4.84 - 1.15}{5} = 0.74$$

4. RESULTS AND DISCUSSIONS

Products of the project are 5 landslide risk maps due to the separate factors and a map due to integrated all drivers in A Luoi district, as shown in Figure 3 and Figure 4.

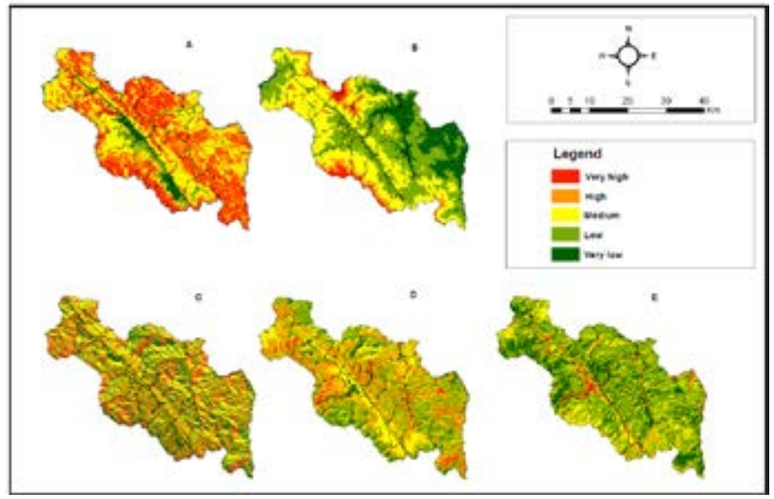

Figure 3. Landslide risk maps due to each factor in A Luoi district. A: Landslide risk map due to slope; B: Landslide risk map due to elevation; C: Landslide risk map due to aspect; D: Landslide risk map due to land cover; E: Landslide risk map due to NDVI density.

As shown in Figure 4, the landslide probability zoning map in A Luoi district, Thua Thien-Hue province, Vietnam, includes 5 levels of landslide risk: very low in dark green, low in light green, medium in yellow, high in orange and very high in red.

Statistical results in Table 9 show that areas with very low landslide risk account for 19.86 % (corresponding to 24,297.5 ha) of the entire district area, low landslide risk accounts for 19.86 % (corresponding to 24,297.5 ha) of the entire district. 2.15 % (equivalent to 2635.11 ha), the medium risk of landslides accounts for 46.55 % (equivalent to 56954.02 ha), the high risk of landslides is 30.02 % (36726.14 ha), the very high is about 1.41 %, accounting for 1724.37 ha).

The results of landslide risk zoning in the district A Luoi show that the communes identified as having a very high risk of landslides are Hong Thai, with an area of 495.91 ha, followed by Hong Kim, accounts for 243.93 ha, Hong Trung 197.61 ha, Dong Son 129.31 ha, Hong Thuong 100.69 ha,…

Areas with high risk of landslides concentrated in several communes, mostly in Huong Nguyen (4869.4 ha), Hong Ha (4130.97 ha), Hong Trung (2871.23 ha), Hong Kim (2043.71 ha), A Roang 1625.71 ha, followed by A Luoi, Dong Son, Hong Bac, Hong Thuy, Hong Thai, Hong Thuong, Hong Van, Phu Vinh, Hong Lam,…

+ Landslide risk at medium level distributed in 3 communes, including Huong Nguyen commune accounts for 8748.33 ha, Hong Ha commune accounts for 7018 ha, Hong Thuy commune accounts for 6164.07 ha. In addition, there are a number of communes with large areas of moderate risk of landslides, such as A Roang, Hong Thai, Hong Trung, Hong Van, Huong Lam, Huong Phong and Nham.

+ Communes with low risk of landslides are Huong Nguyen, Dong Son and Huong Lam and very low risk such as Huong Nguyen, Hong Ha, Huong Phong and Huong Lam.

Table 9. Areas according to levels of landslide risks in A Luoi district

Levels	Scale of landslide risks	Point distance	Area (ha)	Percentage (%)
1	Very low	1.15-1.89	24,297.5	19.86
2	Low	1.89-2.63	2,635.11	2.15
3	Medium	2.63-3.36	56,954.02	46.55
4	High	3.36-4.10	36,726.14	30.02
5	Very high	4.10-4.84	1,724.37	1.41
			122,337.14	100

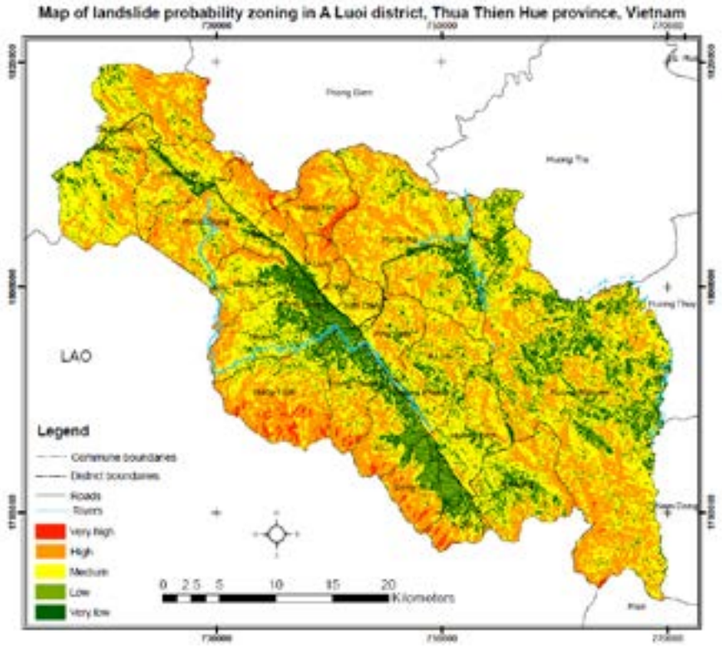

Figure 4. Map of landslide probability zoning in A Luoi district.

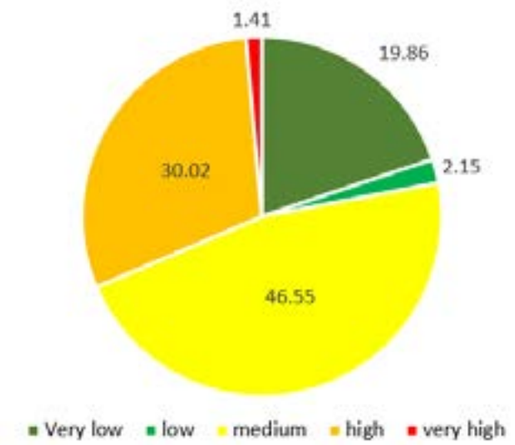

Figure 5. Percentage of area by levels of landslide risks.

Table 10. Area of landslide risk zones by commune in A Luoi district.

Commune	Area of landslide risk zones (ha)				
	Very low	Low	Medium	High	Very high
A Dot	444.67	53.93	583.19	499.29	99.00
A Luoi	285.64	52.40	435.40	546.77	51.31
A Ngo	196.09	45.82	359.08	292.87	3.74
A Roang	1,179.79	93.06	2,703.19	1,625.71	9.29
Bac Son	128.67	9.72	462.63	466.16	39.27
Dong Son	591.17	281.13	677.80	1,023.18	129.31
Hong Bac	607.88	68.39	1,515.64	927.54	4.38
Hong Ha	2,493.48	178.38	7,018.96	4,130.97	68.98
Hong Kim	378.06	40.81	1,474.24	2,043.71	243.93
Hong Quang	302.33	71.13	194.39	34.26	0.24
Hong Thuy	1,385.32	49.45	6,164.07	4,082.45	93.67
Hong Thai	872.18	77.63	2,526.11	2,911.42	495.91
Hong Thuong	1,171.12	209.31	1,521.05	1,043.76	100.69
Hong Trung	656.55	24.52	2,846.44	2,871.23	197.61
Hong Van	606.46	36.99	2,020.92	1,371.19	54.92
Huong Lam	1,405.05	272.96	2,501.03	924.40	1.00
Huong Nguyen	3,839.21	327.51	8,748.33	4,869.40	93.73
Huong Phong	1,861.32	256.27	3,664.91	2,290.07	69.81
Nham	829.11	40.63	2,125.43	815.75	3.41
Phu Vinh	535.46	34.81	1,330.52	900.87	1.36
Son Thuy	410.92	101.36	773.55	446.76	1.33

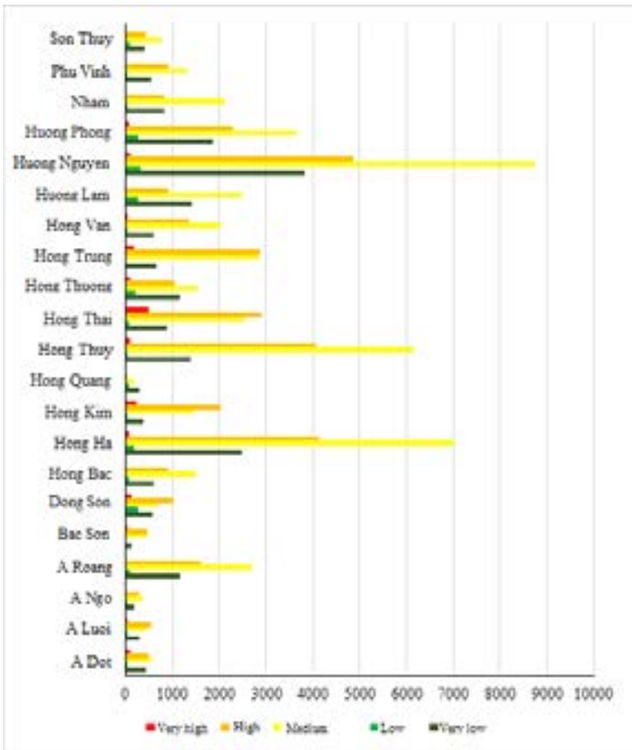

Figure 6. Area chart of landslide risk zones by commune in A Luoi district.

According to the landslide risk map (Figure 4), sites with a very high risk of landslides are distributed to the East of the Truong Son range, where the terrain is rugged, has steep slopes, high mountain peaks and the upstream area of three large rivers consists of Da Krong river, Bo River and Ta Trach river, specifically in Hong Thai, Hong Thuong, Dong Son and A Dot communes. This result is completely consistent with the practical situation as mentioned below:

Historical documents indicated that landslides at many mountainous rivers and stream sites in A Luoi district became more serious after annual rainstorm seasons, threatening people's lives and damaging property. Landslide risk points occurred along Highway 49A, passing through Hong Ha, Phu Vinh and Hong Thuy communes; A Co Pass area, along Ho Chi Minh road through communes Hong Thuy, Hong Van, Trung Son, Hong Kim, A Ngo, Quang Nham, Son Thuy, A Luoi town, Phu Vinh, Huong Phong, Dong Son, Lam Dot, A Roang; on the banks of A Sap and Bo rivers. In addition, there are very high-risk points for landslides on the sides of the Ho Chi Minh road, the segment through the Peke Pass area (Hong Thuy commune), Hong Kim commune, A Roang commune and border Quang Nam province; landslide area behind Bot Do market (Phu Vinh commune), key points on A Co Pass,...

In recent years, landslides have been increasing and the consequences to people, property and the environment are serious as some following events :

- On September 19th, 2013, heavy rains in A Luoi district caused landslides at several sites:

+ Ho Chi Minh road: 8 points were eroded, with a volume of soil and rock of about 1,000 m^3.

+ National Highway 49A from Hong Ha commune to Bot Do intersection: Landslides at 03 points are at Km 67+700, Km73+100 and Km75+150, causing traffic jams long time, with a volume of soil and rock of an estimated 1,500 m^3.

+ 03 bridges in Dong Son commune (Khe Chai Bridge, Khe Triet Bridge, Ti Nghieu Bridge) collapsed.

+ Underwater dam from village 4 to village 6 in Hong Thuy commune was swept away.

- On October 28th, 2021, due to prolonged heavy rain, more landslides occurred on the sides of Ho Chi Minh road. Preliminary statistics showed that there are approximately 80 landslide locations, with soil and rocks spilling onto the road surface, causing traffic jams, including many locations that have collapsed 4-5 times.

- On October 10th, 2022, landslides happened at Km75+150 on National Highway 49. Hundreds of cubic meters of soil and rock flowed from the slopes, covering most of the road surface. In the mountainous communes of Dong Son, Hong Thuy, A Roang and some villages in Hong Thuong and Hong Quang communes, many roads were flooded and water swept soil and rocks onto the road surface.

- In September 2023, A Luoi district currently has 18 landslide risk points in mountains, rivers and streams, with hundreds of households affected. Among them, the 4 most critical and dangerous sites include the Bot Do market area, A Luoi hydropower resettlement area, Tru Phi village, Hong Thuy commune and behind the People's Committee headquarters of Quang Nham commune, affecting the lives of 200 households. Notably, many deep and wide cracks appeared and stretched hundreds of meters on the high mountain, affecting 105 households living in Tru Phi village, Hong Thuy commune, two years ago.

The results also indicated landslides in A Luoi district caused tremendous consequences on every aspect of life, such as loss of farmland, damage to the transportation system, schools, hospitals, communication system and many other facilities, particularly many deaths. The map of zoning landslide probabilities supports local authorities and people's in order to minimize vulnerabilities. We would recommend some solutions, such as enhancing local people's education on landslide awareness, such as recognizing the signatures before a landslide occurs, prevention measures, evacuation and possibly building an early warning system in sites with high risk of landslides. Besides, it is necessary to actively green up bare land and reduce human activities that probably cause landslides.

5. CONCLUSION

This study has established a map of zoning landslide probabilities in A Luoi district, Thua Thien-Hue province, Vietnam, due to the influence of 5 typical factors, including slope, elevation, aspect, land cover and NDVI density, based on the application of the AHP model and integrating GIS-remote sensing technology.

The landslide risk map classified according to the natural fault method consists of 5 risk levels: very low, low, medium, high and very high, corresponding to an area of 19.86 %, 2.15 %, 46.55 %, 30.02 % and 1.41 % of the total area of A Luoi district. The areas at high and very high risk are distributed along Highway 49A, rugged terrain, bare land and spare vegetation cover areas.

The landslide risk zoning map is a useful tool for the authorities to provide measures guiding people's in responding and minimizing damage when landslides occur in A Luoi district. Furthermore, the research results are also an important reference in land use planning and environmental resource management, aiming for sustainable development and reducing the risk of landslides in the locality.

Verification results in A Luoi district using historical data show high reliability, so we propose that the AHP model can be applied to study landslides in other localities in Vietnam.

6. REFERENCES

Alaska Satellite Facility. https://search.asf.alaska.edu/#/. Accessed on 26th Aug, 2023.

Alvioli M., and Baum R. L., (2016). Parallelization of the TRIGRS model for rainfall-induced landslides using the message passing interface. *Environ. Model. Softw,* Vol. 81, 122-135.

Ayalew L., Yamagishi H., Marui H., Kanno T., (2005). Landslides in Sado Island of Japan: Part II. GIS-based susceptibility mapping with comparisons of results from two methods and verifications. *Eng. Geol,* Vol. 81, 432-445.

Bhushan N., and Rai K., (2004). Strategic decision making: Applying the analytic hierarchy process. New York: *Springer*.

Chalkias C et al., (2014). GIS-based landslide susceptibility mapping on the Peloponnese peninsula, Greece. *Journal of Geosciences,* Vol. 4, 176-190.

Cirianni F., Leonardi G., Scopelliti F., (2008). A methodology for assessing the seismic vulnerability of Highway systems. *AIP Conf. Proc,* Vol. 1020, 864-871.

Cirianni F., Fonte F., Leonardi G., Scopelliti F., (2012). Analysis of lifelines transportation vulnerability. *Procedia Soc. Behav. Sci,* Vol. 53, 29-38.

Dahal R. K., Hasegawa S., Nonomura A., Yamanaka M., Masuda T., and Nishino K., (2008). GIS based weights-of-evidence modelling of rainfall-induced landslides in small catchments for landslide susceptibility mapping. *Environ. Geol,* Vol. 54, No. 2, 311-324.

Doan V. L., Nguyen, C. C., Nguyen Q. B., Nguyen T. C., (2020). Assessing the current situation and research solutions on landslides in Vietnam in the period 2010-2020. *Journal of Irrigation Science and Technology,* Vol. 61, 119-128.

ESA, 2023. https://scihub.copernicus.eu. Accessed on 21st Aug, 2023.

Guzzetti F., Reichenbach P., Cardinali M., Galli M., and Ardizzone F., (2005). Probabilistic landslide hazard assessment at the basin scale. *Geomorphology,* Vol. 72, Issues 1-4, 272-299.

Hansen A., (1984). Landslide hazard analysis. *Slope Instab,* 523-602.

Hansen A., Franks C. A. M., Kirk P. A., Brimicombe A. J., and Tung F., (1995). Application of GIS to hazard assessment, with particular reference to landslides in Hong Kong. Geographical Information Systems in assessing natural hazards, *Springer,* 273-298.

Huang Y., and Zhao L., (2018). Review on landslide susceptibility mapping using support vector machines. *Catena,* Vol. 165, 520-529.

Jazouli A. El., Barakat A., Khellouk R., (2019). GIS-multicriteria evaluation using AHP for landslide susceptibility mapping in Oum Er Rbia high basin (Morocco). *Geoenviron. Disasters,* Vol. 6, 3.

People's Committee of A Luoi district. Information portal A Luoi district. https://aluoi.thuathienhue.gov.vn/?gd=21&cn=89&tc=1804. Accessed on 23rd Oct, 2023.

Pourghasemi H. R., Yansari Z. T., Panagos P., and Pradhan B., (2018). Analysis and evaluation of landslide susceptibility: A review on articles published during 2005-2016 (periods of 2005-2012 and 2013-2016). *Arab. J. Geosci,* Vol. 11, Issue. 9, 193.

Reichenbach P., Rossi M, Malamud B. D., Mihir M., and Guzzetti F., (2018). A review of statistically-based landslide susceptibility models. *Earth-Science Rev,* Vol. 180, 60-91.

Saaty T. L., (2008). Relative measurement and its generalization in decision making: Why pairwise comparisons are central in mathematics for the measurement of intangible factors - The analytic Hierarchy/Network Process. Madrid: Review of the Royal Spanish Academy of Sciences, Series A, *Mathematics*. Available at http://www.rac.es/ficheros/doc/00576.PDF.

Saaty T. L., (1990). Decision Making for Leaders: The Analytic Hierarchy Process for Decisions in a Complex World. RWS Publications: *Pittsburgh,* PA, USA.

Saaty T. L., (1990). How to make a decision: The analytic hierarchy process. *Eur. J. Oper. Res,* Vol. 48, 9-26.

Varnes D. J., (1984). Landslide hazard zonation: A review of principles and practice. Commission on landslides of the IAEG. *Nat. hazards,* Vol. 3, 61.

Youssef A. M., Pourghasemi H. R., El-Haddad B. A., and Dhahry B. K., (2016). Landslide susceptibility maps using different probabilistic and bivariate statistical models and comparison of their performance at Wadi Itwad Basin, Asir Region, Saudi Arabia. *Bull. Eng. Geol. Environ,* Vol. 75, Issue. 1, 63-87.

Zaruba Q., Mencl V., (2014). Landslides and Their Control. *Elsevier,* New York, NY, USA.

GEOSPATIAL OVERVIEW OF THE VEGETATION ENVIRONMENT SUGGESTED BY COMMUNITY LEVEL PLACE NAMES IN THE AREA OF NORTHEASTERN THAILAND AND NORTHERN CAMBODIA

Nagata Yoshikatsu

Graduate School of Informatics, Osaka Metropolitan University, Japan
Corresponding author. Email: nagatay@omu.ac.jp

ABSTRACT

Community place names frequently incorporate descriptive words related to the local environment, including features such as topography and vegetation. Such names also incorporate keywords relevant to the village's cultural and historical background. To build a comprehensive spatio-temporal database of community-level place names, the author has collected historical place names primarily from North-Eastern Thailand as well as from surrounding areas in Cambodia, Laos and Vietnam.

This report details the frequency and distribution of place names that feature vegetation-derived terms in North-Eastern Thailand and Northern Cambodia. Data, inclusive of word meanings, is currently being organized in these targeted areas. The analysis shows that the interpretation and spatial pattern of these place names, especially the early ones, may provide important information about the vegetative setting of these communities.

1. INTRODUCTION

The North-Eastern region of Thailand and the Northern region of Cambodia share a border along the Dangrek Mountains that run East to West. Not a few villages located in North-Eastern Thailand on the North side of the Dangrek Mountains have many place names that are difficult to translate from the Thai language. For instance, there are some villages on the Thai side that are labeled as "Ban Ampun". In this context, "Ban" refers to a village. However, "Ampun" is a proper noun that cannot be understood as a Thai word. In the 1920s, the RSD, Royal Survey Department, published maps featuring another village located on the Cambodian side of the neighboring region across the Dangrek Mountains, which is also denoted in Thai characters as "Ban Ampun". This settlement is labeled as "Phum Ampil" in Khmer script on the L7011 series maps dating to the 1960s in later decades. The term "Phum" translates to village, giving "Ampil" a proper noun identity. The Thai form of "Ampil" in Khmer script becomes "Ampul", while in Romanized form, it is "Ampun", to fit the Thai pronunciation. Thus, we can infer that "Ban Ampun", located on the Thai side, originates from the Khmer word "Ampil", meaning Tamarind (Figure 1). The report (Nagata, 2022) discussed the potential for understanding village place name meanings on the Thai side through pronunciation links, despite differing notations between the Thai and Khmer scripts.

Subsequently, over 2,500 positional coordinate-tagged village place names have been collected, covering not only the Dangrek Mountain area but also Northern Cambodia. Topographic maps featuring both Khmer and Roman characters were utilized in this endeavor. Many of these place names describe geographical features and vegetation. In addition, the author has data on about 29,000 village names in North-Eastern Thailand and can extract words that suggest geographical features and vegetation.

This study investigates the frequency of vegetation-related words in village place names and their spatial distribution in North-Eastern Thailand and Northern Cambodia.

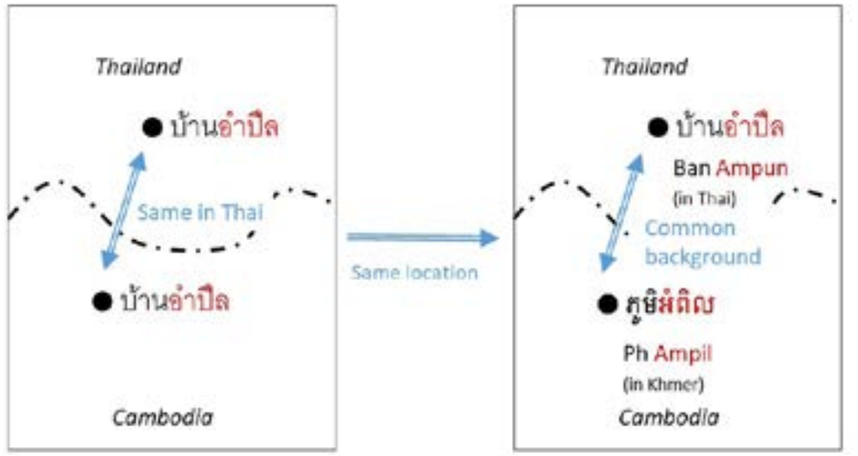

Figure 1. Village name that originates from the same meaning.

2. MATERIALS

For North-Eastern Thailand, approximately 29,000 village place names in the 1990s were extracted from the KCC2K database, which is the result of a village-level national survey conducted by the Thai government (Community Development Department, 1993). This database, however, does not possess positional coordinates for village-level data. As a result, the author's surveyed information was assigned (Nagata, 1996).

Approximately 2,500 village place names were collected from the L7011 series 1:50,000 topographic maps published by the AMS, U.S. Army Map Service, in the 1960s for Northern Cambodia. The collection currently encompasses the area north of 12.5 degrees North latitude. The Khmer meanings were interpreted using the dictionary (Headley, 1977).

3. DISCUSSIONS

Edible fruit tree terms commonly found in village names in Northern Cambodia are Tamarind, Fig, Banana, Gooseberry, Jambolan plum and Mango. Mango, in particular, is frequently used not on in Northern Cambodia but also in North-Eastern Thailand. Another word, lotus, although not a fruit tree term, is widely used in village names in both regions.

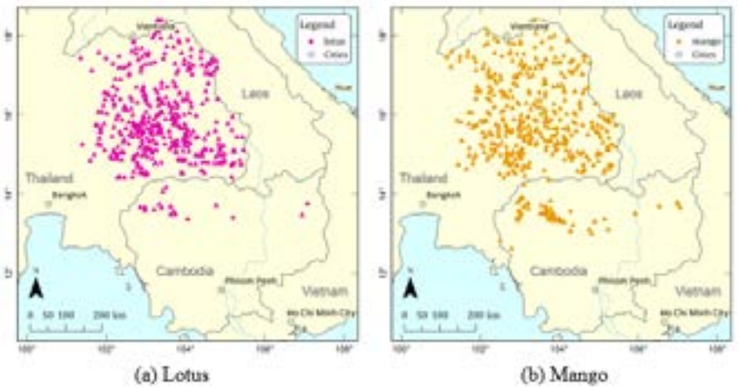

(a) Lotus (b) Mango

Figure 2. Widely preferred village names in both regions.

Figure 3. Village name containing 'Bamboo'.

Table 1 displays the word frequency examined in this report for North-Eastern Thailand and Northern Cambodia. Figure 2(a) exhibits the distribution of villages including the term lotus in their names, while Figure 2(b) demonstrates the distribution of villages including the term mango. Despite the similar spatial extent, lotus appears more commonly in North-Eastern Thailand, whereas mango is over three times more prevalent in Northern Cambodia. Lotus frequently accompanies terms like "Ban Nong Bua", or lotus pond village, in reference to water sources such as lakes and marshes, while mango is highly esteemed as a tree yielding edible fruit.

Some words, such as lotus and mango, are commonly used in place names in both regions, as shown in Figure 2. Conversely, certain words are rarely used in North-Eastern Thailand. For instance, the term "Bamboo" is frequently employed in 27 place names in Northern Cambodia but in only 2 cases in North-Eastern Thailand, as depicted in Figure 3.

Table 1. Number and frequency of villages with specific words in their names.

Word	N.E. Thailand		N. Cambodia	
Lotus	511	(1.76 %)	18	(0.71 %)
Mango	436	(1.50 %)	62	(2.46 %)
Bamboo	2	(0.01 %)	27	(1.07 %)
Tamarind	19	(0.07 %)	18	(0.71 %)

Word	N.E. Thailand		N. Cambodia	
Ceylon oak	30	(0.10 %)	23	(0.91 %)
Samrong/Samraong*	151	(0.52 %)	29	(1.15 %)
Sadao/Sdau*	36	(0.12 %)	7	(0.28 %)
Sompoi/Sambuor*	25	(0.09 %)	7	(0.28 %)

**word in Thai/ in Khmer, respectively*

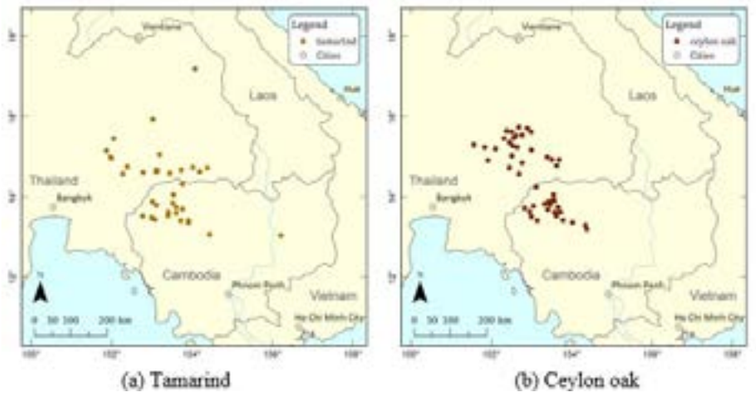

(a) Tamarind (b) Ceylon oak

Figure 4. Village names showing similar concentrated distribution.

In certain cases, the term appears in place names in both regions, but its usage is limited to a smaller area. The Tamarind and Ceylon oak are both examples of this, with the latter being a valuable timber tree (see Figure 4). In Cambodia, these words are predominantly used in the North-Western portion of the country and in the Southwestern portion of Northeast Thailand, including the provinces of Nakhon Ratchasima and Buriram.

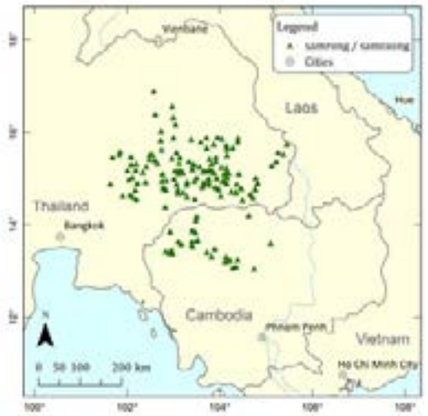

Figure 5. Village name containing "Samrong" or "Samraong".

Place names that include the term "Samraong" in Khmer and "Samrong" in Thai can be found in both regions. The distribution of these names in North-Eastern Thailand is broader than that of Tamarind and Ceylon oak (refer to Figure 5). These distributions imply a similarity in the initial landscapes during the establishment of the villages. Figure 6 depicts two examples of the distribution of villages named after beneficial tree species. Both varieties are broadly distributed

in both regions, although not as frequently as Samrong/Samraong.

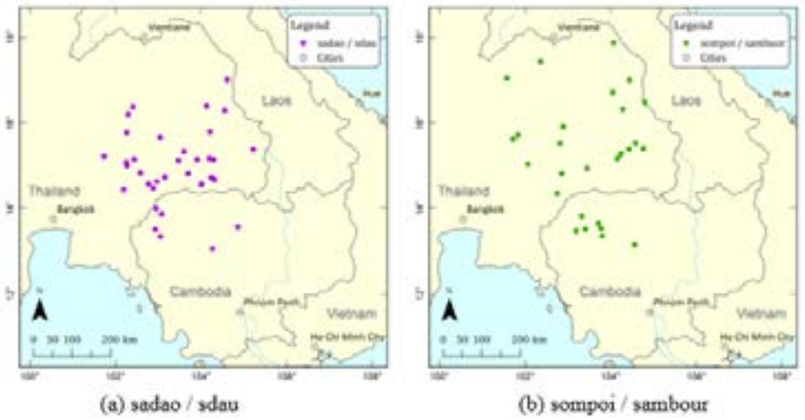

(a) sadao / sdau (b) sompoi / sambour

Figure 6. Village names with widely scattered distribution.

Furthermore, it is reasonable to presume that numerous additional names for trees are frequently used in both regions, although compiling the names of indigenous tree species is challenging.

4. FUTURE WORKS

Given the Mekong River and its tributaries' historical role in supporting regional human mobility for centuries, village place names in Southern Laos, situated on the left bank of the Mekong, must also be taken into account. It is worth noting that similar to the Khmer-derived village names on the Thai side, Thai- and Lao-derived village names also exist in North-Eastern Cambodia (Nagata, 2022). It is essential to consider the meaning of these village names to ensure the inclusion of all pertinent information in local contexts.

Future research will further investigate the impact of the geographical distribution of villages with shared names on the reconstruction of their original ecological surroundings and the analysis of their historical development.

5. ACKNOWLEDGEMENT

Appreciation is given to the Library of Congress for the availability of a number of maps from its collection. This study was supported by JSPS KAKENHI Grant Number JP19K12700.

6. REFERENCES

Community Development Department (CDD), Thailand, 1993. *Muban chonnabot Thai pi 2535* [Villages of the Rural Areas of Thailand, 1992].

Headley R.K., 1997. Cambodian-English Dictionary. *Catholic University of American Press*.

Nagata Y., 1996. Mapping the Village Database: Spread of Economic Growth to Rural Areas of Northeast Thailand. *Southeast Asian Studies*, *33*(4), 138-156.

Nagata, Y., 2022. A Spatio-Temporal Study on the Community Level Place Names of around the Dangrek Mountains Area. *Proceedings of the 2022 Pacific Neighborhood Consortium Annual Conference and Joint Meetings*, 27-32.

PRESENTING OF THE MILITARY TERRAIN ANALYSIS BETWEEN THAILAND AND MYANMAR'S HISTORICAL BATTLEFIELD, OVER 200 YEARS (THE 9 -ARMIES WAR) WITH GEO-INFORMATIC TECHNIQUES

Kittitouch Naksri, Rangsan Ket-ord, Gistada Panumonwatee, Chaiwiwat Vansarochana*

Department of Agriculture, Natural Resources and Environment,
Geography Section Naresuan University, Phitsanulok, Thailand.
*Corresponding author. Email: ChaiwiwatV@nu.ac.th

ABSTRACT

This study applies the Military terrain analysis with the OCOKA concept to remote sensing and GIS techniques to examine the military situation in Thailand and Burma. The War of the Nine Armies, which took place over two hundred years ago, was used as a case study. We obtained data from Google Earth, Google Maps, GIS and historical battle data.

By analyzing the integration of these data, we found that the OCOKA concept can be effectively applied to geo-informatics technology, mentioned cross-country movement (CCM. This study serves as an example of how historical data can be integrated with online geospatial data to provide a more visual representation of past spatial studies.

1. INTRODUCTION

Military terrain analysis is a crucial study that evaluates how a particular operating area affects a mission using the OCOKA framework. This framework considers the actions of both the enemy and our forces and how the terrain impacts the outcome of these actions. Even in a "neutral" area, understanding, predicting and exploiting the terrain can be the difference between victory and defeat. The U.S. Armed Forces have formalized the connection between the battlefield landscape and military tactics through the OCOKA process. This concept has also been applied in many team organizations, including the National Park Service. The OCOKA principle has many interesting features. We applied this principle to GIS techniques to analyze historical battle data between Thailand and Myanmar. It originated over two hundred years ago in the western border area of Thailand and stands for Observation, Cover and Concealment, Obstacles, Key terrain and Avenues of approach.

The system acronym stands for:

O - Observation and Fields of Fire

C - Cover and Concealment

O - Obstacles

K - Key Terrain

A - Avenues of Approach

The research aims to apply the OCOKA principles to analyze historical war data. To carry out the analysis, the QGIS program will be used. This approach is considered innovative, as few people in Thailand use it yet. The research's primary objective is to explore this method's potential

in analyzing war data.

2. STUDY AREA

During the 9-Armies War (1785-1786), Thung Lat Ya in Kanchanaburi Province between Thailand and Myanmar was a historical battlefield. It is located at 14°08'17"N, 99°23'12"E. (Wittayarat, 1992; Wyatt, 2003; Thiphakorawong, 2019; Lat Ya Subdistrict Administrative Organization, 2023)

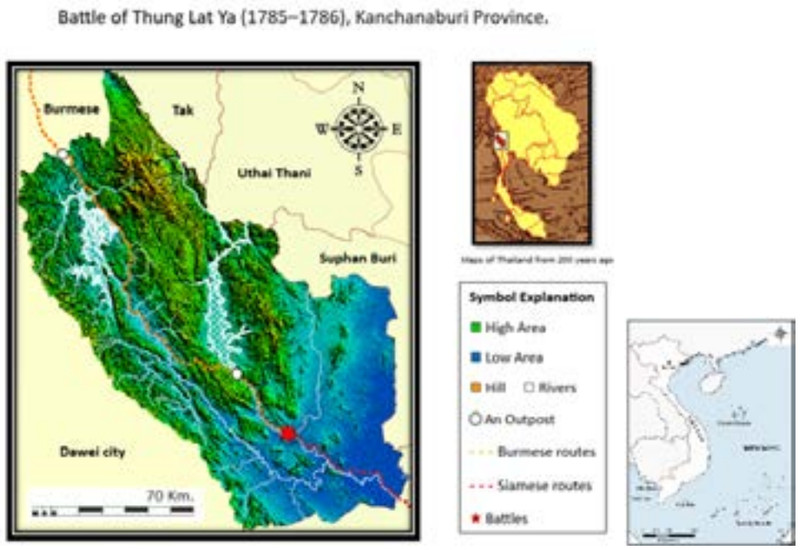

Figure 1. Topographical map of the study area.

- Data source

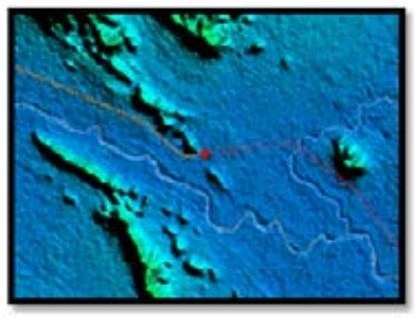

Figure 2. Study area (DEM), 1:50,000.

Figure 3. Land cover layers.

Based on the desired spatial information about the terrain for a specific military operation, rules have to be established. In order to achieve this, spatial and topographic data from Google Earth, Google Maps, GIS and historical battle data have been collected. Let's analyze their integration together. A vector data layer is created and a certain amount of spatial digital elevation model (DEM) data can be found at http://www.mitrearth.org. The data for the study area has been primarily collected from the topographical map mentioned above.

3. GIS DATA LAYERS

The topographic map is transformed into data layers using OCOKA principles in QGIS.

- Observation and fields of fire

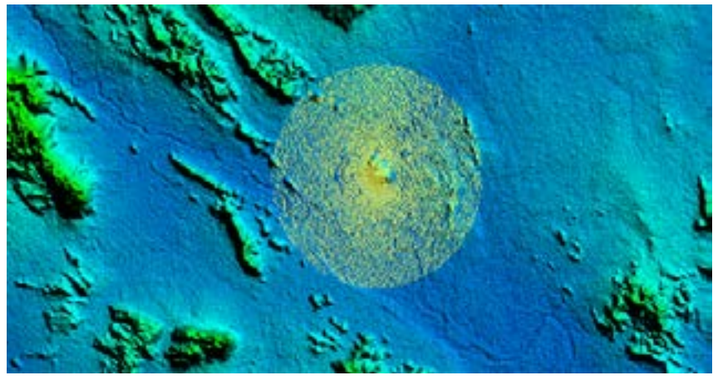

Figure 4. Created viewshed analysis for observation and fields of fire.

- Cover and concealment

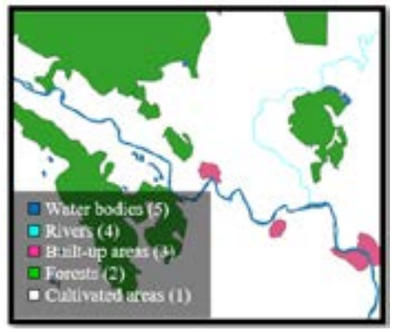

Figure 5. Thematic layer of land use and land cover.

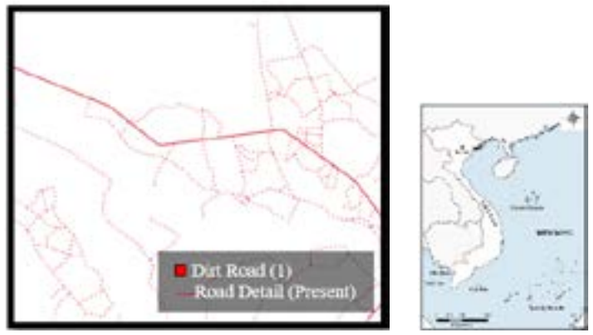

Figure 6. Thematic layer of road network.

- Obstacles

Figure 7. Thematic layer of water bodies.

- **Key terrain**

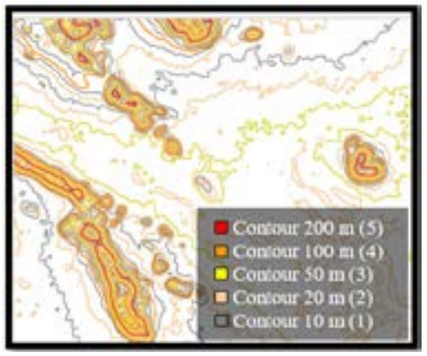

Figure 8. Thematic layer of contour map.

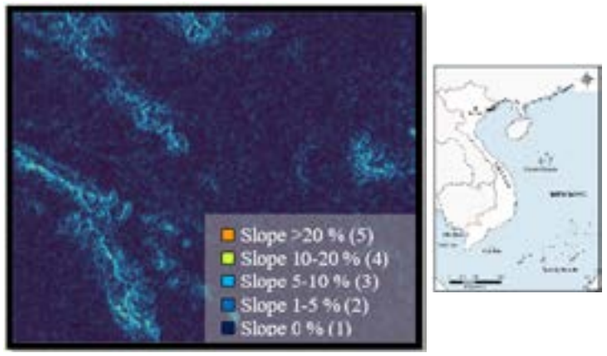

Figure 9. Thematic layer of slope map.

4. METHODS

The knowledge base rules are derived by transforming the GIS data layer information into rules. Each data layer contributes a parameter or condition that is utilized to form rules and ultimately reach the final hypothesis. The analysis technique employs the weighted overlay principle based on the four concepts of OCOKA mentioned earlier. The knowledge base is depicted in Figures 6, 7, 8, 9 and 15.

Figure 10. Knowledge base for selection of observation.

Figure 11. Knowledge base for selection of cover and concealment.

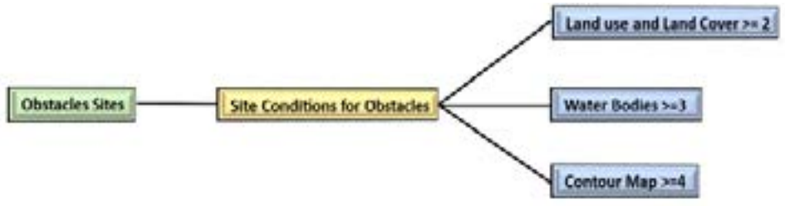

Figure 12. Knowledge base for selection of obstacles.

Figure 13. Knowledge base for selection of key terrain.

5. RESULTS AND DISCUSSION

In order to launch an observation site, several parameters need to be taken into consideration. These include the type of contour map, land use, land cover and the availability of viewshed analysis. An example rule written in text form may look like this:

IF the contour is equal to or greater than 4 and is at a height of 100 m or more

AND

the land cover is forests (land cover code 2)

AND

the viewshed analysis shows the visibility of more than 70 %

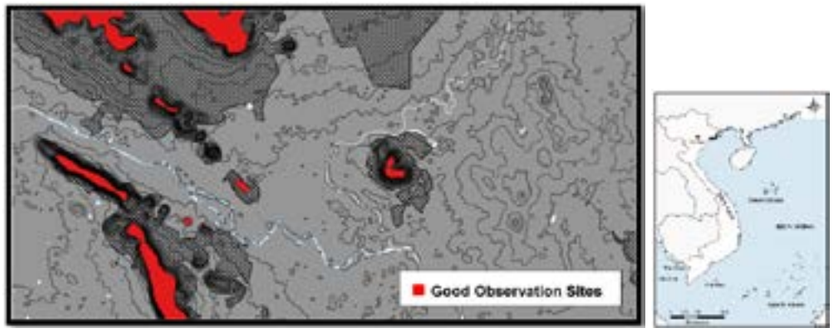

Figure 14. The OCOKA map shows good observation sites.

Figure 15. The OCOKA map shows cover and concealment sites.

Figure 16. The OCOKA map shows obstructions sites.

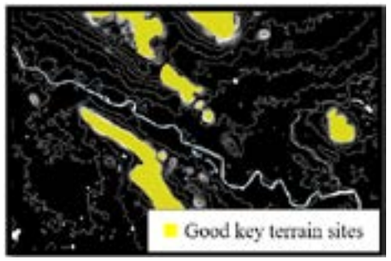

Figure 17. The OCOKA map shows key terrain sites.

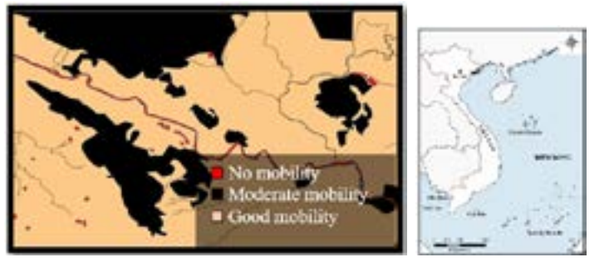

Figure 18. The OCOKA map shows avenues of approach.

- Avenues of Approach

Figure 19. Knowledge base for selection of mobility

6. CONCLUSIONS

Accurate and timely terrain analysis is crucial for the fast-paced mobile battlefield of today. Conventional techniques need updating with the availability of data products like digital maps and high-resolution satellite imagery. The interpretation of terrain features through a knowledge-based approach will prove to be extremely useful for modern-day war planning.

- For Cross County Movement (CCM)

By overlaying each layer of data on top of each other and comparing the results, a Mobility map can be created to determine the appropriate marching route Baijal, M.R et al., (2018). This map can then be compared with the OCOKA principle to ensure that the information obtained is consistent with the principle. When the map aligns with the OCOKA principle, the Thai army can ambush from various mountains, as per historical assumptions. The CCM technique can be applied to transportation and movement in numerous beneficial ways, such as transporting goods, basic necessities for living and medical and public health units. This would be particularly useful for people who face various challenges in today's world.

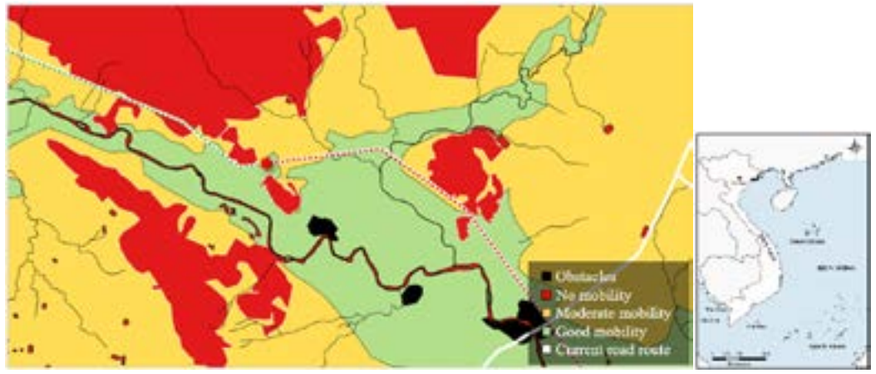

Figure 20. Mobility of combat units map.

7. REFERENCES

Baijal M.R., Arora M.K., and Ghosh S.K., 2018. A GIS-Assisted Knowledge-Based Approach for Military Operations. Retrieved August 12, 2023, from https://www.geospatialworld.net/article/ a-gis-assisted-knowledge-based-approach-for-military-operations/

ERDAS., 1999. Field Guide, 5th Edition, *ERDAS*, Inc., Atlanta.

Lat Ya Subdistrict Administrative Organization, 2023. Khao Chon Kai Area: 9 Armies Battle Field. Retrieved August 12, 2023, from https://www.ladya-sao.go.th/Main/PlaceotopPreview/id/9.

National Park Service, 2009. Cultural Landscape Report: Vicksburg National Military Park. *Atlanta*, Georgia, USA. Retrieved August 12, 2023, from https://parkplanning.nps.gov/document.cfm?parkID=411&projectID=19204&documentID=27908.

Nikolopoulos C., 1997. Expert Systems: Introduction to First and Second Generation and Hybrid Knowledge-Based Systems. *Marcel Dekker Inc*, USA.

Pailoplee S., 2021. Kanchanaburi: Geography, Maps. Retrieved August 12, 2023, from http://www.mitrearth.org/m3-kanchanaburi/

Thiphakorawong, Chaophraya (Kham Bunnag), 2019. The Royal Chronicles of Rattanakosin, King Rama I. *Thai quality books*, Bangkok.

Tourism Authority of Thailand., 2023. The Nine-Army battle historical park. Retrieved August 12, 2023, from https://www.tourismthailand.org/Attraction/the-nine-army-battle-historical-park

Wittayarat P., 1992. Geography Miscellaneous. *R. printing*, Bangkok.

Wyatt D. K., 2003. Thailand: A Short History (Second ed.). *Yale University Press*. New Heaven and London.

OPTIMIZING BROILER HOUSE MANAGEMENT TO REDUCE COSTS AND REDUCE LOSSES WITH THE INTERNET OF THINGS TECHNOLOGY AND WIRELESS SENSOR NETWORK

Sittichai Choosumrong[1]*, Rhutairat Hataitara[1], Kampanart Piyathamrongchai[1], Tossaporn Incharoen[1], Venkatesh Raghavan[2], Thanwamas Phasinam[3], Khongdet Phasinam[4]

[1]Department of Natural Resources and Environment, Faculty of Agriculture Nature Resources and Environment, Naresuan University, Phitsanulok, Thailand
[2]Graduate School of Science, Osaka Metropolitan University, Japan
[3]Agricultural Land Reform Office, Bangkok, Thailand
[4]Faculty of Food and Agricultural Technology,
Pibulsongkram Rajabhat University, Phitsanulok, Thailand
*Corresponding author. Email: sittichaic@nu.ac.th

ABSTRACT

Effective broiler house management is imperative for sustainable and profitable poultry farming. To optimize broiler house operations, this research examines the combination of Internet of Things (IoT) technologies, Closed-Circuit Television (CCTV) powered by artificial intelligence (AI) and wireless sensor networks. The primary objectives encompass cost reduction, loss mitigation and performance evaluation of feeding and watering devices. This proactive approach significantly reduces potential losses. Furthermore, the research evaluates cost implications. IoT technology's ability to regulate variables like feed utilization and energy consumption aids cost reduction. The study's findings offer practical insights for efficient resource allocation.

The combination of IoT, AI-powered CCTV and wireless sensor networks presents a multifaceted solution for holistic broiler house management. The real-time data, predictive insights and automated controls collectively contribute to cost reduction, loss mitigation and informed decision-making. By concurrently evaluating feeding and watering devices, the study enhances farm efficiency and bird welfare.

1. INTRODUCTION

Effective broiler house management is a pivotal determinant of success in modern poultry farming. The broiler industry has witnessed remarkable growth to meet the increasing global demand for poultry products. However, this expansion has brought with it a multitude of challenges that demand innovative solutions. Chief among these challenges are cost control, efficient resource utilization, disease management and the welfare of broiler flocks. Broiler house management is a multifaceted endeavor that extends beyond mere oversight of poultry facilities. It involves the orchestration of environmental conditions, feeding and watering systems, disease prevention and the overall well-being of the broiler flock. The consequences of poor management are substantial, ranging from reduced profitability to ethical concerns regarding animal welfare. In response to these challenges, this research explores the integration of advanced technologies to optimize broiler house management. Specifically, it investigates the convergence of three transformative technologies: the Internet of Things (IoT), artificial intelligence (AI) and wireless sensor networks.

The integration of these technologies offers a multitude of advantages (Chen L. et al., 2019). IoT-equipped wireless sensors continuously monitor critical parameters within the broiler house environment, such as temperature, humidity and air quality. AI algorithms, operating on data collected from strategically positioned cameras, analyze broiler behavior to detect early signs of stress, disease, or anomalies. These technologies provide comprehensive insights into the well-being of the broiler flock, allowing for informed decision-making. One of the primary objectives of this research is cost reduction. IoT technology enables precise control over environmental variables and resource utilization, leading to significant cost savings (Choosumrong et al., 2022).

Additionally, this research explores the application of Web Application to further enhance broiler house management. Web Application technology enables the monitoring of broiler house conditions and operations in real-time through interactive maps and data visualization. It offers a holistic view of the poultry farm, providing insights into the spatial distribution of environmental factors, disease outbreaks and the performance of feeding and watering systems. The integration of Web Applications into broiler house management not only enhances decision-making but also facilitates remote monitoring and data-driven interventions. This technology empowers poultry farmers with the ability to assess the health and productivity of their flock and make informed adjustments to environmental conditions and operational settings. In summary, this research delves into the integration of IoT, wireless sensor networks and Web Application technologies to revolutionize broiler house management. These technologies collectively contribute to cost reduction, loss mitigation and improved broiler welfare. The application Web Application extends the capabilities of broiler house monitoring, providing a comprehensive solution to the multifaceted challenges faced in modern poultry farming.

2. METHODOLOGY

In this work, we have developed sensors for testing a system that measures various vital parameters in the broiler house. These basic sensors include light sensors, temperature sensors, humidity sensors and ammonia gas sensors. We have developed sensors for testing a system designed to monitor various critical parameters within a chicken farm facility. The basic sensors used include light sensors, temperature sensors, humidity sensors and ammonia gas sensors. In addition to these, we have introduced new sensors to enhance the system. These include sound sensors and AI-powered closed-circuit cameras. The sound sensors are employed to measure the intensity of sounds that may arise due to events such as chicken disturbances, potential threats, or hunger. The functioning of the sound sensors involves detecting sound levels and sending notifications through LINE Notify in case of louder-than-normal noises. This enables poultry farm operators to receive real-time alerts and access closed-circuit cameras promptly for visual verification when notified. This integrated system not only helps in maintaining optimal environmental conditions but also enhances the overall security and welfare of the broiler flock. The data Communication will be facilitated using an MQTT Broker, with Node-Red serving as the operational manager for various tasks once data is received from the sensors. Node-Red allows for the straightforward and rapid configuration of conditions for notifications, forwarding data to databases, or displaying information on a dashboard. Another significant aspect of this project involves the development of object detection using OpenCV and the Python programming language. This system is capable

of detecting various entities, including humans and animals. Specifically, the program has been configured to detect dogs and humans. When a person or a dog enters the vicinity of the egg-laying chicken farm, the system will transmit this information to MQTT, Node-RED and send notifications via LINE Notify (Choosumrong et al, 2023). This functionality serves to mitigate potential losses resulting from unauthorized intrusions by dogs or other individuals. The overview of the entire system is presented in Figure 1.

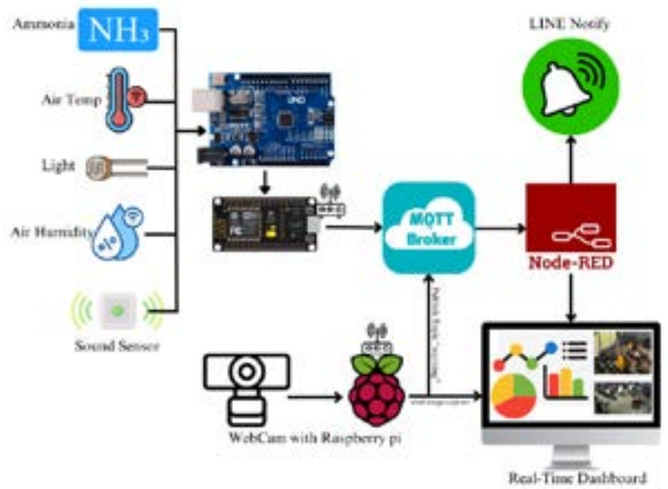

Figure 1. Integrated IoT, AI and Web Application framework for broiler house management.

2.1 Hardware description

2.1.1 Microcontroller

In this integrated system, the utilization of three microcontrollers, Arduino UNO, NodeMCU ESP8266 and Raspberry Pi4, plays a pivotal role in ensuring seamless data acquisition, processing and communication. Arduino Uno, acting as the primary controller, serves as the interface between the various sensors and the broader network. It is responsible for collecting data from a range of sensors, such as light sensors, temperature sensors, humidity sensors and gas sensors, which are fundamental for monitoring critical parameters within the environment. The Arduino Uno gathers this data, converts it into a format suitable for transmission and then communicates with the secondary controller, the NodeMCU ESP8266, via serial communication.

The NodeMCU ESP8266, a compact yet powerful Wi-Fi-enabled microcontroller, takes center stage in facilitating wireless communication and connectivity to the broader IoT infrastructure. Its role is twofold: first, it acts as a bridge connecting the Arduino Uno to the Wi-Fi network, enabling the transmission of data to external servers and services. Secondly, it provides the means to establish secure connections with an MQTT broker, a central hub for data exchange. Through the MQTT protocol, the NodeMCU ESP8266 efficiently transmits the data collected by the Arduino Uno to a centralized MQTT broker.

The Arduino Uno and NodeMCU ESP8266 together form a robust and efficient data acquisition and transmission system. The former excels at sensor interfacing and data aggregation, while the latter leverages its Wi-Fi capabilities to establish connections with external networks and services. This synergistic partnership enables real-time data monitoring and seamless integration into the broader Internet of Things ecosystem, making it a versatile and adaptable solution for various applications, including environmental monitoring, industrial automation and smart agriculture, among others.

Incorporating the Raspberry Pi into the system introduces a powerful dimension of visual intelligence and real-time object detection. The Raspberry Pi serves as the central hub for camera interfacing and object recognition, leveraging the capabilities of the OpenCV library. Raspberry Pi assumes the role of a dedicated computer vision unit connected to a webcam. This setup enables real-time monitoring of the surroundings for specific objects of interest, namely humans and dogs. The OpenCV framework, running on the Raspberry Pi, provides the essential tools for object detection and tracking. As soon as the camera identifies these objects within its field of view, the Raspberry Pi processes the visual data, extracts relevant information and triggers immediate actions.

2.1.2 Sensor

As mentioned before, the basic sensors used include light sensors, temperature sensors, humidity sensors, ammonia gas sensors, sound sensors and Webcam. Light sensor we are using Photosensitive Resistor Sensor Module Light Detection Light Sensing. For temperature and humidity sensors, we are using DHT22. The MQ-137 is a gas sensor module that is primarily used for detecting ammonia (NH3) gas in the air. The KY-037 High Sensitivity Sound Sensor Module is an electronic component designed to detect sound or acoustic signals in its surroundings. It is commonly used in various electronics projects and applications that require sound detection or audio sensing capabilities.

2.2 Monitoring System

2.2.1 Message Queuing Telemetry Transport (MQTT)

Message Queuing Telemetry Transport (MQTT) is a lightweight, efficient and widely used messaging protocol designed for reliable communication between devices and applications in situations where network bandwidth and device resources may be limited. MQTT was developed by IBM in the late 1990s and has since become an open standard with multiple implementations and broad industry support.

MQTT is an open-source pub/sub communication protocol. It is most commonly run over TCP/IP stack, but there are MQTT implementations that use other protocols (e.g. Bluetooth). Since the protocol handles more than “Message Queuing” and “Telemetry Transport”, the term MQTT is commonly used as the protocol’s name instead of being thought of as an acronym for a longer name. The pub/sub model is at the core of MQTT communication. Information is organized by topics. Client devices can publish data to a topic to send messages to any subscribers. Similarly, clients can subscribe to a topic to be notified when a message is published.

2.2.2 Node-RED

Node-RED is an open-source, flow-based development tool that provides a visual programming interface for connecting and automating devices, APIs and online services. It is particularly popular in the field of IoT and is used to create flows that can handle data transformation, communication between devices and the integration of various software and hardware components. Node-RED

plays a central role in this work by providing an intuitive, adaptable and interactive platform for configuring and managing the system's parameters. It empowers users to take control of the system's behavior, enabling them to tailor it to their specific needs and ensuring that notifications sent via LINE Notify align precisely with desired criteria and conditions. This user-centric approach enhances the system's usability and responsiveness, making it a valuable tool for a range of applications, from IoT management to automated alerting and beyond.

2.2.3 LINE Notify

At present, almost of Thai people who have smartphones are using LINE to communicate more than Sky, Email, etc. LINE in Thailand nowaday reaches 50 million users, ranking itself as the number one and most trusted smartphone application for daily use. Especially during the COVID-19 pandemic, LINE stresses its positioning as an infrastructure for all living aspects in the digital era. LINE also sees huge growth in various dimensions as a communication feature, lifestyle and business services platform a solid proof of the transformation of all Thais to become "Digital Citizens" who can use the digital platform to bring their living to the next level under the Life on LINE concept. In this work, we employ LINE Notify to alert the user in the event of an abnormality in the boiler house. LINE Notify is a messaging service provided by LINE Corporation, the company behind the popular LINE messaging app. LINE Notify allows users to send customizable notifications and alerts from various web services and applications to their LINE messaging app.

3. RESULT

Figure 2 shows the system developed utilizes a power source derived from solar energy. This choice is particularly advantageous for certain farmers who may not have access to a conventional electricity supply or seek to reduce operating costs. Installation of the developed prototype is straightforward, convenient and swift. The system components, as illustrated in the image, represent an example of the system's composition and its application in a poultry farm. These components include a breaker, solar charger, a power inverter (12V to 220V) and a pocket Wi-Fi device. The breaker serves as a protective component in the system, ensuring electrical safety. The solar charger harnesses solar energy, converting it into electrical power for use within the system. The power inverter transforms the generated power from 12V to 220V, enabling it to be used for various applications. Lastly, the pocket Wi-Fi device facilitates wireless communication, allowing for remote monitoring and control of the system's functions.

This system design is particularly advantageous in agricultural settings where access to a conventional power grid may be limited or impractical. It offers an efficient and sustainable means of powering essential equipment and devices, ensuring reliable operation while minimizing energy costs.

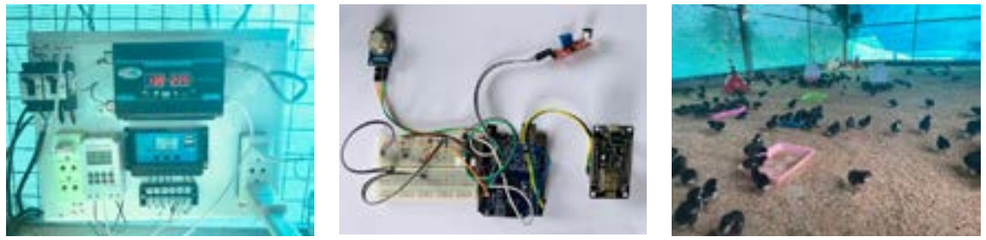

(a) (b) (c)

Figure 2. System experiment (a) is a solar power supply equipment, (b) is a hardware device to collect the data and (c) is inside the chicken house.

A webcam with a Raspberry Pi can detect and count the objects and then send the data, including image capture and number, through an MQTT broker. The MQTT broker connected with Node-RED will store the number in the database using PostgreSQL and at the same time, it will send image captures to the server. The user not only gets the notification from LINE Notify but can also see the real-time monitoring on the web interface, as shown in Figure 3.

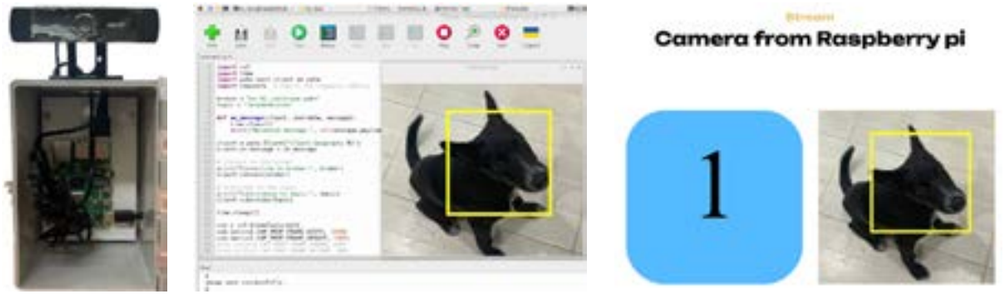

(a) (b) (c)

Figure 3. AI-driven CCTV system (a) is a webcam with Raspberry Pi, (b) is a backend experiment system and (c) is a near real-time dashboard on a web application.

This system can operate on a 24-ampere battery throughout the night. Data transmission to MQTT is scheduled to occur every hour. The low-cost sensors developed as part of this system can reliably read and transmit data without any loss during transmission. Wireless sensors, equipped with IoT capabilities, continuously monitor essential parameters such as temperature, humidity and environmental conditions. Simultaneously, AI-powered CCTV cameras analyze bird behavior, detecting signs of stress, disease, or anomalies. This combined data provides comprehensive insights into the well-being of the flock. An integral component of the study involves comparing feeding and watering devices. Performance evaluation considers factors like feed consumption rates, water availability and operational efficiency. By leveraging data from IoT sensors and AI-driven CCTV, the study offers informed recommendations for optimal device selection. Remote monitoring through IoT technology empowers farmers to access real-time data, facilitating timely adjustments to environmental conditions. Automated controls further ensure precise management, contributing to broiler growth and well-being. The integration of AI-powered CCTV extends beyond health monitoring. It detects aberrant behaviors, enabling early intervention and disease prevention. This proactive approach significantly reduces potential losses. Furthermore, the research

evaluates cost implications. IoT technology's ability to regulate variables like feed utilization and energy consumption aids cost reduction. The study's findings offer practical insights for efficient resource allocation. The Webcam developed for this system may exhibit occasional inaccuracies in detecting certain objects. Further development may be required to enhance its accuracy in the future.

4. REFERENCES

Chen L. et al., 2019. Applications of Artificial Intelligence in Poultry Production: A Review. *Animals*, Vol 9(12), 1012.

Choosumrong S., Hataitara R., and Pothong P., 2022. Development of Smart Agricultural Monitoring and Irrigation System using IoT and Mobile Applications. *The Journal of Spatial Innovation Development*, Vol 3(1), 81-87.

Choosumrong S., Hataitara R., Panumonwatee P., Raghavan V., Nualsri C., Phasinam P., and Phasinam K. 2023. Development of IoT based smart monitor and control system using MQTT protocol and Node-RED for parabolic greenhouse solar drying. *International Journal of Information Technology,* Vol 15(4), 2089-2098.

DEVELOPMENT OF WATER LEVEL MEASURING SENSOR PROTOTYPE EQUIPMENT FOR ANALYSIS AND ALERTING FLOOD RISK SITUATIONS IN THE FORM OF A 3D SIMULATOR ON A WEB GIS APPLICATION

Natima Udon, Kampanart Piyathamrongchai, Sittichai Choosumrong*

Department of Natural Resources and Environment, Faculty of Agriculture Nature Resources and Environment, Naresuan University, Phitsanulok, Thailand.
*Corresponding author. Email: sittichaic@nu.ac.th

ABSTRACT

Flooding is regarded as a serious issue that significantly affects people's lives. Resources and national assets given Thailand's geography, position and natural diversity. Thailand thus deals with flooding on a constant basis when planning for environmental restoration, particularly threats brought on by flood problems, etc. A prototype water level sensor device will be studied and developed in this project to analyze and alert a flood risk scenario in 3D simulation will be investigated and created on web GIS applications.

The development of this prototype water level sensor device involves the application of geoinformatics and Internet of Things (IoT) technology, including the design and creation of a database. This utilizes sensors and devices connected to the Internet to collect and send data to an analysis system, displaying the results in a three-dimensional format on an online map system (Web GIS). This allows relevant organizations or stakeholders to use this prototype device for real-time monitoring of water level situations. The IoT prototype device was developed for two main purposes: 1) to develop IoT devices integrated with Big Data analysis and 2) to develop an online map for displaying real-time data from monitoring devices. The results of this research show that it is possible to develop a prototype sensor device capable of measuring water levels and sending real-time data to a database server, enabling analysis, notification and visualization in the form 3D simulation that can be displayed in Web GIS Application.

In conclusion, the combination of IoT, Spatial data and geoinformatics for developed water level measuring sensor prototype equipment. Water level sensor, the produced prototype equipment can evaluate and detect water levels and the data may be shown in real-time via web GIS application. The findings from this research can support relevant organizations or stakeholders in monitoring water levels that are at risk of flooding in a particular area.

1. INTRODUCTION

The problem of natural disasters in Thailand can be considered a significant disaster issue that has persisted from the past to the present. Currently, especially during the late monsoon season from August to November, heavy and continuous rainfall occurs, leading to flooding issues. Thailand's geographical location in the tropical region exposes it to the influence of monsoon rains according to seasonal patterns. Additionally, the central region, characterized by low-lying areas, is particularly prone to flooding. Therefore, Thailand consistently faces the tendency for flooding. "Large floods have happened several times, producing huge effects on the people, numbering in

the millions, as well as considerable damage to the economy and society as a whole. Here are several examples: Flooding occurred in more than 40 provinces in 1942. A large flood occurred in the northern, central and northeastern areas in 1995. The most severe flood was probably in 2011 when water inundated more than one-third of the nation. The losses were enormous. Even in 2021, a major flood affected 44 provinces. Flooding will strike roughly 69 regions in Thailand in 2022. Natural disasters occurrences caused by global climate change have shown an increasing tendency of disasters each year. This has had a huge impact on Thailand, inflicting substantial damage to the agriculture, production, commerce and tourist industries. Property and human. Furthermore, there is damage to the country's infrastructure, such as roads deteriorating from flooding, bridges collapsing and airports being damaged. The risk of disease outbreaks due to water accumulation on the roads is also a concern. Various activities come to a halt, significantly affecting the economy. This can be seen as having a worrisome impact on both the population and the country.

Over the past several years, it has been observed that Internet of Things (IoT) technology has rapidly grown and played a significant role in various sectors. It is a widely recognized and utilized technology with the potential to analyze, predict and mitigate the occurrence of natural disasters in different areas. This is achieved by using sensors and devices connected to the Internet to collect and transmit data for further analysis. Through the process of ideation and design using the principles of spatial data, which emphasize analyzing and utilizing spatial data for decision-making and problem-solving, we aim to develop a prototype sensor device for water level measurement. Subsequently, data from the sensors will be transmitted over the Internet to be analyzed and stored on a server, presenting the information in a three-dimensional model on an online mapping platform. This enables monitoring and tracking of water level situations that are at risk of flooding in the area.

According to the preceding debate, the topic of natural disasters in Thailand is a major problem that demands immediate resolution as well as the investigation of preventative or developmental methods that incorporate various technologies and innovations. Therefore, in this research, the investigators will study natural disaster occurrences in Thailand and develop a prototype water level sensor device for analyzing and alerting about risk situations of potential disasters in a three-dimensional model on an online mapping platform. The research will encompass the development of IoT devices along with the analysis of Big Data to provide real-time analysis and visualization using Digital Twins, which can be displayed in a Web GIS format. This aims to support relevant agencies and stakeholders in utilizing the model to monitor real-time water levels at risk of flooding, effectively mitigating the impact of disasters in the future.

2. METHODOLOGY AND METHODS

In this study, we developed a sensor for testing a system for measuring water levels. It combines Internet of Things (IoT) technologies and database administration. The sensors utilized have the following features.

This water level measuring device is a prototype that was created to test water level readings in flood-prone locations or river basins. The device functions on solar energy via a solar cell and offers notifications for rising water levels in areas in danger of floods via an alert light. Furthermore, utilizing MQTT, this sensor prototype sends data to a server database via the Internet, linking the prototype device to the database system. Following that, the data supplied from the prototype device is evaluated and a Web GIS is developed to show the information in the form of a 3D simulator using the R language's ray shader software, allowing the data to be viewed on a web GIS Application.

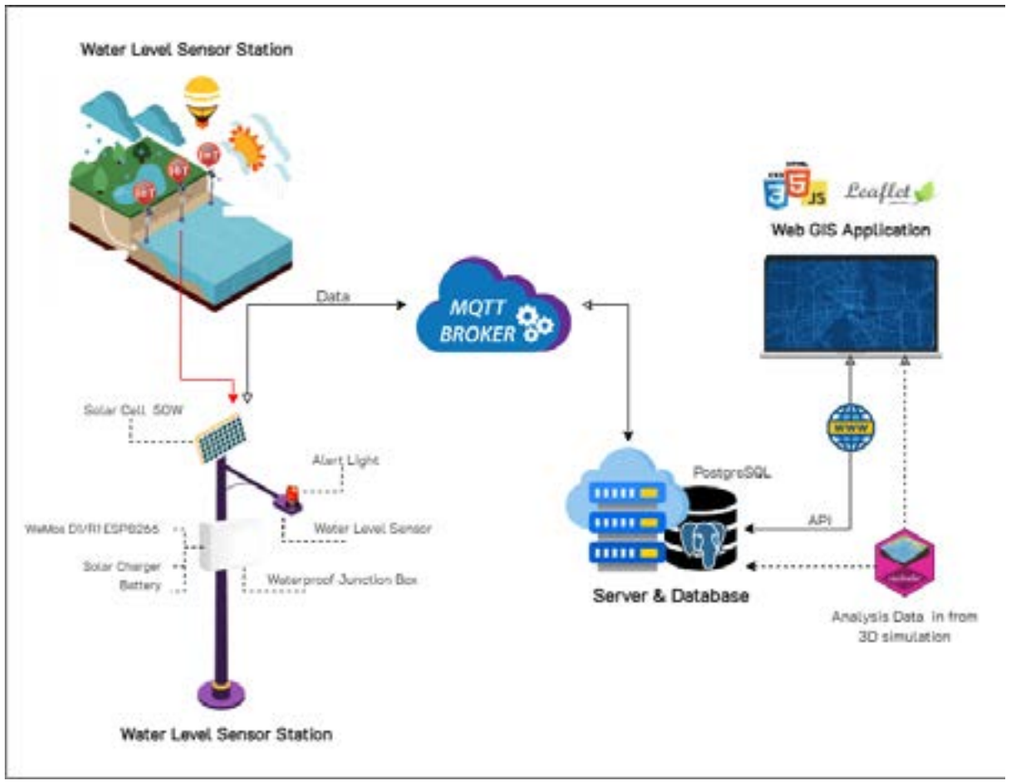

Figure 1. Integrated IoT and Web GIS application framework for developing water level measuring sensor prototype.

The operating principle of this prototype is that the sensor will measure the water level. When the water level exceeds the specified standard or height, it will notify you through a red-light signal to indicate that the water source in that area is higher than the standard. The data is then sent to the real-time database system. The ray shader program retrieves data from the database to analyze water level results and create a 3D model for display on an online map. The map displays the prototype's coordinates, device status, operation and real-time measurement results. The equipment utilized in building the water level sensor prototype in this study focuses on using low-cost sensors that can efficiently function according to the defined objectives and specifications.

2.1 Components

2.1.1 WeMos D1 R2 V2.10 Wifi ESP8266 Arduino

In this research, a prototype device has been developed using a microcontroller board, WeMos D1 R2 V2.10 WiFi ESP8266 Arduino. The ESP8266 D1 R2 WiFi board utilizes the ESP8266 WiFi-enabled processor and puts it onto an Arduino Uno board footprint. It provides a way to

work with the ESP8266 in a familiar setup and does not require a breadboard in order to make interconnections since it has the typical on-board female headers. It will also work with some Uno shields that have compatible I/O pin-outs. This board was originally produced by WeMos. This board is the 2nd generation R2 compatible version. There is also an earlier R1 version, which uses a different pin-out on some of the I/O. The pin-out on the R2 version was made to be more compatible with the NodeMCU pin-out. If working with examples, you may need to reassign some pins depending on which version you are working with. One of the images shows the difference in the pin mappings between the two versions.

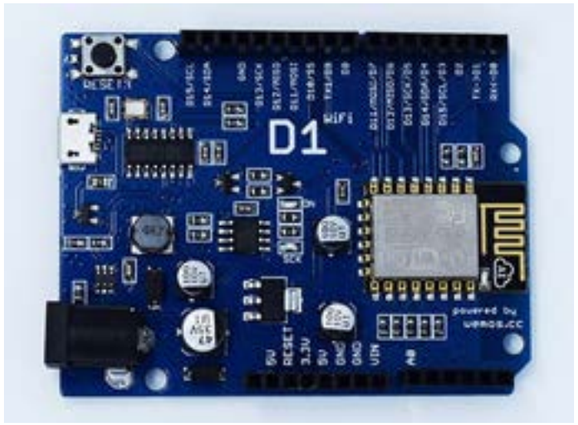

Figure 2. WeMos D1 R1 Pinout.

A great feature of this board is that, in addition to the normal female headers for bringing out I/O, each female header has a row of holes next to it to which soldered male headers, a second row of female headers, or even wires may be attached. These can be soldered to the board's top or bottom side. The board has a strip of male headers that are generally soldered to the board's top side. The board cannot be installed directly into a breadboard if the male headers are soldered to the bottom of the board because the various pieces of headers on one side are not spaced apart on 0.1centers and the holes are offset significantly.

2.1.2 TF-Luna ToF LiDAR Module

In this research, the selected sensor for measuring water levels is TF-Luna ToF LiDAR Module - 8 meters Distance. TF-Luna is a single-point ranging LiDAR, based on TOF principle. With unique optical and electrical design, it can achieve stable, accurate and highly sensitive range measurement.

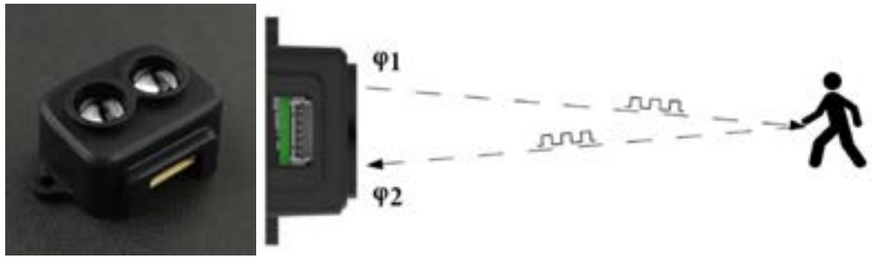

Figure 3. Tf-Luna ToF LiDAR Module with a process of working.

The product is built with algorithms adapted to various application environments and adopts multiple adjustable configurations and parameters so as to offer excellent distance measurement performances in complex application fields and scenarios. TF-Luna is based on TOF, namely, the Time Of Flight principle. It emits modulation waves of near-infrared rays on a periodic basis, which will be reflected after contact with an object. The LiDAR obtains the time of flight by measuring the round-trip phase difference and then calculates the relative distance between the LiDAR and the detected object.

2.1.3 Web GIS

In this study, we created a Web GIS to show the sensor data outcomes. Web Geographic Information Systems (WGIS) are GIS that use the World Wide Web to store, visualize, analyze and distribute geographical data via the Internet. The World Wide Web, or the Web, is an information system that hosts, shares and distributes documents, pictures and other material via the Internet. Web GIS is the use of the World Wide Web to ease GIS processes that were previously done on a desktop computer, as well as the sharing of maps and spatial data. While the terms Web GIS and Internet GIS are frequently used interchangeably, they are not the same thing. Web GIS is a subset of Internet GIS, which is a subset of distributed GIS and so on.

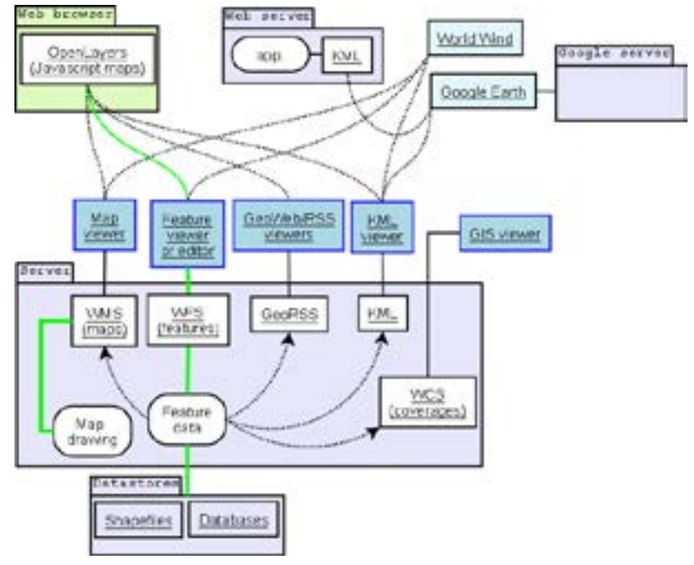

Figure 4. OGC standards help GIS tools communicate.

3. RESULT AND DISCUSSION

The research on the development of a prototype water level sensor device for analyzing and alerting to risk situations of natural disasters in a three-dimensional model on an online map focuses on developing the prototype device and displaying data on a web-based system. This integration aims to integrate geographical information science and Internet of Things (IoT) technology to address issues related to natural disasters. The research objectives are as follows.

1. To develop IoT devices along with Big Data analysis.
2. To develop an online map for real-time display of data from monitoring devices.

Actions		Id	sid	dtime	wlevel	image
Edit	Delete	577	office	12-06-2022-180919	30.21	office_12-06-2022-180919.jpg
Edit	Delete	578	office	12-06-2022-181008	37.23	office_12-06-2022-181008.jpg
Edit	Delete	579	office	12-06-2022-181302	64.46	office_12-06-2022-181302.jpg
Edit	Delete	580	office	12-06-2022-181350	30.49	office_12-06-2022-181350.jpg
Edit	Delete	581	office	12-06-2022-181537	30.49	office_12-06-2022-181537.jpg
Edit	Delete	582	office	12-06-2022-181652	46.49	office_12-06-2022-181652.jpg
Edit	Delete	583	office	12-06-2022-182034	30.49	office_12-06-2022-182034.jpg
Edit	Delete	584	office	12-06-2022-182322	30.49	office_12-06-2022-182322.jpg
Edit	Delete	585	office	12-06-2022-182551	30.49	office_12-06-2022-182551.jpg
Edit	Delete	586	office	12-06-2022-184738	30.77	office_12-06-2022-184738.jpg
Edit	Delete	587	office	12-06-2022-191435	20.95	office_12-06-2022-191435.jpg
Edit	Delete	588	office	12-06-2022-191531	20.95	office_12-06-2022-191531.jpg
Edit	Delete	589	office	12-06-2022-192750	20.95	office_12-06-2022-192750.jpg
Edit	Delete	590	office	12-06-2022-194119	37.79	office_12-06-2022-194119.jpg
Edit	Delete	591	office	12-06-2022-194225	37.51	office_12-06-2022-194225.jpg
Edit	Delete	592	office	12-06-2022-194450	37.51	office_12-06-2022-194450.jpg
Edit	Delete	593	office	12-06-2022-195238	36.67	office_12-06-2022-195238.jpg
Edit	Delete	594	office	12-06-2022-195730	37.51	office_12-06-2022-195730.jpg
Edit	Delete	595	office	13-06-2022-070002	38.07	office_13-06-2022-070002.jpg
Edit	Delete	596	office	13-06-2022-070202	38.07	office_13-06-2022-070202.jpg
Edit	Delete	597	office	13-06-2022-070402	40.04	office_13-06-2022-070402.jpg
Edit	Delete	598	office	13-06-2022-070602	26	office_13-06-2022-070602.jpg
Edit	Delete	599	office	13-06-2022-070802	26	office_13-06-2022-070802.jpg
Edit	Delete	600	office	13-06-2022-071002	25.44	office_13-06-2022-071002.jpg
Edit	Delete	601	office	13-06-2022-071202	34.7	office_13-06-2022-071202.jpg
Edit	Delete	602	office	13-06-2022-071402	31.89	office_13-06-2022-071402.jpg
Edit	Delete	603	office	13-06-2022-071602	27.4	office_13-06-2022-071602.jpg
Edit	Delete	604	office	13-06-2022-071803	27.96	office_13-06-2022-071803.jpg
Edit	Delete	605	office	13-06-2022-072002	34.42	office_13-06-2022-072002.jpg
Edit	Delete	606	office	13-06-2022-072203	34.42	office_13-06-2022-072203.jpg

Figure 5. The results of the water level data measurement and validation using IoT.

Evaluating the accuracy of data collected using the IoT involves assessing the reliability and precision of the measurements obtained from the sensor. To do this, you can follow a systematic approach that includes calibration, testing and validation. Calibrate the LiDAR sensor in the environment where it will be used. Take into account factors including temperature, humidity and ambient light conditions and Compare the measured distances with the actual distances to assess the accuracy of the LiDAR module.

The research and development process began with a review of fundamental facts on flooding problems in Thailand, the elements that contribute to them and monitoring. This includes researching several sensor technologies that may be utilized to create a water-level sensor prototype. Examining the tools, reviewing software program circumstances and referencing current research was also part of the study. This prototype was successfully constructed using the discussed approach and is capable of presenting data via an online mapping system.

4. CONCLUSION

This project presents an idea that emphasizes technological innovation to develop a prototype sensor device capable of efficiently and accurately measuring water levels. Displaying data obtained from the sensor on an online map allows users to access information quickly and report on the situation in a timely manner. We are committed to creating technology that benefits society and promotes the efficient use of water resources. Simultaneously, we strive to enhance measurement and data analysis to enable efficient and sustainable water resource management. Utilizing online maps as a platform for presenting data is a tool that can lead to improved decision-making and systematic prediction and analysis for effective water resource management.

5. REFERENCES

Adda Siva Priya Gayathri, V Satya Sri, Parupalli Sai Vineela, Kondapalli mvvnv Lakshmi and B Mamatha, 2023. Flood forcasting and warning systems using IoT. *International Journal of Creative Research Thoughts (IJCRT)*, Vol. 11, No 3, 2018-2222.

Baraa I. Farhan, 2018. Design and Construct Intelligent Tank “Water Level Sensor”. *Journal of Al-Qadisiyah for Computer Science and Mathematics, 10*(3).

Muhammad Ridzuan Idris, Irdayanti Mat Nashir, Alif Haikal bin Mohd Nordin and Mohd Hasyrah Bin Ramlee, 2021. The Internet of Things (IoT) Practical Book using Arduino WeMos D1 R1 Microcontroller. *Dicetak di Malaysia oleh*, Malaysia.

Rhutairat Hataitara, Kampanart Piyathamrongchai, Rapikorn Chalongsuppunyoo and Sittichai Choosumrong, 2021. Development of real-time river overflow monitoring and warning system using IoT based on Web and Mobile Application. *The 5th Conference on Natural Resources, Geoinformation and Environment*, Mahasarakham University, Mahasarakham Province. May 6-7, 2021.

Sangyal Lama Tamang, Victor Saikhom and Zigmi Bhutia, 2014. 3D Flood Simulation System using RS & GIS. *International Journal of Creative Research Thoughts (IJCRT)*. Vol. 3. No 5 May 2014.

IMPACTS OF URBANIZATION AND POPULATION GROWTH ON LAND COVER AND COASTLINE CHANGES BASED ON REMOTE SENSING AND GIS TECHNIQUE FOR VIETNAMESE COASTAL REGIONS

Le Thi Thu Hang*, Nguyen Hong Quang, Vu Anh Tuan, Nguyen Manh Hung, Nguyen Thi Phuong Hao

Vietnam National Space Center, Vietnam Academy of Science and Technology
*Corresponding author. Email: ltthang@vnsc.org.vn

ABSTRACT

In recent years, urbanization and population have been increasing rapidly in coastal areas of Vietnam. Various development projects are carried out along the coastal areas, putting significant pressure on these areas leading to many coastal hazards such as coastline erosion, saltwater intrusion, seawater pollution,... Continuous monitoring of urbanization in coastal areas is essential to monitor the loss of natural areas due to urban development and to support planning activities, helping local authorities to raise awareness of environmental protection and people's safety. These issues and concerns are the main focuses of this research.

This study applies two methods to assess the effects of urbanization through land use change and coastline change in Rach Gia, one of the country's fastest-growing cities in recent decades:(1) Assessment of land use changes: The study utilizes medium-resolution Landsat satellite imagery (30 m) observed at multiple time points from 2010 to 2020. An advanced machine learning method, the Support Vector Machine (SVM) algorithm, is employed to estimate land use area in conjunction with population survey data. The results demonstrate the proportion of urban land use and urban land use density relative to population growth rates, thereby confirming the influence of urbanization on land use patterns.(2)Assessment of coastal shoreline changes: A series of Landsat satellite images are used to detect changes and fluctuations in the Rach Gia coastline. The technology interprets coastal changes using calculation indices, threshold images and shoreline analysis, integrated within the ArcGIS environment via the DSAS software provided by the United States Geological Survey (USGS). Coastal changes are evaluated using a five-year cycle change index, including erosion and accretion processes from 2010 to 2020. The coastal change index is quantified by three functional analysis variables within DSAS: End Point Rate (EPR), Nearshore Movement (NSM) and Linear Regression Rate (LRR). These variables clearly illustrate the dynamics of the Rach Gia coastline during the study period. The research results demonstrate the advantages and reliability of the research methods and their ability to effectively and timely support the assessment of changes resulting from urbanization in coastal areas.

1. INTRODUCTION

Currently, urbanization and rapid population growth are occurring in coastal areas of Vietnam. Many different development projects are implemented along coastal areas, putting significant pressure on these areas, leading to many coastal hazards such as shoreline erosion, saltwater intrusion and affecting water quality, water quantity,... Regular monitoring of urbanization of coastal areas is essential to monitor the loss of natural areas due to urban development, support regional planning activities and help local authorities in environmental protection and safety.

Remote sensing satellite data are commonly used to analyze changes in urbanization and can provide more information quickly. Several studies using satellite data have demonstrated its effectiveness in understanding various urbanization processes (Guo et al., 2012; Coskun, Alganci and Usta, 2008; Mohan and Kandya, 2015; Sharma and Joshi, 2016). Remote sensing technologies have the ability to provide information over a large area on a repeated basis and are therefore useful in identifying and monitoring areas of urbanization and affecting shoreline change by urbanization. Currently, these technologies are indispensable when developing appropriate action plans for the development of coastal areas. Users and policymakers can easily access the information provided in digital format for various applications and decision-making purposes.

In a review of the literature covering the issues of urban remote sensing and data fusion (Gamba, Dell'Acqua and Dasarathy, 2005), it is shown that nowadays, the increasing availability of remote sensing data sources has promoted the development of urban remote sensing. Data from these satellites helps improve the ability to detect small changes as well as rapid urban expansion to easily distinguish types of urban landscapes, especially in dense cities and heterogeneous land use. These issues and concerns are the focus of our research. Overall, effective approaches to exploit and research the urbanization process from optical image data to support rapid assessment of landscape changes to serve urban planning and management decisions for the towns on the coast of Vietnam.

2. STUDY AREA

Rach Gia city is a coastal city. The city has a fast development rate. The city is one of the cities with developed economic and tourism activities in the country. The city's location typically includes both mainland and islands with coastal biosphere reserves. Implementing the strategy for sustainable development of Vietnam's marine economy until 2030, with a vision to 2045, Rach Gia focuses on investing in developing industrial parks and coastal urban areas (https://Rachgia.Kiengiang.gov.vn/). However, the rapid urbanization process has created multifaceted pressures and is one of the causes of changes in the coastal landscape and environment. The coastal landscape is rapidly changing due to the construction of urban infrastructure to serve commercial, service and tourism activities. Therefore, studying the urbanization process in this city is very important.

Figure 1. Study area: Rach Gia city.

3. DATA

Population data of Rach Gia city in 1989, 1999, 2009 and 2019 were collected (https://www.gso.gov.vn/dan-so/). In 2005, we collected population data from the Decree establishing Rach Gia city of Kien Giang province (97/2005/ND-CP). We estimate the population to obtain analytical data as follows: First, we calculate the population growth rate in the periods from 1989 to 1999, from 1999 to 2005, from 2005 to 2009 and from 2009 to 2019 to 2020. Next, using the population growth rates for the respective periods, we estimated the population in 1990, 1995, 2000, 2010, 2015 and 2020 to match the selected Landsat image. For example, the growth rate calculated for 1989-1999 was used to estimate the population in 1990 and 1995. The same goes for the years. The exception is 2020, where the growth rate of the previous period (2009-2019) is used.

Selected Landsat images are used for land use classification and shoreline change monitoring (Table 1).

Table 1. Landsat data used in study areas.

Satellite data	Band	Path/Row	Resolution	Acquisition Date
Landsat 5	B1-B7	126/53	30 m	05 December 1990
Landsat 5	B1-B7	126/53	30 m	26 December 1995
Landsat 5	B1-B7	126/53	30 m	23 December 2000
Landsat 5	B1-B7	126/53	30 m	12 June 2005
Landsat 5	B1-B7	126/53	30 m	09 May 2010
Landsat 8	B1-B11	126/53	30 m	17 December 2015
Landsat 8	B1-B11	126/53	30 m	20 May 2020

4. METHODS

4.1 Image processing

All the Landsat imageries were pre-processed to the land surface reflectance using the FLASSH tool by choosing relevant sensor types (TM of Landsat 5 and OLI of Landsat 8), date, time of image acquisition and atmospheric (tropical) and aerosol (urban) models. The corresponding sampling data sets were selected and validated from various sources: (1) a geographic database established from aerial photos and verified by field surveys in 2005 and 2010; (2) topographic maps provided by the Ministry of Natural Resources and Environment (MONRE) for 2015, 2020 and (3) reference to Google's historical cloud-free images data in other years.

4.2 Changes in urban area

Four main land use types are selected for classification: agricultural land, bare land, residential, water and cloud cover image layers are classified for each selected Landsat image. The Support Vector Machine (SVM) (Ben-Hur et al., 2001) machine learning classification algorithm is used to classify land use. SVM is a non-parametric supervised machine learning algorithm based on the Kernel function, making spatial transfer methods more flexible. This method is widely used and reliable to classify satellite images (Mountrakis, Im and Ogole, 2011; Sheykhmousa et al., 2020). In contrast to deep-learning approaches that require many samples (Zafari, Zurita-Milla and Izquierdo-Verdiguier, 2019), SVM requires a small number of samples. This method is very suitable for classifying time series of images when sample data is not always available. SVM is also recommended for urban area classification and object detection as it achieves comparable accuracy compared to other machine learning methods (Turker and Koc-San, 2015; Mboga et al., 2017). The research area is Rach Gia city, which has heterogeneous land use types. Accordingly, SVM provides a hierarchical process to shorten processing time without reducing result accuracy (Quang et al., 2020). We set the Kernel style SVM options of the basic radial function, the Gamma in the Kernel function to 0.27 and the Penalty parameter (C) to 100. There are 120 sample regions taken per image and 30 test regions taken to classification model of each image (calibration) and evaluate the results (validation).

The level of accuracy of land use classification was evaluated based on the most common method of assessing accuracy using error matrices. It will calculate the accuracy of measurements on a sample of pixels with known values compared to the corresponding classification on reference land use map data, including Overall accuracy (OA), Omission errors (OE), Commission error (CE) and kappa coefficient (K) (Congalton, 1991). Accuracy overall is the simplest and one of the most frequently used measures of accuracy. Identification error represents the probability that a pixel is classified. In contrast, omission error represents the percentage of a certain class is incorrectly identified on the map (Chen et al., 2013). Kappa is an index that estimates the correlation between two data (Landis and Koch, 1977; Jensen, 2005). Kappa is defined as:

$$K = \frac{(P_0 - P_c)}{(1 - P_c)} = \frac{s/(n - P_c)}{(1 - P_c)} \quad (1)$$

where, P0 is the overall accuracy, which is the ratio of matched pixels and the total number of compared pixels (n); Pc is the probability of random agreement, expressed as:

$$P_c = \frac{(a_1 * b_a + a_0 * b_0)}{(n * n)} \quad (2)$$

where, a_1 and b_1 are the pixels of built-up area on classified images and ground-truth data, respectively and a_0 and b_0 are the pixels of other classes on classified images and ground-truth data, respectively. $K > 0.80$ represents a strong agreement, $0.60 < K \leq 0.80$ represents a substantial agreement, $0.40 < K \leq 0.60$ represents a moderate agreement and a value $K \leq 0.40$ represents a poor agreement (Landis and Koch, 1977; Jensen, 2005).

Finally, the land-use categories and associated area statistics for every five years from 1990 to 2020 for Rach Gia city were refined to remove rough-classified errors, mapped and displayed on ArcGIS.

4.3 Shoreline changes influenced by urbanization

After collecting data and pre-processing the data (1), we calculate and produce The Modified Normalized Difference Water Index (MNDWI) index image (2) (Vu et al., 2019). From the index image, we proceed to select thresholds and separate water, smooth and delete objects not related to the study, separate shorelines from year to year and build a baseline. The DSAS tool is used to create cross-sections to calculate the change of the shoreline using the NSM model (Net Shoreline Movement), that is distance (m) between the oldest and the youngest of the shoreline. The EPR model (End Point Rate) is the endpoint rate simply calculated by dividing the NSM distance (m) by the number of years between those two shorelines. The Linear Regression Rate (LRR) determines the linear regression rate of change determined by fitting a least squares regression line to all shoreline points of a transect. The linear regression rate is the slope of the line (which represents the rate of coastline change) [18]. Models are built in the DSAS tool (3) and integrated

into ArcGIS software. Finally, analyze and evaluate the results (4) (Figure 2). Negative values of EPR, LRR and NSM represent shoreline accretion and positive values represent erosion.

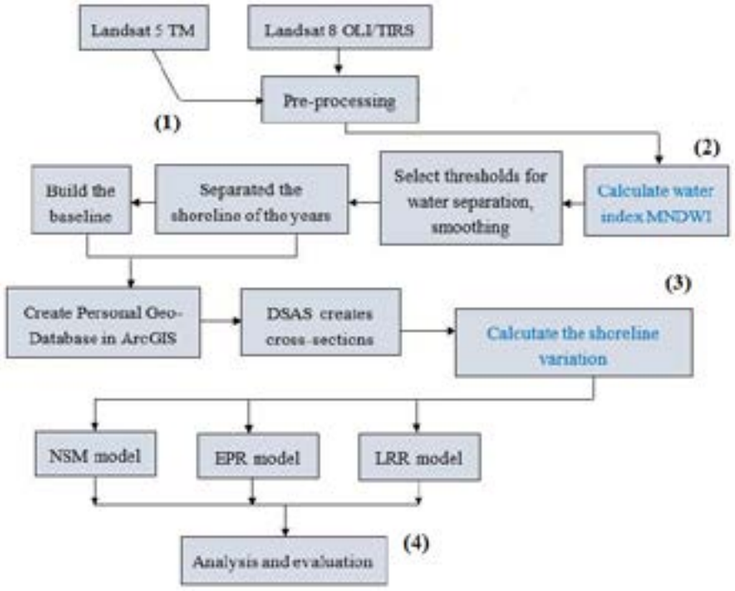

Figure 2. Workflow of methodology.

5. RESULTS AND ANALYSIS

5.1 Changes in urban area

With the classification method presented in section 4, land use types and related area statistics for each year from 1990 to 2020 for Rach Gia City are classified. All classifications were mostly reasonable, with OA and K mostly above 85 % and 0.80, respectively. The number of correctly classified pixels in the samples accounts for a very large proportion and the number of classified samples mistaken for other classification samples is insignificant. OE and CE were 18 % and 22 % lower, respectively, for all years. Therefore, the images are well classified and ensure reliability for the creation of land use to assess urban land use changes in the study area.

Table 2. Accuracy evaluation of land-use classification (OE and CE averaged all land-use).

Rach Gia	Samples	Overall Accuracy (%)	Omission Error (%)	Commission Error (%)	Kappa
1990	100	91.23	8.46	12.11	0.90
1995	120	86.40	9.03	19.87	0.84
2000	105	85.35	13.24	19.43	0.83
2005	113	87.98	16.87	20.14	0.86
2010	123	83.03	17.21	21.81	0.80
2015	125	86.97	17.57	20.95	0.84
2020	136	98.56	1.86	2.99	0.97

According to census data (General Statistics Office of Vietnam), the population of Rach Gia city was about 166,800 people in 1990. Since then, it has continuously increased, although at many different levels (Figure 3). Overall, the city's population increased 1.4 times from 166,800 to more than 227,527 people between 1990-2020. It increased very rapidly in the early stages, especially in the period after 2005, because in 2005, Rach Gia decided to recognize it as a city under Kien Giang province. Therefore, the city has been strongly invested in and developed as a coastal city, with many modern urban projects forming the largest new urban areas in the Southwest region (https://Rachgia.Kiengiang.gov.vn/). However, over the next decade (2010-2020), the city's population growth rate seemed to stabilize and slow down, with a population growth rate of about 1-2 % annually. Census data tends to be quite similar to data analyzed from satellite images. The residential area increased 4 times from 632 hectares to 2734 hectares (Figure 3). The rapid expansion of residential area since 2005 (2,130 hectares) and slow increase in the following periods is very consistent with the trend of population statistics. The residential area expanded at a rapid rate in the period 1990-2005. The speed more than doubled in the period 1990-2000 and nearly doubled in the period 2000-2005. The rapid expansion of the city area has caused the population area to increase sharply. In 2010, the image data was contaminated by a lot of clouds, so it was not accurate enough to be included in the analysis.

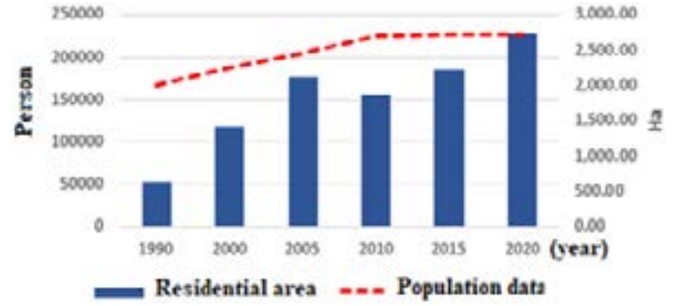

Figure 3. Population data and residential area classification from Landsat images.

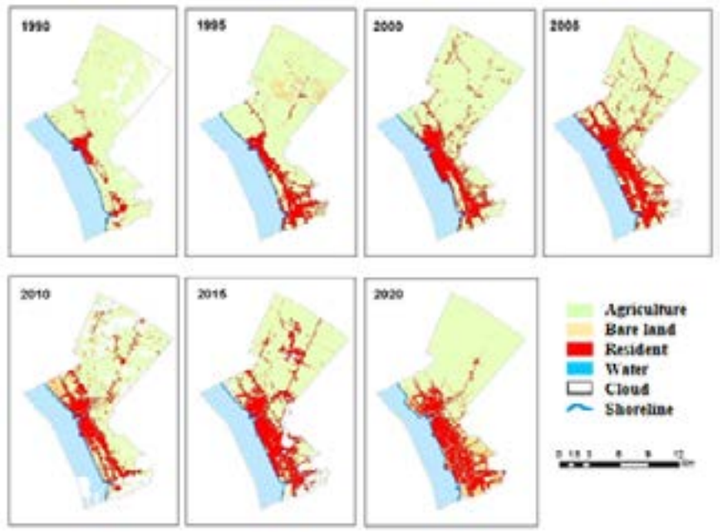

Figure 4. Map of Rach Gia land-use changes in the period 1990-2020.

The impact of urbanization increases the area and changes the structure of urban land use. The rapid expansion and development of Rach Gia's residential area are clearly shown in data obtained from Landsat (Figure 4). The classification method is tested in sampling interpretation, combined with the classification method mentioned in section 4. The classification results are shown in Figure 4.

In 1990, Rach Gia's residential land area was still sparse, often concentrated along main roads. The process of industrialization and urbanization has become clearer over the years. The results show a change in the trend of rapidly increasing residential area (Resident), decreasing agricultural area (Agriculture) and surface water area (Water) (Figure 4, Figure 5).

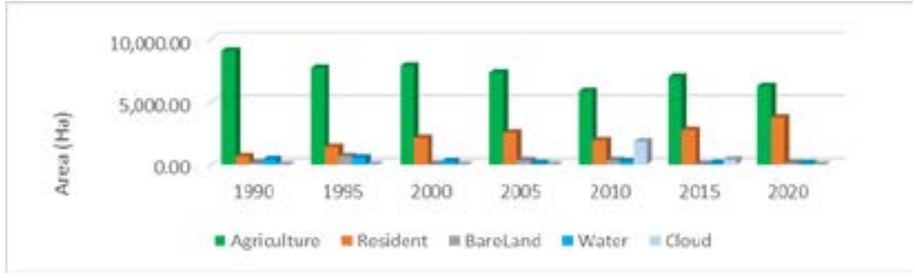

Figure 5. Chart of objects over the years.

With the above results, we see that it is very consistent with the development and urbanization situation of Rach Gia during the research period. Starting from 2000, Rach Gia has been invested and developed quickly. Right in the center of Rach Gia city, a large sea accretion project will be built, with a coastal length of over 10 km, a width extending into the sea of 500 m and a total area of over 500 hectares, expanding the land area for Rach Gia.

We see that in just 5 years, the proportion of residential areas increased significantly from 6 % in 1990 to 25 % in 2005, 27 % in 2015 and 37 % in 2020 (Table 3). In 2010, satellite images captured too many clouds (so the research team did not evaluate the level of change this year).

Table 3. Changes in main land uses of Rach Gia in the period 1990-2020 (unit: ha).

	1990		1995		2000		2005		2010		2015		2020	
	Area	%	Area	%	Area	%	Area	%	Area	%	Area	%	Area	%
Agriculture	9,068.96	89%	7,667.59	75%	7,849.68	77%	7,308.19	71%	5,888.72	57%	6,990.33	68%	6,273.79	61%
Resident	632.59	6%	1,426.76	14%	2,130.58	21%	2,530.65	25%	1,939.41	19%	2,734.13	27%	3,777.28	37%
BareLand	130.58	1%	634.62	6%	30.06	0%	314.46	3%	329.98	3%	34.19	0%	116.05	1%
Water	415.19	4%	518.36	5%	237.01	2%	94.02	1%	235.25	2%	112.70	1%	80.20	1%
Cloud	0.00	0%	0.00	0%	0.00	0%	0.00	0%	1,853.97	18%	375.98	4%	0.00	0%

Evaluation data in two periods (2010-2015 and 2015-2020), investment in coastal areas has rapidly increased the construction area of Rach Gia. With the goal of 2025, Rach Gia will become a class I urban area in Kien Giang province and the most model coastal city in the Mekong delta region. In the construction planning of the Mekong delta until 2020, with a vision to 2050, Rach Gia is located in the urban economic corridor along the southern waterway and in the Long Xuyen Quadrangle. Therefore, in recent times, Rach Gia has received attention from the State and many domestic and foreign investors with many large projects, especially urban development projects("https://Rachgia.Kiengiang.gov.vn/). Therefore, urban change and land restructuring

change drastically. The area of residential areas from more than 2500 hectares (25 %) in 2005 has quickly increased to nearly 3800 hectares (accounting for 37 %) in 2020. The area of agricultural land has decreased clearly due to structural transformation. The city's orientation develops the trend of modernization. We see that the proportion of agricultural land area in 2020 is 61 %, a large decrease compared to 89 % in 1990. The surface water area has decreased significantly due to construction projects and sea reclamation from more than 415 hectares in 2020. 1990 reduced to less than 100 hectares in 2020.

The spatial distribution of urban areas over the years in Rach Gia city has changed rapidly. During the 30 years from 1990 to 2020, the urban area developed strongly in the direction of expanding from the central area to surrounding areas and tended to move gradually to the north and northeast. Urban areas tend to expand in space, covering most of the land in the inner city and gradually moving into neighboring areas. The city has been appearing in many new urban areas. The urbanization process in Rach Gia is increasingly strong, very consistent with the research through the increasing population area with a percentage of area in 1990, 1995, 2000, 2005, 2015 and 2020, respectively are 6 %, 14 %, 21 %, 25 %, 27 %, 37 % (Table 3).

5.2 Shoreline changes affected by urbanization

The water extraction threshold of Landsat pixel images is chosen as water with a value > 0.12 (Vu et al., 2019). The water extraction results are shown in Figure 6. After receiving the surface water vector files of the years, proceed to smooth and remove objects not related to the study to extract the water contours in years and finally create a baseline.

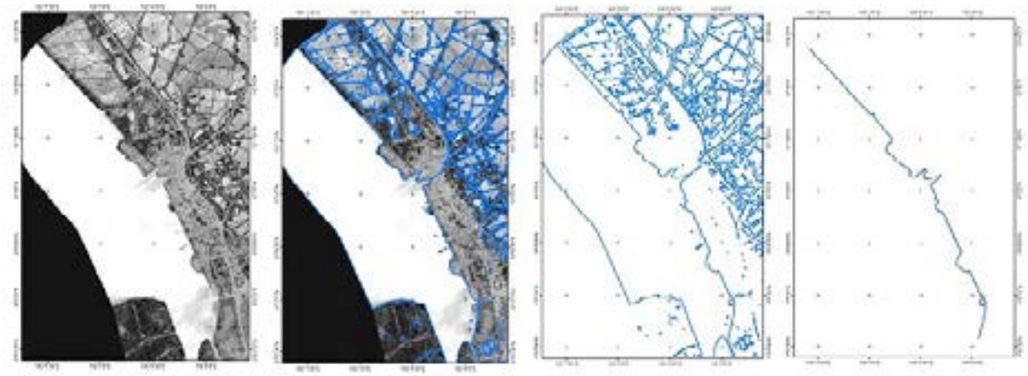

Figure 6. MNDWI index image; Surface water; Received shoreline.

Research shows coastline changes are influenced by urbanization. Figure 7 shows the coastline, baseline and transects along each grid of the Rach Gia coastline. The different shoreline changes along the transects are shown in Figure 7. It can be seen that the rate of change (–) or (+) in the Figure 7 corresponds to accretion and erosion. The study shows that the three statistical methods (EPR, LRR and NSM) for shoreline change rates are relatively similar.

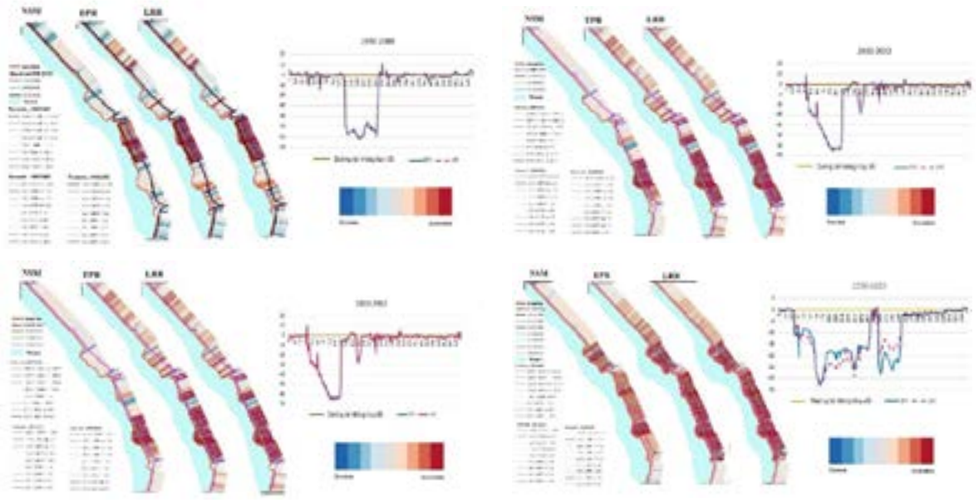

Figure 7. Analysis of the properties of accretion/erosion transects using NSM, EPR, LRR for periods (a)1990-2000; (b)2000-2010; (c)2010-2020; (d)1990-2020.

The NSM, EPR and LRR results are combined with the feature class of the transects according to the model they represent, classifying the transects into two types: accretion (red, orange color lines) and erosion (blue lines) (Figure 7). The delineation of accretional and erosional profiles shows that the coasts of the study area have changed strongly, especially the accretion process (sea reclamation) in the period from 1990 to 2020.

Rach Gia's coastline has a total coastline length of nearly 22 km and the study created 389 transects along the coastline, each transect distance 50 m apart. The results of the study are summarized and shown in Table 4, which represents the average, maximum and minimum change rates of the coastline as well as the transect ratios of erosion and accretion. The negative and positive values of EPR, LRR and LMS shown in Table 4 represent accretional and erosional zones, respectively.

Table 4. Statistical table of combined erosion - accretion from NSM, EPR and LRR models.

	1990-2000	**2000-2010**	**2010-2020**
Total number of Transects	389	389	389
Total length of shoreline (m)	22000	22000	22000
- NSM_avg accretion (m)	-173.52	-111.1	-14342
- NSM_avg erosion (m)	-12.19	10.92	4.2
- NSM_max accretion (m)	-559.18	-560.46	-831
- NSM_max erosion (m)	93.56	86.11	30
Average accretion change rate (m/year)			
- EPR	-18.72	-12.56	-12.08
- LRR	-19.48	-12.82	-11.85
Average erosion change rate (m/year)			
- EPR	1.32	1.24	0.37
- LRR	1.26	1.3	0.38
The ratio of the maximum accretion change value (m/year)			
- EPR	-60.35	-63.35	-70.03
- LRR	-62.3	-65.27	-69.63
The ratio of the maximum erosion change value (m/year)			
- EPR	10.1	9.73	2.57
- LRR	10.06	9.68	2.58
Total accretion transects / Percentage (%)			
- NSM	213/55	329/85	349/90
- EPR	213/55	329/85	349/90
- LRR	211/54	332/85	354/91
Total erosion transects / Percentage (%)			
- NSM	166/43	56/14	32/8
- EPR	166/43	56/14	31/8
- LRR	169/43	53/14	29/7

Studies on the rate of coastline change (Table 4 and Figure 8) show that the coastal area of Rach Gia is accreted (sea encroachment) quite a lot. The coastline along Rach Gia city in the period 1990-2000 (Transect 132 to 209) was especially accreted (sea encroachment) with an average speed of 18 m/year. The distance of accretion location in many places is up to 500 m. The LRR and LMS values are almost the same, indicating strong accretion of the coastline. Negligible erosion was recorded along the coastline of Rach Gia city during this period. During the period 2000-2010 (Transect 54 to 150), it was accreted at an average rate of 12 m/year. The accretion distance was also up to 500 m in many places. In the period 2010-2020, the coastline continued to be improved. Special accretion of two transects (transect 88 to 113 and transect 243 to 341) had an average speed of 12 m/year. The distance of accretion in many places is up to more than 800 m.

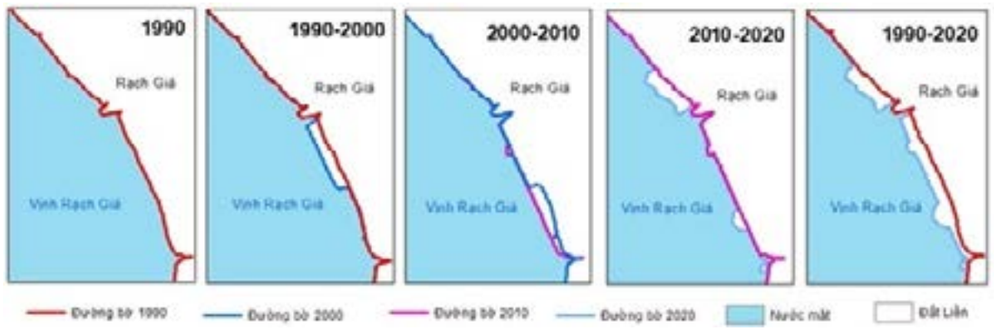

Figure 8. Shoreline changes from 1990-2020 periods.

The sudden rate of coastline change shows that accretion and sea encroachment activities took place firmly during the study period. Shows the rapid urban development in the coastal area of Rach Gia city. In fact, there are many new urban areas built on this sea encroachment area, such as Phu Cuong urban area and new urban area reclamation in the Northwest of Rach Gia city.

6. CONCLUSIONS

The study provides insights into land use, shoreline management, land use change and shoreline change in one of Vietnam's fastest development cities based on change rates. Land exchange and population growth rate. The study calculated the current land use status for Rach Gia city and the rapid change of the shoreline due to the influence of urbanization. Create detailed land

use maps for each 5-year period by classifying Landsat image series with 30 m spatial resolution through machine learning method (SVM) in the period 1990-2020. Create a map to monitor sudden fluctuations of the shoreline.

Although it has limitations regarding both data and approach, census data in Vietnam includes people with official household registrations. These data do not take into account informal workers, which mainly include people from rural areas within the province or other provinces. Therefore, the uncounted population is likely to be significantly larger than the statistical data. At the same time, population estimates also have certain errors. The DSAS forecasting tool calculates through estimated models that account for measurement noise, processing noise and the degree of mismatch between the model and data at each shoreline location. However, because the shoreline is affected by many other factors such as tides, time of image collection, etc., taking a representative shoreline each year for assessment has many limitations in accuracy. Therefore, we should take into account all the influencing factors to model future trends during future model development. Users can consider data specifications and limitations when using this tool to determine shoreline location. However, the research results show compatibility with the reality of the city's urban development and expansion. Seeing the speed of urbanization and construction scale increasing. Small-scale urban projects have been replaced by modern urban area projects and multi-story apartment buildings.

This study's approach to creating land use maps and shoreline monitoring maps to assess urbanization is relatively simple and effective. It is applied to any geographic location as long as similar data about the area and population are available. Furthermore, it can be extended to the regional level to provide comparative analyses in time and space, not only between cities or regions but also between parts of a region or districts in a city.

The research results will be a useful basis to help managers monitor changes and devise strategies for sustainable development and improve urban life while also helping to consider and evaluate the impacts of urbanization on the living environment in the context of current global climate change.

7. ACKNOWLEDGMENTS

The authors would like to thank the Ministry of Science and Technology (MOST) of Vietnam for supporting the project "Supporting Rapid Assessment of Landscape Change to improve planning and decision-making in Vietnam" (Research grant No. NĐT/AU/21/15).

8. REFERENCES

Ben-Hur, Asa, David Horn, Hava T Siegelmann and Vladimir Vapnik, 2001. Support Vector Clustering. *Journal of Machine Learning Research, 2* (Dec), 125-137.

Chen, Yun, Chang Huang, Catherine Ticehurst, Linda Merrin and Peter Thew, 2013. An Evaluation of MODIS Daily and 8-Day Composite Products for Floodplain and Wetland Inundation Mapping. *Wetlands, 33* (5), 823-835.

Congalton, Russell G. 1991. A Review of Assessing the Accuracy of Classifications of Remotely Sensed Data. *Remote Sensing of Environment, 37* (1), 35-46.

Coskun, H Gonca, Ugur Alganci and Gokce Usta, 2008. Analysis of Land Use Change and Urbanization in the Kucukcekmece Water Basin (Istanbul, Turkey) with Temporal Satellite Data Using Remote Sensing and GIS. *Sensors, 8* (11), 7213-7223.

Gamba, Paolo, Fabio Dell'Acqua and Belur V Dasarathy, 2005. Urban Remote Sensing Using Multiple Data Sets: Past, Present and Future. *Information Fusion, 6* (4), 319-26.

Guo, Zheng, S D Wang, M M Cheng and Y Shu, 2012. Assess the Effect of Different Degrees of Urbanization on Land Surface Temperature Using Remote Sensing Images. *Procedia Environmental Sciences,* 13, 935-42.

https://Rachgia.Kiengiang.gov.vn/. Accessed on 16/10/2023.

https://www.gso.gov.vn/dan-so/. Accessed on 16/10/2023.

Jensen, John R., 2005. Digital Image Processing: A Remote Sensing Perspective. *Upper Saddle River, NJ: SPrentice Hall*.

Landis, J Richard and Gary G Koch, 1977. The Measurement of Observer Agreement for Categorical Data. *Biometrics*, 159-174.

Mboga, Nicholus, Claudio Persello, John Ray Bergado and Alfred Stein, 2017. Detection of Informal Settlements from VHR Images Using Convolutional Neural Networks. *Remote Sensing*, *9*(11), 1106.

Mohan, Manju and Anurag Kandya, 2015. Impact of Urbanization and Land-Use/Land-Cover Change on Diurnal Temperature Range: A Case Study of Tropical Urban Airshed of India Using Remote Sensing Data. *Science of the Total Environment,* 506, 453-465.

Mountrakis, Giorgos, Jungho Im and Caesar Ogole, 2011. Support Vector Machines in Remote Sensing: A Review. *ISPRS Journal of Photogrammetry and Remote Sensing, 66*(3), 247-259.

Quang, Nguyen Hong, Claire H Quinn, Lindsay C Stringer, Rachael Carrie, Christopher R Hackney, Le Thi Van Hue, Dao Van Tan and Pham Thi Thanh Nga, 2020. Multi-Decadal Changes in Mangrove Extent, Age and Species in the Red River Estuaries of Viet Nam. *Remote Sensing, 12*(14), 2289.

Sharma, Richa and P K Joshi., 2016. Mapping Environmental Impacts of Rapid Urbanization in the National Capital Region of India Using Remote Sensing Inputs. *Urban Climate, 15*, 70-82.

Sheykhmousa,Mohammadreza,MasoudMahdianpari,HamidGhanbari,FaribaMohammadimanesh, Pedram Ghamisi and Saeid Homayouni, 2020. Support Vector Machine versus Random Forest for Remote Sensing Image Classification: A Meta-Analysis and Systematic Review. *IEEE Journal of Selected Topics in Applied Earth Observations and Remote Sensing, 13*, 6308-6325.

Turker, Mustafa and Dilek Koc-San, 2015. Building Extraction from High-Resolution Optical Spaceborne Images Using the Integration of Support Vector Machine (SVM) Classification, Hough Transformation and Perceptual Grouping. *International Journal of Applied Earth Observation and Geoinformation, 34*, 58-69.

Vu Anh Tuan, Hang Thi Thu Le and Nguyen Hong Quang, 2019. Monitoring Urban Surface Water Bodies Changes Using MNDWI Estimated From Pan-sharpened Optical Satellite Images. *Conference: FIG Working Week 2019, Geospatial information for a smarter life and environmental resilience*. Hanoi, Vietnam, April 22-26.

Zafari, Azar, Raul Zurita-Milla and Emma Izquierdo-Verdiguier, 2019. Evaluating the Performance of a Random Forest Kernel for Land Cover Classification. *Remote Sensing, 11*(5), 575.

THREE-DIMENSIONAL BUILDING MODEL USING DRONE POINT CLOUDS

Sawarin Lerk-u-suke[1], Phaisarn Jeefoo[1]*, Pornthep Rojanavasu[1], Jirabhorn Chaiwongsai[1], Nakarin Chaikaew[1], Bowonsak Srisungsittisunti[1], Niti Iamchuen[1], Wipop Paengwangthong[1], Boonsiri Sukpromsun[1], Watcharaporn Preedapirom Jeefoo[2], Pranorm Khrueawan[1], Jiraporn Kulsoontornrat[1], Suchatri Prasomsuk[1], Chatpong Pachanaparn[1], Nootchararat Thawadee[1]

[1]School of Information and Communication Technology,
University of Phayao, Mae-Ka, Muang, Phayao, Thailand
[2]School of Medical Sciences, University of Phayao, Mae-Ka, Muang, Phayao, Thailand
*Corresponding author. Email: phaisarn.je@up.ac.th

ABSTRACT

The traditional Total Station approach cannot be used to produce a photo-realistic 3D model of an object. This study primarily outlines the theory of high-resolution aerial mapping for 3D construction using drone point clouds of the Provincial Hall in Chiang Rai Province, in northern Thailand. The use of geographic information systems (GIS) to support and convey information to environmental managers and the general public is excellent for presenting data obtained from ongoing location monitoring. The building photos were processed using the Photogrammetry module of Agisoft PhotoScan Professional software. The study progressed through several processing stages with Agisoft PhotoScan Professional, including Align Photos, Build Dense Cloud, Build Mesh, Build Texture, Build Tiled Model, Build DEM, and Build Orthomosaic, respectively. High-quality aerial photographs with a resolution of 2.73 cm were used to create the base map of the building. Moreover, the outcome displayed the 3D texture of the hall.

1. INTRODUCTION

The levels of detail (dimensionality) integrated into digital maps have steadily increased since their introduction. Since they have applications in disaster management, augmented reality, tourism, urban planning, heritage building documentation, gaming visualization, civil engineering, and disaster management, 3D city models have gained popularity as research topics (Döllner et al., 2005; Engel and Döllner, 2006; Kobayashi, 2006; Themistocleous et al., 2014). Reconstructing building structures from façade data has recently been an exciting area of study for survey services. Building model 3D reconstruction has always been dependent on point cloud data from an airborne laser scanner (ALS), which provides precise depth information (Emelianov et al., 2014). One of the most effective methods for recreating planar roof structures is to use ALS. Due to the high altitude at which the data is gathered, ALS is ineffective for modeling building façade information. In addition, the study conducted utilizing ALS is impractical due to the costly equipment and employing a pilot to fly a crewed aircraft.

However, mobile and terrestrial laser scanners (MLS & TLS) can be used to recreate facades. These scanners acquire data from the ground up, unlike ALS. Because the building's façade blocks their line of sight, these scanners are unable to obtain information to map the roof structure (Zakaria et al., 2015). Due to the often inaccurate roof planes, predetermined roof styles must be employed in order to create a 3D building model using only ALS data (Roo et al., 2017).

Because they can gather close-range photogrammetric data in high resolution at cheaper costs, UAVs are gaining a lot of popularity. A tactical advantage over other remote sensing platforms is given by the ability of UAV sensors to be customized based on mission requirements. Though the early developments in this field were primarily focused on military requirements, the gates are now open to many civilian applications, such as building construction, infrastructure documentation and inspection, road maintenance, precision agriculture, monitoring forests, surveillance, disaster mitigation, traffic control, and parcel delivery. UAVs are a practical alternative method for researchers to monitor and record fragile archaeological sites because of their low cost and non-intrusive nature (Themistocleous et al., 2014). Unfortunately, the payload restrictions of UAVs prevented the earlier UAV platform from supporting bigger 3D laser scanners (Palazzolo and Stachniss, 2019).

Drone technology, encompassing all the elements engineers need to create infrastructure, is rapidly advancing in the twenty-first century. These developments are crucial in maintaining a balance between human needs and technological advancements, encompassing aspects of daily life, employment, and socioeconomics. To achieve success in Three-Dimensional (3D) mapping development, thorough preparation and planning throughout and after the completion stages are essential within its specific context. The main objective is to select a model that adequately performs the specified tasks while considering computing, economic, and cognitive constraints without any other significant causes (Sani et al., 2022).

Large-scale urban 3D mapping is now widely used across various application sectors. Proponents in the mapping industry strive to incorporate detailed 3D models that accurately depict the real world into their datasets. Techniques enabling precise mapping of unstructured 3D environments, such as stairwells, tunnels, and caverns, are essential for Unmanned Aerial Vehicle (UAV) navigation. This study presents a system that serves as a starting point in that direction (Rouhani et al., 2017).

Different levels of detail can be generated for 3D architectural models, ranging from bare-bones structures to more complex explicit geometries (Harinish, 2019). For city monitoring, disaster assessment, map updating, etc., automatic building change detection at various times is crucial. To accomplish this task, existing data sources like radiometric satellites or special aircraft photos and 3D geometry models (such as Digital Surface Models and Geographic Information Systems) may be utilized. However, employing these techniques for real-time change detection can be expensive. Nonetheless, the cost of capturing city building images at a low height with high-quality cameras has decreased significantly due to the rapid development of UAV technology.

2. MATERIAL AND METHOD

2.1 Study area

Chiang Rai, Thailand's Northernmost province, shares borders with neighboring nations such as Myanmar and Laos. It is situated between 19°30'00''N to 20°0'00''N and 99°0'00'E to 100°30'00''E. Starting from Doi Tachilek in Shan State, Republic of the Union of Myanmar, it

stretches to Thailand's Southern border. The Mekong River touches the Northeastern side of the region. To the East, it borders the Lao People's Democratic Republic, touching Luang Prabang before extending Southwards to Phayao. The Southern portion connects Phayao, Lampang, and Chiang Mai, while the western region is connected to Chiang Mai (Figure 1).

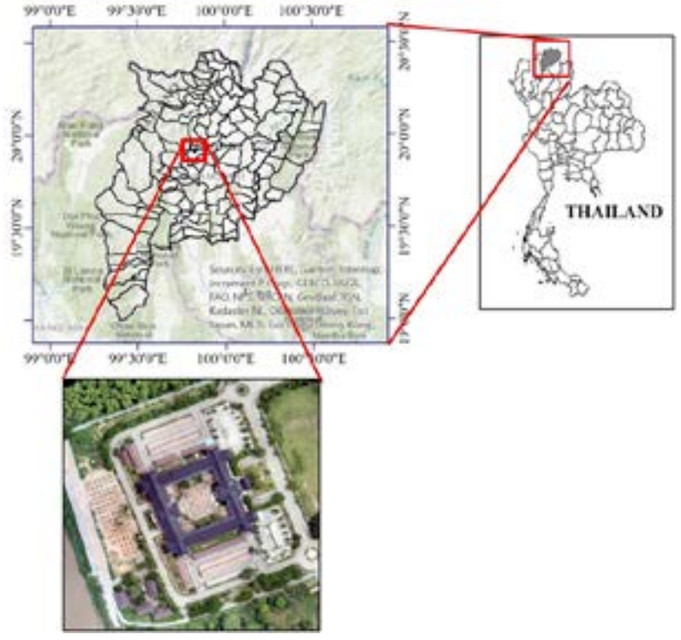

Figure 1. Geographical of the study area, the Chiang Rai Provincial Hall.

Two flight lines with 20 % side lap and more than 60 % end lap make up the panchromatic images. As shown in Figure 2, a total of 197 photos were taken while flying at a height of 100 m above the ground to collect these images.

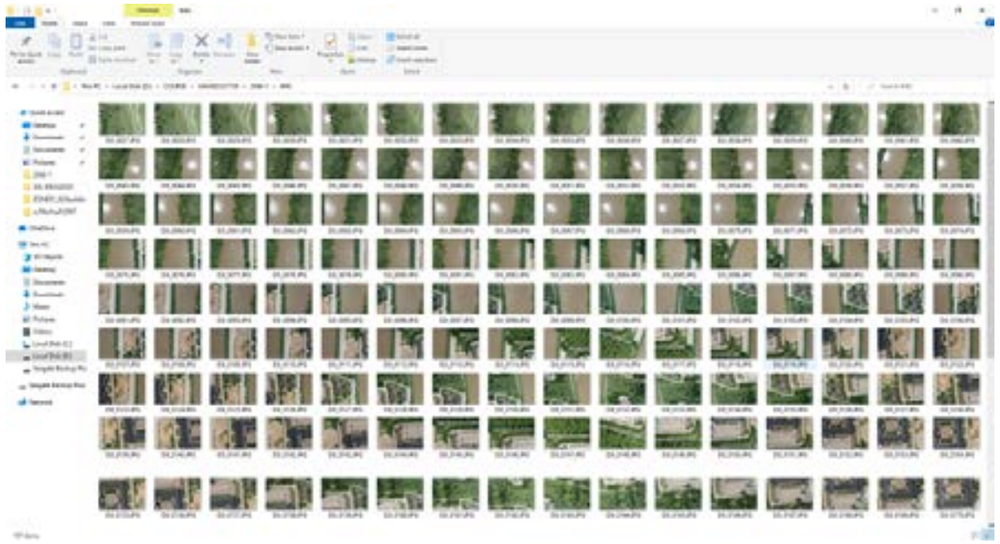

Figure 2. A total of 197 images were over the study area.

2.2 Method

Four basic steps made up the research process. By gathering GCPs and altering the network supplied, the first stage was completed. The second stage involved triangulation using a least squares solution and photo processing. The third stage involved putting procedures into place to perform the spatial analysis and produce a raster surface. The statistical analysis, evaluation, and validation of the created 3D surface were all included in the final stage. Figure 3 provides a summary of the methodology that was employed, and that will be explored in this study.

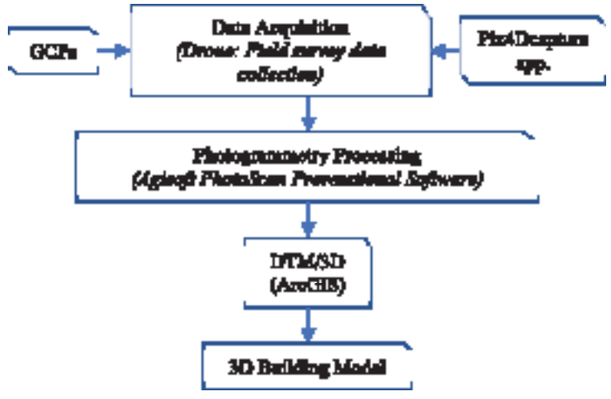

Figure 3. Flow chart of the methodology used in this study.

The DJI Phantom 4 was used to operate the drone most of the time, and extra data was collected in the field using Ground Control locations (GCPs) with six locations. On an iOS smartphone, the Pix4Dcapture app was used for flying control. The photogrammetry software Agisoft PhotoScan Professional (https://www.agisoft.com/) was then used to process the aerial data. The initial application of the Digital Terrain Model (DTM) created from the drone data is to display flood levels using simple elevation.

2.3 Data Acquisition

The data was collected on June 18, 2023, around 10.30 AM, which is the optimal time for collecting data using a DJI Phantom 4 Pro v 2.0 drone, especially for aerial Orthophoto photos of Chiang Rai Hall next to the Kok River, georeferenced using the WGS 1984 system.

The differential global positioning system (DGPS) technique was used to determine the ground control locations, which were then precisely modified using a robust least squares scenario. The Topcon GR-5 GPS unit was utilized to gather the data, and its working mode was real-time kinematic (RTK). Ten ground points' coordinates were gathered, and they were placed on distinct, evenly distributed landmarks throughout the study area. These were measured using the UTM projection reference as a baseline. As shown in Figure 4, only 6 of the total points gathered were used as GCPs, while the remaining 4 points were used as Check Points.

In this study, a large number of Check Points were used since, among other things, the distribution and number of Check Points affect how reliable the accuracy estimates are. A network of 3D coordinates is then given, but without modification, it cannot be post-processed for accuracy in subsequent steps. As a result, the 10 GCPs were all adjusted using a 3D network employing a non-linear solution (variation of the coordinate model). The least squares method was used to

derive a final result that was precise. Later on, the GCPs' corrected coordinates were used for the subsequent processing step.

Figure 4. GCP placement and checkpoint locations within the study region.

During the data collection, the drone was flown at 100 m above ground level, with a total flight time of 18 minutes and 11 seconds, covering an area of approximately 0.16 km^2 (flight plan: 468×346 m). The process of creating an Orthomosaic and various derivative products involved overlapping pictures. In total, 197 pictures were captured. Using the Pix4Dcapture application, a forward overlap of 80 % and a side overlap of 70 % were calculated between the images based on the drone's onboard GPS (Figure 5).

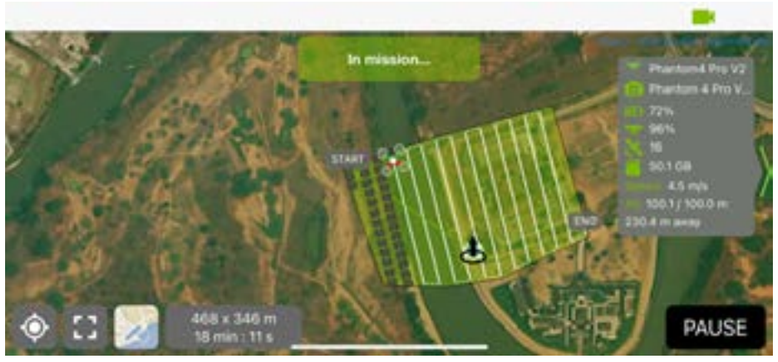

Figure 5. Drone in mission.

2.4 Data Processing: Photo Processing (Bundle Adjustment)

The method for picture processing using Aero-triangulation is also known as the "bundle adjustment technique" since it is based on the notion that a bundle of light rays from the light source (camera sensor) interacts to produce spatial positions. Later, all of the bundles from the related photos are concurrently altered so that the matching light rays cross at the locations of the ground features. The mathematical approach for adjusting these bundles with least squares is based on collinearity equations. For an ideal solution, these equations must be linearized because they are not linear (Wolf et al., 2014). As a starting point for the subsequent processes, this step generates 3D dense point clouds.

Agisoft PhotoScan is a specialized image-based 3D modeler program that aims to produce precise and organized 3D information from fixed photos. Any arbitrary images that meet the requirements will work in both controlled and uncontrolled environments. The photos can be shot using the Agisoft PhotoScan software from any angle, allowing for the reconstruction of the object from a minimum of two photos taken from various angles. According to Figure 6, every step of the procedure, including picture alignment and 3D model reconstruction, is totally automated. Agisoft PhotoScan has developed into a valuable resource for producing accurate 3D data for a variety of applications after receiving recommendations from several users worldwide.

The bundle block adjustment is also used by Agisoft PhotoScan Project Manager when performing triangulation. In contrast to the Leica Photogrammetry Suite (LPS), Agisoft PhotoScan has a significant problem with photo orientation. When the images are strongly orientated from the Nadir (in the direction of Kappa), this is made clear. This can be explained by the absence of the PhotoScan program, which would have allowed for the application of photo calibration and distortion factors during the adjustment process. If the images were not originally in digital form and were later converted into digital form through scanning, as was the case in this study, this could be a significant problem.

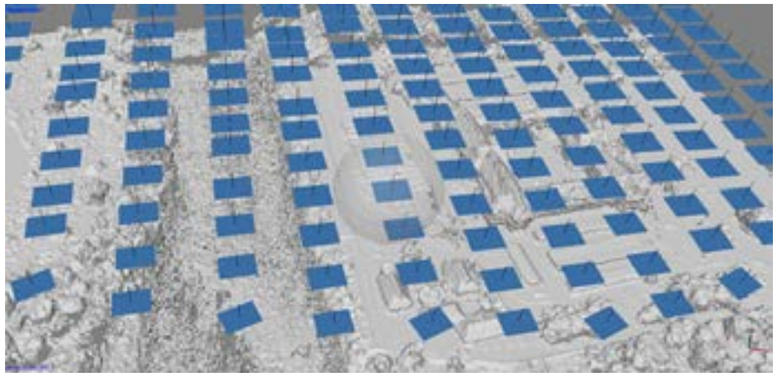

Figure 6. A 3D building model and image alignment examples.

Before being utilized in ArcGIS, the drone imagery underwent pre-processing using Agisoft PhotoScan Professional (Figure 7). This software facilitated the creation of 3D maps and models from RGB photos using photogrammetry and computer vision techniques. Photogrammetry is the science of measuring objects in photographs and utilizing that data to create products like Digital Terrain Models (DTMs) (Preedapirom and Jeefoo, 2021).

With the help of texture topology, using overlapping pictures, Agisoft PhotoScan Professional calculates an object's parallaxes or its movements with respect to the position of the sensor. Due to the smooth DTM generation technique, the software computed the Ground Sampling Distance (GSD) or resolution for the 2D Orthomosaic image to be 2.73 cm. However, it's worth noting that Agisoft's default DTM resolution is 5 times greater than that of the project, resulting in a GSD of 20 cm for the DTM.

Furthermore, the DTM created by Agisoft PhotoScan Professional represents an elevation model of the ground, eliminating surface objects such as houses and trees. After this data assembly was imported, the remaining processing was carried out in ArcGIS.

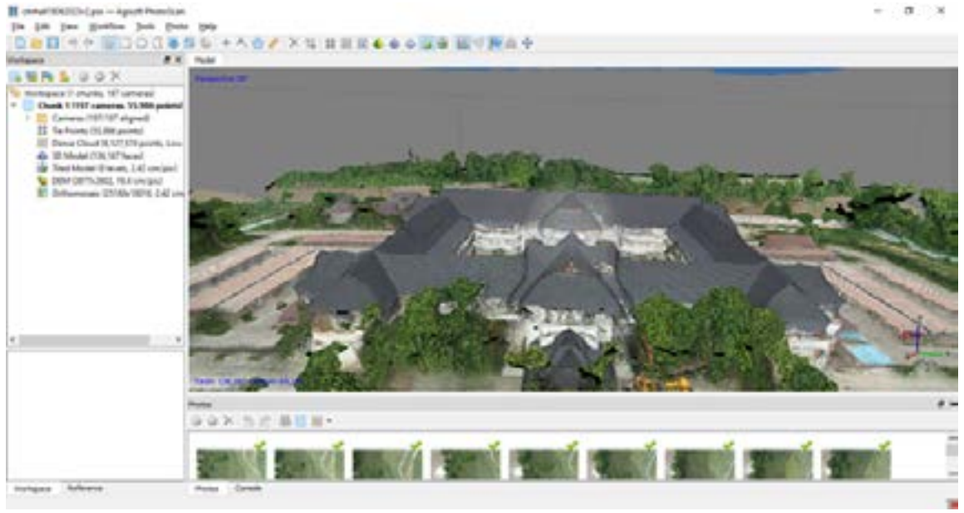

Figure 7. Using Agisoft PhotoScan Professional to process photographs for photogrammetry.

2.5 Spatial Analysis (Digital Terrain Model: DTM)

The process of interpolation is used to predict cell values in areas without sample points. It is founded on the idea of spatial dependency or self-correlation between nearby and far-off organisms. Maps are made using spatial analyst techniques, which are thought to be regarded as one of the crucial GIS tools. The phrase "spatial analysis method" refers to all operations performed on spatial data with the intention of better comprehending the geographic phenomena the data represent. The ArcGIS® Geostatistical Analyst toolbar was used in this study's spatial analysis in order to create a three-dimensional model.

In this research, ArcScene was employed to build this simulation, resulting in a 3D representation with a maximum elevation of 423.265 m and a minimum elevation of 357.663 m (Figures 8a and 8b).

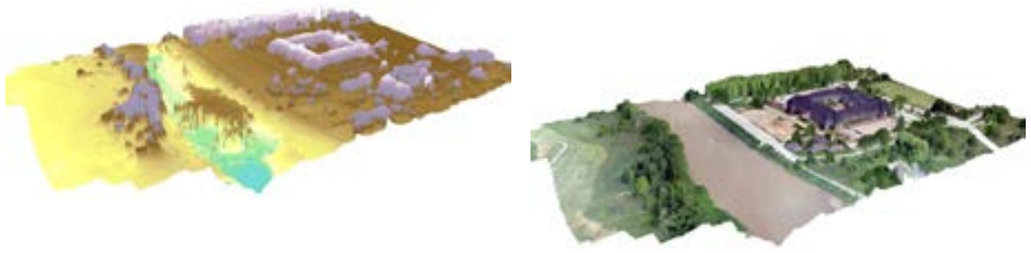

a) Overview of the DTM. *b) Overview of the 3D building model.*

Figure 8. Overview of the DTM (a) and 3D visualization with Orthomosaic (b).

3. RESULTS

One approach for determining the precise location and heights of buildings, or any other kind of point features on the building to be collected, is through a topographic survey. In this study, a total station was utilized to collect point data, providing information about the building's points.

The experimental analysis and assessment conducted in this research served as the study's final conclusion. It was demonstrated that the inaccuracy between point clouds up to the texture model varies, and this inaccuracy is measured in meters. Figure 9 illustrates the relationship between the number of samples on the x-axis and the corresponding error on the y-axis for each output, representing the value of that comparison.

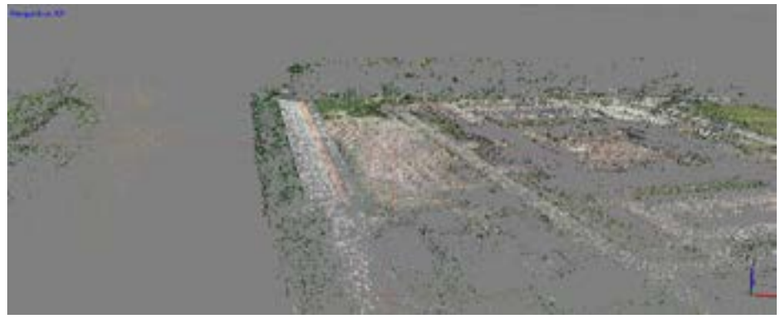

a) Point clouds

b) Texture model

Figure 9. The visualization of texture model of 3D building.

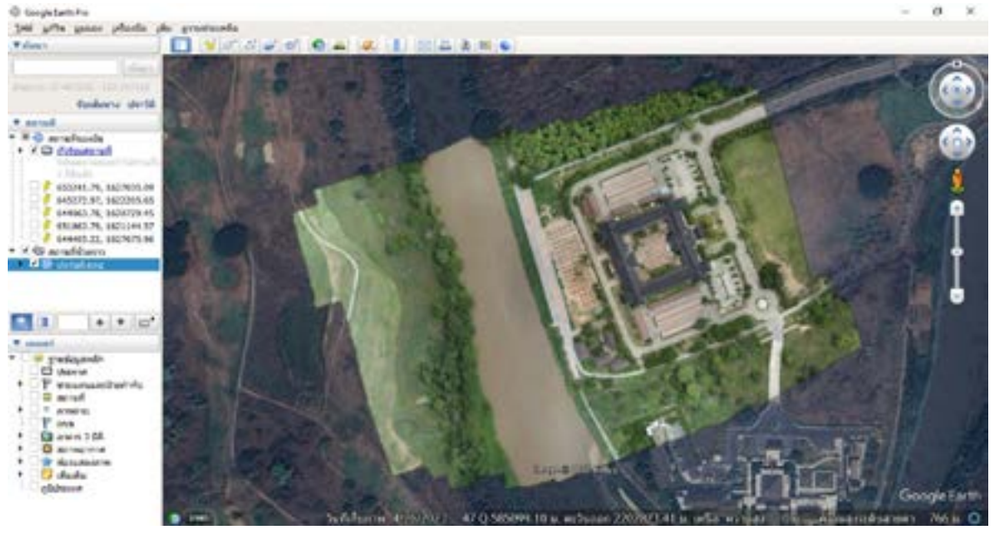

Figure 10. Chiang Rai Provincial Hall mapping with Google Earth Pro.

To capture photos of the Chiang Rai Provincial Hall construction, an indirect method was used, which involved employing a random position for the UAV waypoint. Subsequently, the photos of the Chiang Rai Provincial Hall building were processed using the Photogrammetry feature of Agisoft PhotoScan Professional software. Figure 10 displays the extent of the building as seen on Google Earth.

First-order headings, such as the one above, are bolded in 12 points, placed two lines (12 points) below the paragraph before it and one line (12 points) above the text that follows.

The numbers in your word processor's automated outline heading feature sometimes do not transfer correctly, so please avoid using them. That is, instead of letting the word processor create the heading number for you, manually enter it.

4. CONCLUSIONS

In order to demonstrate the potential of this software for precise 3D modeling, the capacity of Agisoft PhotoScan to extract trustworthy data from aerial photographs was evaluated and examined in this article. A study was conducted in the Chiang Rai Provincial Hall utilizing information gathered from a DJI Phantom 4 Pro with a 100 m flying height to look into this. The utilization of the DJI Phantom 4 UAV/drone for high-resolution flood prevention is undeniably advantageous, as demonstrated in this research. Despite the drone's limited field of view, creating maps at the public level provides significant additional benefits. The study highlights the availability of photogrammetry and GIS software packages, such as Agisoft PhotoScan Professional and ArcGIS, which enable the development of drone data-driven architecture. According to the research purpose and the dataset quality after statistical and validation shape analysis, the Agisoft results indicate promise. The accuracy of the data sent depends on a number of factors, including the caliber of the imagery utilized, image orientation, the scenario chosen, the distribution and availability of GCPs, etc. It is anticipated that the findings of this study will contribute to the advancement of Thailand's earthquake management system. Therefore, based on the findings of the case study, the following conclusions might be drawn:

• The outcomes demonstrate the accuracy and validity of Agisoft PhotoScan software in the triangulation procedure and, consequently, in 3D modeling applications.

• The superior ability of Agisoft PhotoScan software to intensify points during the triangulation process for applications requiring precise 3D modeling.

• The simplicity of the Agisoft PhotoScan software compared to the LPS software since the former doesn't require any approximations for the unknowns, such as the control points and external orientation parameters.

5. ACKNOWLEDGEMENTS

The University of Phayao in Thailand's School of Information and Communication Technology (ICT) is funding this study. We would like to send a special thank you to the provincial administration in Chiang Rai for providing crucial information.

6. REFERENCES

Döllner J., Buchholz H., Nienhaus M., and Kirsch F., 2005. Illustrative visualization of 3D city models. *Proceedings of SPIE - The International Society for Optical Engineering*.

Emelianov S., Bulgakow A., and Sayfeddine D., 2014. Aerial laser inspection of buildings facades using quadrotor. *Procedia Engineering*, *85*, 140-146.

Engel J., and Döllner J., 2014. Immersive Visualization of Virtual 3D City Models and its Applications in EPlanning. *International Journal of E-Planning Research, 1*(4), 17-34.

Harinish K.P., 2019. Optimisation of UAV Flight Plans for Reliable 3D Building (LOD3). *Model Generation*, 6 - 48.

Kobayashi Y., 2006. Photogrammetry and 3D city modelling. *WIT Transaction on the Built Environment, 90*, 209-218.

Palazzolo E., and Stachniss C., 2018. Effective Exploration for MAVs Based on the Expected Information Gain. *Drones*, *2*(1), 9.

Preedapirom W., and Jeefoo P., 2021. Techniques of 3D Visualization using Unmanned Aerial Vehicle for Flood Protection. *International Conference on Digital Arts, Media and Technology with ECTI Northern Section Conference on Electrical, Electronics, Computer and Telecommunication Engineering*, Cha-am, Thailand, 161-164. Doi: 10.1109/ECTIDAMTNCON51128.2021.9425694.

Roo B. De., Bourgeois J., and Maeyer P. De., 2017. Advances in 3D Geoinformation Systems. *In Advances in 3D Geoinformation*, 323-335.

Rouhani M., Lafarge F., and Alliez P., 2017. Semantic Segmentation of 3D Textured Meshes for Urban Scene Analysis. *ISPRS Journal of Photogrammetry and Remote Sensing*, *123*, 124-139.

Sani N.H., Tahar K.N., Maharjan G.R., Matos J.C., and Muhammad M., 2022. 3D reconstruction of building model using UAV point clouds. *The International Archives of the Photogrammetry, Remote Sensing and Spatial Information Sciences*, Volume XLIII-B2-2022 XXIV ISPRS Congress (2022 edition), 6-11 June 2022, Nice, France, 455-460.

Themistocleous K., Cuca B., and Hadjimitsis D. G., 2014. 3D documentation of Fabrica hills caverns using terrestrial and low cost UAV equipment, (November 2014).

Wolf P. R., Bon A. D., and Benjamin E. W., 2014. Elements of Photogrammetry with Applications in GIS. 4th ed. *New York: McGraw-Hill Education*.

Zakaria A., Abdul Shukor S.A., Basah S.N., Rushforth E., and Wong R., 2015. 3D Terrestrial Laser Scanner for Managing Existing Building. *Jurnal Teknologi*, *76*(12).

WEBGL-BASED VISUALIZATION TOOL FOR 3D GEOLOGICAL STRUCTURES IN SHALLOW SUBSURFACE IN URBAN AREAS

Susumu NONOGAKI*, Tsutomu NAKAZAWA

Geological Survey of Japan, National Institute of Advanced Industrial Science and Technology (AIST), Tsukuba, Ibaraki, Japan
*Corresponding author. Email: s-nonogaki@aist.go.jp

ABSTRACT

Shallow subsurface there-dimensional (3D) geological information plays an important role in urban planning, development and management. Recently, we have been working on 3D geological mapping of urban areas in Japan up to tens of meters in depth using a large number of borehole data and have been making 3D maps open to the public on the Web. In this study, to provide 3D geological information in urban areas with an easy-to-understand style on the Web, we have developed a WebGL-based visualization tool for 3D geological maps that consists of shape data of geological boundary surfaces and 3D representations of borehole data. This tool allows us to adjust the visualization style of the 3D geological structure only with mouse operation. When the developed tool for the 3D geological map of central Tokyo was applied, it was confirmed that the tool could effectively demonstrate the distribution of key layers, which are closely related to earthquake-induced disasters. In conclusion, the tool helps to understand the 3D distribution patterns of geological layers and geotechnical properties within the shallow subsurface.

1. INTRODUCTION

3D geological maps that represent shallow subsurface geological structures are essential for the mitigation of earthquake-induced disasters such as amplification of ground motion and liquefaction/subsidence, development and management of infrastructures and assessment of renewable energy potential such as groundwater and geothermal energy. Recently, as part of the intellectual infrastructure development, we have been working on 3D geological mapping of urban plane areas in Japan using borehole data in tens of thousands created for public construction works and for stratigraphic studies, cooperating with local governments and to date have completed 3D geological maps of the Northern area of Chiba Prefecture and central Tokyo, Japan (Naya et al., 2018, 2021). These 3D geological maps are available for free on the website “Urban Geological Map” by the Geological Survey of Japan (GSJ) [URL1]. On this website, users can also browse the two-dimensional (2D) geological map as well as borehole logs used for mapping.

On the GSJ website, the 3D geological maps were originally provided in Virtual Reality Model Language (VRML) format. However, only a few web browsers are capable of handling VRML files. In this study, to make it easy for everyone to use the 3D geological maps on the Web and to understand the 3D distribution patterns of geological layers and geotechnical properties within the shallow subsurface, we have developed a visualization tool for 3D geological maps, combining shape data of geological boundary surfaces and 3D representations of borehole data. In this paper, we will describe details of the functions of the developed tool and show an example of applying the tool to the 3D geological map of central Tokyo.

2. SYSTEM CONFIGURATION

2.1 System requirement and external libraries

The developed tool is a JavaScript-based Web application designed to smoothly render a large number of 3D objects by Graphics Processing Unit (GPU) operations using WebGL, which is standard equipment of web browsers. Table 1 shows a list of open-source JavaScript libraries used in the tool. Here, we used three.js, one of the major libraries in 3D computer graphics, for WebGL programming due to its rich functionality and extensibility.

The tool works on Windows (10 or higher), MacOS and Linux operating systems. Supported Web browsers are Mozilla Firefox, Microsoft Edge, Google Chrome and Safari. The users do not need any external plug-ins to visualize 3D geological maps.

Table 1. List of JavaScript libraries used for system development.

Library name	Download site	License
three.js	https://threejs.org	MIT
jQuery	https://jquery.com	MIT
jQuery-UI	https://jqueryui.com	MIT
jQuery Simple Color	https://github.com/recurser/jquery-simple-color	MIT
jQuery UI Touch Punch	https://github.com/furf/jquery-ui-touch-punch	MIT or GPL Version 2

2.2 Data requirement and data structure

The essential components for rendering 3D geological maps on the Web browser include digital elevation models (DEMs) and color tables of the ground surface and geological boundary surfaces, legend images for rendered objects and an HTML file that contains passes to the stylesheets and JavaScript libraries of the visualization tool. The color of each surface can also be given by texture image with the same range of the DEM. When borehole data are available, the list of locations and lengths of borehole data and texture images of borehole objects are additionally required. As for texture images of borehole objects, two types of images are needed: one for facies that represent the types of soil and rock and another for standard penetration test results, generally called N-values, that represent the softness/hardness of soil and rock. These files should be stored in a data directory with a specific hierarchical structure. The data directory must be provided for each 3D geological map.

The visualization tool is composed of icon images, stylesheets and JavaScript libraries. These files should be stored in an application directory on a different level from the data directory mentioned above. Accessing the HTML file in the data directory invokes JavaScript in the application directory, resulting in the rendering of 3D geological maps on the web browser.

3. FUNCTIONS

The developed tool has several functions useful for better understanding the subsurface geological structure. Figure 1 shows the operation screen of the tool. The screen consists of three parts: the display setting buttons (top left), the legend image (bottom left) and the 3D geological map (center). On the screen, the users can rotate, move and zoom in/out of the 3D geological map, as well as see attributes of geological boundary surfaces and borehole data with simple mouse operations. In addition, the visualization style of the 3D geological map can be controlled from

the display setting buttons. The details of functions available from the display setting buttons are as follows.

3.1 Function for adjusting the vertical-to-horizontal ratio

In cases of wide-area 3D maps, the vertical-to-horizontal ratio of a display screen is one of the most important factors in visualizing and understanding 3D geological structures in detail. This function allows the users to adjust the vertical-to-horizontal ratio of 3D rendering space in whole-number units by moving the slide bar.

3.2 Function for toggling visibility of surfaces

In focusing on the shape of specific boundary surfaces and in understanding the intersection relationship between boundary surfaces, it is often necessary to hide unrelated surfaces. This function allows the users to switch the show/hide mode of individual geological boundary surfaces, including ground surfaces. In show mode, each boundary surface can also be visualized in a solid color style or wireframe style (Figure 2). When a texture image of a surface is available, its color is used instead of solid color.

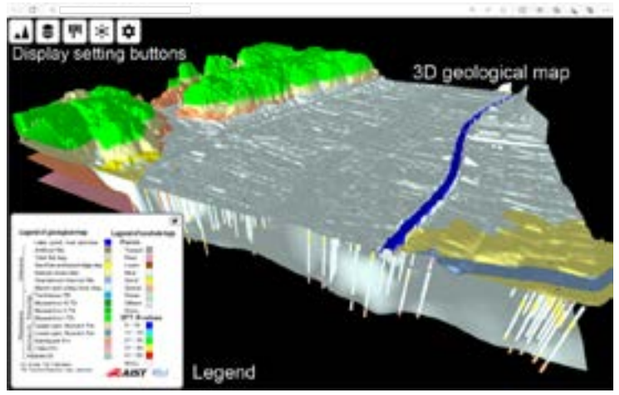

Figure 1. Operation screen of the visualization tool.

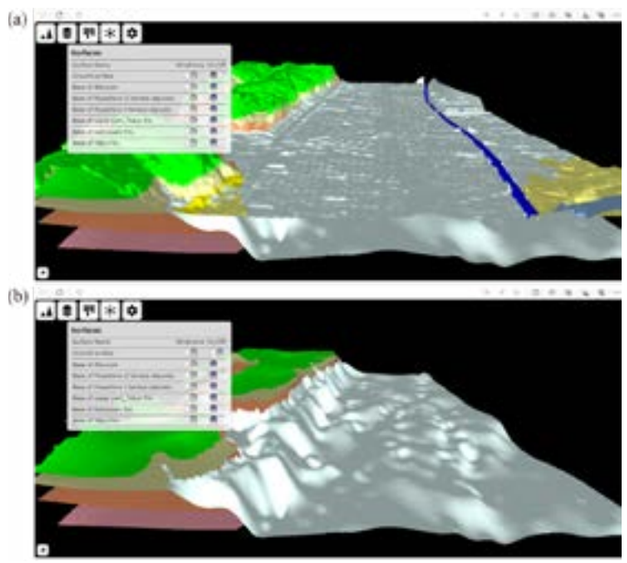

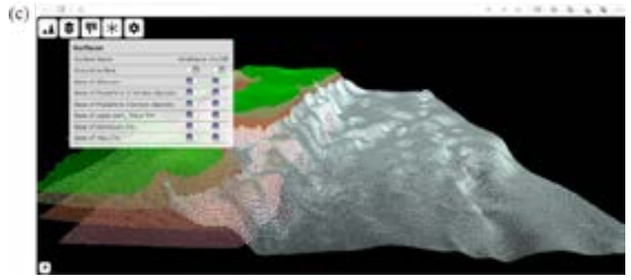

Figure 2. Example of geological boundary surfaces visualization. (a) texture image style with the ground surface, (b) solid color style without the ground surface and (c) wireframe style without the ground surface.

3.3 Function for toggling texture images of borehole objects

The color of borehole objects helps to understand changes in geotechnical properties within geological layers defined by the surface-based geological model. This function allows the users to switch the texture images of borehole objects from two types: Facies and N-values (Figure 3). In the case of N-values, softer and harder parts are colored blue and red, respectively.

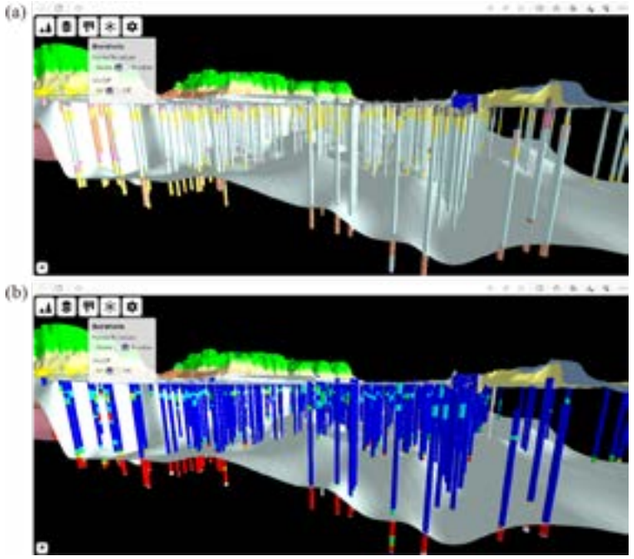

Figure 3. Texture images of borehole objects. (a) Facies, (b) N-values.

3.4 Function for adjusting the position of the light source

The clarity of the visualized geological structure greatly depends on how it is lighted. This function allows the users to adjust the position of the light source in 3D rendering space by giving the azimuth, which represents the horizontal angle from the North and the dip angle.

4. APPLICATION EXAMPLE

The developed tool has been implemented on the GSJ website “Urban Geological Map”. Figure 4 shows an example of the 3D geological structure within the area of 2.5×2.5 km in central Tokyo visualized by our tool. The vertical-to-horizontal ratio of 3D rendering space is eight. Texture images of borehole objects are the ones from N-values.

Figure 4a clearly shows that a geological layer composed of soft sediments, which have a high risk of amplifying earthquake ground motion, thickly distributes in shallow subsurface in the lowland area. In Figure 4b, we can see that the geotechnical properties greatly vary in the geological layers and that soft sediments distribute also in the upland area, where generally expected to be composed of hard ground. Thus, using this tool, anyone can easily understand the distribution patterns of geological layers in shallow subsurface in detail for activities to mitigate earthquake-induced disasters in urban areas.

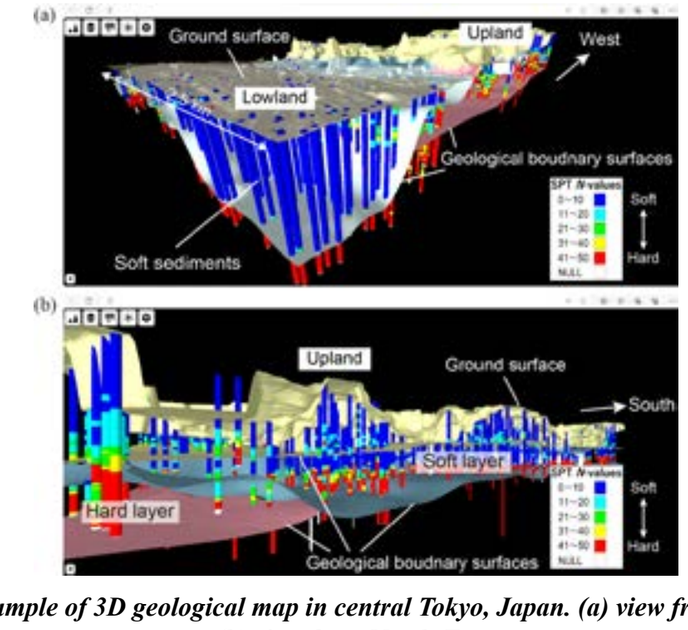

Figure 4. Example of 3D geological map in central Tokyo, Japan. (a) view from North-East, (b) view from North-East.

5. CONCLUSIONS

We have developed the WebGL-based visualization tool for 3D geological structures in shallow subsurface in urban areas. The developed tool not only enhances understanding of shallow subsurface geological structures but also facilitates the utilization of shallow subsurface geoinformation in urban areas. The next works are to implement the function for generating cross-sectional images of geological structures along arbitrary lines and for importing map information from WMS and WMTS into the 3D rendering space.

6. REFERENCES

Naya T., Nonogaki S., Komatsubara J., Miyachi Y., Nakazawa T., Kazaoka O., Shiozaki S., Kagawa J., Yoshida T., Kato A., Yabusaki H., Ogitsu T., and Nakazato H., 2018. Explanatory text of the Urban Geological Map of the Northern area of Chiba Prefecture. *Geological Survey of Japan*, AIST, 55 p.

Naya T., Komatsubara J., Nonogaki S., Ozaki M., Miyachi Y., Nakazawa T., Nakazato H., Suzuki T., and Nakayama T., 2021. Explanatory text of the Urban Geological Map of Central Tokyo (Special Words area). *Geological Survey of Japan*, AIST, 82 p.

The Urban Geological Map of Central Tokyo, Geological Survey of Japan. https://gbank.gsj.jp/urbangeol/en/map_tokyo/index.html.

BUILDING A 3D INFORMATION MODEL FOR UNDERGROUND COAL MINES

Pham Van Chung*, Cao Xuan Cuong, Le Van Canh, Nguyen Quoc Long, Le Thi Thu Ha, Nguyen Viet Nghia

Department of Mine Surveying, Faculty of Geomatics and Land Administration, Hanoi University of Mining and Geology, Vietnam

*Corresponding author. Email: phamvanchung@humg.edu.vn

ABSTRACT

Recently, the digital mine, with a high ability to share mining information through the lifecycle of a mine, has played an increasingly important role in ensuring the safe and effective management and operation of mining activities. Build Information Model (BIM) has been widely used in the field of construction and is considered an advanced technology for construction management. In this study, a 3D information model for a mine is built using BIM. The Industry Foundation Classes (IFC) standard is used to define the mining information model. Point clouds collected by Terrestrial laser scanning (TLS) provide geometric and attributive information for building BIM models. This information model was applied to the NUI BEO underground coal mine. The information model was built for important structures of the mine, including the mine shaft and tunnels. The results show that BIM with the IFC standard can be built for the underground coal mine with a high level of detail and accuracy.

1. INTRODUCTION

The mining industry is one of the important sectors of an economy and plays a key role in the development of each country (Duncan & Abdul Rahman, 2015). As the demand for raw materials for the rapid development of the world economy is often at a high level, the role of the mining industry has been increasingly important. This becomes one of the main driving forces for the development of mining technologies. While the rapid development of mechanical and information communication technologies with heavy semi- or automatic equipment can improve the speed of activities in a mine, this also creates much higher requirements for collecting, storing and representing mining data, including geospatial data. This is because geospatial data is about the spatial information of mines, which is fast and continuously changing as the high productivity of advanced equipment, such as large-scale satellite bulk dozer push, semi-autonomous blast hole drilling, semi-autonomous tractor system (SATS) technology.

Recently, in the technical operation of mines, two-dimensional (2D) AutoCAD drawings are still mainly used. These are the main electronic documents for the management of a mining project. However, this kind of document makes it difficult to find errors and unable to display information, especially in the third dimension. It is noted that 2D drawings are considered traditional tools and have the disadvantage of inefficiency in optimizing mine project operations processes (Li et al., 2021). Therefore, it is necessary to build a 3D information system with functions such as design and display to simulate 3D designs, build virtual reality, computer graphics, construction operation process and finally, the construction and sharing of information for a mining project.

Building Information Modeling (BIM) is a technology for creating, managing and effectively using information about objects characteristic of construction projects throughout the project's life cycle from design, construction, operation and maintenance. Information in BIM includes geometric information and non-geometric information. BIM is widely used in construction such as bridge construction (Qin et al., 2021; Wei et al., 2021; Zou et al., 2016), building houses and heritage and culture structures (Karachaliou et al., 2019; Simeone et al., 2019), tunnels (Li et al., 2021; Zhanping et al., 2019), train line (Xu et al., 2014). With wide applicability in the field of construction engineering, BIM provides new ideas and methods for mine information modeling and positively affects the mining industry (Li et al., 2021).

In this study, BIM is used as the 3D information model for an underground coal mine that has mine shafts to access deep coal beams. For collecting geometric information and other attributes of underground coal mines, terrestrial laser scanning (TLS) is employed. TLS has been used effectively for the 3D data collection of the surface of complex objects, thereby allowing the construction of 3D models (Thomson & Boehm, 2015). This is thanks to TLS's ability to collect millions of 3D surface points of objects in a short time with mm-level accuracy (Cao Xuan Cuong et al., 2021). In addition, the intensity data collected via the RGB camera built into the TLS scanner enables the creation of detailed point cloud data and a highly realistic representation of the scanned object surface. The Scan-to-BIM method (Abreu et al., 2023; Koch et al., 2017) is used to reconstruct 3D models of objects. The accuracy of 3D models is assessed by two methods, comparing with the direct measurement and by comparing its surface mesh with its TLS point cloud.

2. STUDY AREA AND DATA COLLECTION

2.1 Study area

In this study, the study area selected is the mining infrastructure of Nui Beo Coal Joint Stock Company (Figure 1). This is an underground coal mine with an area of 12 hectares for the surface plant infrastructure (SPI), built in 2012 at an altitude of +35 m and access to coal beams by mine shafts and a variety of tunnels. On the site of SPI, two mine shafts are built with a steel structure with a height of 50 m, equipped with a transport system. While an elevator or cage in the primary shaft is used to transport people, the secondary one is used to transport construction materials and rock and coal in and out of tunnels. At the time of this study, the two mine shafts were serving underground mining service from the seam to -350 m, with a design capacity of two million tons of coal/year. In addition to the two mine shafts, to ensure the production of the mine, other ancillary structures were also built, such as plants and office buildings with brick walls and iron roofs. The mine shafts have hoistrooms, headframes and sheave wheels, which have complex structures (Figure 1-a). The underground infrastructure of the mine includes 6.8 km of tunnels for different purposes, such as transportation tunnels, working tunnels and ventilation tunnels (Figure 1b).

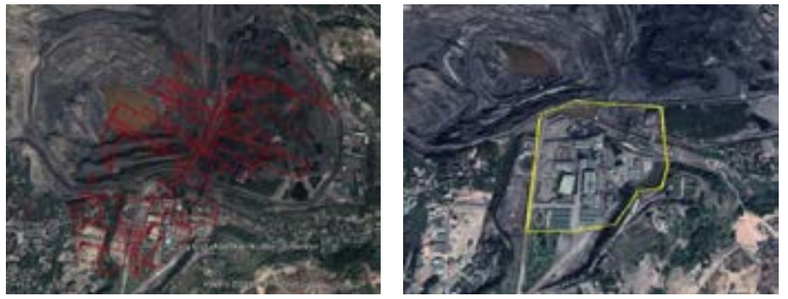

(a) *(b)*

Figure 1. Location of (a) the surface plant infrastructure (the yellow boundary) and (b) the system of tunnels (the red lines).

2.2 Data collection

The procedure of scanning the coal mine's SPI is illustrated in Figure 2. It includes five main steps, such as planning and preparing equipment, designing the TLS laser scanning station, establishing TLS targets for registration, performing TLS scanning and processing data and exporting TLS point clouds. For scanners that provide the centering mode like total stations, each position of the scanner and control points for back-sights can be measured.

Planning is especially important because it is the process that shapes the entire content of the TLS scan. Stemming from the project's requirements, based on the results of the field survey of the TLS scanning area, select appropriate equipment and arrange human resources for implementation. In this study, the following equipment was used (see Table 1).

Table 1. Some comments on tables.

No	Name of survey equipment	Quantity
1	Topcon GLS 2000 scanner	01
2	Faro Focus X130 scanner	01
3	Leica FlexLine TS 09 total station	01
4	Topcon GLS 2000 scanner	01

Based on the characteristics of the TLS scanning area based on the specifications of the TLS scanner, design the scanning stations to cover as many surfaces as possible, thereby reducing the number of scanning stations. It should also be noted to ensure the overlap of scan data between stations to serve later scan registration.

Establish ground control points (GCPs) and targets for each scan pairing. This is for two purposes, including scan registration and transferring the point cloud coordinate system to the geodetic coordinate system. Therefore, at least 3 focal points should be arranged and measured using an electronic total station.

For processing TLS data, each laser scanner has its own software, e.g. Faro scanner with SCENE, whereas the Topcom GLS scanner with Magnet College. However, they have the same processing procedure, including processing for each single scan station before registering all stations and the resulting point clouds (PCs) can be exported to a variety of formats, such as E57, LAS and ptx.

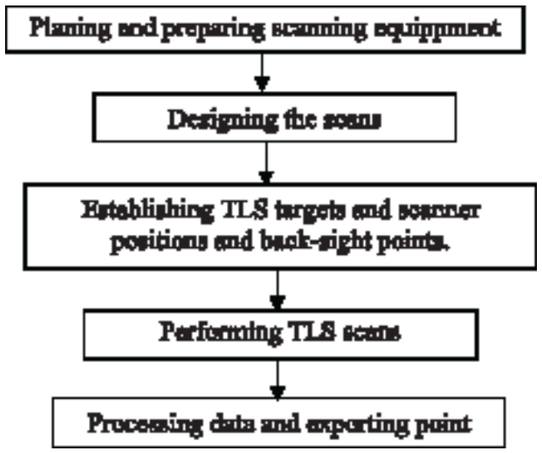

Figure 2. Collecting and processing data procedure.

The data collection is divided into three parts: (1) TLS scanning of the SPI, (2) TLS scanning of the secondary mine shaft and (3) TLS scanning of tunnels. Specifically, part one was performed using a Faro Focus X130, while parts two and three were performed using a Topcon GLS 2000. In part one, there were seven TLS stations to collect data inside the headframe and eight TLS stations collecting data outside the headframe. A number of checkerboards are measured in their coordinates based on survey control points using a Leica FlexLine TS09 total station. Their coordinates are in the VN2000 coordinate system. The GLS 2000 scanner has the function of centering and leveling like a total station, so it can be more useful for the direct registration of point clouds. This scanner was employed to scan the shaft and there were a total number of 86 stations with almost 24 hours of scanning. When scanning tunnels, each tunnel was scanned by the GLS 2000 scanner with its function of resection. The control points in each tunnel were used to position each scan station by resection, so its point cloud was directly measured in the VN 2000 coordinate system. The results were a PC with a number of 172,684,627 points (Figure 3a) with a registration error of 8 mm. PCs were exported to E57 format and ready for the next steps.

(a) *(b)*

Figure 3. Result of TLS scanning for part 1: (a) Outside of the headframe; (b) inside of the headframe.

Scanning data of parts 2 and 3 is performed using Topcon's Magnet College software. The processing results are point clouds for the inside of the shaft (Figure 4) and tunnels (Figure 5). PCs are also exported to the E57 format.

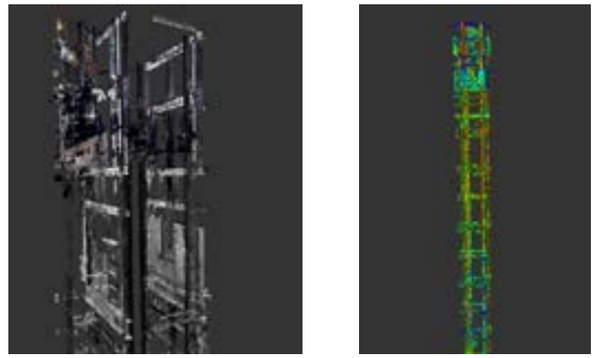

(a) *(b)*

Figure 4. Scanning results of part 2 (displayed in Autodesk RECAP Pro software).

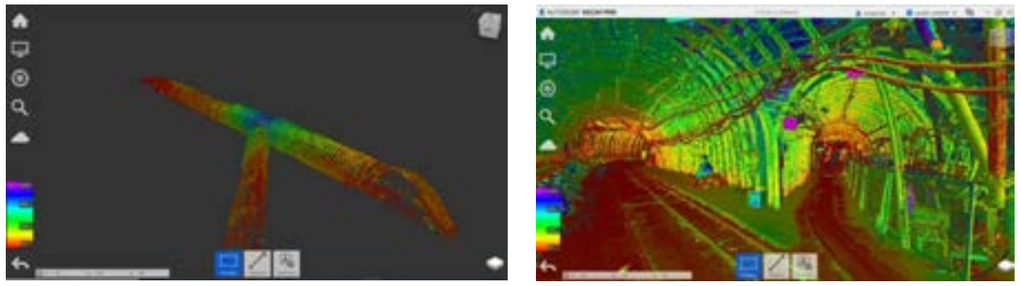

(a) *(b)*

Figure 5. Scanning results of part 3 (displayed in Autodesk RECAP Pro software).

3. METHODOLOGY

3.1 Industry Foundation Classes (IFC) standard of BIM

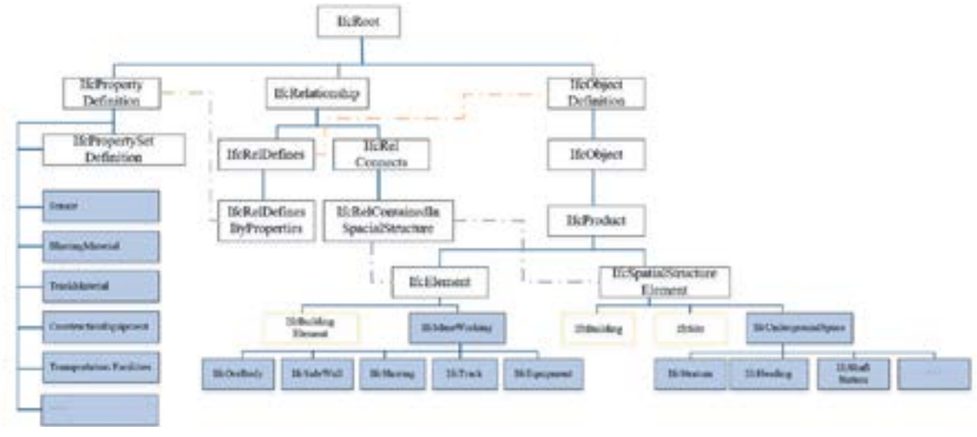

Figure 6. IFC extension for the mine working information model (Li et al., 2021).

In a mining project, there is always a combination of many different fields, such as construction, mining, geology, geodesy, electromechanical, environment and transportation. Therefore, data for BIM can come from a variety of sources and in different formats. To facilitate the exchange of data

between different sources, software, or formats for BIM model management for mining projects, the IFC (Industry Foundation Classes) standard, an open format standard, is used. The IFC uses the EXPRESS language to define the information. The IFC data format contains geometric data and other information, such as the relationship between the Model's elements. The structure of the IFC standard consists of four layers: The domain layer, the interoperability layer, the core layer and the resource layer. However, although many entities and their attribute were developed by IFC to describe objects, services and visual information, they cannot satisfactorily describe our working project. In this study, the mine working information model with IFC extension proposed by Li et al., (2021) was employed (Figure 6).

3.2 Method of BIM generation based on TLS point clouds - Scan-to-BIM

This is a common method for integrating BIM and TLS laser scanning technology. TLS technology provides raw data for BIM, which is point clouds. TLS point clouds, after noise filtering and classified into different objects before extracting their geometrical information. In other words, the model parameters of the objects are estimated. After this step, if there is a lack of objects' important dimensions, direct measurement of these objects can be performed, e.g., the tape or laser meter-based methods. Based on parametric models, a complete BIM model is created after data transformation. For complex objects, the modeling process needs to be done manually with specialized software to produce highly accurate and detailed results. For the objects in the mine, most of them have industrial structures such as beams, trusses and columns, so it is possible to automate the modeling process. However, in fact, there are always many differences between the as-designed and as-built objects due to construction and the impact of environmental factors over time, so to ensure accuracy, the semi-automatic method is suitable for projects in the mining field.

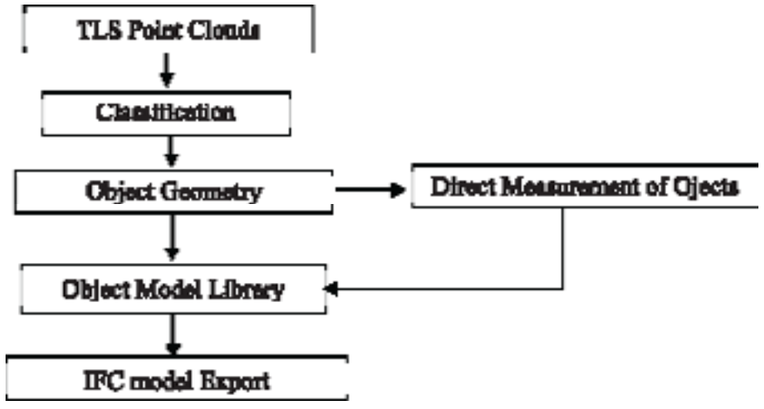

Figure 7. Flowchart of BIM generation from TLS point clouds.

3.3 Level of Details (LOD)

LOD is to determine the quality of models. In this study, a LOD proposed by Trimble (2013) was used. There are five LODs, including LOD 100 (Conceptual), LOD 200 (Approximate Geometry), LOD 300 (Precise Geometry), LOD 400 (Fabrication) and LOD 500 (As-built Model). Table 2 provides some descriptive information about each LOD.

Table 2. Description of BIM LOD (Source: BIM Forum).

LOD 100	LOD 200	LOD 300	LOD 400	LOD 500
Conceptual	Approximate geometry	Precise geometry	Fabrication	As-built
				
The Model Element may be graphically represented in the Model with a symbol or other generic representations but does not satisfy the requirements for LOD200. Information related to the Model Element (i.e., per square meter, etc.) can be derived from other Model Elements.	The Model Element is graphically represented in the Model as a generic system, object, or assembly with the approximate quantities, size, shape, location and orientation. Non-graphic information may also be attached to the Model Element.	The Model Element is graphically represented in the Model as a specific system, object, or assembly accurate in terms of quantity, size, shape, location and orientation. Non-graphic information may also be attached to the Model Element.	The Model Element is graphically represented in the Model as a specific system, object, or assembly that is accurate in terms of quantity, size, shape, location and orientation with detailing, fabrication, assembly and installation information. Non-graphic information may also be attached to the Model Element.	The Model Element is a field-verified representation accurate in terms of quantity, size, shape, location and orientation. Non-graphic information may also be attached to the Model Element.

3.4 Evaluation of Model Accuracy

To evaluate the models' accuracy, Hausdorff's distance from the original TLS point cloud to the Model is calculated based on the "cloud/mesh" distance calculator provided by Cloudcompare software. It is the distance between the TLS point cloud and the corresponding triangular surface of the exported 3D Model in OBJ format.

In addition, the geometric dimensions of the BIM models are compared to truth dimensions. For the ground truth dimension, the distance between shaft rails or guides was measured by a laser meter every 9-meter vertical distance along the shaft. This was performed after each scanning station of the shaft. These distances are used to evaluate the accuracy of the 3D Model of shaft rails using the following equation:

$$\Delta D_i = D_i - d_i;\ (i = 1, 2, \ldots n) \quad (1)$$

$$RMSE = \sqrt{\frac{\sum \Delta D_i}{n}} \quad (2)$$

where Di and di are distances between shaft rails measured in 3D models and by a laser meter, respectively, n is the number of measurements.

4. RESULTS AND DISCUSSIONS

Objects that were TLS scanned include Part 1 (headframes), Part 2 (mine shafts) and Part 3 (tunnels). The model generation was manually performed using AUTODESK REVIT 2023

through three steps: (1) Inserting the point cloud into REVIT; (2) Building the library of REVIT families and BIM objects; (3) Drawing models using Drawing and Editing Tools in REVIT. As this process is to visually superimpose parametric objects onto their corresponding locations in the scan point cloud, it can obtain highly accurate models. However, the limitation of space in tunnels and mine shafts is unavoidable, so some dimensions of objects cannot be collected or measured and their design information can be used. All objects were preprocessed and reconstructed in LOD 500. This LOD is as-built and requires the highest effort of drawing models.

4.1 BIM modeling objects in Part 1

Figure 8 shows the results of drawing BIM models of some objects of the shaft on the ground and in the headframe. This part is mainly formed by columns and beams (Figure 8). REVIT offers a library of REVIT families, such as beams and columns. As they are made according to the industry standard, they are standardized in materials, shapes and dimensions, such as steel I-, C-, U- and L-beams (Figure 9). In addition, REVIT allows users to edit the properties of beams. In this part, I-beams are the most common one and their dimensions, such as flange width, thickness and web thickness are various.

Figure 8. Columns and beams in the headframe of the mine shaft.

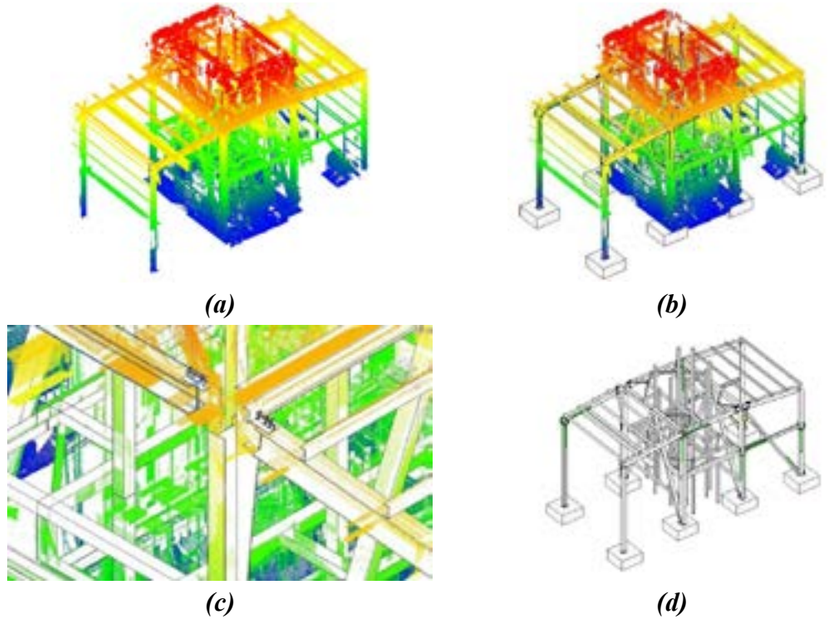

(a) *(b)* *(c)* *(d)*

Figure 9. Generation of BIM models for objects in Part 1: (a) Point cloud extracted for beams, (b, c and d) BIM models of beams built from extracted point clouds.

4.2 BIM modelling objects in Part 2

In Part 2, the BIM model of mine shafts is built (Figure 10). The depth of the mine shaft is 385 m with some components, such as concrete walls, beams at every 9-meter depth and 4 shaft rail tracks running along the shaft. Some features cannot be measured, such as the thickness of shaft walls, then the design information was used. Figure 4 shows that the data collection provided enough points for extracting the dimensions of objects, which in turn were used to reconstruct their models. In this part, IFCWall, IFCBeam and IFCCable are the most commonly used (Figure 11).

Figure 10. Laser scanning beams inside the mine shaft.

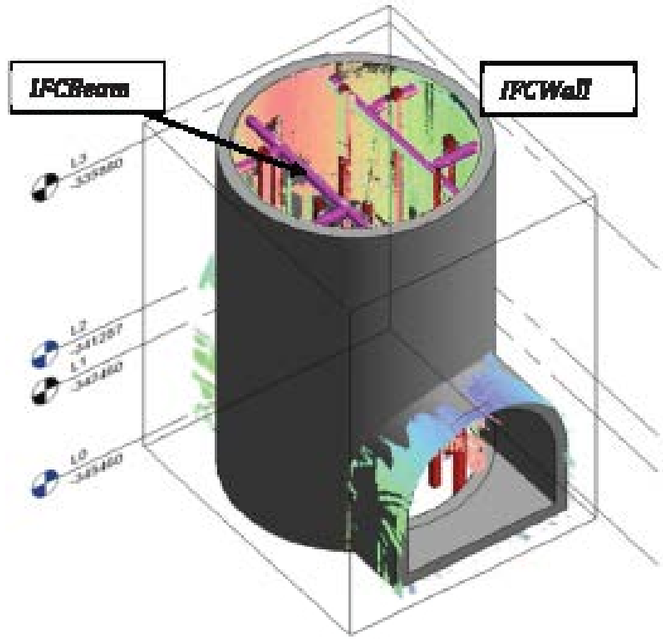

Figure 11. Generation of BIM models for the mine shaft in Part 2.

4.3 BIM modeling objects in Part 3

In Part 3, about 6.8 km length of various tunnels were modeled. They are transportation (3.5 km), working (0.5 km) and ventilation tunnels (2.8 km) (Table 3). In this part, some geometry information about beams can be obtained from point clouds, but some of their dimensions cannot be directly measured, such as flange width, web and flange thickness, so they were measured from beams in the storage place of the mine (Figure 12).

Figure 12. U-beams employed in tunnels and the measurement of their dimension using a tape.

In each tunnel, IFCBeam, IFCCable, IFCPipe and IFCTrack were used to model the tunnel (Figure 13).

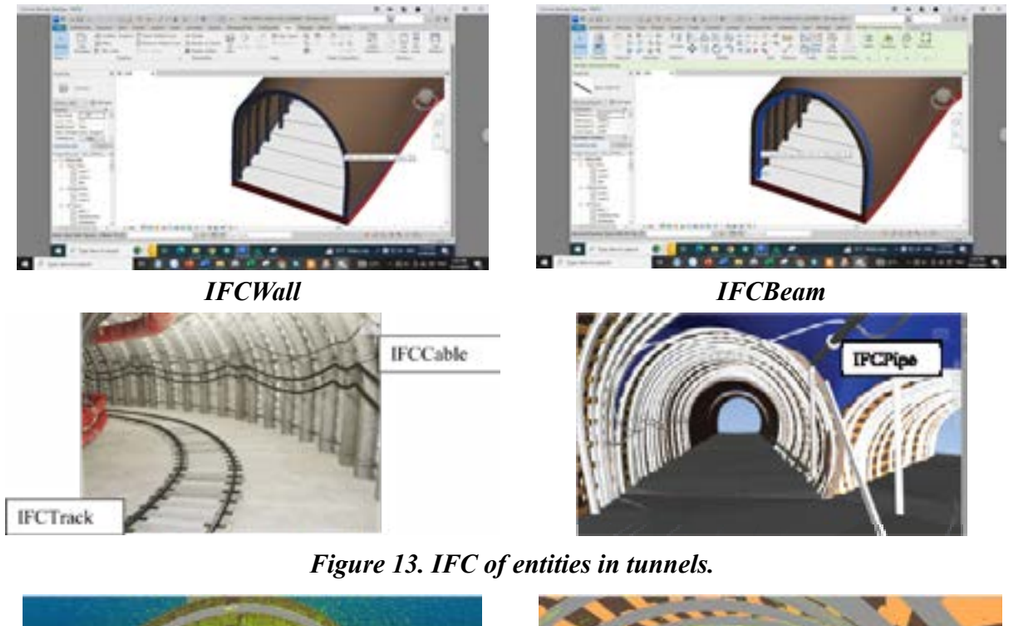

IFCWall *IFCBeam*

Figure 13. IFC of entities in tunnels.

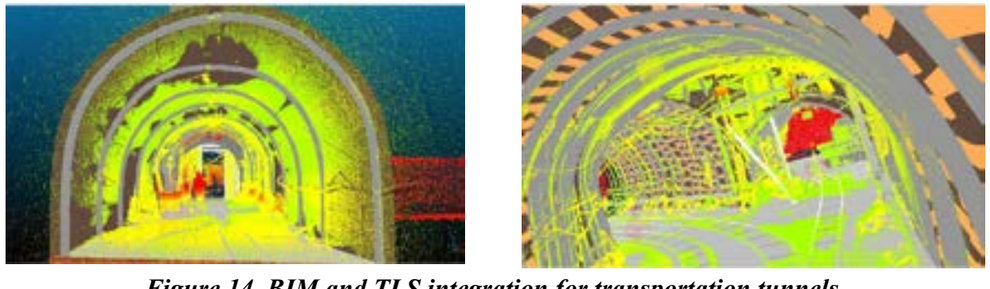

Figure 14. BIM and TLS integration for transportation tunnels.

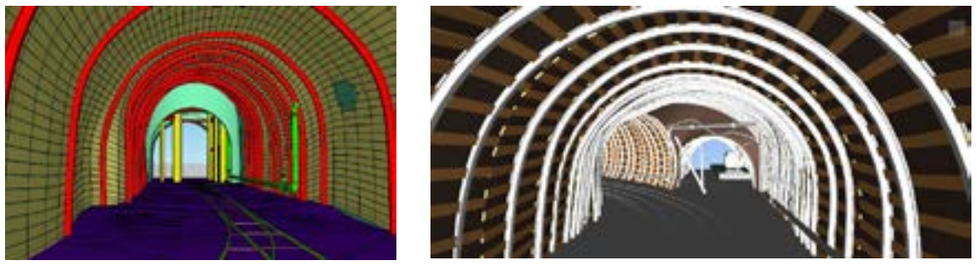

Figure 15. BIM models of transportation tunnels.

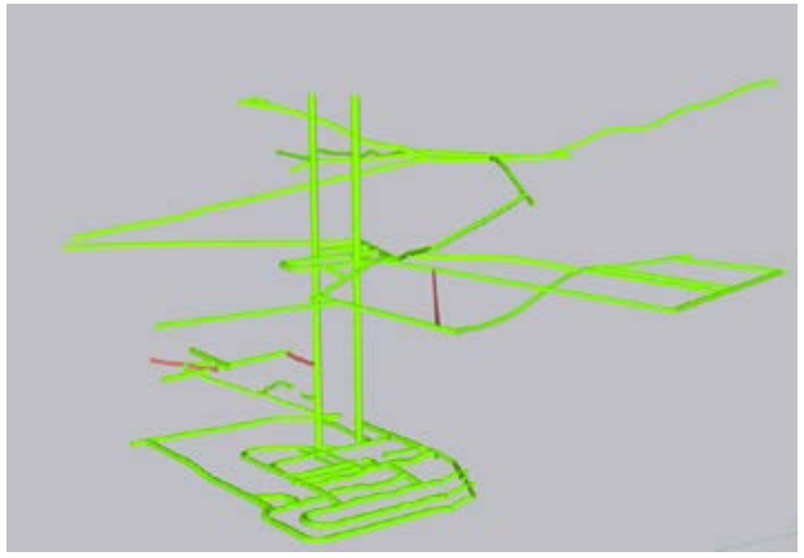

Figure 16. Overview of 3D models of Nui Beo mine shafts and tunnels.

Table 3. Summary information about the 3D model.

No	Objects	Distance (m)
1	Shaft	450
2	Transport tunnels	3,500
3	Working tunnels	500
4	Ventilation tunnels	2,800

Table 3 provides some statistics about the main objects in the underground mine which were modeled. There were 3,500 m of transport tunnels modeled for this project, followed by 2,800 m for ventilation tunnels and there were 500 m of working tunnels. Figure 16 illustrates an overview of the 3D Model of tunnels.

4.4 Model Accuracy Assessment

In order to measure the distance between shaft rail tracks along the shaft, a steel rope with a weight hung in the shaft from the ground. Its weight was put into the sump of the shaft to reduce the oscillation of the rope due to the effect of wind and water. The distance between the steel rope and each track was measured by a laser meter (Figure 17) and then the sum of the two distances is the distance between the two tracks. This distance was also measured from one track to another.

The error of each measurement was calculated by the subtraction of the two distances. The RMSE of this measurement was ± 3 mm. These distances were used to compare with those measured by BIM models (Figure 18). The result is shown in Table 4. The RMSE was ± 8 mm and this accuracy proved that TLS and BIM could be used to monitor the shaft rail tracks. This is important for the maintenance of shaft rail tracks and ensures the safety of the mine shaft's transportation.

Figure 17. Measuring the distance between two shaft rail tracks or guides for accuracy assessment.

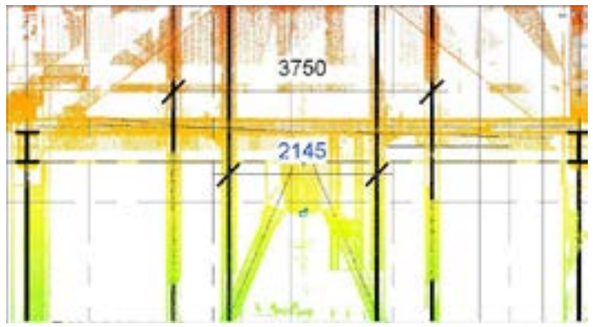

Figure 18. Distance between shaft rails measured from 3D models.

Table 4. Accuracy assessment of the mine shaft model.

Scan Stations	Distances (m)		ΔD (mm)
	Laser meter	3D model	
1	3,745	3,742	-3
2	3,749	3,750	1
3	3,754	3,758	4
…	…	…	…
43	3,740	3,737	-3
RMSE			8

For the accuracy assessment of tunnels' BIM models, Figure 19 illustrates the point cloud, which was created from the BIM model and used to calculate Cloud-to-Cloud (C2C) distances between point clouds of TLS and BIM models (Figure 20).

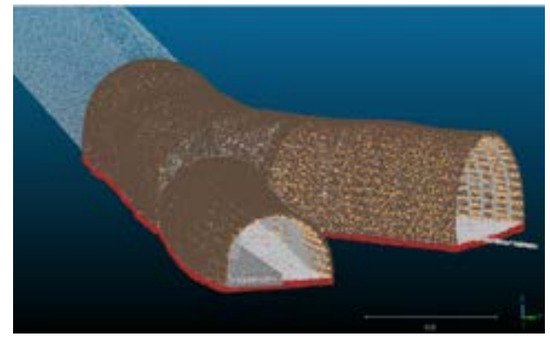

Figure 19. Point cloud of tunnels created from 3D models for comparison with their TLS point cloud.

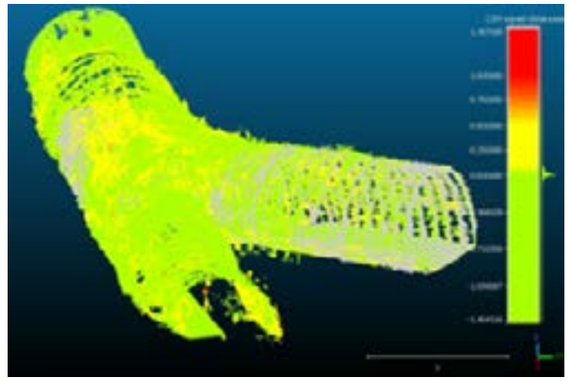

Figure 20. C2C distance map of tunnels.

5. CONCLUSIONS

In this study, we have built a 3D information model of an underground coal mine. The Scan to BIM method was applied in the Nui Beo underground coal mine, which has mine shafts for access to deep coal seams. The result shows that BIM with IFC standard is an effective solution in generating and managing 3D mine information. IFC mine working was extended and inherited from the original IFC standard for the better representation of mine working information model. There were IFCBeam, IFCWall, IFCCable, IFCTrack and IFCPipe, which were most commonly used in this study. TLS point clouds were utilized for two purposes, including reconstructing 3D models of objects and accuracy assessment. With dense and accurate point clouds, underground mining objects were reconstructed in LOD 500. However, as the unavoidable limitation of underground space leads to a lack of data for some objects, the design information was used to have important dimensions of these objects.

The accuracy of the BIM models was assessed using truth dimensions and the cloud-to-cloud distance method. While the former is based on a small number of distances measured using a laser meter and cannot show the modeling accuracy of a whole object, the latter employs point clouds to calculate C2C distances between the BIM model converted point clouds and TLS point clouds and can provide more comprehensive accuracy assessment. The result shows that BIM models were built with an RMSE of 8 mm. In addition, the safe assessment of rail tracks in the mine shaft can

be performed through the rail irregularity, which can be identified using the TLS point cloud of rail tracks and their as-designed BIM models. The comparison between TLS and as-designed BIM was performed by computing their C2C distances.

In conclusion, the integration between BIM and TLS with Scan-to-BIM and Scan-vs-BIM applications is a practical solution for the information management of underground coal mines.

6. ACKNOWLEDGMENTS

This work was financially supported by the Ministry of Education and Training (MOET) in Vietnam under grant number B2022-MDA-10.

7. REFERENCES

Abreu N., Pinto A., Matos A., & Pires M., 2023. Procedural Point Cloud Modelling in Scan-to-BIM and Scan-vs-BIM Applications: A Review. *ISPRS international journal of geo-information*, *12*(7), 260. Retrieved from https://www.mdpi.com/2220-9964/12/7/260.

Cao X. C., Le V. C., Pham V. C., Le D. T., Pham T. D., and Ngo S. C., 2021. Quality assessment of 3D point cloud of industrial buildings from imagery acquired by oblique and nadir UAV flights. *Naukovyi Visnyk Natsionalnoho Hirnychoho Universytetu, 5*, 131-139. Doi:10.33271/nvngu/2021-5/131.

Duncan E. E., & Abdul Rahman A., 2015. 3D GIS for mine development - integrated concepts. *International journal of mining, reclamation and environment, 29*(1), 3-18. Doi:10.1080/17480930.2013.828443.

Karachaliou E., Georgiou E., Psaltis D., and Stylianidis E., 2019. UAV for mapping historic buildings: from 3D modelling to BIM. *ISPRS - International Archives of the Photogrammetry, Remote Sensing and Spatial Information Sciences,* XLII-2/W9, 397-402. Doi:10.5194/isprs-archives-XLII-2-W9-397-2019.

Koch C., Vonthron A., and König M., 2017. A tunnel information modelling framework to support management, simulations and visualisations in mechanised tunnelling projects. *Automation in Construction, 83*. Doi:10.1016/j.autcon.2017.07.006.

Li W., Li S., Lin Z., and Li Q., 2021. Information modeling of mine working based on BIM technology. *Tunnelling and underground space technology, 115*, 103978. Doi:10.1016/j.tust.2021.103978.

Qin G., Zhou Y., Hu K., Han D., and Ying C., 2021. Automated Reconstruction of Parametric BIM for Bridge Based on Terrestrial Laser Scanning Data. *Advances in Civil Engineering,* 1-17. Doi:10.1155/2021/8899323.

Simeone D., Cursi S., and Acierno M., 2019. BIM semantic-enrichment for built heritage representation. *Automation in Construction*, *97*, 122-137. https://doi.org/10.1016/j.autcon.2018.11.004.

Thomson C., Boehm J., 2015. Automatic Geometry Generation from Point Clouds for BIM. *Remote Sensing, 7*(9), 11753-11775. Retrieved from https://www.mdpi.com/2072-4292/7/9/11753.

Trimble, 2013. Project Progression Planning with MPS 3.0. (2023). http://support.vicosoftware.com/FlareFiles/Content/KB/Trimble - Progression Planning V15.pdf. Retrieved from http://support.vicosoftware.com/FlareFiles/Content/KB/Trimble - Progression Planning V15.pdf.

Urda P., Aceituno J. F., Muñoz S., and Escalona J. L., 2021. Measurement of railroad track irregularities using an automated recording vehicle. *Measurement, 183*, 109765. Doi:https://doi.org/10.1016/j.measurement.2021.109765.

Wei J., Chen G., Huang J., Xu L., Yang Y., Wang J., and Sadick A. M., 2021. BIM and GIS Applications in Bridge Projects: A Critical Review. *Applied Sciences, 11*(13), 6207. Doi:10.3390/app11136207.

Xu J., Li A. H., Liu H. Q., Ye M. Z., and Zhang J. R., 2014. Application and risk analysis of BIM in railway systems. *Journal of Railway Engineering Society, 31*, 129-133.

Zhanping S., Shi G., Wang J., Wei H., Wang T., and Zhou G., 2019. Research on management and application of tunnel engineering based on BIM technology. *Journal of Civil Engineering and Management, 25*, 785-797. Doi:10.3846/jcem.2019.11056.

Zou Y., Kiviniemi A., and Jones S., 2016. Developing a tailored RBS linking to BIM for risk management of bridge projects. *Engineering Construction & Architectural Management, 23*, 727-750. Doi:10.1108/ECAM-01-2016-0009.

DETECTION OF LAND SURFACE TEMPERATURE CHANGE IN COAL MINING AREA USING REMOTE SENSING AND GIS TECHNIQUES - A CASE STUDY IN QUANG NINH PROVINCE, VIETNAM

Le Thi Thu Ha[1,2]*, Nguyen Van Trung[1,2]

[1]Hanoi University of Mining and Geology, Vietnam
[2]Geomatics in Earth Sciences Research Group,
Hanoi University of Mining and Geology, Vietnam
*Corresponding author. Email: lethithuha@humg.edu.vn

ABSTRACT

This research explores Land Surface Temperature (LST), which represents the energy exchange between the land surface and the atmosphere, as well as with the biosphere. Variations in surface temperature can lead to the formation of heat islands characterized by higher temperatures compared to surrounding areas. The study focuses on the application of Remote Sensing (RS) and Geographic Information Systems (GIS) to detect changes in LST in a coal mining area in Vietnam. Landsat images spanning from 1986 to 2022 were used to quantify these changes. The analysis revealed that the radiant temperature in 1986 ranged from 14.2℃ to 30.5 ℃, whereas in 2022, it was significantly higher, ranging from 17.4 ℃ to 32.3 ℃. A change map was created to visualize the temporal changes in land surface temperature distribution during the study period. The research employs scientific and efficient methodologies to investigate whether enhancing the ecological environment in coal-mining regions can help alleviate the conflict between human activities and nature, thus fostering sustainable development in these areas.

1. INTRODUCTION

Coal is the most important mineral resource in Vietnam and has made great contributions to Vietnam's economic development and social progress. Coal mining activities that are not well managed will have an impact on the occurrence of environmental damage. The generation and accumulation of heat is the major direct cause of spontaneous coal combustion (Binh, 2017). Open-pit mining operations are processes of denudation, handling and accumulation (Ha, 2020). Therefore, open-pit mining areas are not only affected by vegetation, soil and terrain but also create big pits, transit sites, solid waste and changes in land use land cover (LULC) (Ha et al., 2021).

The land surface temperature (LST) comprehensively reflects the energy exchange between land and the atmosphere, which is an important geophysical parameter in the ground-air system (Li et al., 2016; Zhu et al., 2016). Calculating LST from remotely sensed images is needed since it is an important factor controlling most physical, chemical and biological processes of the Earth (Becker et al., 1990;). Remote sensing instruments are key players in studying and mapping land surface temperature (LST) at temporal and spatial scales (André et al., 2015; Nguyen & Vu, 2019). Remote sensing methodology requires less time and lower cost than field methods to investigate various phenomena on the land surface (Niu et al., 2015).

Standard techniques for detecting coal fire zones encompass both geophysical and remote sensing methods. The geophysical approach involves workers carrying specialized equipment for on-site investigations, demanding significant manpower and material resources. Consequently, these methods prove inadequate for analyzing and monitoring extensive or successive coal fires across wide areas. Nowadays, a diverse range of monitoring sources and remote sensing data is at our disposal and their abundance is progressively growing. This escalation in availability underscores the heightened benefits of utilizing remote sensing technology to identify areas affected by coal fires. The advantages of using remote sensing methodology are the repetitive and consistent coverage, high resolution and evaluation of land surface characteristics (Owen et al., 1998; Trinh et al., 2017). Thermal infrared (TIR) data in remote sensing can help us obtain quantitative information of surface temperature. Coal mining has been most extensively practiced in the area of Cam Pha city, Northeast Vietnam. As a result, the original landscape has been converted to mine spoils.

The aim of the study is to generate a statute of coal mines in the area and estimate LST, then analyze the change in the distribution of LST in the area through the period of 1990-2010 and 2010-2020.

2. MATERIAL AND METHODS

2.1 Study area

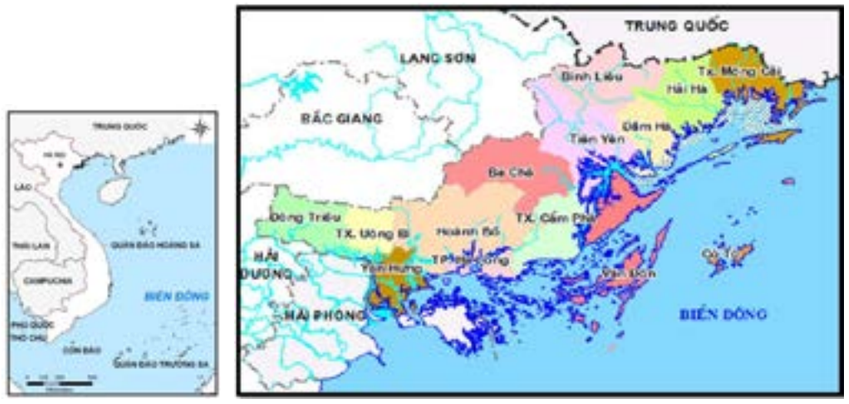

Figure 1. Location of the study area.

Quang Ninh, located in the Northeastern region of Vietnam along the coast, is often compared to a microcosm of Vietnam due to its rich diversity of geographical features, including seashores, islands, plains, hinterlands, hills, mountains and borders (Figure 1). In terms of economic development planning, Quang Ninh holds significance not only as a vital economic hub in the northern part of the country but also as an integral component of the Northern Coastal Region. It is renowned as Vietnam's primary coal mining province and is famous for being home to Ha Long Bay, a UNESCO World Heritage Site and natural marvel. Currently, Quang Ninh is actively promoting tourism as a focal point while simultaneously placing a high priority on safeguarding its marine and island ecosystems. The total economy of the region is highly dependent on coal mining.

Quang Ninh is one of the 25 provinces and cities that share a border. However, it is the only province that shares both land and sea borders with China. Its land border stretches for

118.825 km, while the delineation in the Gulf of Tonkin at sea spans over 191 km. Furthermore, Quang Ninh is one of the 28 coastal provinces and cities, boasting a coastline that extends for 250 kilometers. Within this stretch, there are 40,000 hectares of tidal flats and over 20,000 hectares of bay mangroves. It is also home to 2 out of 12 island districts in the entire country.

2.2 Data and methodology

2.2.1 Data sources

Landsat data were used for this study. Three Landsat data selected to classify land cover of the study area consist of two Landsat-5 TM data acquired in 1990 and 2010 and a Landsat-8 OLI data acquired in 2020 (GLOVIS, 2023).

The details of Landsat data are described in Table 1.

Table 1. Characteristics of satellite data used in the study area.

Sensor	TM, OLI
Spatial resolution	30 m
Processing Level	2A
Acquired Date	26/11/1990 03/12/2010 12/11/2020

While Landsat-5 TM data has 7 spectral bands, including a thermal band:

- Band 1 Visible Blue (0.45-0.52 µm) 30 m
- Band 2 Visible Green (0.52-0.60 µm) 30 m
- Band 3 Visible Red (0.63-0.69 µm) 30 m
- Band 4 Near-Infrared (0.76-0.90 µm) 30 m
- Band 5 Near-Infrared (1.55-1.75 µm) 30 m
- Band 6 Thermal (10.40-12.50 µm) 120 m
- Band 7 Mid-Infrared (2.08-2.35 µm) 30 m

Ground Sampling Interval (pixel size): 30 m reflective, 120 m thermal

The details of Landsat 8-9 OLI and TIRS data are described in Table 2.

Table 2. Landsat 8-9 Operational Land Imager (OLI) and Thermal Infrared Sensor (TIRS).

Bands	Wavelength (micrometers)	Resolution (meters)
Band 1- Coastal aerosol	0.43-0.45	30
Band 2- Blue	0.45-0.51	30
Band 3- Green	0.53-0.59	30
Band 4- Red	0.64-0.67	30
Band 5- Near Infrared (NIR)	0.85-0.88	30
Band 6- Shortwave Infrared (SWIR) 1	1.57-1.65	30
Band 7- Shortwave Infrared (SWIR) 2	2.11-2.29	30
Band 8- Panchromatic	0.50-0.68	15

Bands	Wavelength (micrometers)	Resolution (meters)
Band 9- Cirrus	1.36-1.38	30
Band 10- Thermal Infrared (TIRS) 1	10.6-11.19	100
Band 11- Thermal Infrared (TIRS) 2	11.50-12.51	100

2.2.2 Method of determining the surface temperature from the infrared thermal images

To calculate land surface temperature, in the first step, Landsat 5 TM band data must be converted to TOA spectral radiance using the radiance rescaling factors provided in the metadata file (LANDSAT Conversion to Radiance, Reflectance and At-Satellite Brightness Temperature):

$$L_\lambda = M_L.Q_{cal} + A_L, \quad (1)$$

where:

L_λ - TOA spectral radiance (Watts/[m²*srad*µm]),

M_L - Band-specific multiplicative rescaling factor from the metadata (RADIANCE_MULT_BAND_x, where x is the band number),

A_L - Band-specific additive rescaling factor from the metadata (RADIANCE_ADD_BAND_x, where x is the band number),

Q_{cal} - Quantized and calibrated standard product pixel values (DN).

Table 3. LANDSAT 5 TM and LANDSAT 8 OLI spectral radiance M_L, A_L dynamic ranges.

Data type	LANDSAT 5 TM	LANDSAT 8 OLI
Band	6	7
M_L	0.055×10^{-4}	3.3420×10^{-4}
A_L	1.18243	0.10000

(Note that $\mathbf{M_L}$ and $\mathbf{A_L}$ are derived from the metadata of Landsat 5 TM and Landsat 8 OLIdata)

In the second step, the LANDSAT thermal band data can be converted from spectral radiance to brightness temperature using the following equation (LANDSAT Conversion to Radiance, Reflectance and At-Satellite Brightness Temperature):

$$T = \frac{K_2}{\ln(\frac{K_1}{L_\lambda}+1)}, \quad (2)$$

where: T- At satellite brightness temperature (K)

K_1- Calibration constant 1 [W/(m².sr.µm)]

K_2- Calibration constant 2 [K]

Table 4. LANDSAT 5 TM and LANDSAT 8 OLI thermal band calibration constants.

Data type	LANDSAT 5 TM	LANDSAT 8 OLI
Band	6	7
K_1 (W/(m².sr.µm))	666.09	774.89
K_2 (Kelvin)	1,282.71	1,321.08

For determining a land surface temperature from LANDSAT data, the land surface temperature can be calculated by the following equation (Grishchenko, 2012; Trinh, 2014; Kumar, 2012):

$$T = \frac{K_2}{\ln(\frac{K_1}{L_\lambda} + 1)}, \quad (3)$$

where: T- brightness temperature (K°)

λ- wavelength (11.5 μm)

ε- land surface emissivity, $\rho = \frac{h.c}{\sigma}$

h- Plank's constant ($6{,}626 \times 10^{-34}$ J.sec)

c- velocity of light ($2{,}998 \times 10^{8}$ m/sec)

σ- Stefan Boltzmann's constant, which is equal to 5.67×10^{-8} $Wm^{-2}K^{-4}$.

3. RESULTS AND DISCUSSION

3.1 Evaluate the accuracy of surface temperature extraction results from Landsat satellite images

To assess the accuracy of the current status of land surface temperature values in the study area, the research team collected and compared data from environmental monitoring results in Quang Ninh province in the period 2015-2020 with frequency. Two times/year at 16 locations (Table 5).

In addition, to have a more scientific basis for evaluating the reliability of extracting surface temperature values from remote sensing images, the research team added 16 additional temperature monitoring points in each month, January 2021. Results are summarized in the following Table 5.

Table 5. Assessing the difference in surface temperature values in the Cam Pha - Ha Long area in 2020.

No	Monitoring location	Temperature value		
		Temperature values in December 2020 and January 2021	Temperature value from Landsat 8 OLI image in December 2020	Difference in temperature value (°C)
1	Vietnam-Soviet Friendship Cultural Palace, Ha Long city	23.8 °C	27.1 °C	-3.3
2	Cai Dam market, Bai Chay	24.0 °C	28.0 °C	-4.0
3	Department of Natural Resources and Environment	23.1 °C	24.8 °C	-1.7
4	Ha Tu market, Halong city	23.5 °C	28.8 °C	-5.3
5	Dia Chat market, Campha city	24.2 °C	29.8 °C	-5.6
6	Cam Pha square, Campha city	24.0 °C	29.1 °C	-5.1
7	Mong Duong river, (21°06'04,4" N; 107°33'51,0" E)	22.5 °C	20.9 °C	1.6
8	Mong Duong river, (21°06'08,1" N; 107°34'99,4" E)	22.2 °C	20.2 °C	+ 2.0
9	Cau 2 River, (20°99'96,8" N; 107°29'75,42" E)	22.5 °C	20.5 °C	+ 2.0
10	Cau 2 River, (21°00'97,1" N; 107°29' 94,54" E)	22.5 °C	20.7 °C	+1.8
11	Cau 2 River, (21°00'98,7" N; 107°29'95,48" E	22.9 °C	20.9 °C	+ 2.0
12	Location of the discharge gates behind the Coc Sau mine treatment system (21°00'28,3" N;107°32'51,8" E).	23.5 °C	22.5 °C	1.0
13	Location of the discharge gates behind the Coc Sau mine treatment system (21°00'96,5" N; 107°32'60,0" E);	23.2 °C	22.2 °C	1.0
14	Lo Phong river, (20°95'68,48"N;107°17'32,58" E)	21.6 °C	19.3 °C	2.3
15	Lo Phong river,(20°96'47,8"N; 107°16'03,65"E)	25.0 °C	23.7 °C	1.3
16	Lo Phong river, (20°97'41,9"N; 107°14'54,1" E)	24.9 °C	27.0 °C	-2.1

The assessment results comparing temperature values extracted from remote sensing images with those from monitoring points in 2020 reveal a notable disparity, particularly in regions with high population density. In these areas, the temperature values measured on the images often appear higher than the actual observed values. This discrepancy arises because the surface temperature of objects is pinpointed precisely at that pixel on the image, while field measurements can be influenced by weather conditions, wind, humidity and other factors.

In a general sense, despite some deviations in the baseline temperature values at individual points, the average temperature values across the entire area, as determined from remote sensing images and monitoring data, do not exhibit significant differences. However, variations are more pronounced in coastal regions, areas featuring extensive river and lake systems and densely populated zones. Therefore, these findings underscore the reliability and feasibility of utilizing Landsat image data for constructing large-scale surface temperature maps within the study area.

3.2 Spatial distribution of radiant surface temperature in the Campha-Halong city, Quang Ninh, in 1990, 2010 and 2020.

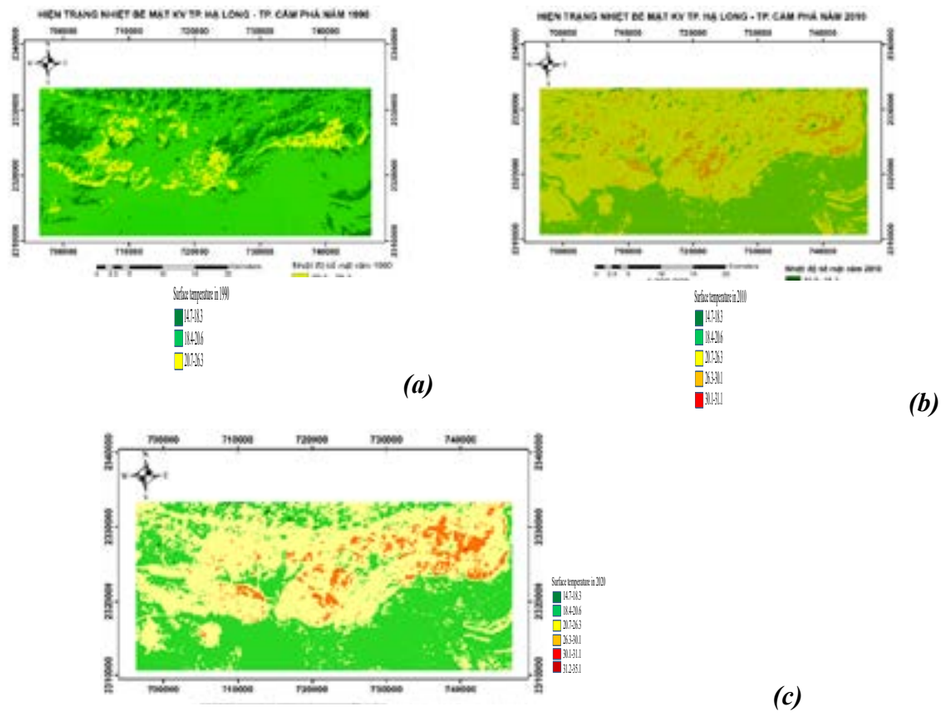

Figure 2. Spatial distribution of radiant surface temperature in the Campha-Halong city.

According to the findings depicted in Figure 2, starting from 1990, the surface temperature remained below 30 °C, indicated by the yellow color on the map (a). However, in the surface

temperature maps for 2010 and 2020, there is a noticeable expansion of regions where temperatures exceed 30 °C and some areas have even experienced surface temperature increases of up to 35 °C (b, c).

This observation underscores the clear connection between surface temperature variations and changes in land use, primarily driven by socio-economic development initiatives in Quang Ninh province. Notably, areas characterized by open-pit mining activities, such as Coc Sau, Deo Nai, Cao Son in Cam Pha City, Nui Fat and Ha Tu in Ha Long city, exhibit a notable and abrupt rise in temperature when compared to their surrounding areas.

3.3 Changes in radiant surface temperature in the Campha-Halong city, Quang Ninh from 1990 to 2020.

The surface temperature fluctuation maps in Figure 3 reveal some noteworthy trends. During the period from 1990 to 2010, surface temperature fluctuations there emerged areas where temperature fluctuations exceeded 6 degrees Celsius, notably in expanded mining regions and areas affected by industrial activities.

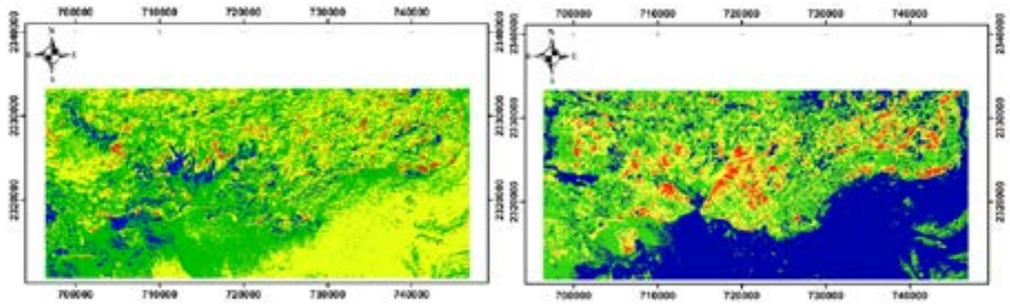

(a) *(b)*

Figure 3. Changes in radiant surface temperature in the Campha-Halong city, Quang Ninh from 1990-2010 (a), from 2010-2020 (b).

Moving forward to the periods from 1990 to 2010 and from 2010 to 2020, the maps illustrate a further expansion of areas experiencing temperatures surpassing 6 degrees Celsius, now encompassing regions with altered surface cover. This clearly demonstrates a correlation between surface temperature alterations and changes in land use driven by socio-economic development initiatives within Quang Ninh province.

The results concerning surface temperature fluctuations in various time spans indicate that coal mining, waste disposal and environmental remediation activities have predominantly expanded over the past two decades. This expansion coincides with a significant reduction in vegetation cover and bare soil areas. Additionally, the area of surface water and bare land has considerably decreased due to reclamation processes along coastal areas for tourist development on residential land. This shift in land use for socio-economic development has contributed to rising surface temperatures, further exacerbated by the context of climate change.

The initial surface temperature maps, depicting temperature changes over ten-year intervals at various locations, provide a visual representation of the distribution of these temperature alterations.

4. CONCLUSION

The approach of using Landsat data's thermal infrared bands to ascertain surface temperature proves highly effective for extensive study areas, yielding historical data. This is particularly valuable for regions where surface cover experiences fluctuations due to activities like mineral extraction and urban expansion, notably in coastal tourism zones.

Landsat satellite images, with their spatial resolution ranging from 60 to 100 meters for thermal infrared channels, offer suitable data for calculating surface temperature across vast study areas encompassing numerous coal mines and an extensive coastline within Quang Ninh province.

The outcomes of the surface temperature analysis reveal that over the past two decades, activities such as coal mining, waste disposal and environmental remediation have expanded their geographical footprint. This expansion has led to significant reductions in both vegetation cover and exposed soil areas. Additionally, the extent of surface water and open land has considerably diminished due to coastal land reclamation for residential and tourist development. The transformation of land use for socio-economic development purposes has contributed to elevated surface temperatures. Moreover, within the context of changing atmospheric conditions, temperatures are experiencing further increases.

The surface temperature maps, showcasing temperature changes over the past 30 years, indicate the need for further investigations into temperature variations across diverse geographical locations. Such studies would provide a more comprehensive understanding of the distribution of these temperature changes.

5. REFERENCES

André C., Ottlé, C., Royer A, and Maignana F., 2015. Land surface temperature retrieval over circumpolar Arctic using SSM/I–SSMIS and MODIS data. *Remote Sensing of Environment*, *162*, 1-10.

Becker F., and Li Z. L., 1990. Towards a local split window method over land surfaces. *International Journal of Remote Sensing*, *11*(3), 369-393.

Binh N. V., 2017. Identify risks and challenges affecting the sustainable development of the coal industry. http://tapchitaichinh.vn/tai-chinh-kinh-doanh/tai-chinh-doanh-nghiep/nhan-dien-nguy-co-va-thach-thuc-tac-dong-den-su-phat-trien-ben-vung-cua-nganh-than-125692.html.

GIS Imagine download free at http://glovis.usgs.gov.

Ha L. T. T., Trung N. V., Lan P. T., and Ai T. H., 2021. Impacts of urban land cover change on land surface temperature distribution in Ho Chi Minh city, Vietnam. *Journal of the Korean Society of Surveying, Geodesy, Photogrammetry and Cartography*, *2*, Vol.39, 113-122.

Ha L. T. T., 2020. Assessing the change in vegetation cover in Cam Pha in the period 2000-2020 due to the impact of coal mining. *Mining Technology Bulletin, 4*, 63-69.

Jeanfmas, (1998). Monitoring land-cover changes: A comparison of change detection techniques. *International Journal of Remote Sensing*, *20* (1), 139-152.

Li Z.L., Duan S.B., Tang B.H., Wu H., Ren H.Z., Yan G.J., Tang R.L., and Leng P., 2016. Review of methods for land surface temperature derived from thermal infrared remotely sensed data. *Journal of Remote Sensing, 20*(5), 899-920.

Nguyen T. T., & Vu T. D., (2019). Use of hot spot analysis to detect underground Coal fires from Landsat-8 TIRS data: A case study in the Khanh Hoa Coal field, North-East of Vietnam: *Environment and Natural Resources Journal*, *17*(3), 1-10.

Niu C.Y., Musa A., and Liu Y., 2015. Analysis of soil moisture condition under different land uses in the arid region of Horqin sandy land, Northern China. *Solid Earth*, *6*, 1157-1167.

Owen T. W., Carlson T. N., and Gillies R. R., 1998. Remotely sensed surface parameters governing urban climate change. *Internal Journal of Remote Sensing*, *19*, 1663-1681.

Singh A., 1989. Review article digital change detection techniques using remotely-sensed data, *International Journal of Remote Sensing*, *10* (6), 989-1003.

Trinh L. H., Zablotskii V. R., 2017 The Application of LANDSAT Multi-Temporal Thermal Infrared Data to Identify Coal Fire in the Khanh Hoa Coal Mine, Thai Nguyen province, Vietnam. *Izv. Atmos. Ocean. Phys, 53*, 1081-1087.

Zhu Z. R, Cheng P. G, Gui X., Teng Y., Tong C. Z., 2016. Overview of surface temperature inversion algorithm. *Geomatics & Spatial Information Technology, 39*(5):70-75.

A COMBINATION OF ALOS-2, SENTINEL-1 IMAGERY FOR RAPID DEFORESTATION DETECTION IN VIETNAM

Ngo Duc Anh[1]*, Vu Anh Tuan[1], Truong Tuan Nghia[2]

[1]Earth Observation Department, Vietnam National Space Center,
Vietnam Academy of Science and Technology
[2]Information Communication and Technology Department,
University of Science and Technology of Hanoi, Vietnam
*Corresponding author. Email: ndanh@vnsc.org.vn

ABSTRACT

In recent years, the socio-economic development in Ha Long city has led to deforestation happening more often and more complicatedly, from clearing forests for vacant land for construction to burning forests for timber and many other purposes to serve human needs. The use of optical remote sensing data has low efficiency in regular forest monitoring due to the influence of tropical climate conditions and cloud cover. To address the need for timely information on lost forest areas, the improvement in monitoring frequency and the combination of multiple types of SAR (Synthetic Aperture Radar) radar images bring about more effectiveness than using a single sensor. The wavelength determines the ability to penetrate the coating object, leading to different scattering mechanisms, thereby obtaining different information about the coating. The longer the wavelength, the better the penetration ability. With the object being the forest cover, the C-band wavelength (~5 cm) receives signals about the canopy and some small branches, generating volume scattering inside the canopy, while the L-band wavelength (~23 cm) acquires information about the tree branches.

This paper focuses on combining two different wavelength SAR data types (C-band and L-band), HV and HH polarizations to detect clear-cut and forest fires. The author uses the method of comparing the backscatter values before and after deforestation to detect forest loss, with the Sentinel-1 time series data using the RCR (Radar Change Ratio) method, while the three ALOS-2 image scenes use the RGB composite method. The results show that the C-band SAR (Sentinel-1) data can detect deforestation due to clear-cutting in Ha Long with monthly frequency. However, it is less effective in finding forest fire areas, while the L-band (ALOS-2) can detect more types of deforestation, including clear-cutting and forest fires. With the C-band (Sentinel-1), HV polarization gives better results than HH, while the L-band (ALOS-2) gives similar results when HV or HH polarization is used. Combining the results from two sets of C-band and L-band SAR data helps to provide more information about the deforested areas, thereby improving the accuracy of the backscatter detection method.

1. INTRODUCTION

According to the definition by IUFRO, Forest Monitoring refers to the periodic and regular measurement of certain parameters of forests (including physical, chemical and biological parameters) to obtain a ground to find out and observe changes over time. If there are insufficient statistics, it will be very difficult to get information on deforestation (which can lead to the

loss of biodiversity and carbon absorption capacity) (O'Grady et al., 2013) (Forest Monitoring Global Forest Atlas). Forest Monitoring has been a critical content in international and national development policies (FAO). Information provided by forest monitoring operations has moved beyond the forest boundary and may be used as an indicator for several environmental and social parameters. However, the capacity for collection, analysis and use of forest resource data in many countries is lacking or inadequate (Forest monitoring and assessment).

Tropical forests are the largest ones in terms of area and play an important role in the global hydrological, biochemical and carbon cycles, as well as make a fundamental contribution to the Earth's biodiversity, global economy and local welfare (Pan et al., 2011; Sasaki et al., 2011). The rapidly growing demands for foods, timbers and biofuels increase serious pressure on tropical forests and lead to deforestation and forest degradation, currently accounting for 20 % of global greenhouse gas emissions (Gullison et al., 2007).

Due to the increasing importance of mitigating the impacts of climate change, the roles of tropical forests in reducing global carbon emissions have led to the REDD+ initiative and subsequently, tropical forest areas are monitored and supervised more often (Kuntz et al., 2011).

Remote sensing to detect forest changes plays an important role in forest monitoring efforts (Kellndorfer, 2019). Optical data has long been a tool for forest monitoring; however, the introduction of SAR data has provided an essential supplementation, using microwave sensors with the capacity of cloud penetration, assuring continuous monitoring even under cloudy conditions; for tropical countries such as Vietnam, this is especially important because the continuous cloud cover is a serious limitation of the optical data regarding the medium resolution (Kellndorfer et al., 2014; Mitchell, Rosenqvist and Mora, 2017).

Many SAR satellites have been launched into the Earth with different duties and missions. In this research study, the team of authors will use different SAR data, ranging from short wavelengths (TerrSAR-X) and Sentinel-1 to longer wavelengths such as ALOS-PALSAR2. Each data type has its own strengths and limitations; however, combining these data sets will provide higher efficacy than using them individually.

2. STUDY AREA

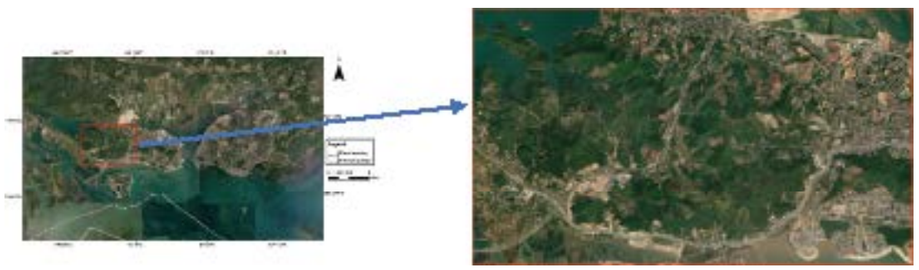

Figure 1. Case study in Ha Long, Vietnam.

Quang Ninh is a coastal province in northeastern Vietnam with a rapidly developing economy and tourism. The swift industrial and service sector growth in Quang Ninh province has placed significant pressure on the environment. The expanding tourism and service industries have necessitated urban infrastructure development. The rapid pace of urbanization has been a positive

factor for the province's socio-economic development. Since 1999, Ha Long has been one of the four urban centers with a high degree of urbanization in the country, alongside Hanoi, Ho Chi Minh city and Da Nang. However, the swift urbanization process has created various pressures and is one of the causes of changes in natural resources, including forest resources. The study area selected for this research is located in Ha Long city, where many forests and various types of forests have been altered due to the impacts of urbanization.

In Ha Long city, various forms of deforestation can be observed. However, in the specific research area, the authors have directed their focus towards two specific types of deforestation: deforestation resulting from the construction of man-made structures, particularly cemeteries and deforestation caused by burning activities. These two forms of deforestation have been identified as significant factors impacting the study area and are, therefore, the primary focus of the research.

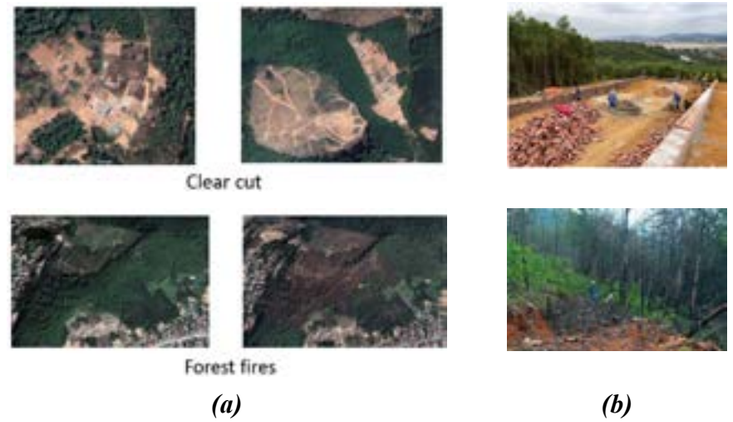

(a) ***(b)***

Figure 2. Two types of deforestation in the study area: (a) Google Earth image, (b) Real-life image.

3. DATA AND METHOD

3.1 Data

The data used in this research includes SAR data to calculate deforested areas and optical data is used to validate the results. The authors used multi-band SAR data (X-band, C-band, L-band). Details are shown in (Table 1)

Table 1. Satellite image data.

No	Sensor	Date	Polarization	Orbit
1	ALOS-PALSAR2	24 Mar 2020	HH, HV	ASC
		23 Mar 2021	HH, HV	ASC
		28 Dec 2021	HH, HV	ASC
2	TerraSAR-X	13 Oct 2020	HH	ASC
		11 Nov 2022	HH	ASC
3	Sentinel-1	Jan 2020 -Dec 2022	VH, VV	ASC

3.2 Principles of using SAR data in forest monitoring

Backscattering (in decibels) obtained from the forest cover is the result of a combination of many mechanisms, in which the total backscattering to be measured is the sum of its compositions

(CEOS Systems Engineering Office 2018):

$$(\gamma^0_{\text{total scattering}} = \gamma^0_{\text{direct scattering}} + \gamma^0_{\text{double-bounce scattering}} + \gamma^0_{\text{volume scattering}} + \gamma^0_{\text{etc}}) \quad (1)$$

According to (Ulaby, 1974; Ulaby, Bush and Batlivala, 1975; Bindlish and Barros, 2001), the backscattering of plants is dominated by radar parameters and surfaces such as frequency, incidence angle, polarization, geometry and surface roughness of objects, complex dielectric properties of objects.

Wavelength determines the penetration capacity of an object, leading to the different scattering mechanisms from which the types of information are different in terms of the cover. The longer the wavelength, the better penetration. TerraSAR-X uses the X-band for ~3 cm wavelength, C-band for ~5 cm wavelength, L-band for ~23 cm wavelength and P-band for ~70 cm wavelength. In this case, the object is a forest and with the X-band, we can only receive signals reflected from the top surface of the objects; the C-band allows us to receive signals from canopies and small branches, generating the volume scattering inside the canopy; the L-band can penetrate branches and the P-band can also penetrate the canopy to obtain information about the trunk.

Polarization: TerraSAR-X uses co-polarization (VV or HH) that is sensitive to flat surfaces, while cross-polarization (VH or HV) is more suitable for volume scattering, which forests are a typical example. Therefore, the cross-polarization application is widely applied for forest monitoring. In addition to the factors mentioned above, other characteristics of SAR also affect forest monitoring, such as angle of incidence, view direction, dielectric properties and surface structures.

Currently, research on forest monitoring using the analysis of backscattering values (dB) often defects large-scale and clear-but situations of deforestation, the cutting down of single trees is still limited. Due to typical characteristics of wavelength, polarization and so on from images taken by TerraSAR-X as mentioned above, only using data from TerraSAR-X for forest monitoring is not appropriate, X-band SAR images have a high resolution and forest monitoring can be implemented on small scale but in more detail, even defecting single trees to be cut down (Science and Summit, 2012), or monitoring the increase/decrease of the forest quality (Airbus Defense & Space, 2014). However, to achieve high efficiency as well as take advantage of each type of SAR satellite, the use of a combination of various types of SAR data (C-band, L-band) is necessary to provide high accuracy and increase the frequency of observations.

3.3 METHOD

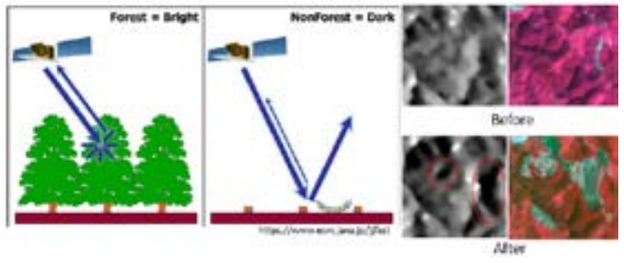

Figure 3. The principle of the backscatter changes on SAR images. Compare SAR and optical images in the deforestation area (Hayashi et al., n.d.).

This study uses a ratio between mean backscatter after deforestation and before deforestation, in which backscatter specifies objects on SAR images and the brightness in the image expresses the roughness. The higher the backscattered intensity, the rougher the studied surface. Hence, the forest area is brighter; conversely, the deforested area is darker, implying low backscattered intensities.

By leveraging a time series of SAR images, it is possible to mitigate the impact of speckle noise and improve the accuracy of detecting deforestation events. The temporal information captured over multiple acquisitions allows for the identification of persistent changes over time, enabling a more reliable assessment of deforestation and other land cover changes. Therefore, the use of a time series of SAR images, like those offered by Sentinel-1, provides a valuable tool for monitoring and analyzing forest disturbances, providing a more comprehensive understanding of the dynamics and changes occurring within the study area.

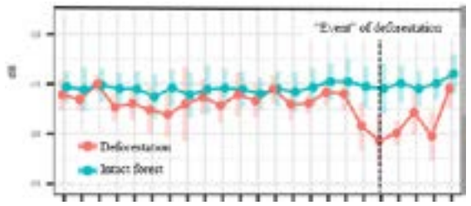

Figure 4. Temporal backscattering profile of intact forest and deforestation area (Anh, Tuan and Hang 2019).

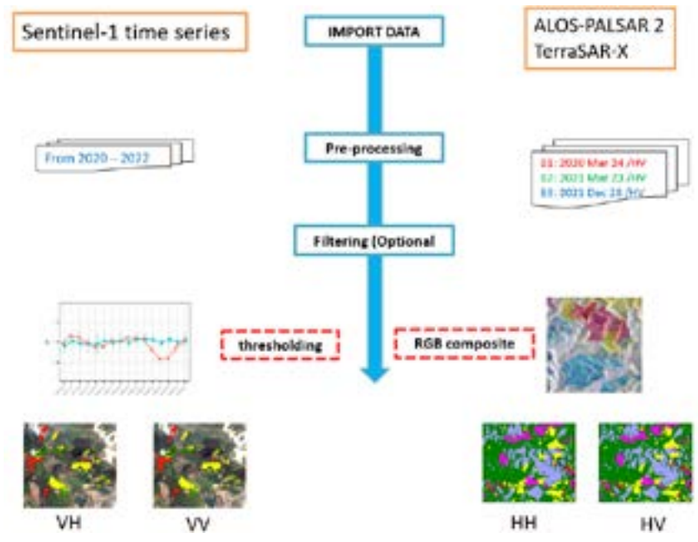

Figure 5. Workflow of methodology.

Sentinel-1 images from the period 2020-2022 were collected and processed collectively using a Python-based tool. Thresholds were constructed through surveying and sample analysis, applying the RCR ratio to determine the deforestation threshold (Anh, Tuan and Hang 2019) and the results of deforested areas were calculated from VH and VV polarization data.

Due to the limited number of ALOS-PALSAR2 and TerraSAR-X images, the method used for deforestation detection was the RGB composite, where red (B1) was assigned to pre-deforestation images, green (B2) was assigned to the deforestation period and blue (B3) was

assigned to post-deforestation images. The result of the RGB composite method is an image of areas with forest changes in different colors, each color corresponding to a different forest change status. After analysis with graphs, a classification method was chosen to categorize different types of deforestation (Figure 10).

The results after classification were calculated from ALOS-PALSAR2 data and TerraSAR-X data were converted to vector format to easy combination with results obtained from Sentinel-1.

4. RESULTS AND ANALYSIS

4.1 Sentinel-1 Analysis

The monthly time series of Sentinel-1 C-band data proved to be a valuable tool in consistently identifying clearings resulting from clear-cut deforestation. However, it had limitations in detecting areas of forest degradation caused by fires. This can be attributed to the fact that the 5 cm wavelength used by Sentinel-1 is not able to penetrate through the canopy effectively, thus making it challenging to detect changes in forest structure. Previous studies, such as the one conducted by (Tanase et al., 2015), have also highlighted this limitation. The C-band SAR primarily captures scatter from the upper canopy and smaller branches, missing out on underlying changes occurring within the forest (Figure 6).

Figure 6. The wildfire areas were not detected using C-band SAR data (Sentinel-1).

4.2 ALOS-2 and TerraSAR-X Analysis

The analysis of the multi-temporal L-band ALOS-2 data yielded valuable insights into forest disturbances that were not captured by Sentinel-1 data alone. By comparing RGB composites of HH and HV polarizations, it became evident that both polarizations contained redundant information (Figure 7). However, a more detailed examination of the HV backscatter time series uncovered nuanced variations among seven distinct land cover classes, including three specific types of forest change: growth, degradation and deforestation (Figure 10). This highlights the added value of utilizing the HV backscatter time series for a comprehensive understanding of forest dynamics and land cover changes.

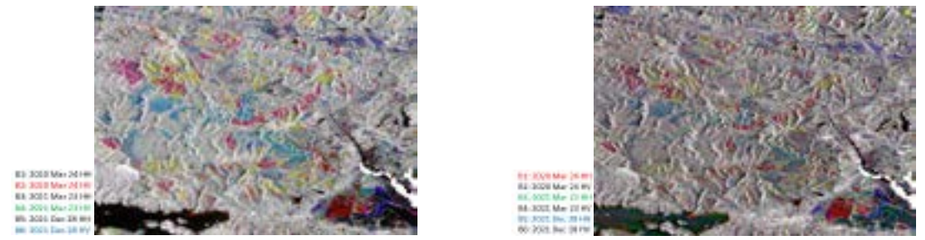

(a) (b)

Figure 7. Similarities of ALOS-2 RGB HV (a) and HH (b) composite images.

Based on the provided results, it is apparent that there are various types of forest changes within the study area, each represented by a distinct color. To gain a deeper understanding of these fluctuations, manual sampling can be conducted, followed by an analysis of the backscatter (in decibels) variation graph.

An intriguing observation arises when considering the ALOS-2 RGB image combination in an area with abundant vegetation cover. Despite the significant differences between the HH and HV polarizations in the individual image channels (Figure 8), their RGB combinations yield similar outcomes, specifically a copper-like color. This similarity has been verified through the author's calculations (Figure 9). This finding highlights the potential redundancy of information between the HH and HV polarizations when combined in an RGB composite. It suggests that both polarizations might convey comparable insights regarding the vegetation cover, possibly indicating the presence of consistent scattering mechanisms across the different polarization channels.

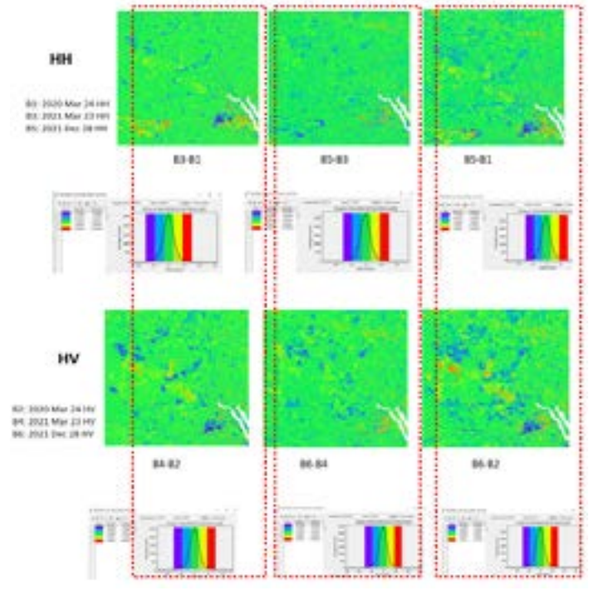

Figure 8. The difference between the HH and HV polarizations by comparing the image bands.

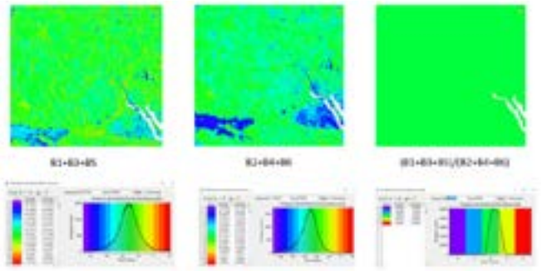

Figure 9. Similarity of RGB combinations for HH and HV polarization.

The 23 cm L-band wavelength was able to penetrate deeper into the canopy and sense structural changes within the forest, enabling the detection of degradation from fires. Supervised classification of the ALOS-2 HV time series extracted thematic maps distinguishing these land cover dynamics (Figure 10). From the above graph, seven levels were classified, in which there are 3 changes in the forest: forest growth, degradation and deforestation.

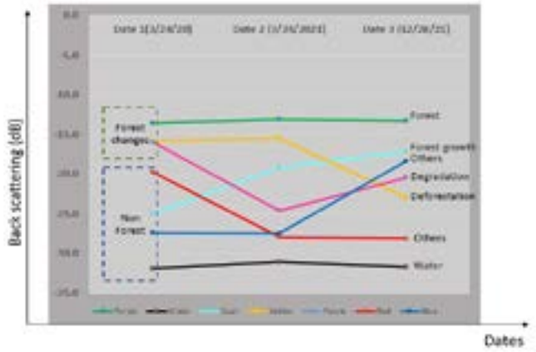

Figure 10. Variation of backscattering values of objects in the study area.

To facilitate the extraction of class information and compute statistics, a Mahalanobis distance classification method was applied in ENVI/SARScape and GIS software. By utilizing these tools, you were able to generate vector results that distinguish thematic classes within the study area, as illustrated in Figure 11.

Figure 11. Map of forest change in the case study using ALOS-2 data.

While the very high 1m resolution TerraSAR-X data holds potential for detailed forest disturbance monitoring, the current method could not effectively utilize the two scenes available.

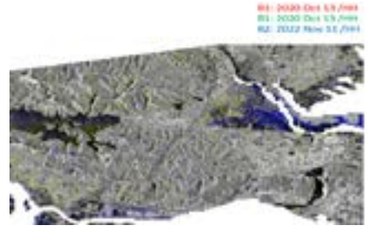

Figure 12. TerraSAR-X RGB composite.

5. DISCUSION AND CONCLUSION

The results demonstrate the usefulness of multi-sensor SAR data for detecting different types of deforestation in the study area. The C-band Sentinel-1 time series was effective at identifying areas of clear-cutting on a monthly basis but less capable of detecting forest degradation from fires, as found in previous studies (Tanase et al., 2015) with Synthetic Aperture Radars (SAR). This is likely due to the shorter 5 cm wavelength having limited penetration through the canopy. In contrast, the L-band ALOS-2 data could detect a wider range of forest disturbances, including clear-cutting, fires, degradation and regrowth. The 23 cm wavelength provided greater sensitivity to changes within the canopy and forest structure.

By combining the capabilities of C-band and L-band SAR data, more accurate and complete deforestation mapping could be achieved. The frequent revisit of Sentinel-1 allowed clear-cut events to be regularly monitored, while ALOS-2 provided complementary information on forest degradation not discernible in the C-band data. As (Tanase et al., 2018) demonstrated, this multi-sensor approach integrating C-band, L-band and optical data strengthens overall deforestation detection. The RGB color composites of ALOS-2 were found to produce similar results for HH and HV polarizations. This suggests the polarization channels contain redundant information when used in this way. However, analyzing the HV backscatter time-series enabled differentiation between seven land cover types, including variations within the forest class. This demonstrates the usefulness of examining polarimetric SAR data across time for forest monitoring, as discussed by (Kellndorfer et al., 2014) natural habitats for biodiverse fauna and flora, and providing food and fiber for human consumption. To obtain sound information for management, protection, and restoration of forests, some core information needs are: 1. While the high-resolution TerraSAR-X data did not yield usable results with the current method, its 1 m spatial resolution could provide detailed forest disturbance monitoring with further algorithm development, as shown in previous X-band studies (Science and Summit, 2012).

Overall, the study successfully demonstrated that integrating multi-sensor C- and L-band SAR can improve the accuracy and completeness of deforestation monitoring. A blended approach is recommended operationally for REDD+ MRV systems. Future research could further exploit the benefits of polarimetric SAR and high-resolution data for detecting early degradation and small-scale disturbances.

6. ACKNOWLEDGMENTS

The authors would like to thank Vietnam Academy of Science and Technology (VAST) for supporting the project No. VAST01.03/21-22. We would like to thank the Remote Sensing Technology Center of Japan (RESTEC) for providing ALOS-PALSAR2 and TerraSAR-X data for this study.

7. REFERENCES

Airbus Defense & Space, 2014. TerraSAR-X Based Monitoring of Forest Degradation in Ghana. www.geo-airbusds.com.

Anh Ngo Duc, Vu Anh Tuan and Nguyen Thu Hang, 2019. Deforestation hot-spot extraction from Radar Change Ratio (RCR) Analysis of Sentinel-1 time series data in Dak G' Long district, Dak Nong province. *International Conference on Earth Observations & Natural Hazards 2019 (ICEO&NH 2019)*. https://sites.google.com/site/iceonh2019/program/proceedings.

Bindlish, Rajat and Ana P. Barros, 2001. Parameterization of vegetation backscatter in Radar-based, soil moisture estimation. *Remote Sensing of Environment*. https://doi.org/10.1016/S0034-4257(00)00200-5.

CEOS Systems Engineering Office, 2018. A Layman's interpretation guide to L-Band and C-Band synthetic aperture radar data. https://doi.org/10.2169/naika.107.contents1.

Forest Monitoring| Global Forest Atlas. Accessed on November 3, 2019. https://globalforestatlas.yale.edu/conservation/forest-monitoring.

Forest Monitoring and Assessment. Accessed on November 4, 2019. http://www.fao.org/forestry/fma/84322/en/.

Gullison R. E., P. C. Frumhoff, J. G. Canadell, C. B. Field, D. C. Nepstad, K. Hayhoe, R. Avissar et al., 2007. Tropical Forests and Climate Policy. *Science 316* (5827), 985-986. https://doi.org/10.1126/science.1136163.

Hayashi, Masato, Miura Mari, Umemiya Chisa and Pantoja Nara, 2022. Joint submission to the first global stocktake a Satellite-based deforestation monitoring system for tropical forests. *JICA-JAXA Forest Early Warning System in the Tropic*s (JJ-FAST) 36, 1-10.

Kellndorfer, Josef, 2019. Using SAR data for mapping deforestation and forest degradation. *SAR Handbook: Comprehensive Methodologies for Forest Monitoring and Biomass Estimation*. Berlin, Boston: DE GRUYTER. https://doi.org/. 10.25966/68c9-gw82.

Kellndorfer, Josef, Oliver Cartus, Jesse Bishop, Wayne Walker and Francesco Holecz, 2014. Large scale mapping of forests and land cover with synthetic aperture radar data. *Land applications of radar Remote Sensing*. In Tech. https://doi.org/10.5772/58220.

Kuntz, Steffen, Felicitas Von Poncet, Thomas Baldauf, Daniel Plugge, Bernhard Kenter and Michael Köhl, 2011. A Multi-Stage Inventory Scheme for REDD Inventories in Tropical Countries. *34th International Symposium on Remote Sensing of Environment - The GEOSS Era: Towards Operational Environmental Monitoring*, No. April.

Mitchell, Anthea L., Ake Rosenqvist and Brice Mora, 2017. Current Remote Sensing Approaches to Monitoring Forest Degradation in Support of Countries Measurement, Reporting and Verification (MRV) Systems for REDD+. *Carbon Balance and Management*. BioMed Central Ltd. https://doi.org/10.1186/s13021-017-0078-9.

O'Grady, Damien, Marc Leblanc, David Gillieson, O'Grady, Damien, Marc Leblanc and David Gillieson, 2013. Relationship of Local Incidence Angle with Satellite Radar Backscatter for Different Surface Conditions. *International Journal of Applied Earth Observation and Geoinformation*, No. 24, 42-53. https://doi.org/10.1016/j.jag.2013.02.005.

Pan Y. D., R. A Birdsey, J. Y. Fang, R. Houghton, P .E. Kauppi, W. A. Kurz, O. L. Phillips et al., 2011. A large and persistent carbon sink in the World's Forests. RID A-1523-2011 RID E-9419-2010. *Science*. https://doi.org/10.1126/science.1201609.

Sasaki N., G. P. Asner, W. Knorr, P. B. Durst, H. R. Priyadi and F. E. Putz, 2011. Approaches to classifying and restoring degraded tropical forests for the Anticipated REDD+ climate change mitigation mechanism. *IForest*. https://doi.org/10.3832/ifor0556-004.

Science, Geo-fct and Data Summit, 2012. X-Band SAR for forestry.

Tanase, M.A. A., R. Kennedy and C. Aponte, 2015. Radar burn ratio for fire severity estimation at Canopy level: An example for temperate forests. *Remote Sensing of Environment, 170* (August 2015), 14-31. https://doi.org/10.1016/j.rse.2015.08.025.

Tanase, Mihai A., Cristina Aponte, Stéphane Mermoz, Alexandre Bouvet, Thuy Le Toan and Marco Heurich, 2018. Detection of windthrows and insect outbreaks by L-Band SAR: A case study in the Bavarian Forest National Park. *Remote Sensing of Environment*, *209* (February), 700-711. https://doi.org/10.1016/j.rse.2018.03.009.

Tanase, Mihai A., Ismail Ismail, Kim Lowell, Oka Karyanto and Maurizio Santoro, 2015. Detecting and Quantifying Forest Change: The Potential of Existing C- and X- Band Radar Datasets. *PLoS ONE 10* (6): e0131079. https://doi.org/10.1371/journal.pone.0131079.

Ulaby, Fawwaz T, 1974. Radar Measurement of Soil Moisture Content. *IEEE Transactions on Antennas and Propagation*. https://doi.org/10.1109/TAP.1974.1140761.

Ulaby, Fawwaz T., Thomas F. Bush and Percy P. Batlivala, 1975. Radar Response to Vegetation II: 8–18 GHz Band. *IEEE Transactions on Antennas and Propagation*. https://doi.org/10.1109/TAP.1975.1141133.

TSUNAMI EVACUATION SIMULATION USING MULTI-AGENT SYSTEM: A CASE STUDY OF WAJIMA CITY, ISHIKAWA PREFECTURE, JAPAN

Tatsuya Nemoto[1]*, Aoi Sato[2], Venkatesh Raghavan[1]

[1]Graduate School of Science, Osaka Metropolitan University, Japan.
[2]Faculty of Science, Osaka City University, Japan.
*Corresponding author. Email: tnemoto@omu.ac.jp

ABSTRACT

A tsunami evacuation simulation model has been developed using a multi-agent system (MAS). MAS is a system composed of multiple agents, where each agent acts autonomously according to the situation under certain rules. In the tsunami evacuation simulation, the agent is an evacuee and the evacuee moves to the safe evacuation site on the road network. Artisoc4, developed by Kozo Keikaku Engineering Inc., was used to generate the simulation model. This software is a simulation platform specialized for MAS that allows users to define the types of agents using GUI and create action rules using Visual Basic.

In this study, the tsunami evacuation simulation was carried out in the port area of Wajima City, Ishikawa Prefecture, Japan. Twelve evacuation sites were established for approximately 12,000 evacuees. There were three types of agents: male, female and tourist, walking speeds were set for each type. As a result of the simulation, all agents completed the evacuation after 2028 seconds.

1. INTRODUCTION

Many natural disasters have occurred in Japan. The tsunami generated by 2011 off the Pacific coast of Tohoku Earthquake caused extensive damage. Recently, Tsunami damage caused by the Nankai megathrust earthquake is predicted. In order to reduce such damage, it is necessary to build a crisis management system based on thorough simulations.

The tsunami evacuation simulations have been conducted using a multi-agent system (MAS). Saito and Kagami, (2005) have constructed the simulation model using MAS and shown its effectiveness. Moreover, their results showed that walking speed and evacuation start time are important parameters to minimize total mortality and missing rate. Kosaka et al., (2017) conducted an evacuation simulation of dispersed evacuees and revealed that evacuation time was shorter if a route with a wider width was selected.

In this study, a tsunami evacuation simulation model has been developed using Artisoc 4 which is a simulation platform specialized for MAS, according to Kosaka et al., (2017). Dijkstra's method was used to find the shortest path to the evacuation site. The simulation was carried out in the port area of Wajima city, Ishikawa Prefecture, Japan to reveal the problem related to evacuation.

2. MULTI-AGENT SIMULATION

A virtual experiment using multiple agents is called a multi-agent simulation. Agents act autonomously according to the situation under certain rules (Figure 1). Models can be constructed to explain complex social phenomena and behavior can be predicted by understanding their mechanisms and characteristics through the simulation. In tsunami evacuation simulation, agents are evacuees and evacuees move to evacuation sites on the road network while influencing each other.

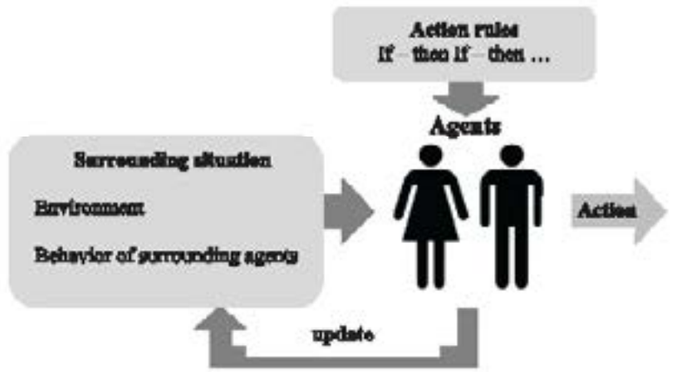

Figure 1. Concept of multi-agent simulation.

3. DEVELOPMENT OF A SIMULATION MODEL

Artisoc 4, developed by Kozo Keikaku Engineering Inc., was used to generate the simulation model. This software is a simulation platform specialized for MAS. It allows users to define the types of agents using GUI and create action rules using Visual Basic (Figure 2).

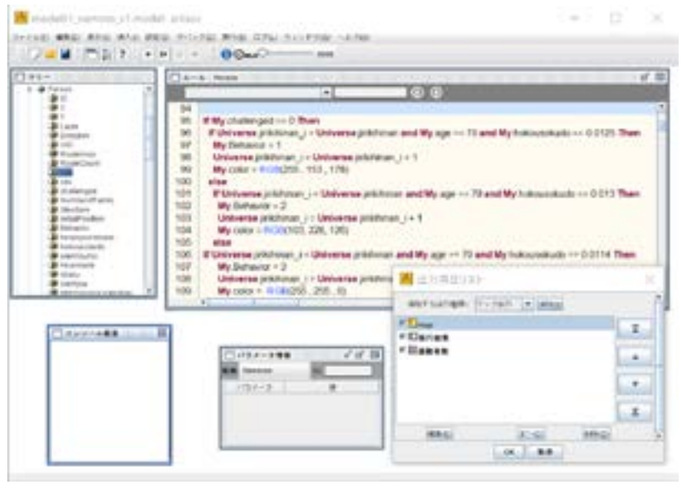

Figure 2. Operation screen of Artisoc 4.

3.1 Study area

The study area is Wajima City, Ishikawa Prefecture, Japan. The simulation area (4×4 km) is shown in Figure 3. Seismic activity has been active in this area since 2020 and there was an M6.5 earthquake in 2023. This area has a port area visited by many tourists and there is a risk of tsunami.

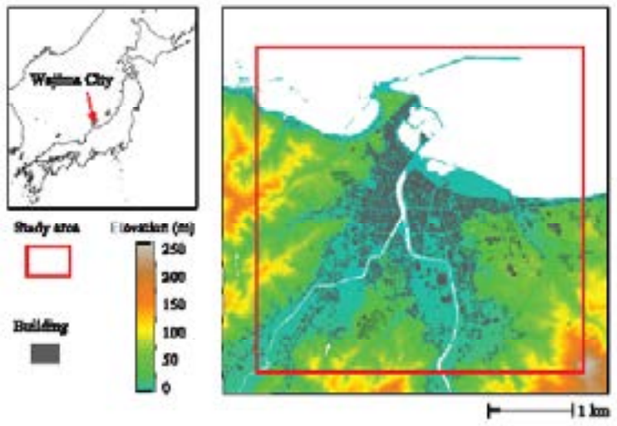

Figure 3. The port area in Wajima city. The map is based on the Fundamental. Geospatial data published by Geospatial Information Authority of Japan.

3.2 Road network and evacuation sites

In tsunami evacuation simulation, evacuees move on a road network consisting of intersections (nodes) and roads (lines). Links can have width information. In this study, road network data was created from OpenStreetMap.

Twelve evacuation sites were set up for the destination of evacuees. These are designated for temporary evacuation. The evacuation sites and estimated tsunami inundation lines are shown in Figure 4.

3.3 Agents setting

The simulation was performed assuming that many local residents are at home and there are many tourists during the daytime on the weekend. The number of evacuees was set at 12,456 based on the total population of the residents and the number of tourists per day. Evacuees were dispersed considering the area and number of buildings in each town.

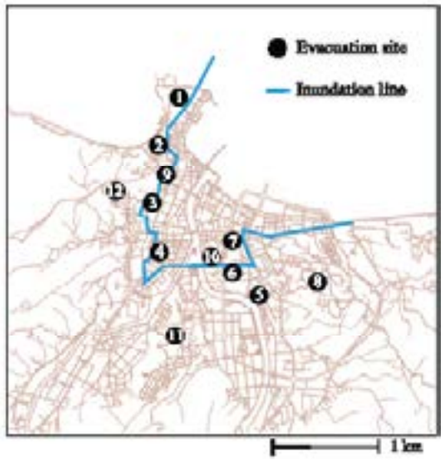

Figure 4. Evacuation sites and estimated tsunami inundation line.

The agent types were female, male and tourist, walking speeds were set to 1.30 m/s, 1.25 m/s and 1.14 m/s, respectively. Under the condition that agents know the position of the evacuation site, they move the shortest route to the evacuation site. The Dijkstra method was used to calculate the shortest path.

4. RESULTS

As a result of the simulation, all agents completed evacuation after 2,028 seconds. The number of people who completed evacuation after 300 seconds, 600 seconds and 900 seconds was 6,976; 11,153 and 11,760, respectively and 90 % of the evacuees had completed their evacuation after about 600 seconds. At evacuation site 4, the number of evacuees exceeded its capacity. The capacity and number of evacuees at each evacuation site are shown in Table 1. The movement of evacuees and time variation of the number of completed evacuations are shown in Figures 5 and 6, respectively.

5. CONCLUSIONS

In this study, a tsunami evacuation simulation model has been developed using MAS. Twelve evacuation sites in the port area of Wajima city were established for 12,456 evacuees. As a result of the simulation, 90 % of evacuees had completed their evacuation after about 600 seconds.

Table 1. Capacity and number of evacuees at each evacuation site.

Evacuation site	Capacity	Number of evacuees
1	1,490	79
2	16,704	92
3	12,017	2,025
4	803	6,437
5	355	144
6	14,346	52
7	8,390	1,264
8	14,346	87
9	540	355
10	550	339
11	13,329	1,296
12	30,000	286

Figure 5. Movement of evacuees.

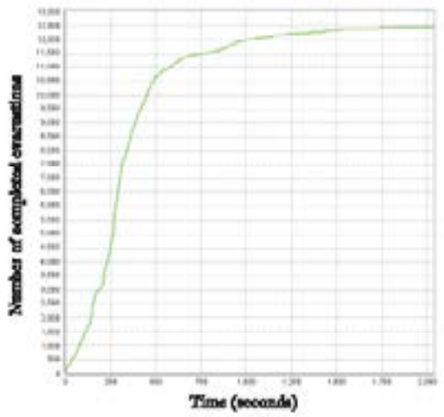

Figure 6. Time variation of the number of completed evacuations.

The attributes of agents were kept simple and classified by gender and status of evacuees (residents or tourists), but it is necessary to subdivide them by age and so on. In addition, it is necessary to consider the occurrence of congestion from road width information and to reflect walking speed differences due to weather conditions and road gradients. More robust simulations using road width and gradient are being examined as a part of ongoing research.

6. REFERENCES

Kosaka Y., Nomura N., Oto A., and Miyajima M., 2017. Analysis of tsunami evacuation by using multi agent system: Case study of Wajima district in Wajima city. *Journal of Japan Society of Civil Engineers, Ser. A1 (Structural Engineering & Earthquake Engineering (SE/EE))*, I_1010-I_1017.

Saito T., and Kagami H., 2005. Simulation of evacuation behaviour from tsunami utilizing multi-agent system. *Journal of Architecture and Planning*, 229-234.

REMOTE SENSING APPLICATION USING GOOGLE EARTH ENGINE PLATFORM TO ASSESS CROP BURN AREAS IN WINTER-SPRING RICE CROP IN THE MEKONG DELTA, VIETNAM

Tran Van Dung[1]*, Lam Dao Nguyen[1], Hoang Phi Phung[1], Dang Pham Bao Nghi[1], Phung Chi Sy[2], Pham Thi Mai Thy[1]

[1]Ho Chi Minh City Space Technology Application Center,
Vietnam National Space Center, Vietnam Academy of Science and Technology
[2]Environmental Technology Center, Ho Chi Minh City, Vietnam
*Corresponding author. Email: tvdung@vnsc.org.vn

ABSTRACT

Straw burning in the Mekong delta has been going on for many years. Rice farmers have the habit of burning straws to free up paddy field space and kill some insects and pathogens before sowing/planting new crops. This not only causes air pollution, reduces soil fertility and harms human health but also increases the risk of widespread fires. The main objective of this study is to apply remote sensing techniques using the Google Earth Engine platform to identify and map straw-burning areas, thereby helping managers have an overall view and make the master plan for suitable agriculture development. The study used FIRMS data (The Fire Information for Resource Management System) extracted from MODIS satellite data using band 21 (MOD14 - Terra and MYD14 - Aqua) for winter-spring rice crops in the Mekong delta. It has the capability to provide near-real-time fire locations. In addition, the rice-age maps are also used to compare and evaluate the reliability of the straw-burning map.

1. INTRODUCTION

The Mekong delta is one of Vietnam's key rice production regions, contributing more than 50 % of the country's rice output. With a large amount of straw after harvest, most farmers choose to burn straw right in the field to free up space to kill insects and pathogens to prepare for the next crop. Piling straw into piles and then smoldering causes widespread air pollution, causing respiratory diseases and affecting people's health (Tham, 2021).

The Mekong delta is located at coordinates 8°35'-10°02'30" N and 104°25'-106°50' E, including 13 provinces and cities: Long An, Tien Giang, Dong Thap, Tra Vinh, Hau Giang, Vinh Long, Soc Trang, Ben Tre, An Giang, Kien Giang, Bac Lieu, Ca Mau and Can Tho city. The Mekong delta region was formed from alluvial sediments and gradually accreted through epochs of sea level change. The terrain of the region is relatively flat. The average height is 3-5 m. Some places are only about 0.5-1 m above sea level.

The Mekong delta has a dense system of rivers and canals, with nearly 40 inter-provincial rivers and canals and nearly 100 intra-provincial rivers and canals. The climate in the Mekong delta is humid tropical, with sub-equatorial monsoon, lots of sunshine and high temperatures all year round. Basically, there are two seasons per year: the rainy season lasts from May to November and the dry season is from December to April next year. Solar radiation is quite abundant and relatively stable, with little variation during the year and within the region. The average annual

total radiation is about 150 Kcal/cm^2. The average annual sunshine hours are about 2,400-2,800 hours. Most of the Mekong delta area is filled with silt every year, making it very fertile creating favorable conditions for rice production. Taking advantage of available advantages, the Mekong delta focuses on rice production and has become the number one granary of our country (Dinh, 2016).

In Viet Nam, there have been several studies related to burning straw, such as the research group Tran Xuan Dung, (2022) and Tran Sy Nam, (2014), with the aim of calculating the amount of gas emitted from burning straw on paddy fields in the Mekong delta region, but only at the level of statistics and document collection without applying remote sensing technology for large-scale assessment. The results of the above studies also show that straw treatment by burning is very common in rice growing areas (accounting for over 98 %), in addition to several other treatment methods such as selling, growing mushrooms and burying in fields, accounting for a very small percentage.

Around the world, in India, there have been studies on the application of satellite data to study straw burning (Das et al., 2023), including detecting changes before and after the time of fire and monitoring fire by vegetation index (NDVI), difference NBR (Normalized Burn Ratio) and other techniques. The purpose of this study is to determine the burning area for the 2021 Winter-Spring rice crop in the Mekong delta using remote sensing methods.

2. DATA USED AND METHODS

2.1 Data

The main data used to study and identify copper burning areas is based on the FIRMS data source (The Fire Information for Resource Management System), which was developed by the University of Maryland with funding from the Fire Information for Resource Management System. Applied research provided by NASA and the Food and Agriculture Organization of the United Nations (FAO) to reveal fire locations in almost real-time to give managers of natural resources around the world fire information (Figure 1). This data is extracted from the MODIS14 (Terra satellite) and MYD14 (Aqua satellite) products of channel 21 (Wavelength 3.96 µm). Each active fire location is represented at the pixel center with a resolution of 1 km.

In addition, the study applied methods to establish rice maps (used to accurately identify straw-burning areas) (Phung et al., 2020) and rice age maps (assess the relevance of study results). The methods are based on research results presented in the article “Monitoring rice growth status in the Mekong delta, Vietnam using multitemporal Sentinel-1 data” (Phung et al., 2020).

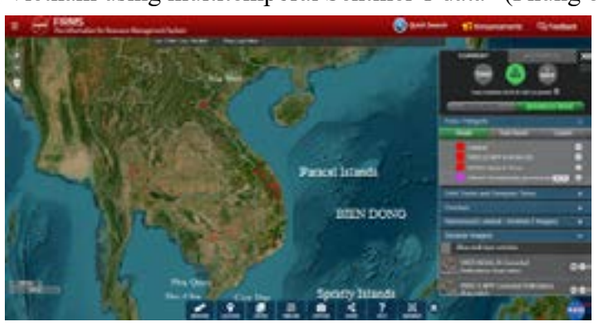

Figure 1. FIRMS data monitoring fire areas in real time.

2.2 Method

To suit study purposes, the above-mentioned FIRMS datasets were extracted through functions of the Google Earth Engine platform, using the global administrative unit layer (FAO GAUL 500 m: Global Administrative Unit Layers 2015, First-Level Administrative Units) during the period March and April 2021 - the harvest time of the Winter-Spring crop in the study area (Figure 2) to filter results in the study area with the support of algorithms. Math is available on the GEE system, such as *ee. Image, clip, Map.addLayer, mean()*. These products are exported into *.tiff format files through the *Export.image.toDrive()* function and store on the computer and opened on GIS applications in the next steps.

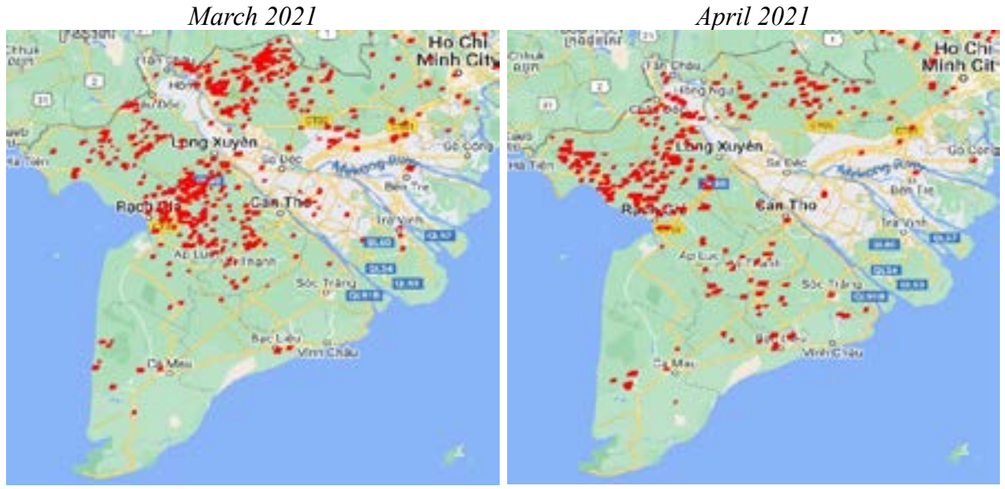

Figure 2. Results of fire areas after extracting from the Google Earth Engine platform.

Fire product data collected from the FIRMS system above is general data about fire areas, which may include straw-burning areas, forest fires, or other unusual fires. Therefore, the study used the results of the distribution of rice areas for the 2021 Winter-Spring crop processed from Sentinel-1 radar remote sensing image data (Figure 3), then performed overlays to accurately identify fire areas caused by straw burning.

Next, to evaluate the relevance of the results obtained, the study used the rice age map (calculated from the time of sowing) last month compared to the map of the straw burning area (rice age map in February to evaluate March straw burning area price; March rice age map for April straw burning area).

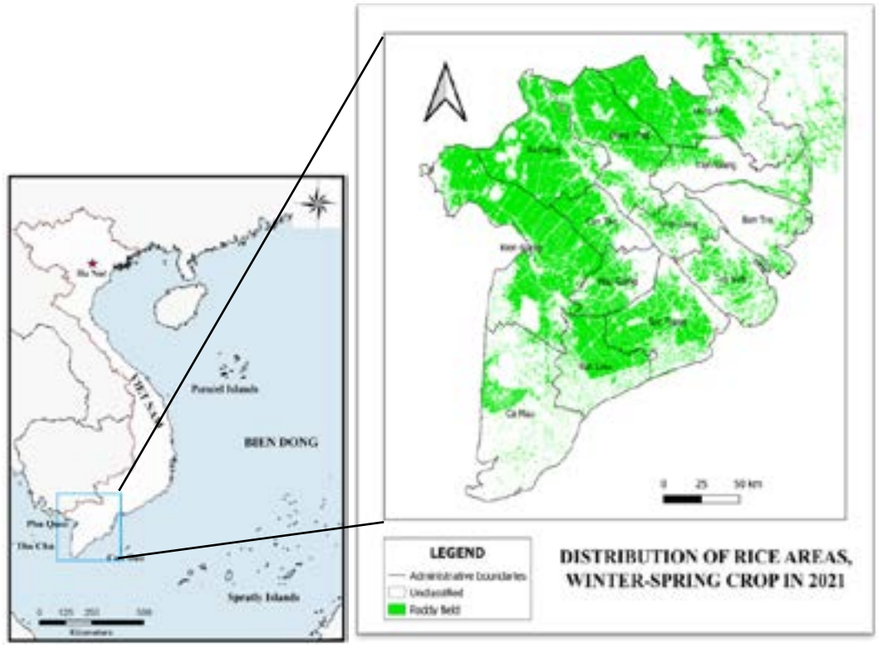

Figure 3. Distribution of rice areas in the Mekong delta.

3. RESULTS AND DISCUSSIONS

The research results have provided information about straw burning areas in March and April 2021 in the Mekong delta region (Figures 4 and 5). These results are largely concentrated in An Giang, Dong Thap, Kien Giang, Hau Giang and Can Tho city.

Also, a comparison between the map of straw burning locations and the map of rice age of the previous month shows that the results are quite suitable, concentrated in areas with rice age from 71 - 120 days, close to harvest time (Figures 6 and 7).

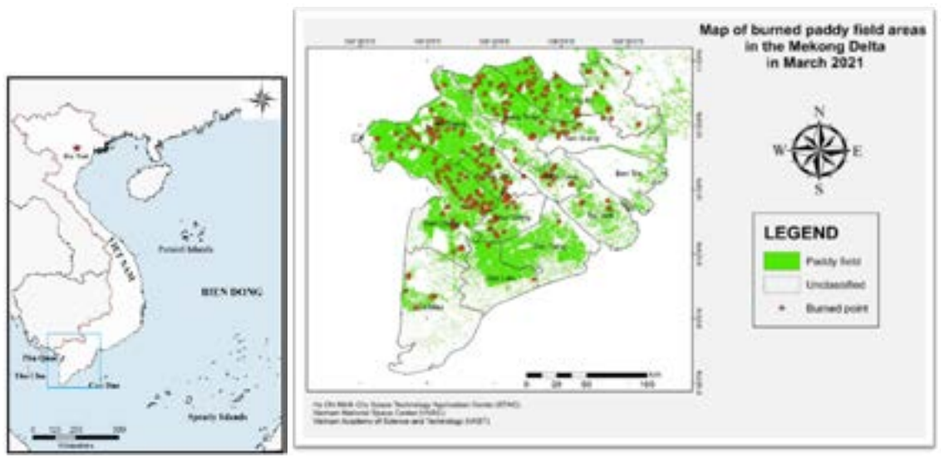

Figure 4. Results of detecting straw burning locations in March 2021.

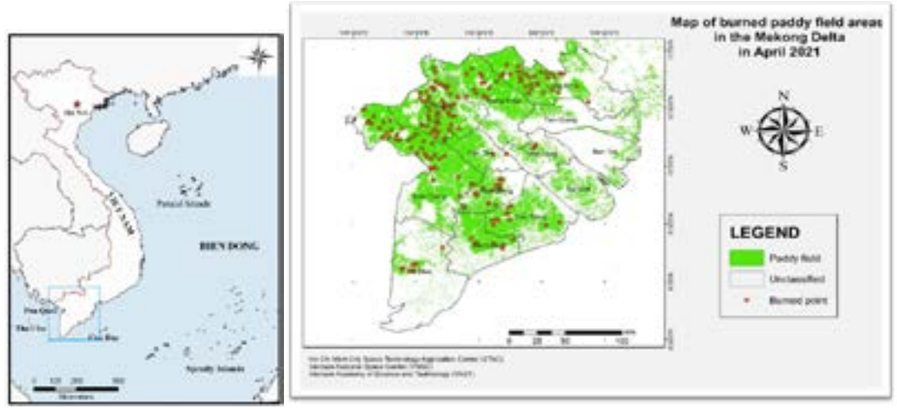

Figure 5. Results of detecting straw burning locations in April 2021.

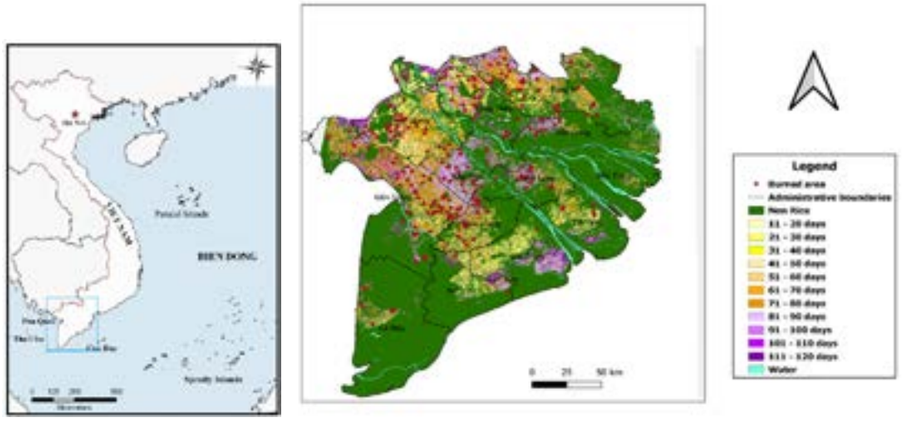

Figure 6. Straw burning locations in March 2021 when overlaying the rice age map in February 2021.

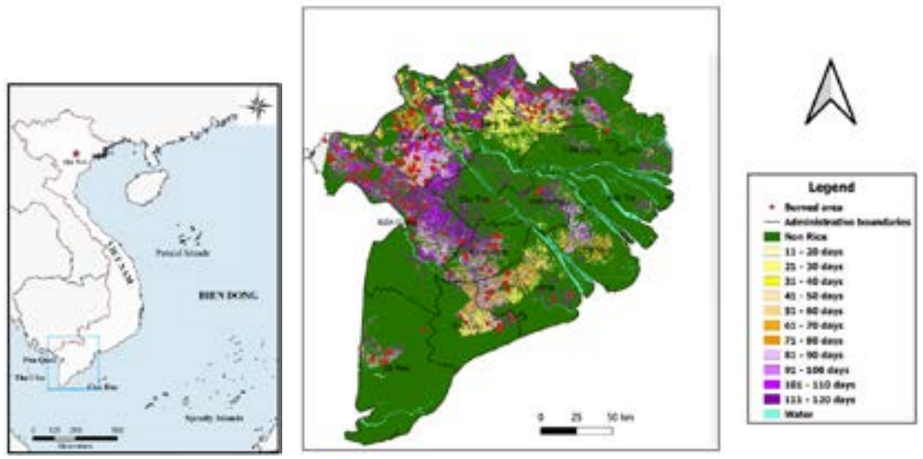

Figure 7. Straw burning locations in April 2021 when overlaying the rice age map in March 2021.

4. CONCLUSIONS

In this study, data from MODIS14 and MYD14 products of Terra and Aqua satellites, respectively, at band 21 (Wavelength 3.96 μm) with the support of cloud platform algorithms Google Earth Engine were used to detect fire locations. In addition, the Rice area distribution map and Rice age map were used, with satellite image data processing methods based on previous studies. The above results reflect that burning straw after harvesting rice in the Mekong delta is extremely common.

From there, we can see an overview of the situation of straw treatment in the Mekong delta region using the open burning method. This result will help the authorities that the government needs to have some policies and measures to minimize it in the future. In the future, the study will conduct field surveys to evaluate the accuracy of the research results and aim to expand the study area throughout the country.

5. ACKNOWLEDGEMENTS

Part of the study result presented in this article is from the project *"Logical Framework and Implementation Organization: reduction of Risks of Open Burning Practices and Unsafe Pesticide Use to the Environment and Human Health in Vietnam"* led by Associate Professor Dr. Phung Chi Sy, Environmental Technology Center (ENTEC).

6. REFERENCES

Dinh L. X., 2016. The Mekong delta's salinity intrusion: causes, impacts and solutions. *National Department of Science and Technology Information, 50*. https://vista.gov.vn/vn–uploads/tong–luan/2016/tl2-2016.pdf.

Dung T. X, Thy, N. H., 2022. Estimated gas emissions from burning straw in fields in the Mekong delta region. *Journal of Hydrometeorology, 736*, 25-35. Doi:10.36335/VNJHM.2022(736).25-35.

https://firms.modaps.eosdis.nasa.gov/map. Accessed on 18 September 2023.

Nam T. S., Nhu N. T. H., Chiem N. H, Ngan N. V. C., Viet L. H., Ingvorsen K., 2014. Estimate the amount and treatment methods of rice straw in some Mekong delta provinces. *Can Tho University Science Magazine, Part A: Natural Sciences, Technology and Environment, 32*, 87-93.

P Das, M. D. Behera, P. C. Abhilash., 2023. A rapid assessment of stubble burning and air pollutants from satellite observations. *International Society for Tropical Ecology*. https://doi.org/10.1007/s42965-022-00291-5.

Phung H. P. and Nguyen L. D., 2020. Rice Crop Monitoring in the Mekong delta, Vietnam Using Multi-Temporal Sentinel-1 Data with C-Band. *ICSCEA 2019*, Lecture Notes in Civil Engineering, J. N. Reddy, C. M. Wang, V. H. Luong and A. T. Le, Eds. S*pringer Nature Singapore Pte Ltd*, 979-986.

Phung H. P., Nguyen L. D., Thong N. H., Thuy L. T., Armando A. Apan, 2020. Monitoring rice growth status in the Mekong delta, Vietnam using multitemporal Sentinel-1 data. *Journal of Applied Remote Sensing,* Vol. 14, Issue 1, 014518.

Tham H., 2021. Status and solutions for handling rice straw after rice harvest. *Environmental management magazine*. http://quanly.moitruongvadothi.vn/1/11821/Thuc-trang-va-giai-phap-xu-ly-rom-ra-sau-thu-hoach-lua.aspx.

SWASH MODEL APPROACH FOR FLOWS INDUCED BY LOW-FREQUENCY WAVES OVER WOODEN FENCES

Hoang Tung Dao[1]*, Ngan Vu Thi Thuy[1], Ngo Thi Thuy Anh[2]

[1]Hanoi University of Natural Resources and Environment, Vietnam
[2]Thuy Loi University, Hanoi, Vietnam
*Corresponding author. Email: dhtung@hunre.edu.vn

ABSTRACT

The Mekong deltaic coasts have been suffering from erosions and massive mangrove reduction for nearly a decade. As considered a natural base solution, wooden fences or permeable structures have been applied for a number of mangrove restoration projects along the coasts. This green structure is often built in front of the mangrove belt to create a lively environment, including low wave energy and high sedimentation for young mangroves. One of the most valuable functions is the wave reduction resulting from the significant reduction due to its resistance generated by densities and thicknesses. This function has also been studied by a number of sites in Vietnam, Thailand and Indonesia. However, the study on the increase of sedimentation in front and behind the fence has been left out due to the complexity of sediment transports, especially for the permeable fences. In this study, the low-frequency wave, which is considered the main contribution to flows, is focused on assessing the possibility of sediment transports through the wooden fence. This study applies the SWASH model developed by Delft University of Technology to carry out a couple of wave scenarios for the southeast and northeast monsoons that were inherited from a previous study. The wave results after distinguishing the high- and low-frequency ones with a cut-off frequency indicate the efficiency of wooden fences on high-frequency waves is significantly higher than on low-frequency waves. Moreover, the amplitudes of low-frequency waves at the upstream and downstream sites of the wooden fences emphasize the roles of these waves in wave-induced flows and sediment transports.

1. INTRODUCTION

The Mekong deltaic coast has been suffering from erosions and unpredictable coastal processes, all due to artificial measures in the past decade. The issues have been noticed since the high demand for food security and accommodation safety became the main target of the local government. Consequently, the coasts along the Mekong delta have been upgraded with traditional (gray) structures, such as concreted dikes, in order to create a safe coast for local civils. However, the downside of these gray structures is the breaking of morpho-dynamic equilibrium (Schoonees et al., 2019), including sediment transport and sedimentation for nurturing both the coast and marine ecosystems, such as mangroves.

In the past decade, nature-based solutions have been applied to the coast to reduce the maximum risks from gray structures and enhance the maximum impact of natural benefits. In the Mekong delta, green structures, such as wooden fences, have become a supportive solution (Albers & Schmitt, 2015; Schmitt et al., 2013; Schmitt & Albers, 2014; Winterwerp et al., 2020) to existing measures to create a livable environment for young mangroves. Studies on green

structures and wooden fences have been significantly raised for a few years, focusing on Southeast Asian areas.

Schmitt and Albers, (2014) carried out a long observation to obtain the efficiency of the wooden fences in preventing erosion and mangrove losses in Soc Trang province, Vietnam. In this study, a system of wooden fences with a T-shape similar to the groins system along the coastal zone. Van Cuong et al., (2015) also practically tested the efficiency of wooden fences made by the combination of Melaleuca and fishing nets for more wave damping. Both two real-scale studies gave out results in a large wave reduction observed inside the wooden fence areas. However, those studies inform a little of the inside understanding of wave reduction mechanisms that occurred inside the wooden fence.

Dao et al., (2020) carried out a series of tests to find the bulk drag coefficients under flow conditions for real- and small-scale wooden fences inherited from observation in coastal areas in Bac Lieu province, Vietnam. This study also results in the resistance coefficients under laminar and turbulent flow conditions, in which the coefficient under turbulent flow is found to be similar to the drag coefficient and dependent on densities under very high turbulence. H. T. Dao et al., (2021) and T. Dao et al., (2022) then validated laboratory data with the SWASH model- an open-source model using the bulk drag coefficients and resistance coefficients found in previous studies. The small-scale validations resulted in a good agreement, but the trust of large-scale simulations still needed to be carried out.

T. Dao et al., (2018) presents an observation of waves at the upstream and downstream site and theoretically states the sediment transport driven by waves. Two main processes of sediment movements are recognized as the net transport as proportional to the odd moment, $\langle u|u|^2\rangle$ (Bosboom & Stive, 2012), where u is the time-average velocity near the bed, including the oscillatory of high-frequency (u_{hf}) and low-frequency (u_{lf}) wave motions. The term $|u|^2$ is shown as the relation to the stirring processes taking place by the oscillatory wave motions and is proportionally calculated by the wave height in the shallow water. In the Mekong deltaic coast, the gentle slopes of 1:500 to 1:800 are commonly found, creating a strong environment for wave dissipations. Therefore, an analysis of high- and low-frequency waves, which are the main objectives, is presented in this study, including results of surface elevation and wave orbital velocity.

2. RESEARCH METHODS

2.1 SWASH Model

SWASH model is an open-source simulator for simulating non-hydrostatic waves and wave-induced currents in the shallow zone based on the non-linear shallow water equations (Zijlema, 2012; Zijlema et al., 2011; Zijlema & Stelling, 2005). This multi-dimensional time-domain model can also simulate other wave processes in shallow water, including wave breaking, reflection and diffraction (Rijnsdorp et al., 2012; Smit et al., 2013). The government equations for wave propagation in a crossed section are expressed as:

$$\frac{\partial u}{\partial x}+\frac{\partial w}{\partial z}=0 \tag{1}$$

$$\frac{\partial \eta}{\partial t}+\frac{\partial}{\partial x}\int_{-d}^{\eta} u\,dz=0 \tag{2}$$

$$\frac{\partial w}{\partial t}+\frac{\partial uw}{\partial x}+\frac{\partial ww}{\partial z}+\frac{1}{\rho}\frac{\partial (P_{nh})}{\partial z}+\frac{\partial \tau_{zz}}{\partial z}+\frac{\partial \tau_{zx}}{\partial x}=0 \tag{3}$$

$$\frac{\partial u}{\partial t}+\frac{\partial uu}{\partial x}+\frac{\partial wu}{\partial z}+\frac{1}{\rho}\frac{\partial (P_h+P_{nh})}{\partial x}+\frac{\partial \tau_{xz}}{\partial z}+\frac{\partial \tau_{xz}}{\partial x}=0 \tag{4}$$

where x and z are the distance in horizontal and vertical directions in the Decade coordinate, respectively; u and w are also the wave orbital velocities relative to x and z directions, respectively. η is the water elevation and t is time; P_h and P_{nh} are the hydrostatic and non-hydrostatic pressure, respectively; τ is the bottom stress and can be linked to the bottom coefficient, c_f, based on the Manning coefficients (Zijlema et al., 2011).

T. Dao et al., (2022) introduced an alternative for simulating wave-fence interactions by implementing the permeable implementation model in the SWASH model. The calibration and validation results in that study that used resistance coefficients obtained from H. T. Dao et al., (2020) inform a good agreement for laboratory data of the study in H. T. Dao et al., (2021).

The real-scale crossed profile used in SWASH includes the gentle slope of 1:500, which is a typical slope found in the Mekong deltaic coast. As shown in Figure 1, wave inputs are set at the west side of the profile, whereas several sponger layers are set at the east side with a length of about 30 m to absorb incoming and reflection waves. Wooden fences are set at x = 70 m with a width of 0.8 m.

In the permeable implementation of the SWASH model, the fence's characteristics are the height, diameter of grain inside the structure, porosity and resistance coefficients. Only one height, diameter and porosity are set for all scenarios, such as 1.6 m for heights, 0.02 m for diameter and 90 % for porosity. Resistance coefficients for both the turbulent and laminar flow conditions were first measured and introduced in the study of H. T. Dao et al., (2020), i.e., in the laminar flow α_{fe} and in the turbulent flow β_{fe}. Both two values are the dependent values of porosity and are unchanged in very high turbulent conditions. In this study, the value of α_{fe} and β_{fe} are chosen as 567 and 2.36, respectively.

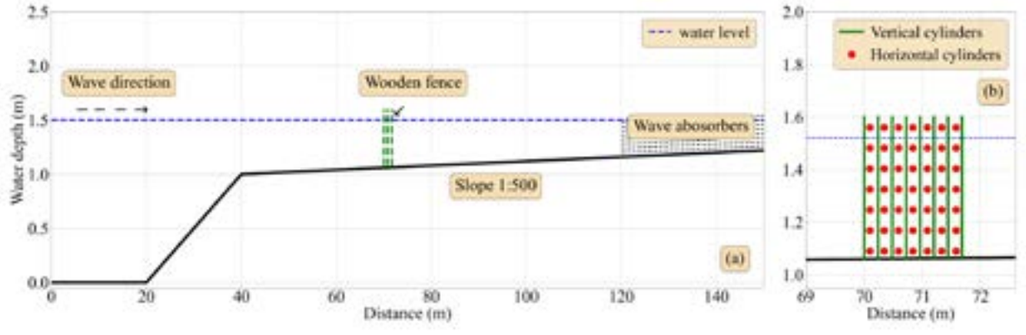

Figure 1. (a) Crossed profile in SWASH model and (b) Schematic view of a wooden fence used in SWASH.

2.2 Wave scenarios

Wave scenarios are based on a few numbers of the wave measured on the coast at Nha Mat, Bac Lieu, Vietnam, located as 9°12'12.75"N - 105°44'39.3"E. In Figure 2, the wooden fences are presented as green lines and a wave gauge was set to obtain wave height and wave period at a location in front of the wooden fence. The data was collected in two seasons, the southeast and northeast monsoons.

Figure 2. Wave collection site at Nha Mat, Bac Lieu, Vietnam. Wave gauges 01 are used to collect wave data.

Wave inputs at the west side of the profile are set from wave collections in Figure 2, where only incoming waves are chosen. The wave settings in the SWASH model include three main characteristics, e.g., wave height (H_i, m), wave period (T_p, s) and water level (d, m) for the southeast and northeast monsoons. Two cases used in the SWASH model are presented in Table 1:

Table 1. List of wave characteristics as model inputs

Case No.	Seasons	(m)	(s)	d (m)
1	Southeast	0.17	4.39	1.21
2	Northeast	0.39	7.71	1.53

Furthermore, for wave analyses, significant wave heights are calculated as $H_{m0} = 4\sqrt{m_0}$, where m_o is the zeroth-order moment of the water surface elevation obtained from modeling outputs. In further analyses, the elevations are separated into low-frequency (LF) and high-frequency (HF), considered as longwave and short-wave, respectively. A cut-off frequency $f_{cut\text{-}off}$ as $0.5f_{peak}$ (Hz), which is estimated from chosen wave periods as 0.2 Hz. As a result, waves are distinguished with $0.005 \leq f_{cut\text{-}off} \leq f_{peak}$ for low-frequency waves and $f_{cut\text{-}off} \geq f_{peak}$ for high-frequency waves. Figure 3 presents wave spectral densities of low-frequency (black dashed line) and total frequency waves (green line) being clearly separated from the cut-off frequency.

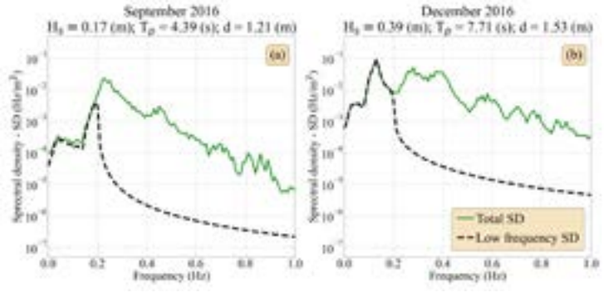

Figure 3. Low-frequency and total-frequency spectral density for a showcase in September and December 2016

3. RESULTS AND DISCUSSION

3.1 Model validation

Previous studies, H. T. Dao et al., (2021) and T. Dao et al., (2022) present the validation results of the SWASH model with laboratory data in a scale of 1:5 that applied the vegetation model and permeable model, respectively. Figure 7 indicates the model validation results from two studies and shows a good agreement between computation and measurement. Even though the error of transmission waves from T. Dao et al., (2022) is slightly higher than its value in H. T. Dao et al., (2021), as shown in Figure 7b, the agreement for the permeable model remains acceptable.

Note that the input in SWASH can only set three parameters: wave heights, periods and water depths (water level). Therefore, the date and time values can only be used for validation and calibration. Additionally, the accuracy between computation and measurement results are calculated to two main parameters, the bias and scatter index (SI), expressed as:

$$bias = \frac{1}{N}\sum_{i=1}^{N}(\sigma_{simulation}^{i} - \sigma_{measurement}^{i}) \quad (5)$$

$$SI = \frac{\sqrt{\frac{1}{N}\sum_{i=1}^{N}(\sigma_{simulation}^{i} - \sigma_{measurement}^{i})^2}}{\frac{1}{N}\sum_{i=1}^{N}\sigma_{measurement}^{i}} \quad (6)$$

where, $\sigma_{simulation}$ and $\sigma_{measurement}$ are the statistical variables computed by SWASH and measured in the field or laboratory, respectively; N is the total number of cases in the considered data set (Zijlema et al., 2011)

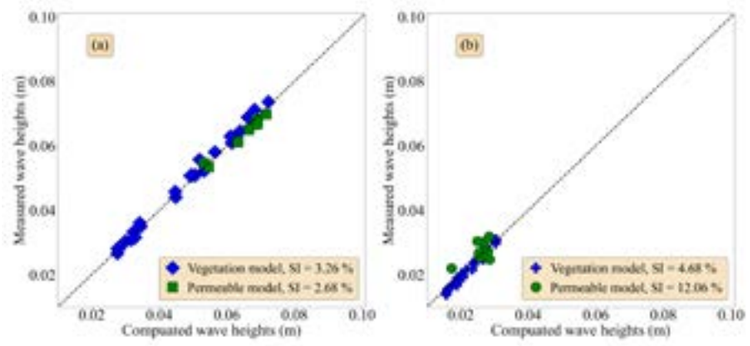

Figure 4. Errors between computation in SWASH and measurement in the laboratory for the Vegetation model (blue and plus sign diamond) and Permeable model (green square and circle). (a) Errors of incoming waves and (b) Errors of transmission waves.

3.2 High- and low-frequency wave heights

Figure 5 presents short- (blue circles) and longwaves heights (red squares) after filtering by the cut-off frequency plotted together in each season. Wooden fences are more effective on short waves than longwaves for both southeast and northeast monsoons. Short wave heights are reduced about 40 % of incoming energies (x= 65 m) when the reduction rates are about 10 % for longwaves. This is also proven by H. T. Dao et al., (2021), that larger waves are damped more than smaller waves. Note that the longwaves always have small wave heights.

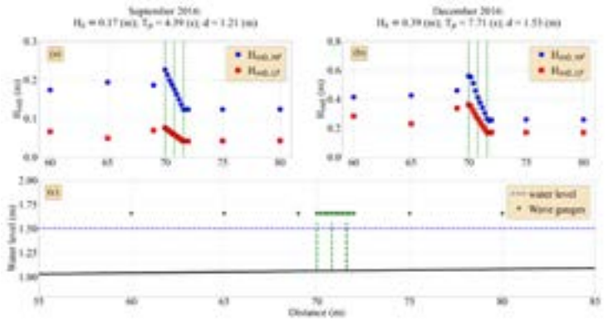

Figure 5. (a) High-frequency and (b) Low-frequency wave height transformation before and after contact with the fences (c).

Even though waves in the northeast monsoon (Figure 5a, December 2016) are larger and longer than in the southeast monsoons (Figure 5b, September 2016), the low-frequency waves follow the same trend. This result will also be an opportunity to assess flows generated by longwaves in the next section.

3.3 Surface elevation and orbital wave velocity

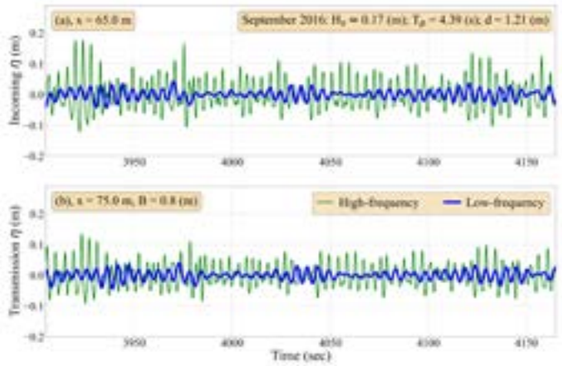

Figure 6. Surface elevation at incoming (a, x= 65 m) and transmitted (b, x= 75 m) location in the southeast monsoon.

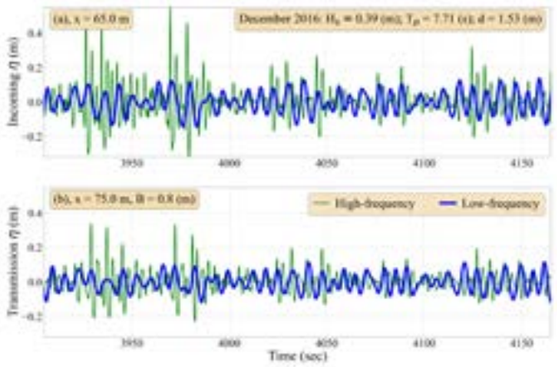

Figure 7. Surface elevation at incoming (a, x= 65 m) and transmitted (b, x= 75 m) location in the northeast monsoon.

Figures 6 and 7 present the surface elevation for the showcase in both southeast and northeast monsoons, respectively. In all of the incoming waves, high-frequency waves (green line) are larger than low-frequency waves (blue line) at x= 65 m. However, there is a difference between the two seasons due to wave inputs in the model. It is shown in Figure 7 that the simulation in northeast monsoon (December 2016) for short waves (Figure 7a) gives similar amplitudes of longwaves (Figure 7b). Moreover, longwaves at both sites (in front and behind) of the fence have similar amplitudes. It can be interpreted that a minor efficiency of wooden fences on longwaves is observed.

Figures 8 and 9 plot the orbital velocity over time at two locations, x= 65 m and 75 m of the fence, for two seasons. It is noticed that the similar trend of the orbital velocities to the surface elevation for the southeast monsoon. The high-frequency velocities are reduced effectively by the wooden fence, but low-frequency velocities seem to remain at their amplitudes. It is easy to notice that orbital velocities in the northeast monsoon at two sites are seemingly unchanged. This result also points out that longwave-induced flows might be the role of further research on sediment transports related to flows.

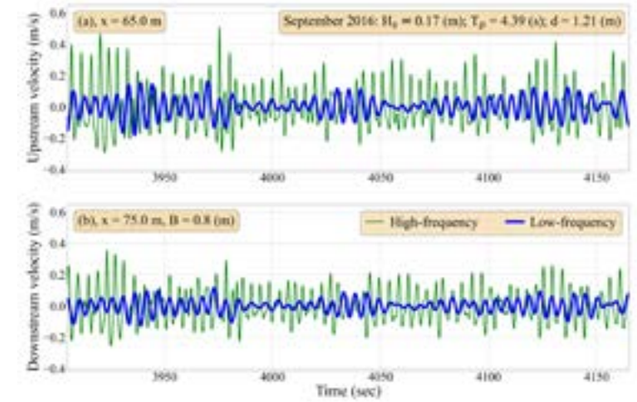

Figure 8. Orbital velocity over time at incoming (a, x= 65 m) and transmitted (b, x= 75 m) location in the southeast monsoon.

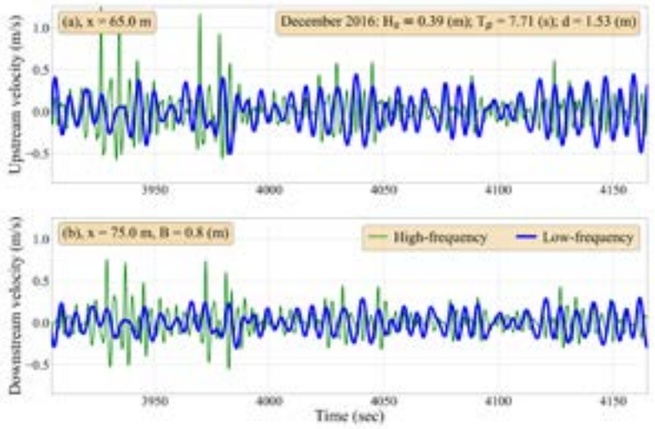

Figure 9. Orbital velocity over time at incoming (a, x= 65 m) and transmitted (b, x= 75 m) location in the northeast monsoon.

4. CONCLUSION

The present study applies the open-source model, SWASH, to simulate wave-fence interactions in the common slope found on the Mekong deltaic coast. The SWASH model was previously validated with laboratory data and proved its skill, giving an open opportunity for further studies. In this study, a new approach for high-frequency and low-frequency waves in order to assess flows over the fences. There are several remarks in this study. Firstly, high-frequency waves are significantly affected by wooden fences when wave heights for two monsoons lose about 40 % of their energies. Additionally, the orbital velocities of both showcases open a new research window for further understanding sediment transport driven by longwave-induced flows. This point of view will be aimed at the future research.

5. ACKNOWLEDGEMENTS

The first author (Hoang Tung Dao) is grateful for being supported by Hanoi University of Natural Resources and Environment (HUNRE), Vietnam and the Project "Research on the efficiency of wooden fences on morphology under southern wave conditions in Bac Lieu province.", project code: 13.01.23.G.02. We all acknowledge all other authors for reviewing and editing the manuscript.

6. REFERENCES

Albers T., & Schmitt K., 2015. Dyke design, floodplain restoration and mangrove co-management as parts of an area coastal protection strategy for the mud coasts of the Mekong delta, Vietnam. *Wetlands Ecology and Management*, *23*(6), 991-1004.

Bosboom J., & Stive M. J. F., 2012. Coastal Dynamics I: Lectures Notes CIE4305. *VSSD*.

Dao H. T., Hofland B., Stive M. J. F., & Mai T., 2020. Experimental assessment of the flow resistance of coastal wooden fences. *Water*, *12*(7), 1910.

Dao H. T., Hofland B., Suzuki T., Stive M. J. F., Mai T., & Tuan L. X., 2021. *Numerical and small-scale physical modelling of wave transmission by wooden fences*.

Dao T., Mai T., Mai C., & Doan T. M. T., 2022. An alternative calibration method for wave-fence interaction in SWASH model. *Journal of Hydro-Meteorology*, *12*, 22-32. https://doi.org/doi:10.36335/VNJHM.2022(12).23-32.

Dao T., Stive M. J. F., Hofland B., & Mai T., 2018. Wave Damping due to Wooden Fences along Mangrove Coasts. *Journal of Coastal Research*, *34*(6), 1317-1327. https://doi.org/10.2112/JCOASTRES-D-18-00015.1.

Rijnsdorp D. P., Smit P. B., & Zijlema M., 2012. Non-hydrostatic modelling of infragravity waves using SWASH. *Coastal Engineering Proceedings*, *1*(33), 27.

Schmitt K., & Albers T., 2014. Area coastal protection and the use of bamboo breakwaters in the Mekong Delta. Coastal Disasters and Climate Change in Vietnam (107-132). *Elsevier*.

Schmitt K., Albers T., Pham T. T., & Dinh S. C., 2013. Site-specific and integrated adaptation to climate change in the coastal mangrove zone of Soc Trang province, Viet Nam. *Journal of Coastal Conservation*, *17*(3), 545-558.

Schoonees T., Mancheño A. G., Scheres B., Bouma T. J., Silva R., Schlurmann T., & Schüttrumpf H., 2019. Hard structures for coastal protection, towards greener designs. *Estuaries and Coasts*, *42*(7), 1709-1729.

Smit P., Zijlema M., & Stelling G., 2013. Depth-induced wave breaking in a non-hydrostatic, near-shore wave model. *Coastal Engineering*, *76*, 1-16.

Van Cuong C., Brown S., To H. H., & Hockings M., 2015. Using Melaleuca fences as soft coastal engineering for mangrove restoration in Kien Giang, Vietnam. *Ecological Engineering*, *81*, 256-265.

Winterwerp J. C., Albers T., Anthony E. J., Friess D. A., Mancheño A. G., Moseley K., Muhari A., Naipal S., Noordermeer J., & Oost A., 2020. Managing erosion of mangrove-mud coasts with permeable dams-lessons learned. *Ecological Engineering*, *158*, 106078.

Zijlema M., 2012. Modelling wave transformation across a fringing reef using SWASH. *ICCE 2012: Proceedings of the 33rd International Conference on Coastal Engineering, Santander,* Spain, 1-6 July 2012.

Zijlema M., & Stelling G. S., 2005. Further experiences with computing non-hydrostatic free-surface flows involving water waves. *International Journal for Numerical Methods in Fluids*, *48*(2), 169-197.

Zijlema M., Stelling G., & Smit P., 2011. SWASH: An operational public domain code for simulating wave fields and rapidly varied flows in coastal waters. *Coastal Engineering*, *58*(10), 992-1012.

DEM GENERATION AND TOPOGRAPHIC CHANGES OF CENTRAL HANOI, VIETNAM

Go Yonezawa[1]*, Tatsuya Nemoto[2], Xuan Luan Truong[3], Susumu Nonogaki[4], Do Thi Hang[3], Muneki Mitamura[2] , Venkatesh Raghavan[2]

[1]Department of Urban Design and Engineering, Graduate School of Engineering, Osaka Metropolitan University, Japan
[2]Department of Geosciences, Graduate School of Science, Osaka Metropolitan University, Japan
[3]Hanoi University of Mining and Geology, Vietnam
[4] National Institute of Advanced Industrial Science and Technology, Japan
*Corresponding author. Email: yonezawa@omu.ac.jp

ABSTRACT

In recent years, urban flooding caused by localized heavy rains has become more frequent in Japan and Vietnam. To solve this problem, it is important to understand the characteristics of the terrain, as well as to improve the drainage function in urban areas. Analyzing the relief of terrain and the micro-topography of Hanoi city can play an important role in explaining its urban transformation.

Yonezawa et al., (2008, 2016) and Yonezawa, (2009) generated a detailed Digital Elevation Model (DEM) of the central part of Hanoi city in Vietnam from about 23,000 points of elevation data. The elevation data is from the topographic maps published by the Department of Survey and Mapping of Vietnam, Ministry of Natural Resources and Environment in 2005 and was provided by Hanoi University of Mining and Geology. The DEM is based on the surface estimation method. The topographical surface is estimated from (x, y, z) based on the surface estimation method (we call it BS-Horizon) using the Cubic B-Spline Function (Nonogaki et al., 2012). BS-Horizon is one of the surface estimation programs for geologic boundary surfaces and geomorphic surfaces. The DEM is generated at a 2-meter resolution and the contour interval is 0.5 meters. The very subtle elevation gaps, which cannot be distinguished on the satellite image, are significantly recognizable on this DEM.

In this research, a DEM is generated using elevation data from a newly published topographic map in 2018. By comparing the two patterns of DEM for 2005 and 2018, the areas of urban transformation can be clarified. These high-resolution DEMs are useful not only for analyzing the urban transformation of central Hanoi but also for urban sustainable development, as in the improvement of urban infrastructure and disaster prevention.

1. INTRODUCTION

Hanoi city, the capital of Vietnam, is one of the fastest-growing cities in Southeast Asia. However, serious urban problems (subsidence, groundwater contamination, flooding, etc.) are increasing every year. In particular, urban flooding is becoming more frequent due to climate change.

The objective of this research is to generate topographic data that can serve as very useful base data for verifying such urban flooding. One type of data that represents the undulations of the earth's surface is the Digital Elevation Model (DEM), which is an important and indispensable data for topographic analysis. In this research, the authors, in collaboration with the Hanoi University of Mining and Geology, generated a high-resolution DEM based on the elevation survey points on an urban planning map published in 2018.

The author also generated a DEM for the central part of Hanoi city from elevation survey points issued in 2005. By comparing the two DEMs, the transformation of the city can be seen. It is hoped that the results of this research will lead to solutions to serious urban problems.

2. RESEARCH AREA AND DATA

The research area is the central part of Hanoi city, Vietnam (Figure 1). The area covers a range of lat. 21°00'00" to 21°04'22.5" and long. 105°47'30" to 105°51'52.5". These coordinates are based on the VN-2000 (UTM).

In this research, we collected the elevation survey data with the Hanoi University of Mining and Geology. Elevation survey points are shown on a 1:2,000 scale city planning map of Hanoi published by the Department of Survey and Mapping of Vietnam, Ministry of Natural Resources and Environment in 2018 (some published in 2017). The study area covers an area of 7,630 m from East to West and 8,110 m from North to South on 49 sheets of this map. A total of 26,579 elevation survey points are included in these maps and their distribution is indicated by the blue dots in Figure 1.

The elevation survey points are provided as digital data in DGN format. We input this data into QGIS and extracted the coordinates and elevation values (*x, y, z*) of the 26,579 elevation survey points. The method for generating the DEM is based on Yonezawa et al., (2008, 2016) and Yonezawa, (2009).

3. GENERATION OF DEM

Nonogaki et al., (2012) propose a gridding algorithm that considers both equality and inequality constraints from elevation data and trend data. The algorithm is designed to approximate a surface using a bi-cubic B-spline and determines an optimal surface using the exterior penalty function method. The optimal surface is the smoothest one that satisfies the given constraints. The program developed based on this algorithm is called 'BS-Horizon'.

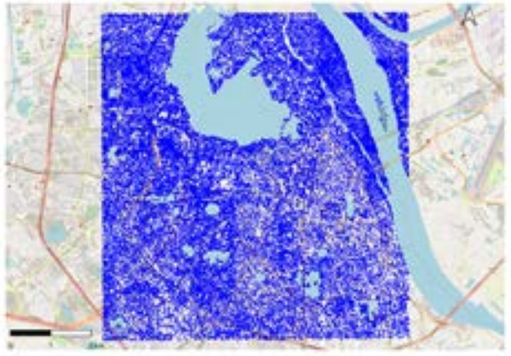

Figure 1. Research area and elevation points in central Hanoi.

The terrain and geological boundary surfaces of the target area can be represented by $z=f(x, y)$. Let $\Omega = \Omega_x + \Omega_y$ be a rectangular domain in x-y plane. M_x and M_y denote the number of sections, respectively. The surface $f(x, y)$ within Ω can be expressed in the quadratic equation (1):

$$f(x,y) = \sum_{i=1}^{M_x+3} \sum_{j=1}^{M_y+3} c_{ij}\, N_i(x)\, N_j(y) \qquad (1)$$

where $N_i(x)$ and $N_j(y)$ are the normalized cubic B-spline bases with respect to x and y, respectively and c_{ij} is constants. An increase in M_x and M_y will enhance the capacity to represent the surface. They are obtained as the optimal solution that minimizes the following equation (2) according to the principle of finding the smoothest surface that satisfies the given measurement data.

$$Q(f;\alpha) = m_1 \iint \left(f_x{}^2 + f_y{}^2\right) dxdy/S + m_2 \iint \left(f_{xx}{}^2 + 2f_{xy}{}^2 + f_{yy}{}^2\right) dxdy + \alpha R(x) \qquad (2)$$

The first and second terms on the right-hand side are functions that evaluate the smoothness of the surface, where S is the area of the region. The third term represents data sufficiency. m_1, m_2 and α adjust the weight of each term and m_1 and m_2 are the surface smoothness and α is the penalty parameter.

In this research, we used this BS-Horizon program to generate a DEM of the terrain surface of the central part of Hanoi city. Extract the (x, y, z) of the elevation measurement points shown in Figure 1 and enter them into the BS-Horizon program. This result was obtained using α=1.000, m_1=0.5, m_2=0.5 as the parameter. However, a detailed verification is in the future. Figure 2 shows an example of visualization of the DEM output from the BS-Horizon program imported into GRASS GIS as an ASCII file. Figure 2 (a) shows an example of a DEM visualization with a resolution of 2 m and 3,816×4,056 grids. Figure 2 (b) shows the visualization with transparency set to 60 % of Figure 2 (a). Figure 2 (c) shows a 3D visualization of the DEM using GRASS GIS.

4. TOPOGRAPHIC CHANGES OF CENTRAL HANOI

Yonezawa et al., (2016) is a DEM generated using elevation survey points from an urban planning map published by the Department of Survey and Mapping of Vietnam, Ministry of Natural Resources and Environment in 2005 for the same area of this research. Figure 3 shows a visualization of the generated DEM of 2005. The composition of the 2005 DEM and the 2018 DEM are shown in Table 1.

Table 1. DEM Parameters.

DEM	Point Number	Grid Number	Resolution (m)
2018	26,579	3,816×4,056	2
2005	23,608	3,211×4,026	2

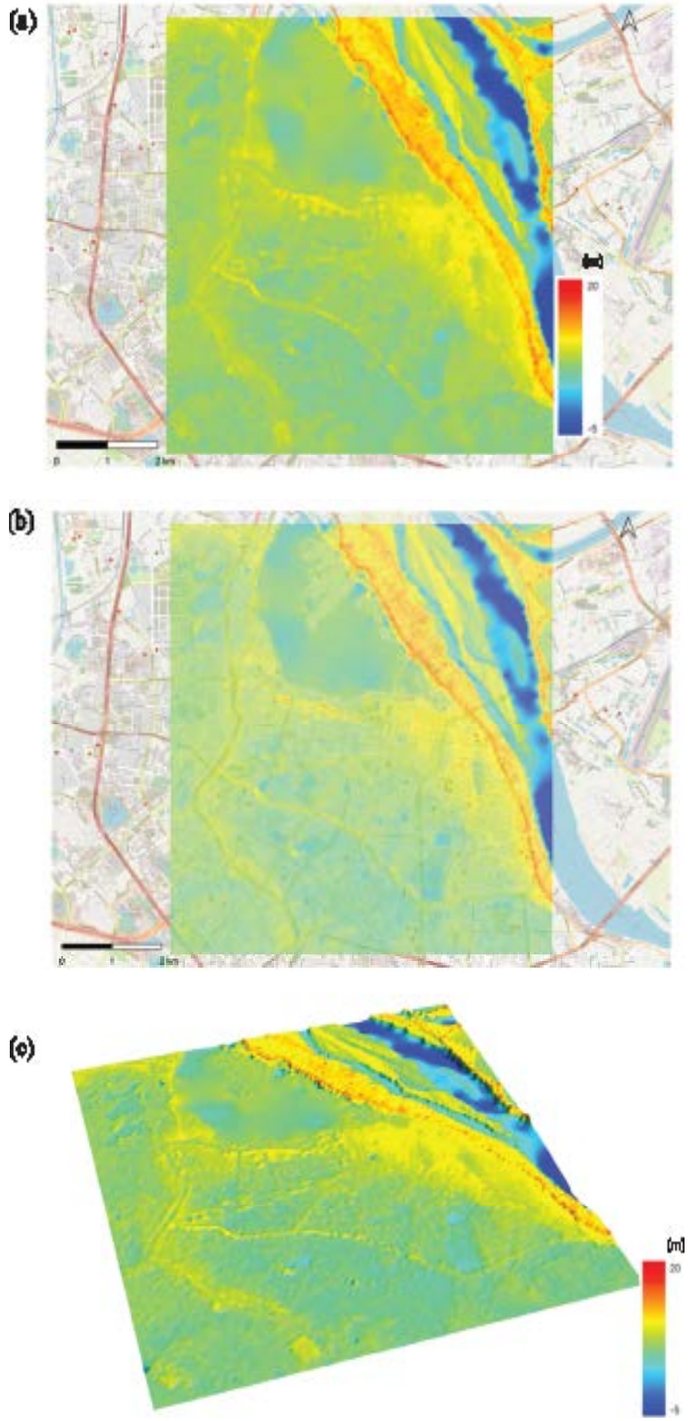

Figure 2. Generated DEM of central Hanoi, (a)Visualization of DEM (3,816×4,056 grid, 2 m resolution), (b) Visualization of DEM with 60 % transparency, (c) 3D visualization of DEM.

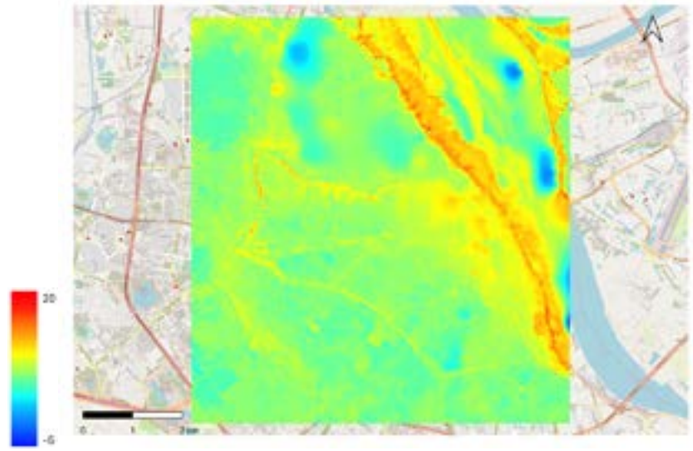

Figure 3. Generated 2005 DEM of central Hanoi.

(a)

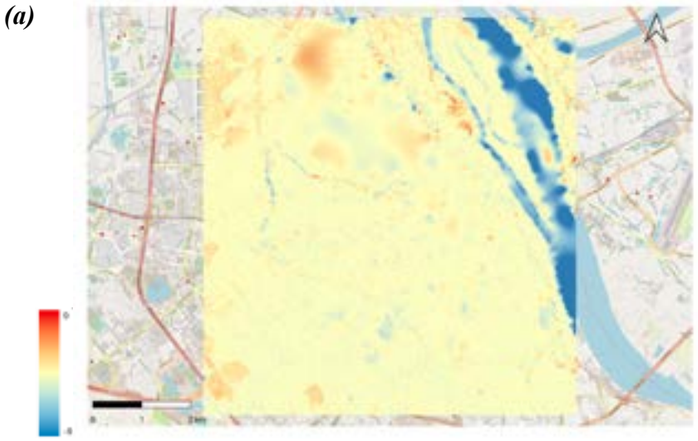

(b)

Figure 4. Difference of DEM by comparing between 2018 and 2005,
(a)Visualization of difference DEM (same region),
(b) Visualization of DEM with 60 % transparency.

We generated the difference of DEM by comparing between 2018 and 2005 (Figure 4). Areas represented in red color are those where the elevation in 2018 is higher than in 2005. Blue color is the area where the elevation in 2018 is lower than in 2005. By comparing the two, it can be seen that the Western side of the lake (Ho Tay) and the Southwestern part of the research area are about 3 or 4 m higher. Also, an area of elevation can be seen between the Great Dike of Hanoi city and the Red River (Song Hong).

5. CONCLUSION

An elevation survey data in 2018 were extracted from a 1:2,000 scale city planning map of Hanoi city, Vietnam and was used for a generation of high-resolution DEM. In this research, we generated a DEM of 2018 with a resolution of 2 m of central Hanoi city. We will validate the parameters used to generate the DEM to improve its accuracy.

Additionally, we compared the generated DEM with the DEM of 2005. The difference between both DEMs generated by using GIS. The topographic changes over the 13-year period were visualized. There was no significant change in the central area of Hanoi city, but 3 or 4 m changes were observed in the suburban areas.

DEMs representing topographic undulations are very important information for urban infrastructure development, building construction and disaster prevention. It is also important for the sustainability of Hanoi city. We hope that the relationship between the DEMs and land use and other infrastructures will be verified in detail in the future, leading to the reduction of urban water damage.

6. ACKNOWLEDGEMENTS

This research was supported by JSPS KAKENHI Grant Numbers 21K01019 and 21K11905.

7. REFERENCES

Nonogaki S., Masumoto S. and Shiono K., 2012. Gridding of Geological Surfaces based on Equality-Inequality Constraints from Elevation Data and Trend Data. *International Journal of Geoinformatics*, *8* (4), 49-60.

Yonezawa G., 2009. 3-D Topographical Analysis in Hanoi, Vietnam. *Southeast Asian Studies*, *46*(4), 519-531.

Yonezawa G., Nonogaki S., Mitamura M., Sakurai K., Truong X. L., Masumoto S., Nemoto T. and Raghavan, V., 2016. Utilization of Elevation and Borehole Data of Hanoi City, Vietnam -Construction of 3D Geological Model-. *Proceedings of GIS-IDEAS 2016,* 190-195.

Yonezawa G., Shibayama M., Nonogaki S., Masumoto S., Raghavan V., and Truong X. L., 2008. Hanoi Urban Transformation in the 19-21 Centuries -Topographic Canges and 3-D Modeling-. *Proceedings of GIS-IDEAS 2008,* 409-414.

DISTRIBUTION, FATE AND ECOLOGICAL TOXICITY OF SOME HEAVY METALS IN SEDIMENT: A CASE STUDY FROM DAY RIVER DOWNSTREAM, VIETNAM

Nguyen Khanh Linh[1,2], Trinh Thi Tham[1], Kieu Thi Thu Trang[1], Trinh Thi Thuy[1], Nguyen Thi Linh Giang[1], Luu Duc Hai[3], Tu Binh Minh[4], Le Thi Trinh[1]*

[1]Hanoi University of Natural Resources and Environment, Vietnam
[2]PhD candidate at VNU University of Science, Ha Noi, Vietnam
[3]Vietnam Association for Environmental Economics
[4]Falculty of Chemistry, VNU University of Science, Hanoi, Vietnam.
*Corresponding author. Email: lttrinh@hunre.edu.vn

ABSTRACT

According to the statistics of management agencies, the Nhue-Day River basin system is experiencing an increase in the number of polluted sources and wastewater flow from production and living activities. The accumulation of persistent organic substances, heavy metals, etc., in sediments affects the quality of river water and the aquatic living system. In this study, the 50 surface sediment samples were collected along Day River downstream in July 2018 and January 2019 (25 sampling sites) to clarify the status, movement and potential risk of some heavy metals (Cr, Pb, Cu, Cd and Hg). The receptor model of Principal Component Analysis (PCA) was applied to track the source types of these metals. The results show that the trace metal contents in sediment were below the limited values suggested by the National Technical Regulation on Sediment Quality (QCVN 43:2017/BTNMT). However, some of those were between the threshold effect level (TEL) and probable effect level (PEL), indicating that heavy metals have been able to cause negative effects on the water organisms. The order of potential ecological risk factors () for each metal in the sediment was arranged as follows: Hg > Cd > Pb > Cu > Cr. This research area overall suffered from a "low-to-moderate" pollution status. The elements Hg and Cd were a major concern for the ecosystem's health because of their high toxicity. Sedimentation of materials at Day Estuary is affected by hydrodynamic factors and the distribution of heavy metals can be well correlated to the sedimentary dynamic environment. Human activities and hydrodynamic conditions are, therefore, important factors that influence the distribution of heavy metals in this study area. Metal source apportionment would control the metal input into the river and estuary and can inform sediment quality management.

1. INTRODUCTION

Day River - the main river of the Nhue-Day River system that originates in the Hanoi province and flows through the Ha Nam, Ninh Binh and Nam Dinh provinces before transforming to the Day River mouth (MONRE, 2020). Playing an important role in crucial river transportation and the socio-economic development of the Nhue-Day River basin, the water quality of Day River is significantly affected by discharged pollutants from pollution sources.

Human development activities and natural processes have released some of the quantities of metals into the aquatic environment. The secondary source of heavy metal pollution in soil and water originates from the use of pesticides, insecticides, fertilizers and more in agriculture. Metals from wastewater transported in currents accumulate in sediments of water bodies because of their non-biodegradable properties. In river basins, more than 97 % of the mass transport of heavy metals to the ocean is associated with river sediments (Jain & Sharma, 2001). The key factors influencing the overall amount of heavy metals from the river to the continental shelf are the coastal current's barrier effects in the sea self and the estuary's filtration of the estuary (M. Liu et al., 2019). Many heavy metals are highly toxic to humans and ecosystems, even in trace concentrations (J. Liu et al., 2019). The toxicity of heavy metals depends on many factors, such as metal species, characteristics, the biological role of the metal, the exposed organism and the lifespan of the exposed organism.

Research on heavy metal distribution and transportation in river sediments was conducted in different regions. Research at the Yangtze River (YR) showed that higher concentrations of metals were discovered in the Yangtze River Estuary (YRE) and the nearshore sloppy region, but lower concentrations were discovered in the Yangtze River channel and the East Sea offshore. However, most heavy metals from the YR showed no change or a slight increase from the inland surface water to the estuary during the pathway cycle. However, they ultimately decreased outside the estuary, particularly in the silt of the East Sea shelf. The information on factors affecting heavy metal transport in sediments, including physicochemical conditions of the environment, was also reported (M. Liu et al., 2019). Similarly, research at the Dagu River Estuary in Jiaozhou Bay, Qingdao, China, also showed that the trace metal content in estuary sediments was much higher than in river sediments; concentrations (mg/kg) of heavy metals in the Dagu River were as follows: Cr ranged from 6.7 to 71.2 with an average of 34.9, Cd ranged from 0.04 to 0.13 with an average of 0.05, Cu ranged from 5.2 to 50.2 with an average of 15.7, Pb ranged from 10.5 to 33.3 with an average of 23.3 and Hg ranged from 0.005 to 0.14 with an average of 0.02 (J. Liu et al., 2019). Besides, the important factors affecting the distribution of heavy metals in the Bohai Sea and the Yellow Sea have been shown to include human activities, particle size and hydrodynamic conditions (Lv et al., 2021). Research results in estuarine shelf regions of the East Sea indicate that heavy metal concentrations are higher in the South than in the North. The distribution of the six heavy metals (Cr, Zn, Ni, Pb, Cu and Cd) can be divided into four groups that correspond well to different sediment compositions, suggesting that hydrodynamic sorting plays an important role in the selective transport of sediment heavy metals (Wang et al., 2018).

In Vietnam, studies on the distribution and transport of heavy metals in river sediments have been carried out in some large rivers such as the Red River (Nguyen et al., 2016), estuaries near Cua Ong port (Ho et al., 2010), Cau River (Duong & Cao, 2015) and Rach River - Ho Chi Minh city (Hoang et al., 2007). The content distribution of some heavy metals such as Pb, Cd, Cu and Zn in sediments in the estuary was slightly higher than in inland river areas. The assessment of the potential risks of some heavy metals was conducted in the Mekong delta (Wilbers et al., 2014), Red River (Trinh et al., 2022), Nhue-Day River basin (Ngo et al., 2021), Vam Thuat river (Le & Nguyen, 2022) and tropical mangrove forests in Can Gio (Nguyen et al., 2019) and coastal areas in the South (Costa-Böddeker et al., 2017). Enrichment factors (EF) of some metals, including Cu, Cd, Pb, Ni and Zn, have shown significant pollution of Cd, Cu and Pb metals in the upstream area of the Red River (Nguyen et al., 2016); (Trinh et al., 2022). Besides, the pollution of some metals

in sediment samples taken at Cua Ong, Ha Long Bay (Vietnam) was confirmed when the I_{geo} value was high and positive for As (Nguyen et al., 2019). Sediment and fish samples from the Nhue Day basin were analyzed to determine the levels of Zn, Cu, Pb and Cd pollution and their potential ecological (EF, modified Pollution Index-mPI and expanded, modified potential ecological risk index-emRI) and human health risks (THQ, HI and TR indices). The metal levels in sediment upstream of Day River indicated moderate to severe contamination (Ngo et al., 2021).

Heavy metals are easily adsorbable on the surface of sediment particles and their concentration is regulated by sediment movement and water flow. Therefore, revealing the transportation and accumulation trend of heavy metal in rivers requires a detailed study of the depositional properties of surface sediments and heavy metal concentrations. The following objectives are specific to this study: (1) to describe the distributions and transportation of heavy metals (Cr, Pb, Cu, Cd and Hg), (2) to analyze the ecological risk of these heavy metals in surface sediments of the Day and (3) track the source of the metals in aquatic systems using the model of Principal Component Analysis (PCA).

2. MATERIALS AND METHOD

Along the Day River downstream (about 130 km from Phu Ly City, Ha Nam province to the Day River estuary), 50 surface sediment samples were collected in July 2018 and January 2019 (Fig. 1). The Peterson grab (Wildco 1750-G30) was used to take sediment samples at a depth of about 5 - 10 cm following the US-EPA sediment sampling Guide and Methodologies (US-EPA, 2010). After mixing evenly on a plastic tray, about 500 grams of the sample was put into the wide-mouth glass container with a Teflon-lined cap. All samples were stored in a specialized sample storage box with ice gel according to TCVN 6663-15:2008 (ISO 5667-15:1999) and transported to the laboratory.

In the laboratory, sediment samples were naturally dried at room temperature. Sediment samples were pretreated in the laboratory using the natural drying method. During the drying process, impurities were removed. Then, the dry sediment samples were crushed according to TCVN 6647:2007 into particle sizes less than 63 µm to determine the humidity (TCVN 4048:2011) and heavy metals contents.

Sediment samples were processed to determine the concentration of some heavy metals according to EPA guidelines 3050B (1996). Sediment samples were treated by in organization of wet samples with strong acid HNO_3 at a ratio of 1:1 and 30 % H_2O_2 solution. The experimental process is described in detail in the publication of Lap et al., (2021). The flame atomic and cold vapor absorption spectroscopy (F-AAS and CV-AAS) with optimized conditions were applied to measure the concentration of heavy metals. The standard deviation of the concentration of quality control samples of heavy metal was less than 7.3 % and the recovery rate of heavy metal content was between 90 % and 112 %.

2.1 Risk assessment

In this study, three parameters, the Geo-accumulation index (I_{geo}), the Potential Ecological Risk Index (RI) and the Degree of Contamination (Cd), were calculated to evaluate the degree of contamination on the sediments. The I_{geo} was first studied by Müller and Suess, (1979) to determine the extent of metal accumulation in sediments. Many scientists use this index to evaluate the level of contamination of individual metals in sediments.

The Potential Ecological Risk Index (RI) was proposed by Håkanson, (1980) to comprehensively assess the ecological risk caused by toxic metals, a useful indicator reflecting the status and degree of environmental contamination. The calculation equations of RI can be presented as the following:

$$C_f^i = \frac{C_n^i}{C_0^i} \quad (1)$$

$$E_r^i = T_r^i \times C_f^i \quad (2)$$

$$RI = \sum E_r^i \quad (3)$$

where C_f^i is the single metal pollution index; C_0^i is the reference value for the metal; C_n^i: is the concentration of metal in the samples; E_r^i: is the monomial potential ecological risk factor; T_r^i is the metal toxic response factor, according to Hakanson, (1980). The values for each element are in the order Zn = 1 < Cr = 2 < Cu = Ni = Pb = 5 < As = 10 < Cd = 30 < Hg = 40.

The four categories of RI and five categories of E_r^i were shown in many previous studies (Lap et al., 2021). To describe the contamination of toxic substances in the studied region, we may define a contamination factor (C_f^i). The following terminology may be used to describe the degree of contamination (Cd) proposed by Håkanson, (1980): $C_d < 8$ indicates a low degree of contamination; $8 \leq C_d \leq 16$ is a moderate degree of contamination; $16 \leq C_d \leq 32$ is a considerable degree of contamination; $C_d \geq 32$ is a very high degree of contamination indicating anthropogenic severe pollution.

2.2 Data analysis processing

All data collected were processed and analyzed using Origin Pro 9.5. The distribution map of metals was built on ArcGIS software using the Kriging interpolation model. The 25 sampling points were divided into 4 site clusters, with 2 first clusters in the inland river area (from SD1 to SD12), a second cluster in the estuary area (from SD13 to SD18) and a last cluster in the coastal area (from SD 19 to SD25). To evaluate the correlation between metal concentrations in sediment.

PCA examines the correlations among heavy metals and identifies their potential sources (Zhao et al., 2017); (Zhao et al., 2020). The related factor scores of PCA, calculated by the regression method, help to understand the associations of environmental variables and to identify source types (Wu et al., 2021). Pearson correlation analysis and Data preparations for PCA were both performed using the statistical package IBM SPSS Statistics 26 for Windows (IBM-Corp, Released 2019).

3. RESULTS AND DISCUSSION

3.1 Spatial distribution of some heavy metals in sediment

Table 1 gives information about the concentrations of five heavy metals in sediments. Compared to the environmental quality standard in marine Vietnam National Technical Regulation on Sediment Quality (QCVN 43:2017/BTNMT), all concentration values are within acceptable ranges. This study divided samples into two groups based on water type (freshwater or salt water

and brackish water) in July 2018 and January 2019. Group one includes sampling sites from SD1 to SD12, which are places with freshwater sources. The average metal concentration in group one varied for Cr, Cu, Cd, Hg and Pb from 27.9 to 92.4 mg/kg (mean 60.6 ± 18.3 mg/kg), from 8.80 to 60.1 mg/kg (mean 38.7 ± 15.0 mg/kg), from 0.310 to 1.06 mg/kg (mean 0.670 ± 0.240 mg/kg), from 0.110 to 0.492 mg/kg (mean 0.260 ± 0.131 mg/kg) and from 15.8 to 39.5 mg/kg (mean 26.4 ± 8.18 mg/kg) in July 2018 and from 29.4 to 98.3 mg/kg (mean 62.7 ± 17.5 mg/kg), 9.02 to 62.0 mg/kg (mean 36.2 ± 14.4 mg/kg), 0.292 to 0.623 mg/kg (mean 0.441 ± 0.102 mg/kg), from 0.060 to 0.470 mg/kg (mean 0.230 ± 0.135 mg/kg) and 14.8 - 44.9 mg/kg (mean 27.7 ± 9.95 mg/kg) in January 2019, respectively. Thus, the results of group one showed that at the time of sampling in 2018, the average concentrations of metals Cu, Cd and Hg in the sediment had higher values, while the concentrations of metals Cr and Pb had lower concentrations in 2019. Group two, which includes sampling sites from SD13 to SD25, showed that the average concentrations of heavy metals Cd and Hg in 2018 were higher than in 2019. In contrast, concentrations of heavy metals Cr, Cu and Pb in 2018 were lower than in 2019.

Table 1. Summary of concentration of some heavy metals in sediment.

	Heavy metal element (mg/kg)									
	July 2018					January 2019				
	Cr	**Cu**	**Cd**	**Hg**	**Pb**	**Cr**	**Cu**	**Cd**	**Hg**	**Pb**
SD1-SD12										
Average	60.6	38.7	0.668	0.259	26.4	62.7	36.2	0.435	0.233	27.7
Min-Max	27.9-92.4	8.80-60.1	0.310-1.06	0.109-0.490	15.8-39.5	29.4-98.3	9.02-62.0	0.285-0.624	0.060-0.470	14.8-44.9
SD	18.3	13.0	0.237	0.127	8.18	17.5	14.4	0.099	0.126	9.95
LEL	26	16	0.6	0.2	31	26	16	0.6	0.2	31
Reference values* (Freshwater sediment)	90	197	3.5	0.5	91.3	90	197	3.5	0.5	91.3
SEL	110	110	10	2	250	110	110	10	2	250
SD13-SD25										
Average	47.7	33.2	0.469	0.251	33.9	49.2	35.7	0.259	0.239	41.0
Min-Max	28.6-68.8	13.1-50.5	0.219-1.02	0.094-0.429	20.9	31.8-72.6	18.6-70.2	0.154-0.465	0.090-0.466	19.7-79.3
SD	12.2	14.2	0.244	0.115	9.08	10.2	14.5	0.080	0.119	20.0
LEL	26	16	0.6	0.2	31	26	16	0.6	0.2	31
Reference values* (Saltwater and brackish water sediment)	160	108	4.2	0.7	112	160	108	4.2	0.7	112
SEL	110	110	10	2	250	110	110	10	2	250

**Reference values of heavy metals in the marine were specified in Vietnam National Technical Regulation on Sediment Quality (QCVN 43:2017/BTNMT)*

Besides, the spatial distribution of heavy metals is shown in Fig.1. The concentration of all five metals was higher at estuaries and coastal zones. Comparison threshold effect levels (TEL) taken from Canadian Sediment Quality Guidelines for the Protection of Aquatic Life (CCME, 1999), NOAA. Screening Quick Reference Tables (Buchman, 2008), the contents of heavy metals except for Hg in all sediments samples transcended the TEL values by 1.04 - 4.39 times. However, the concentration of heavy metals in surface sediments was lower than severe

effect levels (SEL). The distribution map shows a visual image of the impact level of metals in sediments in the study area.

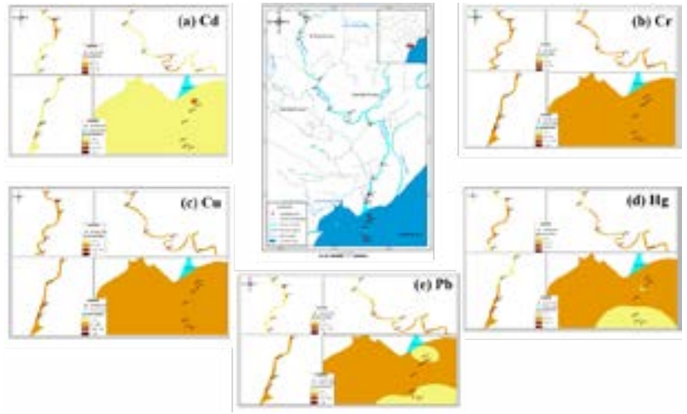

Figure 1. Map of the Day River downstream with sampling locations and concentrations of heavy metals in sediment.

According to the results, Pearson correlation analysis between heavy metals, Cr, Pb and Cu are significantly correlated at the 0.01 level (R_{Cr-Cu} = 0.640, R_{Cu-Pb} = 0.409), meaning they may have similar input sources. Hg has a negative correlation with Cd and has no significant correlation with Cr, Cu and Pb, indicating Hg may have a different source with Cd, Cr, Cu and Pb.

3.2 Ecological risk assessment

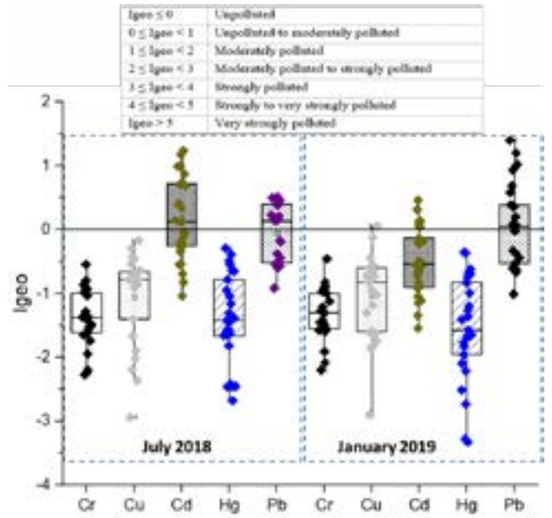

Figure 2. The box-and-whisker plot of I_{geo}.

Figure 2 illustrates the outcome of calculating I_{geo} and demonstrates how the levels of pollution for five heavy metals decrease in the order shown: Cu > Pb > Cd > Hg > Cr (in July 2018) and Pb > Cu > Cd > Hg > Cr (in January 2019). The average of I_{geo} indicated that Cr, Cd and Hg contamination reached class 0 levels (unpolluted) with I_{geo} range from -2.23 to -0.547 (mean -1.39 ± 0.460) (in July 2018) and -2.20 to -0.458 (mean -1.331 ± 0.402) (in January 2019); -1.04

to 1.24 (mean 0.179 ± 0.670) (in July 2018) and -1.55 to 0.472 (mean -0.485 ± 0.54) (in January 2019); -2.68 to -0.293 (mean -1.40 ± 0.71) and -3.33 to -0.353 (mean -1.55 ± 0.83) respectively. Meanwhile, I_{geo} of Cu in January 2019 was classified as class 1 (unpolluted to moderately polluted) because the average of I_{geo} was -2.95 to -0.167 (mean -1.05 ± 0.720). Especially, the I_{geo} value of Pb in the two rounds of sampling varied from -0.923 to 0.519 (mean -0.055 ± 0.461) (in July 2018) and -1.02 to 1.40 (mean 0.057±0.66) (January 2019), hence they were assigned to class 1 (unpolluted to moderately polluted).

Table 2. Ecological risk of heavy metals in sediments.

ID sample	July 2018							January 2019						
	E^i_t					RI	Cd	E^i_t					RI	Cd
	Cr	Cu	Cd	Hg	Pb			Cr	Cu	Cd	Hg	Pb		
SD1	1.58	1.06	3.39	32.3	1.09	39.4	1.74	1.53	1.09	3.53	30.7	1.03	37.9	1.69
SD2	1.17	0.997	6.35	35.1	1.11	44.7	1.66	1.12	1.02	4.24	30.3	1.05	37.7	1.49
SD3	1.60	1.40	9.10	17.6	1.90	31.6	1.98	2.18	1.57	4.82	9.6	1.21	19.4	1.93
SD4	2.05	1.53	7.05	**55.9**	1.27	67.8	2.52	0.653	0.229	3.40	**54.3**	0.813	59.4	1.33
SD5	0.621	0.222	6.27	**46.6**	0.867	54.6	1.32	1.25	1.049	3.48	**41.8**	2.11	49.7	1.89
SD6	1.17	1.04	4.87	17.5	2.16	26.7	1.61	1.62	1.028	3.30	16.8	1.05	23.8	1.55
SD7	1.65	0.966	6.18	37.0	1.11	46.9	1.91	1.69	0.997	4.06	32.2	1.06	40.0	1.80
SD8	1.72	0.945	3.75	17.9	1.13	25.5	1.63	1.58	0.552	2.44	9.9	1.87	16.3	1.48
SD9	1.52	0.958	3.67	**78.4**	1.93	86.5	2.44	1.50	1.17	3.32	**75.2**	2.46	83.6	2.53
SD10	0.898	0.916	7.68	**73.4**	1.12	84.0	2.03	1.38	0.486	5.35	**60.6**	2.11	70.0	2.15
SD11	1.14	0.649	7.68	**49.8**	1.85	61.1	1.95	1.22	0.697	4.22	**48.2**	1.74	56.1	1.84
SD12	1.03	1.11	2.66	35.8	1.84	42.4	1.64	0.993	1.14	2.58	37.4	1.72	43.8	1.62
SD13	1.46	0.924	3.56	30.9	2.17	39.0	1.48	1.29	0.870	1.86	22.4	3.14	29.6	1.45
SD14	1.04	0.993	3.04	27.2	2.30	34.6	1.36	1.08	0.891	2.75	24.7	3.33	32.7	1.47
SD15	1.53	1.07	4.26	**43.0**	2.33	52.2	1.70	1.61	1.78	2.34	**40.1**	4.34	50.2	2.24
SD16	1.16	1.28	5.11	**61.1**	2.26	70.9	1.85	1.24	1.26	3.99	**57.7**	3.78	68.0	2.05
SD17	1.07	0.422	4.21	**68.6**	1.21	75.5	1.38	1.00	0.844	2.65	**62.6**	1.13	68.2	1.41
SD18	0.780	0.538	3.26	30.3	1.17	36.1	0.97	1.06	1.16	2.06	**74.5**	2.64	81.4	1.87
SD19	0.824	1.69	2.96	22.1	1.77	29.3	1.65	0.728	1.59	1.55	16.0	2.56	22.4	1.42
SD20	0.585	1.81	2.53	19.5	1.88	26.3	1.34	0.606	1.63	2.29	17.6	2.72	24.9	1.20
SD21	0.860	1.95	3.55	30.7	1.90	39.0	1.44	0.908	3.25	1.95	28.6	3.54	38.3	1.37
SD22	0.651	2.34	4.26	**43.6**	1.84	52.7	1.72	0.696	2.30	3.32	**41.2**	3.08	50.6	1.07
SD23	0.601	0.770	3.50	**49.0**	0.986	54.9	1.37	0.565	1.54	2.21	**44.7**	0.925	49.9	0.91
SD24	0.439	0.982	2.71	21.7	0.952	26.8	0.88	0.595	2.11	1.72	**53.2**	2.15	59.8	0.91
SD25	0.539	1.991	7.30	**44.0**	0.935	54.8	0.78	0.576	1.77	2.16	**42.4**	0.878	47.8	0.93

According to Table 2, sediments in this region showed a low level of contamination (Cd <8) based on the categorization approach for interpreting Cd described in the method section above. Table 2 also showed that RI values were at a low-risk level for any factors examined (RI <110). Besides, almost all values of the E^i_t were at the grade "low risk" with values under 40, but there were some values of E^i_t of Hg confirmed at level "moderate risk" ($40 \leq E^i_t < 80$).

3.3 Influence of human activities on the distribution of heavy metal

Identifying the pollution sources of heavy metals is significantly valuable for environmental risk management. In the Day River downstream, heavy metals were imported through several pathways, such as pollutants from agriculture activities, river transport activities and wastewater from some craft villages and industrial parks along the river banks. The results of PCA determined the most common pollution sources and contribution rates of heavy metals in the Day River downstream (Table 3 and Fig. 3). In July 2018, the two principal components accounted for 100 % of the total variance. PC1 (36.0 % of the total variance) was highly correlated with Cu, Cr and Pb, with significant correlations exhibited by the paired elements of Cu, Cr and Pb (R =0.496-0.926), indicating that this group had similar contamination levels or similar pollution sources. Previous studies have suggested that Cu, Cr and Pb were mainly from industrial wastewater sewage irrigation and agricultural pollution.

The other principal component, PC2 for samples taken in 2018 and PC3 for samples taken in 2019, accounting for 65.8 % and 87.7 % of the total variance, included the high loading of Cd and Hg, with slight correlations (R = 0.285) demonstrating a different pollution source. Hg in the environment originated mainly from natural sources (volcanoes, the weathering of rocks, forest fires and soils) and human activities such as fuel and oil combustion. Both EF and I_{geo} results suggested that Cd was influenced by anthropogenic input due to the use of chemical fertilizer in agricultural production and sewage irrigation.

Table 3. Source identification of heavy metals in the sediments using PCA.

	PCs	Eigenvalue	Variance	PCA
July 2018	PC1	1.80	36.0 %	Cu, Cr, Pb
	PC2	1.49	29.6 %	Cd, Hg
January 2019	PC1	1.95	39.0 %	Cu, Cr
	PC2	1.28	25.7 %	Pb
	PC3	1.15	23.0 %	Cd, Hg

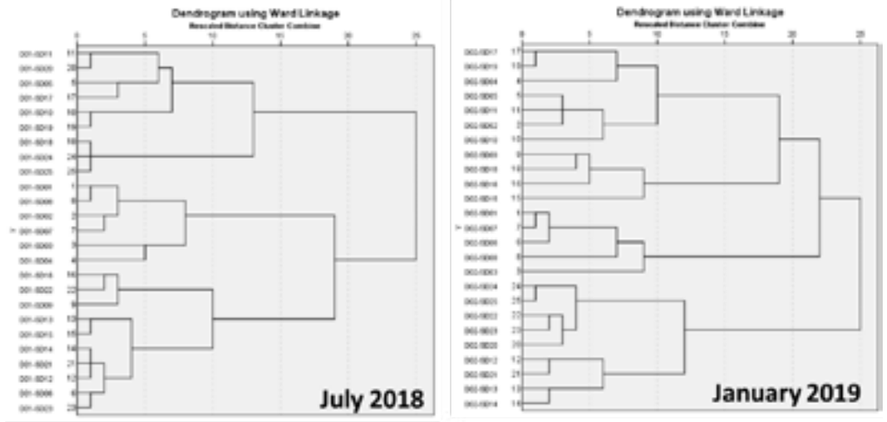

Figure 3. Analysis Clusters results between sediments samples.

Cluster analysis provides information about groups of samples that may have effects from similar waste sources (See Fig.3). The cluster of samples SD12, SD13, SD14, SD21, SD22, SD23 with slightly polluted Cr, Cu, Pb and Hg is a group of sampling points affected by transportation through the main tributaries and river networks. The sampling sites cluster SD01, SD03 and SD06 - SD08 with non-polluted Cd, Pb and Hg have a similar source of contamination from wastewater from residential areas and craft villages along the river. The remaining clusters correspond to sites close to various sources. Some studies have used PCA and geographically

weighted regression (GWR) models to identify the pollution source of metals in the environment (Mohammadi et al., 2019); (Dabgerwal & Tripathi, 2016). The results also reveal that land use types are highly related to human activities and sediment pollution in river systems. The positive correlation between heavy metals and human activities was observed for almost all heavy metals, which varies with the agricultural and urbanization development level at the sub-watershed. Based on the findings, appropriate policies and decisions should be taken on land use to prevent the transfer of heavy metals by sediment to aquatic environments. The classification of sampling sites in the whole research area based on cluster analysis suggests a reduction in sampling sites in the monitoring network without affecting the reliability of the results (Dabgerwal & Tripathi, 2016).

4. CONCLUSION

The research team has built a distribution map of some heavy metals in the downstream area of the bottom river, with input data being the content of those metals in sediment at 25 sampling locations. The metal content is within the allowable limits according to QCVN 43:2017. As a consequence, the sampling sites from SD1 to SD12 demonstrated that, at the time of sampling in 2018, the average concentrations of the metals Cu, Cd and Hg in the sediment were higher than those of Cr and Pb in 2019, while those from SD13 to SD25, the average concentrations of heavy metals Cr, Cu and Pb were lower in 2018 than in 2019, the concentrations of Cd and Hg were higher in 2018. The risk calculation results confirm that the metals pose a low or moderate risk to aquatic ecosystems. I_{geo} and EF values indicate metals that mainly enter surface water and accumulate in sediment from human activities. Clusters of waste sources are also indicated and the main sources of heavy metal in the study area are mainly livestock farming and agricultural production. The results obtained in the study should be a helpful information source, which could be used to monitor measurements and manage the water environment in river basins.

5. ACKNOWLEDGEMENTS

This study was supported by the Project "Comprehensive Assessment of Bioaccumulation Potential and Ecotoxicological and Human Health Risk of Multiple Organic Micro-pollutants in Estuarine and Coastal Areas of Vietnam by Using Paired Biota-sediment Indicators" supported by Vietnam's National Foundation for Science and Technology Development (NAFOSTED) under grant number 104.04-2021.09.

6. REFERENCES

Buchman M. F., 2008. Screening Quick Reference Tables (SQuiRTs).

Canadian Council of Ministers of the Environment (CCME), 1999. Canadian Sediment Quality Guidelines for the Protection of Aquatic Life.

Costa-Böddeker S., Hoelzmann P., Thuyen L. X., Huy H. D., Nguyen H. A., Richter O., & Schwalb A., 2017. Ecological risk assessment of a coastal zone in Southern Vietnam: Spatial distribution and content of heavy metals in water and surface sediments of the Thi Vai Estuary and Can Gio Mangrove Forest. *Mar Pollut Bull*, *114*(2), 1141-1151. https://doi.org/10.1016/j.marpolbul.2016.10.046.

Dabgerwal D., & Tripathi D. S., 2016. Assessment of surface water quality using hierarchical cluster analysis. *International Journal of Environment*, *5*, 32. https://doi.org/10.3126/ije.v5i1.14563.

Duong T. T. A., & Cao V. H., 2015. Study on the distribution of heavy metals in sediments under the Cau River basin. *Vietnam Analytical Sciences Society*, *20*(4), 36-43.

Håkanson L., 1980. An Ecological Risk Index for Aquatic Pollution Control-A Sedimentological Approach. *Water Research*, *14*, 975-1001. https://doi.org/10.1016/0043-1354(80)90143-8

Ho H. H., Rudy S., & Damme A., 2010. Distribution and contamination status of heavy metals in estuarine sediments near Cua Ong harbor, Ha Long Bay, Vietnam. *Geologica Belgica*, *13*.

Hoang T. T. T., Tu T. C. L., & & Nguyen N. H. V., 2007. Study on environmental geochemistry of some heavy metals in river and canal sediments of Ho Chi Minh city. *VNUHCM Journal of Science and Technology Development*, *10*(01), 1-10.

IBM-Corp, 2019. IBM SPSS Statistics for Windows, Version 26.0. *Armonk*, NY: IBM Corp..

Jain C. K., & Sharma M. K., 2001. Distribution of trace metals in the Hindon River system, India. *Journal of Hydrology*, *253*(1), 81-90. https://doi.org/https://doi.org/10.1016/S0022-1694(01)00484-X.

Lap B., Thi Tham T., & Huong N., 2021. Ecological Risk Assessment of Heavy Metals in Sediments of Duyen Hai Seaport Area in Tra Vinh province, Vietnam. *Water Air and Soil Pollution*. https://doi.org/10.1007/s11270-021-05014-5.

Le H. T., & Nguyen V. P., 2022. Assessment of heavy metal pollutants in downstream Vam Thuat River. *Journal of Science and Technology, Industrial University of Ho Chi Minh city*, *59*(5). https://doi.org/https://doi.org/10.46242/jstiuh.v59i05.4601.

Liu J., Yin P., Chen X., & Cao K., 2019. Distribution, Enrichment and Transport of Trace Metals in Sediments from the Dagu River Estuary in the Jiaozhou Bay, Qingdao, China. *Minerals*, *9*(9), 545. https://www.mdpi.com/2075-163X/9/9/545.

Liu M., Chen J., Sun X., Hu Z., & Fan D., 2019. Accumulation and transformation of heavy metals in surface sediments from the Yangtze River estuary to the East China Sea shelf. *Environ Pollution*, *245*, 111-121. https://doi.org/10.1016/j.envpol.2018.10.128.

Liu M., Chen J., Sun X., Hu Z., and Fan D., 2019. Accumulation and transformation of heavy metals in surface sediments from the Yangtze River estuary to the East China Sea shelf. *Environmental Pollution*, *245*, 111-121. https://doi.org/https://doi.org/10.1016/j.envpol.2018.10.128.

Lv J., Hu R., Wang N., Zhu L., Zhang X., Yuan X., & Liu B., 2021. Distribution and movement of heavy metals in sediments around the coastal areas under the influence of multiple factors: A case study from the junction of the Bohai Sea and the Yellow Sea. *Chemosphere*, *278*, 130352. https://doi.org/10.1016/j.chemosphere.2021.130352.

Mohammadi M., Khaledi Darvishan A., & Bahramifar N., 2019. Spatial distribution and source identification of heavy metals (As, Cr, Cu and Ni) at sub-watershed scale using geographically weighted regression. *International Soil and Water Conservation Research*, *7*. https://doi.org/10.1016/j.iswcr.2019.01.005.

Ministry of Natural Resources and Environment (MONRE), 2020. Decision No. 1757/QD-BTNMT dated August 11, 2020 on a List of inter-provincial water sources and a List of inter-country water sources (surface water sources).

Müller P. J., & Suess E., 1979. Productivity, sedimentation rate, and sedimentary organic matter in the oceans: I. Organic carbon preservation. *Deep Sea Res.*, *26*, 1362-1374.

Ngo T. T. H., Tran T. L. A., Nguyen D. Q., Nguyen T. H. T., Le T. T., & Gao a. Y., 2021. Metal Pollution and Bioaccumulation in the Nhue-Day River basin, Vietnam: Potential ecological and human health risks. *International Journal of Environmental Research and Public Health*, *18*(24). https://doi.org/https://doi.org/10.3390/ ijerph182413425.

Nguyen T. N., Marchand C., Strady E., Truong V. V., & Tran T. N. T., 2019. Metals geochemistry and ecological risk assessment in a tropical mangrove (Can Gio, Vietnam). *Chemosphere*, *219*, 365-382.

Nguyen T. T., Zhang W., Li Z., Li J., Ge C., Liu J., Bai X., Feng H., & Yu L., 2016. Assessment of heavy metal pollution in Red River surface sediments, Vietnam. *Mar Pollution Bull*, *113*(1-2), 513-519. https://doi.org/10.1016/j.marpolbul.2016.08.030.

Trinh T. T., Le T. T., & Trinh T. T., 2022. Ecological risks of some heavy metals in sediment samples collected from downstream of the Red River. *Vietnam Journal of Science, Technology and Engineering*, *64*(11), 48-53. https://doi.org/DOI: 10.31276/VJST.64(11).48-53.

US-EPA, 2010. Sediment Sampling.

Wang C., Zou X., Feng Z., Hao Z., & Gao J. (2018). Distribution and transport of heavy metals in estuarine-inner shelf regions of the East China Sea. *Sci Total Environ*, *644*, 298-305. https://doi.org/10.1016/j.scitotenv.2018.06.383.

Wilbers G. J., Becker M., Nga T., Sebesvari Z., & Renaud F. G., 2014. Spatial and temporal variability of surface water pollution in the Mekong delta, Vietnam. *Sci Total Environ*, *485-486*, 653-665. https://doi.org/10.1016/j.scitotenv.2014.03.049.

Wu H., Xu C., Wang J., Xiang Y., Ren M., Qie H., Zhang Y., Yao R., Li L., & Lin A., 2021. Health risk assessment based on source identification of heavy metals: A case study of Beiyun River, China. *Ecotoxicol Environ Saf*, *213*, 112046. https://doi.org/10.1016/j.ecoenv.2021.112046.

Zhao G., Ye S., Yuan H., Ding X., & Wang J., 2017. Surface sediment properties and heavy metal pollution assessment in the Pearl River Estuary, China. *Environmental Science and Pollution Research*, *24*(3), 2966-2979. https://doi.org/10.1007/s11356-016-8003-4.

Zhao L., Gong D., Zhao W., Lin L., Yang W., Guo W., Tang X., & Li Q., 2020. Spatial-temporal distribution characteristics and health risk assessment of heavy metals in surface water of the Three Gorges Reservoir, China. *Sci Total Environ*, *704*, 134883. https://doi.org/10.1016/j.scitotenv.2019.134883.

MANGROVE DEGRADATION ASSESSMENT USING WORLDVIEW-2 IMAGERY FOR MEKONG DELTA, VIETNAM

Pham Hong Tinh[1]*, Tran Dang Hung[2], Richard A. MacKenzie[3], Truong Van Vinh[4], Bui Thanh Huyen[5], Mai Huong Lam[1], Nguyen Thi Hong Hanh[1]

[1]Hanoi University of Natural Resources and Environment, Vietnam
[2]Vietnam Institute of Meteorology, Hydrology and Climate Change, Vietnam
[3]USDA Forest Service, Pacific Southwest Research Station,
Institute of Pacific Islands Forestry, USA
[4]Faculty of Forestry, Nong Lam University, Ho Chi Minh, Vietnam
[5]Department of Water-Environment-Oceanography,
University of Science and Technology of Hanoi, Vietnam
*Corresponding author. Email: phtinh@hunre.edu.vn

ABSTRACT

Mangrove forests have been widely acknowledged for their significant roles in protecting coastal areas from soil erosion, storms and strong waves, as well as providing seafood, aiding in land reclamation and sequestering carbon. Vietnam boasts a considerable expanse of mangrove forests, spanning approximately 170,000 ha along its 3,260 km coastline, with the majority, three-quarters of the total, concentrated in the provinces of the Mekong delta. An examination of time-series WorldView-2 images reveals that between 2015 and 2020, the Vietnamese Mekong delta experienced a loss of around 16,200 ha of mangroves, accounting for approximately 20.3 % of its total mangrove area. However, during the same period, there were efforts to restore mangrove forests, leading to a gain of approximately 27,200 ha. In terms of quality, Vietnamese Mekong delta has about 6,900 ha of degraded mangrove forest (equivalent to about 7.6 % of the total mangrove area) where tree density, structure, or species composition were decreased. Degraded mangrove forests were mainly in the districts Ngoc Hien, Dam Doi, Nam Can (Ca Mau province) and An Minh (Kien Giang province). Anthropogenic factors, particularly harvesting activities constituting thinning and clear felling for wood and charcoal on a 10-15 year rotation in production forest, infrastructure construction, mangrove forests conversion to other purposes, hydrological regime changes or illegal exploitation in protected and special-use forested areas were major drivers of mangrove degradation.

1. INTRODUCTION

The Mekong delta elta coastal region has around 90,777 ha of mangrove forests, accounting for three-quarters of Vietnam's entire mangrove forest area (Tinh et al., 2022b). Mangrove ecosystem services such as coastal protection from storms, floods and erosion; the provision of fuel and raw material products; and habitat for aquatic species play an important role in the sustainable socio-economic development of the Mekong delta and the whole country. Additionally, other ecological services provided by mangroves, such as carbon sequestration for climate change adaptation and mitigation, as well as other social, human, financial and physical capital for local livelihoods, have been highly valued in recent years (Hawkins et al., 2010; Tinh et al., 2022a). However, mangrove

forests in the coastal Mekong delta have fluctuated significantly from 185,800 ha before 1973 (Phan and Stive, 2022) to 90,777 ha (Tinh et al., 2022b) due to the impact of natural conditions and anthropogenic activities. Mangrove forests were severely damaged by the Second Indochina War from 1955 to 1975 (Hong and San, 1993), then significantly converted to shrimp farms in the 1990s (de Graaf and Xuan, 1998) and have been greatly affected by expressions of climate change such as sea level rise and increased storms in recent decades (Truong et al., 2017).

In the Mekong delta region, there have been a number of studies on mangrove area changes (Tong et al., 2004; Thu and Populus, 2007; Bullock et al., 2017; Hong et al., 2019; Liu et al., 2020; Phan and Stive, 2022; Tinh et al., 2022b) and the reasons for these changes (Binh et al., 2005; Truong and Do, 2018; Quyen, 2011; Tinh et al., 2022a). However, research on changes in the quality of mangrove forests is still quite restricted and needs to be expanded. Meanwhile, the study of vegetation indices derived from satellite images, such as the Normalized Difference Vegetation Index (NDVI), is considered to effectively evaluate and identify changes in the quality, growth and development of terrestrial plants (Jackson et al., 1983; Janssen et al., 2018; Li et al., 2018) and coastal mangroves (Fuazi et al., 2019; Akbar et al., 2020).

The study reported research findings on mangrove degradation assessment using WorldView-2-based NDVI and NDVI differencing techniques. NDVI was estimated through analysis of satellite images band ratio to give an indication of greenness and healthy forests. The findings contribute to identifying areas with high levels of degradation that need to prioritize restoration and conservation solutions.

2. MATERIALS AND METHODS

2.1 Study area

This study was carried out in mangrove areas along the coast of the Vietnamese Mekong delta, which includes seven provinces of Tien Giang, Ben Tre, Tra Vinh, Soc Trang, Bac Lieu, Ca Mau and Kien Giang (Figure 1).

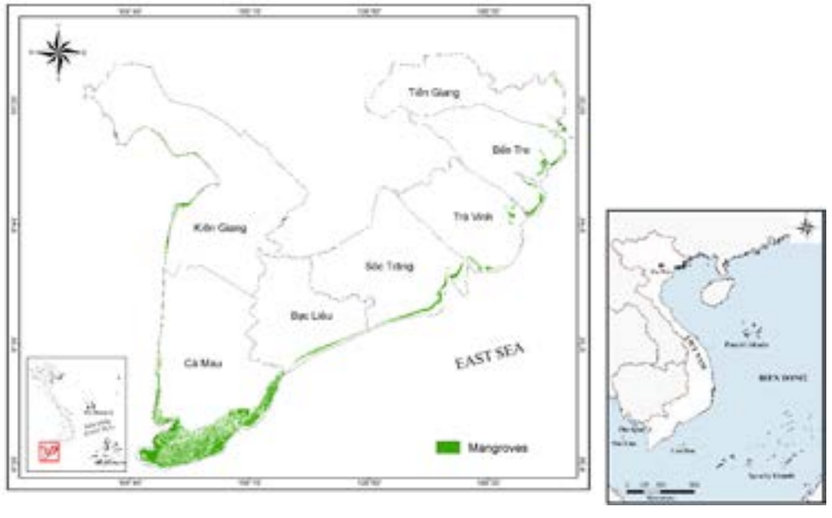

Figure 1. Study area in Mekong delta, Vietnam.

Mekong delta's mangroves were classified into three types of forest: Protection forest, special-use forest and production forest. In 1973, this region had a mangrove extent of up to 185,800 ha (Phan and Stive, 2022). Efforts to rehabilitate mangrove forests have increased in recent years (Tinh et al., 2022b); Nevertheless, the pressures of socio-economic development and variating natural conditions are also driving the mangrove forest area to diminish in quality. Tinh et al., (2022b) reported that the total area of mangroves in the Mekong delta is about 90,777 ha and is dominated by *Rhizophora apiculata, R. mucronata, Avicennia alba, A. officinalis, Sonneratia alba, Bruguiera cylindrixa and B. parviflora*.

2.2 Satellite data

This study was conducted using multi-temporal WorldView-2 images acquired during 2015 and 2020. As the average cloud cover of the WV-2 images over the study area for 2015 and 2020 were 16.38 % and 23.94 %, respectively, we used eight Sentinel-2 images with an average cloud cover of less than 5 % to compensate for frequent cloud cover of WV-2 images. The Sentinel images were georeferenced to the WV's resolution to ensure proper alignment and compensated for the frequent cloud cover of WV-2 images (Alm et al., 2020). The detailed description of the images can be found in the study of Tinh et al., (2022b).

2.3 Satellite imagery processing

The satellite images for 2015 and 2020 were subsets to the mangrove boundary that were classified and reported in the study of Tinh et al., (2022b) to reduce the file size and improve the processing times. Then, NDVI was calculated for each image using the equation (1)

$$NDVI = (NIR - RED) / (NIR) + RED) \quad (1)$$

where NDVI is the Normalized Difference Vegetation Index, NIR is the reflectance of the near-infrared bands and RED is the reflectance of the red bands. NDVI is based on the canopy density model (Umarhadi and Syarif, 2018) and presents the amount of photosynthesizing vegetation. The greenness of the vegetation in the image is correlated with the density of the vegetation canopy. NDVI ranges from -1 to 1, where the positive values show the different health status of vegetation, though close to zero and negative qualities demonstrate non-vegetation. On the other hand, the healthy vegetation has greater near-infrared reflectance; thus, NDVI is close to +1 (Lillesand et al., 2004).

NDVI reflects the health and density of mangrove forests. Its high value represents the healthy status of mangroves, while its lower value is associated with unhealthy mangrove sites (Zhang et al., 2005). The mangrove health changes during 2015-2020 were measured by comparing the NDVI value of the year 2015 ($NDVI_{2015}$) with the NDVI value of the year 2020 ($NDVI_{2020}$) using the NDVI differencing method, where NDVI values are compared and calculated from different images (Mancino et al., 2014). In which, the $NDVI_{2015}$ was subtracted from the $NDVI_{2020}$ (equation 2).

$$\Delta NDVI = NDVI_{2020} - NDVI_{2015} \quad (1)$$

The results obtained were used as parameters to determine the health of mangroves in the Vietnamese Mekong delta. In general, the zero value is deemed a non-change area, while positive or negative values are deemed to be changing areas of healthier or degraded mangroves (Nordhaus et al., 2019; Akbar et al., 2020).

3. RESULTS AND DISCUSSION

Figure 2 indicates the changed and unchanged mangrove areas based on the differential assessment of 2015-2020 NDVI results. The green, red, blue and orange colors are assigned to areas that have experienced changes, while yellow indicates areas with no changes. The red areas are regions that have lost their mangroves, while green areas represent the gain in mangroves extended for the period 2015-2020. There was about 16,138 ha of mangrove area loss in the period of 2015 to 2020, accounting for 20.3 % of the total mangrove area in the Vietnamese Mekong delta. This decrease was offset by an increase in the cover of newly planted and regenerated mangroves in the 27,322 ha area, resulting in a net gain of 11,184 ha. The results also indicate that the area of 63,455 ha remained unchanged. However, 22,093 ha with an NDVI value increase (positive ΔNDVI) and an area of 6,899 ha with an NDVI value decrease (negative ΔNDVI) represented healthier mangroves and degraded mangroves, respectively.

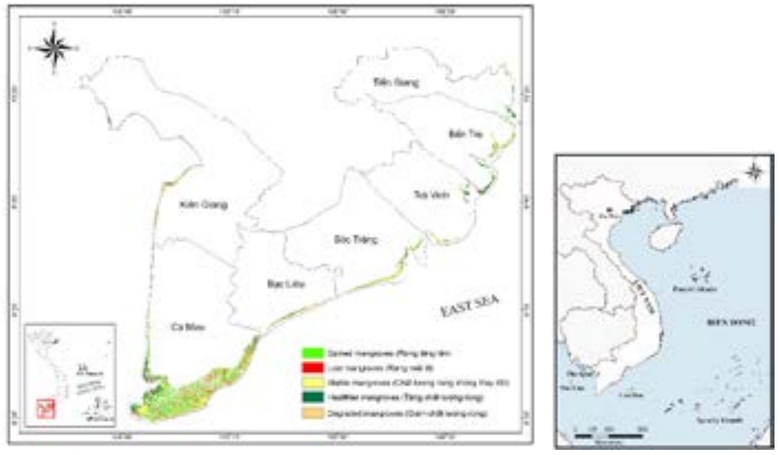

Figure 2. Change in mangrove health during 2015-2020.

In detail, the area of degraded mangrove forests at the commune level was calculated in order to identify priority regions for mangrove restoration efforts (i.e., areas with a high rate of degraded forests). Figure 3 depicts degraded mangroves in all communes with variations in the area and rate of degradation.

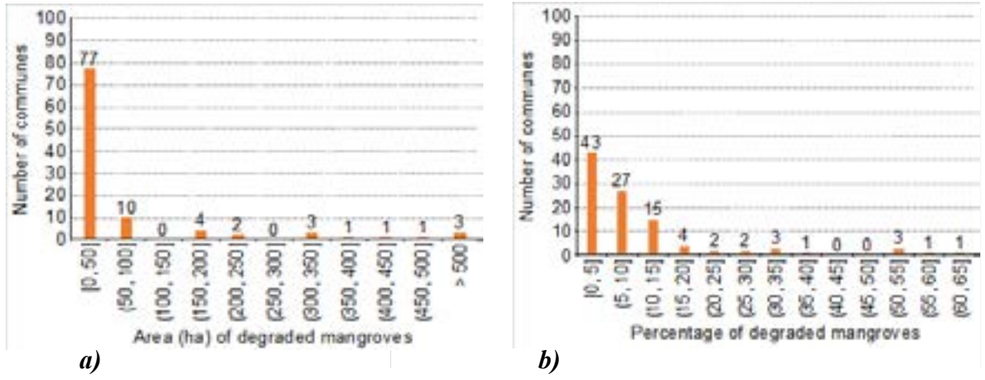

a) ***b)***

Figure 3. Number of communes by area and percentage of degraded mangroves.

The most degraded forest area was found mainly in communes of Ca Mau province; For example, in 682 ha of Vien An Dong (Ngoc Hien district), 644 ha of Tam Giang (Nam Can district), 604 ha of Tam Giang Tay (Ngoc Hien district), 490 ha of Tan An Tay (Ngoc Hien district) and 434 ha of Nguyen Huan (Dam Doi district). Meanwhile, the communes with the highest rate of degraded forest area were mostly in An Minh district, Kien Giang province; For example, Dong Hung A 63.8 %, Van Khanh Dong 55.4 %, Van Khanh Tay 55.0 %, Van Khanh 54.7 % and Tan Thanh 54.5 %.

Regarding the initial assessment of the mangrove degradation causes, ΔNDVI data was overlaid with a map of three types of forests as described in Circular No. 34/2009/TT-BNNPTNT of the Ministry of Agriculture and Rural Development (MARD) and field observation data. The findings demonstrated that all mangrove forests in communes with large degraded mangrove areas belonged to the production forests (i.e., forests for production and trading of timber or non-timber forest products). Meanwhile, mangrove forests in communes with the most significant proportion of degraded mangrove areas were protection forests (i.e., forests for protecting soil and water resources, preventing erosion and desertification, limiting disasters, regulating climate and protecting the environment) and special-use forests (i.e., forest for natural preservation of national ecological standard samples and forest biological gene sources; scientific research; protection of historical and cultural relics and places of scenic beauty). Harvesting activities constituting thinning and clear felling for wood and charcoal on a 10-15 year rotation in production forest (Figure 4a), infrastructure construction activities (Figure 4b), mangrove forests conversion to other purposes (Figure 4c), or hydrological regime changes or illegal exploitation (Figure 4d) in protected and special-use areas were major drivers of mangrove degradation.

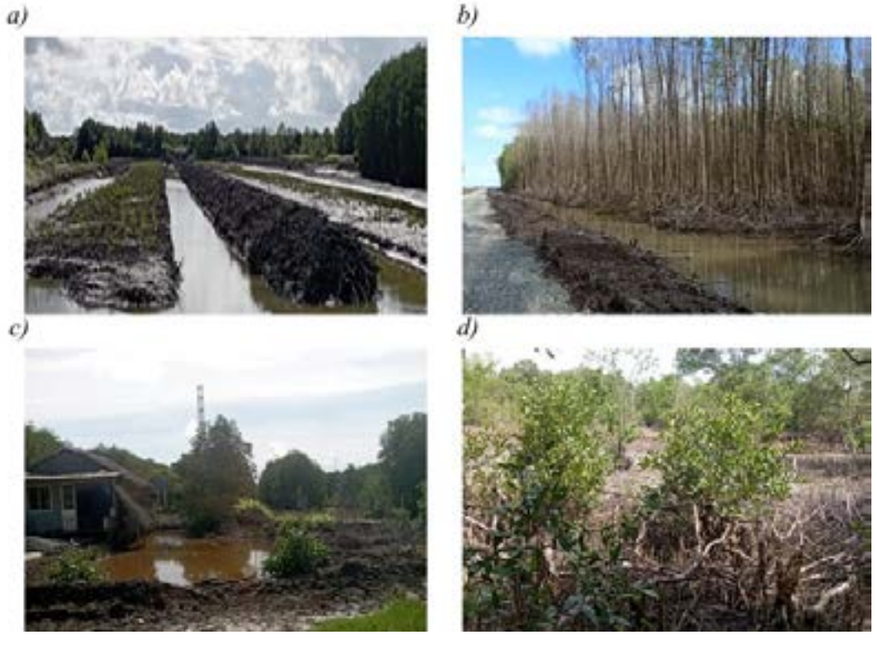

Figure 4. Field observations of the mangrove degradation in the Mekong delta, Vietnam.

4. CONCLUSIONS

This study demonstrated that WorldView-2 imagery and NDVI differencing techniques can produce reliable results in the assessment of mangrove health over time, thereby monitoring the mangrove dynamics. The findings show that there were up to 6,899 ha of degraded mangrove forests between 2015 and 2020, accounting for 7.6 % of the total mangrove forest area in the Mekong delta. Mangrove forests, as production forests, were in the communes with the most degraded areas, while they, as special-use and protection forests, were in the communes with the greatest percentage of degraded forest areas. Although ground-measured data and accuracy evaluation are likely to improve the accuracy of these assessments, the outcomes of this study are still presentable. Besides, future studies in monitoring mangrove dynamics based on the combination of satellite imagery and ground-based vegetation indices are needed to support mangrove management and restoration effectively.

5. ACKNOWLEDGEMENTS

We would like to thank the Polar Geospatial Center, University of Minnesota, for providing the WorldView-2 images. We also express our gratitude to the local authorities for supporting us with the field survey. This study was conducted with financial support from the US Forest Service International Programs (USFS/IP).

6. REFERENCES

Akbar M. R., Arisanto P. A. A., Sukirno B. A., Merdeka P. H., Priadhi M. M., and Zallesa S., 2020. Mangrove vegetation health index analysis by implementing NDVI (normalized difference vegetation index) classification method on sentinel-2 image data case study: Segara Anakan, Kabupaten Cilacap. *IOP Conference Series: Earth and Environmental Science, 584*: 012069.

Alm J., Masjkur M., Arifatmi B., Arquero A., Artz R., Ballhorn U., Boole J-J., Beer F., Coupar A., Couwenberg J., Crosher I., Dannunzio R., Evans C, Fox J, Gerrand A, Goodyear E, Groom A, Hoekman D, Hooijer A and Sulaiman A., 2020. Peatlands mapping and monitoring: Recommendations and technical overview. *Food and Agriculture Organization of the United Nations (FAO)*, Rome.

Binh T. N. K. D., Vromant N., Hung N. T., Hens L., and Boon E. K., (2005) Land cover changes between 1968 and 2003 in Cai Nuoc, Ca Mau peninsula, Vietnam. *Environment, Development and Sustainability 7*: 519-536.

Bullock E. L., Fagherazzi S., Nardin W., Vo-Luong P., Nguyen P., and Woodcock C. E., (2017) Temporal patterns in species zonation in a mangrove forest in the Mekong delta, Vietnam, using a time series of Landsat imagery. *Continental Shelf Research, 147*: 144-154.

de Graaf G.J., and Xuan T. T., 1998. Extensive shrimp farming, mangrove clearance and marine fisheries in the southern provinces of Vietnam. *Mangroves and Salt Marshes, 2*: 159-166.

Fuazi M., Azmi A., and Zakaria M., 2019. Evaluation of Matang mangrove forest loss and gain in 10 years time using multi-temporal satellite derived vegetation index. *The 40th Asian Conference on Remote Sensing (ACRS 2019)*, 14-18 October 2019, Daejeon, Korea

Hawkins S., To P. X., Phuong P. X., Thuy P. T., Tu N. D., Guong C. V., Brown S., Dart P., Robertson S., Vu N., and McNally R., 2010. Roots in the Water: Legal Frameworks for Mangrove PES in Vietnam. Katoomba Group's Legal Initiative Country Study Series. *Forest Trends*: Washington, DC.

Hong H. T. C., Avtar R., and Fujii M., 2019. Monitoring changes in land use and distribution of mangroves in the southeastern part of the Mekong River delta, Vietnam. *Tropical Ecology, 60*: 552-565.

Hong P. N., and San H. T., 1993. Mangroves of Vietnam. *IUCN*, Bangkok, Thailand.

Jackson R. D., Slater P. N., and Pinter P. J., 1983. Discrimination of growth and water stress in wheat by various vegetation indices through clear and turbid atmospheres. *Remote Sensing of Environment, 13*: 187-208.

Janssen T. A. J., Ametsitsi G. K. D., Collins M., Adu-Bredu S., Oliveras I., Mitchard E. T. A., and Veenendaal E. M., 2018. Extending the baseline of tropical dry forest loss in Ghana (1984-2015) reveals drivers of major deforestation inside a protected area. *Biological Conservation, 218*: 163-172.

Li D., Lu D., Wu M., Shao X., and Wei J., 2018. Examining Land cover and Greenness Dynamics in Hangzhou Bay in 1985-2016 using Landsat Time-Series Data. *Remote Sensing, 10*: 32.

Lillesand T., Kiefer R., and Chipman J., 2004. Remote Sensing and Image Interpretation (Fifth Edition). *John Wiley*, New York.

Liu Sa, Li X., Chen D., Duan Y., Ji H., Zhang L., Chai Q., and Hu X., 2020. Understanding Land use/Land cover dynamics and impacts of human activities in the Mekong delta over the last 40 years. *Global Ecology and Conservation, 22*: e00991.

Mancino G., Nolè A., Ripullone F., and Ferrara A., 2014. Landsat TM imagery and NDVI differencing to detect vegetation change: Assessing natural forest expansion in Basilicata, Southern Italy. *iForest, 7*: 75-84.

Nordhaus I., Toben M., and Fauziyah A., 2019. Impact of deforestation on mangrove tree diversity, biomass and community dynamics in the Segara Anakan lagoon, Java, Indonesia: A ten-year perspective. *Estuarine, Coastal and Shelf Science, 227*: 106300.

Phan M. H., and Stive M. J. F., 2022. Managing mangroves and coastal land cover in the Mekong delta. *Ocean & Coastal Management, 219*: 106013.

Quyen N. H., 2011. Land cover change assessment in the coastal areas of the Mekong delta 2004-2009. *IUCN*, Hanoi, Vietnam.

Thu P. M., and Populus J., 2007. Status and changes of mangrove forest in Mekong delta: Case study in Tra Vinh, Vietnam. *Estuarine, Coastal and Shelf Science, 71*: 98-109.

Tinh P. H., MacKenzie R. A., Hung T. D., Hanh N. T. H., Hanh N. H., Manh D. Q., Ha H. T., and Tuan M. S., 2022a. Distribution and drivers of Vietnam mangrove deforestation from 1995 to 2019. *Mitigation and Adaptation Strategies for Global Change, 27*: 29.

Tinh P. H., MacKenzie R. A., Hung T. D., Vinh T. V., Ha H. T., Lam M. H., Hanh N. T. H., Tung N. X., Hai P. M., and Huyen B. I., 2022b. Mangrove restoration in Vietnamese Mekong delta during 2015-2020: Achievements and challenges. *Frontiers in Marine Science, 9*: 1043943.

Tong P. H. S, Auda Y., Populus J., Aizpuru M., Habshi A. A., and Blasco F., 2004. Assessment from space of mangroves evolution in the Mekong delta, in relation to extensive shrimp farming. *International Journal of Remote Sensing, 25*: 4795-4812.

Truong S. H., Ye Q., and Stive M. J. F., 2017. Estuarine Mangrove Squeeze in the Mekong delta, Vietnam. *Journal of Coastal Research, 33*: 747-763.

Truong T. D., and Do L. H., 2018. Mangrove forests and aquaculture in the Mekong river delta. *Land Use Policy, 73*: 20-28.

Umarhadi D., and Syarif A., 2018. Regression model accuracy comparison on mangrove canopy density mapping. *Physical Sciences and Engineering*: 1-11.

Zhang Q., Xiao X., Braswell B., Linder E., Baret F., Moore B., 2005. Estimating light absorption by chlorophyll, leaf and canopy in a deciduous broadleaf forest using MODIS data and a radiative transfer model. *Remote Sensing of Environment, 99*: 357-371.

UTILIZATION OF BOREHOLE DATA FOR CORRELATION SYSTEM OF STRATA: A CASE STUDY OF HANOI, VIETNAM

Kenichi SAKURAI[1,2], Go YONEZAWA[1], Luan Xuan Truong[3]*, Tatsuya NEMOTO[4], Shinji MASUMOTO[5]

[1]Graduate School of Engineering, Osaka Metropolitan University, Japan.
[2]Department of Information Engineering, College of Industrial Technology, Japan.
[3]Hanoi University of Mining and Geology, Vietnam.
[4]Graduate School of Science, Osaka Metropolitan University, Japan.
[5]Professor Emeritus of Osaka City University, Japan.
*Corresponding author. Email: truongxuanluan@gmail.com

ABSTRACT

In order to build cities that are resilient to natural disasters and man-made disasters, urban planning using a variety of subsurface data is essential, such as identifying weak ground and providing land improvements and considering groundwater utilization based on groundwater flow and level increase/decrease. In general, such subsurface data in urban areas can be obtained by a borehole survey to determine and accurately record the geological structure, N-values, groundwater levels and flows.

In Japan, the data obtained from borehole survey is currently formatted as XML files. The author has developed a system for visualization and stratigraphic comparison of borehole data using a Web browser by simply importing borehole data in this format to a server. The system works not only with PCs running web browsers but also with tablet computers such as iPads. Therefore, it is possible to immediately visualize the borehole information at that location as long as the device is connected to the Internet.

In this research, the actual data of the investigation where the system was put into practice in order to estimate the subsurface structure of an area of approximately 7 km in length and 7 km in width in the city of Hanoi, using 275 borehole data, will be provided. In the stratigraphic comparison, the names of the Vietnamese soil types correspond to the Japanese soil types.

1. INTRODUCTION

In order to build cities that are resilient to both natural and man-made disasters, urban planning using a variety of subsurface data is essential, such as identifying weak ground, improving the land and considering groundwater utilization based on groundwater flow and level increase/decrease. In general, such subsurface data in urban areas can be obtained by borehole investigations to determine and accurately record the geological structure, N-values, groundwater levels and flow. However, a borehole survey at a single location provides only a mere piece of information at that point and cannot be used for urban planning, no matter how accurately it is recorded. In order to use the data for urban planning, borehole investigations should be conducted at as many points as possible within a city and the data should be correlated so that the underground structure, level and flow in the area can be sufficiently understood.

In Japan, the data obtained from borehole investigations are formatted in XML file format, which has been standardized by the Japan Construction Information Center (JACIC) and is now

compiled by the Ministry of Land, Infrastructure, Transport and Tourism (MLIT) as Guidelines for Electronic Delivery of Geological and Geotechnical Survey Results (Draft).

The author has developed a system for visualization and stratigraphic comparison of borehole data using a Web browser by simply importing borehole data in this format to a server (Sakurai et al., 2023).

In this research, the actual data of the investigation where the system was used to estimate the subsurface structure of an area of 7 km in length and 7 km in width in the city of Hanoi, using 275 borehole data, will be provided.

In the stratigraphic comparison, the names of the Vietnamese soil types correspond to the Japanese soil types.

2. GEOLOGICAL STRUCTURE OF THE RESEARCH AREA

The target area for this research is the central part of Hanoi, Vietnam. The area covers the range of lat. 21°00′00″ to 21°04′22.5″ and long. 105°47′30″ to 105°51′52.5″. These coordinates are based on the VN2000. The area is located in the Red River delta and its geological structure has been studied by Tran (1991) and Haruyama (2004) in their papers and books. According to their issue, the research area is covered mainly by sedimentary rocks from the Quaternary Holocene and Pleistocene. The Holocene strata consist of the Thai Binh Formation and the Hai Hung Formation and the Pleistocene strata consists of the Vinh Phuc Formation, the Hanoi Formation and the Lechi Formation. (Figure 1).

The research area has also been subjected to 3D geological modeling using GRASS GIS by Yonezawa et al. (2016).

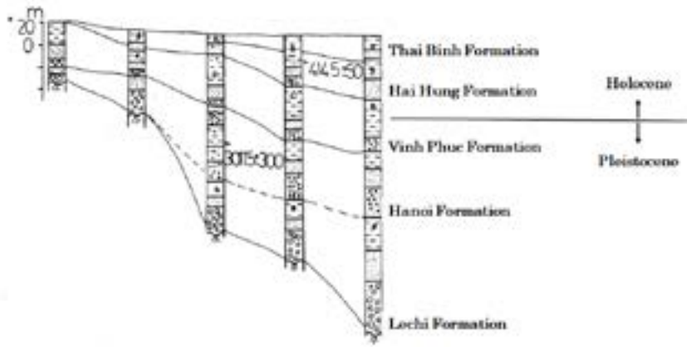

Figure 1. The outline profile section of Red River delta.

3. DATA USED IN THE RESEARCH

The actual data used in this research consists of 275 borehole data collected by Hanoi University of Mining and Geology, covering the area of 7×7 km in Hanoi. The data obtained from borehole investigations in Japan is arranged to be formatted as XML files specified by the Ministry of Land, Infrastructure, Transport and Tourism (MLIT). In order to conduct this research, we converted the borehole data from Hanoi into the file format specified by MLIT. The borehole locations used in the research are shown in Figure 2.

Figure 2. The distribution map of collected borehole data.

4. OVERVIEW OF THE SYSTEM

The entire process from the comparison of the strata to the 3D visualization of the data can be divided into four major steps, as shown in Figure 3.

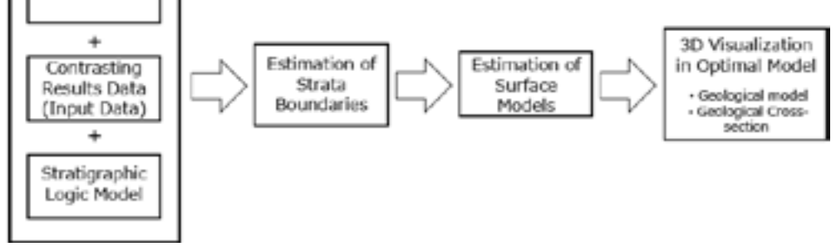

Figure 3. The entire process from the comparison of the strata.

Step 1. Various Types of Data:

The step starts with the collection of the data used to estimate the stratigraphic boundaries. The data includes the elevation of the borehole and each core, the contrasting results associated with the stratigraphic classification of each core and the logical data model showing either the deposition or the erosion of the strata.

Step 2. Estimation of Strata Boundaries:

The formation boundaries for each stratum are to be estimated based on the data created in Step 1. The method of estimation includes the Cubic B-spline (Nonogaki et al., 2008).

Step 3. Estimation of Surface Models:

The results estimated in Step 2 are to be displayed in 3D and to be compared and contrasted to verify whether the estimation is appropriate.

Step 4. 3D Visualization in Optimal Model:

All surface models are to be visualized and checked for inconsistencies. If a discrepancy occurs in Step 4, each step up to Step 4 should be carried out again as needed. Software used for visualization includes GRASS-GIS, Geomodel2003 (Yonezawa et al., 2004) and Terramod_BS (Sakamoto et al., 2012).

By performing the above steps, the borehole data can be used to contrast the strata and be visualized in 3D. In this research, the process mentioned in Step 1, "Various Types of Data", was conducted to create the contrast result data. The borehole data was displayed using a Web-GIS-based comparison system, with some of the system and data being customized especially for this research.

Figure 4 shows the overview of the system used in this research. This system has the function of displaying borehole information in 3D and as a geologic log on a Web browser by simply importing geotechnical information published in the borehole exchange data (XML) format specified in the "Guidelines for Electronic Delivery of Geological and Geotechnical Investigation Results (Draft)" to the server. The entire system is based on OSS (Open-Source Software), so they can be built on on-premises servers or cloud servers at no cost, as long as the user has knowledge of server construction.

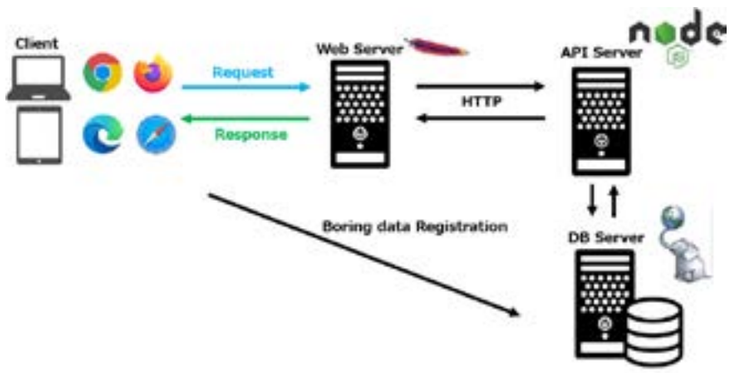

Figure 4. System configuration diagram.

Table 1 shows the name of the service and the version used for the service.

Table 1. List of Server Services and Versions.

Server Name	Server Version
Server OS	Ubuntu 18.04.6 LTS 64bit
Web Server	Apache 2.4.29
API Server	Node.js v17.9.1 + Express
DB Server	PostgreSQL10.23 + PostGIS2.4

The system can be divided into two components - Backend and Frontend. A major feature of this system is that the two components were developed separately. The Backend uses Rest API to reference data stored in the database. If an HTTP request is sent to the API server, the necessary data can be received in GeoJSON format based on the information sent.

On the Frontend, the use of a development language that enables HTTP socket communication enables the system to be developed freely without depending heavily on the OS or development language. The system also works with tablet computers such as iPads, making it easy to refer to borehole information immediately in the field.

The main functions of the API currently available are shown in Table 2. These APIs were designed to display borehole data on Web-GIS in order to retrieve borehole data within a specific area using latitude and longitude and to select and display borehole data in 3D or as a geologic log.

Table 2. Web API service list.

No.	API Service	Service Description
1	Location information for all borehole data	Provide information such as latitude and longitude of all borehole data stored in the database.
2	Location information of borehole data within a specified range	Provide information such as latitude and longitude of borehole data contained within the specified range.
3	Location information for the selected borehole data	Provide information such as latitude and longitude of the borehole data specified by the borehole registration number.
4	Information on borehole core data	Provide all core information, including soil/rock type and borehole classification specified by the borehole registration number.
5	Information on N-value data	Provide N-value information for a specified borehole.

5. ACTUAL USE OF THE SYSTEM

The flow of displaying borehole data in Web-GIS using the system and contrasting the strata will be explained in sequence.

5.1 Startup initial screen

As shown in Figure 5, the boreholes registered in the database are displayed on a map using Web-GIS. When the number of boreholes is large, the marker clustering function is used to display how many boreholes are in close range. Maps that can be used for the background include Google Maps and OSM (Open Street Map). These maps can be changed on the background map selection tab in the upper right corner of the web page.

5.2 Enlarged view of registered borehole data

When the display is enlarged, the marker clustering function is deactivated and the points with borehole data registered on the database are circled in blue on the map (Figure 6).

5.3 Selection of borehole location for display

By clicking on the start and end points of the borehole range to be displayed, a rectangle that shows all the boreholes selected within the area can be displayed based on the width pre-defined in the selection area on the upper right section of the screen (Figure 7). The selected borehole data turns orange and the number of selected borehole data is also displayed in the top right corner of the screen.

To change the width of the selected range, retype the value in the text box on the top right corner of the screen. This changes not only the width of the selection but also the number of selected boreholes accordingly.

Finally, a list of the selected borehole data can be displayed by clicking on the “Confirm” button on the top right corner of the screen.

5.4 Selection of borehole data for display

The borehole data to be displayed can be selected by using the checkboxes on the left side of the screen. The respective buttons on the upper right side of the screen can then be pressed to convert the chosen borehole data into either a 3D visualization or a geological log view (Figure 8).

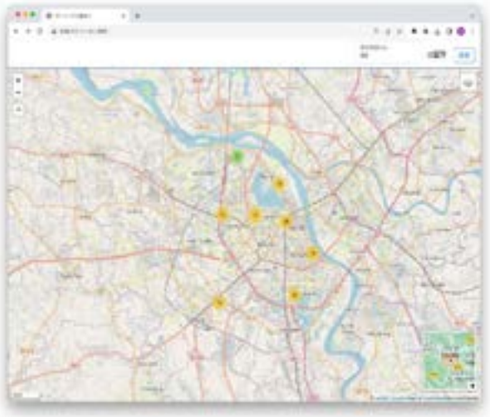

Figure 5. Startup initial screen.

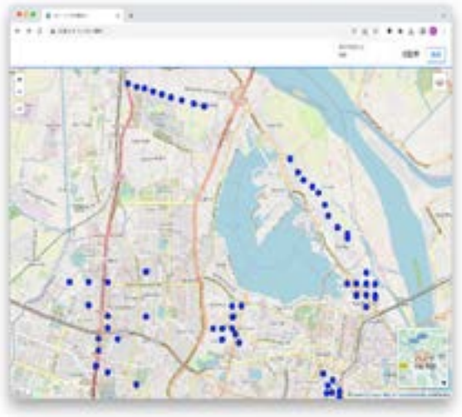

Figure 6. Enlarged view of registered borehole data.

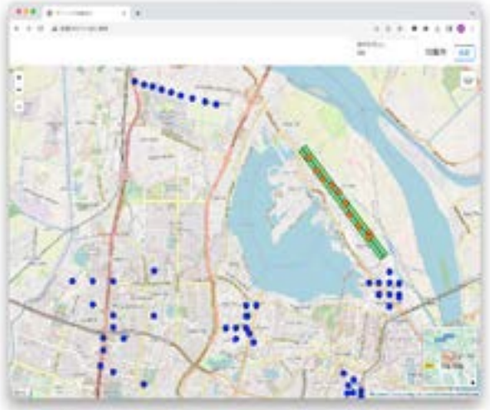

Figure 7. Selection of borehole location for display.

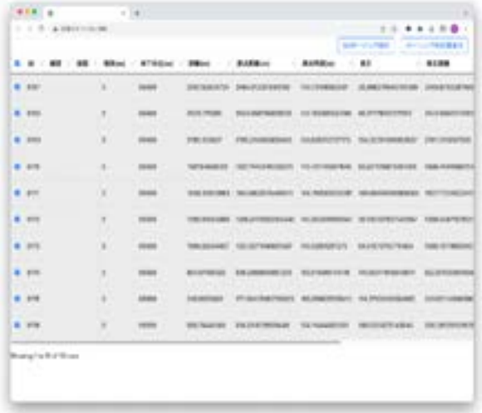

Figure 8. Boring selection for display.

5.4.1 Output Example 1: 3D geologic log view

As shown in Figure 9, the borehole data displayed in 3D can not only be enlarged, reduced, rotated and moved by mouse operation but also be viewed from anywhere in 360°, including horizontally and diagonally. The cores are colored according to the soil classification patterns in the “Guidelines for the Organization of Geological Survey Data” defined by MLIT.

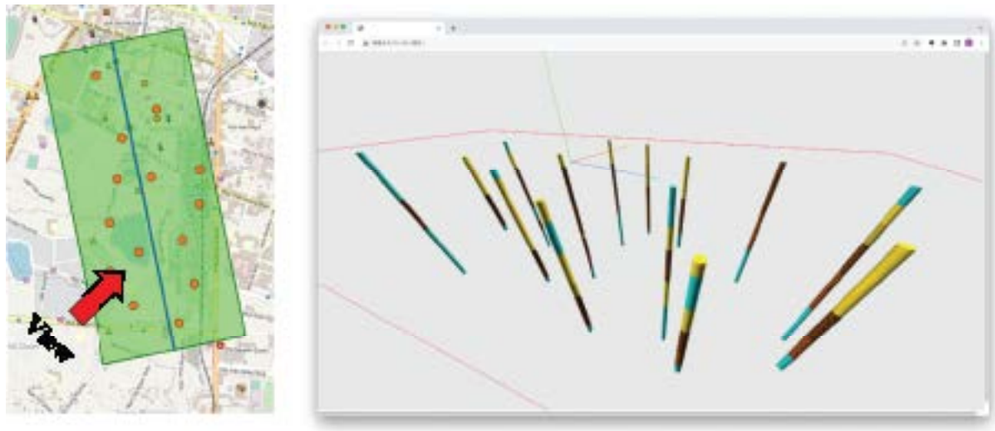

Figure 9. 3D View Screen (Vicinity of Hanoi Station).

5.4.2 Output Example 2: Geologic log view

The borehole core can be displayed reflecting the actual distance as shown in Figure10. The N-values are not shown as they are not included in the data of this research. However, the N-values can also be shown on the right side of the columnar map if the data is available. In addition, as shown in the enlarged Figure 10, detailed data such as the names of soil types and upper/lower depths can be displayed by hovering the mouse over each soil data.

Figure 10. Geologic log view screen, side note: Borehole log view (Enlarged).

6. CONCLUSION

The system has been modified to be compatible with geological data from Vietnam. As a result, a successful operation of both the 3D and the contrast display was achieved.

Borehole data can now be displayed respectively on a map, in 3D, or as a columnar map. This makes it possible not only to compare the geologic logs while viewing them but also to compare them from various viewpoints, viewing data on the map and 3D-display at the same time on a single screen.

In addition, it is now possible to view the borehole data in 3D and as multiple geologic logs on tablet computers such as iPads in the field, accelerating the speed and improving the efficiency of the survey required in geologic study.

In the future, we would like to develop an efficient system for producing geological comparison results and to verify the operation of this system in regions other than Japan.

7. ACKNOWLEDGMENTS

This work was supported by JSPS KAKENHI Grant Number 21K01019 and Japan Construction Information Center (JACIC) Research Grant Number 2023-7.

8. REFERENCES

Haruyama S., 2004. Natural environmental study applied for agriculture in the Northern Vietnam: Natural Hazard and their Diffence Policy against Disaster, the Red River delta, *KOKONSHOIN*, 131.

Nonogaki S., Masumoto S., and Shiono K., 2008. Optimal determination of geologic boundary surface using cubic B-spline. *Geoinformatics, 19*(2), 61-77.

Sakamoto M., Nonogaki S., and Masumoto S., 2012. Terramod-BS: Visual Basic Program for Determination and Visualization of Geologic Boundary Surface Including BS-Horizon Module. *Geoinformatics, 23*(4), 169-178.

Sakurai K., Yonezawa G., Nemoto T. and Masumoto S., 2023.Visualization of Borehole Data for Correlation System of Strata. *Geoinformatics, 34*(2), 37-38.

Tran M., Ngo Q. T., Do T. V. T., Nguyen D. M., and Nguyen V. V., 1991. Quaternary Sedimentation of the principal deltas of Vietnam. *Journal of Southeast Asian Earth Science, 6*(1), 103-110.

Yonezawa G., Masumoto S., Nemoto T., Sakamoto M., and Shiono K., 2004. Visualization of Geologic Boundaries Based on Generalized Geologic Function. *Geoinformatics, 15*(4), 193-208.

Yonezawa G., Nonogaki S., Mitamura M., Sakurai K., Xuan X. T., Matumoto S., Nemoto T., and Raghavan V., 2016. Utilization of Elevation and Borehole Data of Hanoi city, Vietnam -Construction of 3D Geological Model. International Conference on GeoInformatics for Spatial-Infrastructure Development in Earth & Allied Sciences (GIS-IDEAS). *Proceedings of the GIS-IDEAS 2016*, 190-195.

DROUGHT MONITORING USING MODIS DATA AND THE GOOGLE EARTH ENGINE PLATFORM, CASE STUDY IN DAK LAK PROVINCE

Nguyen Ngoc Anh[1,2]*, Hoang Ngoc Khac[1], Tran Thi Ngoc Lam[1], Vu Thi Thuy Ngan[1]

[1]Ha Noi University of Natural Resources and Environment, Vietnam
[2]Graduate University of Science and Technology, Vietnam Academy of Science and Technology
*Corresponding author. Email: nnanh@hunre.edu.vn

ABSTRACT

The study was conducted to monitor drought conditions in Dak Lak province using satellite data and the GEE platform. Various drought indicators, such as the Vegetation Health Index (VHI) and the Normalized Differential Drought Index (NDDI), were obtained from multi-time MODIS satellite data and used to analyze the spatial and temporal distribution of dry conditions in Dak Lak province during the period from 2001 to 2020. This study demonstrates the potential application of GEE computing technology, which gives users access to geospatial big data, not only in drought monitoring but also in other environmental monitoring applications. The study findings reveal that between 2001 and 2020, the NDDI index for Dak Lak province fluctuated between -0.55 and 0.95. The most severe drought was recorded in April 2005, with the NDDI value reaching its peak at 0.95. The years 2002-2003, 2007, 2015-2016 and 2019 experienced significant droughts. According to the VHI index calculations, Dak Lak province underwent moderate drought conditions in March 2003, from March to May 2005, April 2007, April 2010, March 2011 and July 2015. The NDDI index identified the drought frequency as 36.5 %, ranging from mild to extreme levels of drought. In contrast, the VHI index identified a lower drought frequency of 29.5 % during the research period, with most instances being of a mild drought level.

1. INTRODUCTION

Drought is a common and recurring natural disaster that significantly impacts Vietnam's socio-economic development. With climate change leading to increased average temperatures, greater evaporation and more extreme rainfall patterns, the threat of severe droughts is escalating, posing a significant risk to agricultural production. The Central Highlands region, including Dak Lak province, is among the areas most affected by this phenomenon. Drought monitoring and surveillance typically depend on observations from terrestrial meteorological stations (Gu et al., 2007). However, these stations' distribution and density are insufficient for detecting essential spatial data and they lack continuity and interconnectivity. As a result, satellite imagery has proven to be a more effective tool for monitoring and assessing the impacts of drought, as it provides updated information across various spatial ranges and time scales. Google Earth Engine (GEE), a free cloud computing platform, facilitates the storage and processing of large volumes of satellite images. GEE excels at tracking and monitoring long-term changes in land surfaces across extensive regions. It is extensively used to monitor drought through drought indices or variables related to drought, such as rainfall, temperature, humidity and vegetation index (Mutanga, 2019).

Drought is a complex event and its monitoring depends on the availability of high-quality data. The effectiveness of drought indices can vary from one location to another. Therefore, it's crucial to select a suitable index for early detection of drought in challenging basins. This study focuses on

evaluating the efficiency of various satellite-based vegetation indices for tracking droughts in Dak Lak province from 2001-2020 utilizing the cloud-based computational platform Google Earth Engine (GEE). The study selected six common drought indices used to assess agricultural drought. These indices are based on the use of NDVI and LST and are divided into four main groups: (i) *Greenness Related Vegetation Indices* (including the Normalized Difference Vegetation Index (NDVI) and Vegetation Condition Index (VCI), (ii) *Water Related-Vegetation Indices*, including Normalized Differential Water Index (NDWI), (iii) *Temperature Related Vegetation Indices*, including Land Surface Temperature (LST) and Temperature Condition Index (TCI), (iv) *Combined Vegetation Indices*, including Vegetation Health Index (VHI) and Normalized Difference Drought Index (NDDI).

2. MATERIALS

2.1 Study area

Dak Lak pProvince, situated in the heart of the Central Highlands region of Vietnam, encompasses the origin of the Serepok River system and a portion of the Ba River. The terrain of Dak Lak descends gradually from southeast to northwest, with an average elevation ranging between 400 and 800 m above sea level. The region experiences a tropical monsoon climate typical of the Central Highlands, with two distinct seasons annually. The dry season commences in November and lasts until April of the subsequent year, accounting for approximately 15 % of the total annual rainfall. The province's average total annual rainfall varies between 1,500 mm and 2,000 mm.

Figure 1. Location of study area.

The province's unique geographical position and climate result in frequent droughts and water shortages, primarily during the dry season. Several factors exacerbate the drought risk, including climate change impacts, diminishing forest areas, rapid population growth, large-scale production needs and increasing water resource exploitation for production and daily life. The severity of drought-induced water shortages in Dak Lak has escalated, with significant droughts recorded in the past, notably in 2004-2005, 2007-2008, 2011-2012, 2013 and especially in 2015, 2016 and early 2020. These droughts have caused substantial damage to agricultural production and the economic livelihood of the people.

2.2 Data resources

This research utilized datasets that are freely accessible from the Google Earth Engine (GEE) repository, specifically from the MODIS satellite's Terra sensor. The study employed images from the Moderate Resolution Imaging Spectroradiometer (MODIS), which features 36 spectral bands ranging from 0.4 μm to 14.4 μm and was launched in 1999. The datasets used included MOD09A1, which provides 500 m resolution surface reflectance data in 8-day composites and MOD11A2, which offers 1 km resolution land surface temperature data in 8-day composites (Didan, 2015).

The NDVI dataset, derived from Google's MODIS/006/MCD43A4 surface reflection composites, was utilized. The Terra MODIS data was employed for the period 2001-2020. The spatial resolution of Terra MODIS is 250 m and it has a temporal resolution of 16 days (Tucker, 1980).

The MODIS Land Surface Temperature (LST) product, which is a 16-day composite with a spatial resolution of 1 km (MOD11A2) (Wan, 2018), was utilized to derive the daytime land surface temperature. The MOD11A2 product includes quality checks for both daytime LST and emissivity.

Spatial and temporal relationships between MODIS spectral indices and drought conditions were analyzed for the period 2001-2020.

2.3 Methodology

2.3.1 Selected Vegetation Indices for Drought Monitoring

Using the GEE Platform and data series collected from the Modis satellite, we employed various algorithms and functions to derive Vegetation Indices for Drought Monitoring:

(i) Greenness Related Vegetation Indices, including the Normalized Difference Vegetation Index (NDVI) and Vegetation Condition Index (VCI);

(ii) Water Related-Vegetation Indices, including Normalized Differential Water Index (NDWI), *(iii) Temperature Related-Vegetation Indices*, including Land Surface Temperature (LST) and Temperature Condition Index (TCI);

(iv) Combined Vegetation Indices, including Vegetation Health Index (VHI) and Normalized Difference Drought Index (NDDI).

2.3.2 Calculation Formulas for Drought Indices

The calculation formulas for the drought indices are presented in Table 1.

Table 1. The calculation formulas for the indices are from MODIS images.

Indices		Formula	Parameters	Sources
Greenness Related Vegetation Indices	NDVI	$= \frac{\rho NIR - \rho RED}{\rho NIR + \rho RED}$	ρRED, ρNIR are the reflectances for MODIS band 1 (620-670 nm) and band 2 (841-876 nm)	Tucker, 1979
	VCI	$= 100 \text{ x } \frac{NDVI_i - NDVI_{min}}{NDVI_{max} + NDVI_{min}}$	$NDVI_{max}$ and $NDVI_{min}$ are the multiyear absolute maximum and minimum NDVI, respectively, while $NDVI_i$ is the monthly NDVI value at time of observation	Kogan, 1995

Water Related Vegetation Indices	NDWI	$= \frac{\rho NIR - \rho SWIR}{\rho NIR + \rho SWIR}$	ρNIR and $\rho SWIR$ are the reflectances for MODIS band 2 (841-876 nm) and band 7 (2,105-2,155 nm), respectively	Gao, 1996
Temperature Related Vegetation Indices	TCI	$= 100 \text{ x } \frac{LST_{max} - LST_i}{LST_{max} - LST_{min}}$	LST_{min} and LST_{max} define minimum and maximum values of LST (Land Surface Temperature) values in this study period; LST_i defines the LST value belonging to the observed month	Kogan, 1995
Combined Vegetation Indices	NDDI	$= \frac{NDVI - NDWI}{NDVI + NDWI}$	NDDI calculations were made from calculated NDVI and NDWI values	Gu et al., 2007
	VHI	$= a \times VCI + b \times TCI$	Equal importance is given to the Vegetation Condition Index (VCI) and Temperature Condition Index (TCI), each having a weight of 0.5 ($a = b = 0.5$)	Kogan, 1995

The results of the drought index calculations are then classified according to specified thresholds, serving as the basis for determining the drought level in Dak Lak province. The classification of drought indices is indicated in Table 2.

Table 2. Classification of drought indices.

Drought indices	NDDI	TCI / VCI / VHI
Extreme Drought	> 0.8	< 0.1
Severe Drought	0.6-0.8	0.1-0.2
Moderate Drought	0.4-0.6	0.2-0.3
Mild Drought	0.2-0.4	0.3-0.4
Non Drought	< 0.2	> 0.4

3. RESULTS

3.1 Results of calculating NDVI, NDWI and NDDI indices for drought monitoring in Dak Lak province

The calculation results show that the NDDI index for Dak Lak province, from 2001 to 2020, ranges from -0.55 to 0.95. An extreme drought occurred in April 2005 (with the highest recorded NDDI value = 0.95). Severe droughts occurred in the years 2002-2003, 2007, 2015-2016 and 2019. Regarding the annual drought progression, drought conditions in Dak Lak province commonly occur in the months of February, March and April (the period of activity of the Northeast monsoon, which is the dry season in the research area).

Figure 2 shows the time series of NDVI, NDWI and NDDI drought indices. The peaks of the NDDI index correspond to extreme and severe drought events in April 2005, February 2003, April 2016 and March 2019, which are also the times when the NDWI index reaches its lowest values. This suggests that NDDI is more closely correlated with NDWI and these two indices are more sensitive to drought conditions than NDVI (Figures 2 and 3).

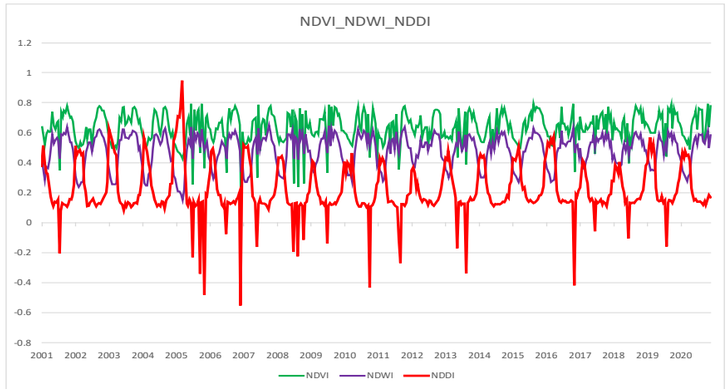

Figure 2. Time series of NDVI, NDWI and NDDI indices for Dak Lak province.

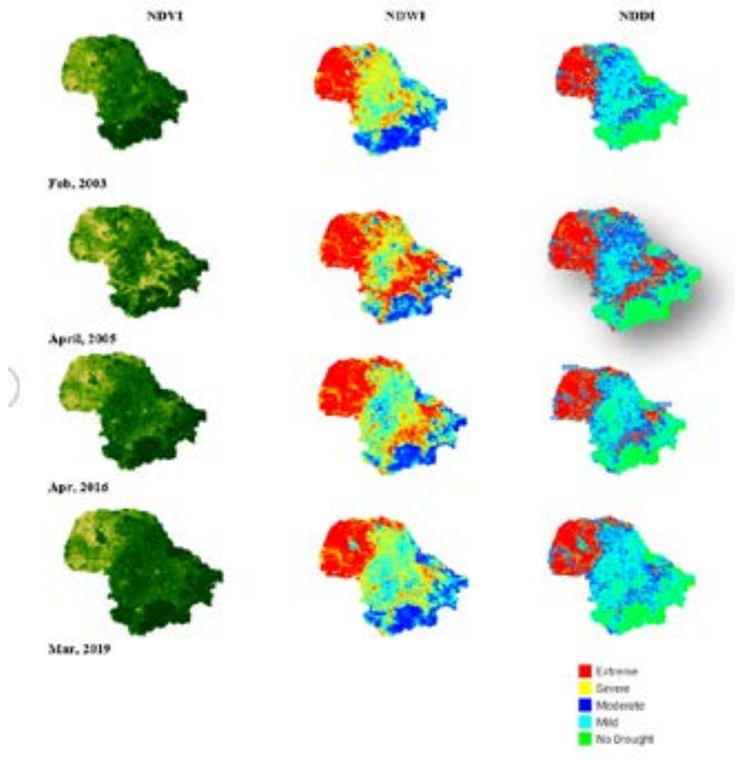

Figure 3. Extreme and severe drought events were identified based on the NDDI indices in the years 2003, 2005, 2016 and 2019.

3.2 Results of calculating the TCI, VCI and VHI indices for drought monitoring in Dak Lak province.

The calculated VHI index results indicate a moderate drought condition in Dak Lak province in March 2003, March - May 2005, April 2007, April 2010, March 2011 and July 2015. The TCI detected more severe plant stress in the years 2002, 2003, 2005, 2016 and 2020. The VCI detected

a higher level of plant stress compared to the other two indices and the stress period also lasted longer, possibly until November or December (Figure 4).

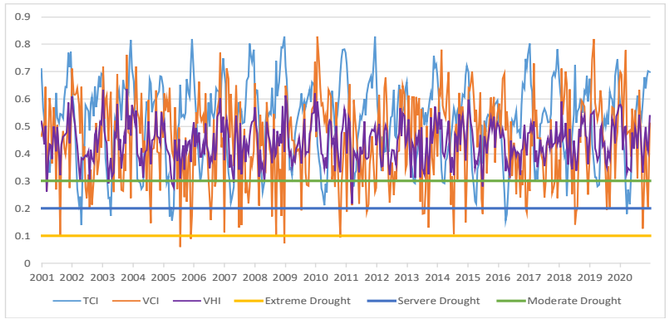

Figure 4. Time series of TCI, VCI and VHI indices for Dak Lak province

Regarding the annual drought trends, the calculated drought indices mostly indicate that drought conditions in Dak Lak province commonly occur in the early months of the year, especially in February, March and April. Only the VCI index shows that plant stress conditions can extend to the end of the year by taking the drought year 2005 as an example to analyze the drought trends within the year (Figure 5). Figure 5 (a) indicates that NDDI shows severe and extreme drought levels in February, March and April 2006 (NDDI > 0.6), corresponding to the relatively lower NDVI and NDWI values in these months compared to other times of the year. While the TCI and VHI values show stress levels mainly occurring from March to May, VCI indicates a more severe plant stress level in the later months of the year (with VCI values in August and December less than 0.1) (Figure 5(b)). As the VCI index attempts to directly measure the health of the vegetation cover, the plant stress condition indicated by the VCI could be caused by reasons other than water shortage.

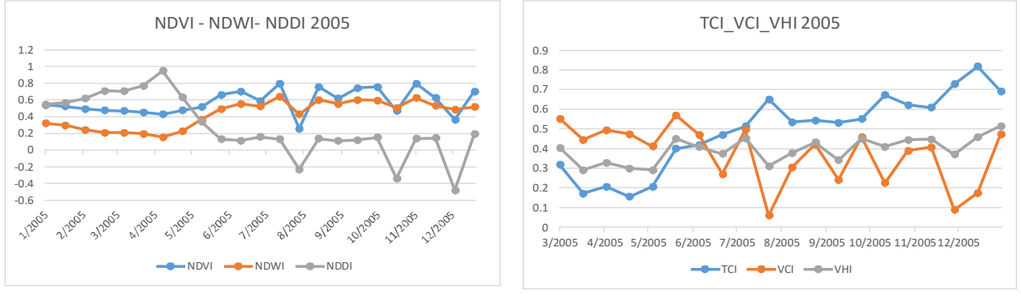

(a) ***(b)***

Figure 5. Drought trends within the year in Dak Lak province in 2005, for example.

Regarding the frequency of drought: During the research period from 2001 to 2020, only the NDDI and VCI indices extracted from MODIS satellite data indicated extremely severe drought events (with NDDI > 0.8 and VCI < 0.1). Severe drought events were detected based on the analysis of NDDI, TCI and VCI drought indices, which were 1.52 %, 1.53 % and 5.25 %, respectively, while VHI did not identify extreme and severe drought levels. Drought at a moderate level was identified based on the NDDI index with a frequency of 15.65 %, followed by VCI (12.68 %) and TCI (8.97 %). The VHI value also only detected a moderate level of plant stress at a rate of 1.75 % throughout the research period (Figure 6).

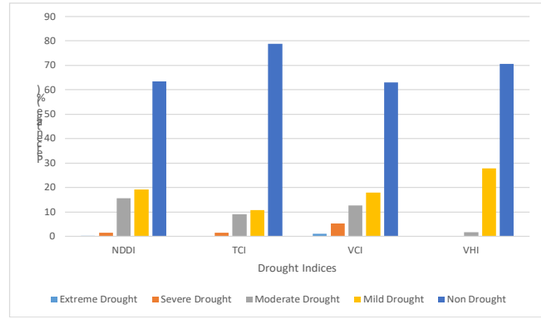

Figure 6. The frequency of drought is determined by the drought indices NDDI, TCI, VCI and VHI.

3.3 Spatial distribution of drought in Dak Lak province

The calculation results of the VHI index only determine drought levels from Mild to Medium during the research period. In reality, Dak Lak province, in particular and the Central Highlands region, in general, are areas that have suffered and are suffering severe impacts from drought compared to other regions across the country, so we chose to use the NDDI index to analyze the spatial distribution of drought in Dak Lak province.

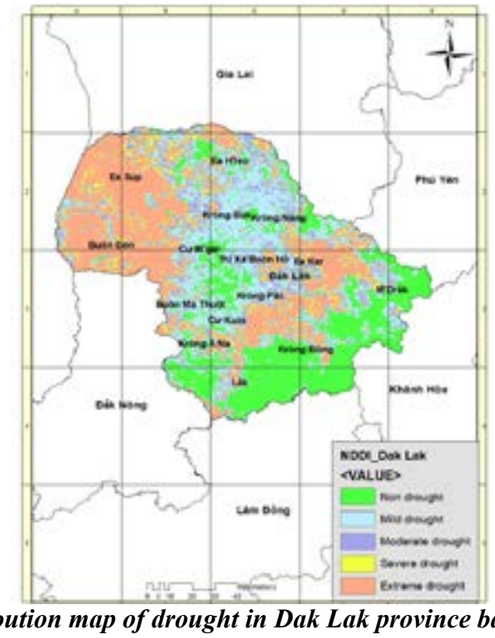

Figure 7. Spatial distribution map of drought in Dak Lak province based on the NDDI index.

Although drought conditions vary between years, generally, Dak Lak province can be divided into three areas with different levels of drought:

(i) Districts located in the southeast of the province (including Lak, Krong Bong and M'Drak districts) belong to the less dense area of the province. This is also an area with a relatively large amount of rainfall and a dense hydrological network.

(ii) The northern districts (including the districts of Ea'Hleo and Krong Nang) and the center of the province (including the following districts: Krong Pak, Buon Ho, Cu Kuin and Ea Kar) are also in the drought area; however, mild to moderate drought occupies most of this area's surface.

(iii) The driest area of Dak Lak province, concentrated in the West, occupies most of the Ea Sup district, the Buon Don district and part of the Cu M'gar district. This is the semi-plateau region of Ea Sup, with low and relatively flat terrain conditions with a relatively rich temperature background (at Ea Sup region, the average annual air temperature is 24.2 °C and the average temperature of most months is not below 20 °C), average annual rainfall below 1400 mm.

4. CONCLUSION

This study aims to monitor drought in Dak Lak province over a 20-year period from 2001 to 2020. The methodology employed Google Earth Engine, data from the MODIS satellite and various algorithms and scripts to analyze and calculate the Vegetation Health Index (VHI) and the Normalized Difference Drought Index (NDDI). The calculation results reflected past drought events in the research area quite accurately. However, the indices showed differences in the frequency and intensity of drought levels. While the NDDI identified extreme and severe drought events in the past, the VHI only determined plant stress levels from Mild to Medium during the research period. The NDDI was chosen to construct a spatial distribution map of drought and identify three different drought-level areas in Dak Lak province. The driest area is identified as the western region of the province, occupying most of the Ea Sup and Buon Don districts. The Southeastern region of the province is an area where drought rarely occurs. Some northern and central districts experience drought, but mainly at mild and moderate levels.

5. REFERENCES

Didan K., 2015. MOD13Q1 MODIS/Terra vegetation indices 16-day L3 global 250m SIN grid V006. *NASA eosdis land processes daac, 10*(730), p.415.

Gao B., 1996. NDWI-A normalized difference water index for remote sensing of vegetation liquid water from space. *Remote Sensing of Environment, 58*(3), 257-266.

Gu Y., Brown J. F., Verdin J. P., & Wardlow B., 2007. A five-year analysis of MODIS NDVI and NDWI for grassland drought assessment over the central Great Plains of the United States. *Geophysical Research Letters*, *34*(6).

Kogan F. N., 1995. Application of vegetation index and brightness temperature for drought detection. *Advances in Space Research*, Vol.15, No.11, 91-100.

Mutanga O., and Kumar L., 2019. Google Earth Engine Applications. *Remote Sensing*, *11*(5), 591.

Tucker C. J., 1980. Remote sensing of leaf water content in the near infrared. *Remote Sensing of Environment, 10*(1), 23-32.

Tucker C. J.,1979. Red and photographic infrared linear combinations for monitoring vegetation. *Remote Sensing of Environment*, *8*(2), 127-150.

Wan Z., 2018. Collection-6 MODIS Land Surface Temperature Products Users' Guide. *University of California, Santa Barbara.*

Tucker C. J., 1979. Red and photographic infrared linear combinations for monitoring vegetation. *Remote Sensing of Environment, 8*(2), 127-150.

Gao B., 1996. NDWI-A normalized difference water index for remote sensing of vegetation liquid water from space. *Remote Sensing of Environment, 58*(3), 257-266.

Kogan F. N., 1995. Application of vegetation index and brightness temperature for drought detection. Advances in Space Research, Vol. 15, No. 11, 91-100.

THAILAND COVID-19 CASE FATALITY SPATIAL CLUSTER AND DIRECTION ANALYSIS

Athitaya Sakunmungmee*, Tanyaluck Chansombat, Pathana Rachavong

Department of Natural Resources and Environment,
Faculty of Agriculture Natural Resources and Environment, Naresuan University, Thailand
*Corresponding author. Email: athitayas63@nu.ac.th

ABSTRACT

The global situation has been dominated by COVID-19 for 4 years. As of August 12, 2023, there were 4,755,443 confirmed cases and 34,437 deaths, equivalent to 491 per million population. The fatality rate was 0.724 percent. This study analyzes CFR: Case Fatality Rate using the COVID-19 death toll data together with the number of confirmed cases, the regional monthly change percentage and the average monthly change percentage. The results of the study are found to have seen regional changes. Areas with extremely dense and sparse deaths are analyzed using Getis Ord Gi and spatial direction analysis to demonstrate the direction of COVID-19 death distribution from the center.*

1. INTRODUCTION

The People's Republic of China announced the discovery of a new strain of coronavirus in Wuhan, Hubei province, in December 2019, or perhaps even since mid-November. The epidemic then spread to many areas around the world. The 2019 novel coronavirus, or SARS-CoV-2, causes severe pneumonia in patients and can lead to death. This virus can spread from person to person through coughing, sneezing, or contact with patient secretions. The virus first spread in Thailand on January 13, 2020, from a female patient who traveled from Wuhan.

Public health agencies usually use R0 and Rt as numbers to indicate the severity of an outbreak. However, outbreaks do not stop with the initial outbreak numbers. It also leads to the death of infected patients. Therefore, it is necessary to have numbers showing the severity of the disease-causing deaths in each area. There are 3 main indices that show death from epidemics as they are used to explain them: 1) CMR: Crude Mortality Rate refers to the probability that each person out of the entire population will die from the disease. 2) CFR: Case Fatality Rate means the risk of death of a confirmed infected person and 3) IFR: Infective Fatality Rate means the risk of dying from a particular disease if infected with that disease. However, each Index has different benefits and limitations in its use.

Current data on COVID-19 infections and deaths worldwide includes 700 million cases, 6.9 million deaths and 13,492 million vaccine doses received. In Thailand, there are 4 million cases, 34.000 thousand people have died 146 million doses of vaccine have been received. The number of deaths worldwide is 9.043 deaths per thousand and Thailand has a proportion of 7.239 deaths per 1.000 people. The purpose of this research is to analyze case fatality rates using spatial cluster and direction analysis.

2. METHODOLOGY

The data analysis process begins with searching for information about the number of deaths in 2021 in each province in Thailand to serve as the basis for the analysis as follows.

2.1 CFR-case fatality rate is calculated from the proportion of deaths from COVID-19 and the number of people infected with SARS-CoV-2 per thousand people in the population.

2.2 Moran's I analysis is a spatial cluster analysis used to find the spatial relationship of deaths and how they are related to the characteristics of the area. Global Moran's I is a measure of the overall clustering of the spatial data. It is defined as:

$$I = \frac{n}{S_0}\frac{\sum_{i=1}^{n}\sum_{j=1}^{n} w_{i,j}(x_i - \bar{x})(x_j - \bar{x})}{\sum_{i=1}^{n}(x_j - \bar{x})^2} \quad (1)$$

$$S_0 = \sum_{i=1}^{n}\sum_{j=1}^{n} w_{i,j} \quad (2)$$

The value of *I* can depend quite a bit on the assumptions built into the spatial weights matrix. The matrix is required because, in order to address spatial autocorrelation and also model spatial interaction, we need to impose a structure to constrain the number of neighbors to be considered. This is related to Tobler's first law of geography, which states that Everything depends on Everything else, but closer things more so - in other words, the law implies a spatial distance decay function, such that even though all observations have an influence on all other observations, after some distance threshold that influence can be neglected.

The idea is to construct a matrix that accurately reflects your assumptions about the particular spatial phenomenon in question. A common approach is to give a weight of 1 if two zones are neighbors and 0 otherwise, though the definition of 'neighbors' can vary. Another common approach might be to give a weight of 1 to k nearest neighbors, 0 otherwise. An alternative is to use a distance decay function for assigning weights. Sometimes, the length of a shared edge is used for assigning different weights to neighbors. The selection of the spatial weights matrix should be guided by the theory of the phenomenon in question. The value of I is quite sensitive to the weights and can influence the conclusions you make about a phenomenon, especially when using distances.

2.3 Cluster and Outlier Analysis (Anselin Local Moran's I or LISA: local indicators of spatial association) is a detailed analysis of spatial dependence and neighbor relations that goes into detail about whether deaths are consistent with the surrounding area or not.

Global spatial autocorrelation analysis yields only one statistic to summarize the whole study area. In other words, the global analysis assumes homogeneity. If that assumption does not hold, then having only one statistic does not make sense, as the statistic should differ over space. Moreover, even if there is no global autocorrelation or no clustering, we can still find clusters at a local level using local spatial autocorrelation analysis. The fact that Moran's I is a summation of individual cross-products is exploited by the "local indicators of spatial association" (LISA) to evaluate the clustering in those individual units by calculating Local Moran's I for each spatial unit and evaluating the statistical significance for each Ii. From the equation of Global Moran's I, we can obtain.

The Local Moran's I statistic of spatial association is given as:

$$I_i = \frac{x_i - \bar{X}}{S_i^2}\sum_{j=1,j\neq i}^{n} w_{i,j}(x_j - \bar{X}) \quad (3)$$

where, X_i is an attribute for feature *i*, *X bar* is the mean of the corresponding attribute, $w_{i,j}$ is the spatial weight between feature *i* and *j* and:

$$S_i^2 = \frac{\sum_{j=1,j\neq i}(x_j - \bar{X})^2}{n-1} \quad (4)$$

Cluster and Outlier Analysis in ArcGIS Pro 3.1 uses Input Feature Classes and Analysis Fields to identify clusters of spatial features with high or low values. The tool also identifies spatial outliers by calculating local Moran's I, z-score, pseudo-p-value and cluster type codes for each statistically significant feature. The z-score and pseudo-p-value indicate the statistical significance of the calculated index values and display the spatial pattern as a choropleth map.4.

Directional Distribution Analysis measures the trend of data points by calculating distances separately in the x and y directions, both of which determine the size of the ellipse or standard deviation of the ellipse. Standard deviational ellipse (SDE). The value obtained by calculating the standard deviation of the x-coordinate point and y-coordinate point from the center mean determines the size of the axis of the ellipse. The distribution of incidents can be seen from the shape of the elliptical standard deviation, which can be calculated as shown in the equation below. The standard deviation of the ellipse can also indicate the angle of rotation of the ellipse or the direction of the distribution of data.

$$SDE_y = \sqrt{\frac{\sum_{i=1}^{n}(y_i - \bar{Y})}{n}} \quad (5)$$

$$SDE_x = \sqrt{\frac{\sum_{i=1}^{n}(x_i - \bar{X})}{n}} \quad (6)$$

where, x_i are the coordinates of phenomena at point *i* on the *x*-axis; y_i are the coordinates of phenomena at point *i* on the *y*-axis; *X-bar* is the mean of phenomena at point *i* on the *x*-axis; *Y-bar* phenomena at point *i* on the *y*-axis; *n* is the number of all phenomena

The angle of rotation of the ellipse is calculated using the following equation.

$$tan\,\theta = \frac{A+B}{C} \quad (7)$$

$$A = \left(\Sigma_{i=1}^{n}\bar{X}_i^2 - \sum_{i_1=1}^{n}\bar{Y}_i^2\right) \quad (8)$$

$$B = \sqrt{\left(\Sigma_{i=1}^{n}\bar{X}_i^2 - \sum_{i=1}^{n}\bar{Y}_i^2\right)^2 + 4\left(\sum_{i=1}^{n}\bar{X}\bar{Y}\right)^2} \quad (9)$$

$$C = 2\sum_{i=1}^{n}\bar{x}_i\bar{y}_i \quad (10)$$

where, X_i-*bar* are deviations of *x* coordinates from the mean; Y_i-*bar* are deviations of *y* coordinates from the mean.

The elliptical degree of the data obtained from the calculation will have the direction of rotation of the long axis (rotation) starting with the measurement clockwise from noon. For example, a degree equal to 90° will have a direction of distribution toward the east. while degrees equal to 180° will have a direction of distribution to the south.

3. RESULTS

The Pandemic continues from mid-January 2020 to the present in Thailand. A total of more than 4 million people have been infected with SARS-CoV-2, with 34,000 thousand deaths and 146 million doses of COVID-19 vaccine have been administered. The death rate per capita of those who died in Thailand is 7,239 deaths per 1,000 people, which is less than the global death toll rate of 9,043 deaths per 1,000 people.

As for the case fatality rate (CFR: Case Fatality Rate) of Thailand, it appears as shown in Table 1 which shows descriptive statistics. It can be seen that the case fatality rate is 17.04 cases per 1,000 people, with a standard deviation of 65.01 cases per 1,000 people. Provinces with the lowest and highest death rates were 0.05 and 545.08 cases per 1,000 people, respectively.

Table 1. The CFR descriptive statistics.

	CFR
Average	17.0360
Standard deviation	65.0111
Minimum	0.0538
Maximum	545.0808
n	77

Table 2. Global Moran Index of CFR.

Regions	Parameters				
	Moran's I	**Expected Index**	**Variance**	**z-score**	**p-value**
Thailand	0.3508	-0.0132	0.0072	4.2889	0.0000
Northern Thailand	-0.1782	-0.1250	0.1302	-0.1476	0.0027
Central Thailand	0.0963	-0.0477	0.0138	1.2252	0.2205
North Eastern Thailand	-0.0481	-0.0526	0.0455	0.0213	0.8041
Eastern Thailand	-0.3646	-0.1667	0.1219	-0.5670	0.5707
Western Thailand	0.1316	-0.2500	0.0248	2.4221	0.0154
Southern Thailand	-0.0873	-0.0769	0.0738	-0.0382	0.9695

Table 2 shows the results obtained from the analysis of the geographic distribution of COVID-19 deaths in Thailand, which is an overview of the entire country, divided into 6 parts according to different regions of the country. Thailand's Moran's Index has a value of 0.35, indicating that the distribution of COVID-19 death patients in Thailand is somewhat clustered according to one region of the country with statistical significance. Meanwhile, the central and western regions of Thailand have Moran's Index values of 0.10 and 0.13, which are similar, indicating that the distribution of COVID-19 death patients is random and not related to the characteristics of the region. It appears to be similar to the northern, northeastern and southern regions, with Moran's

Index equal to -0.18, -0.05 and -0.09, respectively, indicating that the distribution of deceased patients is also random. The eastern region of the country has a Moran's Index of -0.37, indicating that the distribution of COVID-19 death patients in this region is not clustered in any one area but rather scattered throughout the region. All of this appears in Figure 1a.

The following Table 3 shows the results obtained from the provincial CFR directional distance analysis. It was found that there was a deviation of 8.7399 degrees from the central axis, indicating that the orientation of the distribution of Deaths from COVID-19 in Thailand appears to follow a north-south line with only slight deviations. This is because the shape of the country forces it to tilt approximately 9 degrees north-south, as shown in Figure 1b.

Table 3. The provincial CFR directional distance.

	Center X	**Center Y**	**X Std Distance**	**Y Std Distance**	**Rotation**
Thailand	717,821.45	1,574,919.17	251,597.03	55,519.55	8.74

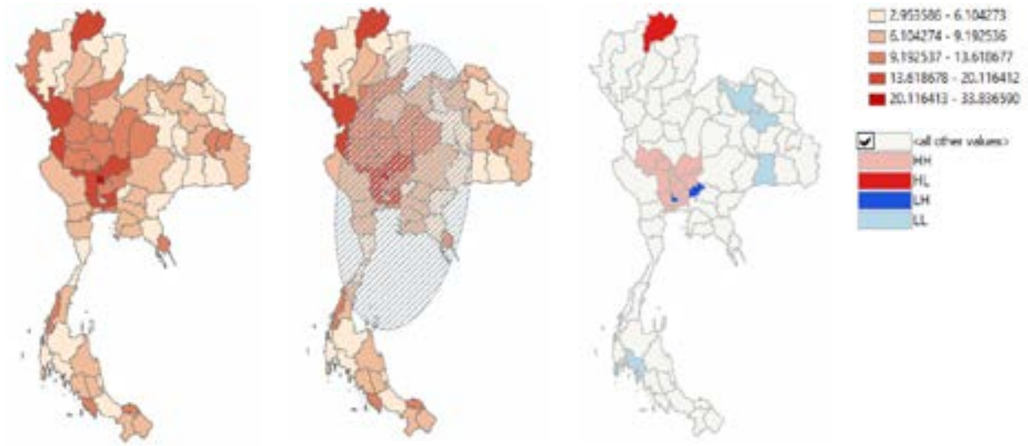

(a) (b) (c)

Figure 1. Thailand Covid-19 CFR spatial distribution (a) direction orientation (b) and local spatial association (c).

In terms of Cluster and Outlier Analysis or LISA: Anselin Local Moran's I - local indicators of spatial association, the results are divided into 4 parts: HH, LL, HL and LH, shown in Figure 1c. This shows that the distribution of CFR at the local level, where HH refers to areas with a high frequency of illness and death from SARS-Cov-2 infection, with surrounding areas having a high frequency of illness and death, which consists of an area of 12 provinces: Samut Sakhon, Bangkok, Pathum Thani, Nakhon Pathom, Phra Nakhon Si Ayutthaya, Saraburi, Lopburi, Ang Thong, Singburi, Suphanburi, Chainat and Uthai Thani.

HL refers to an area with a high frequency of illness and death from SARS-Cov-2 infection, with surrounding areas having a low frequency of illness and death, which consists of an area of 1 province, Chiang Rai. The LL refers to an area with a low frequency of sickness and death from SARS-Cov-2 infection, with surrounding areas having a low frequency of sickness and death, which consists of 5 provinces: Udon Thani, Kalasin, Surin, Phuket and Krabi. Finally, the LH refers to the area with a low frequency of sickness and death from SARS-Cov-2 infection, with

surrounding areas having a high frequency of sickness and death, which consists of the areas of 2 provinces: Nonthaburi and Nakhon Nayok.

4. DISCUSSION

Analysis of the Global Moran Index shows that COVID-19 deaths among Thai people distributed in various provinces have a clustering pattern, where areas that are clustered together were analyzed using Directional distance analysis. It was found that It has a north-south distribution with only a slight tilt angle. Moreover, analyzing the distribution at the local level using Cluster and outlier analysis, it is clearly seen that areas with a high frequency of deaths from SARS-Cov-2 infection, surrounding areas with a higher frequency of deaths from SARS-Cov-2 infection. High cases of sickness and death include the Bangkok area and four provinces surrounding Bangkok, namely Samut Sakhon, Pathum Thani, Nakhon Pathom and Phra Nakhon Si Ayutthaya, including areas of Saraburi, Lopburi, Ang Thong, Singburi, Suphanburi, Chainat and Uthai Thani provinces, a total of 7 other provinces with similar geographic relationships.

However, in explaining death from COVID-19, the spatial relationship pattern resulting from the Cluster and outlier analysis that shows only the connection of the distribution of deaths with the surrounding region does not fully cover the important issues of controlling and preventing disease outbreaks. The research of Derara Girma et al., (2022) studied Factors Contributing to Mortality in Ethiopia. The research of Lucas Almeida Andrade et al., (2021) studies the relationship in spatiotemporal pattern of COVID-19-Related Mortality in Brazil by bringing in the Social Vulnerability of each region to analyze and find relationships and research by Yaowen Luo et al., (2021) that brings together the environmental and socioeconomic risk factors that play a large role in the COVID-19 death rate in the United States. All these studies are good examples that the Geographical Society of Thailand should take into account and encourage further detailed research. This will be very beneficial to public health management to be as comprehensive as possible.

5. CONCLUSION

Analysis of the Global Moran Index shows that illness and death from COVID-19 among Thai people scattered in various provinces have a clustering pattern. Areas that are clustered together are analyzed for Directional distance and are found to be oriented in the north-south direction with a slight angle of inclination. The results obtained from analyzing the distribution at the local level with Cluster and outlier analysis found that areas with a high frequency of death from SARS-Cov-2 infection, with surrounding areas having a high frequency of sickness and death. It consists of 12 provinces: Samut Sakhon, Bangkok, Pathum Thani, Nakhon Pathom, Phra Nakhon Si Ayutthaya, Saraburi, Lopburi, Ang Thong, Singburi, Suphanburi, Chainat and Uthai Thani.

6. ACKNOWLEDGEMENTS

This research was supported by The Geographic Association of Thailand

7. REFERENCES

Derara Girma, Hiwot Dejene, Leta Adugna, Mengistu Tesema and Mukemil Awol., 2022. COVID-19 Case fatality rate and factors contributing to mortality in Ethiopia: A systematic review of current evidence. Retrieved February 26 2023. https://doi.org/10.2147/IDR.S369266.

Djalma de Sigueira junior, Tassiane Cristina Morais, Isabella Portugal, Matheus Paiva Emidio Cavalcanti, Blanca Elena Guerrero Daboin, Rodrigo Daminello Raimundo, Lucas Cauê Jacintho, Jorge de Oliveira Echeimberg, Khalifa Elmusharaf and Carlos Eduardo Siqueira., 2021. Trends in COVID-19 mortality and case-fatality rate in the State of Parana, South Brazil: Spatiotemporal analysis over one year of the Pandemic. Retrieved January 7 2023. http://dx.doi.org/10.36311/jhgd.v31.12792.

Lucas Almeida Andrade, Wandklebson Silva da Paz, Alanna G. C. Fontes Lima, Damião da Conceição Araújo, Andrezza M. Duque, Marcus Valerius S. Peixoto, Marco Aurélio O. Góes, Carlos Dornels Freire de Souza, Caíque J. Nunes Ribeiro, Shirley V. M. Almeida Lima, Márcio Bezerra-Santos and Allan Dantas dos Santos., 2021. Spatiotemporal pattern of COVID-19-Related mortality during the first Year of the Pandemic in Brazil: A population-based study in a region of High Social Vulnerability. Retrieved January 15 2023. https://www.ajtmh.org/view/journals/tpmd/106/1/article-p132.xml.

Yaowen Luo, Jianguo Yan and Stephen McClure., 2021. Distribution of the environmental and socioeconomic risk factors on COVID-19 death rate across continental United States: A spatial nonlinear analysis. Retrieved February 12 2023. https://doi.org/10.21203/rs.3.rs-61369/v1.

APPLICATION OF REMOTE SENSING AND GIS TO ESTABLISH SURFACE TEMPERATURE MAP OF PHU THO PROVINCE

Tran Thi Ngoan

Hanoi University of Natural Resources and Environment, Vietnam
Corresponding author. Email: ttngoan@hunre.edu.vn

ABSTRACT

Phu Tho is a province with great potential for economic and tourism development. Along with that development comes the warming of the province's surface temperatures. This study used Landsat 8 images to calculate the surface temperature of Phu Tho province. The data used in the study are Landsat 8 images combined with geographical data of the area. Calculation results of Phu Tho province's surface temperature range from 26.79-46.32 ^oC. Places with high temperatures are concentrated in the city. Viet Tri is a place with high population density and rapid urbanization. The temperature in the high mountains is relatively cool.

1. INTRODUCTION

Surface temperature is an extremely important input parameter for climate models in studying drought soil moisture as well as monitoring urban temperature inversion phenomena. Ground observations only reflect the temperature at actual measuring stations at a certain location. Therefore, it is necessary to have an effective solution to collect information on a large scale. Remote sensing images are the top choice in solving research problems in the field of resource management, extracting data quickly and accurately. Landsat satellite images have good resolution and are continuously updated, so they are increasingly widely used in surface temperature research.

In recent years, research into the application of remote sensing in surface temperature research has achieved outstanding results. In 2011, in the research project "Research on land surface temperature in Da Nang city from Landsat 7 ETM+ image data," the authors used Landsat 7 ETM+ images to calculate in combination with the emission valence algorithm (Emissivity Normalization Method, NOR), which gave highly accurate results (Tran An Thi, 2011). In 2018, Trinh Le Hung and his colleagues built a surface temperature calculation program based on combining Landsat 8 and Sentinel 2 satellite images to calculate the conversion of the integer value (digital number) of the thermal infrared channel. Landsat images to the actual value of electromagnetic radiation (spectral radiance), determine brightness temperature, determine NDVI vegetation index, surface emissivity and calculate surface temperature. The results give higher accuracy when using an independent type of image (Trinh Le Hung, 2018; Nguyen Dinh Thuan, 2015). In the research work "Analysis of factors affecting the surface urban heat island phenomenon in the Bangkok metropolitan area, Thailand", the study used remote sensing image analysis method to extract temperature. Surface from thermal infrared images on the Landsat satellite determines the spatial distribution, magnitude and main factors affecting the urban heat island, including urban density, the proportion of high-temperature areas, proportion of Vegetation cover area ratio, water surface area ratio, cool surface area ratio (Can N. T., 2019), research on the evolution of urban surface heat island in the northern region of the city. Ho Chi Minh city from thermal infrared channels (Van T. T., 2017). Using thermal infrared channel and NDVI index from Landsat to estimate surface temperature and build city land surface temperature map (Tuyet N. H. A., 2019; Hung N. V., 2019). In addition, there are many research works related to surface temperature and urban heat island phenomenon in Vietnam (Van T. T., 2011).

.In the context of limited actual measurement data, using remote sensing images to calculate and determine surface temperature will bring high economic efficiency. The calculation can be done quickly. Landsat images were taken at a relatively close time period, collecting data for free, so the project focuses on using Landsat images to create a surface temperature map of Phu Tho province.

2. STUDY AREA AND DATA

2.1 Study area

Phu Tho is a Northern midland and mountainous province of Vietnam, located in the center of the region and is the northwest gateway to the capital, Hanoi. Phu Tho province is located on the economic corridor of Hai Phong - Hanoi - Kunming (China), bordering Vinh Phuc Province to the East, Hanoi City to the West, Hoa Binh Province to the South, Hoa Binh Province to the North. Yen Bai, Tuyen Quang and Phu Tho are 50 km from the Noi Bai International Airport, 80 km from Hanoi city center, 170 km from Hai Phong port, from Ha Khau international border gate (between Lao Cai - Vietnam and Yunnan - China), respectively. Thanh Thuy - Lang Son is 200 km and is the confluence of three large rivers: Red River, Da River and Lo River. Phu Tho's geographical location has created favorable conditions for Phu Tho and great potential for production, business, exchange and economic development both domestically and internationally.

Figure 1. Location of Phu Tho province on Vietnam map.

Like other localities, Phu Tho is also greatly affected by global climate change. Tourism development, urbanization, industrialization and modernization have made the area's temperature increasingly hotter. According to hydrometeorological data series, climate change in Phu Tho province is increasingly evident. Therefore, determining surface temperature in Phu Tho province is essential for monitoring temperature changes to control warming in the province.

2.2 Data

A data set used in the project includes Landsat 8 (EarthExplorer.usgs.gov) and administrative boundaries and roads (https://www.diva-gis.org/gdata). The image was acquired on September 6, 2022, at 30 m spatial resolution. The ID of the images is LC08_LITP_127045_20220906_20220914.

The image channels used in the surface temperature calculation are 4,5 and 10.

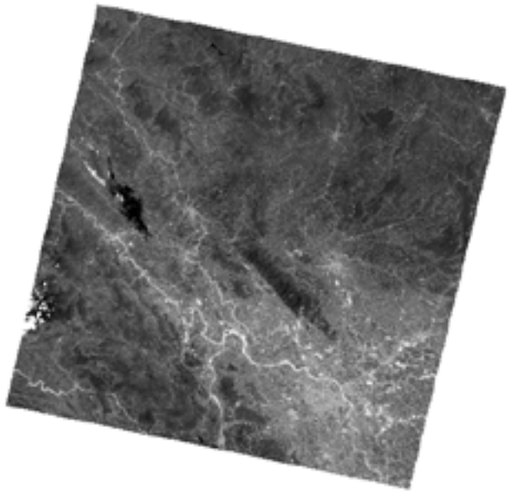

Figure 2. Landsat 8 images serve to calculate the surface cover of Phu Tho province.

3. METHODS

The surface temperature map of Phu Tho province was calculated and built through Landsat 8 image data and vegetation index values. The steps to build a surface temperature map are shown in Figure 3 (https://giscrack.com/how-to-calculate-land-surface-temperature-with-landsat-8-images/).

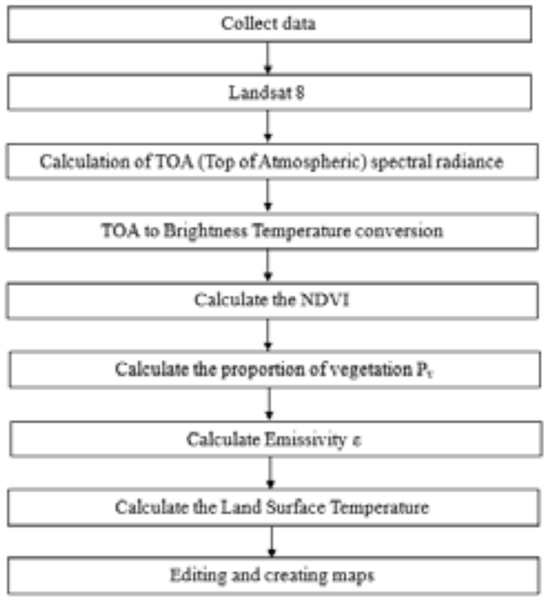

Figure 3. Steps to create a surface temperature map from Landsat 8 images.

3.1 Calculation of TOA (Top of Atmospheric) spectral radiance

$$TOA\ (L) = ML \times Qcal + AL$$

where:

ML = Band-specific multiplicative rescaling factor from the metadata. (RADIANCE_MULT_BAND_x, where x is the band number).

Qcal = corresponds to band 10.AL; with AL = Band-specific additive rescaling factor from the metadata (RADIANCE_ADD_BAND_**x**, where x is the band number).

$$TOA = 0.0003342 \times \text{“Band 10”} + 0.1$$

3.2 TOA to Brightness Temperature Conversion

$$BT = (K2 / (\ln (K1 / L) + 1)) - 273.15$$

where:

K1 = Band-specific thermal conversion constant from the metadata (K1_CONSTANT_BAND_**x**, where x is the thermal band number).

K2 = Band-specific thermal conversion constant from the metadata (K2_CONSTANT_BAND_**x**, where x is the thermal band number).

$$L = TOA$$

Therefore, to obtain the results in Celsius, the radiant temperature is adjusted by adding the absolute zero (approx. -273.15 °C).

$$BT = (1321.0789 / Ln ((774.8853 / \text{“\%TOA\%”}) + 1)) - 273.15$$

3.3 Calculate the NDVI

$$NDVI = (Band\ 5 - Band\ 4) / (Band\ 5 + Band\ 4)$$

Note that the calculation of the NDVI is important because, subsequently, the proportion of vegetation (Pv), which is highly related to the NDVI and emissivity (ε), which is related to the Pv, must be calculated.

$$NDVI = Float\ (Band\ 5 - Band\ 4) / Float\ (Band\ 5 + Band\ 4)$$

3.4 Calculate the proportion of vegetation Pv

$$Pv = Square\ ((NDVI - NDVImin) / (NDVImax - NDVImin))$$

Usually, the minimum and maximum values of the NDVI image can be displayed directly in the image (both in ArcGIS, QGIS, ENVI and Erdas Imagine); Otherwise, you must open the properties of the raster to get those values.

$$Pv = Square((\text{“NDVI”} - 0.216901) / (0.632267 - 0.216901))$$

3.5 Calculate emissivity ε

$$\boldsymbol{\varepsilon = 0.004 \times Pv + 0.986}$$

Simply apply the formula in the raster calculator. The value of 0.986 corresponds to a correction value of the equation.

3.6 Calculate the Land Surface Temperature

$$LST = (BT / (1 + (0.00115 \times BT / 1.4388) \times Ln(\varepsilon)))$$

3.7 Editing and creating maps

After calculating the LTS value, use that result to create a surface temperature map of the mantle in Phu Tho province.

4. RESULTS AND DISCUSSIONS

After calculating the temperature value of Landsat 8 images, the temperature value ranges from 13.7566 to 47.68 ^{o}C. Cropping images along the boundary of Phu Tho province obtained thermodynamic values in the range of 26.7926 to 46.3271 ^{o}C.

Open the background geographic data layers in ArcMap, edit the map and we get the map we need to create, as shown in Figure 4.

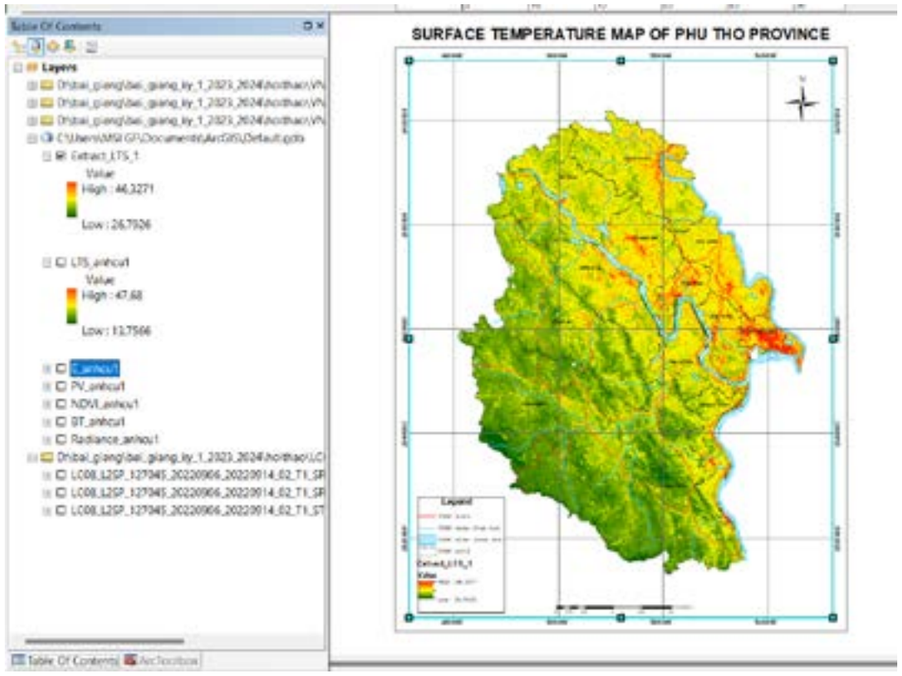

Figure 4. Surface temperature map of Phu Tho province.

Based on the temperature calculation results, it is clear that the background temperature of Phu Tho province is relatively high. Some places reach over 46 degrees. High temperatures are concentrated in the city area. Viet Tri, where there is a dense population, the process takes place quickly. In addition, high temperatures also appear along the main roads where the population lives. From this, we can draw the conclusion that in places with high population density, a high level of concrete will increase the heat. In places with many trees, such as forests and fields, the temperature is lower. In addition, the photo was taken on June 9, 2022, which is the hottest spot of the year, so the overall temperature of the whole province is high.

5. CONCLUSION

The use of remote sensing and GIS technology in creating temperature maps gives quick, highly accurate results. The visual image of the map clearly shows which areas have high temperatures and which areas have low temperatures. Through this, it also helps us identify and evaluate the main causes of the rapid increase in surface temperature.

Areas with high temperatures are often areas with high population density and rapid urbanization. This is a useful finding that helps managers understand the causes to have more effective urban planning and management measures.

6. REFERENCES

An T. T., Dieu N. T., and Minh T. P., 2011. Research on land surface temperature in Da Nang city from Landsat 7 ETM+ satellite image data. *National GIS Application Workshop 2011*.

Anh L. V., and Anh T. T, 2014. Research on land surface temperature using the method of calculating emissivity from vegetation index. *Journal of Earth Sciences, 36*(2), 184-192.

Can N. T., Diep N. T. H., Sanwit I., Pariwate V., Minh V. Q., 2019. Analysis of factors influencing the surface urban heat island phenomenon in the Bangkok area, Thailand. Science magazine of Hanoi National Palm University. *Earth and Environmental Sciences, 1*(35), 53-62.

EarthExplorer.usgs.gov. https://www.diva-gis.org/gdata. Accessed on 4 October 2023.

https://giscrack.com/how-to-calculate-land-surface-temperature-with-landsat-8-images/. Accessed on 4 October 2023.

Hung N. V.; Hoa N. H.; and Nghia N. H, 2019. Using landsat images to build a land surface temperature map in Son La city area for the period 2015-2019. *Journal of Forestry Science and Technology, 6*, 77-87.

Le Hung T., Tai V. V., Long D. N., & Duan D. N., 2018. Building a program to calculate surface temperature based on a combination of Landsat 8 and Sentinel 2 satellite images. *Journal of Surveying and Mapping Science*.

Snow N. H. A., Than N. H., 2019. Remote sensing application to assess surface temperature fluctuations in Dau Tieng district, Binh Duong province in the context of climate change in the period 2004-2019. *Proceedings of the conference Scientific research in Earth science Soil and Environment*, 357-360. https://doi.org/10.15625/vap.2019.000154.

Thuan N. D., and Van P. V., 2015. Application of remote sensing technology and geographic information system to study surface temperature changes in 12 urban districts, Hanoi city in the period 2005 - 2015. *Vietnamese Journal of Science and Agriculture South, 8*(14), 1319-1330.

Van T. T., Bao H. D. X., Dinh Thi Kim Phuong, Mai N. T. T., Nhung D. T. M., 2017. Thermal environment characteristics and urban surface heat island developments in the Northern region of the Ho Chi Minh city. *Can Tho Science Magazine, 49*(A), 11-20.

Van T. T., Lan H. T., and Trung L. V., 2011. Research on urban surface temperature changes under the impact of urbanization in Ho Chi Minh city using remote sensing methods. *Journal of Earth Sciences, 33*(3), 347-359.

THE ROLE OF OROGRAPHIC EFFECTS ON HEAVY RAINFALL EVENT OVER CENTRAL VIETNAM IN OCTOBER 2021

Phong Le Van[1], Phong Nguyen Binh[2], Thuong Le Thi[2]*

[1]Vietnam Institute of Meteorology, Hydrology and Climate Change
[2]Hanoi University of Natural Resources and Environment, Vietnam
*Corresponding author. Email: ltthuong.kttv@hunre.edu.vn

ABSTRACT

In this paper, we use observation data and high-resolution (3 km) simulations from the WRF model, driven by FNL data, to investigate the causes of heavy rain over Central Vietnam from 22nd to 29th October 2021. Our findings confirm the significant role of topography in causing heavy rain. In terms of the atmosphere's vertical structure, the surface's northeast wind, almost perpendicular to the Central region's topography, combined with the east wind and trade winds above, caused strong convection. Additionally, medium-scale formations such as tropical cyclones also contributed to heavy rainfall over a short period in this area.

1. INTRODUCTION

The heavy rainfall in recent years has shown significant changes in both its distribution and quantity. These transformations are increasingly challenging for weather forecasting and early warning efforts. Numerous forecasting technologies have been implemented; however, heavy rain events occurring over short periods of time continue to result in substantial consequences.

Meanwhile, the influence of low-level cold air combined with various atmospheric patterns and disturbances, such as storms, tropical depressions, the Inter-Tropical Convergence Zone (ICTZ) and eastward wind disturbances, has led to substantial rainfall in the Central region of Vietnam (Anh V. P., 2002 and Quang L. D., 2005). However, to assess the causes of heavy rainfall and the vertical structure of the atmosphere during these events, relying solely on synoptic charts is insufficient. Hence, numerical models have emerged as a solution. In 2011, Toan N. T., (2011) utilized the WRF model as a powerful tool for weather prediction. The author ran the WRF model for the Central region days in advance of heavy rain events, comparing cases with and without local data updates for 14 heavy rainfall episodes. The results indicated that better local data improved the model's accuracy.

Additionally, in a recent study, Tuan B. M., (2019) reanalyzed ECMWF data for 30 years and employed dynamic statistical methods to demonstrate that wave-like atmospheric disturbances within the East Asian monsoon zone are a major factor contributing to heavy rainfall in Vietnam. The development of these disturbances can sometimes intensify into storms or tropical depressions and, at other times, only persist in regions of weak convergence and divergence. However, when these wind convergence zones combine with tropical extratropical factors or high terrain in Vietnam, rapid enhancement occurs, creating a favorable environment for heavy rainfall events.

On the other hand, during the heavy rainfall event in October 2020 in the Central region of Vietnam, Mau N. D et al., (2022) pointed out that the activity of the monsoon trough, coupled with the presence of the Madden-Julian Oscillation (MJO), created favorable conditions for the development of tropical cyclones. Furthermore, during the La Niña period, there was an increase in the activity of the eastward winds (trade winds) in the Northwest Pacific, playing a leading role in directing the monsoon trough directly towards the Central region, resulting in historic heavy rainfall in this area.

2. DATA AND METHODS

2.1 Data

This research utilizes two datasets to assess and understand the factors leading to heavy rainfall. Firstly, daily rainfall observations from 8 weather stations in the Central region are employed. Additionally, the "Final" dataset (FNL) from the U.S. National Centers for Environmental Prediction (NCEP), a global reanalysis data set with a spatial resolution of 0.25×0.25 degrees longitude and latitude, is used as input for the WRF model in this study.

2.2 Methods

Synop Method: The Synop method involves the analysis of Synop charts at various pressure levels, combined with observational data from 8 weather stations in the Central region. This approach is employed to investigate and comprehend large-scale circulation patterns and weather configurations contributing to heavy rainfall.

Modeling Method: The modeling method utilizes the high-resolution numerical model WRF (Weather Research and Forecasting) with input data derived from the global reanalysis dataset known as FNL (Final) provided by the U.S. National Centers for Environmental Prediction (NCEP). This modeling approach aims to simulate the occurrence of heavy rainfall during the period from October 22 to October 29, 2021, in order to elucidate the dynamic and thermodynamic mechanisms responsible for rainfall, both in cases with and without geographical influences.

2.3 Experimental design

The WRF model is a numerical weather prediction and research model developed through the collaboration of the United States National Center for Atmospheric Research (NCAR), the National Centers for Environmental Prediction (NCEP), the Forecast Systems Laboratory of the National Oceanic and Atmospheric Administration (NOAA) and a group of scientists at various universities. The clWRF version is a development from the WRF model for the purpose of climate research and prediction. In this study, the WRF model is utilized with three nested grids, each having different resolutions: 27 km, 9 km and 3 km. Region 1 extends to approximately 26°N and off the coast of the Philippines to "capture" large-scale processes, specifically the intrusion of cold air and tropical cyclones. Region 2, with a resolution of 9 km, covers the entire territory of Vietnam and the East Sea. Region 3, with a high resolution, covers the entire Central region to simulate heavy rain events (Figure 1)

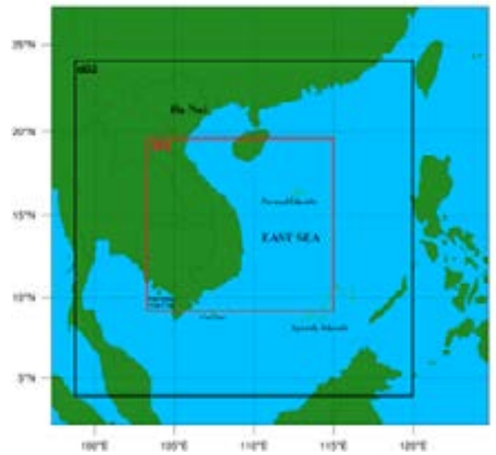

Figure 1. The three nest domains employed in the model.

3. RESULTS

During the heavy rainfall event from October 22 to October 29, 2021, in the Central region of Vietnam, various types of rainfall occurred, including light rain, moderate rain and heavy rain. In some areas from Quang Tri to Quang Ngai, extremely heavy rainfall was observed, with total precipitation ranging widely from 300 to 500 mm and, in many places, exceeding 500 mm.

Furthermore, Vietnam stretches across multiple latitudes and features complex terrain, making the interaction between topography and weather patterns a significant and frequently discussed issue in studies. One of the notable geographical features that influence Vietnam's climate is the Truong Son Mountain Range, which runs along the country's length and acts as a barrier that obstructs lower-level airflows. During the summer, the Truong Son Range blocks the southwest monsoon winds from the west, resulting in the Foehn effect and intensifying heat in the Central region. Therefore, summer is not the main rainy season in this area. However, during the autumn, when the monsoon disturbances within the East Asian monsoon combine with the northeast monsoon winds at lower levels, the Truong Son Range once again plays a critical role in blocking low-level airflows and causing heavy rainfall in the Central region. Consequently, the rains in the Central region are often of high intensity and frequently lead to flash floods and landslides.

In this study, the interaction between topography and weather patterns is also considered and calculated using numerical modeling experiments. In these experiments, two scenarios are run: one with the presence of topography and one without topography. This approach allows for an assessment of how terrain influences weather conditions in the region, helping to elucidate the role of geography in heavy rainfall events.

The simulation ran from October 22 to October 29, 2021, during a period of intense rainfall in the Central region of Vietnam. This was due to a combination of factors: the intrusion of cold air, disturbances in the eastward wind and the emergence of tropical cyclones. The outcomes of the simulation are presented in Figure 3.

From October 22 onwards, potent easterly and northeasterly winds from the East Sea had a direct impact on the Central region of Vietnam. The downward movement of the cold air mass caused what is known as front rainfall over the East Sea. Despite the circulation patterns being similar, there was a significant difference in rainfall between the two simulation scenarios. In the scenario without topography, the majority of the rainfall occurred over the sea and was relatively light. However, in the scenario with topography, the simulated rainfall was considerably heavier, with a tendency for the precipitation to accumulate on the eastern slopes of the Truong Son Mountain Range, extending from Ha Tinh to Quang Ngai.

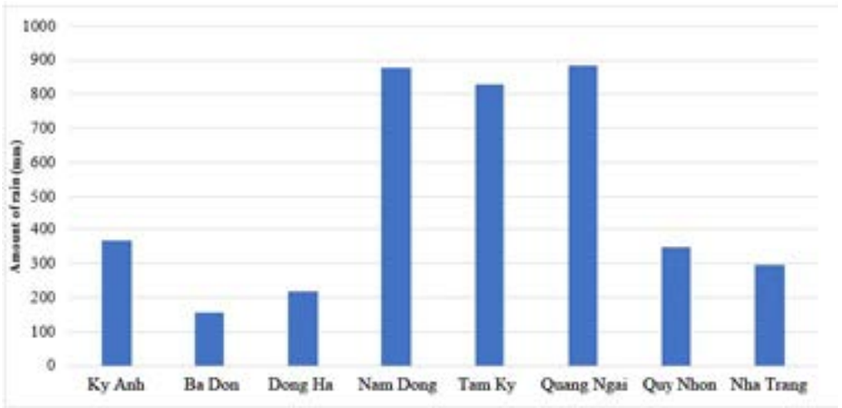

Figure 2. Shows the total daily rainfall at several weather stations in the Central region from October 22 to October 29, 2021.

In the days that followed, the scenario without topography did see some rainfall over land, but it was significantly less than in the scenario with topography. These results clearly highlight the role of topography in obstructing low-level airflows, which results in heavy rainfall.

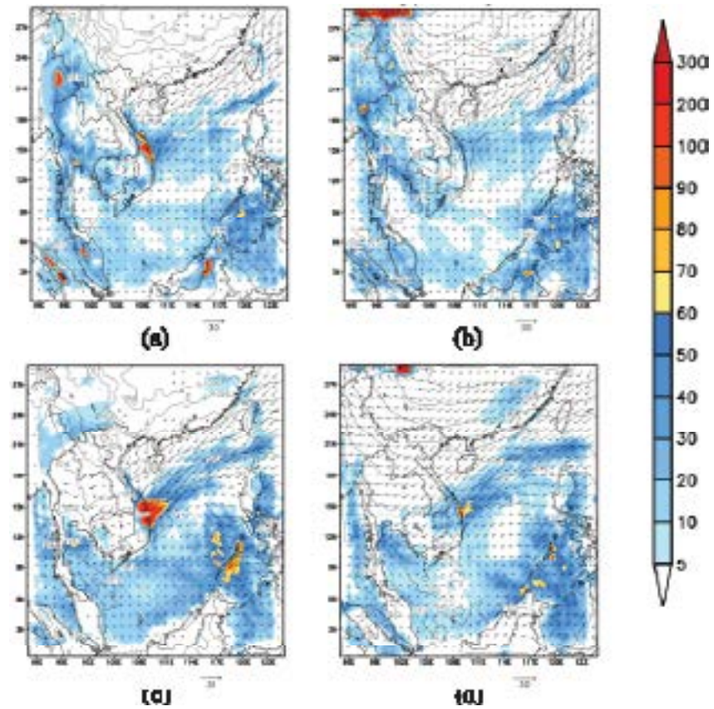

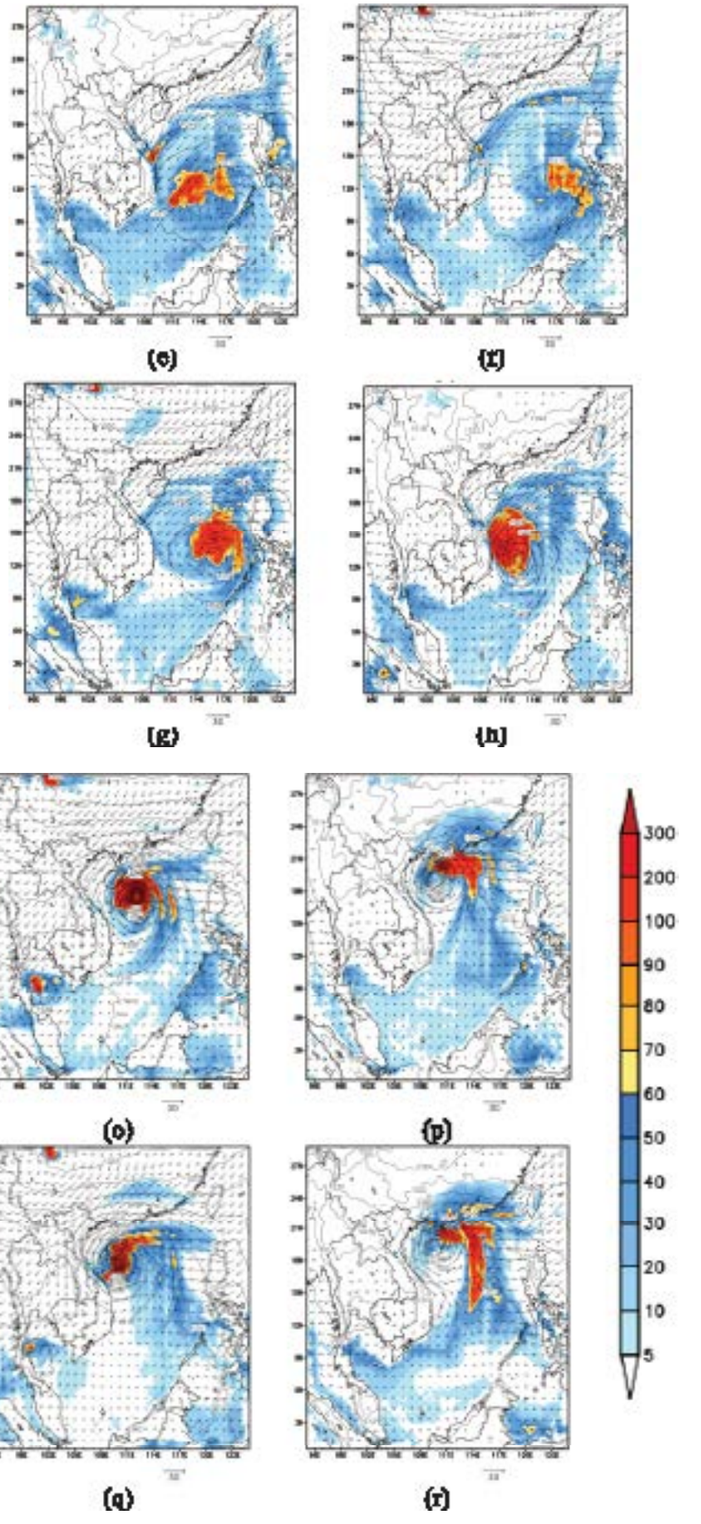

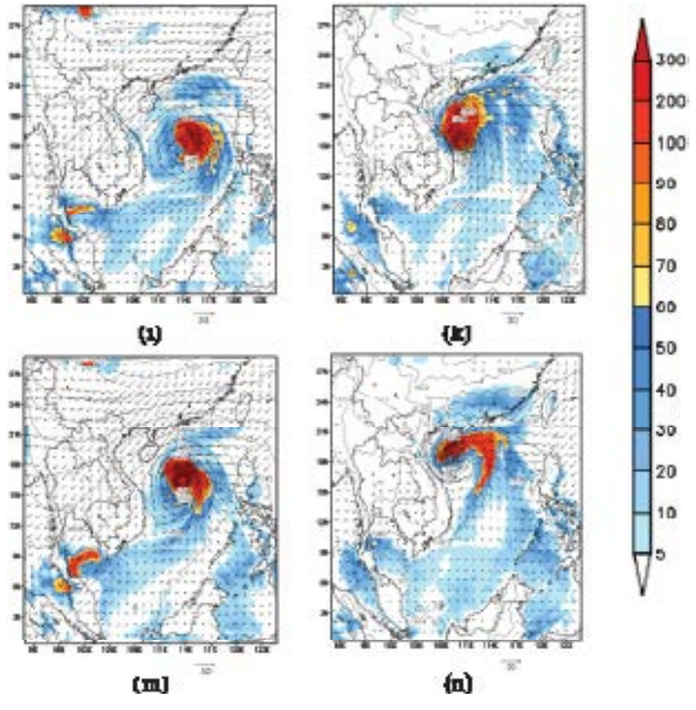

Figure 3. Illustrates the interaction between topography and the weather patterns that contributed to heavy rainfall from October 22 to October 23, 2021 in two cases with terrain (left) and without terrain (right).

To better understand the relationship between topography and weather patterns that result in heavy rainfall, an analysis of the atmospheric vertical structure at 14.8 degrees North Latitude and 108.0 degrees East Longitude was carried out in two scenarios: one incorporating topography and one without. Figure 4 displays the findings.

The scenario that includes topography, cold air and disturbances in the East Asian monsoon converged at a height of 1,500 meters on the eastern side of the Truong Son Mountain Range. The Convective Available Potential Energy (CAPE) index was extremely high over the eastern Truong Son area and the coastal regions of the Central region. This suggests that the convergence of cold air and eastward wind disturbances, which blow almost perpendicular to the Truong Son Range's topography, played a significant role in the very heavy rainfall experienced in this region.

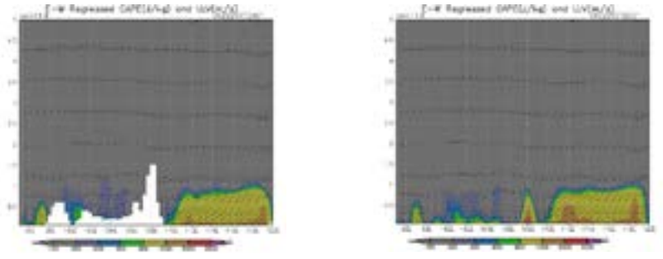

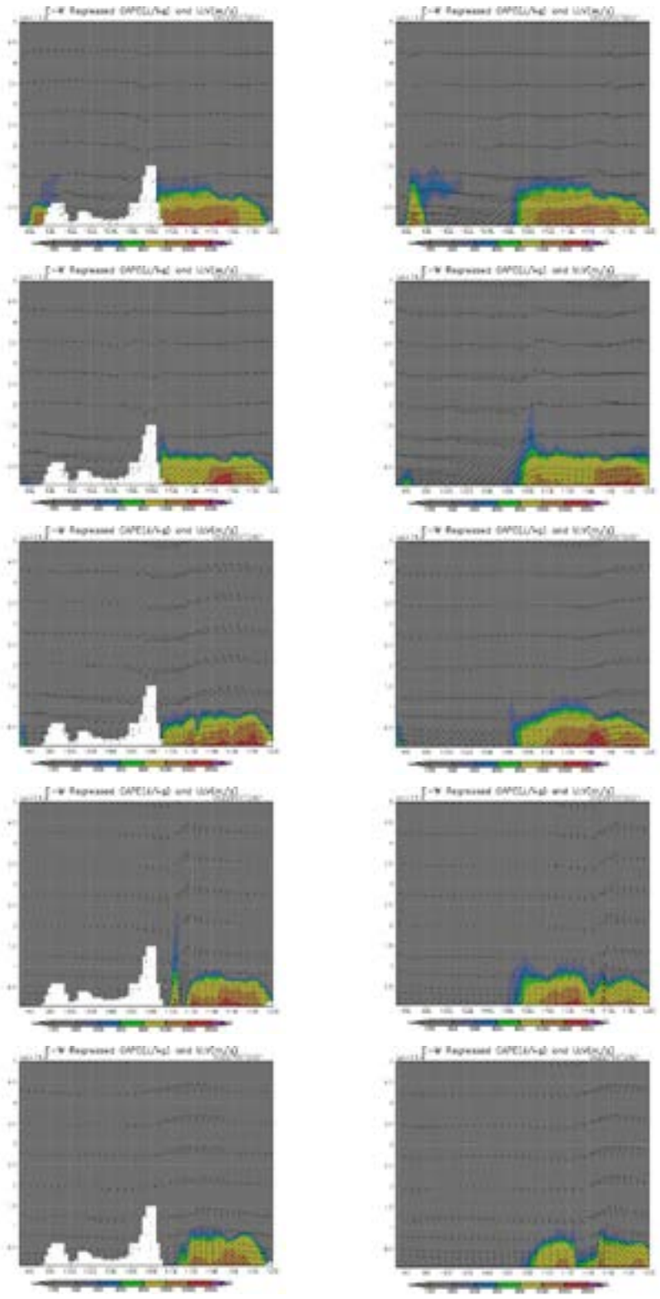

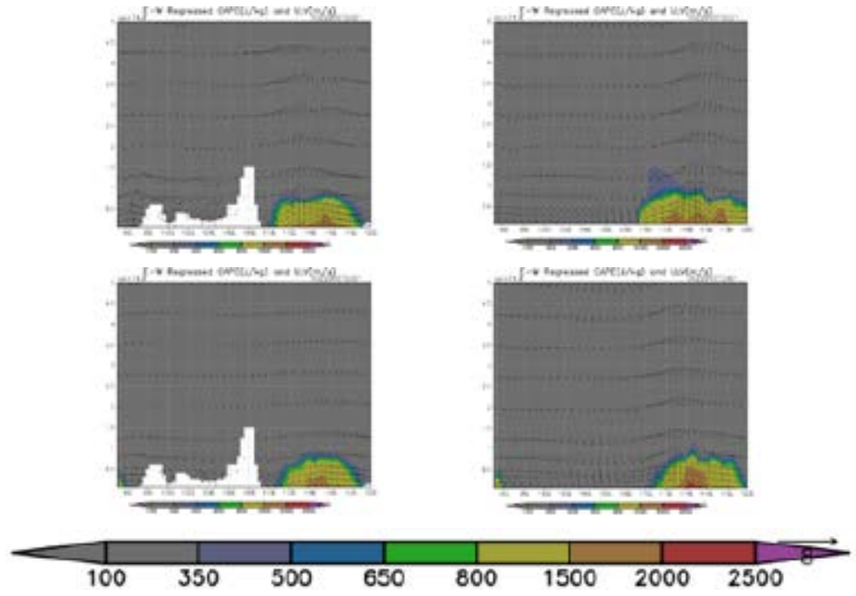

Figure 4. Depicts the vertical atmospheric cross-section at 14.8N in two scenarios: One with topography (left) and one without topography (right), simulated during the heavy rainfall event from October 22 to October 29, 2021 in two cases with terrain and without terrain.

To delve deeper into the interplay between topography and weather patterns that result in heavy rainfall, an analysis was performed on the vertical atmospheric structure at 14.8 degrees North Latitude and 108.0 degrees East Longitude under two conditions: one incorporating topography and one without. The findings are shown in Figure 4.

The scenario that includes topography, cold air and disturbances within the East Asian monsoon converged at a height of 1,500 meters on the eastern side of the Truong Son Mountain Range. The Convective Available Potential Energy (CAPE) index was extremely high over the eastern Truong Son area and the coastal regions of the Central region. This suggests that the convergence of cold air and eastward wind disturbances, which blow almost perpendicular to the Truong Son Range's topography, played a significant role in the very heavy rainfall experienced in this region. Moreover, on October 26, due to the influence of the tropical cyclone circulation combined with disturbances within the East Asian monsoon, rainfall continued in this region. The convergence process was strong and prominently focused around the center of the tropical cyclone.

In contrast, in the scenario without topography, at 14.8 degrees North Latitude, cold air with a stable northeasterly wind pattern affected the Central region of Vietnam. The entire region was directly impacted by a relatively strong cold wave. The CAPE index also showed clear signs but did not exhibit the same convection around the center of the tropical cyclone as in the topography scenario. This suggests that the energy provided by the environment for convergence into the center of the tropical cyclone was relatively weak.

When analyzing the atmospheric structure along the longitudinal axis at 108.0 degrees East Longitude, similar observations were made. In the topography scenario, there was clear convergence between the northeasterly winds and the terrain of the Central region, extending to approximately

16 degrees North Latitude (Bach Ma Range). Furthermore, a relatively well-defined low-level trough (convergence between the Northeast monsoon and the Southwest monsoon) was observed from October 26 in the region from 16 to 18 degrees North Latitude. In the following days, this low-level trough gradually moved Northward following the motion of the tropical cyclone. At this time, the convective potential index primarily existed over the Southern East Sea and the Gulf of Thailand.

Conversely, in the scenario without topography, even though there was still a Northward shift of the low-level trough, the influence of the northeasterly wind was considerably strong, dominating most of the Central region. In this case, the low-level trough was positioned much lower, at around 12 to 14 degrees North Latitude. The CAPE index in this scenario also differed significantly from the topography scenario. On October 22, this index was very strong in the 14 to 16 degrees North Latitude region, indicating strong convergence in this area, but it rapidly weakened in the following days.

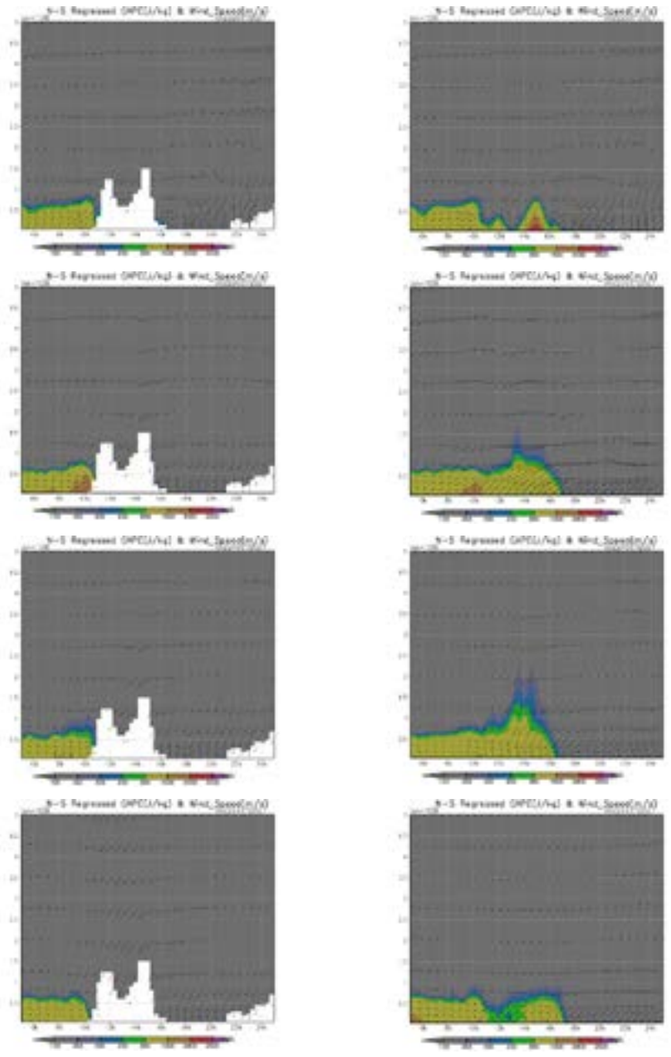

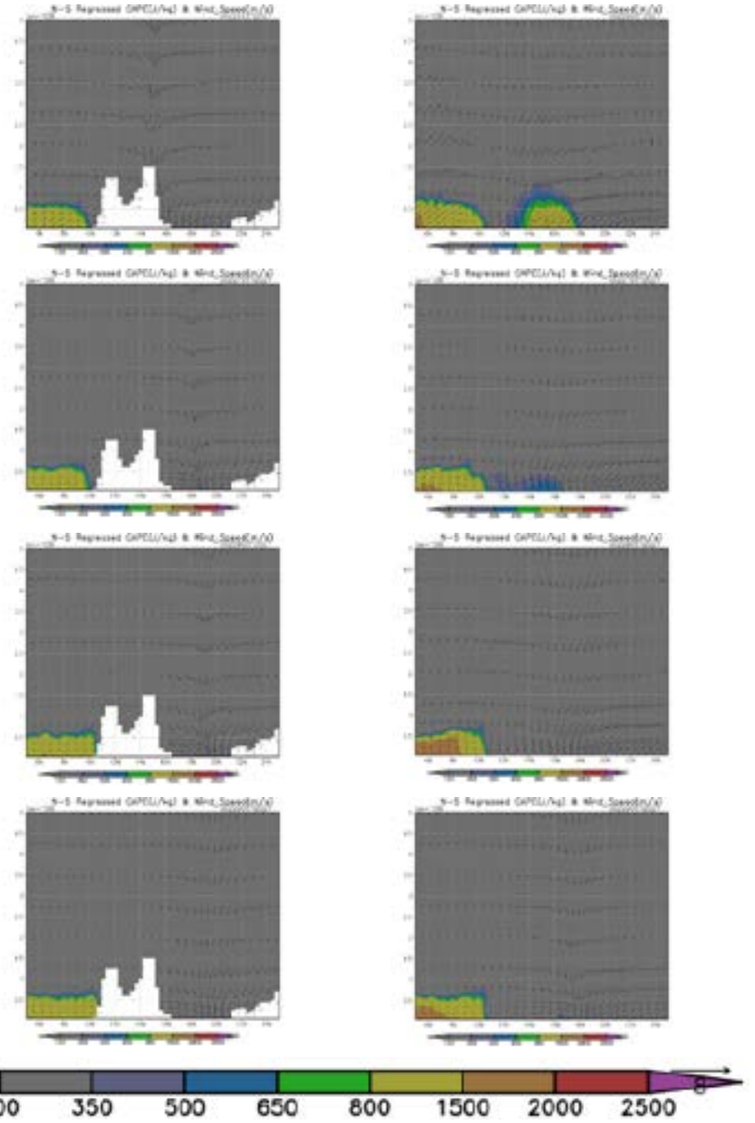

Figure 5. Displays the vertical atmospheric cross-section at 108.0E in two scenarios: one with topography (left) and one without topography (right), simulated during the heavy rainfall event from October 22 to October 29, 2021, in two cases with terrain and without terrain.

4. CONCLUSION

The results from the analysis of observational data and high-resolution WRF model simulations regarding the interaction between heavy rainfall and topography in the Central region during the period from October 22 to October 29, 2021, indicate the following:

(1) Heavy rainfall in the Central region is attributed to the influence of cold air in combination with the topography, as the Truong Son Mountain Range acts as a barrier, enhancing convective activity and rainfall in this area.

(2) The impact of tropical cyclone circulation is one of the factors leading to an increase in both the extent and amount of rainfall over a short period.

(3) In the case of topography, the simulated rainfall field using the high-resolution WRF model is significantly more intense. Additionally, the rainfall tends to concentrate on the eastern slope of the Truong Son Range, spanning from Ha Tinh to Quang Ngai. Conversely, in the scenario without topography, rainfall is primarily distributed over the sea and the amount of rainfall is relatively weak over the Central region.

(4) When analyzing the vertical atmospheric structure at 14.8N and 108.0E, the study observed that during this rainfall event, the Northeasterly winds blew almost perpendicular to the topography. This, combined with upper-level eastward wind disturbances and the influence of the tropical cyclone carrying abundant moisture, created a strong upward converging flow, resulting in widespread heavy rainfall.

5. REFERENCES

Anh V. P., 2002. Trade wind and the research situation of heavy rainfall influenced by trade wind in the Central Region. *Meteorological and Hydrological Journal*, Vol. 499, 22-28.

Mau N. D., Thang, N. V., Duong T. H., Tuan B.M., Tuan V. Q., Hien D. T., 2022. Large-scale circulation associated with heavy rainfall on October 2020 in Central Viet Nam. *Climate Change Science Journal*, Vol. 21, March 2022.

Quang L. D., 2005. Characteristics of Heavy Rainfall in Central Vietnam. *Meteorological and Hydrological Journal*, Vol.536, 1-6.

Toan N. T., 2011. Prediction of Heavy Rainfall due to KKL combined with ICTZ for 1 to 3 days in the Central Central Region using the WRF model. *Master's thesis*, University of Natural Sciences, Hanoi National University.

Tuan B. M., 2019. Extratropical Forcing of Submonthly Variations of Rainfall in Vietnam. *J. Climate*, 32, 2329-2348.

INVESTIGATE SAR INTENSITY AND OPTICAL IMAGES TO RAPIDLY DETECT SMALL AND MEDIUM LANDSLIDES IN MU CANG CHAI DISTRICT YEN BAI PROVINCE

Xuan Quang Truong[1],Van Anh Tran[2,3]* , Cam Chi Nguyen[4], Manh Dat Truong[1], Chi Cong Nguyen[1], Thi Phuong Anh Dao[1], Thi Thanh Thuy Pham[1]

[1]Information Technology Faculty,
Hanoi University of Natural Resources and Environment, Vietnam
[2]Faculty of Geomatics and Land Administration,
Hanoi University of Mining and Geology, Vietnam
[3]Geomatics in Earth Sciences Group, Hanoi Univerisity of Mining and Geology, Vietnam
[4]Faculty of Interdisciplinary Sciences, Hanoi National University, Vietnam
*Corresponding author. Email: tranvananh@humg.edu.vn

ABSTRACT

Synthetic Aperture RADAR (SAR) imagery remains unaffected by weather conditions and enables day-and-night observations, making it particularly suitable for studying landslides, especially in regions with cloud cover, such as tropical climates like Vietnam. On the other hand, optical images can be utilized to create land cover/use maps and monitor changes over time. This paper presents a combination of methods to determine changes in SAR intensity between two time periods and track land use/coverage changes before and after landslides, aiding in the rapid detection of small and medium landslide points in the mountainous areas of northeastern Vietnam. In the study, Sentinel-1 Radar images and Sentinel-2 images from the period before and after July 2022 were utilized. The research leveraged the Google Earth Engine (GEE) cloud computing platform as the primary tool, enabling efficient and rapid mining of image data. The findings from this study can contribute to the improvement of the landslide inventory dataset and the swift identification of potential landslide points during landslide disasters. The study area is located in Mu Cang Chai district, Yen Bai province, known as one of Vietnam's landslide hotspots.

1. INTRODUCTION

One of the landslide hot spot zones in Vietnam is the mountainous region of Northern Vietnam. According to the report of the Vietnam Institute of Geosciences and Mineral Resources (VIGMR, 2023) indicates that several provinces within this region face a significantly high risk of landslides. Notably, Son La and Yen Bai stand out as the two provinces with the most substantial landslide vulnerability, each hosting over 1,000 identified landslide points. Additionally, research conducted at the district level highlights Mu Cang Chai district, situated within Yen Bai province, as particularly susceptible, with 287 documented landslides (Figure 1). In order to reduce the damage caused by landslide hazards, landslide susceptibility maps are useful tools for solving this problem. The main purpose of landslide susceptibility analysis is to identify high-risk areas (Nanehkaran et al., 2021). The main important factor for landslide susceptibility mapping is landslide inventory (Tang et al., 2020).

Synthetic Aperture Radar (SAR) offers several advantages in remote sensing and Earth

observation applications, in which data is captured by radar sensor on the SAR system itself. The sensor transmits microwaves to the Earth's surface and records the backscattered signals. SAR operates effectively in all weather conditions, including heavy cloud cover, rain and fog (Tsokas et al., 2022). It is not dependent on sunlight, making it suitable for day and night imaging. SAR image is evaluated as the best data source for tropical regions such as Vietnam (Tran et al., 2021). Besides that, optical images can be utilized to create land use and land cover (LULC) or NDVI maps and monitor their changes over time. The changes in the NDVI or LULC between pre and post-landslide events can be used to identify landslide-prone areas (Ariza et al., 2021). However, due to after landslide event, the spectral response changes shortly, especially over zones with fast reactivation in the vegetation cover. Therefore, in order to improve the outcome of the landslide susceptibility map, (Yordanov and Brovelli, 2021) recommended using slope to find non-landside and landslide zones. Upon a geological evaluation determined areas which are considered to be less likely to involve mass movements, the slope of very low (< 20°) hillslopes are unlikely to host landslides and very high slopes (> 70°) generally composed of rock unlikely to retain soil deposits prone to land-sliding.

To mitigate landslide damages in the Mu Cang Chai district. In this paper, we present small and medium-size landslide identification based on a combination of the SAR amplitude change detection with slope threshold and NDVI changes detection during pre- and post-events. We used Google Earth Engine (GEE) to compute and process data since it is a free cloud-based online platform, using only freely available data (Gorelick et al., 2017) and (Handwerger et al., 2020).

2. METHODS

2.1 Study area

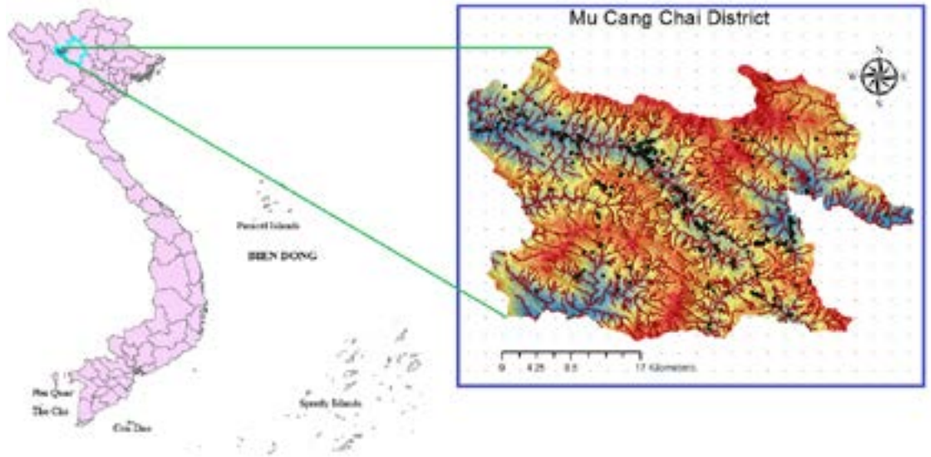

Figure 1. Study area, Mu Cang Chai district, Yen Bai province.

Mu Cang Chai district has an area of 1,199 km² with geographical coordinates ranging from 21°64′37″ to 21°96′38″ North latitude and from 103°89′82″ to 104°89′82″ East longitude. Mu Cang Chai district is located in the Northern part of Yen Bai province. The district is in the high mountains of the Northwest of VietNam and situated at the foot of the Hoang Lien Son mountain range, at an altitude of 1,000 m above sea level. Most of the area of Mu Cang Chai district is located in the distribution of magma eruption formations of the Tu Le complex (ιλKtl), Ngoi Thia (γτKnt), Mu Cang Chai district has a very complex geological structure, strong neo-tectonic activities, with 3 major faults, Weathered crust has a common thickness of 4.5-17 m, the degree of weathering ranges from complete to strong (Figure. 1). According to the report of the district's Department of Agriculture and Rural Development and the results of field investigations, the coverage of the entire area is about 60 % and is on the way to regenerating forests. Based on reports and field surveys in 2021 and 2022, in Yen Bai province, many landslides have occurred along national and province roads due to human activities, where the farmers need more land for agriculture and building houses (VRIM, 2022).

2.2 Data sources

We used The Shuttle Radar Topography Mission (SRTM, see Farr et al., 2007) because this SRTM V3 product (SRTM Plus) is provided by NASA JPL at a resolution of 1 arc-second (approximately 30 m). The Sentinel-1 collects C-band synthetic aperture radar (SAR) imagery from the European Space Agency (ESA) within the Copernicus Programme at a variety of polarizations and resolutions. The data for the optical image, Sentinel-2, also from the Copernicus Programme, was applied in this study, which is an Earth observation mission that systematically acquires optical imagery at high spatial resolution (10-60 m). The detail of the data used is presented in Table 1. According to the classification of landslide size obtained from the Viet Nam Institute of Geosciences and Mineral Resources, landslide sizes are separated into small ones having < 200 (m^3) and medium sizes ranging from 200-1,000 m^3.

Table 1. Data used.

No	Pre-event (T_{pre})	Post-event (T_{post})	Description
Sentinel-1	2019-10-01 2020-05-31	2020-10-01 2021-05-30	VH polarization, ascending + descending, Resolution 10 m
Sentinel-2	2019-10-01 2019-05-31	2020-10-01 2021-05-30	Resolution 10 m
SRTM	Not used		1 arc-second (~30 m) resolution
Landslide points	Filed trip in 2021 along National Road 32		By using a handy GPS

2.3 SAR Amplitude-based change detection using GEE

The tool used in this study is Google Earth Engine (GEE). GEE operates through an online JavaScript Application Programming Interface (API). Through this interface, scripts can be executed, shared and used to replicate geospatial data processing and analysis workflows. The code editor facilitates users to fully implement the functions accessible in Earth Engine. Furthermore, the advantage of GEE also lies in the ability to directly import input data from websites, eliminating the need to download data to the user's computer. This feature allows for rapid data analysis without being limited by the computer's data and memory capabilities (Van Anh. T., 2022).

The methodology of this research is based on the research of (Handwerger et al., 2020) combined with our experience with landslides in the study areas. This method was associated with NDVI changes of the pre- and post-landslide events and slope threshold, which can divide space into two zones (landslide and none-landslide zone) to identify landslide-prone areas. The flow chart of the method is presented in Figure 2.

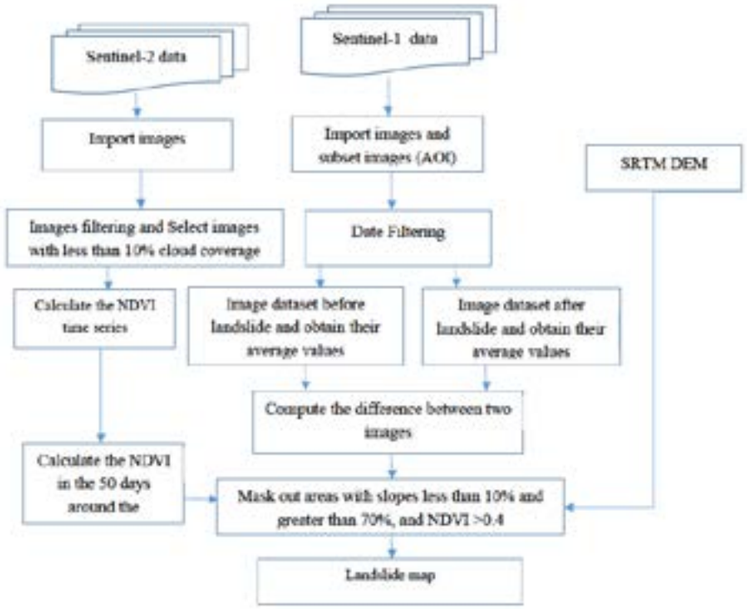

Figure 2. Flow chart of the method presented in this paper.

GEE can access format (GRD) products processed to remove thermal noise and radiance data correction and topography using the SRTM DEM or (ASTER) DEM for areas above 60 degrees latitude. The S1 GRD collection is updated daily and new data are uploaded to GEE within two days of their availability. GEE imports all ascending and descending images. The spatial resolution of the (IW) type GRD products is 20×22 m and the images have a pixel pitch of 10, 25 or 40 m and up to four polarization modes: (VV), (HH), (VV + VH) and (HH + HV). In this study, we only used SAR data in the VH polarization (Handwerger et al., 2020).

The area of interest is Mu Cang Chai district (AOI) and the time period before (Tpre) and after (Tpost) the landslide. Furthermore, Tpre and Tpost will differ depending on the project goal. In this study, we select time during fieldwork time periods. To reduce noise from poor-quality data, we removed all pixels with values ≤ -30 dB (based on recommendations from GEE Data Catalog S1). In addition, we reduce noise by calculating the "Median" operation for the set of images before and after the event. Each data set is calculated as a time average of the data. We created image sets using ascending data and descending data and combined ascending data + descending data (also known as asc + desc) is the average of the ascending and descending sets.

We identify potential landslides (and other types of land surface changes that can be mixed in this task) by examining the change in amplitude, Aratio, defined as the pre-event image set minus the post-event image set, Apre-Apost. Since GEE provides amplitude data in dB, Apre-Apost is equivalent to the standard amplitude ratio approach Aratio (Eq. 1). Therefore, the difference before and after the event will be determined by the formula Jung and Yun, (2020) and Handwerger et al., (2020). The value of Aratio can be positive or negative, in which the positive values represent a decrease in SAR amplitude after a landslide event. Because the changes on the ground surface, such as hillslope geometry, roughness and dielectric properties, can alter the radar reflectance, the SAR amplitude changes after landslide events (Adriano et al., 2020; Rignot and Van Zyl, 1993)

$$Aratio = \log10 (Apre / Apost) \quad (1)$$

where, Aratio: Change in amplitude, A_{pre}: Image before the landslide occurred, A_{post}: Image after the landslide occurred

To reduce false positives as a result in which indicate that a certain condition is present (actually, it is not usually there), we removed areas that are unlikely to correspond to landslides, such as flat areas, agricultural land and lakes, by using threshold-based masks made from (a) topographic slope ($E_{threshold}$= 10 degrees) this threshold was selected based on experiences of the landslide expert in study area) and (b) curvature from SRTM DEM ($C_{threshold}$ = -0.005). This threshold was recommended by (Handwerger et al., 2020). In the pre-processing step, to reduce the noise (image smoothing filters), we also calculated the curvature by taking the Gaussian spatial filter (standard deviation = 60 m and radius = 120 m) as part of our processing in GEE. In all the steps above, we refer to this step as the DEM mask.

Finally, due to that NDVI can assess and monitor vegetation health and coverage vegetation changes (Xie et al., 2017), we use the "NDVI mask" to make the final decision for identifying new landslide points in the study area. The NDVI mask is in areas with high vegetation cover that are approximately 50 days closer to the landslide. The reason for using masks for areas with high vegetation cover is that after landslides, in those areas, there will be no vegetation or sparse vegetation. (Figure 3).

In Figure 3, the highlighted pink areas represent regions where the difference in scattering response between the two periods of Sentinel-1 images has been masked by a slope of less than 10 degrees and green vegetation (NDVI > 0.4). These pink areas are areas where landslides or land cover changes due to agricultural production are likely to have occurred. To more accurately determine landslide locations, we took NDVI charts at some locations suspected of landslides. If NDVI changes according to the plant's growth cycle, it is considered constant, but if there is a sudden change, it can be considered as the landslide point and the final conclusion is yes.

3. RESULTS AND DISCUSSION

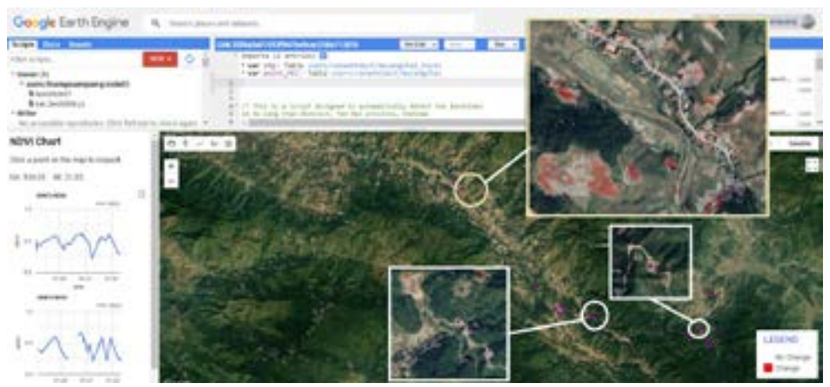

Figure 3. Interface of GEE contains the results showing in Red polygons (landslide polygons) from SAR intensity result of pre-and post-landslide combined with the DEM mask and frequency of NDVI changes (in the left side).

Using GEE for landslide detection, we applied SAR amplitude change combined with both DEM mask and NDVI masks over the latest 50-day post-landslide period to eliminate landslide-free zones in the study area. The results show that SAR-based amplitude change in GEE can be used to detect landslides over large areas. The tool was developed in GEE and is easy to use and develop. This tool can be used to quickly identify landslides for updating the landslide inventory data set (Figure 4). The final result was collected after removing tiny polygons that are around 4,000 polygons were selected and needed to investigate the accuracy of those points which could be real landslide or not.

4. VALIDATION RESULTS AND CONCLUSION

In order to decide which areas detected by SAR amplitude changes are correctly landslide zones, on-site field investigations were conducted. We utilized a set of 16 verification points, which were obtained during fieldwork in January 2021 (refer to Table 2 for details). Data used in the study contains Sentinel-2 (228 images), post-event ascending and descending images 81 scenes and 20 scenes and pre-vent includes ascending and descending images 82 and 19 scenes. The date for collection data of pre-event is about 5 months before events (time to collect data).

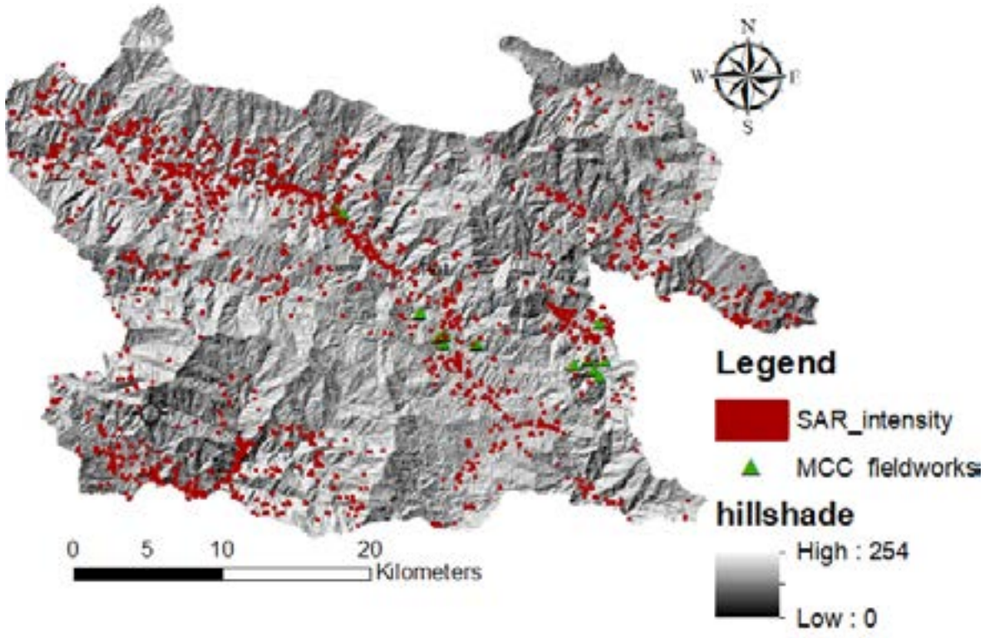

Figure 4. Landslide detection based on SAR amplitude changes combined with DEM mask and NDVI mask.

Table 2. A list of landslide locations was collected on 17 Jan 2021

PointID	X	Y	PointID	X	Y
MCC01	104.2743	21.77521	MCC09	104.1572	21.78039
MCC02	104.271	21.74681	MCC10	104.1013	21.84431
MCC03	104.2738	21.74298	MCC11	104.1019	21.84369
MCC04	104.2665	21.75336	MCC12	104.1069	21.84067
MCC05	104.2579	21.74984	MCC13	104.173	21.76253
MCC06	104.1951	21.76139	MCC14	104.1731	21.76779
MCC07	104.1942	21.76196	MCC15	104.1741	21.76731
MCC08	104.1692	21.766	MCC16	104.2778	21.75265

The results of the SAR amplitude combined with the DEM mask and NDVI have eight polygons that almost cover the six landslide points collected from the field. They are MCC01, MCC04, MCC05, MCC07, MCC09, MCC10, MCC11, MCC13, MCC14 and MCC15. The other MCC points are very close to the result from SAR amplitude. We recognized the distance from landslide points to the nearest red polygons, around 100 meters.

5. CONCLUSION

By integrating Sentinel-1 and Sentinel-2 imagery to assess landslides in the Mu Cang Chai, Yen Bai province, we have concluded:

Utilizing a multi-temporal sequence of Sentinel-1 images, divided into two distinct periods for detecting backscatter discrepancies within both ascending and descending orbits, has proven to be an effective approach for identifying changes in terrain surface.

An additional crucial factor that enhances the ability to identify alterations in topographical features, such as landslides, is the variation in vegetation cover. The normalized differential vegetation index NDVI was employed for this purpose. In areas devoid of vegetation or recently affected by landslides, the NDVI value tends to be low. Combining this with the masking of areas with dense vegetation within 50 days of the landslide event aids in eliminating false positives.

The fusion of different image types and supporting algorithms within the GEE platform represents a revolution in multi-source, multi-resolution data analysis. This approach spares users the need to struggle with data download and processing on personal computers, saving valuable time. The application of GEE offers an overarching view to managers, enabling quick, near-real-time monitoring of landslides.

6. ACKNOWLEDGMENTS

This work is partially funded by the Italian Ministry of Foreign Affairs and International Cooperation within the project “Geoinformatics and Earth Observation for Landslide Monitoring”-CUP D19C21000480001 (Italian side) and partially funded by the Ministry of Science and Technology of Vietnam (MOST) (Vietnamese side) by the Bilateral Scientific Research project between Vietnam and Italy, code: NĐT/IT/21/14.

7. REFERENCES

Adriano B., Yokoya N., Miura H., Matsuoka M., and Koshimura S., 2020. A semiautomatic pixel-object method for detecting landslides using multitemporal ALOS-2 intensity images. *Remote Sens., 12*(3), 561. https://doi.org/10.3390/rs1203056.

Ariza A., N. A. Davila, H. Kemper and G. Kemper, 2021. Landslide Detection in Central America Using the Differential Bare Soil Index. International Archives of the Photogrammetry. *Remote Sensing & Spatial Information Sciences* XLIII-B3-2021:679-684. https://doi.org/10.5194/isprs-archives-XLIII-B3-2021-679-2021.

Gorelick N., Hancher M., Dixon M., Ilyushchenko S., Thau D., and Moore R., 2017. Google Earth Engine: Planetary-scale geospatial analysis for everyone. *Remote Sens. Environ., 202*, 18-27. https://doi.org/10.1016/j.rse.2017.06.031.

Handwerger A. L., Jones S. Y., Huang M. H., Amatya P., Kerner H. R., and Kirschbaum D. B., 2020. Rapid landslide identification using synthetic aperture radar amplitude change detection on the Google Earth Engine. *Nat. Hazards Earth Syst. Sci*. Discuss. [preprint]. https://doi.org/10.5194/nhess-2020-315.

Jung J., and Yun S. H., 2020. Evaluation of Coherent and Incoherent Landslide Detection Methods Based on Synthetic Aperture Radar for Rapid Response: A Case Study for the 2018 Hokkaido Landslides. *Remote Sens., 12*(2), 265. https://doi.org/10.3390/rs12020265.

Nanehkaran Y. A., Mao Y., Azarafza M., Kockar M. K., Zhu H. H., 2021. Fuzzy-based multiple decision method for landslide susceptibility and hazard assessment: A case study of Tabriz, Iran. *Geomech. Eng. 24*, 407-418.

Rignot E. J., and Van Zyl J. J., 1993. Change detection techniques for ERS-1 SAR data, IEEE Trans. Geosci. *Remote Sens, 31*(4), 896-906. https://doi.org/10.1109/36.239913.

Tang Y. M., Feng F., Guo Z. Z., Feng W., Li, Z. G., Wang J. Y., et al., 2020. Integrating principal component analysis with statistically-based models for analysis of causal factors and landslide susceptibility mapping: A comparative study from the loess plateau area in shanxi (China). *J. Clean. Prod, 277*, 124159. Doi:10.1016/j.jclepro.124159.

Tran V. A., Truong X. Q., Nguyen D. A., Longoni L., and Yordanov V., 2021. Landslides monitoring with time series of Sentinel-1 imagery in Yen Bai province-Vietnam. Int. Arch. Photogramm. *Remote Sens*. Spatial Inf. Sci., XLVI-4/W2-2021, 197-203, https://doi.org/10.5194/isprs-archives-XLVI-4-W2-2021-197-2021.

Tsokas, Arsenios, Maciej Rysz, Panos M. Pardalos and Kathleen M. Dipple, 2022. SAR data applications in earth observation: An overview. *Expert Syst. Appl, 205*: 117342.

Van Anh T., Hanh T. H., Nga N. Q., Nghi L. T., Quang T. X., Dong K. T., & Anh T. T., 2022. Determination of Illegal signs of coal mining expansion in Thai Nguyen province, Vietnam from a Combination of Radar and Optical Imagery. In International Conference on Geospatial Technologies and Earth Resources (p. 225-242). Cham: *Springer International Publishing*.

Vietnam Institute of Geosciences and Mineral Resources landslide warning system http://canhbaotruotlo.vn/ (Accessed, Jul 2023)

Xie M., Ma W., Li Z., & Zhou W.,2017. Vegetation recovery after landslides in the Wenchuan earthquake area: Temporal and spatial characteristics. *Natural Hazards, 86.*

Yordanov V., Brovelli M. A., 2021. Application of various strategies and methodologies for landslide susceptibility maps on a basin scale: the case study of Val Tartano, Italy. *Appl Geomat 13*, 287-309. https://doi.org/10.1007/s12518-020-00344-1.

REGIONAL POST-EARTHQUAKE DAMAGE ESTIMATION USING GAUSSIAN GEOSTATISTICAL SIMULATION

Sunanthacha Pholkerd, Pathana Rachavong, Tanyaluck Chansombat*

Department of Natural Resources and Environment,
Faculty of Agriculture Natural Resources and Environment, Naresuan University, Thailand
*Corresponding author. Email: tanyalaks@nu.ac.th

ABSTRACT

Earthquakes can strike suddenly and without warning. An earthquake is a violent and abrupt shaking of the ground caused by movement between tectonic plates along a fault line in the earth's crust. Earthquakes can result in ground shaking, soil liquefaction, landslides, fissures, avalanches, fires and tsunamis. The extent of destruction and harm caused by an earthquake depends on magnitude, intensity and duration, the local geology, the time of day that it occurs, building and industrial plant design and materials and the risk-management measures put in place.

The objective of this research study is to estimate post-earthquake damage at the regional level using Gaussian geostatistical simulation in the study area of 2 provinces: Phitsanulok and Phichit. This study is useful in providing warnings to those involved in the area as well as planning responses in the event of an earthquake occurring on a fault that has not yet been discovered. The results of the study found that there were approximately 1,418 buildings affected by the damage in the risk area. The risk areas can be divided from the perception of earthquake vibrations into 4 levels: the most-risk area with 278 buildings, the high-noise area with 741 buildings, the medium-risk area with 356 buildings and the low-risk area with 36 buildings. The roof of the house. From the survey, it was found that there was no impact to the point of causing damage to the main structure of the building. However, it was found that buildings had cracks or broken cement in areas near the epicenter.

1. INTRODUCTION

Earthquakes can strike suddenly and without warning. An earthquake is a violent and abrupt shaking of the ground caused by movement between tectonic plates along a fault line in the earth's crust. Earthquakes can result in ground shaking, soil liquefaction, landslides, fissures, avalanches, fires and tsunamis. The extent of destruction and harm caused by an earthquake depends on magnitude, intensity and duration, the local geology, the time of day that it occurs, building and industrial plant design and materials and the risk-management measures put in place.

The magnitude-4.5 earthquake, which struck at approximately 12:17 a.m on June 29, 2023, was centered near the tiny town of Phai Lom Subdistrict, Bang Krathum district, Phitsanulok province, Thailand. According to a report from the Department of Geological Resources of Thailand, the cause is due to the movement of hidden underground faults (Hidden Fault), which are apart from the 16 active fault groups. There has never been an earthquake in 100 years. This event was a very shallow earthquake. The earthquake shook people in the areas of Phitsanulok, Phichit, Kamphaeng Phet, Phetchabun and Nakhon Sawan provinces. Vibrations can be felt throughout the area. Damage was found to the walls of houses and churches around Ban Ratcha

Chang Khwan, Pak Thang subdistrict, Mueang district, Phichit province, with slight cracks. These effects correspond to an intensity of V or VI*. These levels of intensity may be reached with earthquakes with a magnitude of around 4 or greater. Likelihood of damage to buildings, such as cracks in plaster. High likelihood of larger cracks in walls and interior walls collapse in less stable buildings. Damage is likely to be caused by falling objects in buildings. The earthquake is felt across a wide area, people are alarmed.

The study was unable to highlight the factors that caused the fault to move because it would take geologists between a year and two years to determine the cause of the earthquake because it is a hidden fault. Underground and has not been discovered before, the study will focus on measuring the magnitude of the vibrations that can be felt and assessing the damage caused. The objective of this research study is to create people's perceptions of seismic hazard maps to estimate post-earthquake damage at the regional level using Gaussian geostatistical simulation in the study area of Phitsanulok and Phichit provinces. This study is useful in providing warnings to those involved in the area as well as planning responses in the event of an earthquake occurring on a fault that has not yet been discovered.

2. STUDY AREA

The study area of about 468 km^2 was located in Phitsanulok and Phichit provinces (Figure 1). The area has communities scattered along the canal. Most of the land has been converted to farmland. And it is an area that is frequently flooded. Such factors are the reason why it is difficult to observe the characteristics of faults on the ground.

Figure 1. The study area is located in Phitsanulok and Phichit provinces.

3. MATERIALS AND METHODS

According to Figure 2, The conceptual framework of regional post-earthquake damage estimation using Gaussian geostatistical simulation involves several key components. Firstly, data on the affected region must be collected and analyzed, including information on the earthquake's magnitude, the type of land use in the area and the distribution of buildings and infrastructure.

Once this data has been collected, it can be used to develop a geostatistical model that can simulate the distribution of damage across the region. This model uses a Gaussian distribution to estimate the probability of damage occurring at any given location based on the data collected during the analysis stage.

The model is then validated using real-world data from previous earthquakes to ensure that it accurately predicts the distribution of damage. Once validated, the model can be used to estimate the likely distribution of damage following future earthquakes, allowing emergency responders and other stakeholders to plan for and respond to potential disasters. Overall, the conceptual framework of regional post-earthquake damage estimation using Gaussian geostatistical simulation is a powerful tool for predicting and mitigating the effects of earthquakes on communities and infrastructure. By combining data analysis, statistical modeling and real-world validation, this approach provides a robust and reliable method for estimating the impact of earthquakes and other natural disasters.

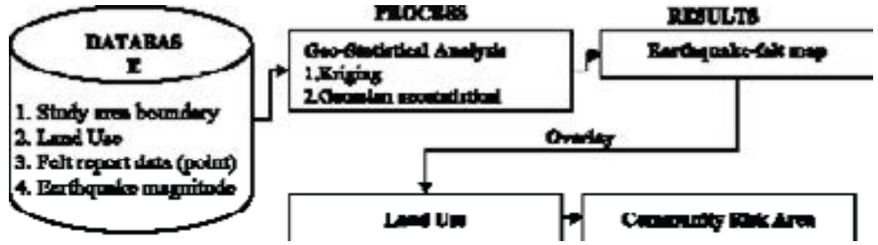

Figure 2. Conceptual framework of regional post-earthquake damage estimation using gaussian geostatistical simulation.

3.1 People's perceptions of seismic hazard map

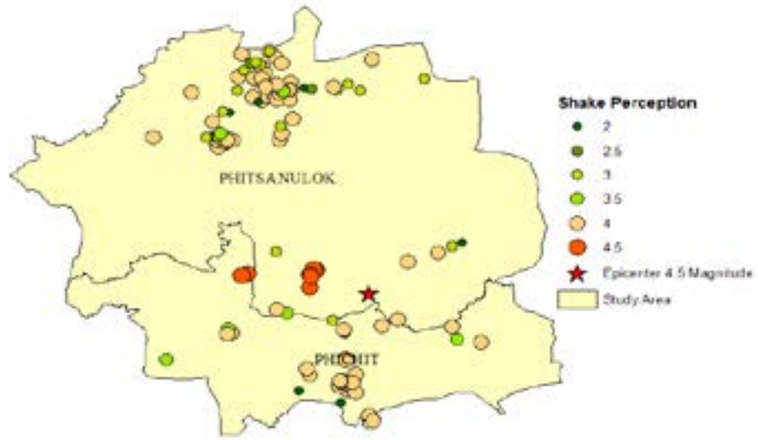

Figure 3. Shaken map from people's seismic perception reports of the Thailand Meteorological Department's earthquake monitoring system.

A map of people's perceptions of seismic hazards (Figure 3) was created from people's seismic perception reports of the Thailand Meteorological Department's earthquake monitoring system. According to the shaking report data, the map is a translation of sensation data and

extrapolated from the Mercalli vibration measurement base. The map is a representation of how people perceive the intensity of seismic activity in different parts of Thailand. It is important to note that the map is not a direct measurement of seismic activity, but rather a reflection of people's subjective experiences. This information can be valuable for disaster preparedness and response, as it provides insight into areas where people may be more vulnerable to the effects of earthquakes. Additionally, the map can be used to identify regions where further research and monitoring are needed in order to better understand and mitigate seismic hazards. Overall, the map serves as a useful tool for understanding the intersection of human experience and natural phenomena.

3.2 Gaussian geostatistical simulations

The Gaussian geostatistical simulations tool is used to create a grid of randomly assigned values drawn from a standard normal distribution (mean = 0 and variance = 1). The covariance model, derived from the semi-variogram specified in the simple kriging layer, is subsequently applied to the raster. This process ensures that the raster values adhere to the spatial structure found in the input dataset. The resulting raster constitutes one unconditional realization and the process can be repeated using a different raster of normally distributed values each time to produce numerous realizations. Further details on this method can be found in Dietrich and Newsam, (1993). If the simple kriging model includes measurement error, the input data values will not be honored in the simple kriging layer or in the simulated realizations. Moreover, the Gaussian geostatistical simulations tool uses a continuous (or smooth) search neighborhood to avoid discontinuities in the simulated surfaces caused by changes in the local neighborhood used in kriging. For more information, refer to Aldworth, (1998) and Gribov and Krivoruchko, (2004). The general workflow for Gaussian geostatistical simulation involves data preparation, realization creation, back-transformation of results into original units and post-processing of results. Alternatively, the results can be used as input to a transfer function (model) to assess variability in the model's output. Figure 4 illustrates this process.

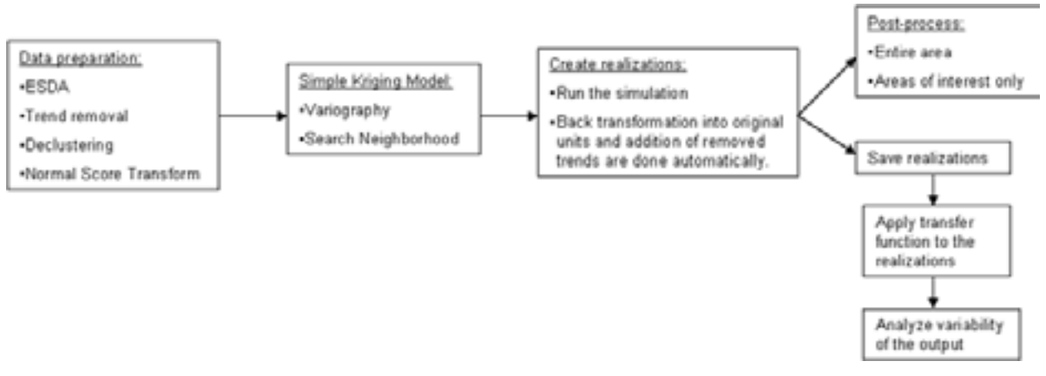

Figure 4. Gaussian geostatistical simulation process.

4. RESULTS

This study is a study of estimating and predicting damage after an earthquake in the study area by analyzing the distribution of vibration-sensing points, which is used as earthquake reporting data and analysis of the distribution of buildings and structures within the earthquake radius using statistical methods. The research results are divided into data analysis as follows:

Firstly, the study analyzes the distribution of vibration-sensing points in the study area to gather information on the intensity and location of the earthquake. This data is then used to estimate the potential damage that may have occurred in different areas. Secondly, statistical methods are used to analyze the distribution of buildings and structures within the earthquake radius. By examining the location, age and construction materials of these buildings, the study can estimate the potential damage that may have occurred to them during the earthquake.

Overall, this study provides valuable insights into the potential damage that can occur after an earthquake in the study area. By analyzing both the earthquake data and the distribution of buildings and structures, researchers can better prepare for future earthquakes and minimize the impact on communities and infrastructure.

4.1 Estimating the perception of earthquakes from the point where the vibrations are perceived.

People's perceptions of seismic hazard maps (Figure 5) were created from people's seismic perception reports of the Thailand Meteorological Department's earthquake monitoring system. According to the shaking report data, there were more than three hundred people reporting the information in total. From the information, it was found that reports were in the areas of Phitsanulok and Phichit provinces. The map is a translation of sensation data and extrapolated from the Mercalli vibration measurement base (Table 1).

Table 1. Data regarding People's Perception of seismic vibrations based on the mercalli scale.

Mercalli scale	Area (km²)
II	5.23
III	130.44
IV	112.55
V	33.80

4.2 Analysis of post-earthquake risk data using Gaussian geostatistical simulation

When it comes to assessing risk in a given area, one crucial factor to consider is the state of the buildings within that area. Using a combination of Gaussian geostatistical simulation and Land use data can help provide a more accurate estimate of the buildings in the area that are at risk. By analyzing the land use data, we can gain a better understanding of the types of buildings and structures in the area, as well as their current condition. The Gaussian geostatistical simulation method allows us to create a spatial model of the area, which can be used to predict the likelihood of certain events occurring, such as natural disasters or human-made accidents. By combining these two methods, we can gain a more comprehensive understanding of the risks facing the buildings in the area and take action to mitigate those risks before they become a problem.

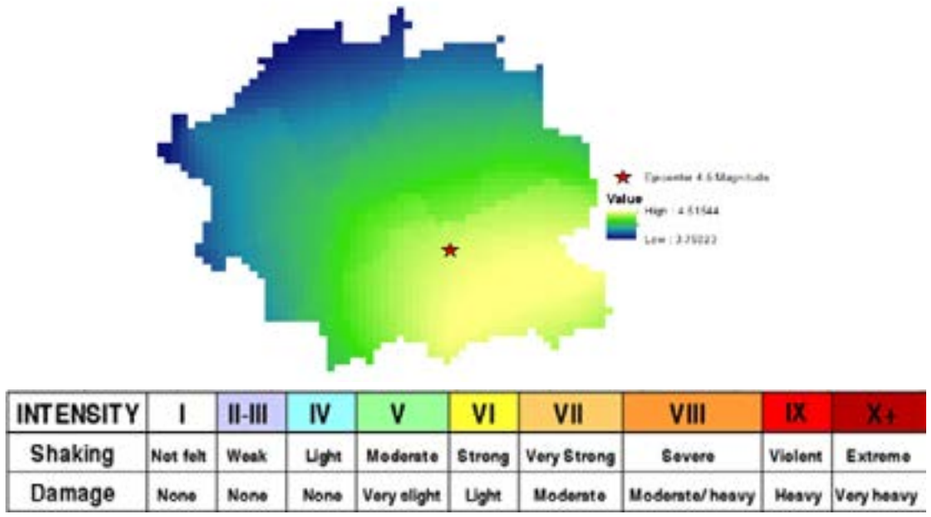

Figure 5. Estimating the damage of earthquake using Gaussian geostatistical simulation.

Table 2. Size of community areas and buildings in risky areas.

Risk level	Area (km^2)	Number of Buildings
Low	115.69	36
Medium	36.69	356
High	82.24	741
Very high	40.10	278

According to Figure 6 and Table 3, the study indicates that the earthquake in Phai Lom subdistrict and Noen Kum subdistrict, Bang Krathum district, Phitsanulok province, impacted community areas and buildings, resulting in a total affected area of 274.72 sq. km. This area is considered to be at risk, with the most significant damage occurring in 40.10 sq.km, equivalent to 25,062.5 rai. The analysis categorizes the areas at risk into high damage (82.24 sq.km.), moderate damage (36.69 sq.km.) and low risk (115.69 sq.km.) respectively.

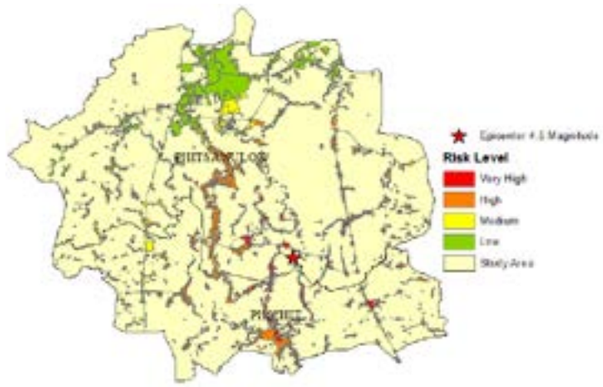

Figure 6. Estimating buildings in the risk area using Gaussian geostatistical simulation and Land use data.

5. CONCLUSION

Estimating the damage after the June 29, 2023 earthquake in the study area is based on the distribution of scores based on the public's perception of the shaking. In collecting data, the criteria were divided according to the Mercalli intensity scale as follows: most at-risk area (VI), very high-risk area V, medium-risk area IV and low-risk area II. Findings on the Impact of Earthquakes on Phai Lom and Noen Kum Subdistricts in Phitsanulok Province

According to a study conducted, the earthquake that occurred in Phai Lom and Noen Kum subdistricts, Bang Krathum district, Phitsanulok province, affected community areas and buildings in total 274.72 sq.km. This area is considered to be at risk, with 40.10 sq.km suffering the most damage. The study categorized the area based on the level of risk: high risk (82.24 sq.km.), moderate risk (36.69 sq.km.) and low risk (115.69 sq.km.). Additionally, approximately 1,418 buildings were found to be in the area of risk. The shaking force magnitude was divided into four levels of risk: the riskiest area with 278 buildings, the high-risk area with 741 buildings, the medium-risk area with 356 buildings and the low-risk area with 36 buildings.

Despite the main structures of the buildings not being damaged, the earthquake affected the area near the epicenter. Cracks and fallen cement were found on buildings, most of which were old buildings and ancient objects such as temples and pagodas. The results of the study were consistent with Lucas Bodenmann et al., (2023) research, which examined the dynamic post-earthquake damage assessment in the Zurich (Switzerland), Pollino (Italy) and Kraljevo (Serbia) earthquakes using the Gaussian model.

6. REFERENCES

Bodenmann L., Reuland Y., and Stojadinović B., 2023. Dynamic post-earthquake updating of regional damage estimates using Gaussian Processes, The Author(s). *Elsevier Ltd*, 109-210.

Khanmohammadi M., Eshraghi M., Mashhadinezhad M.,Sayadi S., and Zafarani H., 2023. Post-earthquake seismic assessment of residential buildings following Sarpol-e Zahab (Iran) earthquake (Mw7.3*)* - Part 2: Seismic vulnerability curves using quantitative damage index. *Elsevier Ltd*. All rights reserved, 108-120

Ma J., and Wang G., 2022. Prediction of fragility deterioration of earthquake-damaged RC structure based on damaged section analysis. Institution of Structural Engineers. *Elsevier Ltd*. All rights reserved, 83-98

Nato J., Ia S., Tea G., Irakli G., and Dimitri A., 2022. Ground motion prediction equations based on shallow crustal earthquakes in Georgia and the surrounding Caucasus. *Earthquake Science*, 497-509.

BA LAT DELTA EVOLUTION IN RESPONSE TO CHANGING FLUVIAL SEDIMENT SUPPLY BY THE RED RIVER, VIETNAM

Nguyen Hao Quang[1]*, Ha Nam Thang[2], Nguyen Van An[3], Nguyen Thanh Luan[4]

[1]Coastal and Estuarine Sediment Dynamics Group, Port and Airport Research Institute, Yokosuka, Japan

[2]Faculty of Fisheries, University of Agriculture and Forestry, Hue University, Vietnam

[3]University of Science and Education, The University of Danang, Vietnam

[4]The Key Laboratory of River and Coastal Engineering, Hanoi, Vietnam

*Corresponding author. Email: ri.nguyenri@gmail.com

ABSTRACT

We discovered the morphological evolution of the active Ba Lat delta in spatial correlation with changes in river sediment load using Landsat images and nautical charts from 1975 to 2022. Suspended sediment load entering the sea via the mouth is estimated based on a combination of a one-line model. Our analysis reported a significant reduction of about 91.5 % in annual sediment load over the period 1958-2021. The delta evolution was found to be highly correlated with sediment load. Between 1975 and 1990, rapid reclamation in the delta combined with a huge sediment supply from the Red River caused the delta to move seaward at a rate > 100 m/yr and the deltaic land area to accrete at a rate of 117 ha/yr. This situation, however, was in a contrasting trend in the early 1990s, in which more than 50 % of the delta's shoreline has undergone severe erosion and the land area and subaqueous delta have also been actively eroding.

1. INTRODUCTION

River deltas, known as coastal landforms, are constructed by a huge accumulation of terrestrial sediment, providing unworthy natural fertile soil and abundant resources (Evans, 2012; Wu et al., 2017; Besset et al., 2019), which offer a great livelihood for hundreds of millions of people worldwide. During the last decades, many large river deltas have retreated under significant anthropogenic pressure and climate change with an alarm vulnerable rate of habitat destruction (Tian et al., 2019; Nguyen and Takewaka, 2022) and declining physical and biological resilience (Anthony et al., 2019).

Among the two largest river deltas in Vietnam, the Red River delta plays a great role in economic development and social resilience in the Northern part of Vietnam, including the Ba Lat mouth, located in the central place of the Red River delta coast, is the largest, most developed and naturally accreting tidal flat in the Red River system. With reference to the decreasing river sediment discharge, any changes in the shoreline of the Ba Lat delta are considered indicative, to some degree, of the evolution of the entire delta system. It would also be interesting to know if large dam-reservoir operations in the Red River basin have had any impact on the shoreline behavior and deltaic land area in the respective delta. The aim of this study is, therefore, to (i) estimate the amount of sediment discharge via the Ba Lat mouth, (ii) quantify changes in the active Ba Lat delta, including the delta-front shoreline, deltaic land area and (iii) explore the statistical relationship between these changes and the river sediment loads before and after all the large dam-reservoir operations upstream of the Red River system.

2. METHODS

2.1 Study area

The Red River system is a monsoon river that discharges 85 % of its water and 96 % of the total sediment load during the wet season (June-October) (Van Maren and Hoekstra, 2004). The Ba Lat is the main mouth and the largest among the six tributary mouths of the Red River system (see Figure 1). The Ba Lat delta is lobate with a bidirectional spit system, characteristic of intermediate wave energy conditions. The Red River flow decelerates as it enters the receiving basin, depositing sandy sediments that form the river mouth bar. It suggests that significant long-term changes in sediment deposited from the Red River will lead to a reduction in the development of the entire river mouth.

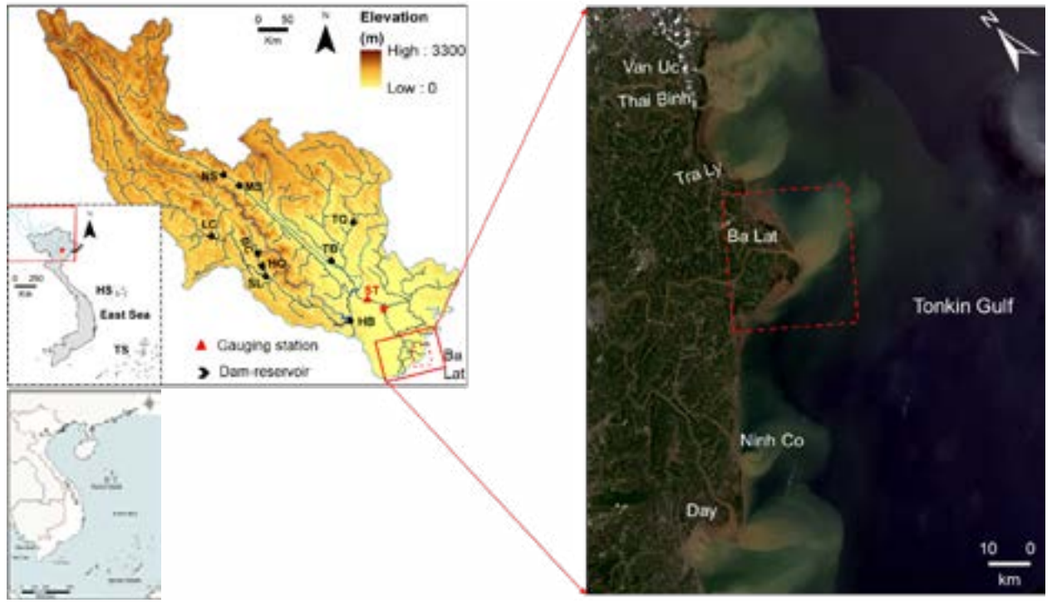

Figure 1. (a) The location of the Red River basin and Red River coast with six major river mouths. Nine major dams upstream (NS-Nansha, MS-Madushan, TQ-Tuyen Quang, TB-Thac Ba, HB-Hoa Binh, SL-Son La, HQ-Huoi Quang, BC-Ban Chat and LC-Lai Chau). The Son Tay (ST) is the hydrological gauging station (red triangle). The Ba Lat mouth is the main mouth of the Red River system. Ha Noi capital is the red star. Red River coast with the Ba Lat delta (red dashed line) viewed from a Landsat scene on 24/8/2020.

2.2 Data sources

We used multi-temporal remote sensing data from Landsat Multispectral Scanner (MSS), Thematic Mapper (TM), Enhanced Thematic Mapper (ETM+) and Operational Land Imager (OLI) satellite images from 1975 to 2022, which were acquired from the United States Geological Survey (https://earthexplorer.usgs.gov/) to evaluate the dynamics of Ba Lat shoreline and land area. The daily water and sediment discharges between January 1, 1958 and December 31, 2021, at the Son Tay gauging station (Figure 1) were obtained from the Vietnam Ministry of Natural Resources and Environment to support the modeling of dynamic water discharge and sediment loads.

2.3 Shoreline change detection

A total of 38 no-cloud Landsat images from 1975 to 2022 were retrieved to extract mean water level-based shorelines. The Normalized Difference Water Index (NDWI), calculated using the Near-Infrared and Short-Wave Infrared channels, *NDWI = (NIR – SWIR) / (NIR + SWIR)*, was used to distinguish land from water and mangrove edge from water (Maglione et al., 2014). The methodology of shoreline change detection based on satellite data is detailed in Nguyen and Takewaka, (2020). Assessment of the evolution of coastal linear features was implemented using the Digital Shoreline Analysis System (DSAS) to evaluate (Thieler et al., 2017; Nguyen and Takewaka, 2021).

2.4 Sediment discharge via the Ba Lat mouth

Since the nearest gauging station (ST) is located approximately 120 km away and there is no gauging station near the Ba Lat mouth, this study first aims to estimate the sediment load carried by the Red River as it enters the sea via the Ba Lat. This amount is estimated based on long-term observations of water and sediment discharge at an upstream hydrological gauging station (Son Tay, Figure 1) and theoretical analysis using the one-line model (Larson et al., 1987). The one-line model is expressed as follows:

$$y = \frac{q_0}{D}\sqrt{\frac{t}{\pi\varepsilon}}e^{\frac{-x^2}{4\varepsilon t}} - \frac{q_0}{D}\frac{|x|}{2\varepsilon}erfc\left(\frac{|x|}{2\sqrt{\varepsilon t}}\right) \quad (1)$$

where: y: shoreline positions; x: longshore coordinate with the origin at the river mouth; t: time; q_0: sediment supply rate from the river; $D=DB+DC$ (DB: berm height, DC: depth of closure); ε: diffusion coefficient related to the longshore sediment transport coefficient; *erfc:* complementary error function. The Maximum shoreline position, y_0:

$$y_0 = \frac{q_0}{D}\sqrt{\frac{t}{\pi\varepsilon}} \quad (2)$$

The position of the shorelines in the 1800s can be determined largely by Minh et al., (2014), Nguyen and Takewaka, (2022), whilst the position at the beginning of the 1980s was detected using Landsat imagery. The estimated sediment load via the Ba Lat mouth is compared with previous studies as shown in Table 1.

Table 1. Statistics on riverine budgets load via the Ba Lat mouth

Studies	Methods	Period	Sediment load (10^6 m^3/yr)
Pruszak et al., (2002)	Measurement and Simulation	N/A	17.4
Van Maren and Hoekstra, (2004)	Measurement and Simulation	1960-1998	15.9
Le et al., (2007)	Measurement and Simulation	1997-2003	7.7
Vinh et al., (2014)	Measurement and Simulation	1960-1979	16.0
Vinh et al., (2014)	Measurement and Simulation	1989-2010	5.9
Kudo and Takewaka, (2017)	Satellite images	1787-2000	9.4
Nguyen and Takewaka, (2022)	Old maps combined Simulation	1000-2000	15.8
This study	Measurement, One-line theory and Satellite images	1800-1980	16.0

3. RESULTS

3.1 Trend analysis for water and sediment discharges at Ba Lat

Figure 2 indicates a significant impact of the constructed upstream dam reservoirs on the temporal annual sediment load and water discharge. A 64-year analysis determined a 91.5 % reduction in the annual sediment load, plummeting from 16.0×10^6 to 1.4×10^6 m^3/yr via the Ba Lat. Notably, the decreasing trend of sediment load has become particularly pronounced since 1988. During the period of 1989-2008, coinciding with the operation of the Hoa Binh dam reservoir, there was an observed annual sediment flux decrease of approximately 57 %, from 16.0×10^6 to 6.9×10^6 m^3/yr.

Starting from the end of 2008 until the conclusion of 2016, a series of dam reservoirs commenced operation, including Nansha (NS) and Madushan (MS) within China's territory, as well as Tuyen Quang, Son La, Ban Chat, Huoi Quang and Lai Chau. In conjunction with previous dam constructions, this marked the onset of a significant second phase of sediment reduction within the Red River system. As a result, dam construction was attributed to about an 80.2 % reduction in annual sediment loads, which dropped the annual sediment load to approximately 1.4×10^6 m^3/yr (Figure 2).

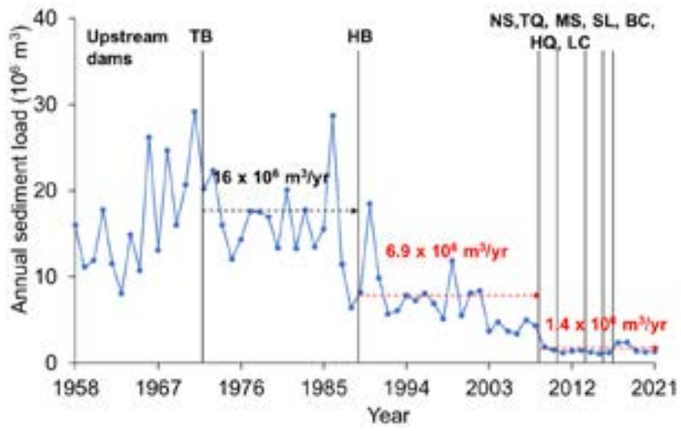

Figure 2. Annual sediment load at the Ba Lat estimated from 1958 to 2021. The black dashed lines represent the starting year of upstream dam-reservoir operations.

3.2 Multi-decadal shoreline changes

Using Landsat images, we are capable of presenting the shoreline dynamics between the north and south sections of the Ba Lat delta (Figure 3). The rates of shoreline position change exhibit notable variations across the three periods for both the north and south sections. In the initial period (1975-1990), the Ba Lat delta was built up with the seaward movement at average rates exceeding 100 m/yr and 200 m/yr for the north and south segments, respectively. During this phase, the right bank demonstrated dominant accretion compared to the north bank. Since the early 1990s, both subsections have encountered significant erosion, characterized by a retreat rate of approximately 20 m/yr. The rate of landward retreat, however, has reduced to around 12 m/yr over the last decade.

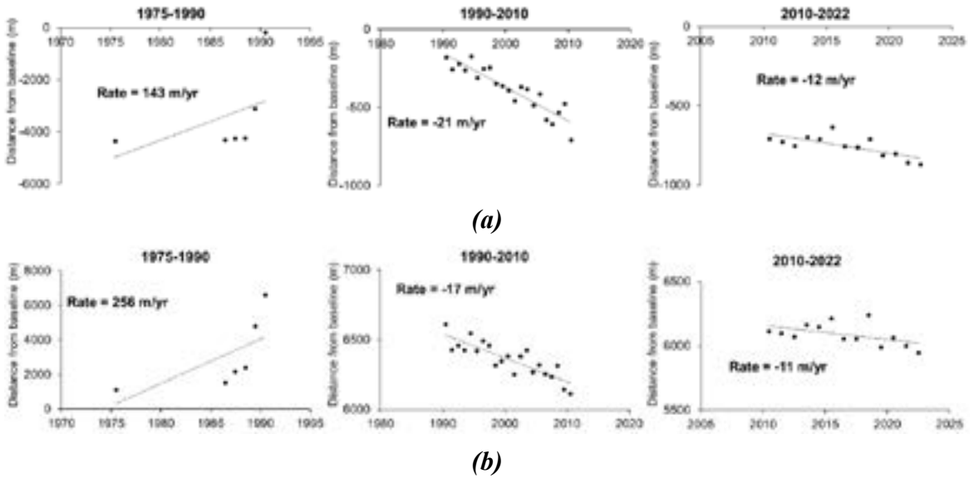

Figure 3. Rates of shoreline change in three different periods, 1975-1990, 1990-2010 and 2010-2022, for the north (a) and south (b), calculated based on the mean shoreline position.

3.3 Evolution of the active Ba Lat delta

The area of active deltaic land has undergone a substantial increase, expanding from approximately 1,050 hectares in 1975 to nearly 3,777 hectares in 2022. This growth is associated with an average net accretion rate of 58 hectares per year, as indicated in Figure 4. Up until 1990, there was a sharp rise in land area from 1,050 hectares in 1975 to 2,820 hectares in 1990, marked by an average accretion rate of 117 hectares per year. Following this, from 1990 to 1993, the active delta entered a phase of severe erosion, coinciding with the commencement of operations at the Hoa Binh dam reservoir in December 1988 and a number of great typhoons during this period. Consequently, a loss of approximately 1,220 hectares, with an average rate of -407 hectares per year, was measured. Nevertheless, owing to human interventions such as mangrove reforestation and the establishment of sanctuary areas, notably when the south and north sections were designated as nature reserves in 1989 and 1995, respectively, the active deltaic land area began to gradually expand from 1993 onwards. This expansion occurred at an average rate of 80 hectares per year.

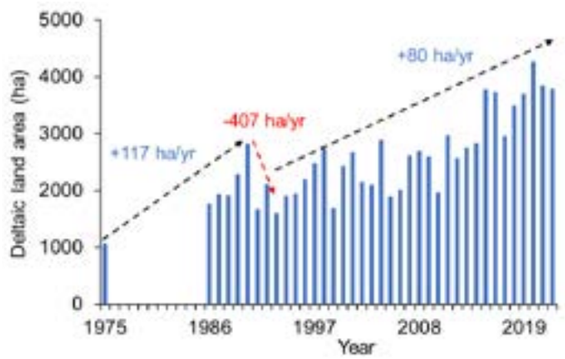

Figure 4. Variations in the land areas in the active Ba Lat delta lobe during the period of 1975-2022 illustrate three stages of delta evolution: a rapid accretion stage (1975-1990), a dramatic erosion stage (1990-1993) and a slow accretion stage (1993-present).

4. DISCUSSION

4.1 Relationship between shoreline variation and sediment load

The shoreline of the Ba Lat delta is strongly varied with the acceleration of the fluvial sediment originating from the Red River, which helps to balance the marine forces of sediment dispersal, subsidence, sea level rise, typhoons and other factors (Nguyen and Takewaka, 2020). Here, we discovered a significant decline in sediment load in the Red River after the construction of the Hoa Binh dam reservoir (December 1988) in a spatial correlation with the shoreline dynamics. The mean shoreline position at an 11-kilometer stretch was calculated from the mouth to the North and to the South of the Ba Lat delta to illustrate the relationships between the mean shoreline position, the annual sediment load and the cumulative annual sediment load.

Generally, there is no straightforward relationship between fluvial sediment supply and shoreline mobility, as the latter can also be influenced by other factors acting at various timescales (Anthony et al., 2019). Nevertheless, we found that fluvial sediment supply is the primary driver of shoreline mobility in the Ba Lat delta (Figure 5), with sediment redistribution processes by monsoon-generated waves and currents along the coast, including regional trapping in the Gulf of Tonkin, playing a complementary role. The high correlations (in both the North and South) between the mean shoreline position and sediment load (Figure 5) for cumulative sediment load from 1990 to the present suggest that the sediment supply from the Red River is a major source and the controlling factor in the evolution of the modern Ba Lat delta during the recent decades. In other words, the shorelines along the mouth are moving landward, mainly due to the dramatic decline in the sediment load of the Red River.

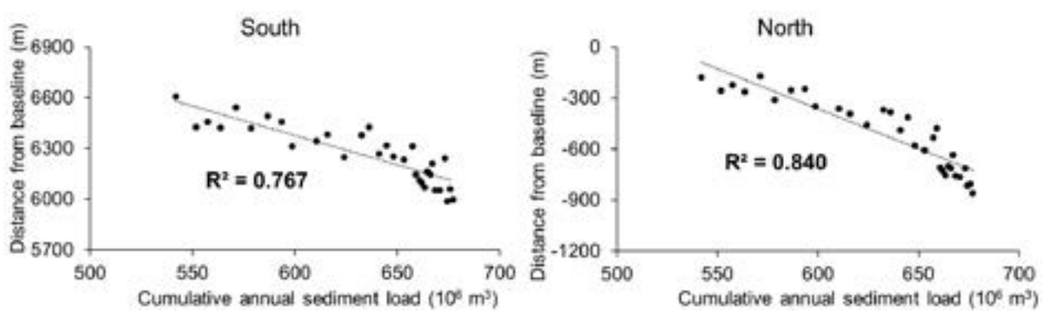

Figure 5. Correlations between the mean shoreline position and cumulative annual sediment load via the Ba Lat mouth from 1990 to present, North and South.

During the phase 1958 - 1987, when the Hoa Binh dam and reservoir were not in operation, the Ba Lat delta front received a substantial sediment load, totaling approximately 16.0×10^6 m^3/yr. This notable influx of sediment played a pivotal role in driving the relatively swift accretion of the active delta. However, the subsequent period spanning from 1989 to 2008 witnessed a significant decrease in fluvial sediment supply, with quantities dwindling to only around 6.9×10^6 m^3/yr. This reduction triggered pronounced erosion along the delta's shoreline.

When the sediment sourced from the river fails to counterbalance the sediment removal from the subaqueous delta or other coastal regions, the natural response tends to be a landward retreat of the shoreline. Evidently, the volume of sediment carried to the sea during the past decade, totaling

1.4×10^6 m^3/yr, proved insufficient to facilitate the progradation of the delta. This insufficiency creates the potential for on going land loss in the future. As a result, the persistent erosion observed in both the North and South sectors of the delta, as illustrated in Figure 5, serves as a clear indication that the sediment supply to the Ba Lat delta's shoreline is no longer capable of maintaining the necessary balance.

4.2 Relationship between deltaic land area and river sediment supply

The relationship between the deltaic land area and the cumulative annual sediment supply during the period from 1975 to the present (Figure 6). Notably, the correlation between land area and river inputs exhibits significant variations across different time spans.

Particularly, during the period spanning from 1975 to 1990, there was a strong correlation between deltaic land area and sediment supply. This suggests that the substantial sediment discharges carried by the Red River played an important role in steering delta development. The detrimental effects of the upstream dam reservoirs on the deltaic land area became distinctly evident during the phase of severe erosion from 1990 to 1993. Throughout this interval, the sediment load estimated to reach the sea through the Ba Lat experienced a drastic decline of approximately 51 % (from 16.0 to 7.9×10^6 m^3/yr). Even the implementation of human activities like mangrove reforestation and delta reclamation could not offset the pronounced reduction in sediment supply from the Red River since 1989. Consequently, a substantial land area was lost during this period, quantified at approximately-07 hectares per year.

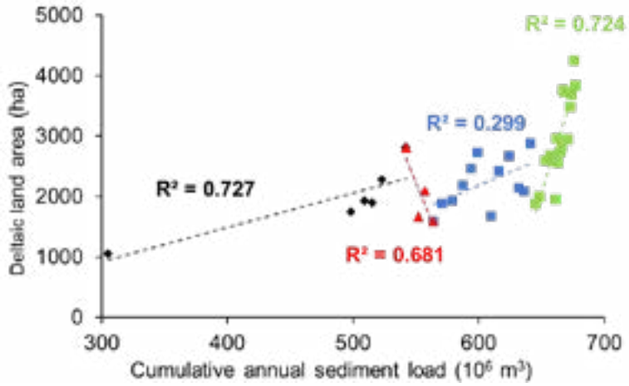

Figure 6. Deltaic land area and cumulative annual sediment load via the Ba Lat mouth during the period 1975-2021.

5. CONCLUSIONS

The sediment supply by the Red River to the sea (Tonkin Gulf) is strongly influenced by the construction and operation of upstream dam reservoirs. Here, we clarified a significant reduction of over 90 % in sediment supply due to the retention of fluvial loads in a closed relationship with the dam reservoirs in the Red River basin, dropping from 16.0×10^6 to 1.4×10^6 m^3/yr.

In addition, we discovered an active erosion in the Ba Lat delta since the early 1990s by using a time-series Landsat image with shoreline dynamics analysis, which can be attributed to the pronounced decline in sediment load that began after the Hoa Binh dam-reservoir started its operation in December 1988. Over the most recent decade, a minimal sediment load of 1.4×10^6 m^3/yr was markedly insufficient to facilitate seaward progradation of the delta or counteract marine forces, resulting in a continuous loss of land.

Without the implementation of effective sediment management strategies on the operational dams, the coastal sediment balance is poised to face further negative impacts in the future. The majority of the delta's sections will continue to experience erosion, amplifying the vulnerability of the delta to cyclones and rising sea levels.

6. ACKNOWLEDGEMENTS

The first author thanks the Japan Society for the Promotion of Science (JSPS) postdoctoral fellowship (ID No. P22057) and Grant-in-Aid for JSPS Fellows relating to the JSPS Postdoctoral Fellowship for Foreign Researchers (Grant number: 22F22057).

7. REFERENCES

Anthony E. J., Besset M., Dussouillez P., Goichot M., & Loisel H., 2019. Overview of the Monsoon-influenced Ayeyarwady River delta and delta shoreline mobility in response to changing fluvial sediment supply. *Marine Geology, 417*, 106038.

Besset M., Anthony E. J., & Bouchette F., 2019. Multi-decadal variations in delta shorelines and their relationship to river sediment supply: An assessment and review. *Earth-science reviews, 193*, 199-219.

Evans G., 2012. Deltas: The fertile dustbins of the continents. *Proceedings of the Geologists' Association, 123*(3), 397-418.

Larson M., Hanson H., & Kraus N. C., 1987. Analytical solutions of the one-line model of shoreline change. Technical report. *US Army Corps of Engineers*.

Le T. P. Q., Garnier J., Billen G., Théry S., & Chau V. M., 2007. The changing flow regime and sediment load of the Red River (Vietnam). *J. Hydrol, 334*, 199-214.

Maglione P., Parente C., and Vallario A., 2014. Coastline extraction using high resolution WorldView-2 satellite imagery. *European Journal of Remote Sensing 47*(1), 685-699.

Minh V. C., N. K. Nghia, and N. H. Thinh, 2014. The changes of Ba Lat and Ha Lan estuaries in past period and Its influences on accretion-erosion of Hai Hau region, Nam Dinh province. *Journal of Science and Technology*. Vietnam academy of water resources. https://www.vawr.org.vn/bien-dong-cua-ba-lat-cua-ha-lan-trong-thoi-ky-can-dai-va-anh-huong-cua-chung-toi-dien-bien-boi-tu-xoi-lo-khu-vuc-hai-hau-nam-dinh.

Nguyen Q. H., & Takewaka S., 2021. Shoreline changes along northern Ibaraki coast after the great East Japan Earthquake of 2011. *Remote Sensing*, *13*(7), 1399.

Nguyen Q. H., & Takewaka S., 2022. Historical reconstruction of shoreline evolution at the Nam Dinh Coast, Vietnam. *Coastal Engineering Journal*, 1-18.

Nguyen Q. H., & Takewaka S., 2020. Land subsidence and its effects on coastal erosion in the Nam Dinh coast (Vietnam). *Continental Shelf Research, 207*, 104227.

Pruszak Z., Szmytkiewicz M., Hung N. M., & Van Ninh P., 2002. Coastal processes in the Red River delta area, Vietnam. *Coastal Engineering Journal, 44*(02), 97-126.

Thieler E. R., Himmelstoss E. A., Zichichi J. L., and Ergul A., 2017. Digital Shoreline Analysis System (DSAS) version 4.0-An ArcGIS extension for calculating shoreline change (ver. 4.4, July 2017). *U.S. Geological Survey Open-File Report*, 2008-1278.

Tian S., Xu M., Jiang E., Wang G., Hu H., & Liu X., 2019. Temporal variations of runoff and sediment load in the upper Yellow River, China. *Journal of Hydrology, 568*, 46-56.

Van Maren D. S., & Hoekstra P., 2004. Seasonal variation of hydrodynamics and sediment dynamics in a shallow subtropical estuary: The Ba Lat River, Vietnam. *Estuarine, Coastal and Shelf Science, 60*(3), 529-540.

Vinh V. D., Ouillon S., Thanh T. D., & Chu L. V., 2014. Impact of the Hoa Binh dam (Vietnam) on water and sediment budgets in the Red River basin and delta. *Hydrology and Earth System Sciences, 18*(10), 3987-4005.

Wu X., Bi N., Xu J., Nittrouer J. A., Yang Z., Saito Y., & Wang H., 2017. Stepwise morphological evolution of the active Yellow River (Huanghe) delta lobe (1976-2013): Dominant roles of riverine discharge and sediment grain size. *Geomorphology, 292*, 115-127.

SPATIAL PATTERN ANALYSIS OF THE SPREAD OF SARS-COV-2 VARIANT IN HANOI CITY, VIETNAM

Thi Quynh Nguyen

Faculty of Nursing, East Asia University of Technology, Hanoi, Vietnam
Corresponding author. Email: quynhnt@eaut.edu.vn

ABSTRACT

Since coronavirus disease 2019 (COVID-19), brought on by the SARS-CoV-2 variant, emerged in Wuhan City and rapidly spread throughout China in December 2019. The global outbreak of the COVID-19 pandemic has spread worldwide, affecting almost all countries and territories. This study aimed to analyze spatial patterns of the SARS-CoV-2 variant on a winter day in Hanoi city (Vietnam) using spatial auto-correlation analysis. The spatial clustering, including spatial clusters (high-high and low-low), spatial outliers (low-high and high-low) and hotspots of the COVID-19 pandemic, were explored using the local Moran's I and Getis-Ord's-statistics. The local Moran's I statistics were first employed to identify spatial clusters and spatial outliers of COVID-19. The Getis-Ord's-statistic was then used to detect hotspots of COVID-19. A case study of locally transmitted cases confirmed in Hanoi city indicated that (i) high-high spatial clusters and low-high spatial outliers and hotspots of COVID-19 were mainly detected in the central area of Hanoi city where the population density is dense, (ii) low-low spatial clusters and coldspots were mostly detected in the west and north of the city. The findings of this study provide important insights into how to apply spatial statistics in general and spatial auto-correlation analysis, in particular, to better understand the spread of the spread of SARS-CoV-2 variant through space.

1. INTRODUCTION

Since early 2020, the COVID-19 pandemic has posed a major risk to public health on a global scale. The COVID-19 pandemic was brought on by SARS-CoV-2, the coronavirus that causes severe acute respiratory syndrome (Shi et al., 2020). The COVID-19 pandemic has caused a global pandemic and has contributed to many deaths worldwide, posing a massive threat to global public health and the economy that may take several years to recover (Martin et al., 2020). According to the most recent data, the World Health Organization had reports of more than 770.4 million confirmed cases of COVID-19 as of September 13, 2023, including more than 6.9 million fatalities (WHO, 2023). With the increasing availability of high-quality data and improved computational capabilities, numerous geospatial methods and tools have been developed and used in infectious diseases, including COVID-19 surveillance (Carballada and Balsa-Barreiro, 2021; Carroll et al., 2014). As a result, attempts have been made to examine the COVID-19 pandemic, especially in studies of the COVID-19 epidemic's hotspots (Hoang and Nguyen, 2022; Vu et al., 2021).

Geographical analysis is also a powerful automated system for the analysis of spatial data. Methods for geographical analysis, including spatial analytical methods and geographic information systems, have been widely used in health research (Kirby et al., 2017; Moore and Carpenter, 1999) and epidemiology (Kirby et al., 2017). Geographical analysis has been successfully applied to study the distribution of specific diseases such as lung cancer (Khazaei et al., 2017; Youlden et al., 2008), heart attack mortality rate (Businge, 2011; Lamprecht and Lamprecht, 1976), cardiovascular diseases (Rezaeian et al., 2008) and particularly respiratory

diseases (Cook et al., 2017; Ferrante et al., 2017; Gambaryan et al., 2017; Gay and Barnouin, 2009; Jindal, 2006). Recently, geographical analysis has revealed that the assessment of the scale of the COVID-19 pandemic from a geographical perspective can offer a better understanding of the spatial distribution, better manage the COVID-19 infection and effectively study its impacts (Kieu et al., 2021). Therefore, it is geographical analysis has been widely applied to study the spatial distribution and the spread of the COVID-19 epidemic at different scales, such as the global scale (Asongu et al., 2021; Kadirvelu et al., 2022; Mayer and Lewis, 2020), regional scale (De Cos et al., 2022; Xie et al., 2021) and the country or state scale (Kodge, 2021; Saeed et al., 2021). Recently, spatial autocorrelation analysis is one of the most commonly used geographical analysis methods in the study of the spread of infectious diseases. In spatial epidemiology, spatial clustering analysis plays an important role in identifying spatial aggregation of disease cases by identifying whether geographically grouped cases can be explained by chance or are statistically significant to find evidence of etiologic factors (Marshall, 1991; Rosli et al., 2018). Previous research has shown that several social processes connected to the space of occurrence frequently determine the dispersion of infectious diseases (Elliott and Wartenberg, 2004; Jones et al., 2008). COVID-19 infections may vary in both space and time due to the complex interactions of various influences, including socioeconomic vulnerability, rapid population increase and urbanization, as well as environmental factors (Rozenfeld et al., 2020). To conduct a study of outbreaks, spatial analysis and the identification of areas with COVID-19 clusters, followed by the characterization of the causes of the dynamics in these clusters, have been encouraged (Krieger, 2003; Nykiforuk and Flaman, 2011). The resulting maps from these spatial methods can help prevent and control cases with targeted public health action plans and guided interventions in areas with higher than expected disease risk while motivating the population with various public health programs with advanced knowledge of disease etiological characteristics (Krieger, 2003). The most frequently used method for spatial clustering and hotspot analysis was local Moran's I, followed by *Getis-Ord's* G_i^*-statistic, Kulldorff's spatial scan statistic and Kernel density (Nazia et al., 2022). For example, using *Getis-Ord's* G_i^*-statistic and geographically weighted principal component analysis, the impact of living environment deprivation on COVID-19 hotspots was successfully examined in Kolkata megacity, India (Das et al., 2021). The exploratory spatial data analysis and the geodetector method was employed to analyze the spatial and temporal differentiation characteristics and the influencing factors of the COVID-19 epidemic spread in mainland China based on the cumulative confirmed cases, average temperature and socio-economic data (Xie et al., 2020). The global (Moran's I) and local indicators of spatial autocorrelation (LISA), both univariate and bivariate, were successfully applied to derive significant clustering of COVID-19 pandemic (Ramírez-Aldana et al., 2020). The global Moran's I statistic and the retrospective space-time scan statistic were also successfully used to analyze spatio-temporal clusters of COVID-19 (Castro et al., 2021). Apart from local Moran's I and *Getis-Ord's* G_i^*-statistics, spatial and space-time scan statistics and the Joinpoint analysis was also employed in a study in the United States where it was found that that higher risks of clustering and incidence of COVID-19 were consistently observed in metropolitan versus rural counties, counties closest to core airports, the most populous counties and counties with the highest proportion of racial/ethnic minorities (Wang et al., 2021).

The objective of this study was to detect the spatial clustering of the spread of SARS-CoV-2 using spatial autocorrelation analysis. This study was divided into five sections. An overview and background of COVID-19 and methods for spatial pattern analysis will be provided in the first section. It will then go on to briefly introduce the study area of Hanoi city and the data used in this study. The third section will discuss the methodology employed in this work, which includes the use of local Moran' I statistics to identify spatial clustering of SARS-CoV-2 and the use of *Getis-Ord's* G_i^* to detect hotspots of SARS-CoV-2 in Hanoi city. The fourth section analyses the findings and provides a discussion on the spatial clustering of the spread of SARS-CoV-2. The final section presents the findings and conclusions of the research.

2. STUDY AREA, DATA USED AND METHODS

2.1 Study area and data used

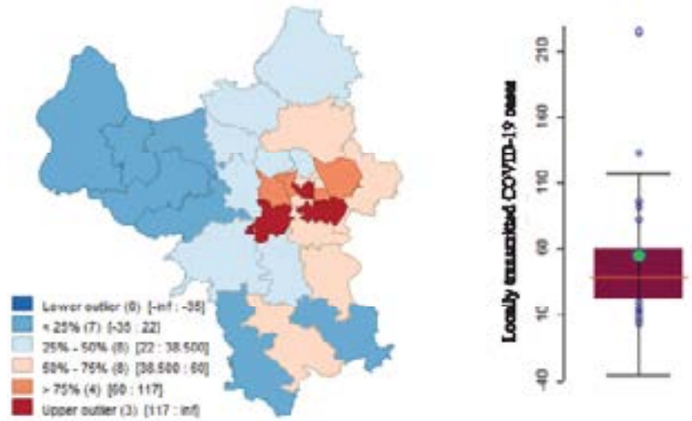

Figure 1. Boxmap (left) and boxplot (right) of COVID-19 cases.

Hanoi, Vietnam's second-largest city and capital, is located in the low floodplain of the Red River Delta in the country's northeast (Fig. 1). Geographically, it is situated between 21°30′35″N to 21°22′25″N latitudes and 105°10′15″E to 106°00′08″E longitudes, covering an area of approximately 3,360 square kilometers. In 2020, Hanoi was reported as one of the worst-affected cities by SARS-CoV-2 in Vietnam. To investigate the spatial clustering of SARS-CoV-2 in this study, a dataset of locally transmitted COVID-19 cases collected on December 21, 2022 in Hanoi was used. The spatial distribution of these COVID-19 cases is shown in Figure 1. Data from Figure 1-left illustrates that the COVID-19 cases were mainly reported in the northeast of Hanoi city. In particular, high numbers of COVID-19 cases were mainly confirmed in the Hanoi metropolitan where the population density is dense such as Hoang Mai (225 cases), Dong Da (223 cases), Ha Dong (133 cases) and Nam Tu Liem (97 cases). On the other hand, a low and very low number of COVID-19 cases were reported in suburban districts such as Ba Vi (12 cases), My Duc (8 cases), Quoc Oai (5 cases) and Phuc Tho (3 cases). Data from the boxplot shown in Figure 1 (right) demonstrates the distribution of COVID-19 cases. This figure shows that the minimum, maximum, mean and median values were 3, 225, 55.6 and 38.5 (COVID-19 cases), respectively. The mean value was greater than the median value, which shows that districts having a large number of COVID-19 cases were larger than districts having a small number of COVID-19 cases. This was also shown by the boxplot being skewed to the top (skewed towards where the highest number of

COVID-19 cases are).

2.2 Methods

2.2.1 Local Moran's I statistic

This study employed global *Moran's I* statistic to identify the spatial clustering of the COVID-19 pandemic at a global scale (Cliff and Ord, 1981; Getis and Ord, 1996). The definition of the global *Moran's I* statistic is expressed in equation (1):

$$I = \frac{n}{S_0}\frac{\sum_{i=1}^{n}\sum_{j=1}^{n} W_{ij}(x_i - \bar{x})(x_j - \bar{x})}{\sum_{i=1}^{n}\sum_{j=i}^{n} W_{ij}\sum_{i=1}^{n}(x_i - \bar{x})^2} \quad (1)$$

where, x_i and x_j are the number of new COVID-19 confirmed cases for district i and district j; $\bar{x}$ is the mean of COVID-19 cases and be given by $\bar{x} = \sum_{i=1}^{n}\frac{x_i}{n}$; n is the total number of districts in the whole study area; and W_{ij} is a ($n \times n$) spatial weight matrix (Vu et al., 2021).

The range of values of global *Moran's I* coefficient is in the interval [-1, +1] (Vu et al., 2021). Positive values of *Moran's I* result from the data's positive spatial autocorrelation., whereas *Moran's I* values are negative when there is a negative spatial autocorrelation (Nguyen and Vu, 2019a). The absence of spatial autocorrelation or random COVID-19 epidemic distribution is shown by values of the global *Moran's I* coefficients that are near zero.

The global *Moran's I* reflect the presence or lack of spatial autocorrelation as a whole. The regional *Moran's I* statistic was used to quantify the spatial clustering of low and high COVID-19 pandemic levels in each district (Vu et al., 2021). The local *Moran's I* statistic (I_i) for COVID-19 pandemic at district i is given by the following equation (Anselin, 1995):

$$I_i = \frac{(x_i - \bar{x})}{\sigma^2}\sum_{j\#i, j\in J_i}^{N} W_{ij}(x_j - \bar{x}) \quad (2)$$

where x_i, x_j, $\bar{x}$ and W_{ij} are defined in equation (1); N is the total number of neighborhood districts (Vu et al., 2021); J_i denotes the neighborhood set of COVID-19 confirmed cases at district i; $j\#i$ implies that the sum of all (x_j - $\bar{x}$) of nearby neighbourhood districts of district i but not including x_j; and σ^2 is the variance of x, given in equation (3). W_{ij} defines neighbor connectivity and can be constructed using first order and second of contiguity (Figure 2).

$$\sigma^2 = \frac{1}{N}\sum_{j=1}^{N}(x_i - \bar{x}) \quad (3)$$

The level of spatial clustering of the COVID-19 pandemic in each district is indicated by local *Moran's I* statistics. Similar to the global *Moran's I* statistic, the local *Moran's I* value at district i (I_i) also ranges between -1 and +1. There is no spatial autocorrelation of COVID-19 causes if the local *Moran's I* coefficient at district i equals zero ($I_i = 0$). If $I_i > 0$, then there will be a positive spatial autocorrelation of COVID-19 cases (Vu et al., 2021). If $I_i < 0$ then there will be a negative spatial autocorrelation of COVID-19 cases. A high positive I_i shows that district i has a similarly high or low number of COVID-19 cases as its neighbors and is called the ‘‘spatial cluster’’(Nguyen and Vu, 2019a). In this case, when there is a positive local spatial autocorrelation, the local *Moran's I* statistic indicates two types of spatial clusters for COVID-19 cases, including high-high spatial clusters and low-low spatial clusters. Low-high and high-low clusters are also two forms of spatial outliers that are identified using the local Moran's I statistic when there is a negative local spatial autocorrelation.

2.2.2 Getis-Ord's G_i^* statistic

Getis-Ord's G_i^*-statistic characterizes the presence of hotspots (high clustered values) and coldspots (low clustered values) over an entire area by looking at each feature within the context of its neighboring features (Nguyen and Vu, 2019b). It is, therefore, *Getis-Ord's* G_i^*statistic was used to identify the counties with high and low numbers of COVID-19 cases (Hoang and Nguyen, 2022; Vu et al., 2021). The form of *Getis-Ord's* G_i^*statistic is defined as follows (Cliff and Ord, 1981):

$$G_i^* = \frac{\sum_{j=1}^{N} W_{ij}\, x_j - \bar{x}\sum_{j=1}^{N} W_{ij}}{S\sqrt{\frac{N\sum_{j=1}^{N}[W_{ij}^2 - (W_{ij})^2]}{N-1}}} \quad (4)$$

$$\text{with } \bar{x} = \frac{1}{N}\sum_{j=1}^{N} x_j \quad (5)$$

$$\text{and } S = \sqrt{\frac{\sum_{j=1}^{N} x_j^2}{N} - (\bar{x})^2} \quad (6)$$

where: G_i^* is computed for the number of COVID-19 cases at county i; x_i, x_j, $\bar{x}$ and W_{ij} are defined in Equation (1) and N is the total number of neighborhood counties as defined in equation (2). W_{ij} can be constructed using the methods of the first order and second of contiguity (shown in Figure 2).

Similar to those obtained from global and local *Moran's I* statistics, the *Getis-Ord's* G_i^* coefficient at county i (G_i^*) also ranges between -1 and +1. If $G_i^* > 0$ and $p(G_i^*) < \alpha$, then there exists a spatial clustering of high-high values (Hoang and Nguyen, 2022; Vu et al., 2021). In this case, these high-high values, so-called a hotspot, reflect the presence of high numbers of COVID-19 cases among county i and its neighborhood counties ($j \in J_i$). Whereas, if $G_i^* < 0$ and $p(G_i^*) < \alpha$ then there exists a spatial clustering of low-low values (Hoang and Nguyen, 2022; Vu et al., 2021). These low-low values are called a coldspot indicating low numbers of COVID-19 cases among county i and its neighborhood counties ($j \in J_i$). Similar to those in the definition of local Moran's I statistic, if the value of G_i^* close to zero and $p(G_i^*) < \alpha$ then there will be neither hotspots nor coldspots or random distribution of COVID-19 cases (Vu et al., 2021).

A lot of attempts have been put on the use of *Getis-Ord's* G_i^*-statistic with the help of ArcGIS software using *Getis z-scores* (Alves et al., 2021; Mitchell, 1999; Nguyen and Vu, 2019b) defined in a study by Mitchel (Mitchell, 1999). However, as discussed above, the presence of a strongly skewed distribution in the dataset fails the test. It is, therefore, testing for the significance of the *Getis-Ord's* G_i^* statistic in this study was also carried out by a randomization test using 999 permutations. In this work, with the help of the spatial statistics software GeoDA, developed by (Anselin et al., 2009), a randomization test was used to test the significance of spatial autocorrelation statistics. Spatial autocorrelation statistics were generated and tested at the significance of 0.05 using 999 permutations.

3. RESULTS AND DISCUSSION

3.1 Spatial Clustering of COVID-19

The Boxmap in Figure 2 (left) demonstrates the spatial distribution of local Moran's I statistics obtained from locally transmitted COVID-19 cases on December 21, 2022. Data from Figure 2 (left) illustrates that low values of local Moran's I coefficients were mainly distributed in the west, north and south of the city. It can be seen that high low values of local Moran's I coefficients were found in districts of Hai Ba Trung (0.61), Son Tay (0.57), Phuc Tho (0.56), Dong Da (0.55), Thach That (0.55) and Ba Vi (0.54). Low values of local Moran's I statistic were mainly concentrated in the east and center of the city, such as Thanh Xuan (-0.41), Ha Dong (-0.39), Hoan Kiem (-0.09), Tay Ho (-0.09), Gia Lam (-0.06) and Thanh Tri (-0.04). The boxplot in Figure 2 (right) demonstrates the spatial distribution of local Moran's I statistic. It can be seen that the minimum, maximum, mean and median values of local Moran's I statistics were -0.4, 0.6, 0.18 and 0.18, respectively. The mean value was equal to the median value, which shows that the data for local Moran's I were quite balanced on both sides. The boxplot of the local Moran's I statistic was not almost skewed to the top or bottom.

Data from Figure 3 (left) shows that there were two high-high clusters, four low-low spatial clusters, three low-high and no high-low spatial outliers and 21 districts and a town with insignificant spatial clustering. Also, it can be seen that two high-high clusters were in the central area of Hanoi city, where the population density is dense. Four low-low spatial clusters were distributed in the northwest and south of the city in suburban districts. Data from Figure 3 (left) illustrates that high-high spatial clusters were detected in the districts of Ba Dinh (60 cases) and Ha Ba Trung (82 cases). Low-low spatial outliers were found in Son Tay (zero cases), Phuc Tho (3 cases), Thach That (20 cases) and Ung Hoa (40 cases). Three low-high spatial outliers were detected in Thanh Xuan (39 cases), Hoan Kiem (51 cases) and Gia Lam (52 cases). Data from Figure 3 (right) shows the statistical significance of Local Moran's I statistics for each district of Hanoi city. Data Figure 3 (right) illustrates that all of the high-high and low-low spatial clusters and low-high spatial outliers were statistically significant at the level of 0.05, of which one low-low spatial cluster and one low-high spatial outlier were statistically significant at the level of 0.001. Two low-low and one high-high spatial clusters were statistically significant at the level of 0.01. A high-high, low-low spatial clusters and one low-high spatial outliers were statistically significant at the level of 0.05. Significant levels were expressed on four different scales, including insignificance (p-value > 0.05) and significance at the levels of 0.05, 0.01 and 0.001 levels. Data from Figure 3 (right) demonstrates the districts of Thanh Xuan and Thach That were detected with statistical significance at the level of 0.001. Son Tay, Phuc Tho and Hai Ba Trung were found with a significant change at the level of 0.01. Four districts of Ba Dinh, Long Bien, Gia Lam and Ung Hoa were discovered to be statistically significant at the level of 0.05.

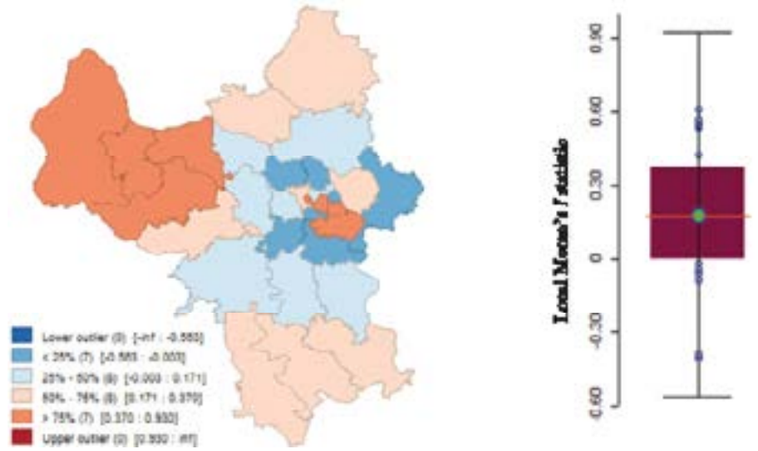

Figure 2. Map (left) and boxplot (right) of local Moran's I statistic.

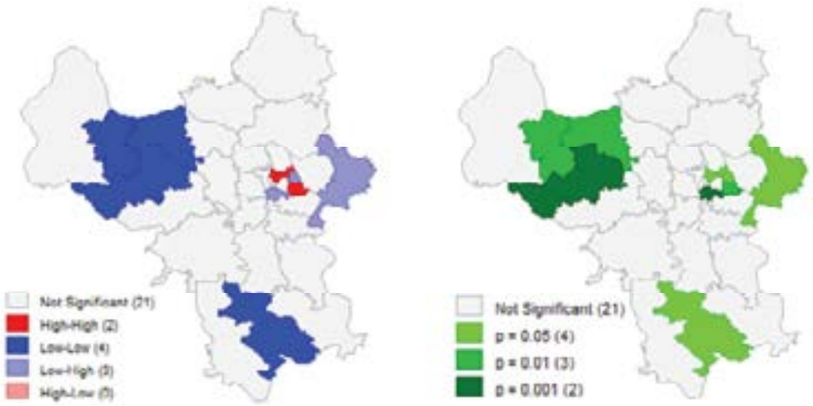

Figure 3. LISA cluster map (left) and significant map (right) of COVID-19.

3.2 Hotspots of COVID-19

Boxmap from Figure 4 (left) shows the distribution of *Getis-Ord's G**-statistic. Data from Figure 4 (left) illustrates that the chart shows that *Getis-Ord's G**-statistics were mainly distributed in the central and eastern districts of the city. Several districts were found with high values of *Getis-Ord's G** were Hai Ba Trung (0.071), Thanh Xuan (0.071), Hoan Kiem (0.061), Gia Lam (0.056), Ba Dinh (0.055), Dong Da (0.055) and Hoang Mai (0.054). Among these districts, Dong Da and Hoang Mai were detected with the largest number of COVID-19 cases, with 298 and 266 COVID-19 cases, respectively. The low values of *Getis-Ord's G**-statistic were mainly concentrated in the suburban districts such as Thach That (0.007), Son Tay (0.007), Ba Vi (0.009), Phuc Tho (0.012) and Ung Hoa (0.014). Among the districts having high values of *Getis-Ord's G**, several districts were detected with low and very low numbers of COVID-19 cases such as Phuc Tho (3 cases), Ba Vi (12 cases) and Son Tay (16 cases). Data from the boxplot in Figure 4 (right) show the distribution of *Getis-Ord's G** statistic. It can be seen that the minimum, maximum, mean and median values of *Getis-Ord's G** statistic were 0.007, 0.071, 0.033 and 0.029, respectively. The mean value was greater than the median value, which shows that districts with high values

of *Getis-Ord's G** statistic were more numerous than districts with low values of *Getis-Ord's G** statistic. It can be seen from Figure 4 (right) that the boxplot was skewed to the bottom.

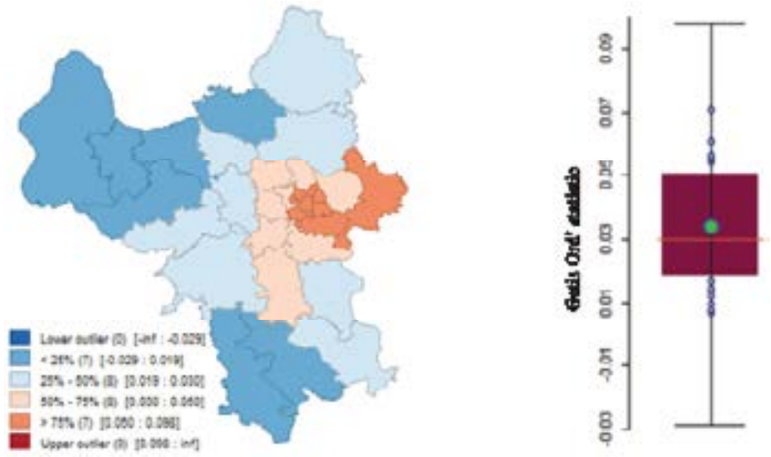

Figure 4. Boxmap (left) and boxplot (right) of Getis Ord's G* statistic.

Hotspots of COVID-19 on December 21, 2022 in Hanoi city are shown in Figure 5 (right). Data from the hotspot map shown in Figure 5 (left) illustrates a total of 5 hotspots, 4 coldspots and 21 insignificant districts. Hotspots were mainly discovered in the central and eastern districts of the city. The five hotspots were detected in Hai Ba Trung (82 cases), Ba Dinh (60 cases), Hoan Kiem (52 cases), Gia Lam (52 cases) and Thanh Xuan (39 cases). Whereas Hoang Mai (225 cases), Dong Da (223 cases) and Ha Dong (133 cases) were districts having a large number of COVID-19-infected cases, no hotspots were detected in these districts. The reason for this was that surrounding districts had a smaller number of COVID-19-infected cases. In addition, coldspots were detected in three western suburban districts and one southern district of Hanoi. Among these suburban districts, some districts had a low and very low number of COVID-19 cases, such as Phuc Tho (3 cases) and Son Tay (16 cases). In addition, the remaining 12 districts were detected with no hotspots and coldspots because they were not statistically significant at the level of 0.05.

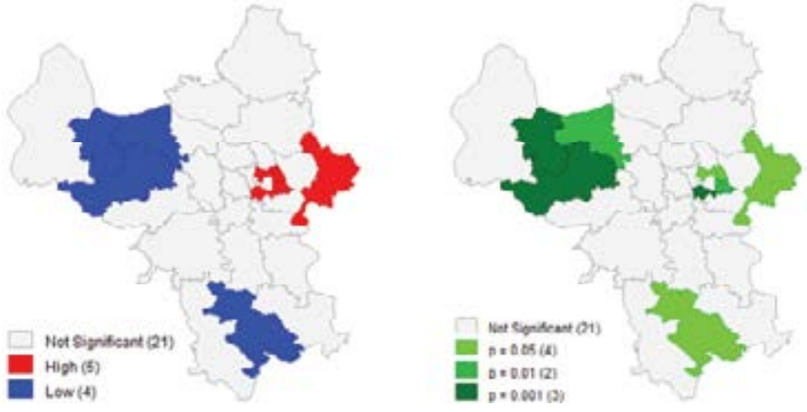

Figure 5. Hotspot map (left) and significant map (right) of COVID-19.

Data from Figure 5 (right) shows the statistical significance of the Getis index for each district of Hanoi city. Statistical levels are expressed on 4 scales, from not reaching statistical significance (p-value > 0.05) and reaching statistical significance at the levels of 0.05, 0.01 and 0.001. Data from Figure 5 (right) shows that a total of four districts (Thanh Xuan, Thach That and Son Tay) were detected with significance at the level of 0.001. Two districts were found with high significance at the level of 0.01 including Hai Ba Trung and Phuc Tho. Districts of Gia Lam, Ung Hoa, Hoan Kiem and Ba Dinh were detected with statistical significance at the level of 0.05.

4. CONCLUSION

This study set out to investigate spatial patterns of the SARS-CoV-2 variant collected on a winter day in 2022 in Hanoi city (Vietnam) based on spatial auto-correlation analysis. In this study, the spatial clustering, including spatial clusters (high-high and low-low), spatial outliers (low-high and high-low) and hotspots of the COVID-19 pandemic were explored using the local Moran's I and Getis-Ord's G_i^* statistics. The local Moran's I statistic was first employed to identify spatial clusters and spatial outliers of COVID-19. The Getis-Ord's G_i^* statistic was then used to detect hotspots of COVID-19. A case study of locally transmitted cases confirmed on a winter day in Hanoi city in 2022 indicated that high-high spatial clusters and low-high spatial outliers and hotspots of COVID-19 were mainly detected in the central area of Hanoi city where the population density is dense, whereas low-low spatial clusters and coldspots were mostly detected in the west and north of the city. The findings of this study provide important insights into how to apply spatial statistics in general and spatial auto-correlation analysis, in particular, to better understand the spread of the spread of SARS-CoV-2 variant through space. This study confirms the effectiveness of spatial autocorrelation analysis in the study of the spread of the SARS-CoV-2 variant.

5. REFERENCES

Alves J. D., Abade A. S., Peres W. P., Borges J. E., Santos S. M., and Scholze A. R., 2021. Impact of COVID-19 on the indigenous population of Brazil: A geo-epidemiological study. *Epidemiology & Infection, 149*, e185.

Anselin L., 1995. Local indicators of spatial association-LISA. *Geographical Analysis, 27*(2), 93-115.

Anselin L., Syabri I., and Kho Y., 2009. GeoDa: An introduction to spatial data analysis. In: Handbook of applied spatial analysis: Software tools, methods and applications, 73-89. *Springer*.

Asongu S. A., Diop S., and Nnanna J., 2021. The geography of the effectiveness and consequences of Covid-19 measures: Global evidence. *Journal of Public Affairs, 21*(4), e2483.

Busingye D., 2011. Spatial epidemiology and temporal trends of heart attack and stroke in Middle Tennessee.

Carballada A. M., and Balsa-Barreiro J., 2021. Geospatial analysis and mapping strategies for fine-grained and detailed COVID-19 data with GIS. ISPRS *International Journal of Geo-Information, 10*(9), 602.

Carroll L. N., Au A. P., Detwiler L. T., Fu T., Painter I. S., and Abernethy N. F., 2014. Visualization and analytics tools for infectious disease epidemiology: A systematic review. *Journal of Biomedical Informatics, 51*, 287-298.

Castro M. C., Kim S., Barberia L., Ribeiro A. F., Gurzenda S., Ribeiro K. B., Abbott E., Blossom J., Rache B., and Singer B. H., 2021. Spatiotemporal pattern of COVID-19 spread in Brazil. *Science, 372*(6544), 821-826.

Cliff A. D., and Ord J. K., 1981. Spatial processes: Models & applications. (No Title).

Cook C., Wallin A., Faucett A., Meyers L., and GROUP T.W., 2017. A cloud based epidemiology network to investigate geographical dynamics of respiratory disease. *Open Forum Infectious Diseases, 4*(Suppl 1), S237.

Das A., Ghosh S., Das K., Basu T., Dutta I., and Das M., 2021. Living environment matters: Unravelling the spatial clustering of COVID-19 hotspots in Kolkata megacity, India. *Sustainable Cities and Society, 65*, 102577.

De Cos O., Castillo-Salcines V., and Cantarero-Prieto D., 2022. A geographical information system model to define COVID-19 problem areas with an analysis in the socio-economic context at the regional scale in the North of Spain. *Geospatial Health, 17*(s1).

Elliott P., and Wartenberg D., 2004. Spatial epidemiology: Current approaches and future challenges. *Environmental Health Perspectives, 112*(9), 998-1006.

Ferrante G., Baldissera S., and Campostrini S., 2017. Epidemiology of chronic respiratory diseases and associated factors in the adult Italian population. *The European Journal of Public Health, 27*(6), 1110-1116.

Gambaryan M. H., Shalnova S. A., Deev A. D., and Drapkina O. M., 2017. Chronic respiratory diseases in the regions of northern Russia: epidemiological distinctions in the results of a national population study. *International Journal of Environmental Research and Public Health, 14*(8), 841.

Gay E., and Barnouin J., 2009. A nation-wide epidemiological study of acute bovine respiratory disease in France. *Preventive Veterinary Medicine, 89*(3-4), 265-271.

Getis A., and Ord J. K., 1996. Local spatial statistics: An overview. Spatial analysis: Modeling in a GIS environment. Longley, P., and M. Batty. *Wiley*, New York.

Hoang A., and Nguyen T., 2022. Identifying Spatio-Temporal clustering of the COVID-19 patterns using spatial statistics: Case studies of four waves in Vietnam. *International Journal of Applied Geospatial Research (IJAGR), 13*(1), 1-15.

Jindal S. K., 2006. Respiratory disease epidemiology in India. *Lung India, 23*(2), 93-94.

Jones K. E., Patel N. G., Levy M. A., Storeygard A., Balk D., Gittleman J. L., and Daszak P., 2008. Global trends in emerging infectious diseases. *Nature, 451*(7181), 990-993.

Kadirvelu B., Burcea G., Quint J. K., Costelloe C. E., and Faisal A. A., 2022. Variation in global COVID-19 symptoms by geography and by chronic disease: A global survey using the COVID-19 Symptom Mapper. *EClinicalMedicine, 45*.

Khazaei S., Mansori K., Soheylizad M., Gholamaliee B., Khosravi Shadmani F., Khazaei Z., and Ayubi E., 2017. Epidemiology of lung cancer in Iran: Sex difference and geographical distribution. *Middle East Journal of Cancer, 8*(4), 223-228.

Kieu Q. L., Nguyen T. T., and Hoang A. H., 2021. GIS and remote sensing: a review of applications to the study of the COVID-19 pandemic. *Geography, Environment, Sustainability, 14*(4). Doi: 10.24057/2071-9388-2021-054.

Kirby R. S., Delmelle E., and Eberth J. M., 2017. Advances in spatial epidemiology and geographic information systems. *Annals of Epidemiology, 27*(1), 1-9.

Kodge B. G., 2021. A review on current status of COVID-19 cases in Maharashtra state of India using GIS: A case study. *Spatial Information Research, 29*(2), 223-229.

Krieger N., 2003. Place, space and health: GIS and epidemiology. *Epidemiology, 14*(4), 384-385.

Lamprecht J. L., and Lamprecht S. J., 1976. The geography of heart attack mortality rate in the OECD countries and its relationship to food consumption. *The Professional Geographer*, *28*(2), 178-180.

Marshall R. J., 1991. A review of methods for the statistical analysis of spatial patterns of disease. *Journal of the Royal Statistical Society: Series A (Statistics in Society), 154*(3), 421-441.

Martin A., Markhvida M., Hallegatte S., and Walsh B., 2020. Socio-economic impacts of COVID-19 on household consumption and poverty. *Economics of Disasters and Climate Change, 4*(3), 453-479.

Mayer J. D., and Lewis N. D., 2020. An inevitable pandemic: Geographic insights into the COVID-19 global health emergency. *Eurasian Geography and Economics, 61*(4-5), 404-422.

Mitchell A., 1999. The ESRI guide to GIS analysis: Geographic patterns & relationships, Vol. 1. *ESRI, Inc*.

Moore D. A., and Carpenter T. E., 1999. Spatial analytical methods and geographic information systems: use in health research and epidemiology. *Epidemiologic Reviews, 21*(2), 143-161.

Nazia N., Butt Z. A., Bedard M. L., Tang W. C., Sehar H., and Law J., 2022. Methods used in the spatial and spatiotemporal analysis of COVID-19 epidemiology: A systematic review. *International Journal of Environmental Research and Public Health, 19*(14), 8267.

Nguyen T. T., and Vu T. D., 2019a. Identification of multivariate geochemical anomalies using spatial autocorrelation analysis and robust statistics. *Ore Geology Reviews, 111*. Doi: 10.1016/j.oregeorev.2019.102985.

Nguyen T. T., and Vu T. D., 2019b. Use of hot spot analysis to detect underground coal fires from landsat-8 TIRS data: A case study in the Khanh Hoa coal field, North-East of Vietnam. *Environment and Natural Resources Journal, 17*(3). Doi: 10.32526/ennrj.17.3.2019.17.

Nykiforuk C. I. J., and Flaman L. M., 2011. Geographic information systems (GIS) for health promotion and public health: a review. *Health Promotion Practice, 12*(1), 63-73.

Ramírez-Aldana R., Gomez-Verjan J. C., and Bello-Chavolla O. Y., 2020. Spatial analysis of COVID-19 spread in Iran: Insights into geographical and structural transmission determinants at a province level. *PLoS Neglected Tropical Diseases, 14*(11), e0008875.

Rezaeian M., Dehdarinejad A., Esmaili Nadimi A., and Tabatabaie S. Z., (2008). Geographical epidemiology of deaths due to cardiovascular diseases in counties of Kerman province. *Iranian Journal of Epidemiology, 4*(1), 35-41.

Rosli N. M., Shah S. A., and Mahmood M. I., 2018. Geographical Information System (GIS) application in tuberculosis spatial clustering studies: A systematic review. *Malaysian Journal of Public Health Medicine, 18*(1), 70-80.

Rozenfeld Y., Beam J., Maier H., Haggerson W., Boudreau K., Carlson J., and Medows R., 2020. A model of disparities: risk factors associated with COVID-19 infection. *International Journal for Equity in Health, 19*(1), 1-10.

Saeed U., Sherdil K., Ashraf U., Younas I., Butt H. J., and Ahmad S. R., 2021. Identification of potential lockdown areas during COVID-19 transmission in Punjab, Pakistan. *Public Health, 190*, 42–51.

Shi Z., Chen H., Fan K., and Chen P., 2020. Some thoughts and strategies of planning for the impact of "COVID-19" epidemic in Yunnan plateau basin. E*3S Web of Conferences, 185*, 3044.

Vu D. T., Nguyen T. T., and Hoang A. H., (2021). Spatial clustering analysis of the COVID-19 pandemic: A case study of the fourth wave in Vietnam. *Geography, Environment, Sustainability, 14*(4). Doi: 10.24057/2071-9388-2021-086.

Wang Y., Liu Y., Struthers J., and Lian M., 2021. Spatiotemporal characteristics of the COVID-19 epidemic in the United States. *Clinical Infectious Diseases, 72*(4), 643-651.

WHO, 2023. WHO Coronavirus (COVID-19) Dashboard. https://covid19.who.int/.

Xie Z., Qin Y., Li Y., Shen W., Zheng Z., and Liu S., 2020. Spatial and temporal differentiation of COVID-19 epidemic spread in mainland China and its influencing factors. S*cience of The Total Environment, 744*, 140929.

Xie Z., Zhao R., Ding M., and Zhang Z., 2021. A review of influencing factors on spatial spread of COVID-19 based on geographical perspective. *International Journal of Environmental Research and Public Health, 18*(22), 12182.

Youlden D. R., Cramb S. M., and Baade P. D., 2008. The International Epidemiology of Lung Cancer: Geographical distribution and secular trends. *Journal of Thoracic Oncology, 3*(8), 819-831.

A NOVEL APPROACH OF NEURAL NETWORKS AND USLE IN SMART SOIL EROSION MODELING, CASE STUDY IN SOUTHERN COASTAL OF VIET NAM

Tran Thi Hoa[1]*, Tran Thanh Ha[2,3], Luan Cong Doan[4], Thu Minh Phan[5], Hung Van Nguyen[6]

[1]Faculty of Information Technology, Hanoi University of Mining and Geology, Vietnam
[2]Geomatics in Earth Sciences Research group,
Hanoi University of Mining and Geology, Vietnam
[3]Faculty of Geomatics and Land administration,
Hanoi University of Mining and Geology, Vietnam
[4]Faculty of Electro-Mechanics, Hanoi University of Mining and Geology, Vietnam
[5]Vietnam Academy of Science and Technology, Nha Trang, Vietnam
[6]Ministry of Natural Resources and Environment, Ha Noi, Vietnam
*Corresponding author. Email: tranthihoa@humg.edu.vn

ABSTRACT

Soil erosion is a critical environmental issue with far-reaching consequences. To tackle this challenge effectively, innovative approaches are required for accurate prediction, monitoring and mitigation, such as the integration of remote sensing data and geographic information systems (GIS). In recent years, the application of machine learning techniques in smart soil erosion modeling has gained significant attention due to its ability to learn complex patterns from data without explicit programming. This paper adopted one of the neural networks - the Long Short-Term Memory (LSTM) to analyze temporal variations in erosion patterns over time, aiding in understanding erosion dynamics. Furthermore, another common soil erosion model - the Universal Soil Loss Equation (USLE) was investigated to predict annual soil loss. Our data were extracted from remotely sensed data (DEM - Digital Elevation Model and MODIS) and vector data of the study area. Our case study is located in the Southern coastal areas of Vietnam where the possibility of annual soil loss is relatively high due to the conditions of steep terrain and heavy seasonal rainfall. Our preliminary results showed that the soil erosion process is unevenly distributed over the entire examined area (Quang Nam Province): the northern region is the most highly affected area than the others. The accuracy of the current soil erosion state map and soil erosion potential map showed satisfactory performance. The integration of LSTM with USLE in a smart soil erosion model has provided valuable insights for implementing efficient soil conservation strategies and adaptive management practices, crucial for mitigating erosion's adverse effects on the environment and agricultural productivity. However, challenges related to data availability and interpretability of black-box models warrant further investigation for the continued advancement of smart soil erosion modeling.

1. INTRODUCTION

Soil erosion is a pervasive natural process that results in the detachment, transport and deposition of soil particles from the Earth's surface. It is driven by various factors, including rainfall, wind, topography, land use practices and vegetation cover. Soil erosion has far-reaching

implications for both the environment and human societies. It can lead to reduced soil fertility, land degradation, sedimentation of water bodies and the contamination of aquatic ecosystems. As such, understanding and mitigating soil erosion is crucial for sustainable land management and environmental conservation.

In soil erosion research, various models play a pivotal role in deciphering the intricate dynamics of erosion processes, offering valuable insights for environmental conservation and sustainable land management. The two most common models are the Universal Soil Loss Equation (USLE) (Wischmeier et al., 1965) and the Revised Universal Soil Loss Equation (RUSLE) (Renard et al., 1997), which use various physical features of soil, water and terrain influenced in the erosion process. Furthermore, the Soil and Water Assessment Tool (SWAT), developed by Arnold et al., in 1998, is a comprehensive model used to simulate hydrology, water quality and erosion in large watersheds. It considers various factors such as land use, climate, soil properties and management practices to estimate erosion rates (Arnold et al., 1998). There are several Geographic Information System (GIS) projects-based erosion models that integrate GIS technology and Remotely Sensed Data for spatial analysis of soil erosion. They combined various data sources and analytical tools to assess erosion risks and develop conservation strategies (Foster et al., 2001; Montgomery, 2007; Dabral et al., 2012). The European Soil Erosion Model (EUROSEM), developed by Morgan et al., in 1998, focuses on predicting sediment transport from fields and small catchments, providing dynamic insights into erosion processes (Morgan et al., 1998). These models form a suite of tools that researchers leverage to analyze and address soil erosion challenges. They offer valuable means for understanding, assessing and mitigating soil erosion's impact on the environment and agricultural lands.

To be more specific, one of the most widely employed models is the Revised Universal Soil Loss Equation (RUSLE). This model, developed by Renard and his colleagues in 1997, provides a comprehensive framework for predicting soil erosion by water. It factors in critical variables such as rainfall, soil erodibility, slope characteristics, land cover and erosion control practices. RUSLE has proven to be a fundamental tool for assessing soil erosion risks and guiding conservation planning efforts, making it a cornerstone in the field of soil erosion research (Renard et al., 1997).

Another influential model worth mentioning is the Universal Soil Loss Equation (USLE). Originally developed by Wischmeier and Smith in 1965, this model provides a framework for estimating soil erosion caused by rainfall and runoff. USLE takes into account various factors, including rainfall erosivity, soil erodibility, slope length and steepness, cover and management practices and support practices to predict soil loss. The USLE model has been instrumental in assessing soil erosion risks, guiding land-use planning and facilitating the design of erosion control strategies, making it a seminal contribution to soil erosion research (Wischmeier et al., 1965). While the Universal Soil Loss Equation (USLE) is a widely used and valuable tool for estimating soil erosion, it does have some disadvantages and limitations, such as it relies on average values of various factors like rainfall, slope and land use but, does not explicitly account for variations in climate conditions like extreme weather events or changes in rainfall patterns; otherwise, there are several concerns of precision and scale - dependency of this model for large areas.

Long Short-Term Memory (LSTM) models, a type of recurrent neural network (RNN), can potentially complement the Universal Soil Loss Equation (USLE) in certain aspects, particularly in addressing the limitations associated with the USLE's temporal dynamics. In detail, LSTM models can seamlessly integrate remote sensing data, climate information and historical erosion data to create more robust predictive models. This integration allows for a more comprehensive analysis of erosion processes. Additionally, LSTM models are well-suited to capture extreme weather events and their impact on soil erosion. They can help assess how climate variability and extreme rainfall events contribute to soil loss, which may not be adequately addressed by the static USLE model. Furthermore, LSTM models can be used to optimize and calibrate USLE parameters based on historical data and temporal patterns, ensuring a more accurate representation of the dynamic erosion processes.

This study integrates the USLE and LSTM to analyze physical factors of the soil erosion process at a regional scale. This process is assessed in Southern Central Vietnam to identify locations of erosion and estimate or predict the potential mass and volume of eroded soil in the research area. The accuracy of the model is handled by using the most current research.

2. METHODOLOGIES

2.1 The study area overview

Our study area extends along the coastal area of Southern Centre Vietnam from the city of Da Nang to the province of Binh Thuan, which is approximately 3,307,000 ha large (see Figure 1). This area has been involved in the recent soil erosion research project in 2022 of which results are used to validate our ones, respectively (Nguyen Duc Lam et al., 2020).

Figure 1. The study area (red shade).

The research area exhibits distinctive geographical and climatic features. To the east, it gently slopes towards the East Sea, featuring numerous deep-sea regions, while its western region enjoys a more subdued topography. Notably, this region encompasses four prominent peaks exceeding

1,000 meters in elevation, including Vong Phu, Hon Me, Hoan Con and Hoan Giao. Moreover, the topography includes transverse mountain ranges that partition the coastal region into narrow plains, giving rise to a succession of peninsulas, lagoons and numerous beaches. The climate is characterized by a climate influenced by the Annamite Range. During the summer, it experiences southwest monsoon winds, while the fall and winter seasons bring regional rains shaped by the complex interplay of topography and the influence of the tropical convergence zone. This climate results in considerable annual precipitation, particularly in areas such as Da Nang and Quang Nam, with the west part reaches of the Thu Bon river witnessing the most substantial rainfall. Nevertheless, the southern part reaches of the coastline often grapples with extended dry periods, contributing to arid conditions, notably in Ninh Thuan and Bình Thuan.

The hydrological system is characterized by a network of relatively short rivers, often marked by steep gradients, which discharge directly into the sea. However, the spatial and temporal distribution of these rivers is non-uniform, leading to fluctuations in water availability. Consequently, certain areas experience water scarcity during specific seasons, while others contend with seasonal water excesses. The brevity and steep inclines of these watercourses also render the region susceptible to flash floods during the rainy season and prolonged dry spells during the dry season, significantly impacting the daily lives, economic activities and overall livelihoods of the local populace. Within this expanse, agricultural land accounts for roughly 16.6 % of the total area, while forested land encompasses about 36.7 %. Specialized land usage represents approximately 6.6 % and residential land occupies roughly 1.3 %. Hills, mountains and sandy terrain collectively dominate the landscape, constituting roughly 83 % of the total area. These lands can be categorized into distinct groups, primarily divided into two primary systems: Alluvial soils deposited by rivers in the plains and Feralit - basaltic soils predicated on the varied geological foundations of the hilly regions.

The vegetation cover within the sandy expanses of the study area manifests substantial diversity in both species' composition and life forms. The vegetation can be categorized based on life forms, dividing it into grasslands, shrublands and forests. Shrubland stands out as the most prevalent and dominant vegetation type in the sandy terrain. Considering local conditions, the vegetation can be further classified into two fundamental categories: Vegetation distributed on dry sand and vegetation in areas subject to recurrent or frequent inundation, with the former predominating the landscape.

2.2 The process flowchart

Our model of mapping soil erosion prediction in the study area was accomplished by integrating the USLE with the LSTM algorithm in 5 steps: (1) Collecting and preparing data input; (2) Extracting 4 main sources of the model which were topography, soil, land use and climate – hydrological system; (3) Calculating parameters of the USLE (P, LS, K C, R); (4) Generating the soil erosion map and severe points; (5) Run the LSTM algorithm to determine most influenced factors and presenting the soil erosion hot spot map.

Figure 2 shows the flowchart of the study, where each color represents each step regarding different sources of data collection and extracted parameters. For example, topography was extracted from DEM and then used to determine slope, aspect and elevation. These indices, then, were used to calculate the parameters P and LS in the USLE model. They were also involved in the LSTM to identify the impact factors for the severe prediction of soil erosion hot spots. Other types of indices such as soil depth, soil AWC (available water capacity), vegetation (NDVI), rainfall and land use types were mainly extracted from satellite images (Landsat) and available regional maps. We also used several local reports for validation and data support. Details of each data collection will be presented in the next sections.

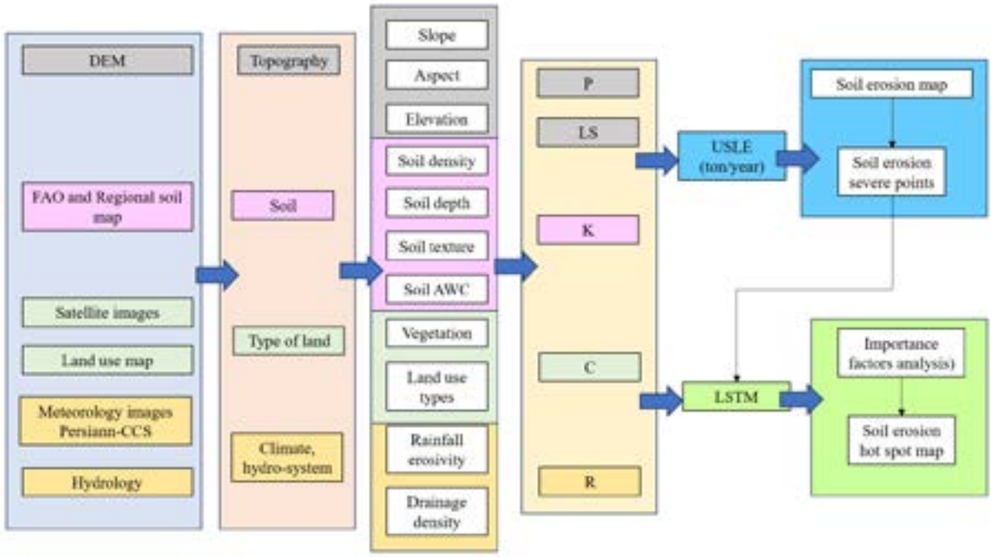

Figure 2. The flowchart of extracting and performing results.

2.3 The USLE model and key variables

The Universal Soil Loss Equation (USLE), established by Wischmeier & Smith in 1965 (Wischmeier et al., 1965), stands as one of the prevalent models employed for the computation of annual average soil erosion and the prediction of mean soil erosion on sloping terrains. The utilization of this model additionally facilitates the projection of variations in soil erosion attributed to changes within the agricultural system and the proposal or estimation of the efficacy of erosion control measures. An advantageous feature of this model lies in its ability to address the individual factors influencing soil erosion (rainfall, topography, soil characteristics, vegetation cover and tillage practices) in a closely interrelated manner, as manifested within the soil loss equation. Specifically, the equation is formulated as follows:

$$A = R \times K \times LS \times C \times P \text{ (ton/arc/year)} \quad (1)$$

where:

A: Annual soil loss (ton/ha/year)

K: Soil erodibility factor (ton.ha.h/ha/MJ/mm)

R: Rainfall erosivity factor (MJ.mm/ha.h/year)

LS: Topographic erosion factors (where L is sloping length in meters and S is sloping steepness in degrees)

C: Cover and management factor

P: Support practice factor

Table 1 represents the data sources and formulas to calculate each variable. In this study, we used QGIS software with its modules to extract, generate and perform their spatial patterns and the soil erosion map.

Table 1. USLE variables.

Variable	Formulas	Source
R	$R = 0.548257 \times P - 59.9$ P: the average annual rainfall; Unit (MJ.mm/ha/h/year)	Persian-CCS satellite images
LS	$LS = (\frac{x}{22.13})^m \times (0.0065 \times s^2 + 0.045 \times s + 0.053)$ where: x is sloping length, s is sloping steepness and m is field-parameter	DEM
K	$K = 0.0293 \times (0.65 - D_g + 0.24 \times D_g^2) \times r$ $r = e^{[-0.0021\frac{OM}{C} - 0.00037(\frac{OM}{C})^2 - 4.02C + 1.72C^2]}$ where: OM is organic matter, C is the clay content in the soil, D_g is the average particle size of soils depending on the classes, such as: - Clay: The average particle size of clay is less than 0.002 millimeters. - Silt: The average particle size of silt ranges from 0.002 to 0.05 millimeters. - Sand: The average particle size of sand ranges from 0.05 to 2.0 millimeters.	Soil maps
C	$C = \frac{-NDVI + 1}{2}$ NDVI: Normalized Difference Vegetation Index	Landsat images
P	Human impacts regarding the slope characteristics. Table 2 illustrates that relationship.	DEM and land use map

Table 2. The P values.

Slope (degree)	P
0-2	0.6
2-5	0.5
5-8	0.5
8-12	0.62
12-26	0.7
16-20	0.8
>20	0.9

2.4 LSTM algorithm

Long Short-Term Memory (LSTM) is a type of recurrent neural network (RNN) architecture designed to address the vanishing gradient problem, a limitation of traditional RNNs (Hochreiter et al., 1997). LSTM networks are capable of learning and remembering over long sequences, making them well-suited for modeling and predicting time series data, such as temporal variations in soil erosion.

LSTM networks consist of memory cells, gates and connections that allow them to capture dependencies in data across various time steps. The key components of an LSTM cell include a cell state, input gate, forget gate and output gate. These components work together to manage the flow of information, decide what to forget and store or output information over time. This architecture enables LSTMs to handle long-range dependencies and effectively model sequential data. LSTM has found application in soil erosion modeling, particularly in addressing the temporal dynamics of erosion processes. Soil erosion is not a static phenomenon; it varies over time due to factors like rainfall patterns, land use changes and land management practices. LSTM can help capture and model these temporal variations (Minacapilli et al., 2018; Pham et al., 2019; Mohammadtaghi Avand et al., 2021). Below are several approaches that LSTM can be applied in soil erosion process research:

- *Temporal Erosion Predictions*: LSTM models can predict soil erosion rates over time, allowing researchers to understand how erosion patterns change seasonally and annually. This is crucial for effective land management and erosion control.

- *Climate Impact Analysis*: LSTMs can analyze the impact of changing climate conditions, such as variations in rainfall and temperature, on soil erosion. Understanding these relationships is vital for climate change adaptation strategies.

- *Land Use Changes*: LSTM models can track the impact of land use changes on erosion patterns. For example, they can assess how deforestation or urbanization affects soil erosion in specific regions.

- *Erosion Forecasting*: LSTMs are used to create erosion forecasting models, which provide early warnings and help in planning and implementing erosion control measures.

- *Data Integration*: LSTMs can incorporate diverse data sources, such as remote sensing data, rainfall records *and* soil characteristics, to provide a holistic understanding of the soil erosion process.

In this study, we used LSTM to predict soil erosion hot spots and patterns over time. We also analyzed the factors of USLE to determine which factor was most impacted by that process. This would help to enhance understanding of the soil erosion context in the study area and to suggest applicable solutions for local authorities.

2.5 Application of LSTM

The key components of the LSTM area:

- *Cell State (C_t):* The cell state is the main horizontal line running through the top of the LSTM. It serves as a memory unit that can store and retrieve information over long sequences. It allows LSTMs to capture long-range dependencies in data.

- *Hidden State (H_t):* The hidden state is the output at a given time step and can be thought of as the current "memory" of the LSTM. It is influenced by both the current input and the previous hidden state.

- *Input Gate (i):* The input gate is responsible for determining which information from the current input and the previous hidden state should be stored in the cell state. It uses a sigmoid activation function to output values between 0 and 1, where 0 means "forget" and 1 means "remember."

- *Forget Gate (f):* The forget gate decides which information to discard from the cell state. It considers the current input and the previous hidden state and uses a sigmoid activation function to determine what to forget.

- *Output Gate (o*): The output gate regulates what information should be passed to the hidden state and, subsequently, to the output. It uses the sigmoid function to decide what to output and a tanh activation function to produce candidate values for the hidden state.

- *Candidate Values (C~t):* This represents the new information that can be added to the cell state. It is computed using a tanh activation function.

The operations within an LSTM cell are governed by the following equations:

$$i(t) = \text{sigmoid}(Wix(t) + UiH_{t-1} + bi) \quad (2)$$

$$f(t) = \text{sigmoid}(Wfx(t) + UfH_{t-1} + bf) \quad (3)$$

$$C_t = \tanh(Wc(x(t) + UcH_{t-1} + bc) \quad (4)$$

$$C_t = f(t) \times C_{t-1} + i(t) \times C_t \quad (5)$$

$$o(t) = \text{sigmoid}(Wox(t) + UoH_{t-1} + bo) \quad (6)$$

$$H_t = ot(t) \times \tanh(C_t) \quad (7)$$

In this study, our LSTM model used points extracted from the soil erosion map as the long-term memory (Cell state); the other variables generated from step 3 of each candidate time were involved in the LSTM as short-term memory (Input Gate). The model decided which insignificant factors would be sent to the "forget gate" and others would be accounted as "candidate values" in the "hidden state". A new set of predicted points were performed in the "output gate".

3. PRELIM RESULTS

3.1 Spatial patterns of USLE variables

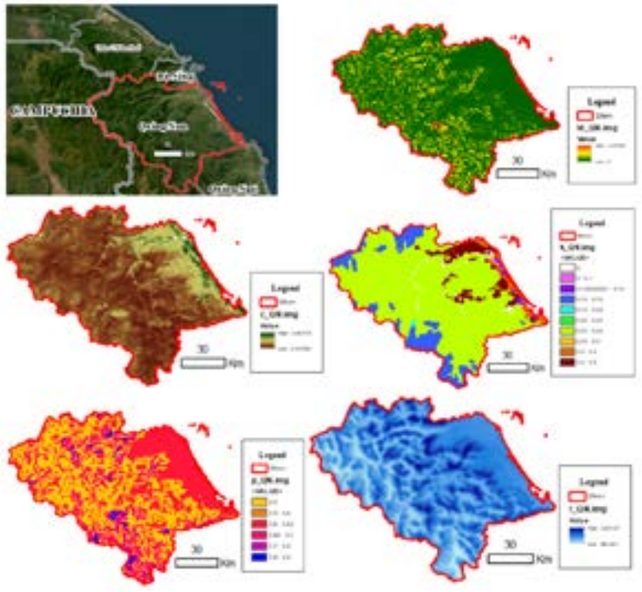

Figure 3. Our tested area - Quang Nam Province (top left) and the USLE variables (from left to right, top to bottom: LS, C, K, P and R).

Due to the high volume of data input and in order to test our proposed methods, we chose Quang Nam province as the testing site. Quang Nam province is in the North of the study area (Figure 3). Following the flowchart shown previously, we loaded data sources into QGIS and then

used Raster Calculation to determine the spatial pixel values of each variable in the test site. Figure 3 represents our testing results of 5 variables of the USLE model: LS, C, K, P and R.

Generally, in terms of topography, Quang Nam province is characterized by its relatively low mountains and a gently sloping terrain towards the sea, with narrow coastal plains. There is no significant variation in slope gradients across the region. Rainfall distribution is uneven, with higher precipitation levels observed in the eastern coastal areas and lower rainfall amounts in the western region. Otherwise, there may be concerns of soil erosion along the coastline.

3.2 Spatial distribution of soil erosion

Figure 4 illustrates the current and predicted state of spatial distribution of soil erosion in the tested area. Based on soil erosion maps in conjunction with statistical data on the extent of eroded land across the entire research area, it is evident that the process of soil erosion is not uniformly distributed throughout the study region. From a spatial distribution perspective, regions such as the mountainous region of Quang Nam province may exhibit extensive soil erosion with rates exceeding 3,200 tons/ha/year and over 100 tons/ha/year, accounting for approximately 60 % of the provincial land areas. The primary reason for this phenomenon is the substantial impact of topography. With a topography that channels the northeasterly winter winds and the southwestern summer winds, these areas experience substantial rainfall, leading to a rapid increase in soil erosion. Furthermore, based on the land cover factor (C), it can be observed that these regions have relatively low C values, indicating a diminishing vegetation cover. Consequently, when it rains, water runs across surfaces without encountering the impediment of vegetation cover, leading to an escalating soil erosion rate.

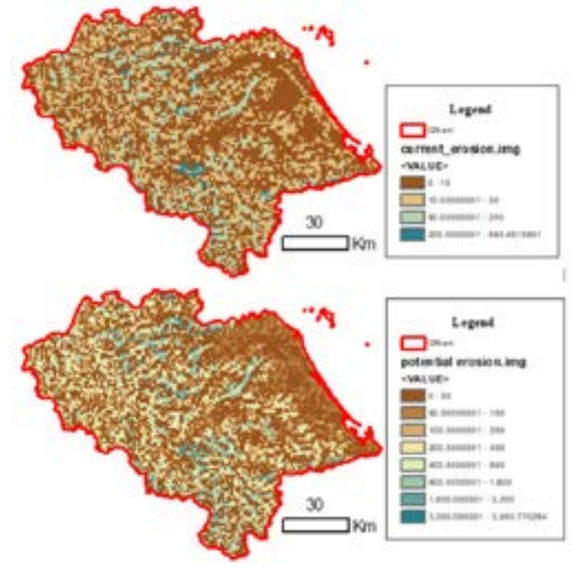

Figure 4. The spatial distribution of the current status of soil erosion in Quang Nam (upper image) in 2022 and a prediction of soil erosion impacts (lower image) projected for 2030.

Unit: ton/ha/year.

In addition, the average annual rainfall in this region is considerably high, owing to their topographical orientation. When these factors are combined, it becomes evident that these areas

are highly susceptible, with high levels of soil erosion exceeding 3,200 tons/ha/year for potential soil erosion and over 200 tons/ha/year for current soil erosion, representing a substantial hazard.

3.3 Future plan

Since we were able to conduct the current and projected state of soil erosion patterns over the tested site, there was a lack of analysis of the role of each factor (P, LS, C, K and R) in the eroded process. Otherwise, the LSTM has not been able to determine the significant "candidate values" due to several uncertainties of data missing and the pixel size. In the next steps, we will investigate (1) analyzing the multi-collinearity of each factor to reveal the relationship between them, (2) determining the most impacted factor in the study area, (3) interpolating and calibrating the hot spots of the model to assess soil erosion risk zone with validation and (4) last but not least, test and apply our strategies entirely the study area.

4. DISCUSSION

The maps of potential soil erosion and current soil erosion in the Quang Nam region are the outcomes of the complex interactions of various natural factors through erosion indices. However, due to our limited time of testing and data resources, the main driving factors have not been revealed yet. Based on our current USLE and LSTM results, we are currently leaning toward the R factor. Rainfall distribution exhibits significant variability and the specific characteristics of each soil type, in conjunction with the influence of the terrain conditions, combined with vegetation cover and land management practices, contribute to the distinct variations in the degree of soil erosion across different regions. Our next steps will test these hypotheses and derive the analysis.

We expect to provide a comprehensive spatial depiction of the susceptibility of various areas to soil erosion, offering invaluable insights for land management and conservation efforts. The integration of these erosion factors, in conjunction with their spatial distribution, serves as a vital tool for understanding the dynamic and complex nature of soil erosion processes not only in the Quang Nam province but also in the South-Central region of Vietnam.

5. REFERENCES

Arnold J. G., Srinivasan R., Muttiah R. S., & Williams J. R., 1998. Large Area Hydrologic Modeling and Assessment Part I: Model Development. *Journal of the American Water Resources Association, 34*(1): 73-89.

Dabral P. P., Baithuri N., & Pandey A., 2012. Soil Erosion Assessment in a Hilly Catchment of the Lesser Himalayas, India, Using USLE, GIS and Remote Sensing. *Environmental Earth Sciences, 66*(7): 1785-1801.

Foster G. R., & McCool D. K., 2001. Modeling Soil Erosion: The Past, Present and Future. *Journal of Soil and Water Conservation, 56*(5): 281-287.

Hochreiter S., & Schmidhuber J., 1997. Long short-term memory. *Neural Computation 9*(8): 1735-1780.

Minacapilli M., Santoro M., & Aucelli P. P., 2018. Soil erosion modeling: A review. *Geosciences 8*(1): 21.

Mohammadtaghi Avand, Maziar Mohammadi, Fahimeh Mirchooli, Ataollah Kavian, John P Tiefenbacher, 2021. A new approach for smart soil erosion modelling: Integration of empirical and machine learning models. research article, research square.

Montgomery D. R., 2007. Soil Erosion and Agricultural sustainability. *Proceedings of the National Academy of Sciences.* 13268-13272.

Morgan R. P., Quinton J. N., Smith R. E., Govers G., Poesen J. W. A., Auerswald K., & E.I.S. S.A., 1998. The European Soil Erosion Model (EUROSEM): A dynamic approach for predicting sediment transport from fields and small catchments. *Earth Surface Processes and Landforms 23*(6): 527-544.

Nguyen Duc Lam, Le Chi Lam, 2020. Using USLE model application and geospatial techonology to evaluate risk of soil loss in Tay Nguyen and Nam Trung Bo in the period of 2000-2018. *Journal of National Resources and Environment* .

Pham H. D., & Pradhan B., 2019. Soil erosion prediction using hybrid integration model of Long Short-Term Memory (LSTM) and Boosted Regression Tree (BRT). *Catena,* 104203.

Renard K. G., Foster G. R., Weesies G. A., McCool D. K., and Yoder D. C., 1997. Predicting Soil Erosion by Water: A Guide to Conservation Planning with the Revised Universal Soil Loss Equation (RUSLE). *US Department of Agriculture*.

Wischmeier W. H., and Smith D. D., 1965. Predicting Rainfall Erosion Losses - A Guide to Conservation Planning. *US Department of Agriculture.*

ASSESSMENT OF THE DYNAMIC IMPACT OF DEBRIS FLOW ON STRUCTURE SAFETY: A CASE STUDY OF CHECK DAM IN VIETNAM

Nguyen Chi Thanh[1] , Vu Quoc Cong[1], Vu Le Minh[1], Do Van Chinh[2]*, Tran Thi Nga[1], Luyen Le Dieu Linh[1]

[1]Hydraulic Construction Institute, Hanoi, Vietnam
[2]Thuyloi University, Hanoi, Vietnam
*Corresponding author. Email: chinhdv@tlu.edu.vn

ABSTRACT

Debris flow is one of the climate-driven natural disasters that has a rising risk of property and life loss. The phenomenon is a combination of high flow velocity and large impact forces in a sudden event of poor temporal predictability. Vulnerable areas to debris flow are mountainous areas with growing populations, such as the Northwest region of Vietnam. Improving the check dams' resistance to debris flow is, therefore, an important task nowadays. Debris flow has been studied worldwide, in which calculating the impact forces of the debris flow on barriers is the core issue. Estimating this impact needs to cover the factors of common flood flow, which are the static debris flow pressure and surcharge from a debris flow moving process and also other dynamic impacts. The dynamic impact factors are the impact and collision of individual components, hits of the debris flow and dynamic debris flow pressure. Current national standards about loads and impact applied for hydraulic construction design in Vietnam have not covered the dynamic impact of debris flow. In this paper, the stability of a check dam located in Vietnam is re-evaluated in two regimes of the debris flow impact: (i) static impacts as conventional flood flow and (ii) dynamic impacts adopting Huebl's approach. The results help to analyze shortcomings of the current design procedure applied for checking dams in particular and hydraulic structures in general. When renovating current check dams or designing new ones, this analysis shows the importance of updating the dynamic impacts of debris flow in the standardized design. In order to upgrade the resistance capacity of the current check dam systems against debris flow, taking those dynamic impacts into consideration is crucial.

1. INTRODUCTION

The northwest region of Vietnam consists of medium and alpine mountains and is vulnerable to debris flow. Rivers here have a considerable hydroelectric power reserve, so hydraulic construction systems have been well developed for multiple purposes, which combine with agricultural development. The total number of check dams in this area is about 12 thousand, resulting in a total irrigation area of 3 million hectares (VAWR, 2008). However, heavy rainfall and debris flow related to climate change are threatening the safety of these constructions. Site investigation of check dams in this area shows average to severe damage.

Statistic research by the Vietnam Academy for Water Resources shows that there is 82 % of the check dams that located in areas with high and very high risk of debris flow. However, their design and construction in the past followed the national standards and did not take that risk into account. Current design and construction procedures applied for check dam in Vietnam follows the national standards of hydraulic dams, which are the TCVN 9137:2012 for concrete dams, TCVN 10777:2015 for local material dams and TCVN 9147:2012 for hydraulic calculation. In these standards, design loads of the flow are considered static loads, which are the hydraulic pressure values at different water levels. The dynamic impact of the debris flow and the impact force of boulders are not taken into account. In addition, climate change has caused extreme weather conditions, including extreme heavy rainfalls. In combination with the typical terrain of the Northwest region, the water level under the current circumstance is clearly higher than the design level at the time of the check dam design. As a result, check dams in the Northwest region of the country are incapable of dealing with debris flow nowadays.

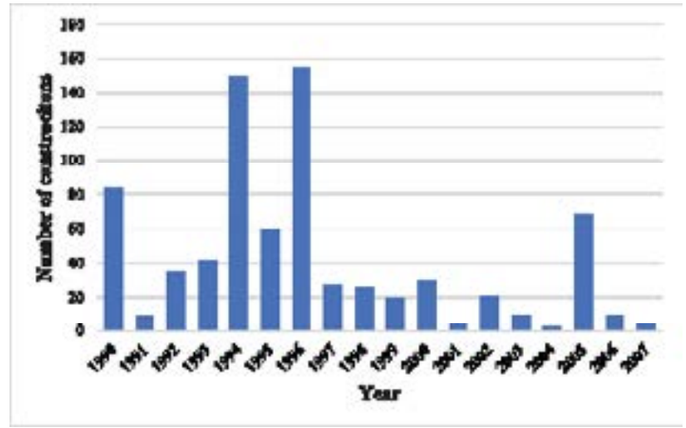

Figure 1. Number of small and average hydraulic constructions damaged by debris flow.

Debris flow mitigation has been well developed in other countries which suffer the high risk of this phenomenon. The Sabo system in Japan is well-known for this problem (Chanson et al., 2004). Debris flow calculation and mitigation are also standardized in Japan, Austria and some other European countries (National Institute for Land and Infrastructure Management - Japan, n.d.) (Huebl and Nagl, 2019) and their standardization is spreading to other countries. The core of the calculation is the model of debris flow and how to evaluate the impact of the flow on the check dam (National Institute for Land and Infrastructure Management - Japan, n.d.) (Huebl and Nagl, 2019; Anggun Lestari et al., 2021; Suda, Hübl and Bergmeister, 2010).

Those approaches have been well studied and applied all over the world, so they can be valuable tools for Vietnam to study and apply to our current circumstances and improve the capability of checking dams to deal with debris flow. For this purpose, this paper will examine the stability of a typical check dam in the Northwest region with and without the impact of debris flow in the design loads.

2. METHODS

2.1 Case study

The Na Muon check dam is located in Na Sang commune, Muong Cha district, Dien Bien province (21.7369N; 103.0831E). It is a rock-filled concrete surface dam with dimensions of

4.0 m high and 14.0 m long. Due to the impact of debris flow over the years, the concrete surface has some damage so severe that the reinforcement inside is clearly visible (as can be seen in Figure 2).

Figure 2. View of Na Muon check dam from downstream (taken in May 2022).

2.2 Vietnamese National Procedure

The dam design was based on Vietnamese National standards, i.e., TCVN 9137:2012, TCVN 10777:2015 and TCVN 9147:2012.

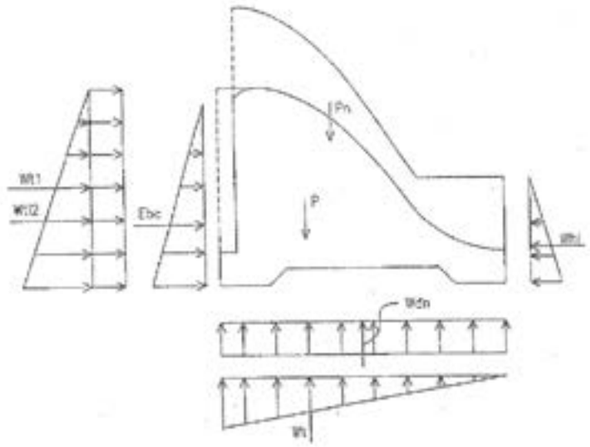

Figure 3. Loads impact map according to Vietnamese standards.

Acting loads on a check dam are listed in Figure 3, including:

P: self-weight of the check dam

P_n: weight of water over the check dam when the upstream water level is higher than the downstream water level

E_{bc}: Lateral earth pressure of the sediment in front of the check dam

W_{TL1}, W_{TL2}: hydraulic pressure of the upstream

W_{HL1}: hydraulic pressure of the downstream

W_{dn}: buoyancy pressure

W_t: seepage pressure

These loads are classified as follows:

- Permanent loads: W_{TL} corresponds to normal upstream water level, W_{HL} corresponds to maximum discharge with normal upstream water level; W_T corresponds to normal upstream water level and waterproofing and drainage devices work normally; soil weight and upstream and downstream lateral soil pressure
- Variable load
  - Long-term variable load: E_{bc}; Thermal impact (only for concrete dams) identified for the year with the average fluctuation amplitude of monthly average temperature.
  - Short-term variable load: Wave pressure corresponding with basic wind velocity; load due to floating objects; Dynamic load when flood discharge overflows the check dam surface
- Accident load
  - W_T corresponding with one of the waterproof and drainage devices is broken
  - Thermal impact identified for the year with maximum amplitude of monthly average temperature
  - Wave pressure corresponding with the maximum wind velocity in a period of years
  - Earthquake action

Depending on the considered working situation of the check dam, the corresponding loads are chosen for a load combination of the design. Check dam design considers 2 types of load combinations:

- Basic load combination: this combination consists of all the permanent loads short-term and long-term variable loads.
- Special load combination: this combination consists of the basic load combination and one of the accident loads.

Depending on the real working condition of the check dam in practice, check dam designs need to consider the basic load combination and special load combination for two of the accident situations.

2.3 Austrian Standard ONR series

Debris flow pressure results from dynamic displacement processes with different proportions of water and sediments, that both are fine and coarse. The debris flows down the channel and interacts with the structure during impact (according to Figure 4). It is assumed that the highest forces act on the barrier during the initial impact. Deposits possibly present behind the barrier have a damping effect and reduce the occurring pressures from a debris flow.

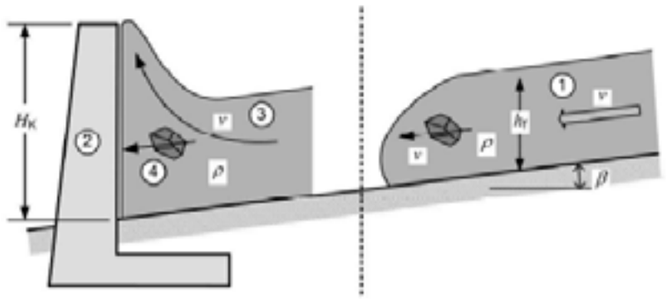

Figure 4. Debris flow in the channel and the impact on the structure (Rudolf-Miklau and Suda, 2011).

in which: (1) - Debris flow in the channel, (2)- Structure (Barrier), (3)- Debris flow hits structure and accumulates, (4)- Collision of individual components.

The newly issued Austrian Standard ONR 24801 provides a standardized model for the design of torrential barriers under debris flow impact, which has been developed from the comparative calculation of common debris flow models from engineering practice in torrent control and calibrated by impact measurements of debris flow events. The model is based on a combined static-dynamic stress approach and also takes into account the impulse by a single object (block, tree, trunk).

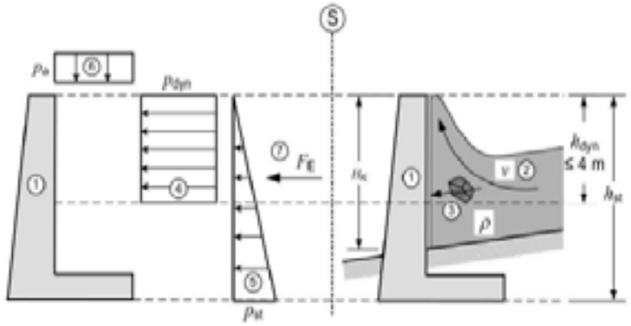

Figure 5. Components of the impact model for debris flow.

in which: (1) - Structure (barriers); (2) - Debris flow hits structure and dams up; (3) Collision of individual components; (4) - Dynamic debris flow pressure; (5) Static debris flow pressure; (6) - Surcharge from debris flow moving process; (7) - Impact of individual components

The impact model shown in Figure 3 is derived from practical experience. Some simplifications are made. For example, the debris-flow pressure is always assumed to act at right angles on the component being impacted. An upward or downward-directed force component during the impact of the debris flow is not taken into account. Forces from the impact of individual components are also always applied normally to the component, even if they impact at an angle.

The loading area of the dynamic debris-flow pressure component is determined from the discharge area (A_{QM}) of the debris flow. The discharge area of the debris flow (A_{QM}) is determined by means of the discharge depth at a characteristic channel cross-section in a flow section immediately above the sedimentation area (Figure 4).

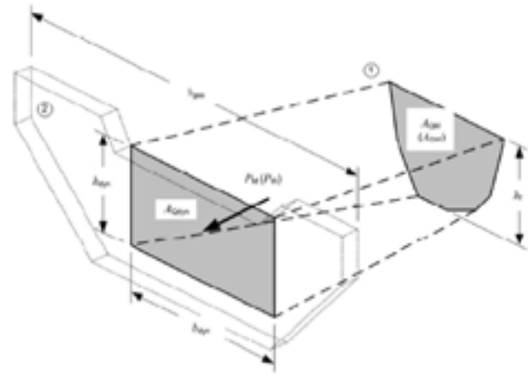

Figure 6. Discharge area of the debris flow and loading area at the structure.

in which: (1)- Typical cross-section of the channel; (2) - Structure

The momentum principle is used to calculate the dynamic debris pressure component. First, the static equivalent force P_M, which acts on the contact area of the dynamic component (A_{Qdyn}), is calculated. The dynamic component of the mudflow pressure P_M can be calculated using the area A_{Qdyn}. This surface load is to be applied to the entire area A_{Qdyn} in the design as a uniform load.

$$P_M = (\rho_M * A_{Qdyn} * v^2) * 10^{-3} \quad (1)$$

$$\rho_{dyn} = \frac{P_M}{A_{Qdyn}} \quad (2)$$

in which:

A_{Qdyn}: Load area on the structure on which P_M acts in m^2

P_M: Static equivalent force resulting from the impact of a debris flow displacement process on the structure, in kN; typical parameters for debris flow displacement processes are given in Table 1

ρ_{dyn}: Dynamic component of the mud pressure in kN/m^2

v: Flow velocity of the displacement process averaged over the discharge cross-section, in m/s

Table 1. The density of the medium of a debris flow relocation process in kg/m³.

Relocation process	Debris-like solid transport	Debris flow	
		Muddy	Stony
Density (kg/m^3)	1,300 to 1,700	1,700 to 2,000	2,000 to 2,300
Average speed (m/s)	3 to 5	3 to 6	5 to 10

3. RESULTS AND DISCUSSIONS

The safety of the Na Muon check dam is recalculated by two different approaches: (1) Evaluating the safety factor based on Vietnamese standards and (2) Evaluating the safety factor based on ONR series.

The stability of this check dam will be reexamined by the two approaches: Calculation 1 using the design loads defined in current national standards, in which the impact of the debris flow

is considered as static load; calculation 2 taking the dynamic impact of the debris flow into account following the instruction of Austrian Standard ONR series.

3.1 Input data

The dam: The main cross-section of the Na Muon check dam is illustrated in Figure 7. The dam is 14.0 m long and 4.0 m high. The outer layer is reinforced concrete M 300 (upstream face) and M 200 (downstream face). The inner part is a combination of concrete M 150 (70 %) and stone (30 %). The dam is 2,0 m over the stream nature ground.

Debris flow: Muddy type, density 1,700 kg/m^3; v = 3 m/s ; load area A_{Qdyn} = 2×14 = 28 m^2

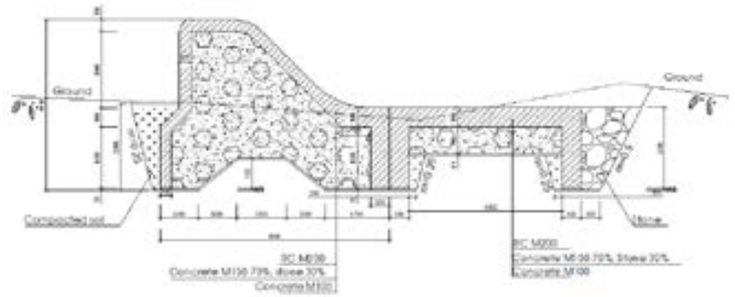

Figure 7. The main cross-section of Na Muon check dam.

Geological conditions of the foundation: Properties of the foundation as in Table 2

Table 2. Geological condition.

Layer	Density	Cohesion	Friction angle
	g/cm^3	kG/cm^2	
	1.93	0.303	20°34’
	2.33	2.083	27°35’

3.2 Results

The maps of loads that have an impact on the Na Muon check dam in those two conditions are illustrated in Figure 8 and Figure 9, respectively.

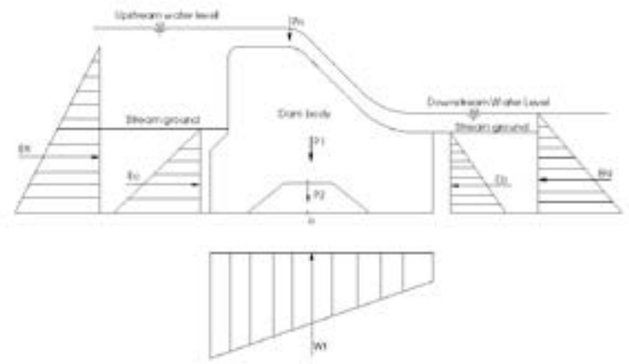

Figure 8. Loads impact map by Vietnamese standards.

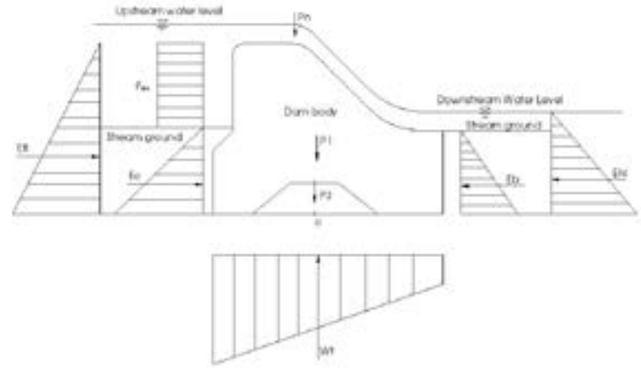

Figure 9. Loads impact map by taking into account dynamic component of debris flow.

Table 3. Summary of load impact.

No	Load impacts	Direction	Value (kN)	Moment arm (m)	Momentum to the dam’s toe (kN.m)	
					M (-)	M (+)
1	P_1	¯	452.59	3.28		1,484.502
2	P_2	¯	36.48	3.35		122.198
3	P_n	¯	42,9	3.85		165.165
4	W_t	↑	213.0	1.48	146.539	
5	E_{tl}	®	99.015	0.88		30.899
6	E_{hl}	¬	35.11	0.75	10.26	
7	E_c	®	13.68	0.72		38,36
8	E_b	¬	53.28	3.25	692.25	
9	ρ_{dyn}	®	30.6	3.35	102.51	
Total					**951.55**	**1,841.124**

Table 4. Results of safety factor.

Safety factor	Approach	
	Vietnamese standards	ONR series
Sliding	**2.74**	**1.97**
Overturning	**2.17**	**1.93**

3.3 Discussions

The main difference between these two methods is the participation of dynamic component of the debris flow ρ_{dyn}, which is illustrated in Figure 5 and calculated in Equation 2.

Table 4 shows the reduction of safety factor between the two approaches, especially the significant change for sliding safety (decreased by 28 %). This result is obviously predicted because of ρ_{dyn}. The value ρ_{dyn} is proportional to the properties of the debris flow (i.e., density, velocity). Thus, it is necessary to include the characteristic factors of debris flow into the design calculations of the check dam because the energy carried by its materials is significant and affects the safety of the dam, especially its anti-sliding capability.

4. CONCLUSIONS

Debris flow is a rising risk to vulnerable areas such as the Northwest region of Vietnam, causing severe damage to current check dams in this area. According to the current design procedure, the national standards (i.e., TCVN 9137:2012, TCVN 10777:2015 and TCVN 9147:2012) do not take into account the dynamic factor of debris flow during its formation and impact on dams. In fact, the dynamic effect is considered the main characteristic component of debris flow and has been standardized and calculated in detail according to the regulations of some countries such as Japan and European countries.

A study case of check dam stability is studied, in which the stability of the check dam is re-evaluated by the two approaches. One calculation considers the impact of the debris flow as static load following the national standards and the other calculation takes the dynamic impact of the debris flow into account following the instruction in the Austrian standard ONR series. There is a drastic drop in safety factor in sliding stability (decrease of 28 %), while the overturning stability also reduces by 11 % when the dynamic impact of the debris flow is taken into account.

This result shows the importance of updating the dynamic impact of debris flow in check dam design in order to increase its resistance under the current situation of debris flow in the region.

5. ACKNOWLEDGMENTS

This paper has used the results of the scientific research project at the Ministry of Science and Technology (MOST): *Research on solutions for multiple purpose check dam in mountainous regions in order to minimize the impact of debris flow*. Code DTĐL.CN-83/21. We would like to thank MOST for creating conditions for the Viet Nam Academy for Water Resources and the Research Team to carry out this study.

6. REFERENCES

Anggun Lestari, Della, Teuku Faisal Fathani, Fikri Faris and Wahyu Wilopo, 2021. Designing Conduit Sabo Dam Series as a Debris Flow Protection Structure. *E3S Web of Conferences*. https://doi.org/10.1051/e3sconf/202133108001.

Chanson, Hubert, 2004. Sabo Check Dams - Mountain Protection Systems in Japan. *International Journal of River Basin Management*. https://doi.org/10.1080/15715124.2004.9635240.

Huebl, Johannes and Georg Nagl, 2019. From Practical experience to national guidelines for debris-flow mitigation measures in Austria. Debris-Flow Hazards Mitigation: Mechanics, Monitoring, Modeling and Assessment. *Proceedings of the 7th International Conference on Debris-Flow Hazards Mitigation*.

National Institute for Land and Infrastructure Management - Japan. n.d., 2022. Technical Standard for Etablishing Sabo Master Plan and Designing Sabo Facilities against Debris Flow and Driftwood. *Technical note of National Institute for Land and Infrastructure Management, 904*.

Rudolf-Miklau, F., and J. Suda, 2011. Technical Standards for Debris Flow Barriers and Breakers. *International Conference on Debris-Flow Hazards Mitigation: Mechanics, Prediction and Assessment, Proceedings*. https://doi.org/10.4408/IJEGE.2010-02.O-02.

Suda, Jürgen, Johannes Hübl and Konrad Bergmeister, 2010. Design and Construction of High Stressed Concrete Structures as Protection Works for Torrent Control in the Austrian Alps. *3rd International Fib Congress and Exhibition, Incorporating the PCI Annual Convention and Bridge Conference: Think Globally, Build Locally, Proceedings*.

VAWR, 2008. Project on Planning for Flash Flood Prevention and Natural Disaster Mitigation in Mountainous Areas of Vietnam.

GIS IDEAS 2023 - HUNRE

GEOSPATIAL INTEGRATED TECHNOLOGIES FOR NATURAL HAZARDS AND ENVIRONMENTAL PROBLEMS

COLLECTION OF ABSTRACTS

COLLECTION OF ABSTRACTS

ESTIMATING ABOVEGROUND BIOMASS USING LANDSAT 8 IMAGERY: A CASE STUDY OF DECIDUOUS BROADLEAF FOREST IN DAK LAK PROVINCE, VIETNAM

Duong Dang Khoi

Quantifying the aboveground biomass (AGB) is essential for understanding carbon sequestration potential. Traditional field-based methods for estimating AGB are often time-consuming, expensive, and limited in their spatial coverage. Recent studies have revealed that using a universal regression model to estimate AGB at a regional or country scale is not feasible. Instead, it is necessary to create local regression models that can accurately estimate AGB locally. However, the spatial distribution of AGB in deciduous broadleaf forests in Dak Lak province must be discovered. Therefore, this study aims to develop regression analysis-based predictive models specifically for estimating the spatial distribution of AGB in the deciduous broadleaf forest in Dak Lak province. Multiple spectral bands and vegetation indices derived from Landsat 8 imagery were used as independent variables, while AGB measurements served as the dependent variable. The statistical analysis results indicate a strong correlation between vegetation indices and field-based AGB data, confirming the effectiveness of using Landsat 8 imagery for estimating AGB. The models show reasonably good performance, achieving R2 values ranging from 0.61 to 0.62 and RMSE values ranging from 30.68 to 31.54. The estimated AGB in the forest averages 100.80 Mg/ha with a standard deviation of 44.27. The regression model-derived spatial distribution of AGB in Dak Lak reveals the variation in AGB across the forest area, highlighting areas with high and low AGB in the province. This map can serve as baseline information for future AGB estimates in the area, contribute to carbon sequestration monitoring efforts, and support improved local forest management practices.

WATER GOVERNANCE AND TRANSBOUNDARY DATA SHARING IN THE LOWER MEKONG REGION. A CASE STUDY OF YALI HYDROPOWER DAM, VIETNAM

Ha Quang Hung, Doan Thi Thanh Thuy, Hong Ha Tran

In recent years, economic growth has led to massive urban sprawl, intensive agricultural production, and environmental degradation and losses in Vietnam. In the Lower Mekong Basin (i.e., a part of Central Highland of Vietnam), agricultural production, urban growth, unsustainable resources (water and soil) management, and industrial activities are the potential pollutants to the regional environment. To regulate human interferences on the environment, environmental taxes and fees based on the "polluter pays principle" (PPP) are the key to environmental protection. However, PPP's efficiencies depend on tracking the pollutants and polluters using spaceborne/airborne monitoring sensors, ground stations, and field sampling. In Vietnam's rural and mountainous, monitoring networks and data are scarce despite efforts to invest in the environmental monitoring system for years. In this research, we examined the use of bio-optical models (i.e., ocean color (OC) and Case 2 Regional Coast Color (C2RCC) methods) and remotely sensed analyses (i.e., Landsat 5, 7, 8 & 9 data) for the case of the environmental incidents in the Yali hydropower dam, Chu Pa, Gia Lai, Vietnam in 2022 and 2009. The research's outputs emphasized revising the environmental monitoring and environmental protection approach in Viet Nam and transboundary data sharing for water governance in the Mekong Region.

GROUNDWATER POTENTIAL ZONING USING LOGISTICS MODEL TREES BASED NOVEL ENSEMBLE MACHINE LEARNING MODEL

Tran Xuan Bien, Pham Thai Binh

In this work, the main aim is to map the groundwater potential zones in the Central Highlands of Vietnam using a novel ensemble machine learning model, CG-LMT, which combines two advanced techniques, Cascade Generalization (CG) and Logistics Model Trees (LMT). For this, the authors collected and selected 501 wells of data and a set of twelve affecting factors for the generation of training and testing datasets used for training and validating the model. The model was validated using various quantitative indicators, including the ROC curve. Results of this study showed that the novel ensemble model performed well for groundwater potential mapping and modeling (AUC = 0.742), its performance is even better than a single LMT model (AUC = 0.727). Thus, the CG-LMT is a promising tool for accurately predicting groundwater potential areas in the study area. In addition, the groundwater potential map generated from the CG-LMT model is a helpful tool for better study area water resource management.

IDENTIFICATION AND DELINEATION OF FLOOD HAZARD AREAS USING THE RELATIVE SLOPE LENGTH DATA: A CASE STUDY OF THE NGAN SAU, NGAN PHO RIVER BASIN, VIETNAM

Nguyen Ba Dzung, Dang Tuyet Minh, Tran Duy Kieu

Flood modeling offers helpful data to support managing flood hazards and reducing the effects of flooding in flood-prone areas. The current study used the Analytical Hierarchy Process (AHP) method and GIS technology to develop flood hazard maps in the Ngan Sau, Ngan Pho river basin. The accuracy of flood simulation results depends on the factors contributing to the flooding. The aim was to monitor and evaluate the importance of relative slope length for flood hazard delineation in the study area. A total of six physical geography and meteorological factors were chosen to calculate relative weights in AHP, including rainfall, slope, soil, land use, drainage density, and relative slope length. When calculating the model, the authors divided these factors into two groups: Group 1 includes five criteria excluding the relative slope length factor, and group 2 consists of all six factors. The authors verified the results of flood hazard zoning based on flood warning levels at hydrological stations in the study area during historical floods. The findings revealed that maps generated from the group of parameters, including the relative slope length, are more accurate than those prepared based on the remaining five variables.

MONITORING THE AREA AND WATER LEVEL OF RESERVOIRS BY REMOTE SENSING AND GIS TECHNOLOGY. CASE STUDY IN VU GIA - THU BON RIVER BASIN

Trinh Thi Hoai Thu, Bui Thi Hong Tham

Managing and efficiently using water resources is a top concern worldwide. Due to drought and increasing water demand, many places have constructed reservoirs on rivers. Although these reservoirs only cover a small part of the Earth's surface, they play a significant role in human health, biodiversity, and watershed ecosystems. Storing water in reservoirs is essential for human livelihoods, agricultural irrigation, and economic development, especially in densely populated and arid regions. However, apart from their positive effects, the construction of reservoirs also leads to water scarcity, causing conflicts over water allocation from upstream to downstream. Therefore, various places with a common water source create and implement water-sharing agreements. Monitoring water resources in general and water quantities at reservoirs, in particular, is critical for developing suitable agreements for sustainable water resource management.

Monitoring a reservoir's water resources requires keeping track of the water body area, water level, and volume. The purpose of the research is to use Landsat 8 images and SRTM elevation data to determine lake surface extent and water levels of A Vuong Lake and Dakmi 4 Lake in the Vu Gia-Thu Bon River basin at various times of the dry season from 2016 to 2020. The results indicate a significant linear relationship between the water levels estimated from DEM data and in-situ hydrologic measurements. The volume of the reservoirs changes as areas and water levels vary. The capacity of A Vuong Lake decreased the most between 2017 and 2018, reaching -58.3 km³.

SOLUTION OF LOW-COST GNSS RTK NETWORK FOR REAL-TIME DEFORMATION MONITORING

Duong Thanh Trung, Do Van Duong

Deformation monitoring is essential for structure health monitoring and early warning of natural hazards such as landslides or Tsunamis. With the requirement accuracy of millimeter or centimeter level, a network of GNSS with static surveying has been widely applied in deformation monitoring. However, the limitation of a fixed network is that it is commonly post-processed and complicated adjustment processing. On the other hand, GNSS RTK can provide real-time data at the centimeter level. However, real-time data transmission between base and rover stations is costly. The limitation in distance from the base and rover is another issue in applying GNSS RTK in vast areas. In general, deformation monitoring using GNSS at centimeter-level accuracy is currently costly. This study introduces a low-cost GNSS RTK network solution for comprehensive range deformation monitoring. An optimal filtering strategy is applied to process data to improve the system's accuracy.

MONITORING URBAN EXPANSION OF THE HANOI AREA BASED ON MACHINE LEARNING ALGORITHMS AND MULTI-TEMPORAL SATELLITE IMAGE DATA SERIES

Dang Thanh Tung, Nguyen Thanh Tung, Hoang Thi Thuy, Ta Minh Ngoc, Dinh Thi Thanh Huyen, Pham Chi Linh

This study monitors urban expansion in the center of Hanoi using GIS and remote sensing techniques based on machine learning algorithms. The results of this study show that the built-up area expanded in different directions during each period. Especially in the last 5-year period, the built-up area expanded rapidly, continuously, and mainly to the East of the center of Hanoi. In contrast, it grew much to the West in the previous period. For the past 10 years, the built-up area has increased by approximately 11.56 square kilometers, of which 5.36 square kilometers were increased from 2013 to 2018, and from 2018 to 2023, this area has increased by 6.20 square kilometers. This result can effectively contribute to urban planning and management, monitoring of environmental protection management, and sustainable development.

RESEARCH AND APPLICATION OF REMOTE SENSING AND GIS TECHNOLOGY TO ASSESS AGRICULTURAL DROUGHT EVOLUTION OVER TIME AND SPACE IN DAK HA AND KON RAY DISTRICT, KON TUM PROVINCE

Tran Van Tinh, Huynh Thi Lan Huong, Nguyen Thi Bich Ngoc

Drought is one of the most damaging natural phenomena. Due to their extensive geographic coverage, monitoring droughts using conventional systems can be challenging. In recent years, Kon Tum province has been experiencing severe droughts and water shortages in the dry season, causing significant damage to agriculture, daily life, and the local economy. This paper presented the method of using NDVI and LST indexes from band 4, band 5, and band 10 of LANDSAT 8 in the exhausted period (from February to April) in the period 2014 - 2023 to calculate the Water Supplying Vegetation Index (SWVI) and Temperature Vegetation Dryness Index (TVDI). The research results performed the remote sensing image processing and calculations on a cloud-based platform - Google Earth Engine (GEE) combined with ArcGIS software. The research results have shown that drought-prone areas correspond to regions with increased LST and decreased NDVI value. In addition, based on the scale of drought severity, two SWVI and TVDI indices have proved that most of the communes in the district are affected by drought during severe drought years. Among these, Dak To Lung commune, Dak To Re commune, and Dak Ruong commune in Kon Ray district are the 3 communes with the most severe drought. Besides the paper also built the agricultural drought map system of the research area. They will be an essential scientific basis, visually displaying the distribution of rural drought serving the local agricultural production planning to cope with drought in the context of climate change.

APPLICATION OF INTERFEROMETRIC SYNTHETIC APERTURE RADAR (INSAR) DATA IN ASSESSING LAND SUBSIDENCE RESULTING FROM HUMAN FACTORS IN NINH BINH PROVINCE, VIETNAM

Nguyen Mai Lan, Lai Hop Phong, Nguyen Duc Anh

Through the method of Satellite Interferometric Synthetic Aperture Radar (InSAR), based on analyzing the phase difference of radar complex images recorded from two different positions simultaneously observing a terrain area where the signals have the same amplitude, frequency, and wavelength but different phases, the deformation of the terrain surface in Ninh Binh province is analyzed and calculated. The preliminary results include the construction of a deformation map of the ground surface in the Ninh Binh province for the period 2020-2021, consisting of 78,077 points. The map shows areas that have been uplifted with values of 3-5 mm/year and >5 mm/year, particularly highlighting areas with significant subsidence velocities of <-10 mm/year (Kim Son and Yen Khanh districts), some areas with subsidence velocities ranging from -5 to -10 mm/year (Yen Nhan commune, Yen Mo district, Nam Binh ward, Ninh Phong district in Ninh Binh city), and subsidence values of 0 to -5 mm/year in the communes bordering between Nho Quan and Gia Vien districts. These results provide a basis for identifying the causes of terrain surface changes and proposing solutions to prevent and mitigate damages in Ninh Binh province in-depth studies continuing in the future.

CO-REGISTRATION OF PRISMA HYPERSPECTRAL IMAGERY FOR ACCURATE LAND COVER CLASSIFICATION

Qiongjie Xu, Vasil Yordanov, Xuan Truong Tran, Xuan Quang Truong, Ludovico Biagi, Maria Antonia Brovelli

The precise and prompt categorization of land cover types holds significant importance in the realm of land resource planning and management, and risk reduction. The utilization of hyperspectral satellite imagery, such as the imagery delivered by PRISMA, plays a vital role in analyzing environmental changes. Even though PRISMA products are distributed at preprocessing Level 2D (radiometrically and geometrically calibrated), the images have inherited registration errors in a few hundred meters range. Co-registration is a crucial preprocessing step before utilizing them. This study used a local co-registration method based on the optical flow estimation technique to co-register the PRISMA images using Sentinel-2 / Landsat 8-9 as references. The results showed that a careful selection of an appropriate reference image holds immense importance in the co-registration process, and the closer the acquisition time of the reference image is to the acquisition time of the image to be co-registered, the higher the quality of the co-registration results. By integrating cutting-edge machine learning techniques, the proposed co-registration approach further enhances the usability and accuracy of PRISMA products for land cover classification. It makes them a valuable source of information for applications in land management and thematic hazard studies, including scenarios such as flood monitoring and landslide analysis.

SURFACE DISPLACEMENT MONITORING UTILIZING SENTINEL-1 TIME SERIES IMAGES AND LEVELING SURVEY DATA IN HANOI'S INNER CITY

Le Minh Hang, Bui Thi Hong Tham, Tran Van Anh, Do Thi Hoai

Surface displacement occurs in many areas worldwide due to factors such as groundwater extraction and infrastructure development, particularly in large cities. The InSAR (Interferometry Synthetic Aperture Radar) technique is being researched and applied for monitoring large-scale surface movement phenomena. In this article, the authors use the PSInSAR method (Persistent Scatterer Interferometry SAR) and Sentinel-1A time series images to determine surface displacement in the inner city of Hanoi from 2018 to 2019. According to the result, the change in subsidence velocity ranges from -15.3 mm/year to +18.5 mm/year in the study area. Besides, we used 55 leveling benchmarks for monitoring subsidence in two areas, such as 43 points in the building area and 12 points in the leveling network, for assessing the precision of the PSInSAR method and monitoring the subsidence level of the inner city of Hanoi. The correlation coefficient (R) between the two datasets, including the subsidence value of PS (Persistent Scatterer) points and the leveling sites, is more significant than 0.80, with Rsqr= 0.8467 at building sites and Rsqr= 0.8589 at leveling networks. In addition, the difference in subsidence value between the two datasets is smaller in building areas than in leveling network areas.

APPLICATION OF MACHINE LEARNING TECHNIQUES IN ASSESSING THE IMPORTANCE OF SALINITY INDICATORS EXTRACTED FROM LANDSAT-8 OLI IMAGERY

Bui Duy Quynh, Hang Ha, Tran Xuan Truong, Chinh Luu

The Mekong Delta region is essential to Vietnam's economy, agriculture, and ecosystem. Salinity has significantly impacted the region's living environment, livelihoods, and productive

activities. Salinity prediction maps are essential in agriculture, environmental management, water resource planning, and ecosystem conservation since they can provide information about the spatial distribution and variability of salinity levels in a specific area. Landsat 8 satellite image data allows for extracting many salinity indicators. However, not all these indicators are necessary for salinity prediction studies. This study aims to contribute to selecting suitable input indicators to enhance the accuracy and precision of salinity prediction modeling. We utilize advanced machine learning techniques, including Bayesian Model Averaging, Extreme Gradient Boosting, Bagging, and Random Forest, to select the most suitable salinity prediction model and evaluate the importance of salinity indicators. The results obtained from the XGBoost model indicate that 18 out of the 20 input variables in the first optimal model made a significant contribution. These variables include two coordinate variables, 12 time-related variables, and four variables derived from the Landsat 8 OLI imagery. The performance evaluation of the selected salinity prediction model was conducted using statistical indicators of determination coefficient (R^2), Root Mean Square Error (RMSE), and Mean Absolute Error (MAE) for both Random Forest and Bagging models. This research establishes a theoretical framework that aids in selecting suitable indicators, thereby enhancing the precision and reliability of salinity prediction maps in the future.

UTILIZING AQUIFER STORAGE AND RECOVERY AS A SUSTAINABLE WATER SUPPLY SOLUTION FOR WATER-SCARCE REGIONS IN THE SOUTHERN PLAIN, VIETNAM

Pham Quy Nhan, Le Viet Hung, Hoang Dai Phuc, Ta Thi Thoang, Tran Thanh Le, Nguyen Quang Son

Currently, in the context of climate change and socio-economic development, the issues of water scarcity and the increasing salinization of groundwater in regions with limited water resources are of substantial concern. In response, the Prime Minister has authorized a program focused on investigating and exploring groundwater sources to fulfill domestic water requirements in these regions, with intentions to expand its implementation scope. Among the areas profoundly affected by these challenges lies the Southern Plain. Internationally and domestically, various solutions have been proposed and examined in research settings to tackle these problems. Nevertheless, specific solutions have proven costly, technically intricate, or incompatible with local customs, resulting in the inefficient utilization of resources. Consequently, the primary objective of this study is to suggest suitable and sustainable approaches to alleviate salinization in groundwater extraction within water-scarce regions of the Southern Plain in Vietnam. The research methodology encompasses comprehensive data collection and supplementary surveys to evaluate groundwater salinization's present status and root causes in water-scarce areas. One such solution is the implementation of Aquifer Storage and Recovery (ASR) technology, involving the recharging of abundant freshwater from dunes along the coastal area in the Vietnam Mekong Delta during the rainy season. This freshwater is then stored in deeper, saline upper Pleistocene aquifers and subsequently extracted during the dry season to meet water supply needs. The authors have conducted additional investigations and a thorough analysis of influencing factors based on prior research to delineate potential areas for the ASR solution using GIS overlay mapping techniques, which have been drafted into 03 regions with low, medium, and high applicable. A pilot project at the household level in My Chanh village, Chau Thanh district, Tra Vinh province, has been tested and validated as a potential area for this solution. The results from the pilot project and simulation outcomes affirm the promise of the identified potential areas for the ASR solution, warranting further investment.

BUILDING A WEB GIS FOR MANAGEMENT OF AQUATIC RESOURCES PROTECTION ZONES SEREPOK RIVER, DAK LAK PROVINCE

Nguyen Huy Anh, Nguyen Trinh Minh Anh, Tran Van Son

WebGIS is a geographic information system used on the Internet environment, which can integrate, distribute, and transmit geographic information, perform queries, and perform spatial analysis. Internet users can access and use GIS applications without installing GIS software. Databases through WebGIS technology allow many people to access simultaneously, managing data over time with large, unified capacity and without generating "versions" like traditional databases. Based on research findings, Webgis was developed to address the aquatic resource protection zones of the Serepok River in the Dak Province. Its key features include an interactive map, search, the ability to add layers, display, query, and see real-time data. Local assistance for managing natural resources and the environment is based on research findings.

DROUGHT HAZARD ANALYSIS USING SPI INDEX AND GIS-BASED ANALYTICAL HIERARCHY PROCESS IN THE CAI-PHAN RANG RIVER BASIN, SOUTH-CENTRAL COAST OF VIETNAM

Hoang Le Huong, Rex Victor O. Cruz, Juan M. Pulhin, Roger A. Luyun, Nathaniel C. Bantayan

Drought is a naturally occurring event associated with a significant decrease in water availability over a region. Changes in hydrological conditions in the area, such as climatic changes, especially rainfall, can lead to droughts and floods, which have many negative impacts on life and nature. Adaptation to natural disasters, such as drought, can be effective through an improved understanding of disasters. Understanding their effects is of widespread concern and a great challenge to researchers and policymakers. Comprehensive hazard analysis will deepen the knowledge of disasters. Many factors influence drought hazards, such as precipitation, temperature, flow and water balance, soil structure, land cover, etc. In the Cai-Phan Rang River basin, South Central Coast of Vietnam, the changes in water availability are significant concerns since they often lead to drought, forest fires, reduced agricultural productivity, poverty, and food insecurity. This study uses the Standardized precipitation index (SPI) to analyze the drought characteristics, including Probability, Intensity, and Duration; then apply the analytical hierarchy method (AHP), a multi-parameter modeling, to evaluate drought hazard in the Cai - Phan Rang River basin. The authors made the drought hazard zoning map based on the weight of the selected indicator using GIS (geographic information system). The results showed that drought has expanded and been prolonged in recent years, although the frequency has remained relatively the same compared to the past. In general, in the Cai-Phan Rang River basin, the southeast regions are at high hazard of drought due to low rainfall and high temperature. Due to topographical characteristics, although located in the vicinity of low-elevation streams, the narrow delta area in the central valley of the basin is the area with the most elevated hazard. Besides the local livelihood is closely dependent on agriculture and aquaculture, so this region should be prioritized in drought response strategies.

APPLICATION OF MULTI-CRITERIA ANALYSIS AND GIS IN CENTRALIZED SOLID WASTE DISPOSAL SITES SELECTION IN HANOI

Pham Thi Thanh Thuy, Le Thi Thu Ha, Luong Thanh Thach, Do Mai Quyen

Choosing a waste disposal site significantly impacts urban planning in terms of its economy, environment, and residents' health. Hanoi is the capital of Vietnam, a city with a large area

and a dense population. However, currently, there are only two waste disposal sites: Nam Son Landfill and Xuan Son Landfill. As a result, the amount of waste dumped into these two landfills is excessively high, leading to an overload situation. The Hanoi authority plans to construct 17 solid waste treatment areas covering an area of 430 hectares. However, there are conflicting opinions about the proposed locations for waste treatment areas, as some believe that those sites still need to be optimized. The study combined Geographic Information System (GIS) technology for spatial analysis and the Multi-Criteria Analysis (MCA) method for assessing the importance level of each criterion for the location selection to determine the most suitable location for the solid waste landfill in Hanoi. The research results indicated that the Nam Son waste treatment area was evaluated as the most optimal location. Among the remaining 16 locations proposed by the city's authorities in the planning document, 6 were deemed suitable, while the rest were considered less relevant according to the evaluation.

COMBINING REMOTE SENSING IMAGERY AND GIS TECHNOLOGY ON THE GOOGLE EARTH ENGINE PLATFORM TO CONSTRUCT MAPS AND ASSESS THE IMPACTS OF SALINITY INTRUSION ON AGRICULTURAL PRODUCTION IN BEN TRE PROVINCE

Le Thi Thuong, Nguyen Trong Nhan, Trinh Xuan Manh, Nguyen Tien Quang, Nguyen Binh Phong

Ben Tre is one of the Mekong River delta under the profound influence of saltwater intrusion, especially towards agricultural production. This study uses GIS technology and Sentinel 1 remote sensing images processed on the Google Earth Engine platform by machine-learning algorithms to generate soil salinity maps to track and assess the salinity degree in Ben Tre province. On that basis, we evaluate the influence of saltwater intrusion on agricultural production. The results show that the Random Forest algorithm is appropriate for the study area to categorize the soil salinity with the most significant coefficient: r = 0.912, and the smallest Root Mean Square Error: RMSE = 2.827, compared to other algorithms. The investigation reveals the salinity degree from high to very high (EC > 8 dS/m) that concentrates in coastal districts including Ba Tri, Thach Phu, and Binh Dai. This causes considerable damage to the agricultural production in Ben Tre province. The result of this study aims to assess soil salinity in agricultural production, placing a basis for proposing solutions to reduce the impact of saltwater intrusion on agricultural output in Ben Tre province.

ASSESSMENT OF FOREST CHANGE PATTERNS IN NORTHWESTERN VIETNAM USING REMOTE SENSING AND LANDSCAPE METRICS

Pham Minh Hai, Pham Hong Tinh, Bui Quang Thanh , Pham Manh Ha, Vu Ngoc Phan

Land-cover change, particularly habitat loss and fragmentation, poses significant threats to ecosystem services and biodiversity conservation. Major land-cover changes occurred in the late 20th century in northwestern Vietnam, but their impacts on forests have not been quantified comprehensively. This study aimed to address this gap by selecting an appropriate landscape metric index for monitoring forest fragmentation and characterizing forest transitions over time, focusing on the case study in Muong La district, Son La Province, from 1990 to 2018. The study utilized satellite images and an aggregation metric at the class level to detect land-cover change and examine forest distribution patterns over the specified period. The results revealed a significant decrease in forested areas in Muong La, with forest cover declining from 77 % to 64 %. The main drivers of forest loss were identified as the expansion of agricultural land and the construction of the Son La Dam water reservoir. The analysis of forest transitions indicated that forest areas in Muong La became more isolated and less compact from 1990 to 2008. However, by 2018, there was a trend towards increased aggregation of forested areas. These findings provide valuable insights into the dynamics of forest fragmentation and highlight the importance of monitoring and understanding such changes over time. The research results contribute to identifying the most threatened forested areas and informing prioritization efforts for natural conservation and land-use planning by the local government. By utilizing the selected landscape metric index and analyzing forest transitions, this study provides a technique for assessing the extent and location of forest threats, supporting targeted conservation efforts and sustainable land management practices.

THE RELATIVE IMPORTANCE OF DRIVING FACTORS OF AEROSOL OPTICAL DEPTH IN HANOI CITY USING REMOTELY SENSED IMAGERY AND A MULTILAYER PERCEPTRON MODEL

Nguyen Tien Thanh, Hoang Anh Huy, Vu Danh Tuyen

Aerosol optical depth (AOD), which reflects optical attenuation, poses a danger to regional sustainable development in arid and semi-arid environments, production activity, air quality, and human health. Understanding these driving factors plays a vital role in the reduction of AOD. This study investigates the relative importance of driving factors of AOD in Hanoi city (Vietnam) using remote sensing and a multilayer perceptron model. A total of nine driving factors, including natural (DEM, slope, aspect, SAVI, and MNDWI), social (population density, distances to roads, and NDBI), and meteorological (column water vapor - CWV) factors, were used to assess their effects on the AOD variation. The AOD and column water vapor (CWV) variables were first retrieved from the MODIS product. Landsat-9 Collection 2 Level 2 Science Product was then used to derive SAVI, NDBI, and MNDWI indices. The importance of driving factors of AOD variation was finally investigated using a multilayer perceptron model and Garson's algorithm. Results show a high significance of population density and DEM in the AOD variation, followed by CWV, slope, distances to roads, MNDWI, and NDBI. The importance of vegetation, approached by the SAVI, appears less influential. The findings of this study provide important insights into how to control the influencing factors of the AOD variation in urban areas.

DIFFUSION OF EXHAUST GASSES FROM WASTE-TO-ENERGY PLANT: MODEL AND FIELD MONITORING

Vu Van Doanh, Khuat Thi Hong, Le Tran Duong, Pham Phuong Thao, Ngo Tra Mai, Le Van Linh, Le Thi Trinh, Thao Ly Do, Trinh Thi Tham

Municipal solid waste (MSW) incinerators that generate electricity are one of the most effective solutions for reliable waste treatment in urban areas of Vietnam. However, the flue gas exhausted from waste-to-energy (WtE) plants may affect ambient air quality and public health. This study evaluated the emissions from the Soc Son WtE plant in Vietnam during the trial operation period using the AERMOD model and field measurements. The authors collected air samples at six locations, 200-2500 m from the plant's stack, in four different directions to measure total suspended particles (TSP), nitrogen dioxide (NO_2), carbon monoxide (CO), and sulfur dioxide (SO2) levels. The concentrations of TSP, NO_2, CO, and SO_2 extracted from the model were well correlated with those collected from the field measurements, with correlation coefficients above 0.80 for all pollutants. This research results indicate that the AERMOD model is appropriate for modeling point sources in WtE plants. The concentrations of TSP and gasses were highest at 200 - 300 meters from the plant's stack, exceeding national and international standards. The diffuse pollution of the gasses was mapped with the scenario of the maximum operating capacity of the plant. The assessment of the human health risk using the estimated concentration from the model

provided a scientific basis for air quality management and public health. The low health risk of pollutants at 1000 meters from the factory stack indicates that the plant's exhaust gas treatment system was operating efficiently.

URBAN RESIDENTIAL LAND VALUATION USING MACHINE LEARNING: A CASE STUDY OF HANOI CITY, VIETNAM

Bui Ngoc Tu, Tran Quoc Binh, Bui Thi Cam Ngoc

As the market expands, the demand for rapid and accurate land price valuation under specific market conditions becomes a prominent and socially relevant topic. Among several approaches to land valuation, machine learning has gained attention as the new method that some researchers propose to include in recent drafts of the Land Law of Vietnam. This research utilized three simple machine learning algorithms, including Decision Tree Regression, Random Forest Regression, and Gradient Boosting regression, to construct urban residential land valuation models. The training and testing datasets comprised 1082 observations across 12 districts in Hanoi City, encompassing 20 variables: Area, frontage length, location, road type, business potential, distance to the city center, distance to recreational facilities, etc. Experimental results revealed that the Random Forest algorithm outperformed the other two, exhibiting an estimated land price error of 16.95 %. Furthermore, the Random Forest algorithm has a side effect allowing for the computation of factors' importance on land price. For the collected datasets, the research demonstrated that location, road width, distance to the city center, and road type were the most influential factors on urban residential land prices in Hanoi. Conversely, factors of availability of communication infrastructure and the security environment exhibit relatively minor effects on land price. The research findings affirm the potential of machine learning in urban residential land valuation, mainly when an adequate volume of training datasets is available.

EVALUATION OF GROUNDWATER LOSS FROM THE HOLOCENE AQUIFER AT THE COASTAL SAND DUNE OF AN HOA HAI COMMUNE - TUY AN DISTRICT - PHU YEN PROVINCE - VIETNAM

Nguyen Thanh Cong, Vu Dinh Hung, Nguyen Huy Vuong, Phan Viet Dung, Pham Tuan, Vu Ba Thao, Nguyen Tiep Tan

Groundwater loss refers to the portion of fresh groundwater either flowing towards the boundaries of rivers, ponds, lakes, and the sea within a region or undergoing evaporation and saline intrusion. Groundwater loss beneath the earth's surface is one of the primary factors contributing to the degradation of water resources in terms of both quantity and quality.

In An Hoa Hai commune, Tuy An district, Phu Yen province, the coastal dune currently extends parallel to the shoreline, with an approximate surface area of 1.68 km², an average width of about 700 meters, and a length of approximately 2400 meters. The elevation of the coastal dune varies from one to eight meters above sea level. Freshwater within this coastal dune is found in the Holocene aquifer, characterized by a lithological composition of fine to medium sand with sources originating from river (amQ_2^3) and sea (mvQ_2^3) deposits. The primary source of recharge to this aquifer is rainfall, with the water table depth being shallow and varying seasonally (ranging from 0.3-2.5 meters during the rainy season and 1.1-4.0 meters during the dry season). Notably, the groundwater table in this aquifer typically lies higher than the levels of nearby rivers, the sea, and local ponds and lagoons. Consequently, freshwater within this aquifer tends to discharge towards the coastal boundaries and the margins of adjacent lagoons. Additionally, due to the shallow groundwater table, it is significantly affected by evaporation.

Based on the analysis of hydrogeological structures, groundwater monitoring, seepage measurements using seepage meters, and groundwater evaporation measurements using lysimeters over a year, we found that the natural groundwater recharge to the aquifer amounts to approximately 1,406,260.8 cubic meters. Groundwater loss due to evaporation accounts for 341,040.0 cubic meters, representing 24.3 % of the natural recharge. Groundwater loss towards the coastal boundaries amounts to approximately 413,096.8 cubic meters, constituting 29.4 % of the natural recharge.

EFFECTS OF CONSTRUCTIONS ON SUBMERGED REEFS ON WAVE CHARACTERISTICS

Ho Duc Dat, Nguyen Quang Tao, Nguyen Trung Dung, Nguyen Van Bau, Dao Hoang Tung, Dinh Quang Cuong

A submerged reef is one of the world's most unique wave reduction environments in the world because of its particular function to create high bed drag forces. However, the constructions built on offshore coral reefs, such as sea dikes or sea walls that protect national sovereignty and economic development have recently changed the wave characteristics of the submerged reefs. This study presents the change in wave characteristics on the coral reef before and after the presence of the dike. This study tested 24 experimental scenarios, including 12 scenarios with a dike and 12 scenarios without one, in a wave flume at Thuy Loi University, Hanoi. The results show a significant rise in wave heights due to the appearance of a dike on the reef. Wave heights tend to increase by 10 % to 30 % because of structure obstacles and the effect of relative shallowness. In addition, the study has also given an empirical formula to determine the incoming wave height to serve the design of construction works on the submerged reef.

FLOOD SUSCEPTIBILITY MAPPING BASED ON AHP AND RANKING METHOD WITH REMOTE SENSING AND GIS TECHNIQUES ON CA RIVER BASIN

Nguyen Tien Quang, Truong Van Anh, Hoang Van Dai, Le Thi Thuong

Flood is one of the most severe natural disasters, causing significant loss of life and property and environmental destruction, so it is necessary to build a flood susceptibility map as a basis for proposed solutions to respond to and minimize the impact of floods. The Ca river basin is the typical study basin. Research using data from some remote sensing satellite images - Shuttle Radar Topography Mission (SRTM) Digital Elevation Model (DEM), Sentinel_1,2 and flood thematic classes such as topography, geomorphology, hydrometeorological conditions, etc. were prepared and combined through a GIS-based analytic hierarchy process (AHP) and Ranking method (RM) to build flood susceptibility areas in the basin. The authors validated the two final flash flood hazard maps with the 10/2020 flood map through the Sentinel Application Platform (SNAP). The results produced a spatial distribution of flood susceptibility with four levels: low, moderate, high, and very high. The research results showed the appropriateness of the methods and the integration of remote sensing and GIS techniques showing important flood susceptibility areas in the Ca river basin.

WATER SURFACE TEMPERATURE RETRIEVAL FROM LANDSAT DATA IN GOOGLE EARTH ENGINE: A CASE STUDY AT SHRIMP FARMS IN MONG CAI CITY, QUANG NINH PROVINCE, VIETNAM

Bui Dac Thuyet

Temperature is a fundamental environmental element of all aquatic ecosystems since it affects marine organisms' survival, growth, maturation, and reproduction. It regulates many physical, chemical, and biological processes in water. Global warming, reaching 1.5°C in the near term, and more frequent and intense extreme weather events (e.g., heat waves) have caused widespread adverse impacts across regions and sectors, including shrimp farming. However, the availability of in situ water temperature data typically only represent a small portion of shrimp farms' thermal profile, and this often leads to limitation in investigating the impacts of global warming and climate change on shrimp farming. For this aim, satellite-derived water surface temperature (WST) at shrimp farms in Mong Cai City, Quang Ninh Province, Vietnam, were investigated using Landsat data in Google Earth Engine. Results showed that satellite-derived WST at shrimp farms in Mong Cai City ranged from 9.9°C to 39.0°C, mainly concentrated at 19-33°C (around 82 % retrieved WST from Landsat data acquired in 2000-2023). There was a seasonal variation of WST at shrimp farms, with monthly mean WST ranging from 18.5°C (January) to 29.7°C (September). Annual WST at shrimp farms in Mong Cai City showed an increasing trend from 2000 to 2022. A remarkable warming trend of WST was detected during shrimp farming season (often from April to October each year), which may lead to high risk for shrimp farms there. The findings of this study indicate that greater awareness of shifts in the WST regime at shrimp farms is required if this activity is sustainable in the climate change context.

CHARACTERIZATION OF TOPOGRAPHIC CHANGES DUE TO RAINFALL-INDUCED SLOPE FAILURE USING LIDAR DATA

Mitsunori Ueda, Tatsuya NEMOTO, Venkatesh RAGHAVAN

This paper introduces the characterization of changes in topographic parameters due to slope failure using DEMs of different periods. The research team calculated the topographical parameters of the slope failure site based on the DEM for two periods before and after the slope failure. The slope failure is the actual slope failure caused by heavy rainfall in 2014. The changes in the difference in DEMs before and after the collapse revealed a lot of erosion and sedimentation of less than 5 m, and shallow landslides occurred frequently. The slope angle tended to become steeper overall, both in the scarp and the main body. Comparison of before and after slope failure landforms of failure sites suggests that flat slope has been changed to hollow or spur terrain forms. Regarding the degree of convergence of the topography, the degree of convergence was higher due to slope failure, and the valley topography was more developed. Finally, the geomorphological parameters performed change vector analysis. As a result of this analysis, it has become easier to identify the collapse location and detect changes in the internal structure. The results obtained in this study will aid in the automatically detecting slope failure. Further, the studies also show good potential to generate more descriptive slope failure inventories, including location, shape, morphology, and flow direction information, which will help predict and mitigate failures.

DEVELOPMENT OF AN EFFICIENT OPEN SOURCE CODE WEB-BASED SYSTEM FOR MAXIMIZING MARINE SOCIO-ECONOMIC BENEFITS IN VIETNAM

Nguyen Tuan Anh

In recent years, Vietnam has paid great attention to marine economic development, especially in the fields of renewable energy, mineral exploitation, and aquaculture, and at the same time, has also increased activities such as environmental protection, monitoring of sea level rise disasters due to the effects of climate change, coastal erosion, natural disasters, storm, security, and defense, etc. Therefore, there have been many different survey projects done at sea. However, there still needs to be an online sea mapping system to bring out the available data to provide people across the country to use for various purposes of socio-economic development on the sea.

The article introduces the open-source Web-Map system we built based on the Leaflet online map (OSM) and our MogoDB real-time database on a VPS server located in Vietnam, allowing users to manage and upload unlimitedly positions, boundaries, regions, and maps to the Web-Map for sharing and exploiting. The database is designed to be open, and the system automatically Scales according to the input data; all data is referenced in a consistent mathematical base, users can choose the working coordinate system VN2000 or WGS-84, and they also have their own data partitions to add their data to. In addition, the system also allows users to select the sea area adjacent to the provinces, determine the depth of the chosen location, and measure the length, area, and circumference at sea. Trial version at: http://103.169.34.100/QLGiaoKVB/#/.

INTEGRATED GIS AND MODELING APPROACHES FOR DEVELOPING A FLOOD FORECAST INFORMATION SYSTEM IN THE SMALL RIVER BASIN IN VIETNAM

Truong Van Anh, Truong Xuan Quang, Duong Anh Quan, Nguyen Dinh Hoang

Flood forecasts play an essential role in accelerating an early warning system that helps to reduce the loss and damage of the exposed society and economy. In the small river basin, where the time concentration is very short compared with the flood-leading time, it requires a new approach to make an effective forecast system. This study suggests an integrated GIS and modeling approach to developing a flood forecast information system, tested on a Vietnam city: Can Tho city. Data-driven flood forecast models have been used to reduce computation time and effort via the SCADA system. The outputs of this model provide information to the text creation module to produce an automatic warning message at control locations, which is, in turn, displayed on a GIS-based interface. The result shows that the leading time increases. Therefore, the time preparation for the hazard's response also increases. As a consequence, this system helps shorten the gap between the forecast agency and the end users, who should take relevant actions based on forecast information to reduce their losses and damage.

IDENTIFICATION OF UPWELLING IN THE MARINE REGIONS OF THE SOUTHERN CENTRE OF VIETNAM BY REMOTE SENSING DATA

Phan Minh-Thu, Nguyen Van Hung, Le Thi Hai Nhu, Ho Dinh Duan, Tran Thi Hoa, Tran Thanh Ha, Truong Thi Cat Tuong, Danh Mon

Upwelling is a fascinating oceanic phenomenon that involves the upward movement of nutrient-rich deep waters to the surface, playing a crucial role in marine ecosystems. This article delves into the investigation of upwelling events in the maritime regions of the Southern center of Vietnam. The complex interplay of seasonal Monsoon winds, ocean currents, and seabed topography primarily influences upwelling in this area. The study utilizes Sea Surface Temperature (SST) data collected from satellite images to explore and understand the spatial and temporal variability of upwelling events. It employs the Topographic Position Index (TPI) method. This comprehensive analysis reveals a distinctive pattern, with upwelling events predominantly observed from May to September, peaking between June and August. These summer months harbor the most favorable conditions for upwelling processes, uplifting nutrient-rich waters from the ocean's depths to the surface layers, benefiting the local fishing industry and ecosystem health. Otherwise, the study also considers the influence of El Niño-Southern Oscillation (ENSO) and La Niña on the variation of upwelling regions and local marine ecosystem's productivity and diversity. By unraveling the mechanisms behind upwelling events and their response to climatic oscillations, the research contributes to a deeper understanding of the marine ecosystem's resilience and vulnerability to environmental changes. Ultimately, this knowledge is a foundation for responsible and informed decision-making in marine resource management for policymakers and stakeholders, aiming to safeguard the region's marine biodiversity and fisheries for future generations.

APPLICATION OF GIS TO BUILD A LAND DATABASE: A CASE STUDY OF MOC CHAU DISTRICT, SON LA PROVINCE

Tran Hong Hanh, Nguyen Tien Duong

As a distinctive means of production, the land holds significant value as a national asset. The establishment of a database stands at the core of digital transformation. A land database comprises four key components: a cadastral database, a land statistical and inventory database, a land use planning database, and a land price database. This paper aims to create a land database, enhancing the efficiency of land exploitation and management within the context of the Moc Chau mountainous district in Son La province. The study utilized methodologies such as synthesis and analysis, field investigation and surveying, and integration of multiple software systems to develop the land database. Consequently, the necessary component databases have been established, ensuring the requisite accuracy. These databases are compiled using the VBDLIS online software developed by Vietnam. This research holds practical significance, offering valuable insights for policymakers and aiding in effective land use planning. It establishes a robust data foundation, a crucial step toward operating within a digital government, economy, and society.

GEOSPATIAL APPROACH FOR ASSESSMENT OF HIGH CONSERVATION VALUE FOREST CARBON STOCKS IN TROPICAL REGIONS: A CASE STUDY IN BAC KAN PROVINCE, VIETNAM

Thi-Nhung Do, Lam-Phuong Do Dang, Thu-Ha Nguyen, Diem-My Thi Nguyen, Quang-Thanh Bui, Van-Manh Pham

The world focuses on the connection between carbon density, forest biodiversity, and their significance. The changes in land use have exceeded the level of greenhouse gas emissions into the atmosphere from all terrestrial ecosystems, emphasizing the importance of forest conservation and restoration in the battle against climate change and the protection of biodiversity. The conversion from forests to agricultural land has resulted in a significant carbon loss within the vegetation system. This study demonstrates the significance of quantifying carbon stocks and assessing the landscape at risk of fragmentation in maintaining the functionality and provision of vital ecosystem services like carbon sequestration. By utilizing optical remote sensing and Synthetic Aperture Radar (SAR) data, the research employed extracted indices from satellite images and the Cubist machine learning model to accurately predict ground-level carbon density. The results were employed to assess the spatial variations in carbon quantities based on existing forest use, exploitation, regeneration, and protection measures. The findings indicate that undisturbed primary forests have an average ground-level carbon density ranging from 150 to 200 Mg ha-1. In contrast, previously exploited forests exhibit carbon densities ranging from 50 to 100 Mg ha-1. In addition to providing information about biodiversity within the research area, mapping carbon reserves can also enhance identifying, safeguarding, and restoring high-value conservation forests. Implementing a long-term forest conservation strategy will mitigate climate change, protect biodiversity, and maintain substantial carbon sequestration capabilities, particularly in forest ecosystems within Bac Kan province.

DEVELOPING VOXEL-BASED 3D GIS FOR GHG EMISSION INVENTORIES

Kapil Chaudhery

Greenhouse Gas emissions are of critical concern under the international and national agreements on reduction of the same. Critical to this notion is the ability to establish a clear and defensible baseline of urban GHG emissions, especially from stationary sources of the built urban environment, which theoretically embodies about 35% of these emissions. The estimation, quantification, and documentation of these GHG emissions is a difficult and complex process. Recent works with building energy and building design surveys have provided insight into how data generalization models can be built to cover a large urban extent using GIS-based interpolation methods to create a representative baseline of GHG emissions across an urban landscape. Further, using cartographic modelling techniques, the layering and additionality of GHG emissions from increasing urbanization and reduction of the same through mitigative measures can provide a more authoritative documentation of baseline and changing emission inventory to demonstrate the achievement of declared emission reduction goals. The tactile understanding and cognitive acceptance/ agreement on the baseline GHG emissions, the changes (increase and decrease), represented as 3D raster grid voxels, with thematic renderings of each attribute set, provides an effective visualization and assessment tool, providing the necessary factual basis for decision making, through this visually-interactive 3-dimensional representation model. The modelling and visualization works are still currently in process however it is expected that the progress-to-date should be an effective platform for dialogue and further development.

URBAN CLIMATE RESILIENCE: MAKING INFORMED DECISIONS THROUGH SPATIAL PLANNING

Kapil Chaudhery

Vietnam has been facing increasing challenges and pressures to its economic growth from climate change-related impacts. In urban settings, the loss of economic activity, impact on livelihood, damage to the living environment, and the increasing risks of flood damage have disrupted the urban growth paradigm. Investments (and loans) in addressing flooding impacts take away from what could alternatively be resources allocated toward urban economic growth. Drawing upon examples and experience through ODA-financed projects, we clearly understand that simple acts of making urban development master plans that follow natural landforms, surficial hydrology, and ecological footprints are logical inputs in creating a more resilient urban development plan. Further, understanding the cause-effect relationship between increasing impervious areas and increasing rainfall events is an avoidable circumstance that needs to be adequately appreciated in planning. Using GIS-based spatial analysis, demonstratively through the collaborative working of governmental and consultant agencies, brings this "spatial decision" process into the normative working and potentially into the understanding of the use of nature-based solutions and blue-green infrastructure. This demonstrative and iterative working/ analytical process provides the opportunity to move from theory into practice, drawing upon geospatial technologies (in the web-based environment) to create climate-responsive spatial development plans.

INFLUENCE OF A FEW DISADVANTAGE FACTORS ON LANDSLIDE OF FILL SLOPE IN THE RESETTLEMENT AREAS OF THE SON LA HYDROPOWER PLANT: A TYPICAL CASE STUDY IN TUA THANG COMMUNE, TUA CHUA DISTRICT, DIEN BIEN PROVINCE, VIETNAM

Phung Vinh An

This paper studies the influence of inclination slope, rainfall, etc. on landslide or fill slope in Tua Thang commune, Tua Chua district, Dien Bien province, Vietnam. This is one of the typical resettlement areas of Son La hydropower plant. In this area, fill slopes were created to expand the area for building infrastructure and houses for resettled people. Fill slopes are often based on experience without field surveys or design drawings. Therefore, in recent years, in many resettlement areas of the Son La hydropower plant, many incidents of landslides of fill slopes have occurred, especially in the rainy season, which causes a lot of damage to people and infrastructure. To explain the reason causing landslides in the resettlement zones during the rainy season, this studies the influence of fill slope and extreme rainfall by analyzing seepage changes according to the pore water pressure of a typical slope. The impacts of these changes on the slope stability coefficient are determined. The rainfall used in the analysis was selected based on regular rain, which has caused many landslides in the previous periods. Calculation results show that the slope is unstable when the total rainfall reaches q= 133.8 mm from the rain beginning. Thus, it can be discovered that the inclination of slope and rainfall are the direct factors that impact the stability of the fill slope of the resettlement area of the Son La hydropower plant. When the side slopes are almost from 1:1 to 1:1.2 for most resettlement sites, rainfall is the decisive factor affecting the slope safety factor value. Also, based on the above rainfall, mathematical model, and fundamental structure, it can be found that the fill slope is almost completely saturated at the time of unsafety. From the findings, it is possible to increase the inclination of embankments or drain water in the dams to enhance the stability of these embankment surfaces. However, because the areas of the slopes were built with houses and infrastructure, it takes work to change their inclination. Therefore, the drainage of slopes is the general solution to enhance fill slope stability for the Son La hydropower plant resettlement sites.

IMPACTS OF HUMAN ACTIVITIES IN THE UPSTREAM AREA OF THE BLACK RIVER IN CHINA ON THE FLOW TO VIETNAM USING HYDROLOGICAL MODELS AND REMOTE SENSED DATA

Khuong Van Hai, Nguyen Tien Giang, Nguyen Cao Don, Hoang Diem Quynh

Hydrological modeling plays a crucial role in comprehending the fundamental processes in river basins associated with the effects of climate variability and human activities on water resource availability. This study developed a high-resolution (0.05°, ~5 km) hydrological modeling for the Black River based on the Variable Infiltration Capacity (VIC) model from January 1980 to December 2018. The results of this study show that the approach to studying the change of hydrological regime on the Black River under the impact of urbanization in the upstream area of China can be applied to regions lacking information and in-situ observation data. The study identifies human factors as the causes behind changes in the flow regime of the Black River in Vietnam. It quantifies the resulting alterations in water availability and hydrological processes, providing insights into the impacts of human activities on the basin.

EVALUATING THE SCOPE OF COASTAL EROSION IN THE MEKONG DELTA FROM BAC LIEU TO CA MAU CAPE USING REMOTE SENSING AND GIS

Quynh Le, Duyen Nguyen, Long Bui Ta

The coastal strip from Bac Lieu to Ca Mau is the gateway to the Mekong Delta region and is essential for the country's economic development. However, this area is currently facing increasingly complex landslide threats. Developing shoreline maps is necessary for environmental monitoring in the area. The research uses remote sensing methodology, GIS tools, and ENVI software to extract the shoreline over the years and then analyze this area's accretion/erosion situation. The results showed that erosion along the coasts of Bac Lieu and Ca Mau over the three years 2021 - 2023 is becoming increasingly complicated. Among them, the most erosion area occurred in Ngoc Hien district, Ca Mau province. While the coasts of Bac Lieu province tend to accrete, such as Dong Hai district and Bac Lieu city, erosion occurs in Dat Mui commune (Ngoc Hien district). The application of remote sensing and GIS methods helps bring helpful information to help local authorities find the best solutions to prevent and limit coastal erosion, as well as in regulation work for coastal zone planning and management.

ESTIMATING ABOVE GROUND MANGROVE BIOMASS OF THE NHA PHU LAGOON USING MACHINE LEARNING AND UAV IMAGERY

Le Canh Tuan

Karst poljes is a special landform, formed in the karst regions. This is a concentrated residential area and a critical economic region. The characteristic of Karst regions is that surface water is rare, but groundwater is abundant. The Karst poljes often occur floods, water pollution, rock falls, collapse, erosion, Etc. Researching typical karst landforms, warning of adverse effects, and serving socioeconomic development is essential to specializing in karst geology. The authors present a method to determine karst poljes on Google Earth images. This research result has been our field test applications.

LAND COVER CLASSIFICATION FROM REMOTE SENSING IMAGERY: MACHINE LEARNING APPROACH

Hoa Thanh Thi Pham, Ngoc Quang Vu, Phuong Nam Thi Doan, Nghi Thanh Le

With the rapid development of technology, the term Machine Learning (ML) has become familiar in many fields, for example, education, business, data mining, image processing, and recognition. There are a variety of ML methods that have brought high accuracy for image classification. Therefore, the study proposes a Random Forest (RF), Support Vector Machine (SVM), and Classification and Regression Tree (CART) for extracting land cover in Quang Binh province, Vietnam. Sentinel-2 SR (Surface Reflectance) was collected in the Google Earth Engine platform. Images were acquired in August 2021 with cloud cover less than 30 %. Samples were randomly distributed in the study area and divided into 70 % for training and 30% for validating. The results showed the ability to use Sentinel-2 and Machine Learning in determining the state of land cover.

COASTAL INUNDATION IN THE NORTH CENTRAL REGION OF VIETNAM: A STUDY BY SUWAT MODEL COMBINING OBSERVATIONS DATA OF SATELLITE IMAGERY AND WATER LEVEL AT STATION

Pham Van Tien, Nguyen Ba Thuy, Nguyen Kim Cuong

Coastal inundation is a common natural catastrophe of this type in Vietnam, which causes economic and life loss in the coastal area. Coastal inundation is mainly due to high tides and storm surges and is increasingly common in rising sea levels due to increased typhoon activity. This paper presents the study results of coastal inundation in the North Central region of Vietnam, the simulations done by the SuWAT model. The model results are verified with the observed data at the hydrological station and the observed flood data from satellite images.

OPTIMAL PARAMETER SELECTION FOR SMRF FILTERING OF LIDAR POINT CLOUD DATA IN VARIOUS TERRAINS OF VIETNAM

Trung Anh Tran, Hong Hanh Tran, Hai Au Luu, Manh Tuan Quach

The LiDAR point cloud classification for obtaining the ground surface through SMRF (Simple MoRphological Filter) filtering is relatively simple to implement. However, choosing the optimal parameters for this filter takes a lot of work. This article researches and tests the appropriate input parameters for the SMRF filter using LiDAR point cloud data from Vietnam, with the primary objective of achieving the most accurate classification of land surfaces. The SMRF method utilizes five parameters: the cell size of the minimum surface grid, a percent slope value, an elevation difference threshold, a slope threshold, and a maximum window size. Various types of terrain exist, including areas with dense or sparse forests, different types of trees, regions with residential structures, areas with significant elevation variations, mixed terrains, and more. Experimenting with input parameters allows filtering SMRF in these terrain types and selecting the most suitable parameters for each type. Subsequently, the ground point cloud is continually detected, and noise and outlier points are removed to construct the most precise digital terrain model. This process is facilitated by the author's application software named, ApLAS.

HUMAN HEALTH STRESS AND EMOTION CHARACTERIZATION USING FACIAL IMAGE INTERPRETATION

Vineet Singh, N. K. Tripathi, Kathiravan Srinivasan

Facial emotion recognition is fundamental in computer vision and human-computer interaction, with applications ranging from social robotics to affective computing. Deep-learning techniques have demonstrated remarkable success in this domain in recent years, outperforming traditional machine-learning approaches. This paper comprehensively reviews facial emotion recognition using deep learning methodologies. The review begins by providing an overview of the challenges and importance of facial emotion recognition. It explores the role of facial expressions in conveying emotions and the significance of accurately recognizing and interpreting these expressions in various real-world scenarios.

Next, the paper delves into the core concepts of deep learning, specifically convolutional neural networks (CNNs), recurrent neural networks (RNNs), and their variants, which have been extensively applied to facial emotion recognition. It discusses the architecture, training procedures, and optimization techniques associated with these deep learning models.

Furthermore, the review discusses the widely used benchmark datasets for facial emotion recognition and the evaluation metrics employed to assess the performance of deep learning models. It highlights the limitations and challenges faced in these datasets and proposes potential solutions and future directions to address these issues.

The paper also provides an in-depth analysis of various feature extraction techniques, including handcrafted and learned features. It explores the advantages and limitations of different feature representations and discusses the integration of multiple modalities, such as facial landmarks, facial action units, and audio, for enhanced emotion recognition.

Moreover, the review presents an overview of state-of-the-art deep learning models for facial emotion recognition, including convolutional neural networks (CNNs), recurrent neural networks (RNNs), and their combinations. It discusses recent advancements, such as attention mechanisms, transfer learning, and generative models, and their impact on improving recognition accuracy and robustness.

Lastly, the review summarizes the essential findings and identifies potential research directions to overcome the existing challenges in facial emotion recognition using deep learning. It emphasizes the need for more extensive and diverse datasets, improved domain generalization, and ethical considerations in designing and deploying facial emotion recognition systems. Overall, this comprehensive review provides researchers and practitioners with a valuable resource to understand the advancements, techniques, and prospects of facial emotion recognition using deep learning methodologies.

SEAMLESS INTEGRATION OF REAL-TIME LOCATION SERVICE AND VN2000 COORDINATE SYSTEM FOR DAILY ACTIVITIES IN VIETNAM

Nguyen Tuan Anh, Phung Trung Thanh

The integration of coordinates of locations with maps, time, and attribute values at places, as well as their variation on digital platforms, makes it useful for about 90 % of activities, including infrastructure construction, transportation, environment, trade, services, production, and socio-economic development of each country. Therefore, in the context that hand-held smart mobile devices built-in GNSS have become popular with every citizen and 4G wireless internet has covered most of Vietnam's territory, we need to take advantage of these advantages to build a straightforward, convenient, easy-to-use system that all people can access and use to serve their

specific daily needs in Vietnam in the VN2000 coordinate system.

The article introduces such a system of ours, including Cloud Realtime Database services on servers and Android mobile applications to create an IoT infrastructure that connects users and acts as a virtual assistant to help citizens and businesses determine VN2000 coordinates Geoid and ortho height, save locations with time information, ortho height, and attribute values at any point, and easily manage and save information. Support the management, maintenance, development, and effective exploitation of a nationwide network of coordinates and elevations. Find Landmarks according to the radius around a location and navigate to the landmarks in the field. The latest Map and Satellite Image section allows measuring, locating land parcels and importing KML, PNG, JPG drawing files, and looking up information on land use planning in all provinces of Vietnam.

This system is also used in a variety of other activities such as the management of BTS stations, management and monitoring of environmental pollution points, points of natural disasters, geological hazards, marking and defining maritime boundaries, and marking and searching tasks related to the evolution of location, value and time on the map background. There are nearly 100 thousand users in all regions of Vietnam, with almost 1000 positive feedbacks. The application can be downloaded for free on Android CHPlay at: https://play.google.com/store/apps/details?id=com.nta.dodacbando. We plan to carry out a digital transformation in the field of survey and mapping in Vietnam, helping with the specific practical activities of each citizen.

GEOLOGICAL LINEAMENT EXTRACTION USING SATELLITE IMAGE AND DEEP LEARNING TECHNIQUE

Xuan Luan Truong, Do Thi Hang, Van Anh Tran, Xuan Quang Truong

Geological lineaments are essential for studying the formation of minerals such as gold. This study uses traditional and deep learning techniques to detect lineament from remote sensing data. The study area is in Thanh Hoa Province, where gold minerals are found. Optical and SAR satellite images such as Sentinel-1 and Sentinel-2 are employed to extract lineament. The result is evaluated by comparing the geological fault map of the study area.

PUBLIC AWARENESS CORK PLANTING TO SUPPORT THE MANGROVE FOREST AND ITS ECOLOGICAL PROTECTION AGAINST CLIMATE-RELATED EXTREME WEATHER EVENTS INVOLVING THE LOCAL POPULATION IN TAN NINH COMMUNE, QUANG NINH DISTRICT, QUANG BINH PROVINCE

Vo Thi Nho, Hoang Anh Vu

65-75 % of mangrove forests and significant cork oaks have been destroyed for shrimp farming. Shrimp farming is now closed for economic reasons, but the loss of ecological function has remained as the mangrove forests have not been restored. However, the forests are protected against storms, especially storms and floods. Given the intensification of extreme weather events, which are expected in the context of climate change, the absence of this protective function is particularly problematic. In addition, the area is exposed to an increased risk of landslides, soil degradation, and saltwater advance. Parts of the destroyed forest will be reforested with 1000 cork oaks. The cork oak is a central part of the mangrove forest and contributes significantly to the recovery of the entire mangrove forest. Afforestation focuses on public relations and the climate change context. This study involves the local population, Buddhists, and monks of the Quang Xa Temple who once stood in the middle of the cork oak forest. With the pursuit of the goal of adaptation to climate change, co-benefits such as ecotourism and the revaluation of the place as a spiritual site are also linked.

INVESTIGATING SPATIOTEMPORAL VARIATIONS OF SUSPENDED PARTICULATE MATTER AND TURBIDITY IN LAKES WITH SENTINEL-2 IMAGERY: THE CASE OF VARESE LAKE (ITALY)

Afshin Moazzam, Maria Antonia Brovelli, Mariano Bresciani

The primary emphasis of this investigation centers on the application of Sentinel-2 satellite imagery to evaluate water quality indicators, focusing on the concentration of suspended particulate matter (SPM) and turbidity. This analysis is based on optical models and conducted within Lake Varese's context. The research methodology encompasses the initial processing of satellite images utilizing ACOLITE software to perform atmospheric correction. The analysis of the results involves a detailed inspection of the spatial patterns and trends detected within the maps illustrating SPM concentration and turbidity. Furthermore, the study investigates relationships between the derived parameters and regional local precipitation patterns. In summary, the integration of Sentinel-2 satellite imagery, atmospheric correction through ACOLITE, and the application of bio-optical models for assessing SPM concentration and turbidity has demonstrated effectiveness in evaluating water quality parameters within Lake Varese. The spatial distribution maps, temporal patterns, and correlation analyses yield valuable insights into this lake's evolving water quality dynamics. These findings enhance our comprehension of the ecological condition of Lake Varese and offer support for informed decision-making in the realm of water quality management.

SOLUTIONS TO ENHANCE ACCURACY WHEN USING UAVS TO COLLECT AND CONSTRUCT SPATIAL DATA FOR THE CREATION OF EXTREMELY LARGE-SCALE MAPS IN THE URBAN AREA

Tran Ngoc Huyen Trang, Le Van Trung

Ho Chi Minh City is the largest city in Vietnam that is interested in and pioneered by the government to become a smart city in the future. The application of solutions to support the collection, construction, and updating of spatial databases, creating the basis for urban management, becomes very necessary. Uncrewed Aerial Vehicles (UAVs) are experiencing strong growth in many fields, especially spatial data collection. Problems arising when collecting and processing UAV images in urban areas include distortion in some areas on the ortho mosaic, accuracy unsuitable for creating huge scale maps (1/200, 1/500), the boundary between adjacent objects needing to be clarified, etc. The authors have conducted flight test shooting with many flight altitudes, different shooting angles, and changing the number of Ground Control Points (GCPs) layouts, using and not using the UAV's RTK receiver mode. From the experimental results, we propose solutions to improve the accuracy of data collection and image processing by UAVs.

SPATIAL PREDICTION OF RAINFALL-INDUCED LANDSLIDES USING FAST DECISION TREE LEARNER BY REDUCED ERROR PRUNING (REP) FOR THE MOUNTAINOUS AREA OF NGUYEN BINH COUNTY, CAO BANG PROVINCE, VIETNAM

Nguyen Quoc Phi, Phan Thi Mai Hoa, Nguyen Thi Cuc, Nguyen Minh Quang, Nguyen Thu Phuong, Phi Truong Thanh, Truong Xuan Quang

Decision tree learning is one of the most successful learning algorithms in data mining approaches due to its attractive features, such as simplicity, comprehensibility, no parameters,

and handling mixed-type data. Among decision tree algorithms, a fast tree-growing algorithm without a substantial decrease in accuracy and a significant increase in space complexity as in landslide studies. The quick decision tree learner by Reduced Error Pruning (REP) was used for landslide susceptibility mapping in the Nguyen Binh County of Cao Bang province. In the database, 306 landslides were plotted and classified into training (70 %, 214) and testing (30 %, 92 landslides) subsets randomly to train and validate the models. A total of 12 landslide conditioning factors were considered as model inputs, and the results of each model were categorized under four susceptibility classes. The receiver operating characteristics (ROC) curve and five statistical measures were used to evaluate the model's performance. Experiments show that the REP tree performs competitively with C4.5 in accuracy, with 92.38 % correct prediction of the area under the curve of 0.935, and the running time is significantly faster than C4.5. Indeed, it is as short as naive Bayes but outperforms naive Bayes in accuracy according to the landslide database in the study area. The research shows that REP could be a practical decision tree algorithm used in natural hazard studies with large amounts of data, and the result is helpful in the decision-making process of land use planning.

LANDSLIDE SUSCEPTIBILITY ASSESSMENT USING HYBRID MACHINE LEARNING MODELS: A CASE STUDY OF CAU RIVER WATERSHED IN THAI NGUYEN, VIETNAM

Tran Thanh Thuong, Nathaniel C. Bantayan, Canesio D. Predo, Cristino L. Tiburan Jr., Vladimir Y. Mariano

Landslides are a natural hazard frequently occurring in mountainous areas and have been responsible for numerous fatalities and injuries. They were considered the primary cause of natural disasters leading to loss of life in Asia. In Vietnam, landslides have become increasingly common in recent years, particularly in mountainous regions, posing a direct and significant threat to human life and property. Landslide susceptibility maps are valuable tools for mitigating this risk, improving land-use planning, and establishing early warning systems. Still, they require continuous updating and further development with practical applications to address the complexity of landslide events. Given the importance of landslide susceptibility maps, this study aimed to assess landslide susceptibility using novel hybrid machine learning (ML) techniques. Three ML models have been developed for landslide susceptibility prediction, including KNNSVM, KNNRF, and KNNRFMLP. These models have been constructed based on K-nearest neighbors (KNN), support vector machine (SVM), random forest (RF), and multilayer perceptron (MLP) algorithms. To develop the models, the study has collected nine conditioning factors (slope, elevation, relief degree of land surface, drainage density, lithology, soil, land use land cover, rainfall, and normalized difference vegetation index) that have been based on the correlation between historical landslide occurrences and specific geo-environmental conditions in the study area. The relative importance of these factors has been determined by excluding that factor and then calculating the overall accuracy of the model. The difference in overall accuracy between the models with and without the conditioning factor indicates the quantitative importance of the factor. The performance of the models has been assessed using different statistical measures, including accuracy, sensitivity, specificity, and the area under the receiver operating characteristic (ROC) curve (AUC). Typically, higher values of ACC, SEN, SPE, and AUC indicate better performance of the models. The results have shown that the KNNRFMLP model has been the most appropriate model with the best performance, with an accuracy of 85.33 %, sensitivity of 85.71 %, and specificity of 83.33 %.

Additionally, the KNNRFMLP model has achieved the highest AUC value (86 %.), indicating that it has been the most effective model for predicting landslide susceptibility. Based on the results, the KNNRFMLP model has been used to produce a landslide susceptibility map for the study area. The final results represented 41,973 ha (14.94 %) in very high-susceptibility areas, 14,258 ha (5.08 %) in high-susceptibility areas, 22.159 ha (7.89 %) in moderate-susceptibility areas, 48,334 ha (17.21 %) in low-susceptibility areas and 154,129 ha (54.88 %) in very low-susceptibility areas. This landslide susceptibility map is a valuable tool for analyzing and evaluating landslide risk at the study site, and it provides practical information for land-use planning and early warning systems. This study has provided a feasible approach for assessing landslide susceptibility using hybrid ML models. The results have demonstrated the effectiveness of the KNNRFMLP model and suggest that it has practical implications for evaluating landslide risk in other mountainous regions with similar geo-environmental conditions. Continuously updating and improving landslide susceptibility maps using advanced ML techniques is necessary to mitigate the risk of landslides and protect human life and property in areas susceptible to this natural hazard.

ROCK DETERIORATION RISK ASSESSMENT FOR LIMESTONE GEOSITES AT DAM THUY AREA OF NON NUOC CAO BANG GEOPARK, VIETNAM USING THE TOPSIS APPROACH

Nguyen Quoc Phi, Vu Thi Phuong Thao, Nguyen Thi Hoa, Le Huynh Duc, Tran Thi Thu Ha, Phi Truong Thanh, Van Duc Tung

The geosites at the Dam Thuy area of Non-Nuoc Cao Bang geopark are a valuable natural heritage for their scientific values and their landscape contexts. However, the risk of rock deterioration at those limestone geosites has yet to be studied. The area's geosites (caves, waterfalls, and natural monuments) are located along the limestone slopes, often highly fractured and exposed to the intense activity of aggressive exogenous agents, which occur mainly with the detachment and fall of blocks highly variable in size. The rock mass generally shows a high degree of fracturing, and evidence of previous block falls is also visible all over the study area. Several blocks of different sizes appear to be in conditions of high instability and in proximity of falling. This study aims to evaluate the performance of the widely used multi-criteria decision-making (MCDM) model of Technique for Order of Preference by Similarity to Ideal Solution (TOPSIS) to produce a rock deterioration risk map in the Dam Thuy area of Non-Nuoc Cao Bang geopark, Vietnam. Nine casual layers, including slope angle, slope aspect, lithology, bedding plane, weathering rate, fracture density, distance to faults, rainfall, and land use, were used to produce the rock deterioration map. The weights of the causal factors were also calculated using the TOPSIS method, and the final risk map plays a vital role in integrated geopark management, especially in preserving geosites in hazard-prone areas.

THE ROLE OF GROUNDWATER RECHARGE SOURCES IN GROUNDWATER EXPLOITATION IN THE RED RIVER DELTA PLAIN, VIETNAM

Viet-Hung Le, Quy-Nhan Pham, Tran-Trung Dang

The Red River delta plain, the second largest delta in Vietnam, covers an area of 14,860 km² and is home to over 22.5 million inhabitants. Predominantly extracted from Quaternary sedimentary aquifers, Groundwater amounts to a total discharge of approximately 3 million m3/day. However, some regions, such as Hanoi and Nam Dinh, have shown signs of over-exploitation, leading to potential depletion, subsidence, saltwater intrusion, and water pollution. While several studies have attempted to estimate groundwater recharge in the study area, uncertainties and fragmented information persist, hindering a comprehensive understanding of groundwater recharge sources. Therefore, this study aims to clarify groundwater recharge sources and their roles in groundwater exploitation. We thoroughly reviewed and compared previous studies by examining complementary

groundwater recharge sources from the Red River system and the delta's edge. This research identified a vital groundwater recharge source from rain, irrigation water, and even wastewater, referred to as "groundwater recharge from the surface". We utilized various satellite images and interpreted different thematic layers to assess the groundwater recharge potential. A Geographic Information System (GIS) was employed for zonation analysis and thematic layer integration. Field trips and water sampling were also conducted, including chemical and radioactive 3H analysis. Groundwater recharge potential was verified using ground recharge rates estimated through isotope analysis, dividing the Red River delta plain into three zones with low, moderate, and high groundwater recharge potential (77, 280, and 440 mm/year, respectively).To evaluate the role of groundwater recharge sources in the current groundwater extraction, we employed MODFLOW software. Based on calibrated and validated flow and solute transport models, we used the "Zone Budget" module to determine the contribution of groundwater recharge sources to Quaternary sedimentary aquifers. The results indicate that surface groundwater recharge occurs throughout the year, with the highest contribution during the rainy season (85 %) and a lower contribution during the dry season (14.20 %). Recharge from the Red River system is predominant during the rainy season, accounting for 12.05 % to 20.71 % of the total recharge. Conversely, groundwater recharge from the bedrock at the edge of the plain and the water discharge to the sea from Quaternary sedimentary aquifers occur throughout the year but in smaller quantities. This study provides valuable insights into the groundwater recharge sources in the Red River delta plain and their significance in sustaining groundwater extraction in the region. The findings can aid in developing sustainable groundwater management strategies to mitigate the potential adverse effects of over-exploitation.

LANDSLIDE SUSCEPTIBILITY PREDICTION BASED ON SLOPE-UNIT MAPPING AND ENSEMBLE MACHINE LEARNING MODELS

Dong Khuc Thanh, Van Anh Tran, Xuan Quang Truong

Landslides are natural hazards that cause significant damage to infrastructure and human livelihoods. Machine learning and geospatial data approaches are believed to yield robust results in landslide prediction. This study employs an integrated method by considering multiple factors based on slope-units in Van Yen district, Yen Bai province, Vietnam. Thirteen factors are used to assess their relationships with landslides, including Elevation, Slope, Aspect, Plan Curvature, Profile Curvature, Lithology, Landcover, Distance to Road, Distance to River, Distance to faults, Topographic Wetness Index, Flow Accumulation, and Rainfall. Four ensemble machine learning models, namely Random Forest (RF), Bagging-based Support Vector Machines (BSVM), Gradient Boosting (GB), and Adaboost (AB), are utilized to analyze landslide susceptibility. Performance evaluation metrics such as sensitivity, specificity, and Receiver Operating Characteristic (ROC) curve are employed to compare the performance of these models. Based on the comparison of Area Under the Curve (AUC) values, the results indicate that all four models are suitable for mapping landslide susceptibility by slope-units in the study area, with the random forest model yielding the best performance.

MONITORING AND ASSESSMENT OF REMOTE SENSING ECOLOGICAL INDEX CHANGES IN CAN THO CITY, VIETNAM

Nguyen Thi Hong Diep, Nguyen Trong Nguyen, Duong Co Hieu Nguyen Thi Thanh Huong

The Remote Sensing Ecological Index (RSEI) is one of the widely used indices for evaluating eco-environmental quality. In this study, the Remote Sensing Ecological Index (RSEI) was a calculation of four ecological elements, including greenness (NDVI), wetness (WET), heat (LST), and dryness (NDBSI) based on remote sensing data taking Landsat 8 OLI period from 2015 to 2020. Next, the study normalizes the values of the ecological elements and estimates the RSEI formula according to Principal Component Analysis (PCA) methods. The calculated results of RSEI in 2015 and 2020 reached an average value of 3.66 and 3.60, respectively. The ecological quality (EQ) decreased from 88.78 % in 2015 to 84.75 % in 2020, with the qualification range from good to very good and increasing from 1.97 % in 2015 to 3.49 % in 2020 from very poor to poor. The average RSEI decreasing and the ecological level proportions changing indicated the environmental environment quality has a reducing trend in the city in 2015 - 2020. The results of RSEI effectively reveal the ecological benefits of surrounding environments in the cities, which lead to a more accurate and comprehensive basis for implementing environmental protection policies and development towards local sustainability.

MANGROVE FOREST TYPES MAPPING USING RADAR AND OPTICAL DATA INTEGRATION WITH THE RANDOM FOREST (RF) ALGORITHM FOR CA MAU PROVINCE, VIETNAM

Tran Dang Hung, Pham Hong Tinh, Pham Minh Hai, Nguyen Thanh Bang, Giang Hoang Hiep, Pham Quang Hiep

Mangrove forests, with their unique root structures, play a crucial role in soil retention and coastal protection against erosion and wave impacts. Additionally, they provide a range of ecosystem services, mitigate the effects of climate change, and maintain water quality. Remote sensing technology has been widely demonstrated as an excellent tool for mapping mangrove ecosystems. However, accurately classifying different types of mangrove forests using remote sensing imagery remains a challenge. Clouds can easily affect optical data, while radar data is often difficult to interpret. Combining both datasets for mangrove classification can significantly improve the accuracy of the classification results. The purpose of this study is to develop a classification method using Google Earth Engine (GEE) that simultaneously utilizes ALOS-2 radar satellite data and optical Sentinel-2 data with medium spatial resolution to map different types of mangrove forests in Ca Mau province using the Random Forest (RF) algorithm. The classification results indicate that dominant types of mangrove forests in the province, such as Avicennia and Rhizophora, can be classified quite accurately, along with aquaculture, residential areas, and agriculture classes, resulting in an overall accuracy of 88 %. The classification becomes less reliable for mixed mangrove forests or locations with limited survey data.

ESTIMATING ABOVE GROUND MANGROVE BIOMASS OF THE NHA PHU LAGOON USING MACHINE LEARNING AND UAV IMAGERY

Nguyen Hoang Thai Khang, Do Lan Phuong, Tran Thi Quynh Thi

This study estimates the aboveground biomass of mangroves in Nha Phu Lagoon using Unmanned Aerial Vehicles (UAVs) and a machine learning approach with a random forest

regressor model. Indicators such as vegetation index, canopy height, texture index, and cloud index were used to measure biomass. The main species in the mangrove community are Rhizophora apiculata and Rhizophora mucronata, with average heights of 10.56 m and 3.45 m, respectively. The developed random forest model accurately estimates aboveground biomass with an R-squared value of 0.8321 and a root-mean-square error of 23.8645 Mg/ha. Estimated aboveground biomass ranges from 37.26 to 181.82 Mg/ha, with an average value of 94.35 Mg/ha. The study highlights a trend in biomass distribution within the Nha Phu Lagoon, with biomass levels in the northern region gradually decreasing towards the southern part. The technologies of UAVs and machine learning combination provide valuable insights into the biomass variations of the dominant mangrove species, contributing significantly to our understanding of ecosystem dynamics and aiding conservation efforts.

APPLICATIONS OF REMOTE SENSING IN MONITORING LAND SURFACE TEMPERATURE (LST) IN HO CHI MINH CITY

Nguyen Huu Thanh, Pham Thi Mai Thy, Lam Dao Nguyen

Today, remote sensing technology has been applied in many fields, supporting the monitoring and predicting of climate change, the environment, the Earth's surface, classifying the land cover/ land use, etc. This technique could save time, money, and human labor. In this research, remote sensing technology is applied to monitor the changes in land surface temperature (LST) in Ho Chi Minh City from 1990 to 2022, using the Landsat 5 TM (Thematic Mapper) satellite with band 6 for the first period, from 1990 to 1999. MODIS images (MOD11A2.061) were acquired from 2000-2022; they provide information on land surface temperature for daytime and nighttime in a year so that it could give more precise temperature data of a region throughout the year. This research was conducted with many images over an extended period of over 30 years. Therefore, it was processed and accessed in the Google Earth Engine platform, utilizing JavaScript. The results showed that the LST maps from MODIS and Landsat 5 images have recorded significant alterations over the years in Ho Chi Minh City. These findings demonstrate the usefulness of remote sensing in monitoring land surface temperatures in urban areas.

LANDSLIDE SUSCEPTIBILITY PREDICTION BASED ON SLOPE-UNIT MAPPING AND ENSEMBLE MACHINE LEARNING MODELS

Dong Khuc Thanh, Van Anh Tran, Xuan Quang Truong

Landslides are natural hazards that cause significant damage to infrastructure and human livelihoods. Machine learning and geospatial data approaches are believed to yield robust results in landslide prediction. This study employs an integrated method by considering multiple factors based on slope units in Van Yen district, Yen Bai province, Vietnam. Thirteen factors are used to assess their relationships with landslides, including Elevation, Slope, Aspect, Plan Curvature, Profile Curvature, Lithology, Landcover, Distance to Road, Distance to River, Distance to faults, Topographic Wetness Index, Flow Accumulation, and Rainfall. Four ensemble machine learning models, namely Random Forest (RF), Bagging-based Support Vector Machines (BSVM), Gradient Boosting (GB), and Adaboost (AB) are utilized to analyze landslide susceptibility. Performance evaluation metrics such as sensitivity, specificity, and Receiver Operating Characteristic (ROC) curve are employed to compare the performance of these models. Based on the comparison of Area Under the Curve (AUC) values, the results indicate that all four models are suitable for mapping landslide susceptibility by slope units in the study area, with the random forest model yielding the best performance.

DIGITAL QUANTIFICATION OF ENVIRONMENTAL CHANGE ALONG HANOI'S FIRST URBAN RAILWAY

Nguyen Dinh Minh, Nguyen Viet Huong

Urban railways are crucial in solving public transport problems in densely populated urban areas. However, their impacts on humans and the environment must be assessed and managed effectively using different methods for sustainable development. In recent years, several urban railway development projects have been carried out in the two largest cities in Vietnam, namely Hanoi and Ho Chi Minh city. In Hanoi, the capital of Vietnam, the first urban railway completed and entered into operation in 2021 is called Metro Cat Linh-Ha Dong. It passes through the center of Hanoi and is anticipated to enhance public transportation in the wards and districts of the city with the highest population densities. For sustainable development, the environmental change caused by this railway's construction and operation must be quantified and managed with modern methods.

Aim: The digital quantification of environmental change along Hanoi's first urban railway aims to map, measure, and monitor the ecological impacts of the construction and operation of the railway using digital data, tools, and techniques such as satellite remote sensing and geographic information systems (GIS).

Concepts: Environmental change along an urban railway can be defined as the environmental alterations brought on by the construction and use of an urban railway. These changes could be physical, biological, or chemical and affect ecological components, including the air, water, soil, and ecosystems. It is essential to comprehend these changes and their implications to mitigate environmental harm and enhance sustainable development. Digital quantification of ecological change is the measurement and analysis of environmental changes through time using digital tools and techniques such as remote sensing, GIS, computer modeling, and monitoring devices.

The approach to the digital quantification of environmental change along Hanoi's first urban railway is data-driven. It focuses on acquiring multispectral, multitemporal digital satellite imagery, using digital image processing and GIS techniques to map, measure, and monitor the environmental impacts of the railway.

The use of digital tools for the analysis of optical and thermal satellite imagery such as Landsat, ASTER, and Sentinel helps to compute the changes in normalized difference vegetation index (NDVI), normalized difference water index (NDWI), and land surface temperature along Metro Cat Linh-Ha Dong before, during and after its construction and operation.

The digital quantification of environmental change along Hanoi's first urban railway is a practical approach to understanding the ecological impacts of urban infrastructure development projects. The use of digital satellite imagery, tools, and techniques, such as digital image processing and GIS, allows for a quantitative assessment of the impacts of the railway on the environment and can inform the development of targeted mitigation strategies.

The digital quantification of environmental change along Hanoi's first urban railway is an essential contribution to sustainable urban development, providing valuable insights into the environmental impacts of infrastructure projects and informing decision-making for long-term sustainability. The study enriches the literature on the ecological applications of satellite remote sensing and GIS for sustainable development in the age of digital transformation.

AUTOMATIC DETECTION AND DELINEATION OF SURFACE WATER BODIES USING OPTICAL AND RADAR IMAGES

Le Thi Phuong Hong, Vu Anh Minh, Dinh Nhat Quang, Ho Sy Tam

The requirement to improve accuracy in the operation and management of reservoirs includes asking for regularly and continuously updated data, and the water surface of reservoirs is one of the critical data that needs to be observed and monitored daily. Nowadays, remote sensing image interpretation has been used to determine the surface area of water, thanks to its advantages in comprehensive coverage, high revisit frequency, good historical data, low cost, and sometimes free access. Methods for automatic detection and delineation of the water surface from remote sensing images can be divided into Threshold segmentation and Image classification. While threshold segmentation is mainly based on spectral knowledge to construct various classification models and water body indices to extract water bodies, image classification synthesizes the image's spectrum, texture, and spatial characteristics. It fully uses the ground features' spectrum, shape, structure, and texture to extract water body information. Remote sensing images are divided into two types: optical photos and radar images.

Many methods have been developed regarding the threshold segmentation method to detect and delineate water bodies from optical remote sensing images by adopting water indices such as NDWI, MNDWI, AWEI,... The evaluation of the most suitable thresholds for water surface determination is based on the principle that the reflectivity of water is lower than that of other soils in the infrared channels. For satellite radar images, the threshold value is usually determined by analyzing the SAR (Synthetic Aperture Radar) intensity histogram and estimating the probability distributions of the water and not water pixels. Google's Google Earth Engine (GEE) is one of the widely used geographic information and remote sensing data storage and calculation platforms, allowing to use, calculation, and export of data for the study area from the satellite image database stored on the server system. This study aims to develop a toolkit for automatic detection and delineation of the reservoir's surface water bodies using both optical and radar images based on the Google Earth Engine platform, which is used to automatically collect low cloudiness images, compute proposed indices, and then water body of the reservoir using different threshold values. The accuracy of the extraction results is assessed by calculating the Overall Accuracy (OA) and the Kappa coefficient (kappa) by comparing the delineated water bodies with the ones determined from surveyed bathymetry or observed water level and topography map. In this research, Am Chua reservoir in Khanh Hoa province, with a storage volume of 4.7 mil m3 corresponding with an average water level of 11.6m has been selected to verify the accuracy of the proposed method and the automatic and flexible toolkit. The results reveal that optional thresholds for delineating the water body of Am Chua reservoir are (i) -0.15 and -0.1 with NDWI and mNDWI indicated respectively for optical images and (ii) -20 ÷ -19 dB for radar images. The values of OA and Kappa greater than 0.9 and 0.85 show the satisfaction of extracted results. Remote sensing data such as Sentinel 1, Sentinel 2, and Landsat 8 are all free of charge, combined with the automatic GEE platform, providing a rapid and friendly toolkit that can support relevant agencies in managing and operating the reservoir more efficiently and economically.

MAPPING AQUCULTURE REGIONS WITH SPOT6 IMAGES IN COASTAL WATER OF BA RIA - VUNG TAU, VIETNAM

Phan Minh-Thu, Nguyen Van Hung, Le Thi Hai Nhu, Ho Dinh Duan, Nguyen Van Hoang, Nguyen Minh Giam

The increasing demand for aquatic food sources is a driving force to stimulate rapid aquaculture development inland, coastal areas, and open seas. As a result, some regions have yet to manage aquaculture properly, leading to instability in economic development and disruption of regional planning. Therefore, mapping the aquaculture areas can strengthen socio-economic management in the region. This article used SPOT6 images combined with ground-truthing survey data to determine the distribution of aquaculture regions in the coastal areas of Ba Ria - Vung Tau province, Vietnam. The analysis results have determined that the total area of aquaculture in the study area is 6636.45 ha, of which the marine aquaculture is 115.43 ha, aquaculture in the river is 609.57 ha, and the inland pond culture is 5911.45 ha. In addition, the analysis results also show that other land use has changed over time. The multi-temporal, comprehensive coverage and high spatial resolution of remote sensing data is a reliable source to determine the fluctuations of land use objects more accurately, contributing an influential part in the state management of aquaculture, socio-economic activities, and environmental pollution monitoring.

SPATIO-TEMPORAL PATTERNS OF THE SPREAD OF A SARS-COV-2 VARIANT THROUGH VIETNAM

Thi-Cham Bui, Anh-Huy Hoang, Danh-Tuyen Vu, Thi-Quynh Nguyen, Tien-Thanh Nguyen

The global outbreak of the COVID-19 pandemic has spread worldwide, affecting almost all countries and territories. This study aimed to analyze the spatio-temporal patterns of the spread of SARS-CoV-2 in Vietnam using spatial auto-correlation analysis. The spatial clustering, including spatial clusters (high-high and low-low), spatial outliers (low-high and high-low), and hotspots of the COVID-19 pandemic, were explored using the local Moran's I and Getis-Ord's⟦ G⟧_i^* statistics. The local Moran's I and Moran scatterplot were first employed to identify spatial clusters and spatial outliers of COVID-19. The Getis-Ord's⟦ G⟧_i^* statistic was then used to detect hotspots of COVID-19. A case study of locally transmitted cases confirmed in four COVID-19 waves in Vietnam indicated that the locations of high-high clusters and low-high outliers and hotspots of COVID-19 had rapidly changed. The findings of this study provide important insights into how to apply spatial statistics better to understand the spatio-temporal patterns of the spread of SARS-CoV-2.

GEODIVERSITY, GEOHERITAGE AND GIS

Natraj Vaddadi

Natural diversity encompasses two main components: biodiversity and Geodiversity. The term Geodiversity is a shortened version of the phrase 'geological and geomorphological diversity and has been defined as 'the natural range (diversity) of geological (rocks, minerals, fossils), geomorphological (landform, processes) and soil features. It includes their assemblages, relationships, properties, interpretations, and systems. This concept is comparable to biodiversity, which focuses on the variety of living organisms on Earth.

Geodiversity is essential, as the various Earth's materials, forms and processes that act on them are an integral part of Nature. Earth's material and form are crucial for the sustenance of ecosystems. Earth's diversity, with its landforms and dynamic processes, provides the substrate for habitat development.

The wide array of landforms and ongoing dynamic processes contribute to creating suitable habitats for various life forms. Therefore, understanding and preserving Geodiversity is essential for our planet's overall conservation and ecological balance.

Similar to the concept of geodiversity are the frequently used terms such as Geosites and Geomorphosites (geomorphological features). Geosites are specific geological locations with

unique attributes, offering aesthetic, scientific, and educational value. Geosites and Geomorphosites hold immense importance for scientific research, educational purposes, and tourism.

The study and recognition of Geosites and Geoheritage date back to as early as 1949, and significant efforts have been made at the national and regional levels to identify and conserve them. Many countries have designated certain areas as UNESCO Geoparks, signifying their geological and cultural significance.

Geosites enhance our understanding of Earth's history, natural processes, and cultural heritage. They may also serve as valuable research, education, and reference resources while holding cultural and economic significance for local communities.

In recent years, Geographic Information Systems (GIS) technology has proven itself a precious spatial analysis tool, transcending its everyday use in navigation. Professionals in heritage management, conservation, restoration, architecture, archaeology, and cultural heritage have embraced GIS to support and enhance their work.

GIS has also emerged as a vital tool for Geoheritage conservation. Through GIS, detailed maps and visual representations of heritage sites and geodiversity can be created, aiding in identifying and understanding crucial geological features. This is instrumental in prioritizing conservation efforts and formulating effective management plans to preserve these natural assets.

Additionally, GIS contributes significantly to Geotourism which promotes sustainable tourism by showcasing geological features and processes. By establishing tourism routes and providing interactive maps and location-based services, GIS enhances visitors' experiences at significant sites, enriching their understanding and connection with the geological wonders.

Much of this work is large-scale and focuses on a macro perspective. The intrinsic value of smaller-scale sites of geological significance is often overlooked and not recorded. Such sites provide valuable insights into Earth's evolution and scientific history. As essential resources for research reference and holding cultural significance for local communities, they also serve as valuable educational tools for Earth Sciences students, fostering a deeper appreciation of the Earth's geological heritage.

Considering the above, The Centre of Education and Research in Geosciences (CERG) has launched "Geotrails", an outreach program. Geotrails are field traverses that use GIS and Geospatial maps with attribute information as a base. Each Geotrail documents the navigational information, key attributes, and geological/geomorphological/cultural information at a micro-level of exciting sites along the trail. Two such popular "Geotrails" in Pune and Ahmednagar districts in the state of Maharashtra, India, are detailed in the paper.

The Geotrail maps offer detailed route guidance to the public, allowing them to explore the area from various perspectives. Alongside highlighting geological features, these maps also draw attention to ancient heritage sites, both historical and archaeological, found near the field outcrop or along the field traverse. This approach establishes a meaningful connection between the local geology, architecture, and history, promoting essential awareness of Earth Sciences and its significant contributions to the well-being of society.

DIGITAL ELEVATION MODELS (DEMS) GENERATED FROM RADAR REMOTE SENSING, A TEST CASE OF THE MEKONG DELTA

Hung Q. Ha, Thinh P. Ha

Despite efforts to create various digital elevation models (DEMS) for the Mekong region, an official product has yet to be released. The coexistence of different DEM models, such as MERIT DEM, FABDEM, Google-Earth DEM, SRTM, etc., has led to various development plans and policies being proposed for the area. In this research, we examined the use of Sentinel-1 data for DEM generation for timely terrain monitoring in the case of the Mekong Delta. The outputs confirmed the irrelevance of Sentinel-1 DEM for regular elevation monitoring. Still, it also opened the path for the soon-to-be-launched LOTUSat-1 for deformation monitoring and elevation modeling.

AUTOMATIC EXTRACTION OF LINEAR FEATURES FROM DIGITAL ELEVATION MODEL USING EDGE EXTRACTION AND HOUGH TRANSFORMATION

Venkatesh Raghavan, Tatsuya Nemoto, Shinji Masumoyo

Linear geomorphic features such as valleys and ridges represent geologic lineaments and contribute important information in targeting natural resources, evaluating hazard risk, and elucidating surface deformation caused by tectonic forces. Several algorithms have been proposed for automatically extracting lineaments from digital satellite images and Digital Elevation Models (DEM). Despite the advantages, the limited use of automated linear feature extraction, can be partially ascribed to implementing algorithms as a standalone implementation using proprietary software ecosystems. As a result, the feature extraction workflow remains validated with disparate datasets and in diverse geographical conditions. Further, the refinement of algorithms and optimization of parameter selection remains to be resolved.

This research focused on investigating the process of extracting lineaments from digital images (e.g., satellite images and DEM). The basic steps in three-stage processing involve the differentiation of linear geomorphic features, edge extraction, and vector line extraction from edge maps or raster images. The entire workflow was implemented and tested using the Free and Open Source GRASS GIS framework using existing functions and add-ons.

As a preliminary step, DEM was used to calculate terrain forms and associated geometry using the GRASS r.geomorphon function. The r.geomorphon function categorizes the DEM into 10 terrain forms: Flat, peak, ridge, shoulder, spur, slope, hollow, footslope, valley, and pits. Linear foot slopes, hills, and valleys define features of interest in this research. Such terrain form can be represented as binary images by reclassifying the output raster generated by r.geomorphon.

Terrain form using recognition r.geomorphon is sensitive to search radius and flatness threshold. Additionally, skip radius is used to eliminate the impact of minor irregularities, and flatness distance eliminates the effect of a more extended search radius distance. The selection of parameters for r.geomorphon is subjective and requires a trial and error approach based on visual inspection of the output generated.

As an alternative approach to overcome subjectivity in parameter selection to identify the terrain forms, a more straightforward (fewer parameters) using the Convergence Index was also attempted. The Convergence Index depicts the relief structure as a set of concurrent areas (channels) and divergent areas (ridges). The Convergence Index is beneficial for detecting lineaments mainly represented by ridges or channel systems. In the present experiment, binary images representing valley systems were generated as input for the second step of the data processing workflow.

The test data covering parts of the Rokko mountain range in southeastern Hyōgo Prefecture, Japan, was mainly characterized by linear valley systems potentially representing active faults. Therefore, in the second step, the Canny edge detector algorithm implemented as an i.edge module in GRASS GIS was applied to the reclassified terrain form and Convergence Index images representing only valley systems.

An edge is considered a change in gradient computed from digital values defining the image. Two main differences characterize the Canny filter from other edge detectors. First, different edge

detection algorithms generally produce broad edges, while the Canny filter generates one-pixel-wide line(s) representing the most probable edge position. Secondly, the Canny filter combines several steps, while other algorithms generate edges in a single step that may require some pre- or post-processing to achieve the desired results.

The Canny edge detection algorithm consists of multiple steps. Firstly, the noise is reduced by a Gaussian filter to obtain a smoothed image. Secondly, two orthogonal gradient images are computed. These images are combined to generate a final gradient defining the edge's angle and magnitude. Subsequently, non-maximum suppression is applied to preserve only pixels with a magnitude higher than the magnitude of other pixels in the direction (and the opposite direction) of the gradient. Finally, significant edges are retained by thresholding with hysteresis. The Canny edge detector produces an edge map and an angle map as output, used in the final data processing step.

The Hough Transform algorithm is applied to the Canny edge map and angle map as input in the final step. Hough transformation extracts line segments and is implemented as r.hough transform function in GRASS GIS. The r.hough transform module uses an identify and remove method to extract significant lines from the Hough image. Lines obtained by placing and removing the Hough transform method are further processed to get the line segments from the original image. The subsequent step of line segment extraction involves the elimination of the outlying pixels. The method should show tolerance to smaller gaps because some line segments can be interrupted, for example, by local terrain form. On the other hand, such gaps cannot be too frequent because many interruptions indicate line segments that are probably not part of the target feature. The Hough transform is optimized by providing directions of edges as input. These angles are used to search only pixels in the direction of a particular line.

The results using the data processing workflow were verified for a test site in the Rokko mountain range, and their efficacy for automatic lineament extraction techniques was successfully demonstrated. Further, the algorithm was also tested on multi-direction relief shades that highlight terrain features that not in terrain would form or Convergence Index maps alone. As a future work, optimizing parameter selection using machine learning will minimize subjectivity in linear feature extraction. The paper will highlight the advantages of the approach to extract and validate "geologic" lineaments and demonstrate results obtained using high-resolution DEM.

DEVELOPING A SYSTEM OF LAND PRICE BASING GIS TO STRENGTHEN THE LAND PRICE GOVERNANCE IN PROVINCES. A CASE STUDY IN GIA NGHIA, DAK NONG PROVINCE

Vu Le Ha, Bui Thi Cam Ngoc

The land price information system provides detailed and accurate information about the real estate market. Building a land price information system on the WebGIS foundation is the most appropriate direction, especially in the context of the 4.0 technology revolution and in alignment with the Government's digital transformation objectives. It is a valuable tool that helps users quickly and accurately access land price information, thereby supporting managers and investors in shaping strategies and making intelligent decisions to tap into potential and succeed in this field. This study constructs a land price information system for Gia Nghia City, Dak Nong province. The research has investigated 981 successful transaction prices in the market to serve the construction of the land price database for 19,142 parcels in 8 wards and communes of Gia Nghia City. The authors build the land price information system for Gia Nghia City with functions for querying and displaying various types of land prices. The research team has also developed several land valuation methods, including the standard parcel reference method, one of the most commonly applied batch land valuation methods worldwide. The test results show that the land prices are appropriately assessed, with an error not exceeding 10 % of the successful transaction prices in the market. These advanced functions enable the WebGIS system to be dynamic, facilitating regular updates to the land price database of 8 wards and communes. When the land price information system for Gia Nghia City is successfully established, it will facilitate easy, fast, and accurate access to land price information, enabling effective management and valuation of land prices that align with the market transactions promoting transparency in the local real estate market.

EWEBBING 3D MAP FROM UAV IMAGES IN DALAT CITY, LAM DONG PROVINCE

Tran Ngoc Huyen Trang, Le Van Trung

Big cities are completing the establishment of Spatial Data Infrastructure (SDI) to create an essential foundation to improve their capacity to provide necessary information related to digital economic development and meet all the requirements of innovative city management. With the advantages of high accuracy, low cost, and flexibility in 3D data creation, UAV (Unmanned Aerial Vehicle) images have been researched and applied. This article describes the new opportunities of using UAVs in 3D mapping and then sharing 3D map data through the WebGIS platform. After collecting the UAV images, they will be processed to create ortho mosaics, point clouds, and a Digital Surface Model (DSM). Conduct a classification of ground points to create a Digital Terrain Model (DTM). Combine DSM and DTM to form a calibrated surface numerical model (Canopy Height Model, CHM). Digitize the image map and the object height extracted from the CHM model, and assign attribute data to each object. We edit the map and share it on the web. ArcGIS Online allows you to share information widely, targeting multiple users and reducing the cost of GIS software investment in building thematic classes for urban management.

ASSESSING THE RISK OF LANDSLIDES USING GIS APPLICATION IN KRONG BONG DISTRICT, DAK LAK PROVINCE, VIETNAM

Anh Nguyen Huy, Anh Nguyen Trinh Minh, Trong Tran Van

Krong Bong district is located in the Southeastern part of Dak Lak province, with a predominantly hilly and mountainous terrain covering a significant area, where slopes over 250 accounts for 42 % of the total area. This area is considered one of the most severely affected regions in the province due to recent landslide incidents. The study utilized a combination of GIS technology and remote sensing to assess the risk of landslides, serving early warning efforts and minimizing human and property losses. The results, in the form of a landslide risk map, identified areas with shallow risk covering 308.54 km² (24.54 %), low-risk areas surrounding 260.06 km² (20.68 %), moderate-risk areas surrounding 309.22 km² (24.59 %), high-risk areas covering 270.05 km² (21.47 %), and very high-risk areas covering 109.62 km² (8.72 %). This research successfully constructed a landslide risk map, providing valuable information for disaster prevention solutions and mitigating damages caused by natural disasters.

PUBLISHING HOUSE FOR SCIENCE AND TECHNOLOGY
A16, 18 Hoang Quoc Viet Road, Cau Giay, Ha Noi
Marketing & Distribution Department: **024.22149040**;
Editorial Department: **024.37917148**
Administration Support Department: **024.22149041**
Fax: **024.37910147**, Email: **nxb@vap.ac.vn**; Website: **www.vap.ac.vn**

GIS IDEAS
PROCEEDINGS INTERNATIONAL CONFERENCE GIS-IDEAS 2023
GEOSPATIAL INTEGRATED TECHNOLOGIES FOR NATURAL HAZARDS AND ENVIRONMENTAL PROBLEMS

Hanoi University of Natural Resources and Environment,
Vietnam 07-09 November 2023

Hanoi University of Natural Resources and Environment (HUNRE)
Osaka Metropolitan University (OMU)
Japan-Vietnam Geoinformatics Consortium (JVGC)

Responsible for Publishing
Director, Editor in Chief
PHAM THI HIEU

Editors: **Nguyen Van Vinh, Nguyen Thi Chien**
Ha Thi Thu Trang, Natraj VADDADI
Venkatesh RAGHAVAN

Computing Technique: **Nguyen Duc Manh**

Cover design: **Tran Thu Hien**

Corporate publishing:
Hanoi University of Natural Resources and Environment
Address: 41A Phu Dien Road, Phu Dien Ward, Bac Tu Liem District, Ha Noi

ISBN: 978-604-357-207-0

Printing 400 copies, size 20,5 × 29,5 cm, printed at Consulting Publishing and Media Viet Joint Stock Company. Address: No. 4/20, Lane 156 Hong Mai, Bach Mai Ward, Hai Ba Trung District, Ha Noi City, Vietnam.
Registered number for Publication: 3759-2023/CXBIPH/01-42/KHTNVCN.
Decision number for Publication: 87/QĐ-KHTNCN was issued on 15 December 2023.
Printing and copyright deposit were completed in the 4th quarter, 2023.

GIS IDEAS

Organized by

Hanoi University of Natural Resources and Environment
The Japan - Vietnam Geoinformatics Consortium (JVGC)
Osaka Metropolitan University
https://gis-ideas.org/2023/

ISBN: 978-604-357-207-0
9 786043 572070
NOT FOR SALE